Exploring an oncolytic virus triggered PD-L1 response via immunoPET

Julia Hoebart

A thesis submitted for the degree of
Doctor of Philosophy

Supervisor: Dr. Gabriela Kramer-Marek
The Institute of Cancer Research
University of London

September 2021

Declaration

I, Julia Hoebart, confirm that the work presented in this thesis is my own. Where information has been obtained from other sources, I confirm that this has been indicated in the thesis.

Acknowledgments

At first, I would like to express my sincerest gratitude to Dr. Gabriela Kramer-Marek for giving me the opportunity to pursue a PhD in her research group at the ICR as well as her continuous support and guidance as my supervisor. I would like to thank Prof. Alan Melcher and Prof. Kevin Harrington for their insightful advice and guidance on bridging the gap to translational research. I am also grateful for the contributions from Dr. Chiara Da Pieve who has performed the radiochemistry in my project and Dr. Damian Borys for his effort around introducing me to the field of radiomics. My PhD project would not have been the same without their contributions.

I am grateful to the Oracle Cancer Trust and the Chellaram Foundation for funding my project. It has been an honour and a true pleasure to conduct my project as a member of the 'Oracle family' and I wish Oracle the best of luck for their future endeavours.

Thanks to all present and previous members of the Preclinical Molecular Imaging Team for their support in the lab and their patience in teaching me about PET – it has been an exciting journey. Special thanks go to Gitanjali and Marta - I have been lucky to have the both of you accompanying and supporting me during my thesis writing journey. It has been a pleasure to get to know you and I really hope we stay in touch. Thanks to Justyna for being such a faithful 'office-neighbour' and partner in crime, I am looking forward to many years of long-distance friendship ahead. I would also like to thank Florian for all the hours spent on sharing his knowledge around molecular imaging and his commitment and contributions towards my project. Finally, I would like to thank Daniela, Tom and Stephen for making the CCI labs a cheerful place.

I would like to acknowledge the support received from colleagues at the CCI such as Lisa Patterson for making sure that our labs run so smoothly, Carol Box and Will Court for teaching me about cloning. I would also like to thank Ian Titley for introducing me to flow cytometry - it has paid off in the end - and Louis Howell for her help with microscopy related tasks. Special thanks are directed to Selva: science has never been as fun as with you - stay in tune. I would also like to thank Petros Mouratidis, Krisha Desai and Patrick Lawrence for their support and for sharing experience whenever needed, it has been great to work alongside such passionate and committed colleagues. I am also grateful for having met Lisa, who has been massive support during work hours and beyond. I will miss you a lot. Likewise, I would like to thank Haider, Dana, Emma, Timon and Stephanos for the lunchbreaks and movie nights – it has been a lot of fun and will hopefully be continued. Special thanks go to Elise and Daniela for hosting regular yoga classes which have been key for my personal wellbeing.

I would like to thank my family for their everlasting support which goes far beyond the last four years of my life. Special thanks are directed to my grandmothers who have always had time for a chat over the phone, my sister who is simply the best, my dad who has supported me whenever possible and my auntie for her regular check ins. On this occasion, I would also like to thank my mum for the many years she has supported me like no one else. Moreover, I would like to thank all my friends in Austria who stuck with me albeit the long distance and were always there when needed. Last but not least I would like to thank Matt for his love and care, and for believing in me like no one else does. I am so grateful to have you - this journey would have never been the same without you.

Abstract

Oncolytic virotherapy (OV) exploits viruses which preferentially infect and kill cancerous cells. Moreover, oncolytic viruses stimulate the tumour-immune microenvironment towards an inflammatory phenotype. Therefore, OV is an attractive tool to prime tumours for clinically approved immunotherapies, such as immune checkpoint blockade (ICB). The latter is particularly relevant when ICB alone only moderately improves the therapy outcome over conventional treatment approaches, as observed in head and neck cancer. However, the impact of OV on the expression of programmed death-ligand 1 (PD-L1), a key target of ICB, remains vastly unexplored. Importantly, PD-L1 is expressed across multiple cell types and is sensitive towards various parameters changed in response to OV.

In my PhD project I employed immuno-positron emission tomography (immunoPET) to explore the impact of OV on PD-L1 expression in syngeneic head and neck cancer mouse models (MOC1, MOC2). At first, I established an imaging protocol using a PD-L1 targeted PET tracer, ^{89}Zr-DFO-PD-L1$_{\text{mAb}}$, in mice bearing subcutaneous tumours with varying PD-L1 expression levels. Using this imaging protocol, I investigated the systemic changes of PD-L1 following local injection of the oncolytic herpesvirus RP1 to MOC1 tumours. The MOC1 model was selected based on its sensitivity to RP1 *in vitro*. Remarkably, a single dose of locally delivered RP1 induced a transient systemic increase of PD-L1 early after treatment, which was most pronounced in secondary lymphatic tissue. Surprisingly, these changes could not be linked to distinct serum cytokines. *Ex vivo* histopathology indicated an influx of immune effector cells, however no therapeutic benefit was achieved through an OV-ICB combination.

In summary, PD-L1 immunoPET revealed that a single intratumoural dose of RP1 induces a systemic increase of PD-L1 highlighting that the immune-modulatory effect of this therapeutic approach reaches far beyond the tumour itself.

Table of contents

List of abbreviations

Ab	Antibody
ADCC	Antibody dependent cell-mediated cytotoxicity
APC	Antigen presenting cell
AUC	Area under the curve
BCA	Bicinchoninic acid assay
BFC	Bifunctional chelator
BSA	Bovine serum albumin
CCL	Chemokine ligand
CD	Cluster of differentiation
CK	Cytokeratin
CL	Contralateral
CMV	Cytomegalovirus
CPE	Cytopathic effect
CPM	Counts per minute
CPS	Counts per second
CT	Computed tomography
CXCL	C-X-C motif chemokine ligand
DAMP	Danger-associated molecular pattern
DC	Dendritic cell
DFO	Deferoxamine (or desferrioxamine)
DMEM	Dulbecco's modified Eagle's medium
DMSO	Dimethyl sulfoxide
DNA	Desoxyribonucleic acid
EDTA	Ethylenediaminetetraacetic acid
EGFR	Epidermal growth factor receptor
EpCAM	Epithelial cell adhesion molecule
EPR	Enhanced permeability and retention
$\mathbf{E_{ß+mean}}$	Mean positron energy
$\mathbf{F_{ab}}$	Antigen-binding fragment
FBS	Foetal bovine serum
FC	Flow cytometry
$\mathbf{F_{c}}$	Crystallisable fragment
FcRn	Neonatal Fc-receptor

FcγR	Fc gamma receptor
FDR	False discovery rate
FFPE	Formalin-fixed paraffin-embedded
FMO	Fluorescence minus one
FOV	Field of view
F_v	Variable fragment
GALV	Gibbon-ape leukaemia virus
GAPDH	Glyceraldehyde-3-phosphate dehydrogenase
GFP	Green fluorescent protein
GM-CSF	Granulocyte macrophage-colony stimulating factor
GP	Glycoprotein
H&E	Haematoxylin and eosin
HEPES	4-(2-hydroxyethyl)-1-piperazineethanesulfonic acid
HNSCC	Head and neck squamous cell carcinoma
HPLC	High pressure liquid chromatography
HPV	Human papillomavirus
HSV	Herpes simplex virus
HVEM	Herpesvirus entry mediator
i.v.	Intravenous
ICB	Immune checkpoint blockade
ICP	Infected cell protein
IFN	Interferon
IFU	Infectious units
IgG	Immunoglobulin G
IHC	Immunohistochemistry
IL	Interleukin
IRF	Immunoreactive fraction
ITLC	Instant thin layer chromatography
LDS	Lithium dodecyl sulfate
Ln	Lymph node
LOR	Line of response
mAb	Monoclonal antibody
MFI	Median fluorescence intensity
MHC	Major histocompatibility complex
MIP	Maximum intensity projection

MOC	Murine oral carcinoma
MOPS	3-(*N*-morpholino)propanesulfonic acid
MRI	Magnetic resonance imaging
MWCO	Molecular weight cut-off
NK cell	Natural killer cell
oHSV	Oncolytic herpes simplex virus
OV	Oncolytic virotherapy
p.i.	Post-injection
PAMP	Pathogen-associated molecular patterns
PBS	Phosphate-buffered saline
PC	Polyclonal
PCR	Polymerase chain reaction
PD-1	Programmed death receptor 1
PD-L1	Programmed death ligand 1
PD-L2	Programmed death ligand 2
PET	Positron emission tomography
PFU	Plaque forming units
PRR	Pattern recognition receptors
RC	Radioconjugate
RCF	Relative centrifugal force
RCP	Radiochemical purity
RCY	Radiochemical yield
RES	Reticuloendothelial system
RLU	Relative light units
RNA	Ribonucleic acid
ROI	Region of interest
RPM	Revolutions per minute
RPMI	Roswell Park Memorial Institute
$\mathbf{R_{\beta+mean}}$	Mean positron range
RT	Room temperature
s.c.	subcutaneous
SD	Standard deviation
SDS	Sodium dodecyl suflate
Sp. act.	Specific activity
SPECT	Single photon emission tomography

STING	Stimulator of interferon genes
STR	Short tandem repeat
SUV	Standardised uptake value
$t_{1/2}$	half-life
TBS	Tris-buffered saline
TD	Tumour-draining
TLR	Toll like receptor
TME	Tumour microenvironment
TNF-α	Tumour necrosis factor alpha
T-VEC	Talimogene laherparepvec
UF	Ultrafiltered
VOI	Volume of interest
VSV	Vesicular stomatitis virus
WB	Western blot

Chapter 1: Introduction

1.1 Head and neck cancer

Head and neck cancers comprise a heterogeneous set of malignancies originating from distinct anatomical sites within the head and neck area, including the oral cavity, the sino-nasal cavity, the pharynx and the larynx (Fig.1-1). Most head and neck cancers arise from the mucosal epithelium (~95%) lining the aforementioned anatomical sites and are therefore addressed as head and neck squamous cell carcinoma (HNSCC). HNSCC is among the most common types of cancer worldwide, leading to 890,000 new cases and 450,000 deaths in 2018, thus causing significant morbidity to those affected by the disease (Bray et al., 2018). In Europe, 160,000 new cases of HNSCC were diagnosed in 2018 and 73,000 deaths were recorded (Ferlay et al., 2019). Accordingly, HNSCC was listed as the sixth most common type of cancer in Europe following female breast cancer (523,000 cases), colorectal cancer (500,000 cases), lung cancer (470,000 cases), prostate cancer (450,000 cases) and bladder cancer (197,000). The following sections of this chapter address the aetiological and epidemiological aspects of HNSCC as a disease, its diagnosis and prognosis, as well as current clinical therapy regimen and emerging therapeutic approaches such as immunotherapies.

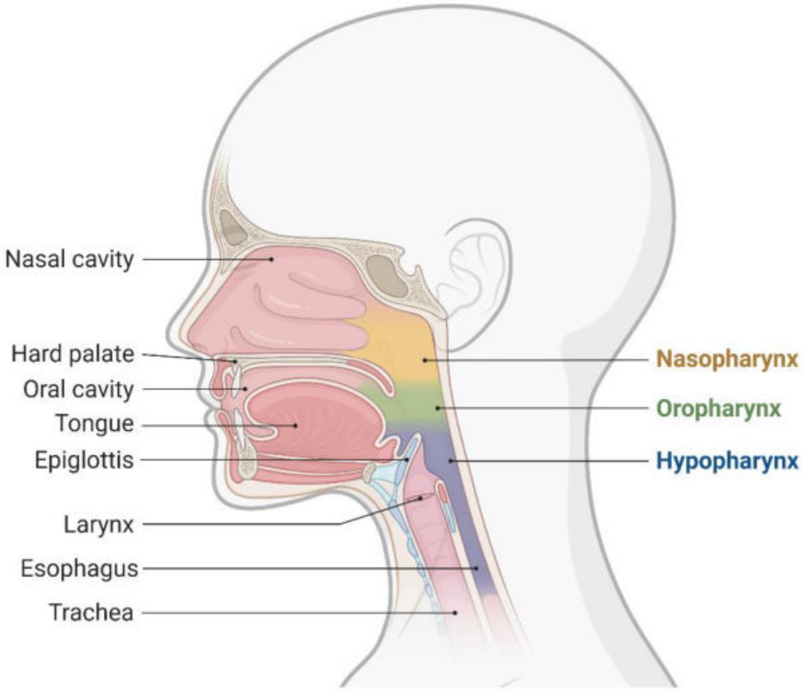

Figure 1 - 1: Anatomical sites of head and neck squamous cell carcinoma (HNSCC). HNSCC comprises cancers arising from the mucosal epithelium lining the oral cavity, the sino-nasal cavity, the pharynx and the larynx. Figure created with Biorender.com.

1.1.1 Aetiology and epidemiology

The most common causes of HNSCC are overexposure to tobacco-associated carcinogens or excessive consumption of alcohol, or both (Hashibe et al., 2009). HNSCC caused by tobacco and or alcohol overconsumption is typically diagnosed in older patients (median age at diagnosis 66 years) and has lately started to decline as a possible effect of decreasing use of tobacco globally (Meza et al., 2020; Pesce et al., 2019). Another significant risk factor for HNSCC is infection with oncogenic human papillomavirus (HPV) strains, primarily HPV-16 and to a lesser extent HPV-18 and other strains (Marur et al., 2010). HPV-positive cases, which predominantly present with cancer in the oropharynx (>70% of oropharyngeal cancers are HPV-positive), have shown a dramatic increase over the last decades, especially in North America and northern Europe (Windon et al., 2018). These cases are frequently diagnosed at a younger age, reflecting a latency period of 10 to 30 years after initial oral infection (median age at diagnosis 53 years). The increased incidence of HPV-positive HNSCC and oropharyngeal cancer in particular is in part due to increased oral HPV exposure, e.g. oral sex (Chaturvedi et al., 2011). Furthermore, increasing awareness for HPV and the availability of HPV-specific diagnostic tests might have contributed to this rise in numbers. Due to their different aetiology, HNSCCs are strictly divided into two subgroups, HPV-positive and HPV-negative cases. It is important to note that men are at twofold to fourfold higher risk of developing HNSCC than women. In HPV-positive disease this is in part explained by a higher number of lifetime sexual partners and a higher chance of persistent oropharyngeal HPV infection among men (Chaturvedi et al., 2015; Gillison et al., 2012; Gillison et al., 2015), whilst in HPV-negative cases the high male to female ratio reflects sex-specific patterns of risk behaviour including the use of tobacco and alcohol (World Health, 2015).

1.1.2 Diagnosis and staging

A diagnosis for HNSCC is established via biopsy of the primary tumour and or neck mass and subsequent routine histopathological assessment (Pynnonen et al., 2017). In specific cases, e.g. poorly differentiated tumours, additional immunohistochemical staining might be required for diagnosis (Yi et al., 2017). HPV testing is usually performed in all oropharyngeal tumours as it is a major determinant of staging and prognosis. Diagnostic approaches include detection of

E6 and *E7* mRNA (by reverse transcription polymerase chain reaction, rtPCR), HPV DNA (by PCR or in situ hybridisation) or the cell cycle protein p16$^{\mathrm{INK4A}}$ (by immunohistochemistry, IHC) (Taberna et al., 2017). Interestingly, patients with HPV-positive HNSCC have a higher chance of survival, i.e. median survival of 131 months in HPV-positive vs. 20 months in HPV-negative disease (Chaturvedi et al., 2011). The significant prognostic advantage of HPV-driven disease might be influenced by several factors including gene expression and mutational profiles (e.g. alterations of *CDKN2A* and *TP53* in HPV-negative vs. loss of *TRAF3* and amplification of *E2F1* in HPV-positive disease) as well as immune contexture (e.g. higher abundance of tumour infiltrating T-cells in HPV-positive than HPV-negative tumours) (Mandal et al., 2016; Network, 2015).

Following histopathological confirmation, a staging evaluation is performed irrespective of HPV status. Staging includes a complete head and neck examination, tomographic imaging by computed tomography (CT) or magnetic resonance imaging (MRI) to assess the extent of the disease and a chest CT to check for metastases. Where available, ^{18}F-fluoro-deoxy-glucose (FDG) positron emission tomography (PET) combined with CT is used to assess the local extension of advanced disease (i.e. cervical lymph node involvement) and for distant metastatic staging (Krabbe et al., 2009; Pfister et al., 2020). Distant metastases most commonly occur in the lung (50-75% of metastatic cases), followed by bone, liver, brain, skin and soft tissue (Ferlito et al., 2001) and constitute an unfavourable prognostic factor (90% of metastatic patients die within two years following detection of the first metastasis) (Dwivedi et al., 2010). A thorough endoscopic examination including laryngoscopy, oesophagoscopy and bronchoscopy is additionally performed in patients with tobacco-related HNSCC, due to the high risk of second primary tumours of the upper aerodigestive tract (Coca-Pelaz et al., 2020). Endoscopic examination is usually omitted in patients with HPV-positive HNSCC as they rarely manifest with second primary tumours (Taberna et al., 2017).

In addition to the aforementioned role of ^{18}F-FDG PET, it is also recommended for the identification of unknown primary disease in patients presenting with cervical lymph node metastases (stages III and IV) (Yoo et al., 2013), as well as for the assessment of therapy response after radiotherapy (with or without chemotherapy) (Castaldi et al., 2012). In the latter setting however, radiation-induced tissue inflammation can substantially reduce the diagnostic accuracy of ^{18}F-FDG PET, thus any positive findings in PET are recommended to be confirmed via biopsy (Mak et al., 2011). Although ^{18}F-FDG PET/CT detects HNSCC with high sensitivity (>95%), its inability to accurately assess the extent of tumour spread and the relationship between the tumour and adjacent structures (due to the poor anatomical resolution and soft tissue contrast of PET in combination with unenhanced CT) still limits its integration in routine diagnostic practice (Castaldi et al., 2013; Roh et al., 2007; Wong et al., 2013). Furthermore, due to current resolution limits in PET/CT, small metastatic lesions might remain undetected. However, technological advances including PET/MRI scanners might overcome some of these limitations (Buchbender et al., 2012).

Following a full diagnostic work up, each HNSCC patient is staged according to the 8th edition Cancer Staging Manual published by the Union for International Cancer Control (UICC) and the American Joint Commission on Cancer (AJCC) (Amin et al., 2017). The staging criteria are based on the tumour-node-metastasis (TNM) system and vary for each anatomical subsite, i.e. oral cavity, oropharynx, hypopharynx, larynx, paranasal sinuses (examples for the oral cavity and the oropharynx are provided in table 1-1). In the case of oropharyngeal HNSCC, the HPV-status is taken into account for disease classification and staging. The TNM classification results are then used to stage the extent of the disease (stages I, II, III, IV) and select a treatment plan accordingly (Table 1-2).

Oral cavity	
Classification	
Tumour	
TX	Primary tumour cannot be assessed
Tis	Carcinoma in situ
T0	No tumour identified
T1	Tumour <2 cm in greatest dimension
T2	Tumour ≤2 cm, the depth of invasion is between 5 and 10 mm Or the tumour is >2 cm but <4 cm, and the depth of invasion ≤10 mm
T3	Tumour >4 cm, or any tumour with a depth of invasion >10 mm
T4	Moderately advanced or very advanced local disease
T4a	Tumour has invaded nearby structures in the mouth, such as the jaw, sinuses, or skin of the face
T4b	Tumour has invaded the muscles and bones that form the mouth or the base of the skull, and/or it encases the internal arteries

Node	
Nx	Regional lymph nodes cannot be assessed
N0	No regional lymph-node metastases
N1	Metastases to 1 or more ipsilateral lymph nodes, none >6 cm in greatest dimension
N2a	Metastasis to a single ipsilateral node, >3 cm but <6 cm in greatest dimension, without extranodal extension
N2b	Metastases to multiple ipsilateral lymph nodes, none >6 cm in greatest dimension, without extranodal extension
N2c	Metastases to bilateral or contralateral lymph nodes, none >6 cm in greatest dimension, without extranodal extension
N3a	Metastasis to a lymph node, >6 cm in greatest dimension, without extranodal extension
N3b	Metastases to one or more lymph nodes, with clinically overt extranodal extension
Metastasis	
M0	No distant metastases
M1	Distant metastases

Oropharynx

Classification	**HPV-positive**	**HPV-negative**
Tumour		
TX	Primary tumour cannot be assessed	Primary tumour cannot be assessed
Tis	Carcinoma in situ	Carcinoma in situ
T0	No tumour identified	No tumour identified
T1	Tumour <2 cm in greatest dimension	Tumour <2 cm in greatest dimension
T2	Tumour >2 cm but <4 cm in greatest dimension	Tumour >2 cm but <4 cm in greatest dimension
T3	Tumour >4 cm in greatest dimension or extension to lingual surface of epiglottis	
T4	Moderately advanced local disease; tumour invades larynx, extrinsic muscle of the tongue, medial pterygoid muscle, hard palate or mandible, or beyond	
T4a		Moderately advanced local disease; tumour invades larynx, extrinsic muscle of tongue, medial pterygoid muscle, hard palate, or mandible
T4b		Very advanced local disease; tumour invades lateral pterygoid muscle, pterygoid plates, lateral nasopharynx, or skull base or encases carotid artery
Node		

Nx	Regional lymph nodes cannot be assessed	Regional lymph nodes cannot be assessed
N0	No regional lymph-node metastases	No regional lymph-node metastases
N1	Metastases to 1 or more ipsilateral lymph nodes, none >6 cm in greatest dimension	Metastasis to a single ipsilateral lymph node, ≤3 cm in greatest dimension, without extranodal extension
N2	Metastases to contralateral or bilateral lymph nodes, none >6 cm in greatest dimension	
N2a		Metastasis to a single ipsilateral node, >3 cm but <6 cm in greatest dimension, without extranodal extension
N2b		Metastases to multiple ipsilateral lymph nodes, none >6 cm in greatest dimension, without extranodal extension
N2c		Metastases to bilateral or contralateral lymph nodes, none >6 cm in greatest dimension, without extranodal extension
N3	Metastases to one or more lymph nodes, >6 cm in greatest dimension	
N3a		Metastasis to a lymph node, >6 cm in greatest dimension, without extranodal extension
N3b		Metastases to one or more lymph nodes, with clinically overt extranodal extension
Metastasis		
M0	No distant metastases	No distant metastases
M1	Distant metastases	Distant metastases

Table 1 - 1:Tumour-Node-Metastasis (TNM) classification for HNSCC tumour types (site-specific to oral cavity and oropharynx as representative, common subsites) adapted from the 8th edition of the Cancer Staging Manual. For TNM classification of other HNSCC sites, see 8th edition of the Cancer Staging Manual.

1.1.3 Therapy

The choice of therapeutic regimen for the treatment of HNSCC is individual to each patient guided by the anatomical subsite, stage (I-IV), disease characteristics (HPV status), functional considerations and patient wishes (Table 1-2) (Johnson et al., 2020a). The following section will address the clinical use of conventional therapies, followed by a section on the incorporation of immunotherapies (immune checkpoint inhibitors) in clinical routine practice.

1.1.3.1 Conventional therapy

The treatment of HNSCC is largely based on conventional therapy modalities including surgery, radiotherapy and chemotherapy. The following two paragraphs address general rules and considerations in the treatment of locally confined, early-stage disease vs. the treatment of metastatic, advanced-stage disease. Anatomical subsite-specific treatment options are addressed in a separate table (Table 1-2).

Patients with *locally or locoregionally confined HNSCC (stages I or II)*, presenting with a small primary tumour and no or limited nodal involvement (of only one lymph node), are frequently cured via a single modality approach, undergoing surgery or radiotherapy (cure rates >80%) (Lee et al., 2018). Accessibility of the lesion site decides whether surgical removal is an option, e.g. lesions in the oral cavity (Wong and Richard, 2019). Recent advances in minimally invasive surgery techniques, including transoral robotic surgery or laser resection surgery, have expanded the indications for primary surgical management (Forastiere et al., 2018; Weinstein et al., 2012). If accessibility is restricted, such as in the case of pharyngeal and laryngeal cancers, radiotherapy regimens are applied (DeVita et al., 2008; Rancati et al., 2010). In all cases, the most curative approach is selected to ensure preservation of function.

For *HNSCC tumours at more advanced tumour or nodal stage (stages III or IV)*, combinations of therapy modalities, such as postoperative radiation or chemo-radiation are selected. These combinations can reduce the risk of recurrence and improve survival (Bernier et al., 2004; Cooper et al., 2004). A combination of surgery and follow-up radiotherapy is usually selected if the lesion site is accessible and no distant metastases exist. If regional, nodal metastases are present or the tumour is considered non-resectable, systemic chemotherapy combined with radiotherapy should be considered. It is important to note that different chemo-radiation regimen exist employing cisplatin or carboplatin/5-fluoroucil alongside radiotherapy (Oosting and Haddad, 2019). In patients with advanced stage disease and increased risk of recurrence, the use of tri-modal therapy, meaning surgery followed by chemo- and radiotherapy may be applied (Forastiere et al., 2013). However, this regimen causes late toxicities from radiation and thus severely compromises quality of life in survivors (Mehanna and Morton, 2006; Rettig et al., 2016).

Owing to the heterogeneity of HNSCC tumours (due to their diverse aetiology and anatomical sites), delicate selection of the treatment approach is key to ensure an optimum therapeutic outcome whilst incurring minimum harm to the surrounding tissue and vital organs. The following table lists state of the art recommendations for the clinical treatment of the major anatomical subsites in HNSCC (Table 1-2).

Oral cavity		Treatment of the primary tumour
• **Early stage** Stages I or II	Small primary tumours without cervical lymph-node involvement (T1 or T2, N0)	OPTION 1: Surgical resection preferred for primary tumour, especially in the absence of coexisting conditions OPTION 2: Definitive radiotherapy only if surgery not feasible; conformal techniques and brachytherapy could have a role
• **Locally advanced stage** Stages III or IV	Large tumours (T3 or T4) or lymph-node involvement (N1, N2, or N3) or both	OPTION 1: Surgical resection preferred OPTION 2: Definitive concurrent radiotherapy and chemo-radiotherapy if patient is unfit for surgery or surgery is not feasible
Oropharynx		Treatment of the primary tumour
• **Early stage**	Small primary tumours with no or minimal lymph-node involvement; Immunohistochemical testing for p16 must be performed **HPV-negative disease** (no p16 expression): Stages I and II without nodal disease (T1 or T2, N0) and stage III with minimal nodal disease (T1 or T2, N1) **HPV-associated disease** (positive p16 expression): Stage I disease (T1 or T2, N0)	OPTION 1: Consider enrollment in clinical trials when feasible, primary definitive radiotherapy alone (common) or consider concurrent systemic therapy with radiotherapy for bulky T2 disease (especially in HPV-positive disease) and N1 disease OPTION 2: Surgical resection of the primary tumour, minimally invasive techniques (e.g., transoral robotic surgery or transoral laser microsurgery) in selected patients may be feasible, well-tolerated, and effective
• **Locally advanced stage** Stages III or IV	Larger tumours, lymph-node involvement, or both; Immunohistochemical testing for p16 must be performed	No randomized trials have compared approaches. Preservation of function, long-term toxic effects, and quality of life are important. There are no current differences in treatment on the basis of p16 or HPV status. Consider enrollment in clinical trials when feasible.

	HPV-negative disease (no p16 expression): Stages III and IV; T3 or T4, N0 or N1; or T1, T2, T3, or T4, and N2 or N3 **HPV-associated disease** (positive p16 expression): Stage I, N1 disease with involvement of one node >3 cm or two or more ipsilateral nodes ≤6 cm; stage II or III, T3 or T4, N1 without distant metastases	OPTION 1: Concurrent chemo-radiotherapy is common, less common and debatable is induction chemotherapy followed by radiotherapy or chemo-radiotherapy for select patients who are not good candidates for upfront chemo-radiotherapy OPTION 2: Surgical resection of the primary tumour (usually reserved for smaller primary tumours)
Larynx		Treatment of the primary tumour
• **Early stage** Stages I and II (T1 or T2, N0) and part of stage III (selected T3N0 tumours)	Smaller primary tumours, without lymph-node involvement (without evidence of thyroid cartilage involvement) suitable for laryngeal preservation therapy	Therapy differs in accordance with the various anatomical sites in the larynx. Limited prospective trial evidence and patient preference, toxic effects, and preservation of function guide therapeutic choices. Consider enrollment in clinical trials if feasible. OPTION 1: Definitive radiotherapy is generally preferred, especially for larger tumours, and can result in good function and voice quality, particularly in tumours in the supraglottic larynx and the glottic larynx or In patients with highly selected, bulky, T2 cancers with invasion and impaired vocal-cord mobility, consider intensified radiotherapy or, in rarer situations, concurrent chemo-radiotherapy; reserve salvage laryngectomy for patients with recurrent or persistent disease or severe functional impairment OPTION 2: For laryngeal preservation, smaller tumours (T1N0 or selected T2N0) can be treated with transoral robotic surgery or transoral laser microsurgery if feasible. Less commonly, partial laryngectomy with laryngeal preservation is possible if tumour-free margins can be ensured, with good tumour control and survival
• **Locally advanced stage** Stages III or IV	Larger tumours with or without lymph-node involvement (T1, T2, or T3) and without evidence of thyroid cartilage involvement are suitable for larynx-preserving surgery or	Therapy and risk may differ according to anatomical site in the larynx and the extent of disease. Multidisciplinary assessment should be performed with the goals of preservation of organ function, survival free of laryngopharyngeal dysfunction (speech, swallowing, and airway patency).

	Patients with bulky, extensive T3 or large T4a tumour with involvement of cricoid or outer cortex thyroid cartilage or patients with poor pretreatment laryngeal function should be considered for upfront surgery and total laryngectomy	OPTION 1: Definitive concurrent chemo-radiotherapy preferred if possible for preservation of function or Perform definitive radiotherapy alone if patient is medically unfit for chemotherapy or Perform sequential chemotherapy and then radiotherapy if concurrent therapy would be associated with an unacceptable adverse-events profile; however, this treatment is associated with a lower rate of larynx preservation and a higher risk of local recurrence OPTION 2: Partial resection, partial laryngectomy, or endoscopic or open resection if indicated in small primary tumours (T1 or T2) if laryngeal preservation is feasible, tumour exposure is adequate, and negative margins can be achieved or Total laryngectomy for extensive T3 or large T4a lesions or thyroid cartilage involvement; this treatment is not amenable to laryngeal preservation OPTION 3: Consider induction chemotherapy followed by radiotherapy alone or sequential therapy with induction chemotherapy followed by concurrent chemo-radiotherapy for larger bulky tumours, with individualisation for anatomical site, response, toxic effects, and locoregional control requirements
Hypopharynx		Treatment of the primary tumour
• **Early stage** Stage I (T1N0) or selected stage II (T2N0)		OPTION 1: Approaches involving preservation of function and laryngeal sparing are preferred. Definitive radiotherapy is the usual treatment of choice OPTION 2: Surgery can be considered in carefully selected cases. Transoral robotic surgery or transoral laser microsurgery may be performed if feasible and if laryngeal preservation is possible. Less commonly, partial laryngopharyngectomy with preservation of laryngeal function is possible if tumour-free margins can be ensured
• **Locally advanced stage** Stages III or IV	T2 or T3, N0–N3, if amenable to pharyngectomy with partial or total laryngectomy or very locally advanced stage T4a, N0–N3	Multidisciplinary assessment with goals of preservation of organ function and survival free of laryngopharyngeal dysfunction survival (speech, swallowing, and airway patency) OPTION 1: Perform definitive radiotherapy alone if patient is medically unfit for chemotherapy or Perform sequential chemotherapy and then radiotherapy if concurrent therapy would be

		associated with an unacceptable adverse-events profile; however, this treatment is associated with a lower rate of larynx preservation and a higher risk of local recurrence OPTION 2: Surgery with partial laryngectomy or endoscopic or open partial resection if indicated for small primary (T1 or T2) tumours if laryngeal conservation is feasible, tumour exposure is adequate, and negative margins can be achieved or Surgery: total laryngopharyngectomy plus neck dissection plus hemithyroidectomy or total thyroidectomy for extensive T3 or large T4a lesions and poor pretreatment laryngeal function OPTION 3: Consider induction chemotherapy followed by radiotherapy alone or sequential therapy with induction chemotherapy followed by concurrent chemo-radiotherapy for large bulky tumours with individualization for site, response, toxic effects, and locoregional control requirements
Paranasal sinuses		Treatment of the primary tumour
• **Early stage** Stages I or II	Small primary tumours without lymph-node involvement (T1 or T2, N0) The treatment outlined below is specific to the histologic features of squamous-cell carcinoma; there is marked heterogeneity and multiple other histologic subtypes in this area	These are rare cancers with heterogeneous histologic features and behaviour; therefore, no randomized, prospective trials are available to define adequate therapy Complete surgical resection is the preferred initial treatment
• **Locally advanced stage** Stages III or IV	Locally advanced disease (T3 or T4, N+) The treatment outlined below is specific to the histologic features of squamous-cell carcinoma; there is marked heterogeneity and multiple other histologic subtypes in this area.	These are rare cancers with heterogeneous histologic features and behaviour; therefore, no randomized, prospective trials are available to define adequate therapy Complete surgical resection is the preferred initial management Perform definitive chemo-radiotherapy only if the patient is not a candidate for definitive surgery

Table 1 - 2: Recommendations for the treatment of HNSCC according to anatomical site (primary tumour only) released by the Massachusetts Medical Society 2020. These recommendations represent globally accepted treatment standards and do not contain

information on recommended follow-up treatments or simultaneous treatment of the neck area which can be found in the original version of this table (Chow, 2020).

Owing to the radical nature of the conventional treatment approaches and the complex anatomy of the head and neck area, the majority of patients suffer from therapy-associated side effects. Frequent side effects following radiotherapy include short- and long-term pain from scarring, difficulty swallowing, changes in voice, loss of appetite, weight loss and a dry mouth due to collateral damage of the salivary glands (Rose-Ped et al., 2002). The most common surgery-associated side effects include temporary or permanent loss of normal voice, impaired speech, hearing loss and difficulty swallowing. The side effects incurred by chemotherapy include fatigue, risk of infection, nausea and vomiting, hair loss, loss of appetite, and diarrhoea, and usually go away after treatment is finished (Adelstein, 2003). Taken together, the substantial side effects incurred by conventional therapy modalities raise the need for less invasive and more targeted approaches, such as the immunotherapies presented in the following section.

1.1.3.2 Immune checkpoint inhibitor therapy

More recently, HNSCC patients at relapsed/metastatic stage of disease are also treated with immune checkpoint inhibitors targeting programmed death receptor 1 (PD-1), namely Pembrolizumab and Nivolumab. Anti-PD-1 therapy reverses cancer immune evasion and thus acts relatively targeted, incurring far less severe side effects than other treatment options for advanced HNSCC (Burtness et al., 2019; Dong et al., 2002; Ferris et al., 2016). The principles of this treatment approach are addressed in detail in section 1.3.4.

The PD-1 targeted monoclonal antibody (mAb) Pembrolizumab (commercial name KEYTRUDA®) is applied in patients affected by metastatic or unresectable, recurrent HNSCC (Burtness et al., 2019; Seiwert et al., 2016). However, Pembrolizumab treatment is only recommended as a first-line monotherapy if the primary tumour expresses programmed death ligand 1 (PD-L1), which was found to serve as a predictive biomarker of response to anti-PD-1 treatment when measured via IHC (Doroshow et al., 2021). Further details on this topic and the differences between IHC-based PD-L1 positivity scores can be found in section 1.3.5. Given the primary tumour expresses PD-L1 (determined via a combined positivity score (CPS) ≥1), patients receive Pembrolizumab as a single agent treatment, whilst patients with low or no PD-L1 expression (CPS <1) are given Pembrolizumab in combination with platinum and 5-fluorouracil chemotherapy (Burtness et al., 2019). Alternatively, HNSCC patients presenting with recurrent or metastatic disease and those progressing on or after chemotherapy, are eligible to receive Pembrolizumab as a second-line treatment, given their tumours express PD-L1 (tumour proportion score (TPS) ≥50 %) (Cohen et al., 2019). As an alternative to Pembrolizumab, Nivolumab (commercial name OPDIVO®) another PD-1 targeted mAb, is licenced for the treatment of recurrent or metastatic HNSCC progressing on or after chemotherapy (Ferris et al., 2016). In contrast to Pembrolizumab, Nivolumab can be applied regardless of intratumoural PD-L1 expression level. Pembrolizumab and Nivolumab are usually delivered via repeat dosing as intravenous bolus infusions (Pembrolizumab: 200 mg over 30 min every three weeks; Nivolumab: 240 mg over 30 min every two weeks) for up to 24 months unless unacceptable toxicities occur (recommended as per the European Medical Agency). In contrast to conventional therapies, severe toxicities are less likely to occur and immunotherapy-associated side effects, so-called immune-related adverse events (IRAEs), including pneumonitis or colitis can either be counteracted via treatment interruption or systemic corticosteroids (immunosuppressives) (Puzanov et al., 2017). Another immunotherapy-related phenomenon called hyperprogression, i.e. dramatically accelerated disease progression, is infrequently observed in HNSCC (Saâda-Bouzid et al., 2017). Taken together, the application of anti-PD-1 checkpoint inhibitors raises hope for a new era of immunotherapy-based management strategies of HNSCC.

The therapeutic improvement achieved with anti-PD-1 monotherapy as compared to conventional treatment regimens (moderately improved therapy, less severe side-effects) is currently being investigated further with a specific focus on combinations of anti-PD-1 ICB with other immunotherapeutic approaches. One example is a recent phase III clinical trial, testing an immunotherapy combination between the anti-cytotoxic T-lymphocyte antigen 4 (CTLA-4) targeted mAb Ipilimumab (commercial name YERVOY®) with Nivolumab versus a conventional therapy regimen (anti-EGFR mAb Cetuximab, cisplatin/carboplatin and fluorouracil chemotherapy) in platinum-ineligible recurrent or metastatic

HNSCC (NCT02741570). Although the immune checkpoint inhibitor combination showed a clear, positive trend towards overall survival in patients whose tumours express PD-L1 (CPS ≥20), it did not show a significant improvement over the control arm (Argiris et al., 2021). The missed effect was partially due to an improved overall survival in the control arm as compared to historical data. After all, other promising treatment approaches with the potential to synergize with anti-PD-1 ICB do exist. One such approach is oncolytic virotherapy which will be addressed in the following introduction subchapter (1.2) including examples for ongoing clinical trials (1.2.7).

1.1.4 The tumour microenvironment

The tumour microenvironment (TME) is composed of cancer cells, the extracellular matrix (ECM), stromal cells, the vasculature and various immune cell types; altogether shaping tumour specific properties such as hypoxia, interstitial fluid pressure, etc. The following section addresses the cellular compartments of the TME and barriers imposed by the TME which are relevant in the context of this thesis, including physical and chemical barriers which may impact the distribution of therapeutic and imaging agents as well as the tumour-immune contexture, which eventually impacts the response to cancer immunotherapies. These aspects are discussed in the context of HNSCC.

1.1.4.1 Compartments of the tumour microenvironment

Cancer associated fibroblasts (CAFs) constitute a major cell fraction of the reactive tumour stroma with a diverse array of functions. These cells modulate tumour progression via the synthesis of growth factors, drive metastasis through the synthesis and remodelling of the ECM and are capable of influencing tumour angiogenesis (Sahai et al., 2020). CAFs have potent immune-modulating effects supporting tumour immune escape via the release of cytokines and chemokines (e.g. TGF-β, IL-6 and CXCL-9) and by abrogating the function of cytotoxic lymphocytes (Monteran and Erez, 2019). Therefore, CAFs have emerged as an attractive intratumoural compartment for therapeutic targeting (Chen and Song, 2019). In HNSCC, a high tumoural density of CAFs has been acknowledged as a poor prognostic factor (Knops et al., 2020).

Solid tumours are infiltrated with varying degrees of *immune cells.* These immune cells play different functional roles and are frequently divided into immunosuppressive and pro-inflammatory subsets originating from both the innate and adaptive arm of the immune system (Labani-Motlagh et al., 2020). Immunosuppressive cell populations tune down or help escape immune responses and are composed of myeloid-derived suppressor cells (MDSCs, innate arm), macrophages of the M2 phenotype (M2 macrophages, innate arm) and regulatory T cells (T_{reg}, adaptive arm) (Gabrilovich and Nagaraj, 2009; Togashi et al., 2019). Pro-inflammatory cell populations promote immune responses against pathogens or 'non-self' including anti-tumour immune responses. Immune cells with pro-inflammatory capacity include antigen presenting cells (APC, innate arm) and immune effector cells, i.e natural killer cells (NK cells, innate arm) and cytotoxic T cells (adaptive arm) and others (Labani-Motlagh et al., 2020). However, tumour cells are equipped with powerful immune escape mechanisms rendering tumour-resident immune effector cells and antigen presenting cells incapable of recognizing tumour cells as 'non-self' (Anderson et al., 2017; Cantoni et al., 2020). It is important to note that far more immune cell subsets may be found within the TME, many of which play context-dependent roles and cannot be assigned to either immunosuppressive or pro-inflammatory populations. Similarly to other solid tumours, HNSCC masses show a highly heterogeneous immune infiltrate making it difficult to identify specific tumour-immune subtypes (Sun et al., 2021). Accordingly, efforts to identify such HNSCC immune subtypes are still ongoing. Interestingly, HPV-status seems to impact the immune infiltrate as lesions from HPV-positive patients show higher T-cell abundance including both effector and regulatory T-cells (Mandal et al., 2016).

The *tumour vasculature* is formed by endothelial cells and pericytes, supplying the tumour with oxygen and nutrients. Tumours tend to become hypoxic when they grow too large in size apparently because the blood supply is insufficient (Petrova et al., 2018). The lack of oxygen stimulates cancer and stromal cells to produce angiogenic growth factors such as vascular endothelial growth factor (VEGF) and fibroblast growth factor (FGF) which in return induce endothelial cell growth and vessel formation (Carmeliet and Jain, 2011; Giavazzi et al., 2003; Nauta et al., 2017). In healthy tissue, vessels are lined by a thin monolayer of endothelial cells, shaping the vascular endothelium, frequently supported by pericytes. In tumours however, blood vessels have abnormal, immature structure with fewer pericytes and weaker cell-cell junctions rendering them dysfunctional and leaky (Klein, 2018). This leakiness increases the interstitial fluid pressure (IFP) eventually affecting the distribution of nutrients and macromolecules in the TME, as addressed in a subsequent paragraph in this section. Tumour vascularisation also promotes metastatic spread as cancer cells have an easier access to the blood stream (Zetter, 1998). Accordingly, tumour micro-vessel density is investigated as a prognostic biomarker for disease survival. Evidently, CD105 (endoglin), a marker of neovascularisation, plays a prognostic role for patient outcome in HNSCC (Martone et al., 2005). Other marker proteins under investigation include CD31 and CD34 (Hasan et al., 2002).

The *ECM* includes collagen, fibronectin, elastin and laminin which provides a physical scaffold for cells and impacts tumour cell dissemination (Anderson and Simon, 2020). In solid tumours, the ECM can constitute up to 60% of the tumour mass. Importantly, large amounts of collagen together with a high rate of fibroblast infiltration result in desmoplasia, which is linked to poor patient prognosis (Bexelius et al., 2020). A desmoplastic phenotype can also be found in HNSCC and has been suggested for investigation as a marker for poor prognosis in oral squamous cell carcinoma (Zainab et al., 2019). An increased density of collagen fibres within a solid tumour leads to higher stiffness and fuels cancer progression (Provenzano et al., 2008a; Provenzano et al., 2008b). HNSCC tumours are considered relatively collagen-rich, whilst the tumour collagen promotes proliferation and migration of HNSCC cells and confers resistance to chemotherapy (Lai et al., 2019). Furthermore, the ECM serves as a depot for cytokines and growth factors which are released by proteases like matrix metalloproteinases (MMPs) (Anderson and Simon, 2020). The aforementioned MMPs also catalyse remodelling of the ECM and facilitate cancer cell migration and metastatic spread (Thomas et al., 1999). Accordingly, specific MMPs have been associated with an increased metastatic potential as evidenced for oral squamous cell carcinoma (Hong et al., 2000).

1.1.4.2 Barriers of the tumour microenvironment

In health the *interstitial fluid pressure* (IFP) is maintained at physiologic levels via a constant transcapillary pressure gradient (slightly negative in healthy interstitium) resulting in a net outward transcapillary flow (Young et al., 1950). In solid tumours, the IFP is often increased imposing a strong physical barrier for efficient drug delivery (Jain, 1987), particularly affecting macromolecules which are primarily transported via convection rather than diffusion (Jain, 1990; Rippe and Haraldsson, 1994). The reasons for the increased IFP in solid tumours are not fully understood but probably involve blood-vessel leakiness, lymph-vessel abnormalities, interstitial fibrosis and an eventual contraction of the ECM mediated by stromal fibroblasts (Heldin et al., 2004). A high IFP has also been described in HNSCC (Gutmann et al., 1992; Less et al., 1992)

Hypoxia is a common feature of solid tumours, primarily due to a dysfunctional and heterogeneous vascular network which fails to provide adequate amounts of oxygen to the growing tumour. In healthy tissue oxygen levels are maintained at 3-7%, whilst in most tumours median oxygen levels fall below 2% (McKeown, 2014). Therefore, it is clear that tumours are well adapted to grow and expand in this persistently oxygen-depleted TME. Hypoxia-inducible factor-1 (HIF-1) is the main regulator of this adaptation process (Semenza, 2012). Under hypoxic conditions, HIF-1 mediates the transition from oxidative to glycolytic metabolism as a primary source to cover cellular energy requirements (Kim et al., 2006; Warburg, 1956). Additionally, hypoxia impacts immune cells in a variety of ways, eventually resulting in an overall immunosuppressive effect (e.g. enhancement of immunosuppressive functions in myeloid derived suppressor cells and effector T cells). Furthermore, hypoxia is associated with resistance to radiotherapy, resulting in a poorer clinical outcome (Gray et al., 1953). HNSCC tumours are also characterised by hypoxia (median oxygen levels ~1.3%) with roughly similar levels between HPV-positive and HPV-negative disease (Sørensen et al., 2013). In line with general observations, high levels of hypoxia in HNSCC tumours portend a poor prognosis and confer resistance to radiation therapy (Göttgens et al., 2019).

An *immunosuppressive immune contexture* can impose a strong immunological barrier in solid tumours (Fridman et al., 2017). It is characterised by the presence of distinct immune cell populations including MDSCs, M2 macrophages and T_{reg} cells as well as inhibitory cytokines secreted by those cell populations, including IL-1, IL-6, IL-10 and transforming growth factor-β (TGF-β) (Fridman et al., 2017; Josephs et al., 2015; Ruffell and Coussens, 2015). Josephs et al 2015). The latter cytokines not only promote the survival of immunosuppressive cell populations but also provide an environment perceived as hostile by proinflammatory immune cell populations or leads to functional impairment of immune effector cells, which was found to play a role in HNSCC (de Ruiter et al., 2017). Furthermore, the density of immunosuppressive cell populations correlates with a poor prognosis across several solid tumour types including HNSCC (Pang et al., 2020). Over the last couple of years efforts to immunologically characterise HNSCC tumours have increased drastically to better understand on how to tailor the application of novel immunotherapies, such as ICB and OV, for the treatment of this disease (Cillo et al., 2020; Li et al., 2019a).

1.2 Oncolytic virotherapy

Oncolytic virotherapy (OV) employs viruses as anticancer drugs (Russell and Peng, 2007). These viruses selectively infect and destroy tumour tissue, a process addressed as oncolysis. Lately however, oncolytic viruses have evolved as powerful tools to awaken the immune system in the fight against cancer, capable of overcoming cancer-associated immunosuppression (Gujar et al., 2018). This introductory subchapter provides an overview on oncolytic viruses including general aspects and tumour selectivity, their mechanism of action and the immune response they can elicit. Furthermore, four viruses which are frequently applied for OV use are presented and their potential ability to upregulate the immune checkpoint PD-L1 is discussed.

1.2.1 General aspects and tumour selectivity

Oncolytic viruses are mostly replication-competent viruses which exhibit a tropism towards cancerous cells. This tropism can either exist as a native trait (e.g reovirus, newcastle disease virus) or it can be introduced via genetic modifications (e.g. adenovirus, herpes simplex virus, HSV) (Russell et al., 2012). The amenability towards genetic modifications depends on the genome size of the virus: while smaller-sized viruses like reovirus (~23.4 kb) are less amenable for genetic modifications, larger-sized viruses like HSVs (~152 kb) allow for such modifications and can additionally accommodate transgenes. Oncolytic viruses are usually categorised according to their genome structure, differentiating between DNA and RNA viruses. Examples for DNA viruses are HSV, adenovirus and vaccinia virus while representative RNA viruses are reovirus, coxsackievirus and measles virus (see also section 1.2.4; table 1-3).

In addition to the aforementioned tropism towards cancerous cells, several other tumour-related features promote the tumour selectivity of oncolytic viruses. Firstly, the presence of virus-specific receptors on the tumour cell surface (e.g. coxsackie-adenovirus receptor CAR or CD46) (Gaggar et al., 2003; McDonald et al., 1999). Secondly, the high metabolic and replicative activity of tumour cells (Hanahan and Weinberg, 2011). Thirdly, the common lack of anti-viral defence mechanisms in cancerous cells, such as type-I interferon signalling (Stojdl et al., 2003). And lastly, the leaky vasculature present in tumours, promoting rapid and unselective extravasation of viral particles (Schaaf et al., 2018). The underlying mechanisms of OV tumour selectivity have been thoroughly discussed elsewhere (Ilkow et al., 2014).

1.2.2 Mechanisms of action

Oncolytic viruses unfold their anticancer effects through multiple mechanisms, some of which are virus-associated and some that relate to the immunological events initiated following virus administration (Fig.1-2). As mentioned earlier on, oncolytic viruses preferentially infect cancerous cells which can be due to the expression of viral entry receptors and or dysfunctional antiviral defence mechanisms present in cancer cells. Upon infection, excessive viral replication leads to cancer cell death, an effect historically referred to as oncolysis. Subsequently, viral progeny is released from the dying cancer cells and eventually re-infects adjacent tumour tissue (Russell and Peng, 2007). In parallel, a wealth of cytoplasmic components is released including specific antigens, cytokines and danger- as well as pathogen-associated molecular patterns (DAMP, PAMP) which can trigger innate and adaptive anti-cancer immune responses (Gujar et al., 2018; Kaufman et al., 2015). Most importantly, their release can convert an immunosuppressive tumour microenvironment (TME) into an inflamed, immune effector cell-rich tumour phenotype. The addition of transgenes encoding inflammatory cytokines (e.g. granulocyte macrophage-colony stimulating factor) or therapeutic cargos (e.g. anti-CTLA-4 mAb) into the viral backbone can further enhance these pro-inflammatory and therapeutic effects (Andtbacka et al., 2015; Thomas et al., 2019). The role of transgenes in OV is discussed in greater detail in section 1.2.5. In addition to the aforementioned effects, certain oncolytic viruses (e.g. HSV-1, vesicular stomatitis virus) can infect and destroy the tumour vasculature and thus provide anti-angiogenic properties (Angarita et al., 2013; Benencia et al., 2005; Breitbach et al., 2011). More precisely, Breitbach *et al* have described direct infection and destruction of tumour-associated but not healthy vasculature following systemic administration of a vesicular stomatitis virus (VSV) in a murine colon carcinoma model (Breitbach et al., 2011). In addition, subsequent immune-mediated effects led to the formation of microclots within tumour vessels enhancing the anti-angiogenic effect on tumours. Hence, the anti-angiogenic effects arising from OV can be of direct and indirect nature, albeit the exact mechanism of tumour vessel targeting by oncolytic viruses remains to be fully understood.

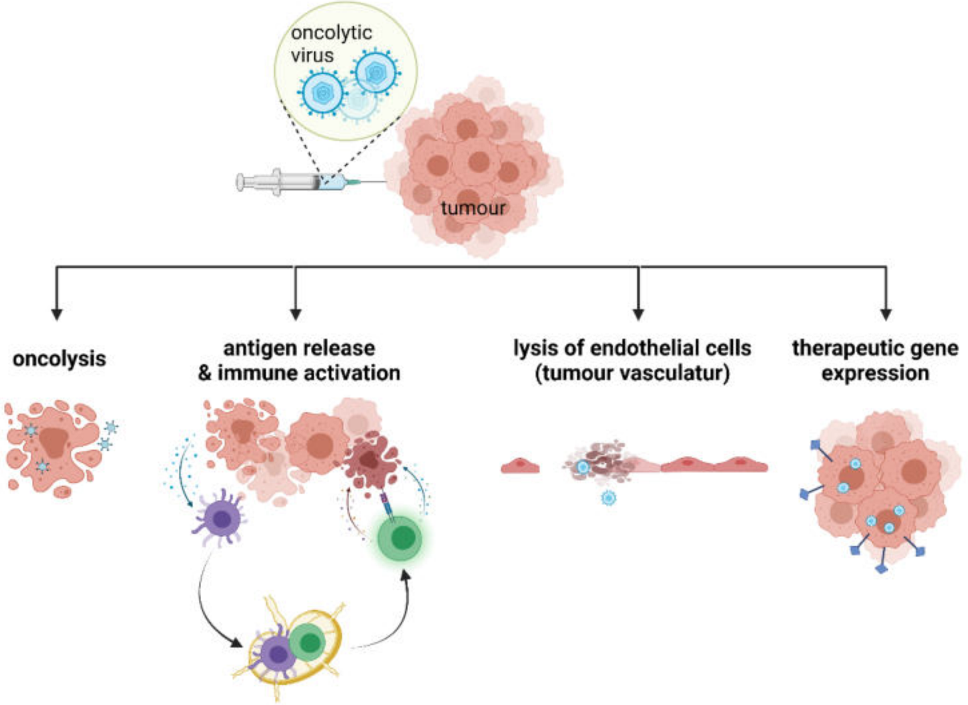

Figure 1 - 2: Four modes of action of oncolytic viruses. Oncolytic viruses cause significant tissue damage through oncolysis, activate the immune system via the release of antigens and other mediators, cause endothelial cell lysis in tumours and can be used for therapeutic transgene overexpression in target cells. Figure created with Biorender.com.

1.2.3 Immune response to OV

The therapeutic effect arising from OV was long believed to be driven by the virus' oncolytic activity. More recently however, the role of the immune response triggered through OV has become increasingly acknowledged and is believed to be critical for the therapeutic success. Like any other viral pathogen, oncolytic viruses trigger a cascade of immunologic events involving the innate and adaptive immune system.

Upon viral infection of the target cell, the oncolytic virus is recognised by receptors of the innate immune system, so called pattern recognition receptors (PRRs). The latter triggers several signalling cascades leading to the activation of interferon regulatory factors (IRFs), nuclear factor-kappa B (NF-κB), activator protein 1 (AP-1) and the production of type I interferons (IFNs). Additionally, type I IFN signalling through the JAK/STAT pathway leads to antiviral effects which can restrict oncolytic virus replication. The latter causes inflammation within the

TME which allows to overcome tumour immunosuppression and promotes the intratumoural recruitment of innate immune cells, such as antigen presenting cells (APCs) and natural killer (NK) cells (Nguyen et al., 2002). The cytokines released during this initial response include the Type I IFNs IFN-α, IFN-β which exhibit potent antiviral activity and can therefore limit viral spread (Yan and Chen, 2012). However, several strategies have been proposed to overcome this first-line measure of antiviral response, e.g. via viral engineering (Evans et al., 2014). At the same time these cytokines activate APCs which phagocytose tumour debris arising from viral oncolysis. The APCs then travel to the draining lymph nodes, where they engage with naïve and effector T-cells. The process called antigen presentation is used to activate (prime) T cells against a specific (e.g. tumoural) antigen (Bedoui and Greyer, 2014; Rosendahl Huber et al., 2014). The latter step basically links the innate immune response (APCs, etc.) with the adaptive immune response (T-cells, etc.). Critically, immune effector T-cells with cytotoxic activity (CD8+ T-cells) can be primed against tumour specific antigens, such as tumour associated antigens (TAA) and neoantigens (Kaufman et al., 2015). Examples for common TAAs in HNSCC which T-cells could be primed against include EGFR (overexpressed in 80-90%), the receptor for hyaluronic acid mediated motility (RHAMM, ~70%) and carbonic anhydrase IX (CAIX, ~80%), or the melanoma antigen gene (MAGE) protein MAGED4B (overexpressed in ~50%) (Chong et al., 2012; Schmitt et al., 2009). TAA-specific cytotoxic CD8+ T-cells can directly attack target cells and destroy them through the release of cytotoxic granules containing granzyme B and perforin. Similarly, NK cells, which have been mentioned previously, also exhibit cytotoxic activity through cytotoxic granule release (Paul and Lal, 2017). However, these potent effects can also be directed against viral antigen and therefore significantly limit viral spread. Other effects such as the pre-existence of neutralising antibodies against the virus used for therapy can additionally impair viral propagation, especially upon systemic administration. This is particularly relevant in the case of viruses with a high seroprevalence among the general population, e.g. HSV-1 seroprevalence 50-60% (Xu et al., 2006). The breadth of immunologic barriers and strategies to overcome limitations of oncolytic virus spread *in vivo* extent beyond the scope of this thesis and are actively investigated by others in the field.

After all, it is important to stress that OV has the capability of inducing an inflamed TME via the secretion of pro-inflammatory cytokines and the infiltration of immune effector cells. As such, it provides an advantageous environment for the onset of other immunotherapies such as ICB, the mechanisms of which are addressed in a separate section (1.3.4). However, the distinct impact of OV on the targets of ICB, particularly the immune checkpoint PD-L1, remain unexplored in HNSCC. Therefore, the exploration of PD-L1 expression upon OV in models of HNSCC was the main aim of my PhD project.

1.2.4 Oncolytic virus candidates

In this section four common oncolytic virus types are presented including their major features, strategy of cell entry and (pre)clinical example candidates (also see Table 1-3).

Adenoviruses (AdV) are dsDNA viruses which display several features rendering them attractive oncolytic agents such as their potent lytic activity and their capability of inducing immunogenic cell death (Uusi-Kerttula et al., 2015). AdVs enter cells mostly via binding to CAR, a receptor which is ubiquitously expressed on all human organs (Coyne and Bergelson, 2005). Other cell entrance receptors to AdV exist such as heparin-sulfate, CD46, CD80/86 or integrins and play a serotype-dependent role (Zhang and Bergelson, 2005). To generate tumour selective AdVs safe for clinical application, several genetic modifications have been proposed. For example, deletion of the *E1B-55kD* gene which usually blocks p53 during AdV infection, leading to selective replication in p53 dysfunctional tumour cells (Bischoff et al., 1996). In healthy tissue, the tumour antigen p53 is the guardian of DNA damage, controlling cell division and apoptosis (Vogelstein et al., 2000). Mutations in the *p53* gene, can lead to uncontrolled cell division and carcinogenesis and occur in an estimated 50% of all tumours. ONYX-015, an oncolytic AdV which harbours the *E1B-55kD* deletion, showed selective replication and oncolysis in p53 mutant HNSCC tumours in clinical testing (Nemunaitis et al., 2000). A close derivative of ONYX-015, the oncolytic AdV H101 (commercial name ONCORINE®), obtained clinical approval for the treatment of late stage nasopharyngeal carcinoma in combination with chemotherapy China (Ganly et al., 2000; Liang, 2018; Xu et al., 2003). More examples for other AdV specific deletions can be found elsewhere (Hemminki et al., 2020; Uusi-Kerttula et al., 2015). A major limitation of AdVs is that human serotype AdVs do not replicate in animal tissues which hampers preclinical studies in immunocompetent models to explore host–vector interactions (Alemany et al., 2000).

Vaccinia viruses (VV) have several attributes which make them attractive for oncolytic virus use including a short lifecycle with rapid cell to cell spread, strong lytic ability and large cloning capacity (~190 kbp) (Guo et al., 2019). Unlike other viruses, VVs do not require specific surface receptors for cell entry, allowing them to infect a wide range of cells (Carter et al., 2005). To confer tumour selectivity, different genetic modifications have been applied. For instance, the VV JX-594 (commercial name PEXA-VEC®), which has been tested clinically in several tumour types such as hepatic carcinoma (Breitbach et al., 2015; Cripe et al., 2015; Heo et al., 2013), had its thymidine kinase gene deleted making it reliant on cellular thymidine kinase expression. Thymidine kinase is constitutively expressed across the majority of cancer cells, whilst in healthy cells it is only expressed during S phase of the cell cycle (Topolcan and Holubec, 2008). This way, JX-594 preferentially infects cancer cells over healthy cells. In addition to this modification, JX-594 also contains GM-CSF for enhanced immune cell recruitment. Another oncolytic VV named GL-ONC1 proved to be safe in patients with locoregionally-advanced HNSCC undergoing standard chemo-radiotherapy (Mell et al., 2017). Based on this, a phase II study was warranted but not further pursued.

Reovirus is a naturally occurring dsRNA oncolytic virus infecting target cells through the interaction of viral attachment protein σ1 and the cell surface receptor junctional adhesion molecule-1 (JAM-1) and mediated by β1 integrins (Forrest et al., 2003; Hashiro et al., 1977; Maginnis et al., 2006). The mechanism determining its cancer specificity is still poorly understood but largely believed to be reliant on overactivation of the Ras signalling pathway (Norman et al., 2004). Due to its small genome, reovirus is difficult to engineer genetically. The reovirus candidate Reolysin (commercial name PELAREOREP®) has shown oncolytic activity across a broad range of human cancer cell lines such as melanoma (Errington et al., 2008), colon and ovarian (Hirasawa et al., 2002), breast (Marcato et al., 2009) and HNSCC (Cooper et al., 2015; McLaughlin et al., 2020; Twigger et al., 2012). It was also tested clinically in combination with chemotherapy (e.g.

paclitaxel) across solid tumours including HNSCC patients (Karapanagiotou et al., 2012; Kyula et al., 2012). However, a follow-up phase III clinical trial in patients with platinum-resistant, recurrent/metastatic HNSCC did not reach approval for this treatment regimen. In a more recent clinical trial, Samson *et al* have demonstrated successful infection of primary brain tumours or brain metastases following systemic administration of Reolysin (Samson et al., 2018).

HSVs are considered very attractive for OV use as they broadly infect cancer cells (both human and mouse), have high lytic and immunogenic potential and provide a large genome (~152 kbp) making them amenable for genetic modifications. Furthermore, HSVs have been studied extensively and all their essential and non-essential genes have been characterised (Peters and Rabkin, 2015). The latter enables targeted manipulation of the HSV genome to render them apathogenic against neurons and enhance tumour selectivity for oncolytic use. In order to confer safety for OV use it is critical to disable their neuropathogenic capacity which is vastly determined via the gene encoding for infected cell protein (ICP) 34.5 (Chou et al., 1990; Chou and Roizman, 1994; Orvedahl et al., 2007). ICP34.5 is dispensable for viral replication in tumour cells and has therefore been deleted in most oHSV constructs (Andtbacka et al., 2015; Critchley-Thorne et al., 2009; Krabbe and Altomonte, 2018; Thomas et al., 2019). Furthermore, HSVs have established several mechanisms to evade an immune response. One such mechanism is driven through the expression of ICP47, a protein which prevents peptide loading onto major histocompatibility complex (MHC)-I and subsequent MHC-I expression. This ensures the evasion of HSV-infected cells from CD8+ T-cells (Goldsmith et al., 1998). Consequently, the ICP47-encoding gene is commonly deleted in oHSV candidates (Andtbacka et al., 2015; Thomas et al., 2019). ICP6 is another protein of the HSV genome which is frequently altered for OV use (Goldstein and Weller, 1988). Whilst ICP6 is essential for HSV replication in noncycling cells, deleting ICP6 makes HSV selective for dividing cells and therefore more specific to tumour tissue, as exemplified by the oHSVs G47△ and G207 (Markert et al., 2000; Todo et al., 2001). Data evidencing oncolytic and anti-metastatic activity of G47△ in tongue cancer mouse models following intralesional injection has recently been published (Uchihashi et al., 2021). A different oHSV candidate namely HF10 worked similarly well when tested in mouse models of tongue and ear cancer, showing evidence of oncolysis, prolonging overall survival and immune-activating potential (Esaki et al., 2020; Takano et al., 2021). Examples for the application of oHSV candidates in clinical testing including the two strains Talimogene laherparepvec or T-VEC (in metastatic melanoma) and G47△ (malignant glioma) which have already obtained clinical approval are provided in section 1.2.7. Another characteristic of HSV is its mode of cell entry which is mediated via several receptors. Glycoproteins expressed on the virus envelope bind several receptors presented on the target cell, including nectin-1 and -2, herpesvirus entry mediator (HVEM) and heparan sulfate binding sites (Spear, 2004). All four proteins are widely expressed across various cell types. Importantly, both nectin-1 and HVEM can be expressed on cancer cells and therefore directly influence the sensitivity towards oHSVs (Ghose et al., 2021; Yu et al., 2007; Yu et al., 2005).

Oncolytic virus	**Adenovirus**	**Herpes simplex virus 1**	**Vaccinia virus**	**Reovirus**
Genome	dsDNA ~36 kbp	dsDNA ~152 kbp	dsDNA ~190 kbp	dsRNA ~23.4 kbp
Cell entry receptor	CAR (mostly), Heparan-sulfate, CD46, CD80/86, integrins (serotype-dependent)	HVEM, Nectin-1, -2, Heparan-sulfate binding sites	none	JAM-1, β1-integrins
Necessary genetic modifications (apathogenicity)	see below	ICP34.5 deletion	none	none
Genetic modifications to enhance tumour selectivity or potency	*E1B* 55kDa deletion *E1A* gene 24-bp deletion	ICP47 deletion, ICP6 deletion	TK gene deletion	None are common
candidates in clinical trials	ONYX-015* H101	T-Vec* G47△*, G207 RP1, RP2, RP3	JX-594, GL-ONC1	Reolysin

*Table 1 - 3: Examples of commonly used oncolytic viruses with virus-specific characteristics. Abbreviations stand for double-stranded desoxyribonucleic acid (dsDNA), double-stranded ribonucleic acid (dsRNA), coxsackie-adenovirus receptor (CAR), cluster of differentiation (CD), herpesvirus entry mediator (HVEM), infected cell protein (ICP), junctional adhesion molecule-1 (JAM-1), thymidine kinase (TK). *Viruses which have already obtained clinical approval in specific countries.*

1.2.5 Common transgenes

One major limitation of oncolytic viruses is their poor therapeutic efficacy when applied as a monotherapy. The expression of transgenes is a strategy to overcome this limitation by providing additional tools to improve their therapeutic effect. Such transgenes can encode various structures including *(1) immune-modulatory molecules* such as cytokines or inhibitors of immune suppressors, *(2) therapeutic agents* (therapeutic cargos) such as immune checkpoint inhibitors or pro-drug converting enzymes or *(3) proteins or molecules enhancing viral spread*. Each category of transgenes is briefly addressed in the following paragraphs.

The incorporation of transgenes encoding *immune modulatory molecules* is aimed to either support a pro-inflammatory tumour microenvironment or reduce signals supporting an immunosuppressive environment. By far the most popular immune-stimulatory transgene added into many different viruses is granulocyte macrophage-colony stimulating factor (GM-CSF). GM-CSF a pro-inflammatory cytokine promoting the maturation and function of dendritic cells (DCs) and improving the activity of macrophages (Dranoff et al., 1993; Kim et al., 2000). Oncolytic virus candidates expressing GM-CSF include the clinically approved oHSV T-Vec (previously known as OncoVex) (Andtbacka et al., 2015), the VV JX-594 (Breitbach et al., 2015) and the AdV CGTG-102 (Kanerva et al., 2013). Moreover, transgenes encoding for pro-inflammatory interleukins (ILs) are frequently overexpressed to support immune cell attraction and expansion to and within the tumour. In this manner, IL-2 which supports T lymphocyte expansion (Boyman and Sprent, 2012) and IL-12 which regulates T lymphocyte and NK cell responses and induces the production of IFN-γ (Trinchieri, 2003) have been integrated in several oncolytic virus constructs including AdVs and VVs respectively (Nakao et al., 2020; Quixabeira et al., 2021). Conversely, the overexpression of inhibitors to immunosuppressive cytokines has been described in several papers. Transforming growth factor-beta (TGF-β) is a cytokine with potent immunosuppressive function inhibiting the activation, proliferation and differentiation of T cells (Li et al., 2006). Yang *et al* have generated an oncolytic AdV which is armed with a soluble receptor for TGF-β, capable of trapping TGF-β and thus abrogating its immunosuppressive function (Yang et al., 2019).

Oncolytic viruses are frequently employed as *therapeutic cargos*, armed with molecules or proteins to enhance their antitumour capacity. From an immunotherapeutic point of view, there is substantial evidence for the synergism between oncolytic viruses and immune checkpoint inhibitors (Liu et al., 2017b; Nakao et al., 2020; Ribas et al., 2017). Thus, engineering oncolytic viruses to encode immune checkpoint inhibitor molecules is a compelling alternative, potentially reducing the need for combination therapies. Furthermore, the capability to selectively infect cancer cells might lead to a more localised production of immune checkpoint inhibitors and thus provide a superior safety profile to systemic administration. Several examples for such checkpoint inhibitor delivering viruses are provided by Thomas and colleagues who compared several oHSV constructs each encoding a different immune checkpoint molecule including CTLA-4 and immune co-stimulatory pathway activating ligands to OX40, 4-1BB and CD40 in a syngeneic mouse model of lymphoma (Thomas et al., 2019). All four candidates provided enhanced tumour control of injected and non-injected tumours as compared to the parental oHSV virus. Clinical evaluation of these constructs in solid tumours is currently underway (NCT03767348, NCT04336241). In another preclinical study an anti-PD-1 encoding oHSV was employed showing promising therapeutic efficacy in a mouse model of glioblastoma (Passaro et al., 2019; Passaro et al., 2020). An alternative approach to use oncolytic viruses as drug-delivering cargos is via the incorporation of prodrug converting genes to facilitate targeted activation of an anti-cancer drug. Simpson *et al* have tested a cytosine deaminase expressing oHSV in several tumour cell lines as well as in a rat gliosarcoma model (Simpson et al., 2006). Cytosine deaminase converts the antifungal fluorocytosine to the chemotherapeutic agent fluorouracil with cytotoxic capacity (Tiraby et al., 1998). Accordingly, the combination of the cytosine deaminase armed oHSV with fluorocytosine enhanced the therapeutic effect compared to the parental virus combined with the prodrug *in vitro* and *in vivo* (Simpson et al., 2006). The same virus was also tested in a panel of HNSCC cell lines but did not show enhanced efficacy through cytosine deaminase prodrug conversion (Price et al., 2010).

A third category of transgenes uses *proteins or molecules which enhance viral spread* in the tumour microenvironment. Solid tumours impose several physical barriers hampering viral propagation throughout the tumour mass.

Several such physical barriers are addressed in section 1.1.4.2 of the introduction. An example for a protein aiding viral spread in the tumour is the fusogenic membrane glycoprotein (GP) from gibbon ape leukaemia virus (GALV), also referred to as GALV-GP-R$^-$ (Krabbe and Altomonte, 2018). Infected, GALV-GP-R$^-$ expressing cells form multi-cell syncytia via PiT1 receptors, thus enhancing viral propagation and tumour cell killing (Higuchi et al., 2000). PiT1 is expressed on all mammalian cells, however, the murine version of PiT1 is not compatible with GALV-GP-R$^-$, thus impairing the fusogenic capability of GALV-GP-R$^-$ expressing virus constructs in mouse cancers (Beck et al., 2009; Johann et al., 1993). The enhanced potency of GALV-expressing oncolytic viruses over the non-GALV expressing virus has been described in several tumour types, including a HNSCC and melanoma following a GALV-encoding oHSV *in vitro* (Roulstone et al., 2021). Another GALV-encoding oHSV, showed 5-30 fold increased tumour cell killing across several cancer cell lines (including a HNSCC cell line) *in vitro* and tumour shrinkage increased 5- to 10-fold *in vivo* (Simpson et al., 2006). As an alternative to GALV-GP-R-, matrix-degrading enzymes have been integrated into the backbone of oncolytic viruses to facilitate viral spread within tumours. According to data published by Tedcastle *et al*, an actin-resistant DNAse I expressing AdV showed improved antitumour efficacy and enhanced intratumoural spread in a mouse xenograft model of colon carcinoma (Tedcastle et al., 2016). A more comprehensive overview on the variety of possible transgenes used in OV can be found elsewhere (Twumasi-Boateng et al., 2018).

1.2.6 PD-L1 upregulation upon OV

The role of OV as an immune-modulatory agent in cancer therapy is increasingly appreciated. Several of those effects including the infiltration of immune effector cells as well as the secretion of pro-inflammatory cytokines, are mentioned in section 1.2.3. This section focuses on the stimulatory effect OV can have on the expression of the PD-L1 protein. The upregulation of PD-L1 in the TME has been reported across a variety of solid tumour types following OV via different virus constructs. The strong interest for agents with PD-L1 upregulating capacity can be explained by its twofold role as a therapeutic target (addressed in 1.3.4) and a biomarker for treatment response to PD-1/PD-L1 targeted ICB (addressed in 1.3.5). When expressed on tumour cells, PD-L1 has potent immunosuppressive capacity which can be exploited therapeutically via PD-1/PD-L1 targeted protein blockade. Accordingly, the upregulation of PD-L1 upon OV alongside other OV-owed therapeutic traits (oncolysis and attraction of immune effector cells to the tumour) are likely to synergize with PD-1/PD-L1 ICB. This section provides a summary of OV-associated mediators of PD-L1 expression and an overview on the literature listing publications which reported increased levels of PD-L1 upon OV (Table 1-4).

The myriad of factors which knowingly mediate PD-L1 expression are addressed in a separate introduction chapter of this thesis (1.3.2). From the sum of these possible factors, cytokines are expected to play a crucial role in the upregulation of PD-L1 upon OV. Specific cytokines, so-called type I interferons (IFN), are released as a first-line measure upon viral infection (Katze et al., 2002; Yan and Chen, 2012). Type I IFNs act as an initial alert signal for the immune system inducing T-cell recruitment and have the capability to inhibit viral replication (Hwang et al., 1995; Sainz and Halford, 2002). Hence, PD-L1 may be upregulated by type I IFNs on infected and neighbouring cells in an autocrine and paracrine manner respectively. It is important to note that some viruses like HSV-1 have developed strategies to inhibit type I IFN signalling (Johnson et al., 2008). In the further course following virus injection, antigen-specific T-cells release IFN-γ which might in turn increase PD-L1 on surrounding tumour cells, as a mechanism to evade the cytotoxic activity of T-cells. This concept of PD-L1 upregulation is acknowledged as a strategy of adaptive immune resistance in tumours (Pardoll, 2012; Ribas, 2015). Data from several studies support this concept reporting a simultaneous increase of activated T-cells (CD8+ T-cells), IFN-γ and PD-L1 upon treatment with different OVs likewise (Ribas et al., 2017; Samson et al., 2018). Other studies report only a singular increase of CD8+ T-cells and IFN-γ, without PD-L1 upregulation in tumours, eventually contradicting the concept of an IFN-γ-triggered PD-L1 increase *in vivo* (Shen et al., 2016). While strong evidence for an IFN-mediated upregulation of PD-L1 exists *in vitro* (Garcia-Diaz et al., 2017; Loke and Allison, 2003), additional mechanistic studies are required to decipher the role of IFNs in the context of an OV-triggered PD-L1 increase in tumours *in vivo*.

As mentioned previously, increased levels of PD-L1 following intratumoural OV were reported on several occasions. For example, two preclinical studies employing an oncolytic marabavirus and a poxvirus respectively have reported increased expression of PD-L1 in murine models of mammary carcinoma (4T1, EMT6 and E0771) (Bourgeois-Daigneault et al., 2018; Chaurasiya et al., 2020). In addition, both viral constructs eventually enhanced the therapeutic effect of subsequent ICB. Similar to the effects observed in the models of mammary carcinoma, intratumoural injection of VV constructs to murine colon carcinoma models (MC38, CT26) led to an increase of PD-L1, followed by improved therapy upon combination with anti-PD-1/PD-L1 ICB (Liu et al., 2017b; Nakao et al., 2020). Importantly, the studies in the CT26 tumour model showed upregulated PD-L1 in both injected and non-injected lesions, evidencing the potential of systemic effects induced by local OV (Nakao et al., 2020). It is noteworthy however, that the oncolytic virus overexpressed interleukin (IL)-7 and IL-12; whereby the latter had been shown to induce PD-L1 expression in systemic organs such as the heart and the lungs following intraperitoneal IL-12 administration (Eppihimer et al., 2002). Another IL-12 overexpressing oncolytic virus, a Semliki Forest virus, upregulated PD-L1 in a mouse model of melanoma (B16-OVA) (Quetglas et al., 2015). Furthermore, the authors showed that IL-12 triggered PD-L1 expression in an IFN-γ dependent manner. The impact of OV on PD-L1 in melanoma was reported on several other occasions. Zamarin *et al* have addressed this subject in the B16-F10 melanoma model using a New Castle Disease virus (Zamarin et al., 2018). They reported high levels of PD-L1 restricted to injected lesions at early times after virus injection (24 h after first injection) and increased PD-L1 levels in both injected and non-injected tumours at a later time point (day 13 after treatment start), supporting both the dynamic nature of PD-L1 expression and potential systemic effects of local OV. The HSV-1 candidates T-VEC (GM-CSF expressing) and RP1 (GM-CSF and GALV expressing) also induce PD-L1 expression in melanoma as reported in clinical and preclinical (4434 model) settings (Ribas et al., 2017; Roulstone et al., 2021; Thomas et al., 2019). RP1 injected to 4434 melanoma tumours has also led to an upregulation of PD-L1 in tumour draining lymph nodes (TD Ln) but not in non-injected tumours on the contralateral flank which might as well have been a matter of measurement timing (Roulstone et al., 2021; Thomas et al., 2019). An upregulation of PD-L1 in tumours upon OV has been observed in several other cancer models, including myeloma (Kelly et al., 2018), acute leukaemia (Shen et al., 2016) and glioma

(Jiang et al., 2017). Clinically, a PD-L1 upregulating effect was described for glioma and melanoma brain metastasis (Samson et al., 2018) as well as for a subset of pancreatic cancer patients (Mahalingam et al., 2020) following intravenous reovirus injection.

Taken together, the current literature strengthens the potential of oncolytic viruses to upregulate PD-L1 across a variety of cancer types, however no publication reporting this effect in HNSCC has been found. Therefore, I chose to study the PD-L1 response to OV in preclinical mouse models of HNSCC. For OV, I chose a novel oHSV-1 candidate which was shown to upregulate PD-L1 in melanoma (Roulstone et al., 2021; Thomas et al., 2019) and is currently tested in clinical trials across solid tumour types including HNSCC (see 1.2.7).

Oncolytic virus	therapeutic transgenes	PD-L1 upregulation and tumour type	Stage of study	Reference
Marabavirus	-	Murine mammary carcinoma 4T1, EMT6 (both mRNA+protein level)	preclinical	(Bourgeois-Daigneault et al., 2018)
Vaccinia virus	-	Murine colon cancer MC38 (protein)	preclinical	(Liu et al., 2017b)
	IL-7, IL-12	Murine colon cancer CT26 (protein)	preclinical	(Nakao et al., 2020)
Reovirus	-	Multiple myeloma 5TGM1 (not stated)	preclinical	(Kelly et al., 2018)
	-	High grad glioma, melanoma brain metastases (both mRNA+protein level)	clinical trial	(Samson et al., 2018)
	-	Pancreatic adenocarcinoma (protein); only in a small subset of patients	clinical trial	(Mahalingam et al., 2020)
Poxvirus	-	Murine mammary carcinoma E0771 (protein)	preclinical	(Chaurasiya et al., 2020)
Herpes simplex virus	GM-CSF, GALV-GP-R-	Murine melanoma: 4434 (protein)	preclinical	(Roulstone et al., 2021; Thomas et al., 2019)
	GM-CSF	Melanoma (protein)	clinical trial	(Ribas et al., 2017)
Vesicular stomatitis virus	IFN-β	Murine acute myeloid leukaemia C1498 (protein)	preclinical	(Shen et al., 2016)

New Castle Disease Virus	-	Murine melanoma B16-F10 (protein)	preclinical	(Zamarin et al., 2018)
Adenovirus	-	Lung adenocarcinoma CMT64 (protein)	preclinical	(Woller et al., 2015)
	OX40L	Mouse glioma GL261 (protein)	preclinical	(Jiang et al., 2017)
Semliki Forest virus	IL-12	Mouse melanoma B16-OVA	preclinical	(Quetglas et al., 2015)

Table 1 - 4: Oncolytic viruses with PD-L1 upregulating capacity in vivo, preclinical as well as clinical examples are provided. Oncolytic virus candidates armed with PD-1 or PD-L1 encoding transgenes have been omitted. Abbreviations stand for interleukin (IL), messenger ribonucleic acid (mRNA), granulocyte macrophage-colony stimulating factor (GM-CSF), gibbon ape-like leukaemia virus glycoprotein R (GALV-GP-R-), interferon (IFN), OX40 ligand (OX40L), ovalbumin (OVA).

1.2.7 Clinical application of oHSVs

HSV-based oncolytic viruses have been spearheading the race for clinical translation. The oHSV Talimogene laherparepvec or T-VEC (commercial name IMLYGIC®) was the first oncolytic virus to gain approval for the treatment of advanced stage melanoma in the United States and Europe (Andtbacka et al., 2015). More recently, another HSV-based oncolytic virus called G47△ (commercial name DELYTACT®) has been approved in Japan for the treatment of malignant glioma (in June 2021). While T-VEC has the genes encoding for ICP34.5 and ICP47 deleted, and GM-CSF overexpressed (Hu et al., 2006), G47△ is triple mutated rendering ICP34.5, ICP47 and ICP6 dysfunctional (Todo et al., 2001). Both oHSVs have been approved for local application, i.e. intralesional delivery. The adverse events occurring alongside intralesional oHSV treatment include local effects at the site of injection (discoloration, oedema and pain) and systemic symptoms (flu-like symptoms, fatigue, shivers, headaches) (Andtbacka et al., 2015). However, the systemic symptoms attenuate with the increasing number of injections. The potential impact of the high HSV-specific seroprevalence in the general population has been addressed in several clinical trials testing oHSVs. Interestingly, no significant difference in therapeutic effect to the oHSV-based treatment between HSV seropositive and seronegative patients was observed (Andtbacka et al., 2015; Ferris et al., 2014).

In regard to HNSCC, several clinical trials investigating the safety and efficacy of oHSVs in combination with clinically approved treatments have been reported. One trial led by Kevin Harrington investigated T-VEC in combination with chemo-radiation in patients with untreated locally advanced HNSCC (Harrington et al., 2010; Hu et al., 2006). The results from this trial showed that the treatment was well tolerated and achieved locoregional control in the majority of patients. More recently, a phase Ib trial investigating the safety and efficacy of T-VEC with or without the immunotherapy Pembrolizumab (anti-PD-1 ICB) in recurrent and metastatic HNSCC was reported (Harrington et al., 2020). It demonstrated a tolerable safety profile, but no enhanced efficacy compared to Pembrolizumab monotherapy in historical control patients with recurrent/metastatic disease. A major limitation was the relatively high number of early deaths after treatment initiation (28% died before the first postbaseline tumour assessment at week 9) due to the assignment of a significant number of patients with high-volume, terminal disease. Even so, a substantial number of patients achieved durable remission, suggesting that more rigorous patient selection and the application of an oHSV candidate with enhanced potency might still warrant enhanced therapeutic efficacy of this combination. Therefore, several clinical trials (NCT03767348, NCT04336241) investigating a group of novel oHSV based viruses are currently underway (Harrington et al., 2021). One oHSV candidate tested in these trials, namely RP1, harbours deletions in ICP34.5/ICP47 encoding genes and expresses GM-CSF (Thomas et al, 2019). The critical improvements as compared to T-VEC are the additional expression of the fusogenic protein GALV-GP-R^- for enhanced virus spread and the delicate strain selection at the start of its development. The latter refers to the fact that RP1 was selected from 29 initial HSV-1 strains following testing across a panel of human cancer cell lines whilst T-VEC was selected from only two HSV-1 strains and selected based on less comprehensive screening (Liu et al., 2003; Thomas et al., 2019). However, to my knowledge no head-to-head comparison of RP1 vs. T-VEC has yet been published. RP1 is currently tested in a range of solid tumours, including HNSCC, in combination with anti-PD-1 ICB (Nivolumab; NCT03767348), where promising anti-tumour activity has been observed in some patients (Middleton et al., 2020). Due to its high translational relevance e and the fact that it is actively in development in a randomised phase II study, RP1 has also been used for the preclinical work presented in this thesis. Next to RP1, there is RP2, (additionally expressing an anti-CTLA-4 antibody-like molecule) which is trialled clinically as a monotherapy and in combination with the anti-PD-1 mAb Nivolumab (Aroldi et al., 2020).

1.3 Programmed death ligand 1

Programmed death ligand 1 (PD-L1) and its binding partner programmed death receptor 1 (PD-1) have been identified as key players in the maintenance of immune homeostasis. In cancer as well as in chronic infection, PD-1/PD-L1 interaction is exploited as a mechanism of immune evasion which in cancer can be tackled therapeutically via ICB. However, little is known about the role of PD-L1 in the acute phase of viral infection which might provide useful indications about the role of PD-L1 following oncolytic virus injections. This introduction chapter covers the background on PD-L1, including its basic features and expression sites, the mediators of PD-L1 expression, its role in immune homeostasis as well as its relevance as a mechanism of immune evasion in the context of cancer. Finally, the role of PD-L1 during acute viral infection is addressed, providing a link to the results presented on its expression behaviour upon oncolytic virotherapy (Chapter 6).

1.3.1 Basic features and expression sites of PD-L1

Programmed death ligand 1 (PD-L1, B7-H1, CD274) is a type I transmembrane protein which belongs to the immunoglobulin (Ig) superfamily (Dong et al., 1999). It consists of two extracellular domains (one Ig-V-like and one Ig-C-like), a transmembrane component and a short cytoplasmic tail, which does not contain canonical signalling motifs (Dong et al., 1999; Keir et al., 2008; Lin et al., 2008). The PD-L1 protein is composed of 290 amino acids and has a molecular mass of 33 kDa (Dong et al., 1999). It is encoded by the *CD274* gene in both human and mouse and the proportion of shared amino acids between the two species is 69% (Latchman et al., 2001). PD-L1 is expressed on a broad range of cells including haematopoietic (APCs, macrophages, T and B cells) as well as non-haematopoietic cells (epithelial, endothelial cells, cancer cell lineages and others) (Eppihimer et al., 2002; Sharpe and Pauken, 2017). Importantly, its diverse expression sites impact its function, an aspect addressed in more detail in section 1.3.3 (Mueller et al., 2010). PD-L1 binds two different proteins: PD-1 (CD279), most frequently expressed by activated T-cells but also other immune cells, and CD80 (B7.1), expressed by APCs and eventually by activated T and B cells (Butte et al., 2007; Park et al., 2010) (Fig.1-3). Interestingly, PD-L1/CD80 interactions only occur in *cis* on APCs (Chaudhri et al., 2018; Sugiura et al., 2019). This *cis* interaction prevents PD-L1 from binding to PD-1 and therefore mitigates its inhibitory effect on T-cells (Sugiura et al., 2022). It should be noted that CD80 also binds to CD28 and CTLA-4 expressed by T-cells in *trans* (Peach et al., 1995).

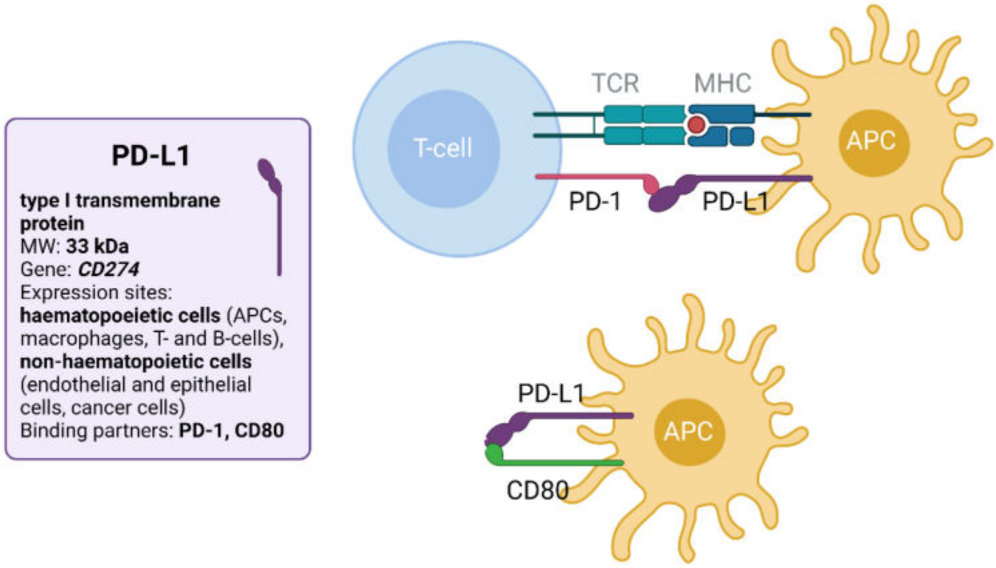

Figure 1 - 3: Basic features and binding partners of PD-L1. PD-L1 expressed on antigen presenting cells (APCs) (or other cell types such as tumour cells) binds to PD-1 expressed on T-cells (or other cell types) as a coinhibitory signal next to major histocompatibility complex (MHC) and T-cell receptor (TCR) binding; PD-L1 expressed on APCs can bind CD80 in cis, i.e. on the same cell. Figure created with Biorender.com.

1.3.2 Mediators of PD-L1 expression

PD-L1 expression is controlled by a complex network of molecular mechanisms including (1) *inflammatory stimuli*, (2) *microbial stimuli*, (3) *genomic aberrations*, (4) *oncogenic signalling*, (5) *microRNA-based control*, and (6) *posttranslational modulation*. For the purpose of this thesis, they have been split into extracellular mediators, including (1) and (2), and intracellular mediators, including (3) to (6), as showcased in Fig.1-4. With a view to the research presented in this thesis, extracellular mediators, which are perceived to play a predominant role in regulating PD-L1 expression during viral infections., will be addressed in greater detail.

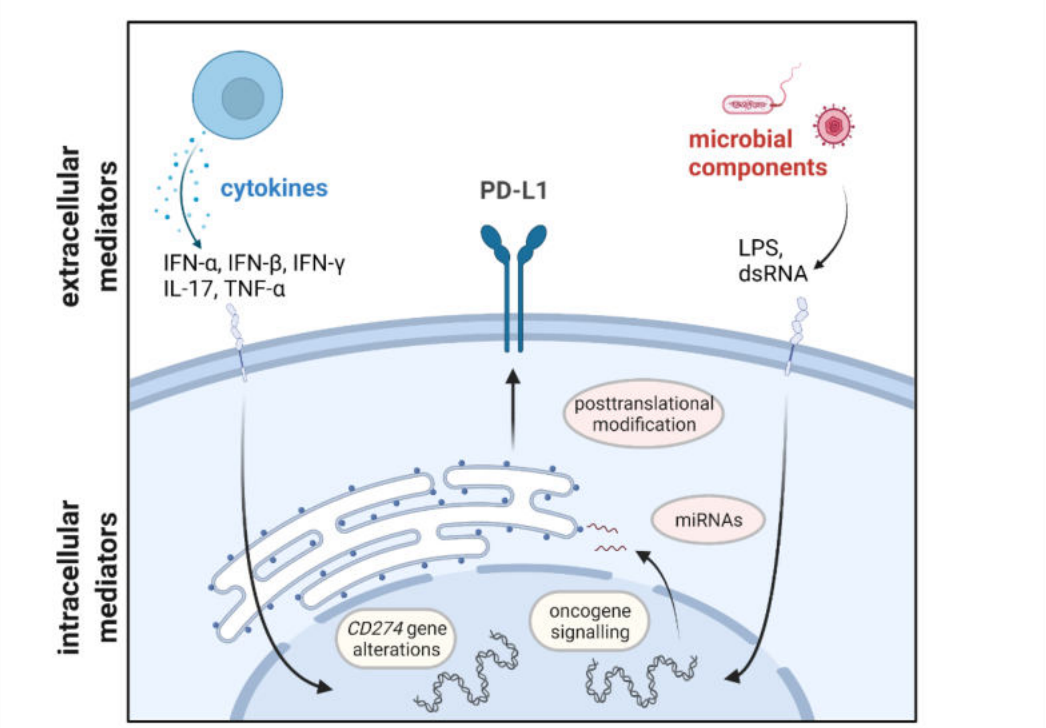

Figure 1 - 4: Mediators of PD-L1 expression. Extracellular mediators include cytokines such as interferon-α (IFN-α), IFN-β, IFN-γ, interleukin-17 (IL-17), tumour necrosis factor-α (TNF-α) and microbial components such as lipopolysaccharide (LPS) and double stranded RNA (dsRNA) which belong to bacteria and viruses respectively; intracellular mediators include CD274 gene alterations, oncogene signalling, micro RNAs (miRNAs) and posttranslational modifications. Figure created with Biorender.com.

As mentioned already, PD-L1 expression is regulated by various extracellular and intracellular mediators. One category of extracellular mediators are *inflammatory stimuli* (1) such as cytokines and a small fraction of chemokines. Cytokines are immune-modulating macromolecules which can be released by several cell types, most importantly immune cells, in response to pathogens or other stimuli. Interferons (IFNs) are one type of cytokines which mediate PD-L1 expression, most notably IFN-γ a pro-inflammatory cytokine (type II IFN) produced by T cells as well as NK cells upon activation (Ivashkiv, 2018). IFN-γ potently upregulates PD-L1 on a variety of cell types, including various tumour types, healthy tissue und immune cells (Brown et al., 2003; de Kleijn et al., 2013; Mazanet and Hughes, 2002). Since IFN-γ is perceived as the most prominent soluble inducer of PD-L1, PD-L1 expression is frequently thought of as a crude measure for local IFN-γ levels *in vivo*. However, it is important to consider that the impact of IFN-γ on PD-L1 expression might be context dependent, e.g. cell type dependent response (Noguchi et al., 2017). Next to IFN-γ, type I IFNs, including IFN-α and IFN-β, also upregulate PD-L1 as evidenced on melanoma cells, endothelial cells, monocytes and DCs (Eppihimer et al., 2002; Garcia-Diaz et al., 2017; Schreiner et al., 2004). Interestingly, type III IFNs, do not impact PD-L1 expression (Garcia-Diaz et al., 2017; Raftery et al., 2018). Other inflammatory stimuli capable of inducing PD-L1 expression involve interleukin (IL)-17 in monocytes, prostate and colon cancer cell lines (Wang et al., 2017; Zhao et al., 2011), tumour necrosis factor-alpha (TNF-α) in endothelial cells, DCs, monocytes and several cancer cell lines (Lim et al., 2016; Mazanet and Hughes, 2002; Ou et al., 2012; Wang et al., 2017; Zhao et al., 2011) and IL-4 in renal cell carcinoma (Quandt et al., 2014). The interleukins, IL-1β, IL-6 and IL-27 collectively induce PD-L1 in DCs (Karakhanova et al., 2010; Kil et al., 2017), while IL-27 also upregulates PD-L1 in ovarian cancer cells (Carbotti et al., 2015). IL-12, a pro-inflammatory cytokine, shows context-dependent effects as it upregulates PD-L1 in endothelial cells and specific macrophage populations but reduces its expression on the THP-1 macrophage cell line (Eppihimer et al., 2002; Xiong et al., 2014). IL-10, an anti-inflammatory cytokine, upregulates PD-L1 in DCs and monocytes (Curiel et al., 2003; Zhao et al., 2011). Interestingly, transforming growth factor-beta (TGF-β), another anti-inflammatory cytokine, seems to have a cell-type dependent effect on PD-L1 expression as exemplified by reduced PD-L1 expression in monocytes and epithelial cells (Ou et al., 2012), but increased expression in DCs following TGF-β exposure *in vitro* (Ni et al., 2012; Song et al., 2014). Several chemokines have also been reported to upregulate PD-L1 expression, including chemokine ligand (CCL) 5 on breast cancer cells (Aboulkheyr Es et al., 2021), C-X-C motif chemokine (CXCL) 5 in several murine and human cancer cells (Li et al., 2019b), CXCL6 in oesophageal squamous cell carcinoma cells (Zheng et al., 2021), CXCL9/10/11 in gastric cancer cells (Zhang et al., 2018). Ongoing and future research might reveal more chemokine candidates as regulators of PD-L1 expression.

Another category of extracellular mediators of PD-L1 expression are *microbial stimuli* (2) comprising of bacterial and viral particles (Fig.1-4). One such example is lipopolysaccharide (LPS), a major surface membrane component of Gram-negative bacteria (Alexander and Rietschel, 2001). *In vitro* treatment studies with LPS have shown increased PD-L1 expression on macrophages, monocytes and bladder cancer cells (Huang et al., 2013; Loke and Allison, 2003; Qian et al., 2008). LPS signals through toll-like receptor 4 (TLR4), a PRR located on the cell surface, which results in the activation of type I IFNs in activated B-cells, possibly explaining the link between LPS and PD-L1 expression (Lu et al., 2008). Furthermore, stimulation of the cytosolic RNA sensor TLR3 via polyinosinic-polycytidylic acid (poly(I:C)), a synthetic dsRNA analogue frequently applied to mimic infections of dsRNA viruses, was shown to upregulate PD-L1 on various cell types, including DCs, endothelial cells and neuroblastoma cells (Boes and Meyer-Wentrup, 2015; Cole et al., 2011; Pulko et al., 2009). Similar to the link between LPS and PD-L1 expression, it remains unclear whether PD-L1 upregulation is directly triggered through TLR3 activation or as a result of collateral effects (i.e. autocrine or paracrine effect). Other viral proteins also induce PD-L1 expression: the human immunodeficiency virus (HIV) Trans-Activator (Tat) protein was shown to upregulate PD-L1 in DCs (Planès et al., 2014) and the hepatitis C virus (HCV) core protein was shown to increase PD-L1 expression in liver macrophages and monocytes (Tu et al., 2010; Zhai et al., 2017). Moreover, the latency-associated transcript (LAT) of HSV-1 was found to upregulate PD-L1 on mouse neuroblastoma cells by a yet unknown mechanism (Chentoufi et al., 2011).

In contrast to the aforementioned extracellular mediators of PD-L1 expression, the expression of PD-L1 is also regulated at several intracellular levels. These include *genetic alterations* (3) of the *CD274* gene via both amplifications and translocations which have been shown to increase PD-L1 levels in several tumour types (Sun et al., 2018). Further, *aberrant oncogenic signalling* (4) might be a driver of PD-L1 expression as a measure of immune evasion to aid tumour outgrowth. Such a relationship was exemplified for the oncogene called *MYC* which contributes to tumourigenesis (Dong et al., 2020). Inactivation of *MYC* has resulted in reduced PD-L1 expression in multiple human and mouse tumour cell models (Atsaves et al., 2017; Casey et al., 2016). Similar effects have also been shown for other oncogenic and pathway mutations which lead to the activation of epidermal growth factor receptor (EGFR) and anaplastic lymphoma kinase (ALK) (Sun et al., 2018). More recently, the role of *micro RNAs* (miRNAs) (5) as regulators of PD-L1 expression has been unveiled: miRNAs act as posttranscriptional regulators of gene expression by inducing target messenger RNA (mRNA) degradation or by inhibiting translation. Their role as regulators of

PD-L1 expression was first highlighted by miR-513 which supresses PD-L1 expression at the level of translation (Gong et al., 2009). *Posttranslational modification* (6) is the final mechanism modulating PD-L1 expression. An example for such regulation is CMTM6 which positively regulates PD-L1 expression, as highlighted across various cell systems (Burr et al., 2017; Mezzadra et al., 2017). After all, the full breadth of mechanisms regulating PD-L1 expression, including novel aspects such as epigenetic control, remain to be completely understood and are addressed in ongoing and future research.

1.3.3 The role of the PD-1/PD-L1 axis in immune homeostasis

The PD-1/PD-L1 axis acts as a key regulator of immune homeostasis. In health, PD-1/PD-L1 interaction is a critical determinant of physiological immune tolerance involved in the modulation of the strength of initial T cell response (Honda et al., 2014), protection from autoimmune diseases (Nishimura et al., 1999; Nishimura et al., 2001) and preservation of foetomaternal tolerance (Guleria et al., 2005). Binding of PD-L1, e.g. expressed on APCs or macrophages, to PD-1 on antigen-stimulated T-cells serves as a potent co-inhibitor of T-cell activation (Chemnitz et al., 2004; Sheppard et al., 2004). As such, it can alter T-cell activity by inhibiting T-cell proliferation, cytokine production and other effector functions (Butte et al., 2007; Chang et al., 1999; Curiel et al., 2003; Dong et al., 1999; Freeman et al., 2000; Keir et al., 2008; Latchman et al., 2004). Sustained presence of antigen such as in chronic infection results in sustained expression of PD-1 on T-cells. Subsequently, continuous engagement of PD-1 by PD-L1 leads to a state of T-cell dysfunctionality, traditionally referred to as ‘exhaustion’, which can culminate in apoptosis or programmed cell death (Sharpe and Pauken, 2017; Wherry and Kurachi, 2015). The role of PD-1/PD-L1 engagement is vastly understood through the effects of checkpoint signalling through PD-1. In contrast, the effects arising from signalling through PD-L1 remain poorly explored, probably owing to the lack of canonical signalling motifs in the cytoplasmic tail of PD-L1. Next to its role in governing immune tolerance the PD-1/PD-L1 axis was found to play a major role in cancer. In contrast, its role during acute infections remains poorly understood.

1.3.4 The role of PD-L1 in cancer

In cancer, PD-L1 expression is exploited as a mechanism of immune evasion. Accordingly, PD-L1 expressing cancer cells bind to PD-1 on activated CD8+ T-cells as a measure to avoid cytotoxic attack (Dong et al., 2002). Furthermore, PD-1/PD-L1 binding contributes towards CD8+ T-cell exhaustion and apoptosis (Iwai et al., 2002), whilst it has also been discovered to convey anti-apoptotic stimuli in tumour cells by a yet unknown mechanism (Azuma et al., 2008). PD-L1 expression renders cancer cells more tumorigenic and invasive *in vivo* (Dong et al., 2018; Iwai et al., 2002). Alongside the inherent expression of PD-L1 in cancer cells, PD-L1 can be upregulated by an inflammatory tumour phenotype such as through increased presence of cytokine-secreting immune effector cells (e.g. IFN released from CD8+ T cells), a concept introduced as adaptive immune resistance (Pardoll, 2012; Ribas, 2015). Regardless of the mechanism of PD-L1 upregulation, therapeutic blockade of either PD-1 or PD-L1 checkpoints leads to tumour control or even tumour remission in several preclinical mouse models of cancer (Dahan et al., 2015; Mosely et al., 2017). Following successful clinical testing of this treatment approach, mAbs targeting the PD-1/PD-L1 axis were clinically approved and are now routinely used to treat non-small cell lung cancer, urothelial carcinoma and advanced stage HNSCC (Bellmunt et al., 2017; Brahmer et al., 2015; Ferris et al., 2016). A more detailed background on its application in HNSCC can be found in section 1.1.3.2. It is important to note that the expression of PD-L1 as assessed via IHC on tumour biopsies serves as a diagnostic marker in some but not all anti-PD-1/PD-L1 responsive cancers (Doroshow et al., 2021). The following section will address this aspect in more detail.

1.3.5 PD-L1 as a predictive biomarker

The utility of tumour PD-L1 expression as a predictive biomarker of response to anti-PD-1/PD-L1 ICB was first observed in the early clinical trials testing the anti-PD-1/PD-L1 checkpoint inhibitors nivolumab and atezolizumab respectively (Herbst et al., 2014; Topalian et al., 2012). Accordingly, higher expression levels of PD-L1 in the tumour were associated with an improved outcome, as observed in patients with non-small cell lung cancer, urothelial carcinoma, HNSCC and other tumour types. Interestingly however, some cancers such as small cell lung cancer, melanoma and hepatocellular carcinoma respond to ICB regardless of PD-L1 status (Doroshow et al., 2021). Therefore, PD-L1 status is considered an imperfect predictive biomarker and approved as a companion diagnostic tool to anti-PD-1/PD-L1 ICB on an individual basis.

In clinical practice, tumour PD-L1 expression is assessed via immunohistochemical staining of tumour biopsy samples which are then scored by a trained histopathologist. To score PD-L1 protein expression, four different parameters have been established including the tumour proportional score (TPS), tumour cells (TC), tumour-infiltrating immune cells (IC) and the combined positivity score (CPS) as listed below (Doroshow et al., 2021).

$$TPS\ (\%) = \frac{Number\ of\ PD-L1\ stained\ tumour\ cells}{Total\ number\ of\ viable\ tumour\ cells} \times 100\%$$

$$TC\ (\%) = \frac{Number\ of\ PD-L1\ stained\ tumour\ cells}{Total\ number\ of\ viable\ tumour\ cells} \times 100\%$$

$$IC\ (\%) = \frac{\substack{Area\ of\ tumour\ infiltrated\ by \\ PD-L1\ stained\ immune\ cells}}{Total\ tumour\ area} \times 100\%$$

$$CPS = \frac{\substack{Number\ of\ PD-L1\ stained\ cells \\ (tumour\ cells, lymphocytes\ and\ macrophages)}}{Total\ number\ of\ viable\ tumour\ cells} \times 100$$

Moreover, several different staining platforms utilising different PD-L1 specific antibody clones have been established, each of which is associated with a specific therapeutic antibody: The Dako 22C3 pharmDx platform is licenced as a companion diagnostic platform for pembrolizumab (anti-PD-1 ICB), the Dako 28-8 pharmDx platform is approved for Nivolumab (anti-PD-1 ICB), the Ventana SP263 for Durvalumab (anti-PD-L1 ICB) and the Ventana SP142 platform is licenced for Atezolizumab (anti-PD-L1 ICB). The following table (Table 1-5) lists diagnostic criteria for ICB patient stratification on a disease-specific basis, following current EMA recommendations (Orellana García et al., 2021).

Tumour type	Disease stage	PD-L1 positivity threshold	Treatment recommendation	Original citation
22C3 pharmDx (Pembrolizumab)				

Non-small cell lung cancer	Metastatic, without EGFR mutations or ALK fusions	TPS ≥50%	Pembrolizumab as a monotherapy	(Mok et al., 2019)
	Locally advanced or metastatic after progression on chemotherapy	TPS ≥1%	Pembrolizumab as a monotherapy	(Herbst et al., 2016)
HNSCC	Metastatic or unresectable, recurrent	CPS ≥1	Pembrolizumab as a monotherapy or in combination with platinum and 5-fluorouracil chemotherapy	(Burtness et al., 2019)
	Recurrent or metastatic, progressing on or after platinum chemotherapy	TPS ≥50%	Pembrolizumab as a monotherapy	(Cohen et al., 2019)
Urothelial carcinoma	Locally advanced or metastatic, cisplatin ineligible	CPS ≥10	Pembrolizumab as a monotherapy	(Balar et al., 2017a; Vuky et al., 2020)
28-8 pharmDx (Nivolumab)				
Non-small cell lung cancer	Metastatic, without EGFR mutations or ALK fusions	TC ≥1%	Nivolumab alone or in combination with ipilimumab (anti-CTLA-4)	(Hellmann et al., 2019)
Ventana SP142 (Atezolizumab)				
Urothelial carcinoma	Locally advanced or metastatic, cisplatin ineligible	IC ≥5%	Atezolizumab as a monotherapy	(Balar et al., 2017b)
Triple-negative breast cancer	Unresectable, locally advanced or metastatic, chemotherapy-naive	IC ≥1%	Atezolizumab in combination with nab-paclitaxel	(Schmid et al., 2018)
Ventana SP263 (Durvalumab)				
Non-small cell lung cancer	Locally advanced or unresectable, no progression upon platinum-based chemo-radiation therapy	TC ≥1%	Durvalumab as a monotherapy	(Antonia et al., 2017)

Table 1 - 5: PD-L1 immunohistochemistry platforms which obtained clinical approval as companion diagnostic assays to PD-1/PD-L1 ICB listed for different tumour types and immune checkpoint inhibitors. IC denotes tumour-infiltrating immune cells, TC tumour cells, TPS tumour proportional score, CPS combined positivity score, EGFR epidermal growth factor receptor, ALK anaplastic lymphoma kinase, CTLA-4 cytotoxic T-lymphocyte antigen-4 and nab-paclitaxel nanoparticle albumin bound-paclitaxel.

Although PD-L1 IHC has now become a routine diagnostic procedure to stratify patients for anti-PD-1/PD-L1 ICB, its application imposes several limitations: First and foremost, the four diagnostic platforms in use differ in sensitivity raising issues of inter-assay heterogeneity (Rimm et al., 2017). Secondly, the application of four different semi-quantitative scores and varying positivity cut-offs lead to major discrepancies in reporting practices (Brahmer et al., 2015; Reck et al., 2016; Rittmeyer et al., 2017). Thirdly, the outcome of these semi-quantitative scores highly depends on the interpreting pathologist (inter-observer heterogeneity), eventually representing a greater source of error than the variation between different assay platforms (Brunnström et al., 2017). The aforementioned variables raise the need for standardisation among staining platforms (including antibody clones), PD-L1 scoring systems and the evaluation process to determine PD-L1 positivity. The latter might particularly benefit from digital pathology solutions and automated image analysis. In addition to the aforementioned limitations, other shortcomings inherent to biopsy based IHC such as its poor representative value in capturing intratumoural heterogeneity and inability to address dynamic expression behaviour should be considered. In an effort to overcome these shortcomings alternative diagnostic approaches to determine PD-L1 expression (within the tumour and beyond) are currently being investigated. These include qPCR to quantify PD-L1 mRNA expression in tissue biopsy specimen as a method to overcome inter-observer variability (Erber et al., 2017) or liquid biopsies to capture the burden of PD-L1 expressing tumour cells in the circulation allowing for repeated sampling and overcoming inter-observer variability (Boffa et al., 2017; Kloten et al., 2019). Moreover, *in vivo* molecular imaging techniques such as positron emission tomography are currently investigated as tools to determine PD-L1 expression across several systemic organs (e.g. primary tumour, metastatic lesions, lymph nodes) (Bensch et al., 2018; Verhoeff et al., 2020). Recent advances of PD-L1 immunoPET are discussed in great detail in the introduction to chapter 4 (4.1) whilst a general overview on the imaging modality is provided in the introduction subchapter 1.4.

1.3.6 The role of PD-L1 during acute viral infection

Viruses are capable of upregulating PD-L1 on haematopoietic and non-haematopoietic cells through PRR signalling. Moreover, PD-L1 expression is mediated by a myriad of pro- and anti-inflammatory signals released over the course of a viral immune response (Sun et al., 2018). This section connects these aspects in the context of the early phase of viral infection, thus providing a foundation for the understanding of the PD-L1 dynamics in response to oncolytic viruses.

In the early phase of virus infection, virus-infected tissues release type I and type III IFNs as a first line measure of antiviral defence (Galani et al., 2017; Lazear et al., 2019). However, only type I IFNs, including IFN-α and IFN-β, but not type III IFNs are capable of PD-L1 upregulation (Garcia-Diaz et al., 2017; Raftery et al., 2018). Type I IFNs additionally improve the cytotoxicity of NK cells and the activity of antiviral cytotoxic CD8+ T-cells thus enhancing an antiviral response (Aichele et al., 2006; Biron et al., 2002; Kolumam et al., 2005). Moreover, the direct upregulation of PD-L1 following the recognition of viral particles through TLRs and the activation of subsequent signalling might also contribute towards an increase of PD-L1 in virus-infected tissue and APCs likewise (Boes and Meyer-Wentrup, 2015; Cole et al., 2011; Pulko et al., 2009). In fact, increased expression of PD-L1 on APCs in this early phase of infection is speculated to be an important measure to fine-tune the activation CD8+ T effector cells and avoid overstimulation. The latter role is further supported by the stimulatory impact of PD-L1 expressing APCs on T regulatory cells which act to confine antiviral responses and prevent an overreaching response (Francisco et al., 2009; Veiga-Parga et al., 2013). Remarkably, the selective lack of PD-L1 on haematopoietic cells results in lethal pathology upon viral infection (Mueller et al., 2010).

In the later phase of an acute virus infection immune cells release IFN-γ, a type II IFN, and other cytokines such as TNF-α and IL-10 (Zhang and Bevan, 2011). IFN-γ strongly upregulates PD-L1 across multiple cell types (Garcia-Diaz et al., 2017; Raftery et al., 2018). In addition, a subpopulation of APCs, so-called plasmacytoid DCs, migrate into virus-infected tissue and secrete large amounts of type I IFNs (Siegal et al., 1999). Apart from their antiviral capacity, type I IFNs also drive an inflammatory response and the secretion of TNF-α, IL-1β and IL-6 (Davidson et al., 2015). The latter can further increase PD-L1 expression and promote virus elimination (Sun et al., 2018). Alongside the changes of PD-L1, the coinhibitory receptor PD-1 is rapidly upregulated on virus-specific T cells upon recognition of viral antigen (Ahn et al., 2018). Schönrich and Raftery suggest that in the late phase of acute viral infection, PD-L1 is strongly upregulated as a measure to mitigate terminal differentiation of CD8+ T-cells. Ultimately, PD-1/PD-L1 binding might prevent excessive tissue damage due to uncontrolled cytotoxic attack by virus-specific T-cells (Schönrich and Raftery, 2019). In contrast, there is no clear evidence supporting the role of PD-L1 expressed by virus infected cells as a mechanism of escape from antiviral immune effector cells through PD-1/PD-L1 triggered co-inhibition.

1.4 Immuno-positron emission tomography

Immuno-positron emission tomography (immunoPET) is a molecular imaging approach combining the high sensitivity of PET with the superior target specificity of antibodies or antibody-derivatives (e.g. antibody fragments, protein scaffolds) as vectors for radioisotopes (Reddy and Robinson, 2010; Wei et al., 2020). As such it provides a non-invasive approach to monitor and quantify the expression of extracellular targets at a systemic level *in vivo*. ImmunoPET plays an increasingly important role in cancer diagnosis as well as treatment selection and monitoring. This chapter will focus on the principles of PET and PET image analysis methods, as well as antibody-based immunoPET agents (defined as PET radioconjugates).

1.4.1 Principles of PET

PET is a molecular imaging technique which relies on the unique characteristics of positron emitting radionuclides. The decay characteristics of these radionuclides allow to track the location of a radiolabelled targeting vector and infer on the expression and the metabolic status of a distinct biological target via PET *in situ*. Therefore, PET as an imaging modality can provide spatial and functional information about the extracellular target of interest and allows for signal quantification *in vivo*. The following paragraphs will address the basic physics of PET including positron emission, positron-electron annihilation, image acquisition and reconstruction, as well as signal quantification.

1.4.1.1 Positron emission and positron-electron annihilation

An uncharged atom with a stable nucleus contains an even number of positively charged protons (and neutrons) and negatively charged electrons in its nucleus and the nucleus periphery respectively (Fig.1-5). Radioisotopes however, have unstable nuclei, either via an excess of protons or neutrons, and therefore undergo radioactive decay in order to reach stability (Phelps and Los Alamos National, 1988). If a nucleus carries an excessive number of protons, it most commonly decays via positron emission (also known as β^+ or beta-plus decay) (Anderson, 1932). These positrons are emitted at a range of energies, from zero up to a maximum endpoint energy ($E_{\beta+\max}$), which is specific to each radionuclide. Proton-rich nuclei can also decay via electron capture which can further lead to the emission of x-rays or gamma-rays (Phelps and Los Alamos National, 1988). Frequently, the two decay modes co-exist, hence the introduction of the positron yield which indicates the fraction of positron emission of the total emission spectrum.

Following positron emission, the positron has a very short lifetime in electron-rich matter such as tissue. Over this short period, it loses kinetic energy via interactions with atomic electrons in the tissue. The distance made is called the positron range ($R_{\beta+\text{mean}}$) and is dependent on the energy of the emitted positron ($E_{\beta+\text{mean}}$) (Levin and Hoffman, 1999). Once most of the positron's energy is lost, it combines with an electron and both particles annihilate. Through positron-electron annihilation the mass of both particles is converted into electromagnetic energy (Phelps and Los Alamos National, 1988). This energy is released via the simultaneous emission of two photons in opposite directions (~180° angle) with an energy of 511 keV. The positron-electron annihilation event and the subsequent emission of two photons is at the heart of PET image acquisition, which will be described in the following section.

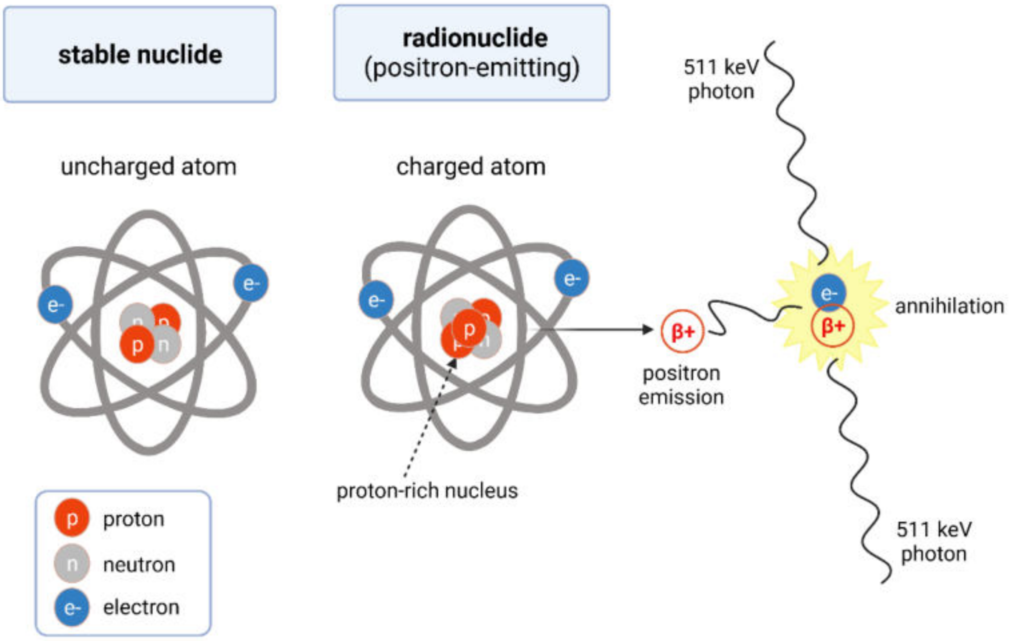

Figure 1 - 5: Schematic of a stable nuclide vs. an unstable, proton-rich radionuclide. Proton-rich radionuclides tend to emit positrons (β+) which, after travelling a short distance in surrounding matter, annihilate with an electron (e-) causing the emission of two simultaneous photons in opposite direction. Figure created with Biorender.com.

1.4.1.2 Image acquisition, reconstruction and registration

PET image acquisition relies on the coincident detection of the 511 keV photon pair emitted from the positron-electron annihilation (Phelps et al., 1975; Ter-Pogossian et al., 1975). Accordingly, the 511 keV photons are recorded as coincident events by opposing elements of the PET camera, whilst allowing for a coincidence time window within the nanosecond range (Fig.1-6). To capture a maximum range of events, the PET camera elements (e.g. scintillation detectors) are most-commonly arranged in ring configuration (Turkington, 2001). Following detection by a scintillation detector coupled to a photo-multiplier tube, the photon is converted into an electrical signal which is then fed into the subsequent electronics (amplifiers, pulse height analysers, high voltage) and a coincidence circuit (Phelps and Los Alamos National, 1988). The geometric orientation of truly coincident events allows to back-trace the origin of annihilation along a so-called line of response (LOR) which is the basis of PET image reconstruction. However, the recorded events also contain a number of undesirable events including random, scattered and multiple coincidences which are excluded at image reconstruction (Shukla and Kumar, 2006). The reconstruction process itself uses mathematical algorithms (e.g. filtered back projection, maximum likelihood expectation-maximisation) and produces a three-dimensional (3D) image volume, where the signal intensity in each voxel is proportional to the amount of radioactivity in the same voxel (Tong et al., 2010). However, it is important to consider that the 511 keV annihilation photons eventually attenuate via the interaction with surrounding tissue, i.e. via Compton scattering and the photoelectric effect (absorption) (Phelps and Los Alamos National, 1988). Photon attenuation depends on tissue density and is therefore specific to each tissue type. In order to account for this effect, a so-called attenuation correction based on a PET attenuation estimation is incorporated in the image reconstruction algorithm. Such attenuation estimation can either be derived from a transmission scan (~511 keV) acquired with the PET camera or from a CT scan (~40-140 keV) in case of PET/CT hybrid instrumentation (Kinahan et al., 1998). In the latter case however, accurate spatial alignment of PET and CT scans at image (co-)registration is required. In PET/CT, and any other dual-modality imaging approach, spatial correspondence between the voxels of two scans taken at different times, from different viewpoints, and/or by different sensors has to be determined in a process referred to as image (co-) registration. Hybrid PET/CT scanners enable sequential image acquisition within narrow time windows with the subject of investigation remaining on the same bed, infinitely enabling a fixed and known coordinate transformation between the images produced (Cherry, 2009). At software level however, the images arising from the two modalities need to be registered which can be achieved via two different approaches: (i) *rigid body transformation* for steady structures (e.g. brain) or (ii) *non-rigid body transformation* for moving structures (e.g. heart, intestine, bladder) (Fox et al., 2008). So-called similarity measures between the modalities have to be defined in order to establish a registration algorithm and may include landmark measures (e.g. fiducial markers placed on the head or skin) or surface and edge markers (usually defined via automated or manual segmentation). Discrepancies in PET/CT image co-registration most frequently arise from organ movement through respiration or peristalsis (Vogel et al., 2007). More details on the subject of image registration in PET/CT can be found elsewhere (Fox et al., 2008). After all, co-registration of functional (PET) and anatomical (CT) images allows to map the spatial distribution and accurately detect radiolabelled vectors in a living subject and measure radioactivity quantitatively. The application of PET without CT lacks the anatomical information required to locate the radiolabelled vector, a requisite for the use of ^{18}F-FDG in tumour staging (Fueger et al., 2009). Furthermore, radiotracer distribution can be visualised and radioactive uptake measured over time via sequential (dynamic) image acquisitions (Muzi et al., 2012).

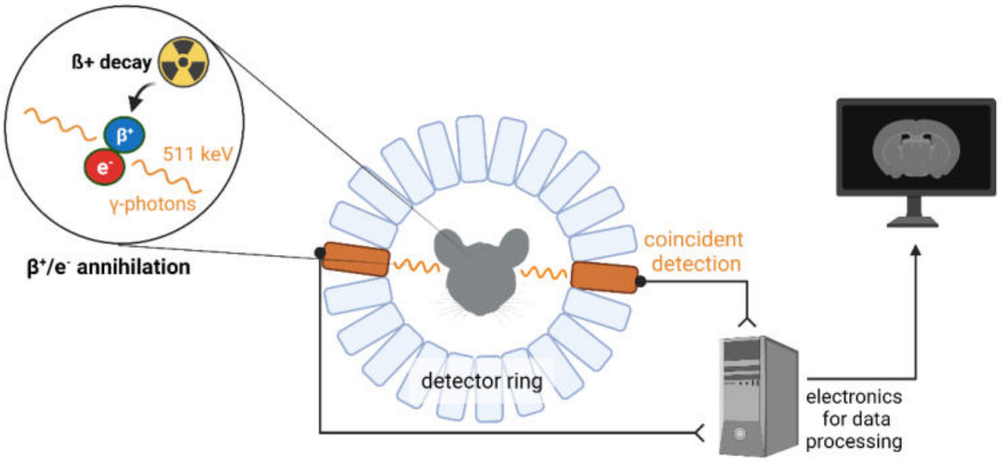

Figure 1 - 6: The principles of PET in a nutshell. Following electron-positron annihilation two 511 keV photons are emitted at a ~180° angle; these photons are then detected as coincident events by opposing elements of the PET camera (configured as a detector ring) and converted into an electrical signal which is further used for image reconstruction. Figure created with Biorender.com.

1.4.1.3 PET resolution, sensitivity and recent advances

Spatial resolution in PET is determined by distinct properties of the PET scanner (detector size), the decay characteristics of the radioisotope (positron range) as well as the annihilation event itself (non-colinearity): (i) The size of the scintillation detectors used in a PET system determines the intrinsic resolution of the scanner, i.e. detectors larger in size achieve higher resolution. (ii) The positron range of a radioisotope determines the distance between ß+ emission and the annihilation event, thus leading to higher resolution in radioisotopes with low positron range, i.e. low energy at emission. (iii) Non-colinearity arises from the deviation of the two annihilation photons from the exact 180° position, a phenomenon that occurs due to the positron having a small residual momentum when the annihilation happens (Saha, 2005). The effects of non-colinearity deteriorate with increasing distance between the detectors. The current resolution limit in small animal PET scanners reaches around 1.0 mm (Spinks et al., 2014; Visser et al., 2009), whilst clinical scanners have a resolution limit of roughly 3.5-5.0 mm (Demir et al., 2018; Moses, 2011).

PET outperforms other clinically approved nuclear imaging techniques in terms of sensitivity, e.g. single photon imaging including SPECT (Adonai et al., 2002). In general, instrument sensitivity is determined by the number of photons counted per unit radioactivity within one second (e.g. counts per second (cps) per megabecquerel (MBq) or cps/MBq). Conventional PET scanners (axial field of view ~0.2 m) have instrument sensitivities between 10-15 kcps/MBq, which is approximately 1 to 2 magnitudes higher than in single photon emission systems (Gambhir, 2002). However, recent technological advances have tremendously improved SPECT system sensitivity. These advances include (i) detectors made of material with enhanced photon-sensitivity (e.g. cadmium-zinc-telluride (CZT) crystals as compared to conventional sodium iodine (NaI)) (Ito et al., 2021) and (ii) the arrangement of multiple detector heads in a fixed location (e.g. ring coordination as used for PET scanners) rather than fewer detector heads attached to a rotating gantry (Wacholz et al., 2020; Yamada et al., 2021). So far, cardiac imaging has profited most from these SPECT advances, but other clinical indications might soon catch up (Abbott et al., 2018).

While most clinical PET systems have a relatively narrow axial field of view (~0.2 m), a recently developed total-body PET scanner (EXPLORER® PET scanner) has an axial extension of 2 metres (Badawi et al., 2019). The scanner is characterised by a tremendous improvement in sensitivity (by a factor of 40 for total-body imaging or a factor of 4-5 for single organs) due to the total-body coverage and an increased solid angle for detection at any point within the body resulting in unprecedented count density (Cherry et al., 2018). For the acquisition of state-of-the-art diagnostic PET images very small amounts of activity and short acquisition times suffice. For instance, a total-body ^{18}F-FDG scan in the EXPLORER® PET scanner requires 9.25 MBq (vs. 370 MBq for a conventional PET scanner) and the acquisition can be completed in 15-30 s (vs. 10- to 20-min total-body protocols in a conventional PET scanner). Taken together, these advances significantly reduce the radiation burden for the patient.

Another recent development in PET investigates the simultaneous use of two or more radioisotopes with different emission characteristics, also referred to as multiple-isotope (MI) PET (Fukuchi et al., 2017). Accordingly, MI-PET may be performed with a pure positron emitter (such as ^{18}F) in combination with a radioisotope that emits prompt high-energy gamma rays along with the positrons (such as Copper-60, ^{60}Cu) (Andreyev et al., 2014). The discrimination of radioisotopes is achieved by combining the PET camera with gamma detectors for the high-energy prompt gamma rays (Fukuchi et al., 2017). MI-PET acquisitions are therefore based on the simultaneous acquisition of double (two annihilation photons) and triple (two annihilation photons and a prompt gamma ray) coincidence events, making use of prompt gamma rays with energies characteristic to each radioisotope.

1.4.1.4 Quantification of radioactive uptake in PET imaging

As mentioned in the previous section, PET allows for the quantification of radioactive uptake based on the principle that the signal intensity in each voxel is proportional to the amount of radioactivity in the same voxel. To assess static radioactive uptake in a defined volume of interest (VOI) of the PET image several methods have been described (Hoekstra et al., 2000). The most widely applied measure is the standardised uptake value (SUV). The SUV is a (semi-) quantitative index for the radioactive uptake measured within a defined VOI (c_{VOI} – radioactivity per volume, e.g. MBq/mL) normalised against the injected radioactivity (*ID* - injected dose, e.g. MBq) per subject weight (BW - body weight, e.g. mL) and is calculated based on the following formula (Lucignani et al., 2004):

$$SUV\ (t) = \frac{c_{VOI}(t)}{{ID(t)}/{BW}}$$

Importantly, the injected dose is decay-corrected to the time (*t*) of the PET acquisition in order to match the time of the VOI-based uptake measurement. Additionally, for the SUV calculation it is widely assumed that the average mass density of body tissue corresponds to 1 g/mL. This mass density conversion relies on the high proportion of water in most body organs, however disregards tissue of different composition such as bone. Several derivatives of the SUV exist including the SUV_{max}, SUV_{peak} and SUV_{mean} and have been widely used to assess ^{18}F-FDG uptake in cancerous lesions in the clinical set-up (Sher et al., 2016). The most widely applied measure is the SUV_{max}, indicating the SUV of the hottest (most tracer-avid) voxel within a VOI. The SUV_{peak} is the average SUV within a fixed-size VOI usually centred on a region of high tracer uptake. The SUV_{mean} is the SUV of the mean average of all voxels within a VOI. Each of the three SUV values has their own advantages and disadvantages. For instance, the SUV_{max} has the advantage of being easy to apply and operator independent but is relatively sensitive to noise (Boellaard et al., 2004). The SUV_{peak}, which provides increased robustness towards noise, is dependent on the choice of VOI and therefore it is subject to operator-dependent variability (Krak et al., 2005; Vanderhoek et al., 2012). Similar to the SUV_{peak}, the SUV_{mean} is robust towards noise but suffers from poor reproducibility due to its dependency on the choice of VOI (Krak et al., 2005). All SUV values are dependent on the instrumentation and reconstruction methods used imposing a challenge of reproducibility, which raises the need for standardisation (e.g. multi-center clinical trials) (Ziai et al., 2016).

Preclinically, radioactive uptake is frequently expressed as the percentage injected dose per gram (%ID/g) or as the percentage injected dose per mL (%ID/mL) respectively. Both uptake measures mirror the radioactive uptake assessed by *ex vivo* biodistribution studies. To obtain the %ID/mL for a distinct organ, the uptake in a VOI defining the organ is measured computationally (c_{VOI} - radioactivity per volume, e.g. MBq/mL), normalised against the decay-corrected injected dose (ID, e.g. MBq) and then multiplied by 100 as shown in the following equation:

$$\% ID/mL\,(t) = \frac{c_{VOI}(t)}{ID\,(t)} \times 100$$

The tissue density is assumed as 1 g/mL, and all radioactivity measures are decay-corrected for the same time point t. VOI-based quantification of tracer uptake on PET images has become a well-established method in both the clinical and preclinical setting.

1.4.2. Radioconjugates for immunoPET

As mentioned previously, immunoPET employs antibodies or their derivatives (e.g. antibody fragments or protein scaffolds) as targeting moieties for radioconjugates (RCs). Each antibody, antibody fragment or protein scaffold binds one specific target and once labelled with a PET-compatible radioisotope, can be used to trace target expression via PET *in vivo*. In order to select an immunoPET targeting moiety which matches the characteristics of the target antigen, it is key to understand the basic features of full-length antibodies and know the range of smaller-sized constructs. Therefore, a detailed overview on the properties of full-length antibodies will be provided and a selection of antibody-based fragments and derivatives will be presented in the following subchapters (1.4.2.1 and 1.4.2.2). In addition, the most commonly used PET-radioisotopes for antibody radiolabelling including some short-lived radioisotopes will be discussed (1.4.2.3). Finally, basic considerations around the choice of chelator and aspects of the radiochemical labelling/conjugation procedure will be addressed (1.4.2.4).

1.4.2.1 Antibodies

Following on from rapid clinical approval of several monoclonal antibodies (mAbs) of the immunoglobulin G (IgG) isotype for therapeutic use, the molecular imaging field has started adopting mAbs as targeting moieties for RCs, especially in the field of cancer imaging (Mestel, 2017). Antibodies of the IgG isotype provide specific features making them attractive targeting agents, including high inherent target specificity and affinity and a serum half-life spanning from several days up to a few weeks (Fig.1-8). On the contrary, due to their relatively high molecular weight (~150 kDa), they penetrate tissue inefficiently (e.g. solid tumours) and frequently accumulate in healthy organs, including the liver and the spleen.

In mammals four other Ig isotypes exist including IgM, IgE, IgA and IgD (Fig. 1-7) (Janeway, 2001). The five Ig isotypes vary in their heavy chain structure determining the difference in effector functions *in vivo*. The basic structural characteristics and antigen binding capacity is relatively similar across all isotypes. While IgD, IgE and IgG exist as monomers and have similar molecular weight (IgD ~184 kDa, IgE ~188 kDa, IgG ~150 kDa), IgA and IgM form dimers and pentamers respectively, which significantly increases their molecular weight (IgA ~390 kDa, IgM ~970 kDa) (Fig.1-7). IgG itself has four subtypes in humans (IgG1, IgG2, IgG3 and IgG4) which are highly homologous, but differ in their constant region, particularly in their hinges. The latter influences their capacity to affect the host immune system via binding FcγR or C1q (as explained in a subsequent paragraph). IgG1, IgG2 and IgG4 have similar molecular mass and serum half-lives (MW ~146 kDa, $t_{1/2}$ ~21 d) as compared to IgG3 (MW ~165 kDa, $t_{1/2}$ ~7 d) (Janeway, 2001). The characteristics of the IgG molecule including high target specificity and affinity, a relatively low molecular mass matched with a long serum half-life as compared to other isotypes, make it a favourable candidate for diagnostic and therapeutic antigen targeting. These advantages also apply for its role as a PET imaging vector and explains its supremacy over other immunoglobulin isotypes. Nevertheless, other Ig isotypes (e.g. IgE, IgM) have occasionally been used as targeting vectors in imaging studies, however with the aim to study immunoglobulin biodistribution during pathologies such as cancer or inflammation rather than exploring their capacity as a diagnostic tool (Man et al., 2021; Oyen et al., 1996). Of note, due to their relevance as an imaging vector in my project and to ease communication, IgGs will be referred to as *antibodies* throughout the thesis.

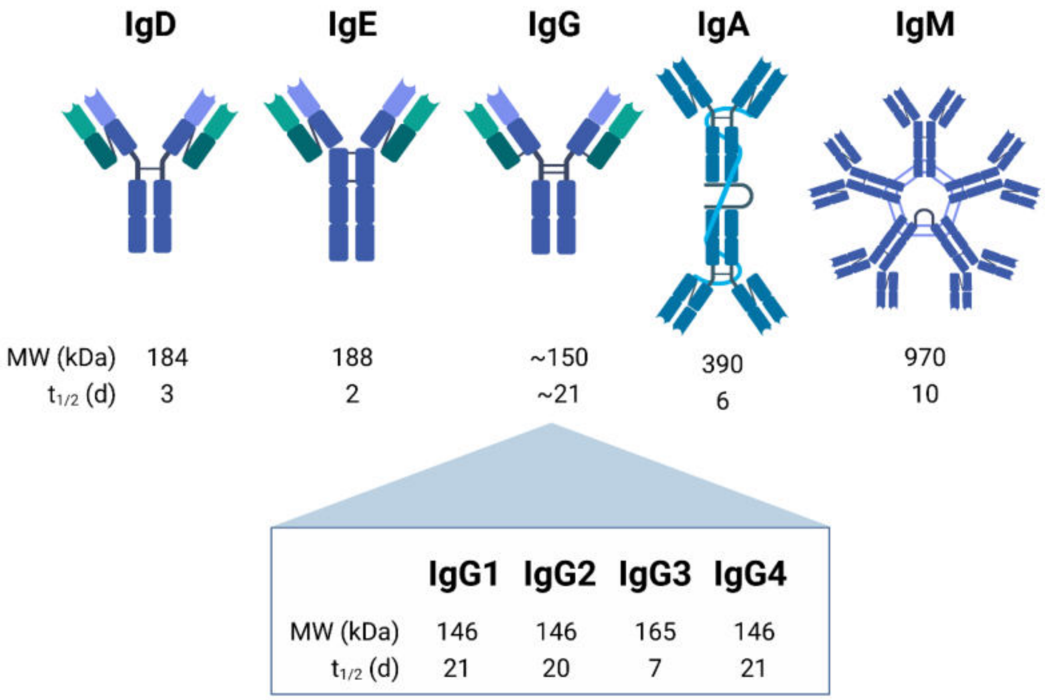

	IgD	IgE	IgG	IgA	IgM
MW (kDa)	184	188	~150	390	970
$t_{1/2}$ (d)	3	2	~21	6	10

	IgG1	IgG2	IgG3	IgG4
MW (kDa)	146	146	165	146
$t_{1/2}$ (d)	21	20	7	21

Figure 1 - 7: Immunoglobulin (Ig) isotypes D ,E, G, A and M and IgG subclasses IgG1, IgG2, IgG3 and IgG4 listed with the corresponding molecular weight (MW) and serum half-life ($t_{1/2}$) (Janeway, 2001). Figure created with Biorender.com.

IgGs are Y-shaped macromolecules which consist of two identical pairs of heavy and light chains linked by disulphide bonds (Fig.1-8) (Janeway, 2001). The two arms of the Y-shaped molecule constitute the antigen-binding fragment (F_{ab}) which includes the variable fragment (F_v) comprised of both a variable heavy chain (V_H) and a variable light chain (V_L). The antigen specificity of a full-length antibody is dictated by the six complementary determining regions (CDRs) located within its F_v domain, three out of six in both chains, the V_H and the V_L. The F_v domains are therefore the key component for therapeutic (e.g. target blockade) and diagnostic (e.g. target detection) antibody exploitation. The stem region of the Y is known as the crystallisable fragment (F_c) and is formed by constant heavy chain (C_H) domains only. This region accounts for antibody binding to Fc-receptors (e.g. Fc gamma receptor, FcγR and neonatal Fc receptor, FcRn) and proteins of the complement system (e.g.C1q protein) (Chan and Carter, 2010). The role of Fc-mediated binding will be discussed later in this section.

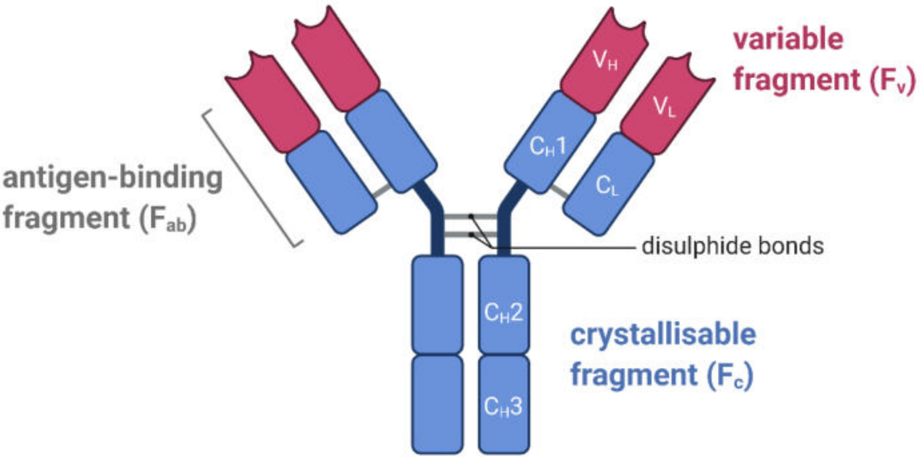

Figure 1 - 8: Simplified representation of IgG structure. Variable light chain (V_L), variable heavy chain (V_H), constant heavy chain (C_H) domains 1-3, crystallisable fragment (F_c), variable fragment (F_v), antigen-binding fragment (F_{ab}). Figure created with Biorender.com.

It is assumed that exogenous antibodies and antibody-RCs follow the same pharmacokinetic behaviour as observed with endogenous antibodies. Upon systemic delivery, antibodies exhibit a biphasic pharmacokinetic profile, a fast distribution phase is followed by a slow elimination phase (Lobo et al., 2004). This profile is driven by the interaction between antibodies and their binding partners (antigen, Fc-receptors). The systemic distribution of intravenously delivered antibodies is usually confined to the vascular system and interstitial space due to their molecular weight and polarity (Lobo et al., 2004). The process of antibody extravasation into the interstitial space is inefficient and happens via diffusion, whereby antibodies cross the endothelial cell membranes lining the blood vessels via convective transport through paracellular pores (Glassman et al., 2015). Antibody diffusion rates are influenced by the antibody`s target affinity and specificity, target internalisation rate, antibody hydrophilicity and charge, and tissue-specific features such as blood flow and membrane structure (Boswell et al., 2010; Deng et al., 2012; Rudnick and Adams, 2009). The latter imposes an advantage for tissue with naturally fenestrated vessels, such as the spleen, the liver and bone marrow, as well as tissue with pathologically 'leaky' vasculature, such as tumours (Tabrizi et al., 2010; Wang et al., 2008). In the case of solid tumours this effect can culminate in the so-called enhanced permeability and retention

(EPR) effect, which has been described as a major driver for non-specific accumulation of systemically administered (macro)molecules in solid tumour masses (Matsumura and Maeda, 1986; Yasunaga et al., 2017). The distribution of antibodies within tumour masses is very slow and happens via diffusion and convection (antibody diffusion coefficient ~1.3 × 10^{-8} cm^2/s) (Brown et al., 2004). Additionally, antibody movement within tumours is further hindered by the interstitial fluid pressure (IFP) and the binding site barrier (Fujimori et al., 1990; Jain, 1990; Jain and Baxter, 1988; Juweid et al., 1992). High IFP is a phenomenon observed across many solid tumours owing to vessel abnormalities, fibrosis and contraction of the ECM (Heldin et al., 2004). High IFP imposes strong physical resistance and can therefore significantly hamper macromolecule movement in tumours. The binding site barrier presents resistance of biochemical nature and limits tumour penetration, particularly of antibodies exhibiting high target affinity. Accordingly, high-affinity antibodies tend to bind targets in very close proximity to the point of extravasation, thus impairing further penetration into the tumour stroma (Fujimori et al., 1990; Juweid et al., 1992). Rudnick *et al* and Glatt *et al* have demonstrated that antibodies with lower target affinity overcome this issue but low target affinity might in return compromise target specificity (Glatt et al., 2016; Rudnick et al., 2011). An alternative approach to overcome the binding site barrier is to increase the dose of injected antibody, to aid target saturation across the whole tumour (Vivier et al., 2018). In molecular imaging, this is frequently achieved via co-injection of unlabelled antibody (Lu et al., 2020). Another component affecting intratumoural antibody distribution is tumour vascularisation and the heterogeneous vascular density as compared to healthy organs (Welti et al., 2013).

Antibodies exhibit an extended serum half-life ($t_{1/2}$=7-21 days in humans, IgG isotype-dependent) due to their slow systemic clearance via intracellular proteolytic degradation rather than glomerular filtration (kidney MWCO ~55 kDa) (Lobo et al., 2004). There are three distinct mechanisms leading to antibody degradation: (i) *target mediated disposition* (TMD) which occurs upon antibody-antigen binding via the F_{ab} portion, (ii) *receptor-mediated endocytosis* via FcγR expressed by macrophages located in the liver (Kupffer cells) or macrophages belonging to the reticuloendothelial system (RES), or (iii) *non-specific fluid phase endocytosis* by vascular endothelial cells. In addition, the extended half-life is owed to the role of FcRn. FcRn can be expressed by a variety of cells (e.g. endothelial cells, hepatocytes, macrophages) and binds to the C_H2-C_H3 domains within the antibody Fc portion (Roopenian and Akilesh, 2007). Once bound to FcRn, the antibody is internalised where it is protected from intracellular lysosomal degradation, followed by translocation to the cell surface where it is released back to the extracellular space or vessel lumen.

Whilst the predominant effector mechanism of antibodies is target-mediated (e.g. receptor blockade or modulation), several other non-target-mediated effects can occur. For example, immune effector cells (NK cells, macrophages) expressing FcγRs become activated upon antibody-FcγR binding and attack surrounding (tumour) tissue, an effect called antibody-dependent cellular cytotoxicity (ADCC) (Clynes et al., 2000; Nimmerjahn and Ravetch, 2008). Similar effects occur via antibody-binding to the complement protein C1q, referred to as complement protein-dependent cytotoxicity (CDC). It is important to note that the affinity towards Fc-receptors (FcγR and FcRn) varies depending on the IgG isotype, allowing to select the isotype which best fits the purpose (Nimmerjahn and Ravetch, 2012).

In summary, antibodies exhibit distinct features (high target specificity and affinity and an extended serum half-life) which render them very attractive targeting moieties for PET RCs but are inefficient in their capability to penetrate tissue which might limit their diagnostic flexibility *in vivo*. As an alternative to antibodies, there is a range of smaller-sized options for targeting moieties including antibody fragments and derivatives.

1.4.2.2 Antibody fragments and derivatives

Molecular engineering techniques and enzymatic digestion procedures have facilitated the production of antibody fragments and derivatives which retain antigen specificity and affinity of the original antibody through the preservation of antigen-binding elements, e.g. F_{ab}, F_v domains (Wu, 2014). Due to their reduced molecular weight, these fragments exhibit faster kinetics *in vivo* (MWCO of the kidney ~55 kDa) which are additionally enhanced through the loss of FcRn binding sites. It is important to note that faster systemic clearance can significantly reduce tumour uptake (Adams et al., 2001). Furthermore, the lack of FcγR binding sites reduces eventual immune-mediated effector functions encountered with full-length antibodies. The absence of such effector functions facilitate the use of antibody fragments for diagnostic purposes. A selection of such antibody fragments will be presented hereafter (Fig.1-9).

The two Fab variants *Fab'* (~55 kDa) or *(Fab')$_2$* (~110 kDa) are both enzymatically derived antibody fragments in which the Fc region has been removed (Lütje et al., 2015). The bivalent (Fab')$_2$ is cleared through the liver, the monovalent Fab' fragment can be excreted via the renal route. In contrast to Fab', (Fab')$_2$ retains the capability to bind the target bivalently which can significantly improve overall target affinity but also induce effector functions (e.g. target cross-linking, inducing activation, signalling and internalisation) (Wu, 2014).

The *single-chain antibody variable fragment (scFv)* molecule (~25 kDa) is a smaller-sized example for an antibody fragment, comprised of the V_H and V_L domains of an antibody (Ahmad et al., 2012). The two domains are joined together by a short peptide linker. It is important to note that scFvs represent the basic building blocks of antibody engineering and are used to construct a wide range of antibody-based structures, e.g. minibodies and diabodies (Hudson and Souriau, 2003; Wu, 2014).

Minibodies (80 kDa) and *diabodies* (55 kDa) are constructed from scFvs to provide larger, bivalent single-chain formats. Their reduced molecular weight facilitates rapid antigen targeting and faster systemic clearance as compared to full-length antibodies (Hu et al., 1996; Sundaresan et al., 2003). Accordingly, high contrast images can be acquired within 21 h or 4 h upon injection of radiolabelled minibodies or diabodies respectively. A CD8-targeted minibody radiolabelled with ^{89}Zr (^{89}Zr-Df-IAB22M2C) has recently been tested clinically and has shown promising lesion-targeting capability rendering it the first immunoPET agent to assess the abundance of CD8+ T lymphocytes in solid tumours (Pandit-Taskar et al., 2020).

Single domain antibodies (sdAbs), more commonly referred to as *nanobodies,* are derived from camelid heavy chain-only antibodies (Hamers-Casterman et al., 1993). They are considered the smallest antigen-binding fragments (<15 kDa) with the potential of an antigen affinity and specificity comparable to a full-length antibody (De Vos et al., 2013). High contrast PET images can be acquired within less than an hour after delivery of the radiolabelled nanobody. Several preclinical and early clinical PET imaging studies employing nanobodies as targeting moieties have reported promising results (Keyaerts et al., 2016; Krasniqi et al., 2017).

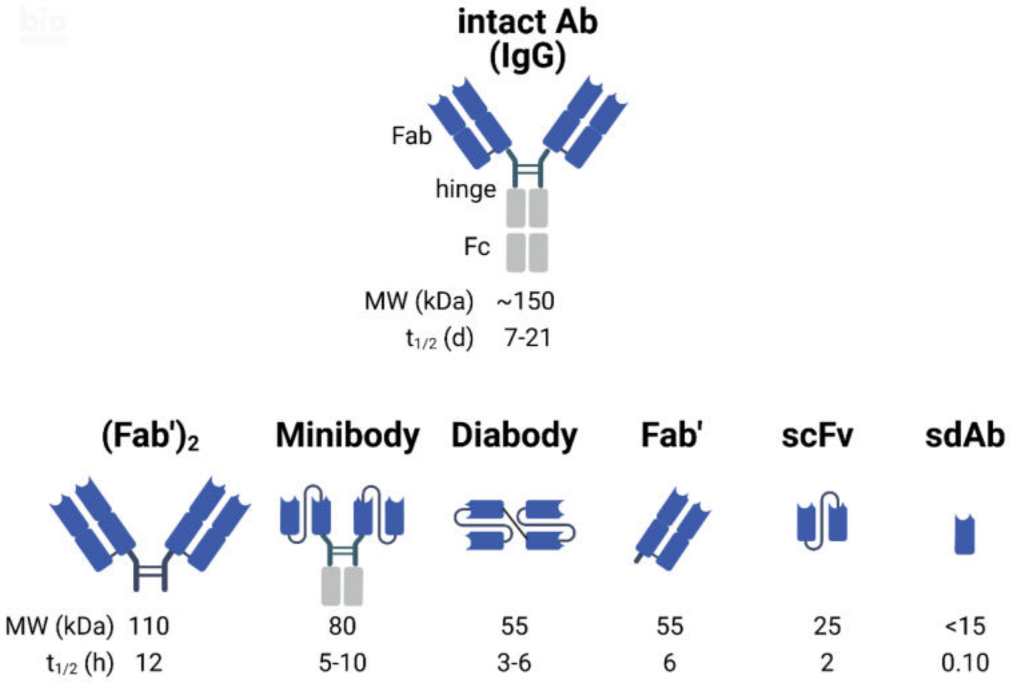

Figure 1 - 9: Selection of antibody-based targeting moieties suited for immunoPET use; antibody (Ab), immunoglobulin G (IgG), antibody-binding fragment (Fab), crystallisable fragment (Fc), single-chain antibody variable fragment (scFv) single domain antibody (sdAb), molecular weight (MW) and circulation half-life ($t_{1/2}$) are listed below each structure and have been derived from the following sources (Holliger and Hudson, 2005; Janeway, 2001; Wu, 2014). Figure created with Biorender.com.

1.4.2.3 PET radioisotopes

The slow kinetics of antibody-based RCs (tumour penetration and systemic clearance) require late imaging time points (>24 h after injection) which go beyond the limits of the most frequently used PET radioisotope, Fluorine-18 ($t_{1/2}$=1.8 h). Therefore, long-lived radioisotopes including Zirconium-89 ($t_{1/2}$=78.4 h), Iodine-124 ($t_{1/2}$=100.2 h) and Copper-64 ($t_{1/2}$=12.7 h) are usually used for antibody radiolabelling purposes (Vivier et al., 2018). Next to the physical decay half-life, each radioisotope has several other characteristics which should be taken into consideration at radioisotope selection. These include the positron yield, the energy of the positron at emission ($E_{\beta+\mathrm{mean}}$), the positron range in tissue ($R_{\beta+\mathrm{mean}}$), as well as the occurrence of other modes of radioactive decay (e.g. electron capture) and the possible emission of gamma-rays (whereby only radiation with abundance >5% is addressed). Considering these characteristics plus the commercial availability, three PET radioisotopes suited for antibody-labelling will be presented (Table 1-6). Furthermore, Fluorine-18 and Gallium-68 will be described as the two, most commonly used short-lived PET radioisotopes for labelling of antibody fragments and derivatives.

Zirconium-89 (^{89}Zr) is a cyclotron produced radioisotope that has a physical decay half-life of 3.27 d which makes it an attractive candidate for antibody-radiolabelling exhibiting a similar serum half-life and slow tissue penetration (Severin et al., 2011). Furthermore, the physical half-life is long enough for national and international isotope shipment to locations that do not have direct access to a cyclotron. However, the positron yield of ^{89}Zr is suboptimal as only 23% of its decay proceeds via positron emission and 77% via electron capture (Fig.1-10). The resulting decay radiations include the 511 keV gamma-rays from positron annihilation and 909 keV gamma-rays arising from intermediate (decay) states (Dilworth and Pascu, 2018). The high energy gamma-rays can incur a substantial radiation burden to systemic organs, especially during extended exposure due to slow tissue clearance as observed with ^{89}Zr-labelled antibodies (Börjesson et al., 2009; Pandit-Taskar et al., 2014). An advantageous aspect of the emitted positron is the relatively low endpoint energy ($E_{\beta+max}$=902 keV) and the consequent short positron range ($R_{\beta+mean}$=1.2 mm), that ultimately allow for high resolution PET images. Of note, additional details on ^{89}Zr with a particular focus on antibody-radiolabelling are provided in the subsequent section (1.4.2.4) and the introduction to chapter 4 (4.1).

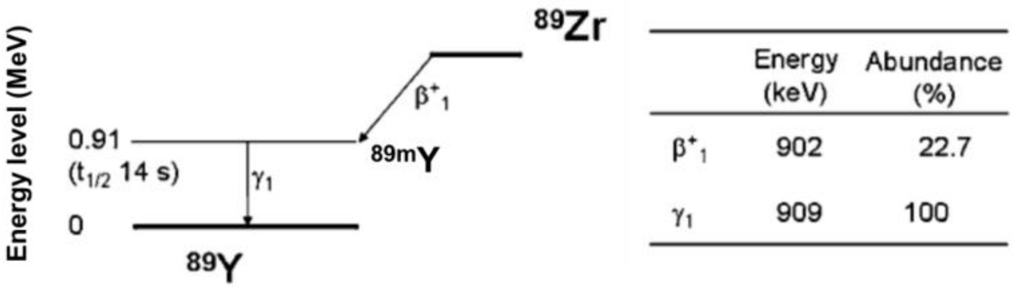

	Energy (keV)	Abundance (%)
β^+_1	902	22.7
γ_1	909	100

Figure 1 - 10: Simplified decay scheme for Zirconium-89. ^{89}Zr decays by positron emission (23%) and electron capture (e.c., 77%), both decay modes lead to an intermediate state (^{89m}Y) which eventually de-excites via the emission of a high-energy gamma ray (909 keV) to ground state ^{89}Y, energy for positrons/gamma rays is shown as maximum energy. Scheme adapted from Lubberink et Herzog (Lubberink and Herzog, 2011).

Iodine-124 (^{124}I) is a cyclotron produced radioisotope that has a decay half-life of 4.18 d and a complex decay profile with dual energy emission: beta radiation emissions ($E_{\beta+max}$) of 1535 keV (12%) and 2138 keV (11%) and gamma emissions ($E_{\gamma+max}$ of the most relevant ones only) of 723 keV (10%), 603 keV (63%), and 1691 keV (11%) (Fig.1-11) (Lubberink and Herzog, 2011). Due to these physical properties, ^{124}I can be used for both imaging and therapy. For its use in PET, several aspects should be considered: firstly, ^{124}I has a low positron yield (23%); secondly, the high positron emission energy and long positron range in tissue ($R_{\beta+mean}$~3.4 mm) affect image resolution; and thirdly, the 603 keV gamma-rays (arising from intermediate decay states) fall into the energy window of most PET scanners, causing prompt gamma coincidences which significantly increase the measured background in images (Herzog et al., 2002). When introduced in the body, ^{124}I, like any iodine anion, accumulates in the thyroid gland. As a consequence, most ^{124}I-labelled agents are characterised by high radioactive uptake in the thyroid gland (following metabolic deiodination of the radioactive compound) thus imposing a dosimetric burden to this organ and limiting the use of ^{124}I probes in head and neck cancer imaging.

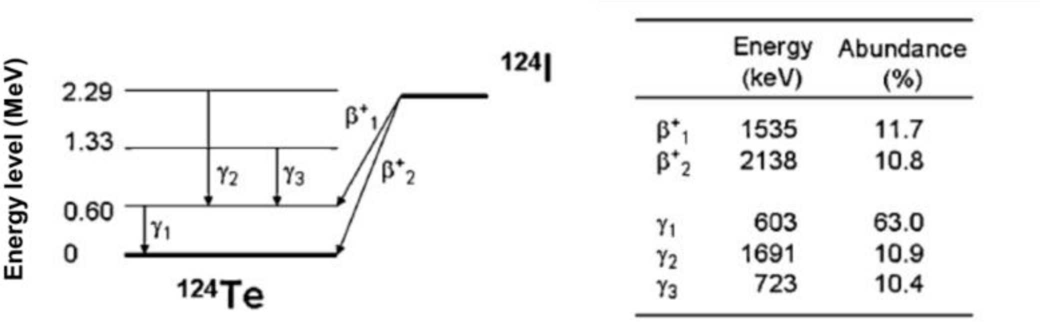

	Energy (keV)	Abundance (%)
β^+_1	1535	11.7
β^+_2	2138	10.8
γ_1	603	63.0
γ_2	1691	10.9
γ_3	723	10.4

Figure 1 - 11: Simplified ^{124}I decay scheme showing its decay via the emission of positrons (at two energy levels β^+_1 and β^+_2) and gamma rays (at two different energy levels γ_2 and γ_3). Both decay modes lead to an intermediate state which eventually de-excites via the emission of gamma rays (γ_1) to ground state ^{124}Te. The emission energy shown for positrons (and gamma rays) is maximum energy. Scheme adapted from Lubberink et Herzog (Lubberink and Herzog, 2011).

Copper-64 (^{64}Cu) is a cyclotron produced radiometal which decays by several modes including β^+ emission (17.8%), electron capture (43.8%) and β^- emission (38.4%) offering the option to be used for both diagnostic and therapeutic purposes (Fig.1-12) (Gutfilen et al., 2018). Due to its physical decay half-life of 12.7 h, it can be used as a label for both smaller antibody fragments and full-length antibodies (Anderson and Ferdani, 2009). Furthermore, its half-life of almost 13 h allows for radioisotope shipment to locations that have no direct access to a cyclotron. Positrons emitted by ^{64}Cu have a favourable endpoint energy ($E_{\beta+max}$) of 653 keV, facilitating high-resolution PET images. Different from other radiometals used in nuclear medicine (e.g. ^{89}Zr, ^{68}Ga), ^{64}Cu has correspondent non-radioactive and naturally occurring isotopes which are essential for biochemical cellular processes. In fact, copper is an essential microelement involved in cellular homeostasis, iron transport, respiration and metabolism (Bartnicka and Blower, 2018; Niculae et al., 2021).

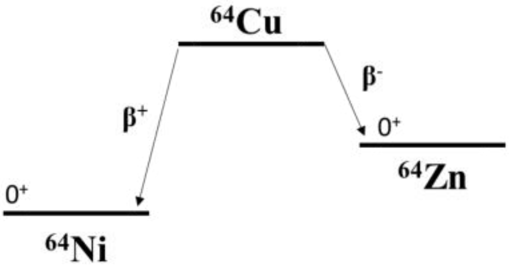

	Energy (keV)	Abundance (%)
β^+	653	17.8
β^-	573	38.4

Figure 1 - 12: Simplified scheme of ^{64}Cu showing its decay via β^+ emission to stable ^{64}Ni and β^- emission to ^{64}Zn. Energy emission energy shown for positrons is maximum energy. Scheme adapted from Be et al (Bé et al., 2012).

Fluorine-18 (^{18}F) is cyclotron produced and is the most widely used PET-radioisotope owing to the use of fluorinated radiopharmaceuticals such as in ^{18}F-FDG for cancer imaging (Jacobson et al., 2015). Due to the following physical characteristics, ^{18}F can be considered an almost perfect PET-radioisotope: it has a short physical half-life ($t_{1/2}$=1.8 h) which is long enough to perform synthesis and imaging over a few hours and short enough to minimize the overall radiation burden; it is characterised by a high positron yield of 97% and the emitted positrons have a short positron range of 0.6 mm owing to the relatively low energy at emission ($E_{\beta+max}$=634 keV) (Fig.1-13). These characteristics allow for PET images with high effective resolution as compared to other radioisotopes. When covalently attached to molecules (e.g. radiofluorinated small molecules), ^{18}F is generally a non-residualising label. However, if introduced for example as part of a complex with aluminium ion (i.e. ^{18}F-AlF), the label shows residualising properties, i.e. accumulation of the radioactive label in cells upon internalisation (Zhou et al., 2021). Finally, 18-Fluoride ($^{18}F^-$), similarly to $^{89}Zr^{4+}$, is a bone-seeker and therefore tends to accumulate in bone tissue *in vivo*.

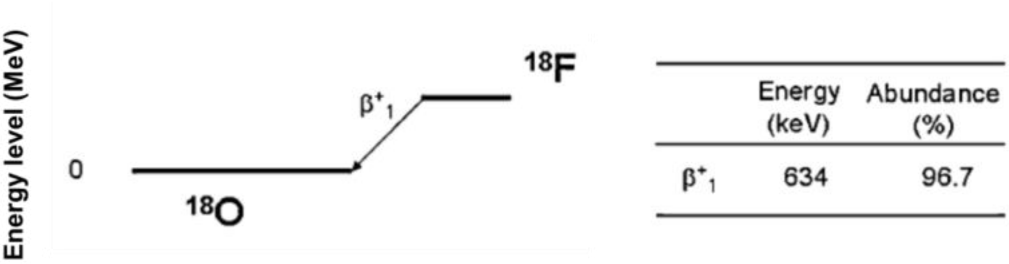

	Energy (keV)	Abundance (%)
β^+_1	634	96.7

Figure 1 - 13: Simplified ^{18}F decay scheme. ^{18}F decays via positron emission at ~97% converting into ^{18}O. Energy shown for positrons is maximum energy. Scheme adapted from Lubberink et Herzog (Lubberink and Herzog, 2011).

Gallium-68 (^{68}Ga) is a generator produced radioisotope with a half-life of 1.1 h (Pagani et al., 1997). The positron yield of ^{68}G is 88% and the emitted positrons are characterised by high energy ($E_{\beta+max}$=1899 keV) and long tissue range ($R_{\beta+mean}$=3.4 mm), thus negatively affecting PET image resolution which is particularly relevant in high resolution preclinical systems (resolution limits ≤1 mm) (Fig.1-14).

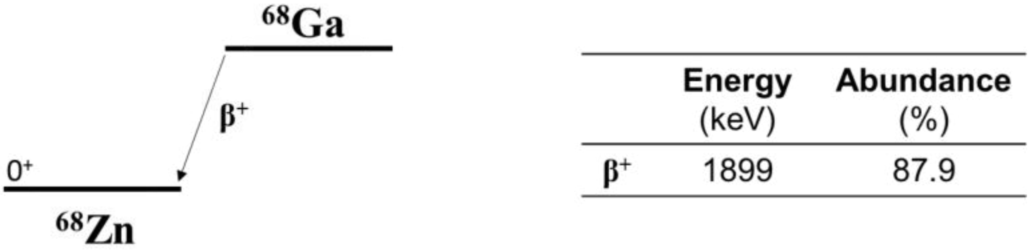

	Energy (keV)	Abundance (%)
β^+	1899	87.9

Figure 1 - 14: Simplified ^{68}Ga decay scheme. ^{68}Ga emits mostly positrons in order to reach stability as ^{68}Zn. Positron energy shown as maximum energy. Scheme based on Marganiec et al (Marganiec-Gałązka et al., 2018).

radionuclide	radioactive half-life (h)	positron yield (%)	max/mean positron energy (keV)	mean positron range (mm)	gamma radiation (keV)	other considerations
Fluorine-18	1.8	97	634/250	0.6	-	most common, cyclotron
Gallium-68	1.1	89	1899/830	3.4	-	generator - produced
Copper-64	12.7	17	653/216	0.6	-	also β^-, Auger electrons
Zirconium-89	78.4	23	902/396	1.2	909	

Iodine-124	100.2	12 11	1535/826 2138/826	~3.4	603 1691 723

Table 1 - 6: Properties of positron-emitting radionuclides commonly used for labelling antibodies and their fragments/derivatives.

The selection of an adequate targeting molecule together with a suitable radiolabel and radiolabelling procedure is very important for the design of radioimmunoconjugates for PET imaging. Some basic aspects around chelator choice and radiolabelling strategies are addressed in the following section.

1.4.2.4 Choice of chelator and radiolabelling strategies

For PET imaging, proteins including antibodies and their fragments are frequently labelled with radiometals such as long-lived ^{89}Zr and ^{64}Cu, short-lived ^{68}Ga or the short-lived radiohalogen ^{18}F (using prosthetic groups or in the form of ^{18}F-AlF) (Boros and Packard, 2019). The introduction of a radiometal is achieved via a bifunctional chelator (BFC) consisting of a metal binding moiety and a chemically reactive functional group that allows coupling to the protein (Fig.1-15a) (Chomet et al., 2021). Ideally, chelating agents are attached in a stable manner and should not affect the protein's integrity, target recognition capability (e.g. target specificity, immunoreactivity), and pharmacokinetic behaviour. Both the BFC conjugation and the following radiolabelling should be performed using the mildest conditions possible (e.g. room temperature and 4-9 pH range) aiming to preserve protein integrity.

Full-length antibodies are mainly modified by random conjugation to lysine residues that are distributed throughout the whole protein. The higher the lysine density and availability outside the antigen binding region, the lower is the chance to perturb the immunoreactivity. However, the attachment of an average of one or two chelators per antibody can generally be achieved without affecting its target recognition (Perk et al., 2010; Sharma et al., 2021). In the case of smaller proteins such as antibody fragments or nanobodies, such random conjugation approach is not ideal. More recently, alternative strategies like site-specific conjugation procedures have been proposed. By controlling the location of the modification on the protein, site-specific conjugation has the advantage to produce consistent and homogenous products. However, it requires the artificial introduction of specific functional groups into the protein structure (e.g. cysteine residues, non-canonical amino acids, tags), which is easier to achieve for small proteins than for full-length antibodies. Therefore, such molecularly engineered antibodies with specific conjugation sites are still not widely accessible (Behrens and Liu, 2014; Park et al., 2021). Alternatively, coupling at the antibody interchain cysteine residues has been proposed as a type of site-specific reaction but it can generate heterogeneous products and requires a chemical pre-treatment of the protein (i.e. reduction of disulphide bonds) prior to the attachment of the BFC (Park et al., 2021).

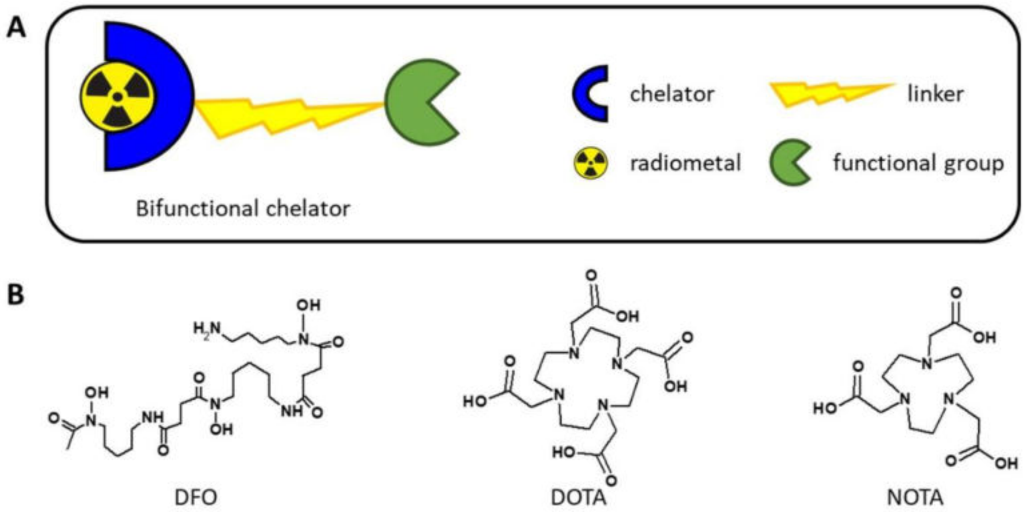

Figure 1 - 15: A. Schematic representation of a bifunctional chelator showing a metal chelating part and a functional group, for the coupling to a protein, connected by a linker. B. Molecular structures of the most commonly used chelators for ^{89}*Zr (i.e. desferrioxamine, DFO), for* ^{64}*Cu and* ^{68}*Ga (i.e. 1,4,7,10-tetraazacyclododecane-N,N',N'',N'''-tetraacetic acid, DOTA and 1,4,7 triazacyclononane-1,4,7 triacetic acid NOTA) and for the* ^{18}*F-AlF complex.*

For the radiolabelling of full-length antibodies (or other proteins with extended biological half-life such as minibodies) with ^{89}Zr, desferrioxamine (DFO) is the most commonly used chelator (Fig.1-15b). DFO is commercially available in bifunctional forms (i.e. DFO-isothiocyanate and DFO-maleimide) and the conjugation and radiolabelling procedures are performed under mild conditions (i.e. room temperature) and have been studied extensively (Vosjan et al., 2010; Zeglis and Lewis, 2015). During the conjugation procedure DFO forms stable linkages with the lysine residues of antibodies (Perk et al., 2010). The chelator coordinates ^{89}Zr using six atoms and the two remaining sites on the metal centre are occupied by molecules of water. Importantly, this type of coordination configuration cannot warrant an optimal stabilisation of the ^{89}Zr-complex. Consequently, variable degrees of demetallation have been observed in rodent models *in vivo* as indicated by the uptake of free ^{89}Zr in the bones (Abou et al., 2011). For this reason, various research groups are focusing on the development of new chelators that could warrant an increased stabilisation of the ^{89}Zr complex (Bhatt et al., 2018). Amongst the alternatives, a couple of promising octadentate bifunctional chelators (i.e. DFO* and HOPO) are available nowadays (Deri et al., 2014; Patra et al., 2014). However, because of factors such as high lipophilicity (which could influence the protein pharmacokinetics) or a costly production due to the lengthy and low yielding synthesis, their accessibility is still limited. Consequently, DFO remains the chelator of choice for ^{89}Zr despite its limitations.

A non-metal alternative for antibody labelling is the positron-emitting radioiodine ^{124}I. Proteins can be directly labelled with ^{124}I by reacting the generated, positive iodine species (I^+) with tyrosine and to a lesser extend histidine residues in the protein (Kumar and Ghosh, 2021). The reaction is usually performed under mild conditions (room temperature, pH~7), however the protein may be damaged during this process (Salacinski et al., 1979). A variety of alternative approaches for ^{124}I-labelling of proteins exist is described in greater detail by Kumar *et* Ghosh (Kumar and Ghosh, 2021).

Antibody fragments such as Fabs and scFvs and other proteins with a medium to short biological half-life can be radiolabelled with ^{64}Cu. Macrocyclic chelators with six coordinating atoms can form stable complexes with the radiometal (Shokeen and Wadas, 2011). Examples of such chelators are 1,4,7,10-tetraazacyclododecane-N,N′,N″,N‴-tetraacetic acid (DOTA) and 1,4,7 triazacyclononane-1,4,7 triacetic acid (NOTA) (Fig.1-15b). Studies showed that, once injected *in vivo*, the ^{64}Cu-DOTA complex has low stability resulting in the premature dissociation of the radiometal. Additionally, the tranchelation of ^{64}Cu from ^{64}Cu-DOTA to liver enzymes such as superoxide dismutase has been observed (Frindel et al., 2017). A more promising chelator alternative to DOTA is NOTA which showed improved *in vivo* stability together with a fast radiolabelling procedure using mild conditions (i.e. room temperature to 40°C) (Price and Orvig, 2014; Zhang et al., 2011).

Short-lived ^{68}Ga and ^{18}F are usually used for the radiolabelling of proteins with a short biological half-life like nanobodies. Macrocyclic chelators such as DOTA and NOTA can form very stable complexes with ^{68}Ga (Fig.1-15b) (Price and Orvig, 2014). Whilst DOTA requires high reaction temperatures (i.e. 90-95°C), NOTA allows radiolabelling at lower temperatures (i.e. room temperature to 40°C). Based on the formation of a very strong bond with the aluminium ion, ^{18}F is often used to radiolabel proteins in the form of the ^{18}F-AlF complex (D'Souza et al., 2011). Stable complexes can be achieved using macrocyclic chelators such as NOTA (and its derivative NODA) (Fig.1-15b) in a short reaction time (approximately 15 min) at high temperatures (approximately 100°C). Although ^{68}Ga and ^{18}F have very short physical half-lives, which are incompatible with the long biological half-life of full-length antibodies, recent research has investigated alternative strategies such as pre-targeting approaches (Evans et al., 2014; Meyer et al., 2016). These are comprised of two major steps: firstly, a functionalised antibody is injected *in vivo* and allowed to bind systemic targets; secondly a small ^{68}Ga- or ^{18}F-radiolabelled reactive molecule is injected to specifically tag the functionalised antibody. Free excess of the reactive molecule is rapidly cleared from circulation. A major advantage of this strategy is the use of short-lived radioisotopes which reduces the radiation burden and enables shorter imaging time frames.

1.5 Hypothesis and aims

The work presented in this thesis is aimed to address the following hypothesis: An oncolytic virus-triggered upregulation of PD-L1 goes beyond tumour-associated cell compartments and exhibits a dynamic behaviour. The following aims were defined to address the main hypothesis as part of aim 4. Each aim was dedicated a separate results chapter in this thesis.

Aim 1: Characterisation and modification of PD-L1 levels in syngeneic mouse tumour models of head and neck squamous cell carcinoma.

Aim 2: Characterisation of ^{89}Zr-DFO-PD-L1$_{mAb}$ binding *in vitro* and pharmacokinetic characterisation and dose optimisation for PD-L1 immunoPET imaging in syngeneic mouse tumour models *in vivo.*

Aim 3: *In vitro* testing of the novel oHSV RP1 on MOC1 and MOC2 cells and follow-up investigations to assess the impact of intratumoural injections of RP1 on tumours *in vivo* (therapy, perfusion).

Aim 4: Applying PD-L1 immunoPET to monitor PD-L1 expression upon intratumoural RP1 injection into MOC1 tumours with follow-up analyses including immunohistochemistry and cytokine analyses. Additionally, flow cytometry and combination therapy studies were used to better understand and eventually exploit the previous finding therapeutically.

Chapter 2: Materials and methods

2.1 Cell culture

2.1.1 Cell lines and culture media

Murine oral carcinoma cell lines, MOC1 and MOC2, were a kind gift of Dr. Ravindra Uppaluri (Dana-Farber Cancer Institute, MA, USA). The murine lung epithelium cell line TC-1 and the squamous carcinoma cell line SCC7 were a kind gift of Prof. Tzyy-Choou Wu (Johns Hopkins University, MD, USA) and Dr. Richard Vile (Mayo Clinic, MN, USA) respectively. CT26 murine colon carcinoma cells and the murine macrophage cell line RAW264.7 were kindly provided by Dr. Esther Arwert (Medicinal Chemistry 3 Team, ICR, UK) and Prof. Molly Stevens (Imperial College London, UK) respectively. The Vero cell line which is derived from an African green monkey kidney was provided by Dr. Shane Foo (Translational Immunotherapy, ICR, UK). Human embryonic kidney (HEK) 293T cells were obtained from Gary Box (Pharma and Stress Response Team, ICR, UK) and were used for production of lentiviral particles. All cell lines were cultured in DMEM medium with GlutaMAX™ (#31966, Thermo Fisher Scientific Inc, MA, USA) supplemented with 10% heat-inactivated foetal bovine serum (FBS) (#10500064, Thermo Fisher Scientific) or RPMI 1640 with GlutaMAX™ (#61870036, Thermo Fisher Scientific) supplemented with 10% FBS, as detailed in table 2-1.

Name	Culture medium	Species	Initial passage no	Source	Original citation
MOC1	DMEM	Mouse	NA	Ravindra Uppaluri	(Judd et al., 2012b)
MOC2	DMEM	Mouse	NA	Ravindra Uppaluri	(Judd et al., 2012b)
SCC7	DMEM	Mouse	NA	Richard Vile	(Hirst et al., 1982)
TC-1	DMEM	Mouse	NA	T.C. Wu	(Lin et al., 1996)
HEK293T	DMEM	Human	p2	Gary Box	(Graham et al., 1977)
RAW264.7	RPMI	Mouse	NA	Molly Stevens	NA
VERO	DMEM	African green monkey	NA	Shane Foo	(Simizu and Terasima, 1988)
CT26	DMEM	Mouse	NA	Esther Arwert	(Brattain et al., 1980)

Table 2 - 1: Cell lines used in this thesis with additional information. NA denotes not available.

2.1.2 Propagation of cell lines in culture

All cells were grown in Nunc™ cell culture flasks (Thermo Fisher Scientific) and kept in a sterilised humidified chamber at 37°C and 5% CO_2 whilst in culture. To ensure sterility throughout the period of culture, all interventions were carried out in an ultraviolet (UV)-irradiated laminar flow Class II hood. Cells were split on a regular basis, i.e. 2-3 times per week, depending on the individual growth rate. For splitting, culture media was removed, the cell monolayer was gently washed with PBS (#10010023, Thermo Fisher Scientific) and then incubated with TryplE™ Express Enzyme solution (#12605010, Thermo Fisher Scientific) in the incubator at 37°C. Once dissociated, cells were collected into a 15 mL conical tube. To ensure high yields at collection, the flask was washed with culture medium once. The cell suspension was spun down (290 RCF, 3-5 min, 21°C) and the supernatant removed. The cell pellet was then resuspended in 1 mL of culture medium and seeded at a cell line-dependent ratio into a flask filled with fresh culture medium. All reagents were warmed up to 37°C in a clean water bath prior to splitting. Cell lines were kept in culture for no more than 12 passages after thawing.

2.1.3 Cell counting

Cultured cells were collected following enzymatic dissociation as previously described (2.1.2) and resuspended in culture medium to reach a volume of 1 mL. An aliquot of 10 µL per chamber was loaded onto the Neubauer improved haemocytometer (#13444890, Thermo Fisher Scientific) and the number of cells manually counted under the microscope (three to four squares per chamber). If required, the cell suspension was diluted prior to counting. The concentration of cells in one chamber was calculated using the following formula:

$$\frac{cells}{ml} = counted\ cells\ \times dilution\ factor\ \times 10^4 \times \frac{1}{counted\ squares}$$

2.1.4 Cryopreservation of cell lines

For long-term storage, cells were collected at 80-90% confluency, washed with PBS (pH 7.4) once and resuspended in a mixture of pure culture medium (DMEM or RPMI; 0.2 mL per 1 mL mix), heat-inactivated FBS (0.7 mL per 1 mL mix) and dimethyl sulfoxide (0.1 mL per 1 mL mix; #D2650, Sigma-Aldrich, MO, USA). 0.5-1 mL aliquots of cell suspension were transferred into cryovials (#375418, Thermo Fisher Scientific) and placed in a Mr. Frosty™ Freezing Container (#5100-0001, Thermo Fisher Scientific). The freezing container filled with isopropanol was stored at -80°C to ensure gradual cooling (-1°C/min) for a minimum of 24 h, whereupon the vials were transferred to a liquid nitrogen depository for long-term storage.

2.1.5 Authenticity and mycoplasma negativity of cell lines

Mycoplasma negativity was routinely confirmed via polymerase chain reaction (PCR) on DNA extracts from each cell line (Surrey Diagnostics, UK). To confirm authenticity of MOC1 and MOC2 cells, short tandem repeat (STR) profiling was performed on DNA extracted from these cell lines (IDEXX BioAnalytics, DE). DNA was extracted from a cell pellet of ~1×10^6 cells in sterile PBS using the DNeasy Blood & Tissue Kit (#69504, Qiagen, NL).

2.1.6 Plasmid quality control

The *pLenti-CD274-mGFP* plasmid carrying the murine *CD274* gene tagged with a monomeric green fluorescent protein (mGFP) reporter also known as mTagGFP or TagGFP2 (#MR 203953L2, OriGene Technologies Inc, MD, USA) (Fig.3-6a) was dissolved in sterile water to reach 0.1 µg/µL and authenticity confirmed via a diagnostic digest, using AsiSI and MluI restriction enzymes (both New England Biolabs, MA, USA). Accordingly, the plasmid was mixed with restriction enzymes (0.5 µL per 1 µg of plasmid each) in CutSmart® buffer (10x; #B72045, New England Biolabs) and incubated at 37°C for 90 min. The digest was stopped via sample storage at 4°C, 40 min. Samples were then mixed with a gel loading dye (6x; #B7024S, New England Biolabs) and loaded onto an agarose gel (1%) supplemented with GelGreen Nucleic Acid Stain (10,000x; #41005; Biotium, CA, USA) and the gel electrophoresis run. Bands were then visualised on an UV transilluminator. Of note, Li *et al* have shown that PD-L1 expression is similar across different plasmids expressing PD-L1 with or without a reporter system, including GFP (Li et al., 2016).

2.1.7 Cell engineering of MOC2 cells

The MOC2*(PD-L1)* cell line was generated by lentiviral transduction of *CD274* to ectopically overexpress the murine PD-L1 protein in MOC2 parental cells. For the transduction, HEK293T cells (8×10^5/per well, in 3 mL of DMEM 10% FBS each) were seeded onto a 6-well plate the day before the experiment. The following day, *pLenti-CD274-mGFP* plasmid (3 µg) was incubated with the Lenti-X™ Packaging Single Shot (VSV-G) (#631275, Takara Bio Inc, JPN) at room temperature (RT) for 10 min and then added to a well of cultured HEK293T cells. The cells were incubated for 24 h, whereupon the supernatant was gently removed and replaced by 3 mL of fresh culture medium. After another 24 h incubation period, the supernatant was harvested and filtered (MilliporeSigma™ Steriflip™ Sterile Disposable Vacuum Filter Units, 0.45 µm, Thermo Fisher Scientific). The presence of lentiviral particles was confirmed using Lenti-X™ GoStix™ (a clear band is detected at viral titres $>5\times10^5$ IFU/mL; Takara Bio). 150-300 µL of supernatant containing packaged lentiviral particles was mixed with culture medium and polybrene (8 µg/mL; Sigma-Aldrich) and added to a well (6-well plate) containing a monolayer of semi-confluent MOC2 cells. A polybrene only control (8 µg/mL) was run alongside to reassure that polybrene does not impact cell viability. After 2-3 d, the supernatant was removed and cells dissociated via trypsinisation. The cell suspension was spun down at 250 g, 3 min and resuspended in sterile PBS containing 2% FBS and placed on ice. The GFP-positive cell population was sorted via fluorescent-activated cell sorting (FACS) on a MoFlo Astrios cell sorter (Beckman Coulter, CA, USA). The target population was directly seeded to one well of a 6-well plate filled with DMEM 10% FBS supplemented with 1% of Penicillin/Streptomycin (#P4333, Sigma-Aldrich) and Amphotericin B (250 µg/mL, #A2942, Sigma-Aldrich). Cells were left in the incubator on antibiotic/-mycotic treatment for 7 days. Thereafter, cells were passaged, counted and seeded to 0.5 cells/well into a flat-bottom 96-well plate to grow populations from single cell clones. After 10-12 d, 25 single cell populations were trypsinised and transferred to T25 flasks for expansion. Once confluent, cells were stained for flow cytometric screening of reporter gene and protein expression. Staining was performed as described in section 2.4.1 using 3×10^5 cells per sample. Stained samples were run on a BD LSRII and results analysed using FlowJo (both BD Becton, Dickinson and Company).

2.2 Treatment studies *in vitro*

2.2.1 IFN-γ stimulation of cells *in vitro*

Recombinant Mouse Interferon-γ (IFN-γ; #IF005, Merck KGaA, DE) was reconstituted in 10 mM sodium phosphate buffer (pH 8.04; strictly no sodium chloride) containing 0.1% bovine serum albumin (BSA; #A9647, Sigma-Aldrich) to a concentration of 0.5 mg/mL. 20 μL aliquots were prepared and stored at -80°C. For *in vitro* stimulation, cell lines were seeded in duplicate to 1-2×10^5 cells/well into 6-well plates the evening before the experiment. The following morning, all media was removed and 1.5 mL of media containing murine recombinant IFN-γ (20 ng/mL) or vehicle (PBS) were added. After 24 h, PD-L1 protein expression was assessed via various techniques, including flow cytometry (2.4.1), western blot (2.5.3) and radioligand binding assays (2.8.1).

2.3 Microscopy of cultured cells

2.3.1 Brightfield microscopy

Brightfield images of cells in culture were acquired at RT using a CytoSMART Lux2 miniature microscope (CytoSMART Technologies B.V., NL).

2.3.2 Confocal immunofluorescence microscopy

For confocal microscopy imaging, 3-4×10^5 cells were seeded into a Nunc™ glass bottom petri dish (Thermo Fisher Scientific) and left to attach overnight. The following day, all media was removed and the primary antibody diluted in DMEM containing 10% FBS (Table 2-2) was added for 30 min on ice. Cells were gently washed with PBS (pH 7.4) and subsequently incubated with the secondary antibody diluted in DMEM containing 10% FBS (Table 2-2) supplemented with Hoechst® 33342 (5 µg/mL; Thermo Fisher Scientific) for 30 min on ice, protected from light. Cells were gently washed with PBS (pH 7.4) and finally covered with buffer (2% FBS in PBS) for imaging. Dishes were placed in a transport box filled with ice and imaged at the ICR Sutton Confocal facility. Images were captured on a Zeiss LSM700 confocal microscope (excitation via lasers at 639 nm, 405 nm and 488 nm of AF-647, Hoechst and GFP respectively; variable dichroic beamsplitter which allows efficient splitting of the emission wavelengths to different photon-multiplier-tubes; Carl Zeiss Inc, DE) by Louise Howell (Confocal Microscopy Core facility Sutton, ICR, UK) or Dr. Justyna Maczynska (Preclinical Molecular Imaging Team, ICR, UK). Image files were exported via ZenBlue software (Carl Zeiss).

Antibody target	Clone	Fluorescent tag	Working dilution	Host species	Company	Catalogue number
PD-L1 (CD274)	MIH5	-	1:200	Rat	Invitrogen	14-5982-81
Anti-rat	PC	AF-647	1:400	Goat	Invitrogen	A21247

Table 2 - 2: Table of antibodies for fluorescent staining of cultured cells, abbreviations stand for programmed death ligand 1 (PD-L1), cluster of differentiation (CD), polyclonal (PC), Alexa Fluor® 647 (AF-647).

2.4 Flow cytometry

2.4.1 Flow cytometry of cultured cells

3-5×10^5 cells were transferred into microcentrifuge tubes (1.5 mL Eppendorf® Safe-Lock microcentrifuge tube, Eppendorf AG, DE) and placed on ice for the following staining procedure. Initially, cells were spun down (135×g, 3 min, 4°C), the supernatant removed and the pellet resuspended in ~100 µL PBS (pH 7.4). This step was repeated once to ensure no residues of culture medium. For staining of extracellular epitopes, cells were carefully resuspended in buffer (PBS, pH 7.4, supplemented with 2% FBS, 10 µL buffer per 1×10^5 cells) and antibodies added as indicated in table 2-3. As a last step, Draq7™ viability dye (1:50 dilution factor; BioStatus, UK) was added. The antibody-cell mix was incubated on an orbital shaker (~60 RPM) for 30 min at 4°C, protected from direct light. For staining of intracellular epitopes, such as cytokeratins, cells were initially incubated with Fixable Viability Dye eFluor™ 780 (#65-0865-14, Thermo Fisher Scientific) following staining and incubation steps as mentioned previously (extracellular epitopes). After the 30-min incubation period, two consecutive washes with PBS 2% FBS were performed and the cells were fixed and permeabilised using the eBioscience™ Foxp3/Transcription Factor Fixation/Permeabilisation Concentrate and Diluent (#00-5521-00, Thermo Fisher Scientific). Cells were resuspended in 100 µL of freshly prepared Fixation/Permeabilisation working reagent for 30 min at 4°C, protected from light. Next, cells were washed with 100 µL of eBioscience™ Permeabilisation Buffer (10x; #00-8333-56; Thermo Fisher Scientific) twice and stained with the antibody targeting the intracellular epitope at the concentration indicated in Table 2-3. The incubation was carried out as previously mentioned and followed by two washes with 100 µL of PBS 2% FBS. For PD-L1 expression analysis following oncolytic virus treatment *in vitro*, cells were permeabilised and fixed in order to reduce the replication competency of residual virus (buffers contain paraformaldehyde). For samples stained with multiple fluorochromes of overlapping emission spectra, compensation beads were stained with single dyes following the same staining procedure as for cell samples. For flow cytometry (FC), cells were resuspended in ~200 µL of PBS 2% FBS and transferred into 5 mL BD Falcon™ tubes (#352058, BD Becton Dickinson and Company, NJ, USA). Tubes were then placed on ice and carried to the Flow Cytometry Core facility (ICR, Sutton). Each sample was briefly vortexed before loading it onto a BD LSRII flow cytometer (BD Becton Dickinson and Company). For acquisition, the stopping gate was set to selectively acquire singlet and viable events (1-5×10^4 events per sample depending on experiment). Data was analysed using FlowJo software (both BD Becton, Dickinson and Company). The median fluorescence intensity (MFI) was measured to determine the expression of the protein of interest. All FC experiments were performed three times unless stated otherwise.

Antibody target	Clone	Fluorescent tag	Working dilution	Host species	Company	Catalogue number
EpCAM (CD326)	G8.8	FITC or APC	1:100	Rat	BioLegend	118201
HVEM (CD270)	HMHV-1B18	APC	1:100	Armenian Hamster	BioLegend	136305
Pan-CK	C11	AF-488	1:50	Mouse	CST	4523
PD-L1 (CD274)	10F.9G2	PE	1:200	Rat	BioLegend	124307
CD44	IM7	PE	1:100	Rat	BioLegend	103007

Table 2 - 3: Fluorescent antibodies for staining of single cell suspensions from cultured cells for flow cytometry, abbreviations stand for epithelial cell adhesion molecule (EpCAM), Herpesvirus entry mediator (HVEM), cytokeratin (CK), programmed death ligand 1 (PD-L1), cluster of differentiation (CD), allophycocyanin (APC), Alexa Fluor® 488 (AF-488), fluorescein isothiocyanate (FITC), phycoerythrin (PE).

2.4.2 Flow cytometry of cells derived from tumours and spleens

Tumours and spleens were collected on day 3 or 7 after intratumoural RP1 or vehicle treatment (n=5-6 per group). Each organ was weighed and subsequently cut into small pieces using a scalpel blade. Tissue pieces were then transferred into 15 mL conical tubes containing ~800 µL of PBS on ice. Tumours were enzymatically digested with Liberase™ TL Research Grade (#5401020001, Merck) as follows: 200 µL Liberase™ (reconstituted at 2.5 mg/mL in sterile water) was added to each sample and incubated at 37 °C for 25 min, while gently shaken every 5 min. Thereafter, 10 mL of cold PBS were added and the suspension spun at 250×g, 3 min, 4°C. The supernatant was removed and 2 mL of PBS with 2% FBS added to the digested tissue chunks. Both, tumour and spleen suspensions, were then strained through a 70 µm mesh (MACS® SmartStrainers, Miltenyi Biotec, DE) mounted onto a 15 mL conical tube using a syringe plunger.

Erythrocytes were lysed using Ammonium-Chloride-Potassium (ACK) lysing buffer (5 mL/spleen, 1 mL/tumour; Gibco/Life Technologies). Samples were incubated with ACK lysing buffer for 5 min at RT and then spun down at 300×g, 10 min, 4°C. The supernatant was removed and samples resuspended in 1 mL of PBS containing 2% FBS and 5 mmol/L ethylenediaminetetraacetic acid (EDTA) (EDTA solution 0.5 M, pH 8; ICR media production) and placed on ice. An aliquot of each sample (5 µL) was resuspended in trypan blue dye (dilution factor of 1:10 or 1:20) and cells counted using a haemocytometer as previously described (2.1.3). 1×10^6 cells per sample were transferred as a 100 µL suspension into a 96-well plate (conical-bottom) and used for FC. The following steps were strictly performed on ice: TruStain FcX antibody (2 µL, BioLegend, CA, USA) was added to each sample and incubated for 10 min, followed by staining with a mixture of five antibodies (Table 2-4) and the Fixable Viability Dye eFluor™ 780 (#65-0865-14; Thermo Fisher Scientific). Samples were incubated on an orbital shaker (~60 RPM) for 25 min at 4°C, and then washed twice with PBS. For washing, the plate was centrifuged at 250×g, 3 min, 4°C and the antibody mix was replaced with cold PBS (150 µL). The cell suspensions were then fixed using the eBioscience™ Foxp3/Transcription Factor Fixation/Permeabilisation Concentrate and Diluent (#00-5521-00; Thermo Fisher Scientific) as previously described (2.4.1). Following two washes with permeabilisation buffer, the samples were resuspended in 50 µL PBS containing 1% paraformaldehyde and stored at 4°C overnight, protected from light. Single stain samples (on tissue or compensations beads) and fluorescent minus one (FMO) control samples (on tissue) were prepared alongside. For FC, the plate was centrifuged, the supernatant removed and the samples resuspended in 200 µL PBS 2% FBS. Each sample was then transferred into a 5 mL BD Falcon™ tubes (BD Becton, Dickinson and Company) and placed on ice. FC was performed on a FACS ARIA™ Ilu sorter equipped with 5 lasers (BD Becton, Dickinson and Company) with the help of Fredrik Wallberg (Flow Cytometry Core facility Chelsea, ICR, UK). At sample acquisition, a gating path was applied to ensure that a consistent number of singlet and alive events were recorded for each sample (minimum of 5×10^5). The flow rate was kept at slow pace and the sample backflush was activated between samples. Data analysis was carried out on FlowJo version 10.6.2 (BD Becton, Dickinson and Company). Data irregularities were excluded from final FlowJo analysis where necessary

(Monaco et al., 2016). Fluorescence spillover was compensated using beads and single-stain controls. Gates were positioned according to fluorescence minus one (FMO) controls stained on organ samples. The role of the controls used in the FC experiments including FMO and IgG isotype controls is briefly discussed in the appendix (section 8.1).

Antibody target	Clone	Fluorescent tag	Working dilution	Host species	Supplier	Catalogue Number
EpCAM (CD326)	G8.8	BB515	1:50	Rat	BD	565425
CD45	30-F11	BV510	1:100	Rat	BioLegend	103128
PD-1	29F.1A12	BV421	1:100	Rat	BioLegend	135221
PD-L1 (CD274)	10F.9G2	PE	1:100	Rat	BioLegend	124307
PD-L2	TY25	APC	1:50	Rat	BioLegend	107210

Table 2 - 4: Fluorescent antibodies for multi-colour staining of single cell suspensions derived from whole tumour or spleen tissue for flow cytometry. Abbreviations stand for epithelial cell adhesion molecule (EpCAM), cluster of differentiation (CD), programmed death receptor 1 (PD-1), programmed death ligand 1 (PD-L1), programmed death ligand 2 (PD-L2), allophycocyanin (APC), Alexa Fluor® 488 (AF-488), Brilliant™ Blue 515 (BB515), Brilliant Violet™ (BV), phycoerythrin (PE).

2.5 Western blot

2.5.1 Cell lysis for protein extraction

Cells (1-2×10^6) were collected into microcentrifuge tubes and washed once with cold PBS. For lysis, cells were resuspended in cell lysis buffer (150-200 µL) and incubated at 4°C for 20 min on an orbital shaker. Cell lysis buffer was freshly prepared by mixing the following components: radioimmunoprecipitation assay (RIPA) buffer (Thermo Fisher Scientific), 1 mM EDTA (0.5 M EDTA solution, pH 8; ICR media production), Halt™ Phosphatase Inhibitor Cocktail (100x, Thermo Fisher Scientific), Protease Inhibitor (25x, cOmplete™ Protease Inhibitor Tablets, Roche Diagnostics Inc, CH) and 0.05 M NaF (1 M NaF solution, ICR media production). Samples were homogenised using a sonicator (Sonic Dismembrator Model 100, Fisher Scientific) and centrifuged at 9.400×g, 4°C for 10 min. Clear sample supernatants were transferred into new microcentrifuge tubes and stored at -20°C until further use. All steps were performed on ice unless stated otherwise.

2.5.2 Tumour lysis for protein extraction

Pieces of frozen tumour tissue (~50 mg) were transferred into tissue grinding tubes containing metal beads (Precellys Lysing Kit; #03961-1-008, Bertin Technologies SAS, FR) and topped up with freshly prepared tissue lysis buffer (300 µL). Tissue lysis buffer contained Tissue Lysis Reagent 1 (#FNN0071; Thermo Fisher Scientific), Halt™ Phosphatase Inhibitor Cocktail (100x; Thermo Fisher Scientific) and Protease Inhibitor (25x, cOmplete™ Protease Inhibitor Tablets, Roche Diagnostics). Samples were then mechanically dissociated on a tissue homogeniser (Precellys 24 tissue homogeniser; #P000669-PR240-A, Bertin Technologies SAS, FR) and homogenates transferred into microcentrifuge tubes. Samples were homogenised using a sonicator (Sonic Dismembrator Model 100, Fisher Scientific) and centrifuged at 9.400×g, 4°C for 10 min. Samples were stored at -20°C until further use. All steps were performed on ice unless stated otherwise.

2.5.3 Western blot

For western blotting, tissue and cell lysates were thawed on ice and their protein concentration determined via bicinchoninic acid assay (Pierce™ BCA protein assay kit) following the manufacturer's protocol. Adequate amounts of protein (20-25 µg/sample for cell lysates, 40 µg/sample for tumour lysates) were pipetted into microcentrifuge tubes and supplemented with NuPAGE™ sample buffer (4x; #NP0007), NuPAGE™ sample reducing agent (10x; #NP0004) and topped up with ultrafiltered (UF) water to reach a volume of 20 µL or 35 µL, depending on gel thickness/well size. For protein denaturation, samples were incubated in a thermomixer at 70°C for 10 min. Samples were loaded into a NuPAGE™ 4-12% Bis-Tris gel securely locked in a blot module (XCell SureLock™ Mini-Cell, #EI0001). A pre-stained protein ladder (3-6 µL, Novex™ Sharp Protein Ladder) was loaded into the outer wells as a molecular weight marker. The blot module chamber was then filled with running buffer containing 50 mL 3-(*N*-morpholino)propanesulfonic acid (MOPS) sodium dodecyl suflate (SDS) concentrate (20x NuPAGE™ MOPS SDS Running Buffer; #NP0001) and 950 mL UF water. NuPAGE™ Antioxidant (#NP0005) was added (1 mL) to the inner chamber and the electrophoresis run at 120 V for ~1.5 h using a PowerPac™ HC High-Current Power Supply (Bio-Rad Laboratories Inc, CA, USA). The gel was removed from plastic frames and the gel sandwich placed in the transfer apparatus (component of Mini-Cell) in the correct orientation to ensure the transfer of the protein bands from the gel onto the nitrocellulose membrane. Filter paper and nitrocellulose membranes (0.45 µm pore size) were purchased together (#LC2001). All components were soaked in transfer buffer prior to layering. The transfer box was tightly locked in the blot module chamber to ensure close contact between the gel and nitrocellulose membrane throughout the wet transfer. The chamber module was filled with transfer buffer containing 50 mL NuPAGE™ Transfer Buffer (20x, #NP0006), 100 mL methanol (#20847.307, VWR International, PA, USA) and 850 mL UF water. The transfer was run at 330 mA for 2.5 h using the PowerPac™ HC High-Current Power Supply. For TBS-T, 50 mL TBS (10x) solution (ICR media production) was mixed with 450 mL UF water and 250 µL TWEEN® 20 (#P7949, Sigma-Aldrich). Post-transfer, the nitrocellulose membrane was transferred into small tray filled with TBS-T containing 5% milk (2.5 g dry milk powder reconstituted in 50 mL TBS-T) and incubated for 1 h at RT under constant movement on a sea-rocker shaker. Thereafter, the solution was removed and replaced by the primary antibody prepared in TBS-T containing 5% milk (Table 2-5). Primary antibodies were incubated at 4°C overnight on an orbital shaker. The following day, membranes were rinsed with TBS-T (three times, 5 min each) and incubated with a horseradish peroxidase (HRP) conjugated secondary antibody (prepared in TBS-T containing 5% milk, see table 2-5) for 1 h at RT on a sea-rocker shaker. Finally, membranes were rinsed with TBS-T (three times, 5 min each) and UF water (2 min) and incubated with chemiluminescent substrate supplemented with a signal enhancing component (SuperSignal™ West Femto/Pico Substrates) for 5 min at RT protected from light. Immunoblots were imaged in a ChemiDoc XRS+ Imaging System (Bio-Rad Laboratories) using a dynamic acquisition mode (1 image/sec over a period of 100 sec) for optimal detection of protein bands. A photographic image was acquired for co-registration. Immunoblots were prepared with Image Lab software (Bio-Rad Laboratories) and densitometric analysis performed using ImageJ software (Schneider et al., 2012). All products listed were purchased from Thermo Fisher Scientific unless stated otherwise.

Antibody target	Clone	Working dilution	Host species	Conjugate	Company	Catalogue number
EGFR	C74B9	1:1000	Rabbit	-	CST	2646
Pan-CK	C11	1:1000	Mouse	-	CST	4545
PD-L1	10F.9G2	1:1000	Rat	-	BioXcell	BE0101
GAPDH	D16H11	1:1000	Rabbit	-	CST	5174
β-Actin	PC	1:1000	Rabbit	-	CST	4967
Anti-rat	PC	1:1000	Goat	HRP	Vector Laboratories	PI-9401
Anti-mouse	PC	1:1000	Horse	HRP	CST	7076
Anti-rabbit	PC	1:1000	Goat	HRP	CST	7074

Table 2 - 5: Antibodies (primary and secondary) used for western blot. Abbreviations denote epidermal growth factor receptor (EGFR), cytokeratin (CK), Glyceraldehyde 3-phosphate dehydrogenase (GAPDH), polyclonal (PC), horse-radish peroxidase (HRP).

2.6 Syngeneic mouse models of cancer

2.6.1 Animal husbandry

All animal studies were approved by the Institutional Review Board (covered by project licence P5B619C3D) and were in line with the National Cancer Research Institute Guidelines for Animal Welfare in Cancer Research (Workman et al., 2010).

Female C57Bl/6J and Balb/c mice were purchased from a commercial breeder (Charles River, UK) at 6 to 8 weeks of age. Animals were caged in groups of 5-6 in type II individually ventilated cages (IVC; 500 cm^2, Allentown Inc, NJ, USA) and allowed to acclimatise for a minimum of 5 days upon arrival. Mice were kept in a specific pathogen free (SPF) facility with a light-dark cycle of 12:12 h, temperature of 21 ± 1°C and humidity of 55 ± 10 %. Sterile water and food (Rodent diet, LabDiet, USA) were provided for *ad libitum* consumption. Environmental enrichment included bedding substrate of Corn Cob 6/8, Aspen chew sticks 5x1x1 cm (#CS3C15, Datesand group, UK) and Bed r'Nest paper wool nesting material (#BEDRNEST, Datesand group). All animal studies were conducted in the Sutton ICR facility.

2.6.2 *In vivo* tumour models

For subcutaneous tumour establishment, cells were harvested at passage 2 or 3 upon thawing at a confluency between 80-100%. Cells were dissociated and counted as previously described (2.1.2 and 2.1.3). The required number of cells was resuspended in sterile PBS (pH 7.4) to reach a concentration of 1×10^6 cells in 100 µL and transferred to a 1.8 mL cryovial. This concentration was used for MOC2, MOC2*(PD-L1)*^{poly} and MOC2*(PD-L1)*^{single} cells. MOC1 cells were initially titrated (5×10^5 - 2×10^6 cells in 100 µL) and then used at 1×10^6 cells in 100 µL. CT26 cells were injected at a concentration of 5×10^5 cells in 50 µL PBS. Injections were performed in a SPF facility in a laminar flow hood equipped with an anaesthetic rig. Mice, shaved in the left flank region on the day before the injection, were anaesthetised with gaseous isoflurane (1.5-2.0% in O_2 v/v). Cells were thoroughly resuspended and drawn up with a 1 mL syringe (Terumo Group, JPN). The syringe was mounted with a 27 G needle (#K2127; BD Becton Dickinson and Company) and 50-100 ul (volume depending on cell number required for injection) injected subcutaneously to the left flank. All MOC cell types were injected to C57Bl/6J mice, whilst CT26 cells were injected to Balb/c mice. Animal weights and tumour growth were monitored on a regular basis, with tumour volumes calculated from calliper measurements taken in two dimensions ($volume = \frac{1}{2} \times length \times width^2$). Humane endpoints for *in vivo* studies were determined by the licence protocol (protocol 02 of project licence P5B619C3D) with any tumour diameter exceeding 15 mm or superficial tumour ulcerations greater than 5 mm in diameter.

2.7 Production of ^{89}Zr-DFO-PD-L1$_{mAb}$ and -IgG$_{mAb}$

The conjugation of *p*-isothiocyanatobenzyl-desferrioxamine (DFO-NCS) to anti-mouse PD-L1$_{mAb}$ (clone 10F.9G2) or anti-mouse IgG$_{mAb}$ (clone LTF-2) and the following radiolabelling of the conjugate with zirconium-89 (^{89}Zr) are described in sections 2.7.1 and 2.7.2 (Fig.2-1). Dr. Chiara Da Pieve (Preclinical Molecular Imaging Team, ICR, UK) kindly performed the procedures following the protocol published by Vosjan *et al* (Vosjan et al., 2010).

2.7.1 Conjugation of antibody to DFO-NCS

At first, a buffer exchange of PD-L1$_{mAb}$ (5.9 mg/mL, clone 10F.9G2, BioXCell, NH, USA) or IgG$_{mAb}$ (7.7 mg/mL, clone LTF-2, BioXCell) into 0.1 M sodium carbonate pH 9 (Na_2CO_3, Sigma-Aldrich) was performed using an Amicon ultra-centrifugal filter (50 kDa MWCO, Sigma-Aldrich), following the manufacturer's protocol. Subsequently, the protein concentration was determined by ultraviolet-visible (UV-Vis) spectrophotometry at 280 nm using a NanoDrop 2000 spectrophotometer (Thermo Fisher Scientific). An average molar extinction coefficient (ε_{280}) of 210,000 $M^{-1}cm^{-1}$ was applied, as widely accepted for IgG antibodies. DFO-NCS (#C121; CheMatech, FR) was dissolved in dry dimethyl sulfoxide (DMSO, Sigma-Aldrich) at a concentration of 10 mM (7.6 mg/mL) and added to the mAb solution at 5-molar excess to achieve an approximate ratio of 1.0 DFO-NCS/mAb. The reaction was incubated in a thermo shaker for 3 h at 24°C. The mAb-conjugate (DFO-PD-L1$_{mAb}$ or DFO-IgG$_{mAb}$) was purified by gel filtration using a Zeba spin desalting column (40 kDa MWCO, Thermo Fisher Scientific) pre-equilibrated in 0.5 M 4-(2-hydroxyethyl)-1-piperazineethanesulfonic acid (HEPES) buffer pH 7 (Sigma-Aldrich), following the manufacturer's protocol. The final concentration of the conjugate was measured by UV-Vis spectrophotometry as previously described. The solution was transferred to 1.5 mL low protein binding microcentrifuge tubes (1.5 mL LoBind microcentrifuge tube, Eppendorf) in aliquots of ~100 µL and stored at -20°C until further use.

2.7.2 Radiolabelling of the DFO-antibody conjugate

The ^{89}Zr oxalate solution (40-45 MBq, 1 M oxalic acid solution, CyclotronVU, NL) was transferred into a 1.5 mL low protein binding microcentrifuge tube (Eppendorf) and neutralised using a 2.0 M sodium carbonate (Sigma-Aldrich) solution (4.5 µL Na_2CO_3 per 10 µL of ^{89}Zr solution) and 0.5 M HEPES pH 7.0 (Sigma-Aldrich) to reach a final pH of 7. Then, the DFO-mAb conjugate was added (~0.20 MBq/µg) and the mixture was incubated for 1 h at RT. At the end of the reaction, a 0.1 M EDTA solution (Sigma-Aldrich) was added at a ratio of 1:20 to the reaction mix and incubated for further 15 min at RT. The product, ^{89}Zr-DFO-PD-L1$_{mAb}$ or ^{89}Zr-DFO-IgG$_{mAb}$, was purified using a Zeba spin desalting column (40 kDa MWCO) equilibrated in PBS. The final protein concentration was determined by UV-Vis spectrophotometry at 280 nm.

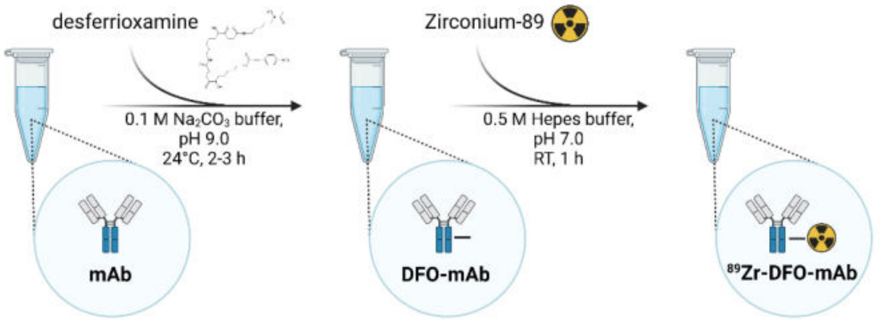

Figure 2 - 1: Schematic of ^{89}Zr-DFO-PD-L1$_{mAb}$ preparation. Abbreviations stand for desferrioxamine (DFO), monoclonal antibody (mAb), Zirconium-89 (^{89}Zr), 4-(2-hydroxyethyl)-1-piperazineethanesulfonic acid (HEPES), room temperature (RT). Figure created with Biorender.com.

2.7.3 Silver staining

Silver staining was used to confirm the molecular weight and integrity of the DFO-mAb-conjugates. The DFO-conjugated and unconjugated mAb samples (0.05-0.5 µg) were mixed with lithium dodecyl sulfate (LDS) sample buffer (NuPAGE™ 4x concentrate) and ultrapure water to reach a total volume of 20 µL in microcentrifuge tubes. For antibody reduction, a sample reducing reagent was added to this mix (NuPAGE™ 10x concentrate) and samples were incubated in a thermomixer at 80°C for 2 min. All samples were loaded onto a NuPAGE™ gel (Bis-Tris gel 4-12%) and run at 120 V for ~1 h, using MOPS SDS as running buffer (NuPAGE™ 20x concentrate diluted in water). For silver staining, the Pierce™ Silver Stain for Mass Spectrometry kit (#24600) was used as follows: the gel was washed with ultrapure water (2×5 min) and fixed in a solution containing 50% ethanol:10% acetic acid (v/v) (2×15 min) under gentle agitation. Thereafter, a sensitising reagent was added for 2 min, followed by staining with silver nitrate solution for 25 min under constant shaking. Thereafter, the gel was washed with ultrapure water (3×30 sec) and developed for up to 2 min using formaldehyde under alkaline conditions (sodium carbonate). As the protein bands appeared, the reaction was stopped with 5% acetic acid solution. Silver impregnated protein bands were visualised on a ChemiDoc XRS+ Imaging System (Bio-Rad Laboratories). All products were purchased from Thermo Fisher Scientific unless stated otherwise.

2.7.4 High pressure liquid chromatography

To determine the homogeneity of DFO-PD-L1_{mAb} (i.e. absence of aggregates and fragments), analytical size exclusion (SEC) high pressure liquid chromatography (HPLC) was carried out on an Agilent Infinity 1260 quaternary pump system equipped with a 1260 Diode array (Agilent Technologies). PD-L1_{mAb} and DFO-PD-L1_{mAb} were analysed on a bioZenSEC3 column (4.6×150 mm, 1.8 μm, Phenomenex, UK), by isocratic elution using 95% 0.1 M phosphate buffer pH 6.8 and 5% of isopropanol as mobile phase, at a flow rate of 0.35 mL/min. The absorbance was recorded at 280 nm. Elution profiles were analysed using the Laura software v.4.4.6.79 (Lablogic, UK). HPLC including the analysis of elution profiles were performed by Dr. Chiara Da Pieve (Preclinical Molecular Imaging Team, ICR, UK). HPLC was performed only once.

2.7.5 Mass spectrometry

The number of DFO molecules per mAb was determined via mass spectrometry. DFO-PD-L1_{mAb} and PD-L1_{mAb} were deglycosylated via enzymatic digestion using Endo S (New England BioLabs) in GlycoBuffer 1 (10x, New England BioLabs) at 37°C for ~1 h. The reaction was heat-inactivated at 55°C for 10 min and the product stored at -20°C until analysis. Mass spectrometry was performed on a 6520 A Series quadrupole Time-of-Flight (qToF) mass spectrometer with a fitted dual electro spray ionisation (ESI) source (Agilent Technologies). Sample preparation was performed by Dr. Chiara Da Pieve (Preclinical Molecular Imaging Team, ICR, UK) and the mass spectrometry measurements and analysis was kindly performed by Meirion Richards (Stuctural Chemistry Team, ICR, UK). Mass spectrometry was performed only once.

2.7.6 Instant thin layer chromatography

The radiochemical purity (RCP) of the radiolabelled product, ^{89}Zr-DFO-PD-L1$_{mAb}$ or -IgG$_{mAb}$, was routinely checked by instant thin layer chromatography analysis (ITLC) using silica gel-impregnated glass microfiber paper strips (ITLC-SG; Agilent Technologies) and 0.1 M sodium acetate buffer with 25 mM EDTA (pH 5; Sigma-Aldrich) as mobile phase. The ITLC strips were analysed using a Cyclone Plus Phosphor Imager (Perkin Elmer). The ^{89}Zr-labelled conjugate appeared at the origin (Retention factor < 0.1) while the free $^{89}Zr^{4+}$ cations were chelated by EDTA and migrated with the solvent front (Retention factor > 0.9). Dr. Chiara Da Pieve (Preclinical Molecular Imaging Team, ICR, UK) kindly performed and analysed the ITLC.

2.7.7 *In vitro* serum stability

The stability of ^{89}Zr-DFO-PD-L1$_{mAb}$ with respect to loss of radioactivity from the radiolabelled mAb was assessed *in vitro* using mouse serum. ^{89}Zr-DFO-PD-L1$_{mAb}$ (~4 MBq) was added to 500 µl mouse serum (Sigma-Aldrich) in a 1.5 mL low protein binding microcentrifuge tube (n=3). ^{89}Zr (~4 MBq) was used as a control. The mixture was incubated in a thermo shaker at 37°C, 800 rpm. Samples (~1 µL) were taken at 0, 24, 72 and 168 h (n=3 for each time point) and analysed by ITLC as previously described (2.7.5). Stability testing and analysis were kindly performed by Dr. Chiara Da Pieve (Preclinical Molecular Imaging Team, ICR, UK).

2.8 Cell binding radioimmunoassays

2.8.1 Specificity of binding assay

MOC1, MOC2 and CT26 cells (2×10^4 cells/well) and MOC2*(PD-L1)*^{poly} and MOC2*(PD-L1)*^{single} (2.5×10^4 cells/well) cells were seeded on 24-well plates (#142475; Nunclon™ Delta-treated; Thermo Fisher Scientific) 72 h prior to binding study. RAW264.7 cells (suspension cells) were cultured in T25 flasks instead. 24 h prior to binding study, all media was gently removed and cells were treated with murine IFN-γ (20 ng/mL, as described in 2.2.1) or standard culture media as a control (1 mL/well for 24 well-plates and 5 mL/flask for T25 culture flask). On the day of the binding study, RAW264.7 cells were harvested and distributed to equal fractions into 1.5 mL low protein binding microcentrifuge tubes to perform the binding study on suspended cells. All eppendorf tubes and plates were placed on ice for the duration of the binding assay. Cells were gently washed with cold PBS once and incubated with ^{89}Zr-DFO-PD-L1$_{\text{mAb}}$ or ^{89}Zr-DFO-IgG$_{\text{mAb}}$ (3.5-7.4 kBq/well prepared as a 2 nM-solution prepared in DMEM supplemented with 1% FBS; n=3) for 1 h on ice. For blocking, cells were pre-incubated (10 min) with 100-fold molar excess of PD-L1$_{\text{mAb}}$ or IgG$_{\text{mAb}}$. After the incubation period, the supernatant was removed, cells rinsed twice with cold PBS twice and trypsinised. Each well of cells was collected into a scintillation vial (PerkinElmer Inc, MA, USA) and loaded onto a Wizard^2 2480 automated gamma-counter (PerkinElmer) to count the radioactivity in each well. One representative sample for each cell line was used to count the number of cells using a haemocytometer (2.1.3). The radioactivity measured in counts per minute (CPM) was divided by the cell number as a measure of normalisation for radioligand binding. Cell-associated radioactivity was normalised to the maximum cell-associated radioactivity of MOC2*(PD-L1)*^{single} cell line, and reported as the mean of n=3 ± SD. At least two biological repeats were performed with all cell lines using ^{89}Zr-DFO-PD-L1$_{\text{mAb}}$. ^{89}Zr-DFO-IgG$_{\text{mAb}}$ specificity of binding was performed only once.

2.8.2 Saturation binding assay

A saturation binding assay was performed to estimate the dissociation constant (K_d) of ^{89}Zr-DFO-PD-L1$_{\text{mAb}}$. MOC2*(PD-L1)*^{poly} cells (2×10^5 cells/well) were seeded on a 24-well plate and cultured overnight. On the following day, cells were incubated with increasing concentrations of ^{89}Zr-DFO-PD-L1$_{mAb}$ (0.7-126 kBq/well; n=3) in non-supplemented DMEM media for 1 h at 4°C. The addition of 100-fold molar excess of non-radiolabelled PD-L1$_{mAb}$ as a 10-minute pre-block, was used to determine non-specific binding. Post-incubation, the cells were rinsed once with cold PBS, trypsinised and collected into scintillation vials. Cell-associated radioactivity was measured on a γ-counter (PerkinElmer). For K_d estimation, gamma-counter measurement data were plotted as the amount of bound versus free radioconjugate (RC). The specific binding (SB) was determined by subtracting the non-specifically bound (NSB) fraction from the total bound (TB) fraction and fitted to a one-site receptor-binding model using GraphPad Prism 8 (GraphPad Software Inc, CA, USA).

2.8.3 Lindmo assay

The immunoreactivity of ^{89}Zr-DFO-PD-L1$_{mAb}$ was determined following the method described by Lindmo *et al.* (Lindmo et al., 1984; Lindmo and Bunn, 1986). Cultured MOC2*(PD-L1)*^{poly} cells were collected via trypsinisation and counted using a haemocytometer (2.1.3). Increasing numbers of cells ranging from 0.313-20×10^6 cells/tube (7 portions in total) were resuspended in PBS containing 1% FBS, transferred into 1.5 mL low protein binding microcentrifuge tubes and placed on ice. Cells were spun down (200 RCF, 3 min, 4°C) and washed with cold PBS once, before incubation with ^{89}Zr-DFO-PD-L1$_{mAb}$. 250 µL of ^{89}Zr-DFO-PD-L1$_{mAb}$ prepared in DMEM containing 1% FBS (~5 kBq per tube; worth 100,000 CPM on the γ-counter) was added to each tube (SB and NSB). To assess non-specific binding, 250 µL of unlabelled PD-L1$_{mAb}$ (1 µM) was added to microcentrifuge tubes (NSB). All remaining tubes were topped up with 250 µL of DMEM 1% FBS only (SB). All vials were placed in a thermomixer for 1 h (300 rpm, 21°C). Thereafter, the samples were centrifuged, the supernatant removed and the cells washed with PBS once before being measured on a gamma-counter (PerkinElmer). The immunoreactive fraction (IRF) of the RC was determined from the intercept value of the fitted line derived from plotting the total/bound counts against the inverse of the cell number using GraphPad Prism 8 (GraphPad Software).

2.9 ^{89}Zr-DFO-PD-L1$_{mAb}$ imaging and biodistribution

2.9.1 Combined PET and CT scanning

^{89}Zr-DFO-PD-L1$_{mAb}$ (2 MBq, 10-18 μg in 100 μL PBS) was co-injected with different amounts of PD-L1$_{mAb}$ (Table 4-1) into the tail vein of anaesthetised (~2.0% isoflurane/O$_2$, v/v) MOC1, MOC2, MOC2*(PD-L1)*^{poly}, MOC2*(PD-L1)*^{single} and CT26 tumour-bearing mice (n=3-5 per group). ^{89}Zr-DFO-IgG$_{mAb}$ (1-2 MBq, 9-15 μg in PBS) was injected alone. Whole body PET and CT scans were performed 24, 48, 72 or 96 h post-injection using an Albira PET/SPECT/CT scanner (Bruker, MA, USA). Mice were anaesthetised 5 min ahead of scanning (~2.0% isoflurane/O$_2$, v/v) and anaesthesia maintained for the duration of each scan. For scanning, mice were placed on a heated mouse imaging bed in prone position. The PET scan was acquired as a static, whole-body acquisition (15 min) with an energy window of 358 to 664 keV and a coincidence timing window of 5 ns (Spinks et al., 2014). Subsequently, a static, whole-body, high resolution CT scan was acquired at 250 projections (X-ray tube set-up at 45 kV and 400 μA; voxels 0.5×0.5×0.5 mm^3). PET scans were reconstructed using a maximum-likelihood expectation-maximisation (MLEM) algorithm (12 iterations) with a voxel size of 0.5×0.5×0.5 mm^3. The reconstruction algorithm included corrections for scatter and random coincidences, as well as attenuation (CT scan served as an anatomic reference) and radioactive decay. No partial volume correction was applied. CT scans were reconstructed using a filtered back projection (FBP) algorithm.

2.9.2 Quantification of radioactive uptake in PET images

Quantification of RC uptake in PET scans was performed via PMOD software version 3.206 (PMOD Technologies Ltd, CH). Each volume of interest was determined by positioning a sphere to cover a specific organ (e.g tumour) in the PET scan. The 50% hottest voxels within this sphere were then iso-contoured and the outcome checked visually. As a measure of radioactive uptake, the mean of the 50 peak counts within the iso-contoured region (PET$_{Max50}$; mean of the 50 'hottest' voxels with highest counts within the tumour volume) was recorded and converted into the percentage of injected dose per gram of tissue (%ID/g) by means of a cylinder calibration factor (MBq/g/counts). Of note, the radioactive uptake in very small organs, i.e. lymph nodes, was determined via averaging the 5 peak counts only ($\mathrm{PET}_{\mathrm{max5}}$). The calibration factor for uptake conversion was obtained from scans of a phantom cylinder (130 ccm) filled with increasing concentrations of ^{89}Zr (0.5-10 MBq; 1 M oxalate solution) of known activity and volume. The below formula was used for PET-based RC uptake measurements (percentage injected dose per gram of tissue - %ID/g, activity in ROI in kBq/cc - $C_{img}(t)$, weight in gram - $W(t)$, volume in cm^3 - $V(t)$, injected dose in kBq – $D_{inj}(t)$, the V(t)/W(t) ratio was assumed to ~1 cm^3/g):

$$\%\frac{ID}{g}(t) = C_{img}(t) \times \frac{V(t)}{W(t)} \times \frac{1}{D_{inj}(t)} \times 100\%$$

2.9.3 Tissue biodistribution studies

For tissue biodistribution studies, mice injected with either ^{89}Zr-DFO-PD-L1$_{\mathrm{mAb}}$ or ^{89}Zr-DFO-IgG$_{\mathrm{mAb}}$ were euthanised between 24 to 96 h after RC administration. Major organs including blood, heart, lungs, thymus, liver, spleen, kidney, small intestine (duodenum), large intestine (colon), bone (femur shaft and epiphysis), muscle and tumour were collected, weighed and their radioactivity measured on a gamma-counter (PerkinElmer). Peripheral blood (>100 uL) was collected via cardiac puncture in deep anaesthesia, whereafter the animal was euthanised via cervical dislocation. Following cervical dislocation, solid organs were collected, washed in water and briefly dipped on a paper towel to remove residual blood before weighing and gamma counting. In the interest of consistency, all organs for each biodistribution study described in this thesis were collected by the same person (Julia Hoebart). At gamma-counting, aliquots of the injected dose (ID) were measured alongside and used as a reference for the total ID to calculate the organ-specific uptake as the percentage ID per gram of tissue (%ID/g). Activity measurements were background- and decay-corrected. The RC uptake in each organ was calculated via the following formula (percentage ID per gram of tissue - *%ID/g*, organ-specific activity in counts per minute - $C(t)$, background activity in counts per minute - $B(t)$, tissue weight in gram - $W(t)$, injected dose decay-corrected in counts per minute - $D_{inj}(t)$):

$$\%\frac{ID}{g}(t) = \frac{C(t) - B(t)}{W(t)} \times \frac{1}{D_{inj}(t)} \times 100$$

2.9.4 Autoradiography

Tumours collected at biodistribution were immersed in optimal cutting temperature (OCT) compound (Tissue-Tek® O.C.T compound, Sakura Finetek Inc, CA, USA) and placed on dry ice until OCT had solidified. Each sample was mounted onto a metal sample holder for sectioning on a cryotome (Thermo Fisher Scientific) on the day of biodistribution. Tissue sections (6-10 µm) were mounted onto microscope slides (SuperFrost Plus™ Adhesion slides, Thermo Fisher Scientific) and exposed to a photostimulable storage phosphor screen (#GE28-9564-75, GE Healthcare, UK). Following a 24 h exposure period, the phosphor screen was scanned on a Typhoon FLA 7000 scanner (25 µm pixel size; GE Healthcare).

2.10 Oncolytic virus

2.10.1 Oncolytic viruses RP1 and RP1-15

The oncolytic HSV-1 used in this thesis is part of a wider platform presented by Thomas *et al* (Thomas et al., 2019). In this thesis, RP1 version 16 and RP1 version 15 (referred to as RP1 and RP1-15 respectively) were used. RP1 expresses murine GM-CSF (mGM-CSF) and the fusogenic glycoprotein GALV-GP-R$^-$, whilst RP1-15 expresses GFP instead of mGM-CSF. Virus stock vials provided from the manufacturer were aliquoted (5-100 µL) into microcentrifuge tubes and stored at -80°C until required for experimental use, to avoid multiple freeze-thaw cycles. Of note, virus aliquots were always thawed on ice. Both viruses were kindly provided by Replimune (Replimune Inc, MA, USA).

2.10.2 Infection capability of RP1-15 *in vitro*

To determine the infection capability of the virus, MOC1 and MOC2 cells were seeded on 6-well plates (1-2×10^5 cells/well) in DMEM 10% FBS (1.5 mL/well). On the following morning, aliquots of increasing concentrations of RP1-15 (0.01/0.1/1.0/10.0 PFU/cell) were prepared in DMEM 10% FBS at RT. All media was removed and well-resuspended RP1-15 dilutions added to each well (1.5 mL/well). Plates were then placed in a humidified incubator (37°C, 5% CO_2) and taken for imaging on a Celigo S Image Cytometer (Nexcelom Bioscience LLC, MA, USA) at 6, 24 and 48 h after treatment. On the cytometer, plates were imaged with the brightfield and the fluorescence microscope (Green 483/536; exposure 29,735 ms; gain 0). Images were analysed and exported using the Celigo software version 5.2.0.0 (Nexcelom Bioscience). The RP1-15 infectiousness was expressed as the ratio of the GFP-positive area over the area of confluent cells. The following settings were used for image analysis: (*Confluency 1+2*: texture algorithm with an intensity threshold of 10 for brightfield and 26 for green fluorescence signal; precision was set to 'high' for both, all other settings were used as suggested by default). The experiment was performed three times (n=1 well per concentration) but image quantification was only feasible on one of three datasets due to technical difficulties.

2.10.3 Cytopathic effect of RP1 *in vitro*

For determination of the cytopathic effect (CPE), MOC1 and MOC2 cells were seeded on 96-well plates (1750 cells/well) on the evening before treatment initiation. For the treatment, aliquots of increasing concentrations of RP1 (0.1/1.0/10.0/100/500 PFU/cell) were prepared in DMEM 10% FBS at RT. All media was removed and RP1 dilutions added to each well (100 µL/well). Plates were then placed in a humidified incubator (37°C, 5% CO_2) for 48 h and cell viability assessed thereafter. To determine cell viability, CellTiter-Glo® assay (#G7570, Promega Corp, WI, USA) was used following the manufacturer's instructions. In brief, CellTiter-Glo® reagent was thawed and allowed to equilibrate at RT for 4 h prior to assay start. Plates with RP1-treated MOC1 and MOC2 cells were placed on the bench 30 min prior to assay start. Then, the volume of medium left in each well was estimated and the content in each well was topped up with the equivalent amount of Glo reagent (~85 µL). To initiate cell lysis, the plates were placed on a sea-rocker shaker (2 min, RT) and left to incubate on the bench (10 min, RT). Thereafter, 85 µL of each well were transferred into a corresponding well in a white, flat-bottomed 96-well plate (Corning® 96-well plate, Sigma-Aldrich). The luminescence intensity in each well was measured using a luminometer plate reader (LUMIstar Omega, BMG Labtech, DE) and expressed as relative light units (RLU). The signal gain was always based on an untreated control. This experiment was performed three times at n=5 per concentration.

2.10.4 Replication of RP1-15 *in vivo*

MOC1 tumour-bearing mice (n=3-6 per group) were injected intratumourally with RP1-15 (1×10^6 PFU, 10 µL). After 72 or 168 h, mice were culled and tumours, spleens and tumour draining lymph nodes (TD Ln) collected. The organs were weighed and placed into tissue grinding tubes (Precellys Lysing Kit, Bertin Technologies SAS, FR) filled with 0.5 mL of protease inhibitor cocktail (complete ULTRA Tablets, Mini, EASYpack; Roche, CH). The organs were then homogenised using a Precellys 24 tissue homogeniser (Bertin Technologies), selecting programs 1 and 2 with a 10 min break on ice in-between. Grinded tissue was centrifuged (16,000×g, 4°C for 15 min) and supernatants were collected and used as a stock to prepare serial dilutions (1 in 5) in serum-free DMEM medium.

Inguinal/mammary lymph nodes or tumours collected from untreated animals were used as a negative control, and neat RP1-15 virus was used as a positive control. Serial dilutions and control samples (50 µL) were added to 100%-confluent Vero cells, which were seeded the day before (2×10^5 cells/well in 100 µL DMEM 10% FBS on a sterile, flat-bottomed 96-well plate, COSTAR, Sigma-Aldrich). The serial dilutions were incubated (37°C, 5% CO_2) for 2 h and plates were manually tilted every 15 min throughout that period. Afterwards, the supernatants were replaced by 100 µL of culture medium (DMEM 10% FBS) and plates incubated for 72 h. In order to determine the presence of replicating RP1-15, the plates were imaged on a Celigo S Image Cytometer (Nexcelom Bioscience) using the integrated brightfield (3,530 ms; gain 0) and fluorescent microscopes (Green 483/536; exposure 70,000 ms; gain 51). Images were analysed using the Celigo software version 5.2.0.0 (Nexcelom Bioscience) as previously described (2.10.2) and RP1-15 positivity expressed as the ratio of the GFP-positive area over the area of confluent cells. The experiment was performed at least three times per time point (n=1-2 wells per concentration, depending on the yield of organ supernatant).

2.10.5 RP1 therapy of MOC1 mouse model *in vivo*

MOC1 tumours were established as described in section 2.6.2, using a number of 1×10^6 cells resuspended in 100 µL PBS for each flank-injection. Once MOC1 tumours reached a volume of 110 ± 61 mm^3 (mean ± SD) mice were randomised into two groups. For the treatment, a single dose or three repeat doses of RP1 (1×10^6 PFU, 10 µL) or vehicle (PBS, 10 µL) were delivered intratumourally using a BD microfine insuline syringe (BD Biosciences). For repeat dosing studies, the injections were performed every other day, i.e. on day 0, day 2 and day 4. Tumour volumes and body weights were measured on a regular basis starting on the day of treatment commencement (day 0). Of note, no blinding was performed. Tumour volumes were calculated from calliper measurements taken in two dimensions ($volume = \frac{1}{2}\times length\times width^2$). Humane endpoints for *in vivo* studies were determined by the licence protocol with any tumour diameter exceeding 15 mm or superficial tumour ulcerations greater than 5 mm in diameter.

2.10.6 Combination therapy study with RP1 and anti-PD-1 ICB

RP1 treatment of MOC1 tumours was performed as previously described in section 2.10.5. The anti-PD-1 ICB or control IgG2a treatment was either started on day 3 or day 7 after RP1 injection and was administered every third day for three times in total. Anti-PD-1 mAb (clone RMP1-14, 200 µg/injection in 100 µL sterile PBS pH 7.4) or IgG2a (clone 2A3, 200 µg/injection in 100 µL sterile PBS pH 7.4) were delivered intravenously via the tail vein under isoflurane anaesthesia. The antibodies for this study were kindly provided by Dr. Petros Mouratidis (Therapeutic Ultrasound Team, ICR, UK). Treatment monitoring and study endpoints were the same as in 2.10.5.

2.10.7 Tumour perfusion after intratumoural RP1 *in vivo*

MOC1 tumour-bearing mice (tumour volumes ranging from 50 to 200 mm^3) received a single intratumoural dose of RP1 (1×10^6 PFU in 10 µL or 5×10^6 PFU in 50 µL) or no injection as a control. To determine tumour perfusion at a given time, isoflurane-anaesthetised mice were injected with Hoechst® 33342 (50 µL, ~15 mg/kg, #H3570, Thermo Fisher Scientific) via the tail vein. The compound was allowed to distribute systemically for 1 min, whereupon mice were culled and tumours collected (Martinive et al., 2006). The tumours were embedded in OCT and stored at -80°C, protected from light until further use. Cryo-sectioning of tumours to 6 µm thick slices was performed as previously described (2.9.4). For fluorescent imaging, tumour sections were rinsed with PBS and covered with VECTASHIELD® antifade mounting medium (#H-1000-10, Vector Laboratories) and a coverslip. Coverslips were sealed around the perimeter using transparent nail polish and allowed to solidify at 4°C, protected from light for several hours. For the imaging itself, the slides were loaded onto a Zeiss/MetaSystems automated fluorescence and brightfield scanning system (Carl Zeiss Inc, DE). The ROI (tumour section) on each slide was delineated manually and fluorescent scans acquired automatically (0.322 µm/pixel, 20-fold magnification, excitation via PhotoFluor LM75 metal halide lamp with filter for 350/50 nm, dichroic beamsplitter, emission filter for 460/50 nm). Images were exported via the ZenBlue software (Carl Zeiss). Louise Howell (Confocal Microscopy Core facility Sutton, ICR, UK) kindly performed image acquisitions.

2.11 Histopathology

2.11.1 H&E staining of frozen tissue sections

Slides with frozen tissue sections (6-10 µm) were kept in the freezer for the period between cutting and staining. For staining, slides were placed in a small rack and immersed in methanol for 5 min for fixation. Slides were briefly washed in tap water (30 sec) and placed in filtered Gill's III Haematoxylin (#PRC/13/3, Pioneer Research Chemicals, Ltd, UK) for 1 min, followed by rinse in running tap water (4 min). For differentiation, sections were briefly immersed in ~0.67% acid alcohol (1-3 sec for 6-10 µm thick sections), followed by another rinse in running tap water (5 min). Slides were placed in Eosin 1% Aqueous (#PRC766/1; Pioneer Research Chemicals) for 30 sec and then incubated in increasing concentrations of EtOH: 90% EtOH 20-30 sec for 6-10 µm and 100% EtOH 30 sec. Slides were then incubated in xylene for 2 min. Finally, each section was covered with 1 drop of Pertex® Mounting Medium (#PRC/R/750, Pioneer Research Chemicals) and a cover glass and left to solidify at RT. All steps were carried out at RT. Haematoxylin and eosin (H&E) stained sections were digitised on a semi-automated slide scanner via the NDP.scan 2 software (40× magnification; NanoZoomer, Hamamatsu Photonics K.K., JPN) and exported for display using the NDP.view 2 software (Hamamatsu Photonics).

2.11.2 Preparation of FFPE tissue sections

Upon tissue collection, organs were immersed in neutral buffered formalin solution (10%, #HT501128; Sigma-Aldrich) for 24 h, briefly rinsed in PBS (pH 7.4) and transferred into 70% EtOH solution until tissue processing. Tissue processing was kindly performed by Dr. Barbara Martins Da Costa, Paediatric Tumour Biology, ICR, UK. The processed tissue was then embedded in paraffin using a Leica paraffine embedding station (Leica Microsystems Ltd, UK). The paraffin-embedded tissue was cut into 4 µm-thick sections using a manual microtome (Leica RM2125 RTS, Leica Microsystems) and mounted on microscope slides (#3800200E, Leica Microsystems).

2.11.3 H&E staining of FFPE tissue sections

Slides with formalin-fixed and paraffin-embedded (FFPE) sections (4 μm) were placed in a slide staining rack and deparaffinised via immersion in pure xylene (2×5 min), followed by specimen rehydration in decreasing concentrations of ethanol (100%, 90%, 70% for 2 min each). Slides were then placed in ultrapure water (2 min), followed by incubation in filtered Harris Haematoxylin (#H356; TCS Biosciences Ltd, UK) for 6 min. Afterwards slides were washed with running tap water (1 min) and dipped into 0.67% acid alcohol (30% HCl in 70% EtOH). Slides were washed with running tap water (5 min) and placed in 1% aqueous eosin for 2 min, whereupon they were placed in ultrapure water (~10 sec). For tissue dehydration, slides were incubated in 95% and 100% EtOH baths for 1 and 2 min respectively and then left in pure xylene (2×2 min). Finally, each slide was mounted with a cover glass as previously described (2.11.1). All steps were performed at RT. H&E-stained sections were digitised and exported as previously described (2.11.1).

2.11.4 Delineation of necrotic fraction on H&E sections

Digitised H&E-stained tumour sections (FFPE, 4 μm thick) obtained from PD-L1 immunoPET studies following RP1 or PBS treatment were used to determine the area of damaged tissue within each sample. Each section was visually inspected and the area of damaged ('necrotic') tissue manually delineated using NDP.view 2 software (Hamamatsu Photonics). Necrotic areas were characterised by structural disintegration, the presence of haematoxylin-rich, nuclear debris and broad eosinophilic staining. The whole section (excluding areas of skin) was delineated as a reference and the necrotic area expressed as the necrotic fraction.

2.11.5 PD-L1 IHC

For immunohistochemical staining, sections were re-hydrated as described in 2.11.2, with a final incubation in UF water (5 min). For antigen retrieval, a pressure cooker filled with reconstituted citrate buffer solution (1200 mL, pH 6.5; #H-3300, Vector Laboratories, CA, USA) was preheated and slides added in a metal rack. The pressure cooker was safely locked and pressure allowed to build up. Once pressure had built up (yellow plunger pointing out) the retrieval was timed for 5 min. Subsequently, the pressure cooker and content were cooled down with running tap-water. Each section was encircled using a hydrophobic barrier pen (#H-4000, Vector Laboratories) and covered with one drop of 3% H_2O_2 (0.86 mL H_2O_2 30% in 9.14 mL PBS) while placed on a slide staining tray. The peroxidase block was incubated for 10 min, followed by washes with TBS-T. For blocking, the sections were incubated with 10% rabbit serum (Vector Laboratories) for 30 min. PD-L1 primary antibody (Table 2-6) was incubated overnight at 4°C. Thereafter, slides were washed with TBS-T, the secondary rabbit anti-goat antibody (Table 2-6) was added for 30 min and slides were again washed with TBS-T. 3, 3′ diaminobenzidine tetrahydrochloride substrate (DAB; #K3467, Agilent) was used for signal detection and left on for 12 min. All sections were counterstained using Gill's III haematoxylin and the staining differentiated as described in 2.11.3. The sections were de-hydrated in increasing concentrations of ethanol (70% and 90% for 30 sec and 100% 1 min) and placed in xylene (2×2 min). Finally, each section was covered with a drop of paramount reagent and mounted with cover slips as described in 2.11.1. All steps were performed at RT. Slides were digitised as previously described (2.11.1). Optimisation steps of the PD-L1 IHC protocol are presented in Suppl.Fig.2 to 7.

2.11.6 CD8 and PD-1 IHC and computer-assisted image analysis

Staining for CD8 and PD-1 proteins was performed in a similar way to PD-L1 unless for a few variations. All steps up until epitope blocking were performed as in 2.11.5. For blocking of CD8a or PD-1 staining 2.5% goat serum (Vector Laboratories) or 3% BSA (Sigma-Aldrich) in PBS were added for 10 min or 90 min respectively. Thereafter, CD8 or PD-1 primary mAbs were applied overnight at 4°C in a humidified chamber (Table 2-6). The slides were washed with TBS-T, followed by incubation with an anti-rat antibody (30 min) or an anti-rabbit antibody (60 min) for CD8 and PD-1 staining respectively. The remaining steps were performed as described in 2.11.5. Of note, optimisation of both CD8 and PD-1 IHC protocols are shown in Suppl.Fig.8 to 9 and Suppl.Fig.10 to 12 respectively.

The number of CD8 and PD-1 positive cells per section was analysed using Definiens Architect XD™ software version 4.4.3 (Definiens Inc, DEU). At first, a ROI was determined for each section via an automatic ROI detection tool. Next, the cellular analysis was run applying the settings as listed in the subsequent sentences. A haematoxylin threshold of 0.1, a typical nucleus size of 53.216 µm (accepting an area <8) and a simulation inside cytoplasmic stain as the simulation mode with a marker threshold of 0.4 were selected. Furthermore, a typical cell size of 54 μm^2 was determined and the threshold for the IHC marker intensity (selected feature) was set to 0.25 as a benchmark value to distinguish between DAB-stained (>0.25) and unstained (<0.25) cells. All parameters were based on a training dataset.

2.11.7 CD31 IHC and computer-assisted image analysis

For CD31 IHC staining all steps including the heat-mediated antigen retrieval were performed as described in 2.11.5. Thereafter, each section was blocked with 3% H_2O_2 for 15 min, followed by incubation with anti-CD31 mAb (0.2 g/l, Table 2-6) for 1 h. Subsequently, 1 drop of Rat Histofine Max PO (ready to use solution, Table 2-6) per section was incubated for 30 min and visualised via DAB as previously described (2.11.5). All further steps including digitisation of the slides were performed as described in 2.11.5. The CD31 IHC protocol had previously been established in the laboratory and did not require further optimisation.

Intratumoural vessel density was analysed using Definiens Architect XD™ software version 4.4.3 (Definiens). The ROI for each tumour section was determined via manual delineation to ensure coverage of the whole section (all tumour tissue) but strict exclusion of connective tissue surrounding the tumours. Image information included the scan magnification (40-fold) and the resolution (0.226 µm/pixel). Vessel detection was based on IHC brown chromogen, with the cytoplasm as the IHC marker. The following parameters were applied: For vessel detection, an IHC chromogen threshold of 0.12 (determining the minimum DAB chromogen intensity to be considered as 'positive', range of 0-1), a minimum stain area of 11 μm^2 and a gap to close of 7 µm; for vessel classification an area below 110 μm^2 was considered a small vessel, and an area above 2000 μm^2 was considered a large vessel, while everything in-between the two cut-offs was considered medium. Additionally, all areas below 70 μm^2 and every structure with a brown chromogen intensity below 0.04 were excluded. All parameters were based on a training dataset.

Antibody target	Clone	Work dilution	Host species	Conjugate	Company	Catalogue number
CD8	4SM16	1:100	Rat	-	eBioscience	14-0195-82
CD31	SZ31	1:30	Rat	-	Dianova	DIA-310
PD-1 (CD279)	D7D5W	1:200	Rabbit	-	CST	84651
PD-L1 (CD274)	PC	1:500	Goat	-	Research and Diagnostic Systems	AF1019
Anti-rat	PC		Goat	HRP	Vectorlabs	PI-9401
Anti-goat	PC		Rabbit	HRP	Agilent	P0449
Anti-rabbit	PC		Goat	HRP	Agilent	P0448
Anti-rat	NA	1 drop	unkown	HRP	Nichirei Biosciences	414311F

Table 2 - 6: Antibodies (primary and secondary) for IHC. Abbreviations stand for cluster of differentiation (CD), programmed death receptor 1 (PD-1), programmed death ligand 1 (PD-L1), polyclonal (PC), horse-radish peroxidase (HRP).

2.12 Cytokine analysis

2.12.1 Multiplex cytokine analysis of tissue samples

The organs used for cytokine analysis (peripheral blood and tumours) were harvested from RP1 and PBS-treated mice at day 3 after a single treatment, alongside biodistribution studies. Peripheral blood was collected into a 1.5 mL microcentrifuge tube and allowed to clot in upright position for ~30 min, at RT. The sample was then centrifuged at 1,000×g for 10 min at 4°C and the serum (clear supernatant) collected into a 1.5 mL microcentrifuge tube. All serum and tumour samples were snap-frozen in liquid nitrogen and stored at -80°C until further processing. For cytokine analysis, protein extracts of tumours were prepared as previously described in tumour lysis for protein extraction (2.5.2). Serum samples were diluted with sterile PBS (pH 7.4; 1:2). All samples were then shipped to EveTechnologies (Calgary; Canada) on dry ice for multiplex cytokine analysis. Tumour and serum samples were analysed via the 10-plex kit (Millipore) including the following cytokines: GM-CSF, IL-1β, IL-2, IL-4, IL-6, IL-10, IL-12, IFN-γ, TNF-α and MCP-1. Tumours were also analysed via the IFN-α/IFN-β 2-Plex Mouse ProcartaPlex™ Panel (Invitrogen™/Life Technologies). Each sample was filtered prior to the experiment start and assayed in duplicate. The mean of each duplicate was used for analysis wherever possible.

2.13 Statistical analysis

All statistical analysis was performed using GraphPad Prism software, version 9 (GraphPad Software, CA, USA). No data was excluded unless stated in the text. A combination of four normality and log-normality tests (including the Anderson-Darling test, D'Agostino & Pearson test, Shapiro & Wilk test and Kolmogorov-Smirnov test) were applied to assess whether the data met the assumptions for normality and homogeneity of variance. In addition, the distribution of the data was explored graphically via a Q-Q plot. Results from both normality tests and graphical exploration were used to choose between parametric (normally distributed data) and non-parametric statistical tests (data departs from normality) for further analysis. The following statistical tests were used in this thesis:

A *Student's t-test* was applied for any comparisons of the means from two datasets regarding a specific variable (e.g. mean body weight of group A vs. group B). Originally, the Student's *t*-test was designed for the analysis of small samples (Student, 1908). An unpaired Student's *t*-test was applied to determine the difference between two independent groups, whilst a paired *t*-test was applied to compare the means of two measurements of one variable for one group (e.g. before-after measurements). For any datasets with unequal variance, a Welch's test (also referred to as Welch's correction) was applied to reduce the probability of a type I error, i.e. the rejection of the null hypothesis by mistake (Derrick and White, 2016; Welch, 1947). To determine similarity of variance between two datasets, an *F*-test, which looks at the ratio between variance of group A vs. variance of group B, was performed. *P*-values of less than 0.05 were considered statistically significant across all unpaired Student's *t*-tests throughout this thesis. An example for an unpaired *t*-tests with Welch's correction presented in Fig.3-1c, Fig.5-6b, Fig.6-5b and Fig.6-8b. Paired *t*-tests were not applied in this thesis.

In scenarios where multiple *t*-tests had to be applied on one and the same dataset, e.g. in biodistribution experiments where radiotracer uptake was compared between group A and group B across a panel of 10+ organs, *multiple unpaired t-tests* were applied. Since multiple testing increases the probability of a type I error, a method to reduce this error needs to be applied. In such case, the estimation of the false discovery rate (FDR) following the Benjamini-Hochberg procedure is a widely accepted method to reduce the probability of a type I error when multiple *t*-tests are applied. The Benjamini-Hochberg procedure provides a potential gain in power over other methods which are aimed at controlling the family-wise error rate (Benjamini and Hochberg, 1995). In the readout, each discovery is associated with a *q*-value, as a measure of statistical confidence (just like the *p*-value) (Noble, 2009). *Q*-values below the maximum false discovery rate (FDR) of 1% were considered statistically significant. Of note, all *q*-values in this thesis are denoted as *p*-values. Examples for multiple unpaired *t*-tests in this thesis are provided in Fig.4-6b, Fig.6-2c, Fig.6-3a, Fig.6-7a and Fig.6-9.

A *one-way analysis of variance* (ANOVA) was applied to compare the means of more than two independent groups in order to determine whether there is statistical evidence that the associated population means of one categorical variable are significantly different (Fisher, 1921; Moran and Smith, 1918). The one-way ANOVA is also considered an omnibus test because it primarily determines whether there are any significant differences in the means between any of the groups overall. Only the post-hoc tests determine which specific pair(s) of means differ significantly. I chose to apply Tukey correction for post-hoc analysis to compare vessel density among different tumour types (Fig.4-10a) as it is considered the best available method if sample sizes are uneven (Tukey, 1949). For the analysis presented in Fig.5-4, I chose to use the Dunnett's test as it allows to compare each of a number of treatment conditions against one single control (Dunnett, 1955). *P*-values of less than 0.05 were considered statistically significant.

The *two-way ANOVA* is an extension of the one-way ANOVA that examines the influence of two different, categorically independent variables on one continuous variable. As such it not only aims at assessing the main effect of each independent variable, but also if there is any interaction between them (Yates, 1934). Just like its one-way counterpart, it requires post-hoc tests to determine significant differences between pairs of groups. I chose to use the Bonferroni method which is considered a relatively conservative and eventually less powerful test, but well suited if only a few comparisons are made (Lee and Lee, 2018), e.g. Fig.4-3c and Fig.6-3b. In the Bonferroni multiple comparisons method α (or adjusted α) directly depends on the number of hypotheses tested enabling to reduce the probability of a type I error whilst decreasing statistical power. *P*-values of less than 0.05 were considered statistically significant. A two-way ANOVA was used to analyse data presented in Fig.4-3c, Fig.6-3b, Fig.6-11a/b/e/f and Fig.6-16a.

The *Bland-Altman plot* describes the agreement between two quantitative measurements by comparing the mean differences and constructing limits of agreement (Bland and Altman, 1999). The resulting graph is a scatter plot in which the difference of the two paired measurements is plotted against the mean of the two measurements with the potential to visualize a bias between the measurement techniques. Ideally however, the mean difference between the two methods equals zero or comes close to zero (Giavarina, 2015). A Bland-Altman plot was used to compare radioconjugate uptake measured computationally on PET scans vs. via conventional biodistribution and gamma-counting as shown in Fig.4-11a-c.

As compared to the Bland-Altman plot, *correlation* studies the relationship between one variable and another, not the differences. Accordingly, correlation can show whether, and how strongly, pairs of variables are related. The latter is expressed through the correlation coefficient r, a numerical value ranging between -1.0 and +1-0, implying two things the magnitude (r close to zero indicates weak correlation while any r close to 1 indicates a strong correlation) and the direction (positive values of r indicate positive correlation while the inverse accounts for negative values of r). Pearson correlation is the most commonly used method for parametric data and was applied on datasets presented in Fig.4-11d-f and Fig.6-16b (Pearson and Heron, 1913). P-values of less than 0.05 were considered statistically significant.

For certain *in vivo* experiments, a *power analysis* was performed to determine the sample size required to detect a particular effect (assuming an expected difference and standard deviation) at a chosen probability and significance level (80% and 5% respectively) using a two-sided test. An example for such power analysis is provided in chapter 6 (6.2.1). G* Power version 3.1 was used for power analysis (Faul et al., 2009; Faul et al., 2007). No power calculations were performed for exploratory *in vivo* studies, e.g. chapter 3 (3.2.4, 3.2.7), chapter 4 (4.2.3, 4.2.4, 4.2.5, 4.2.6) and chapter 5 (5.2.5, 5.2.6) or therapy studies which followed a design previously published in the literature such as the therapy study in chapter 5 (5.2.4), which was in line with the therapy studies published by Thomas et al., 2019. No power calculations were performed for *in vitro* studies. Each *in vitro* experiment shown in this thesis was performed three times unless stated otherwise. Performing three biological repeats to prove validity of an *in vitro* finding is a widely accepted standard in the biomedical science community.

2.13.1 Statistics in chapter 3

An unpaired Student's *t*-test with Welch's correction was used to compare average protein expression (CD44 or PD-L1) on cells *in vitro*.

2.13.2 Statistics in chapter 4

^{89}Zr-DFO-PD-L1$_{\mathrm{mAb}}$ specificity of binding data was analysed via a two-way ANOVA with Bonferroni multiple comparisons test for each cell line. The ^{89}Zr-DFO-IgG$_{\mathrm{mAb}}$'s specificity of binding data was analysed via an unpaired Student's *t*-test with Welch's correction. Multiple unpaired *t*-tests including the Benjamini-Hochberg procedure for FDR correction were applied to compare the tumour uptake achieved following the injection of 4 different doses to MOC2 and MOC2*(PD-L1)*^{poly} tumour-bearing mice. A one-way ANOVA with Tukey's correction was used for variance analysis of CD31^{+} vessel density across tumour models. The Altman-Bland method test was performed to compare quantification strategies for tumour uptake, (biodistribution vs VOI-based PET image quantification). A Pearson correlation of tumour uptake data (biodistribution vs VOI-based PET image quantification) was performed.

2.13.3 Statistics in chapter 5

For analysis of the cytopathic activity of RP1 on MOC1 and MOC2 cell lines, a one-way ANOVA with a follow-up Dunnett's tests for comparison of every mean against the mean of the control condition (0 PFU) was performed. Data was log(10)-transformed for this analysis to meet the assumptions of normality. For comparison of treatment-dependent tumour volume differences, the area under the curve (AUC) from tumour volume measurements of each mouse was assessed. Accordingly, the AUC was determined as a definite integral of each tumour growth curve between day 0 and day 6 and the averages of AUCs of RP1 vs. PBS-treated groups were compared via an unpaired Student's *t*-test with Welch's correction.

2.13.4 Statistics in chapter 6

The biodistribution data was analysed via multiple unpaired *t*-tests (two-tailed) comparing uptake levels between RP1 vs. PBS-treated groups for each organ set including the Benjamini-Hochberg procedure for FDR correction. Data was log(10)-transformed for analysis to meet the assumptions of normality and equal standard deviations (SD) were assumed for each organ set. Similarly, the differences between the cytokine concentrations of RP1 and PBS treated animals were analysed via multiple unpaired t-tests and Benjamini-Hochberg procedure. For analysis of dynamic changes of RC uptake between day 3 and 7 within RP1 and PBS-treated groups, as well as multi-parameter FC results and IHC results (CD8 and PD-1) a two-way ANOVA with Bonferroni multiple comparisons correction was applied. For analysis of the necrotic fraction between RP1 and PBS treated groups, unpaired Student's *t*-tests with Welch's correction were applied. A Pearson correlation was used to calculate a correlation coefficient for CD8 and PD-1 data from IHC.

Chapter 3: Characterisation of syngeneic mouse models of head and neck squamous s cell carcinoma

3.1 Introduction

In my PhD project, I aimed to study the systemic effects of oncolytic virotherapy (OV), a type of cancer immunotherapy which exploits viruses, on programmed death ligand 1 (PD-L1), a protein involved in cancer-immune crosstalk, in the context of head and neck cancer (hereafter referred to as head and neck squamous cell carcinoma, HNSCC). In order to explore these effects preclinically, I required a mouse model of HNSCC which closely recapitulated the human disease, whilst providing a fully intact immune system to capture cancer-immune system interactions. Given the requirements, I opted for a syngeneic mouse model of HNSCC.

Syngeneic mouse models of cancer are still considered the gold standard to study cancer immunotherapies in a preclinical set-up (Lau et al., 2017; Mosely et al., 2017). To generate a syngeneic mouse model, an immortalised mouse cancer cell line is engrafted in the same mouse strain that it was originally derived from (Zitvogel et al., 2016). Histocompatibility between the cancer cell line and the host immune system ensures recapitulation of native cancer-immune system interactions as required for cancer immunotherapy studies (Olson et al., 2018). So far, no alternative mouse model system, including patient-cancer derived xenograft models and humanised mouse models of cancer, provides a fully intact immune system in order to recapitulate these multi-faceted systemic interactions (Olson et al., 2018). In addition, the latter models are difficult to establish, come at a high cost and often incur issues of reproducibility.

Amongst the limited number of murine HNSCC cancer models, I identified the murine oral carcinoma cell lines 1 and 2, namely MOC1 and MOC2, as suitable cell lines for *in vitro* and *in vivo* modelling of the disease. Both cell lines were derived from tumours of the oral squamous epithelium induced by repeat exposure to the chemical carcinogen 7,12-Dimethylbenz[a]anthracene (DMBA) and were described as moderately differentiated squamous cell carcinomas according to a histopathological assessment (Judd et al., 2012b). Given that these cell lines were generated on a C57Bl/6 background, they allowed for allo-engraftment into fully immunocompetent (C57Bl/6) mice, thus providing optimum conditions to explore cancer-immune system interactions preclinically. Furthermore, these models resemble a wide-spread and particularly difficult to treat type of HNSCC, i.e.

human papillomavirus (HPV) negative, carcinogen-associated squamous cell carcinoma of the oral cavity.

Despite their common derivation, the two cell lines behave differently when engrafted as subcutaneous tumours in C57Bl/6 mice *in vivo*. While MOC2 tumours are described as fast-growing, with 100% take-rate and high metastatic potential, MOC1 tumours exhibit an indolent growth behaviour, take at lower rates and do not metastasise (Judd et al., 2012b). CD44 expression levels are higher in MOC2 than MOC1 cells, supporting evidence that MOC2 is more aggressive and has higher metastatic potential (Judd et al., 2012b). Epidermal growth factor receptor (EGFR), a common protein marker of HNSCC, is expressed at low to medium levels in both, but at a higher level in MOC2 than MOC1 (Judd et al., 2012b).

Immunophenotypically, MOC1 tumours show higher expression of MHC-I, and increased levels of CD8+ T-cells, whilst MOC2 tumours exhibit lower MHC-I expression and higher rates of immunosuppressive cell populations, e.g. regulatory T-cells (Judd et al., 2012a). PD-L1 is expressed at low levels in both cell lines *in vitro* but can be significantly increased upon treatment with type I and type II interferons (IFN) (Robbins et al., 2020; Shah et al., 2016). In tumours, PD-L1 is expressed in various cell compartments, including cancer cells, endothelial cells and immunosuppressive cell populations such as myeloid-derived suppressor cells and regulatory T-cells (Shah et al., 2016). In line with *in vitro* results, PD-L1 expression in tumours is relatively low overall, although slightly higher in MOC1 than MOC2 tumour-derived cell populations (Shah et al., 2016). Furthermore, PD-L1 expression only seems to be partly controlled by interferon levels *in vivo* (Shah et al., 2016).

Both cell lines harbour several driver mutations of human HNSCC, including Trp53, mitogen-activated protein kinase (MAPK), phosphoinositide 3-kinase (PI3K), NOTCH, JAK/STAT and Fat1-4 (Onken et al., 2014). Furthermore, distinct genetic differences between the cell lines were found, including the mutation of different RAS isoforms (H-RAS in MOC1 and K-RAS in MOC2) and most importantly, a higher overall mutational burden in MOC1 compared to MOC2 cells (Judd et al., 2012b; Onken et al., 2014). The latter supports evidence that MOC1 cells have higher immunogenicity and are therefore more amenable to be rejected due to immune surveillance (personal communication with Antonio Rullan, Francis Crick Institute, UK).

Therapy studies have evidenced the differential response of MOC1 vs. MOC2 models to various treatments. Vaccination with irradiated MOC1 cells but not MOC2 cells generated immunological memory against unirradiated cells evidenced by successful tumour rejection at re-challenge (Moore et al., 2016a). Whilst both MOC1 and MOC2 showed no response to anti-PD-L1 monotherapy, the addition of STING agonists significantly increased the therapeutic effect in MOC1 but not MOC2 tumour-bearing mice (Moore et al., 2016a). More therapy studies have been reported, however, using only either of the two cell lines, therefore impairing a direct comparison (Greene et al., 2020; Hayman et al., 2021; Moore et al., 2016b; Robbins et al., 2020; Zolkind et al., 2018). Importantly, to my knowledge, no studies have been published so far investigating the effects of oncolytic viruses in either of the two models.

Taken together, MOC1 and MOC2 models represent a carcinogen-induced type of oral squamous cell carcinoma, harbouring mutations which match common genetic alterations found in human HNSCC. They provide a different immune-phenotype; MOC1 is considered as T-cell inflamed or “hot” and MOC2 as T-cell deprived or “cold”. Both show different responsiveness to several immunotherapies. The publication record indicates that both cell lines are well-established and characterised in mouse models compared to other murine cell lines of HNSCC. More importantly, their response to oncolytic viruses has been vastly unexplored, as well as the PD-L1 expression behaviour upon OV, highlighting the novelty of my studies.

In this chapter I describe the characterisation of MOC1 and MOC2 cells, starting with *in vitro* analyses aimed to prove their phenotypic authenticity as compared to already published work. Next, I report on the expression analyses looking at protein markers of HNSCC and further elaborate on the PD-L1 expression behaviour *in vitro* and *in vivo*. Lastly, I describe the generation of a PD-L1 overexpressing variant of the MOC2 cell line, as well as their characterisation *in vitro* and *in vivo*. With the work presented herein, I am laying the foundation for the work in the following chapters.

3.2 Results

3.2.1 Authentication of MOC1 and MOC2 cell lines *in vitro*

The identity of MOC1 and MOC2 cell lines was initially confirmed *in vitro*. Phenotypically, both cell lines showed similar growth behaviour with a fast average doubling time of ~18.6 h and ~16.6 h for MOC1 and MOC2 respectively (Fig.3-1a). When grown as a monolayer, MOC1 and MOC2 cells presented with slightly different morphology as illustrated on brightfield images (Fig.3-1b). To compare the phenotypic similarity of both cell lines against previously published results, their CD44 expression was measured via flow cytometry (FC). Accordingly, CD44 was expressed at higher levels in MOC2 (MFI of 41246 ± 8248, mean ± SD, n=3) than MOC1 (MFI of 2194 ± 445) cells, which was in line with the results published by Judd *et al* (Judd et al., 2012b) (Fig.3-1c). Genotypic identity testing via short tandem repeat (STR) profiling of DNA extracted from MOC1 and MOC2 cells revealed high genetic overlap with original cell batches (MOC1 100%, MOC2 >80%; Suppl.Fig.1).

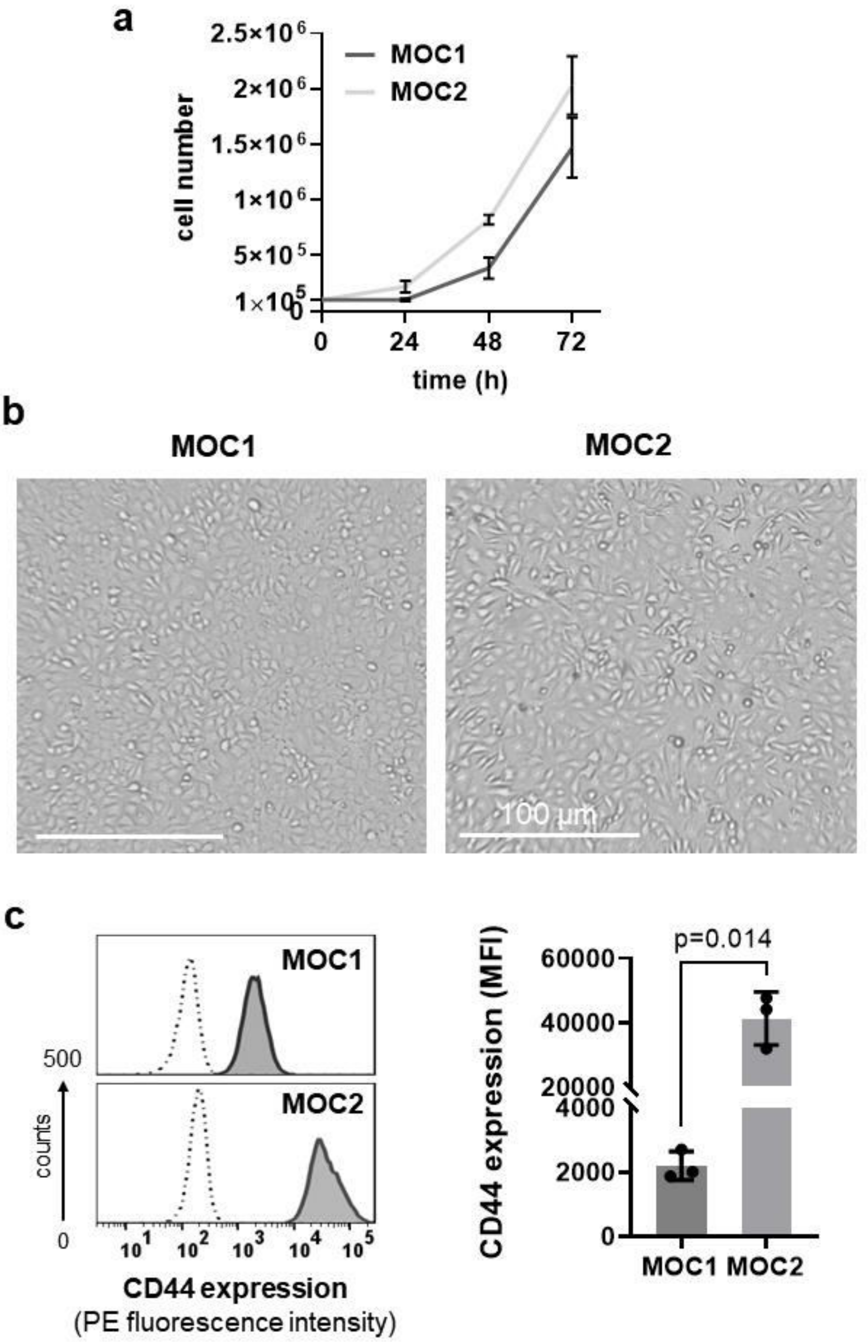

*Figure 3 - 1: **a.** Growth curves of MOC1 and MOC2 cells upon seeding of 1×10^5 cells (6-well plate, n=3) **b.** Brightfield images of MOC1 and MOC2 cells at high confluency in vitro **c.** Representative histograms of CD44-stained (dark grey line) and IgG2b-stained (dashed line) MOC1 and MOC2 cells; bar chart shows median fluorescence intensity (MFI) as mean ± SD of n=3 repeats; unpaired Student's t-test with Welch's correction.*

3.2.2 Expression of select HNSCC markers on MOC1 and MOC2 cells *in vitro*

HNSCC is known to express several marker proteins including epithelial cell adhesion molecule (EpCAM), EGFR and various types of cytokeratins (CK), including type 8 (Andratschke et al., 2015; Ang et al., 2002; Grandis and Tweardy, 1993; Ligtenberg et al., 2018; Lindgren et al., 2017). I aimed to assess the expression level of all three proteins to confirm the phenotypic similarity of MOC1 and MOC2 cell lines towards the human disease. I employed western blot (WB) and FC using anti-EGFR, anti-EpCAM and pan-CK antibodies and investigated expression levels in MOC1 and MOC2 cells, alongside two other murine cancer cell lines, TC-1 and SCC7, which were historically used to model HNSCC (Dillon et al., 2019; O'Malley et al., 1997). The pan-CK antibody targeted multiple cytokeratin epitopes, including types 4, 5, 6, 8, 10, 13, 18. In addition, these experiments enabled the identification of a potential cell line specific marker, which could be used as a tumour cell specific marker in a multi-parameter FC panel.

I found that EpCAM was expressed in all MOC1 (99.6 ± 0.53 % EpCAM-positive events) and a large proportion of MOC2 cells (80.1 ± 3.26 % EpCAM-positive events), with MOC2 cells showing a more heterogenous expression profile (Fig.3-2a/b). The high overall expression of EpCAM in MOC1 cells suggested this protein as a potential marker for this cell line. In contrast, SCC7 and TC-1 cells were vastly EpCAM negative (SCC7 0.08 ± 0.01 % and TC-1 0.06 ± 0.03 % EpCAM-positive events) (Fig.3-2a/b). EGFR expression was very heterogeneous across all tested cell lines, with MOC2 demonstrating relatively high, MOC1 and SCC7 medium and TC-1 negligible levels as evidenced by bands on immunoblots and densitometric quantification of the results (Fig.3-2c/f). Importantly, Judd *et al* also showed a well-defined EGFR band for MOC2 cells, confirming comparatively high receptor expression (Judd et al., 2012b). The pan-CK antibody indicated very low expression of CKs in SCC7 and undetectable expression levels in TC-1 and MOC1 cells (Fig.3-2c/d). However, MOC2 cells demonstrated high intensity bands at both 50 and 55 kDa, suggesting this group of proteins as a potential cell-line specific marker. FC analysis of pan-CK stained MOC2 cells confirmed high overall CK expression (99.9 ± 0.1% pan-CK-positive events, mean ± SD, n=3) (Fig.3-2e).

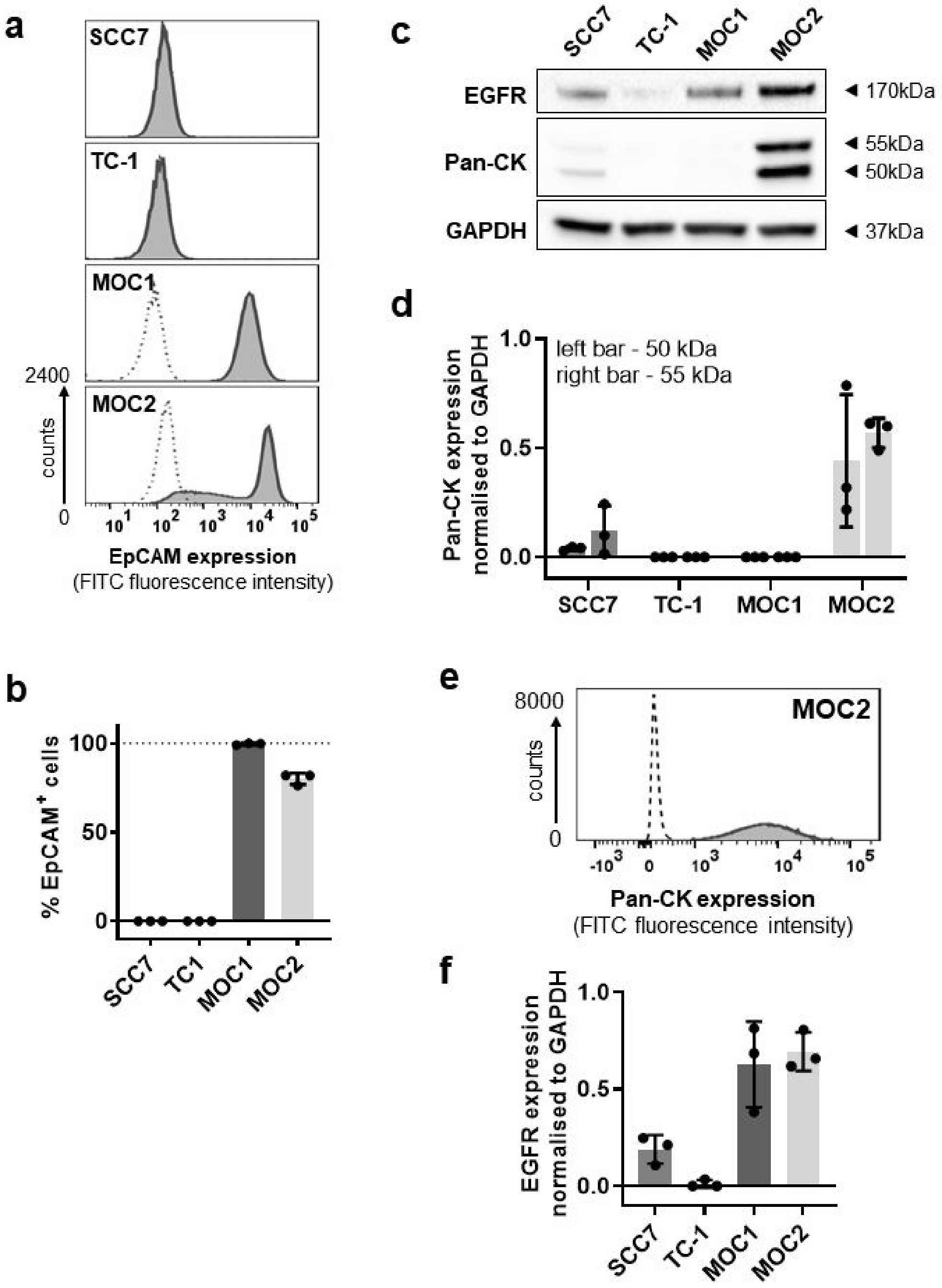

*Figure 3 - 2: **a.** Histograms of EpCAM-stained (dark grey line) and IgG2b-stained (dashed line) cells **b.** Bar chart of EpCAM-positive events as a fraction of all singlet and alive events (mean ± SD; n=3 repeats), gating based on unstained control **c.** EGFR and pan-CK expression levels in cell lysates assessed via western blot (WB) **d.** Bar chart shows pan-CK expression normalised to GAPDH as assessed via densitometric analysis of WB bands (mean ± SD; n=3 repeats) **e.** Histogram of pan-CK stained MOC2 cells (dark grey, coloured histogram) or IgG1 isotype stained cells (dashed line) **f.** Bar chart shows EGFR expression normalised to GAPDH assessed via densitometric analysis of WB bands (mean ± SD; n=3 repeats).*

3.2.3 PD-L1 expression of MOC1 and MOC2 cells *in vitro*

Next, I assessed the PD-L1 expression profile of MOC1 and MOC2 as well as SCC7 and TC-1 cells at baseline and upon IFN-γ stimulation by FC and WB. The cytokine IFN-γ is a potent inducer of PD-L1 expression and is frequently used to assess the capability of cells to upregulate PD-L1 (Loke and Allison, 2003; Shah et al., 2016). Low baseline PD-L1 expression was found in MOC1 (MFI of 269 ± 51; mean ± SD, n=3), MOC2 (MFI of 485 ± 57) and SCC7 cells (MFI of 348 ± 39) and was slightly higher in TC-1 cells (MFI of 743 ± 105) (Fig.3-3a/b). *In vitro* stimulation with murine IFN-γ (20 ng/mL, 24 h) markedly increased PD-L1 expression across all cell lines: MOC1 (MFI of 2656 ± 741, n=3, *p*=0.03), MOC2 (MFI of 2811 ± 759; *p*=0.04), SCC7 (MFI of 4945 ± 2155, *ns*), TC-1 (MFI of 5395 ± 1755; *p*=0.04) (Fig.3-3a/b). This data was corroborated by WB results obtained from cell lysates of cells stimulated the same way (Fig.3-3c). Importantly, these findings are in line with work previously published on PD-L1 expression levels of MOC1 and MOC2 cells with or without IFN-treatment *in vitro* (Robbins et al., 2020; Shah et al., 2016).

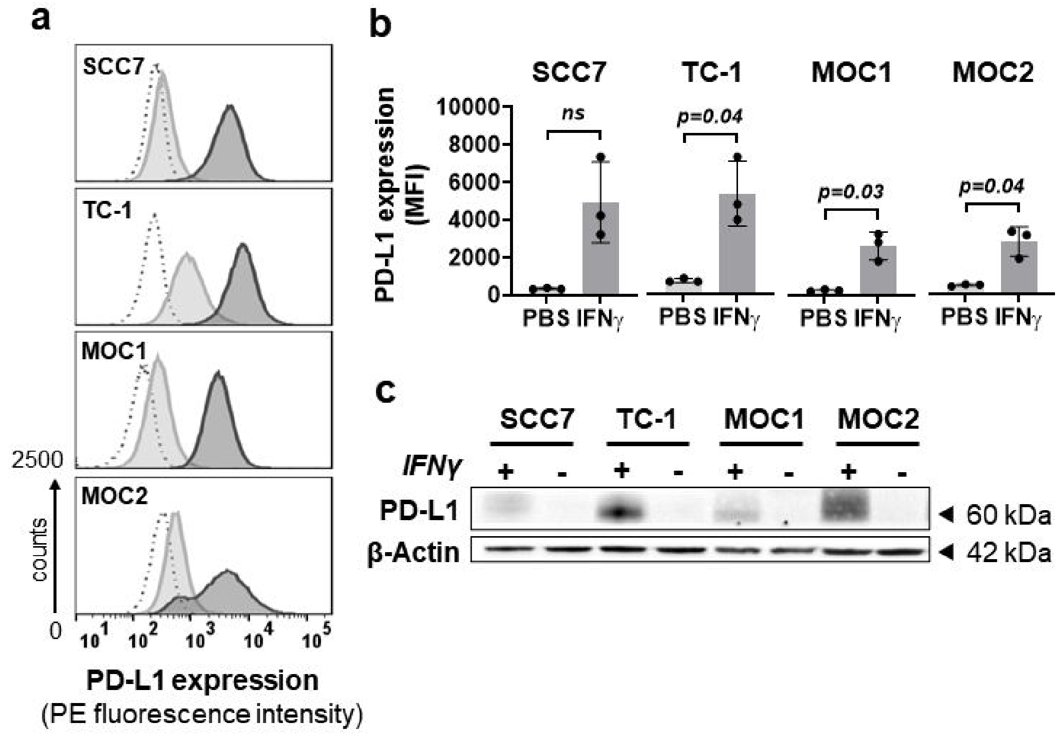

*Figure 3 - 3: **a.** Representative histograms of anti PD-L1-stained cells (grey-coloured histograms) after vehicle (light grey) or IFN-γ (dark grey) stimulation (20 ng/mL for 24 h) and IgG2b-stained cells (black dashed line, no filling), 1 of 3 repeats **b.** Bar charts show PD-L1 expression (MFI) as assessed via FC (mean ± SD, n=3 repeats), unpaired*

Student's t-test with Welch's correction was applied ***c.*** *PD-L1 expression levels assessed on cell lysates of IFN-γ and PBS-treated samples via WB (1 of 3 repeats).*

3.2.4 Growth kinetics and PD-L1 expression of MOC1 and MOC2 tumours *in vivo*

Although orthotopic tumours (i.e. oral cavity) would have been the preferred choice providing a microenvironment matching MOC1 and MOC2 original sites, tumour engraftment at a heterotopic site (i.e flank) was selected instead for the following reasons: (i) accessibility and ease of volume-monitoring (calliper measurements, no anaesthesia required) (ii) stringent size limits for tumours in oral cavity (tumour volumes >100 mm^3 are required for reasonable count statistics in PET and a reasonable range of tumour volumes 100-1000 mm^3 for therapeutic studies) and (iii) welfare concerns with orthotopic tumours (tumours might affect food and water intake) and difficulty monitoring them. The crucial limitation of the heterotopic model was the altered microenvironment for MOC1 and MOC2 cells which eventually impacts tumour growth, angiogenesis and morphology as shown for other tumour types (Erstad et al., 2018). It is important to bear in mind that the use of calliper measurements as a basis for tumour volume assessment can confer a bias (under- or overestimation of the exact tumour volume depending on tumour shape and the volume formula used) and reduce overall sensitivity to detect volumetric changes (Faustino-Rocha et al., 2013; Pollok et al., 2009). However, due to its ease of use it remains the most frequently used tool to monitor tumour volume progression in preclinical *in vivo* studies.

Following subcutaneous flank injection, MOC1 tumours showed an indolent growth phenotype with latent growth onset and a relatively long average doubling time of ~4.1 days, whereas MOC2 tumours showed a more aggressive growth phenotype, with an average tumour volume doubling time of ~2.7 days (Fig.3-4a). All MOC2 tumours reached a volume of 100 mm^3 within less than two weeks, while only one MOC1 tumour exceeded this volume within 26 days post-cell injection. Both tumour types had a take rate of 100% and a subset of animals developed tumour ulcerations (Fig.3-4b). Neither spontaneous regression of tumours nor a substantial decrease in body weight was observed in either of the models (Fig.3-4a). Importantly, these observations matched tumour growth data published by the Uppaluri lab (Judd et al., 2012b). To check whether the growth onset and growth rate of MOC1 tumours could be improved, three different cell numbers (2×10^6, 1×10^6, 5×10^5; n=3 per group) were injected. Animals injected with 1×10^6 or 2×10^6 cells, showed 100% uptake of tumours, and similar growth behaviour as previously reported (Suppl.Fig.13). The take rate with 5×10^5 cells was reduced (1 out of 3 mice). Additionally, a higher cell number seemed to be associated with higher probability of ulceration. Therefore, I decided to inject 1×10^6 MOC1 cells for all future cell implantations.

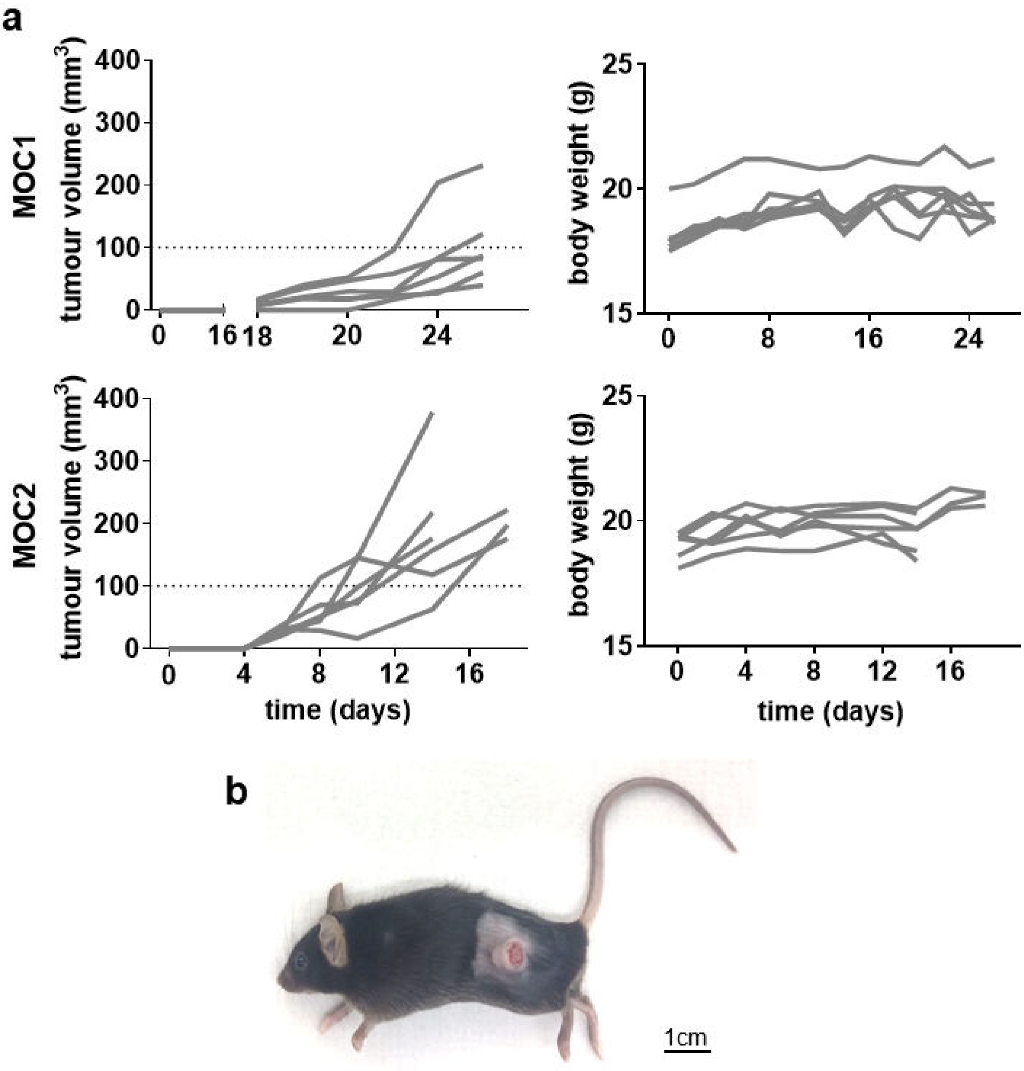

*Figure 3 - 4: **a.** Tumour growth curves of MOC1 (2×10^6 cells s.c.) and MOC2 (1×10^6 cells s.c.) mouse models (n=6 mice per model) together with body weight records. **b.** Representative ulceration (advanced stage) of MOC1 subcutaneous flank tumour.*

Next, I assessed the PD-L1 expression level of MOC1 and MOC2 tumours via immunohistochemistry (IHC) and WB. For PD-L1 IHC, several primary antibodies were tested including clone 10F.9G2 (BioXcell), clone D5V3B (Cell Signaling Technology) and a polyclonal antibody (#AF1019, Research and Diagnostic Systems); however, only the polyclonal anti-PD-L1 Ab showed staining at all. The staining protocol was then optimised to yield an optimal staining outcome with this primary antibody (Suppl.Fig.2-7). Applying the optimised IHC protocol, very low PD-L1 signal was detected across IHC stained tissue sections of both MOC1 and MOC2 tumour types as compared to PD-L1 expressing spleen tissue (Fig.3-5a/b). These results were corroborated by WB of whole tumour lysates showing low expression of PD-L1 (Fig.3-5c). Of note, WB bands revealed higher variability in PD-L1 expression amongst MOC1 as compared to MOC2 tumours (Fig.3-5c). In summary, both MOC1 and MOC2 tumours exhibited low PD-L1 expression thus providing suboptimal conditions to optimise injection conditions of a PD-L1 specific PET radioconjugate for tumour imaging *in vivo*.

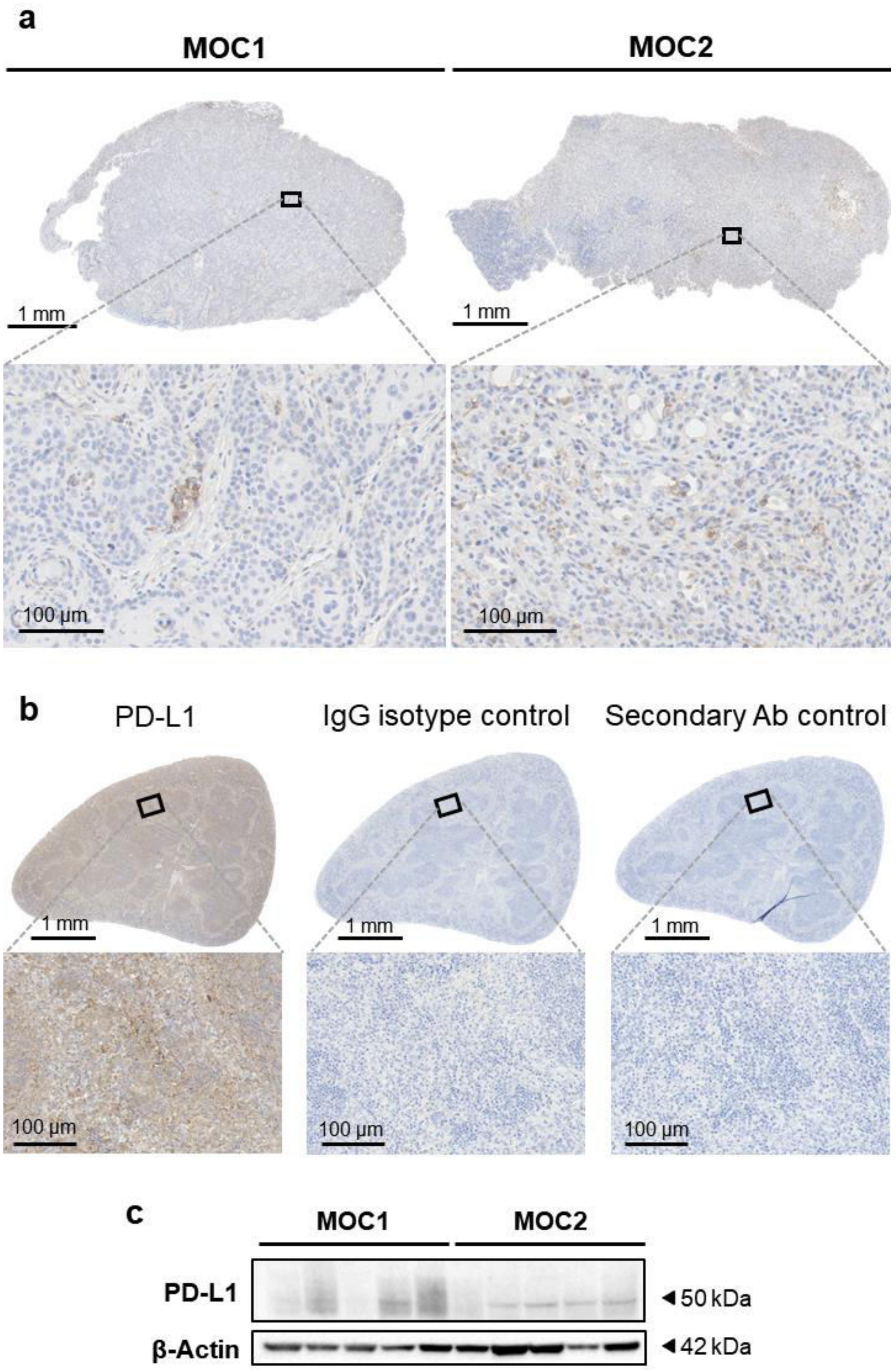

*Figure 3 - 5: **a.** PD-L1 IHC of MOC1 and MOC2 tumour sections as an overview and a zoom of a representative area **b.** Spleen sections used as positive control tissue for PD-L1 IHC, IgG isotype control and secondary antibody (Ab) control (from left to right) **c.** PD-L1 protein levels in tumour lysates assessed via WB (n=5 per model).*

3.2.5 Establishment of PD-L1 overexpressing MOC2 cell line

To obtain a murine model cell line expressing PD-L1 at higher baseline levels, MOC2 cells were transfected lentivirally with *pLenti-CD274-GFP* to ectopically overexpress the PD-L1 protein (Fig.3-6a). Lentiviral transfection was selected as it is considered a potent and reliable tool for the introduction of foreign DNA into mammalian cells, providing stable transgene expression over extended periods of time (Elsner and Bohne, 2017). Furthermore, lentiviruses are capable of infecting both dividing and non-dividing cells but carry the risk of inducing irreversible genotoxic effects. Other viruses, e.g. adenoviruses, can also be used for gene transduction but eventually fail to induce long-lasting gene expression (Fus-Kujawa et al., 2021). Non-viral alternatives for gene transfection are based on physical (electroporation, magnetic beads) or chemical methods (e.g cationic lipids), but might provide lower transfection efficiency whilst bearing a higher risk of cell damage (e.g. electroporation which uses electric current to transiently increase cell membrane permeability).

Initially, a diagnostic digest and subsequent DNA-electrophoresis were performed to confirm the identity of the *pLenti-CD274-GFP* plasmid (Fig.3-6a/b). Single digestion with either AsiSI or MluI restriction enzymes showed one intense band at ~10 kb, which was marginally higher than expected. A double digest with these enzymes, resulted in a faint band at ~0.9 kb and an intense band between 7-8 kb. When no restriction enzymes were added, a non-specific, stretched band was detected.

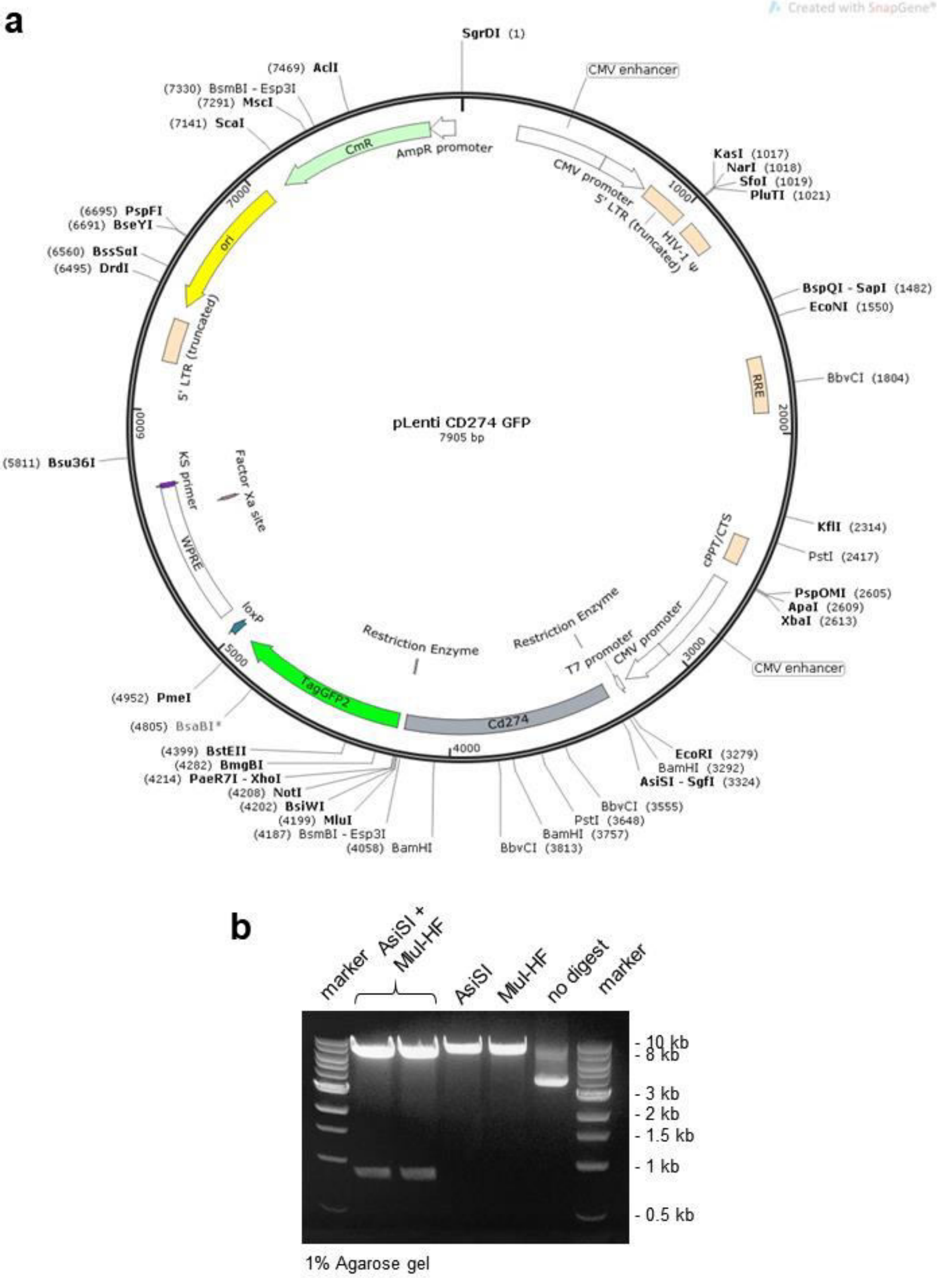

*Figure 3 - 6: **a.** pLenti-CD274-GFP plasmid map with restriction sites **b.** pLenti-CD274-GFP DNA (~0.5 µg) separated via gel electrophoresis on an agarose gel (1%) after digestion with restriction enzymes; marker bands indicated in kilobases (kB).*

Next, viral particles were produced in HEK293T cells, however this resulted in relatively low viral titres, as evidenced by a faint band on Lenti-X™ GoStix™ (Fig.3-7a). Accordingly, incubation of MOC2 cells with *CD274*-positive lentiviral particles achieved low transfection efficiency (<10%). To obtain a green fluorescent protein (GFP)-positive cell population, cells were sorted via

FACS and expanded in culture, and subsequently seeded for single cell clone selection. Following 10-14 days of growth, 25 small colonies were harvested and screened for GFP reporter gene expression via FC. As an alternative to FC, quantitative PCR (qPCR) could have been used to determine the copy number changes of PD-L1 mRNA. However, due to limited resources, I chose to use FC instead (FC reagents and protocols were available from previous experiment whereas qPCR reagents/protocols were not). According to FC results, clone 22 showed very high GFP expression, with a 41-fold increase of GFP fluorescence relative to the autofluorescence level detected in MOC2 parental cells (Fig.3-7b). Clone 7 showed the second highest GFP-expression level with a 9-fold increase over MOC2 autofluorescence, while the remaining 23 clones showed very low GFP-expression (1 to 4-fold increase compared to MOC2).

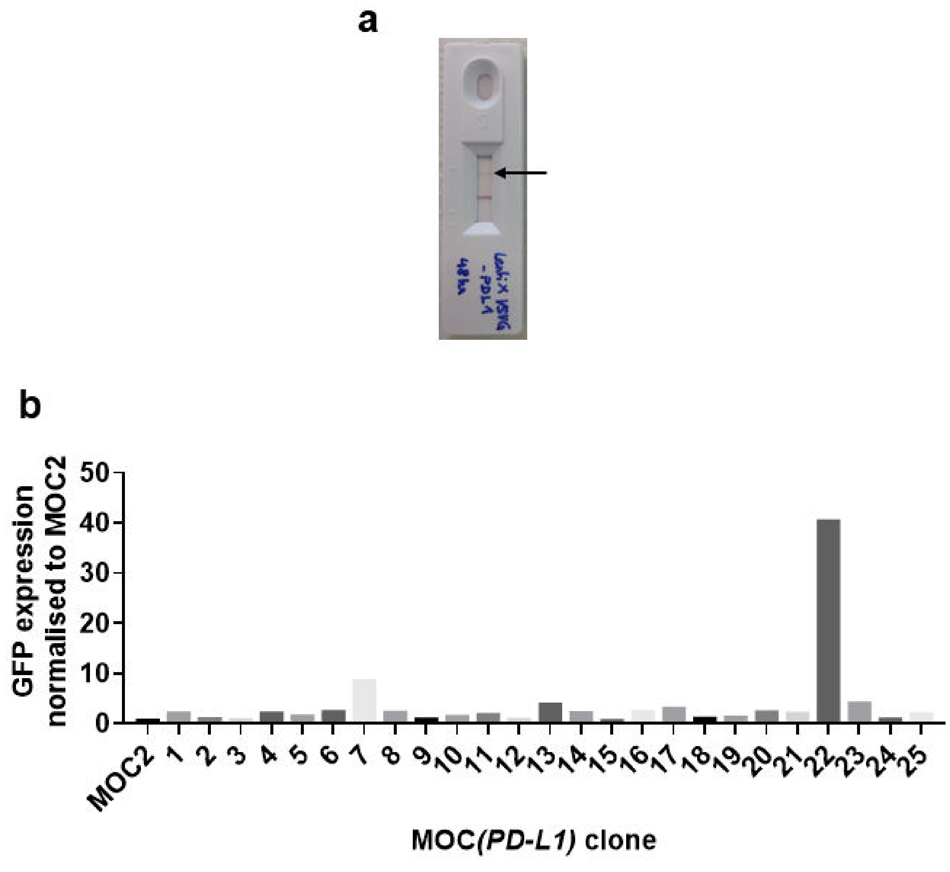

Figure 3 - 7: ***a.*** *Lenti-X GoStix showing a faint band (arrow) indicating the presence of lentiviral particles and an intense band indicating a valid result.* ***b.*** *Expression levels of GFP reporter (GFP expression normalised to MOC2 parental cells) of various single cell clones derived from MOC2(PD-L1)^{poly} cells, GFP expression was measured via FC (n=1).*

3.2.6 Characterisation of PD-L1 overexpressing MOC2 cell line *in vitro*

Due to the exceptionally high PD-L1 expression level, clone 22 (hereafter referred to as MOC2*(PD-L1)*^{single}) was chosen for further characterisation alongside the polyclonal cell population, MOC2*(PD-L1)*^{poly}, and MOC2 cells as a baseline control. Of note, the monoclonal cell population is genetically homogeneous thus providing an ideal PD-L1 expressing positive control (e.g. improved stability and homogenous expression properties). In contrast, the polyclonal counterpart is genetically heterogenous which limits its role as a positive control (e.g. variation in expression level and stability) whilst providing a better recapitulation of the genetic diversity present in the parental cell population (i.e. MOC2). The genotypic similarity between parent and daughter cell lines (except for their differential PD-L1 status) might be of particular relevance for tumour engraftment and the conservation of tumour phenotypic characteristics *in vivo*.

Confocal microscopy showed medium and variable expression of GFP and PD-L1 in MOC2*(PD-L1)*^{poly} cells compared to a higher and more consistent expression of both, GFP and PD-L1, in the MOC2*(PD-L1)*^{single} population (Fig.3-8). In both cell populations, PD-L1 was expressed ectopically, according to the protein's original expression site. Neither GFP-positivity nor PD-L1-stained cells were detected in the parental MOC2 population. MOC2*(PD-L1)*^{poly} cells were stained with the anti-rat IgG secondary antibody as a control and no staining was observed.

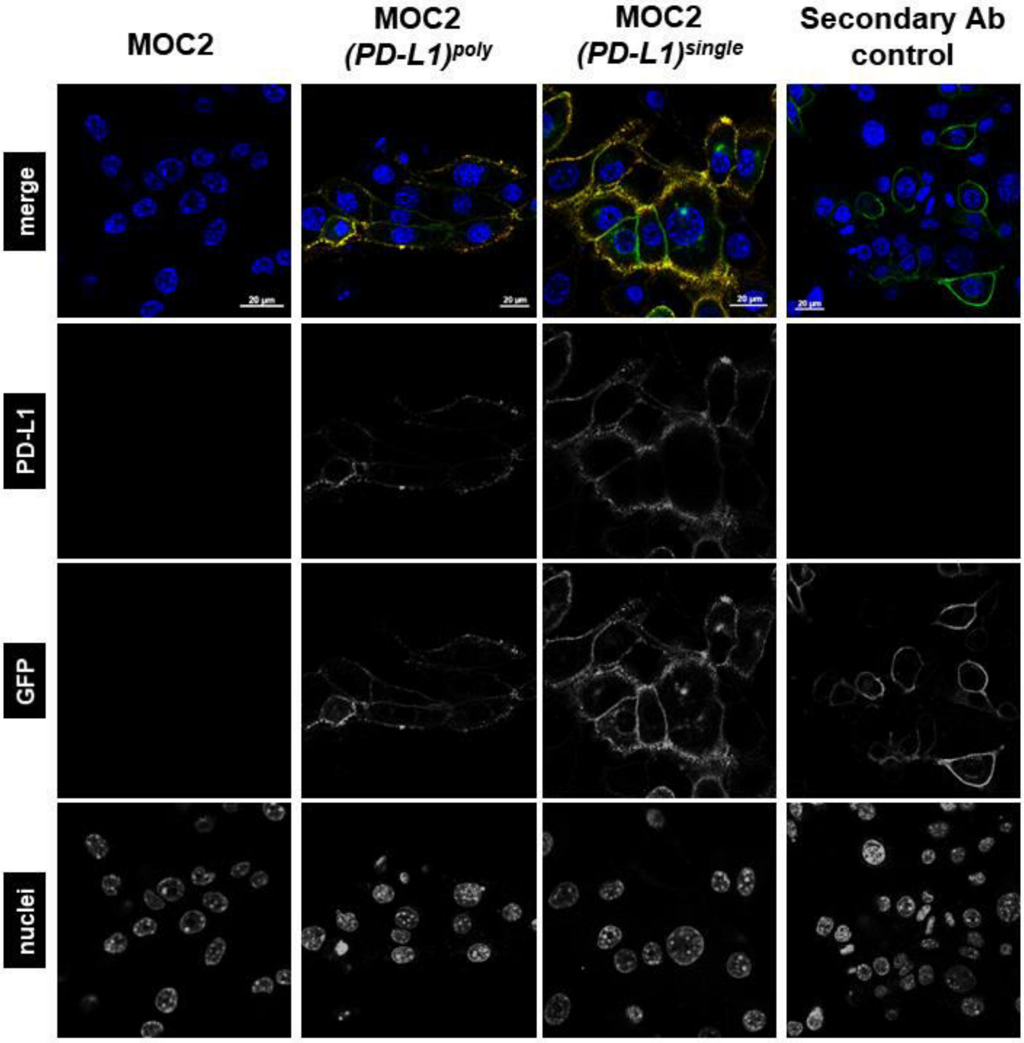

Figure 3 - 8: Confocal microscopy images of MOC2, MOC2(PD-L1)^{poly} and MOC2(PD-L1)^{single} cells, and anti-rat IgG (secondary) control performed on MOC2(PD-L1)^{poly} cells (n=1). Merged channel images (top row) are shown in colour with nuclei represented in blue, GFP in green, PD-L1 in red, while single-channel images are shown in black and white (rows two to four).

The results obtained from further analyses of PD-L1 expression via FC and WB were in line with confocal microscopy findings (Fig.3-9a/b). They confirmed high, intermediate and negligible PD-L1 expression in MOC2*(PD-L1)*^{single} (MFI 27,848 ± 5,253; mean ± SD, n=2-3), MOC2*(PD-L1)*^{poly} (MFI 11,902 ± 6,552) and MOC2 (MFI 318 ± 38) cells respectively. Unexpectedly, longitudinal analysis of PD-L1 expression via FC revealed a passage-dependent decrease of the protein, indicating unstable expression over time (Fig.3-9c). Importantly, this observation was made on untreated cells (no IFN supplement). Therefore, to ensure as little variation as possible, I decided to use only early passages (passages 1 to 3) of

MOC2*(PD-L1)*^{poly} and MOC2*(PD-L1)*^{single} cells for *in vitro* and *in vivo* (i.e. subcutaneous inoculation) studies.

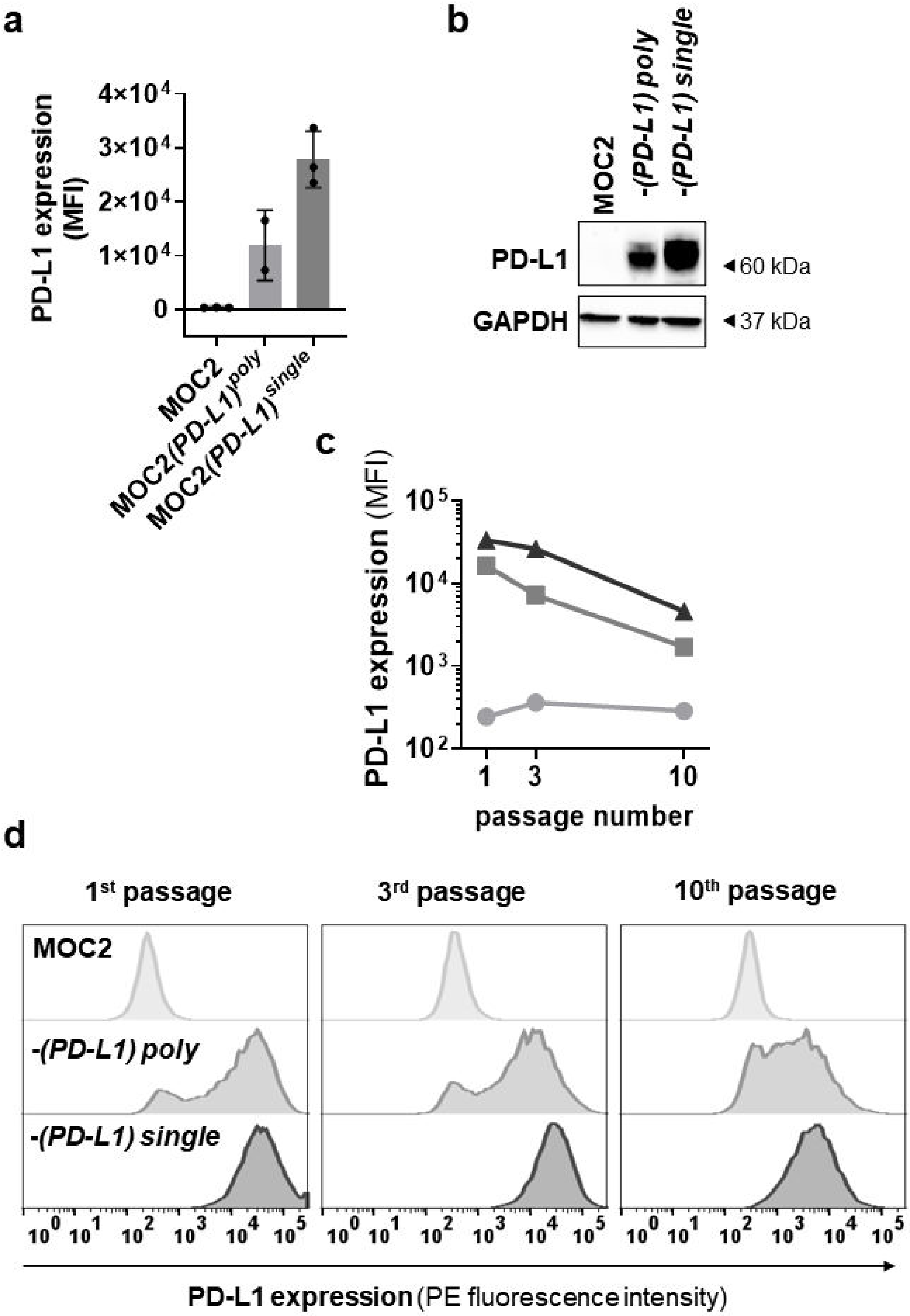

*Figure 3 - 9: **a.** PD-L1 expression (MFI) measured via FC, expressed as mean ± SD of n=3 repeats for all but MOC2(PD-L1)^{poly} (n=2 repeats) **b.** PD-L1 protein levels in cell lysates assessed via WB (1 of 3 repeats) **c.** and **d.** PD-L1 expression (MFI values in c. and histograms in d.) over a period 10 passages measured via FC (n=1).*

3.2.7 Growth kinetics and PD-L1 expression of MOC2*(PD-L1)*^{poly} and MOC2*(PD-L1)*^{single} tumours *in vivo*

Following characterisation of cells *in vitro*, MOC2*(PD-L1)*^{poly} and MOC2*(PD-L1)*^{single} cell lines were inoculated subcutaneously *in vivo*. The take rate was 100% for both and the majority of tumours reached a volume of 100 mm^3 at 15-16 days post-injection (Fig.3-10). As previously observed in MOC1 and MOC2 tumours, a small fraction of tumours developed ulcerations and neither spontaneous regression of tumours nor a decrease in body weights was observed (Fig.3-10).

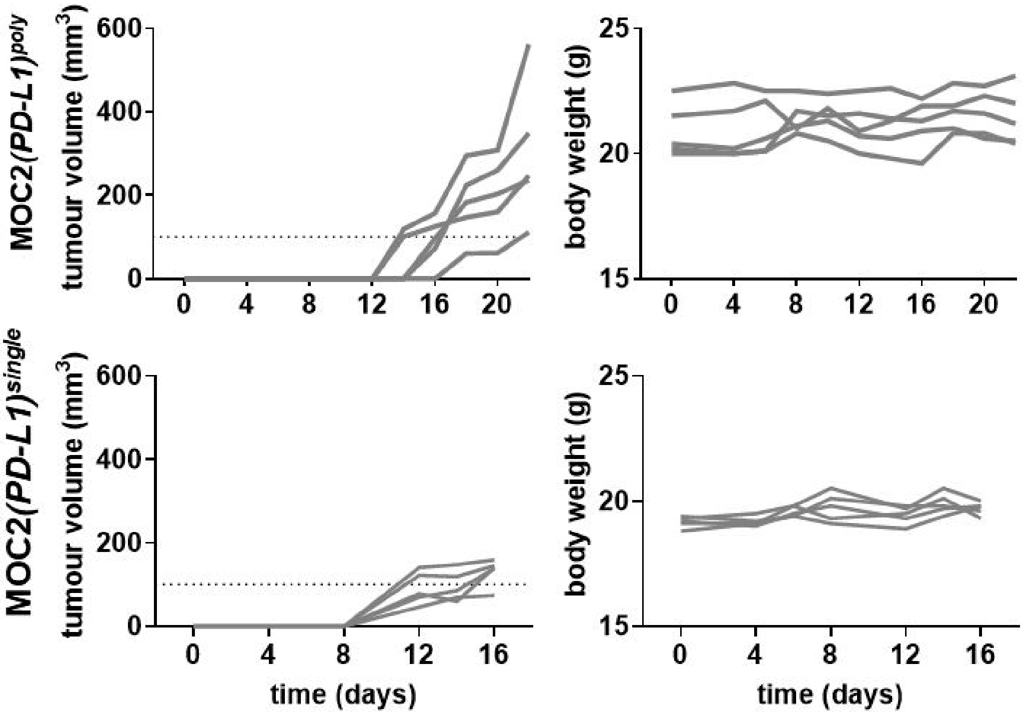

Figure 3 - 10: Tumour growth curves of MOC2(PD-L1)^{poly} (1×10^6 cells s.c.) and MOC2(PD-L1)^{single} (1×10^6 cells s.c) mouse models (n=5 per model) alongside body weight records.

PD-L1 expression of MOC2*(PD-L1)*^{poly} and MOC2*(PD-L1)*^{single} tumours was assessed via IHC and WB. PD-L1 IHC-stained MOC2*(PD-L1)*^{poly} tumours showed a slight increase of PD-L1, spread heterogeneously across the tumour section (Fig.3-11a). In comparison, MOC2*(PD-L1)*^{single} tumours showed markedly higher levels of PD-L1, however, with intrasectional heterogeneity (Fig.3-11a). Of note, PD-L1 expression patterns across IHC-stained tumour sections were assessed via visual inspection only. Isotype control and secondary antibody only stained spleen sections were used to confirm specificity of primary and secondary antibodies (Fig.3-11b). The difference in overall PD-L1 expression was corroborated by WB analysis of tumour lysates (Fig.3-11c) In summary, both tumour types showed an intermediate or high increase of PD-L1 expression, which revealed to be heterogeneous as evidenced by confined areas with enhanced PD-L1 staining across the whole tumour section.

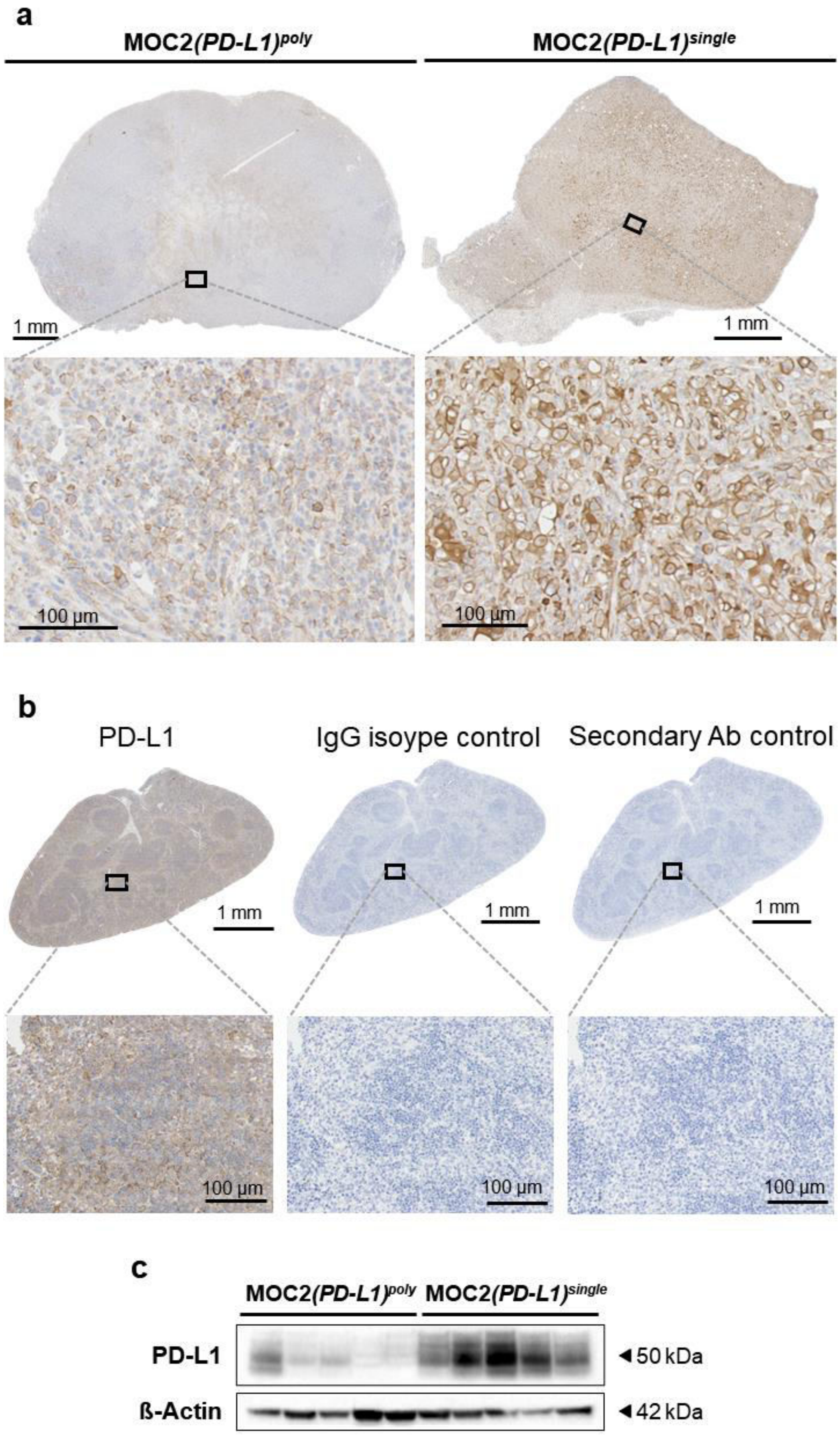
a
MOC2(PD-L1)poly
MOC2(PD-L1)single
1 mm
1 mm
100 µm
100 µm
b
PD-L1
IgG isoype control
Secondary Ab control
1 mm
1 mm
1 mm
100 µm
100 µm
100 µm
c
MOC2(PD-L1)poly
MOC2(PD-L1)single
PD-L1
ß-Actin
◄50 kDa
◄42 kDa

*Figure 3 - 11: **a.** PD-L1 IHC of MOC2(PD-L1)^{poly} and MOC2(PD-L1)^{single} tumour sections shown as an overview and a selected zoomed area. **b.** Spleen sections used as positive control tissue for PD-L1 IHC, IgG isotype control and secondary antibody (Ab) control (from left to right). **c.** PD-L1 expression assessed on tumour lysates via WB (n=5 samples per model).*

3.3 Conclusion and discussion

Sensible selection and characterisation of syngeneic murine cancer models is key to ensure both the optimum recapitulation of the human disease as well as the best-fit model for the research purpose. For cancer immunotherapy purposes, syngeneic mouse models are still the most widely used *in vivo* model systems, as they enable recapitulation of cancer-immune system interactions. In regard to HNSCC, MOC1 and MOC2 syngeneic models provide key features of the human disease and have a significant track record in the field of cancer immunotherapy research (Moore et al., 2016b; Onken et al., 2014; Robbins et al., 2020). Additionally, they resemble a very common and difficult to treat subtype of HNSCC, so-called carcinogen-induced, HPV-negative oral carcinomas.

Analyses aimed to confirm the authenticity of MOC1 and MOC2 cell lines *in vitro*, revealed higher expression levels of CD44 and EGFR proteins on MOC2 as compared to MOC1 cells (Fig.3-1c, Fig.3-2c/f), which was in line with work published by Judd *et al* (Judd et al., 2012b). Phenotypic authenticity was further corroborated by the growth behaviour of both cell lines *in vivo*, showing that MOC1 cells grew at slower pace than MOC2 (Fig.3-4a), when engrafted subcutaneously in female C57Bl/6J mice (Judd et al., 2012b). Finally, STR profiling of DNA extracts confirmed high genetic overlap with reference profiles obtained from original stocks (>80% for both; see Suppl.Fig.1).

In an effort to investigate the expression levels of common markers of HNSCC, I found that MOC1 expressed EpCAM at high levels across all cells and could therefore be used as a marker in multi-parameter FC panels (Fig.3-2a/b). Likewise, EpCAM expression was high on MOC2 cells but not across the whole cell population. Pan-CK, a common marker of squamous cell carcinomas, showed high binding to MOC2 cells via WB and FC, confirming its potential as a specific marker for this cell line (Fig.3-2d/e). EGFR expression levels were intermediate in both cell lines, albeit higher in MOC2 than MOC1 (Fig.3-2c/f), and matched previously reported results (Judd et al., 2012b). The direct comparison with SCC7 and TC-1 cells, both derived from anatomical sites other than the head and neck, revealed negligible expression levels of all three HNSCC-specific marker proteins (Fig.3-2a-f). According to this expression analysis, MOC1 and MOC2 cell lines resemble common features of HNSCC well, as evidenced by the expression of EGFR, EpCAM and cytokeratins.

PD-L1 expression analysis revealed low inherent levels of PD-L1 across MOC1 and MOC2, *in vitro* and *in vivo* (Fig.3-3a-c, Fig.3-4b-c). These findings are supported by results previously published on MOC1 and MOC2 models (Robbins et al., 2020; Shah et al., 2016). In contrast, a selection of HNSCC cell lines of human origin, including JHU-011, JHU-022, JHU-029, were found to have relatively high levels of PD-L1 expression in culture (Chen et al., 2019; Lyford-Pike et al., 2013). I also performed IFN-γ stimulation experiments *in vitro* and confirmed that the cytokine potently upregulates PD-L1 across MOC1 and MOC2 cell lines (Fig.3-3a-c) as previously shown by others (Robbins et al., 2020; Shah et al., 2016). Remarkably, Shah *et al* report a differential correlation of PD-L1 expression on tumour-resident cell populations and tumour IFN-γ transcript levels *in vivo*, which seemed cell type dependent across MOC1 and MOC2 tumours (Shah et al., 2016).

In prospect of the next steps in my project, i.e. the characterisation of a PD-L1 targeted PET radioconjugate for which I required a positive control cell line, I generated a PD-L1 overexpressing variant of MOC2 cells. I selected a *CD274*-encoding plasmid controlled by a cytomegalovirus (CMV) promoter to achieve stable overexpression of PD-L1. Characterisation of the polyclonal and monoclonal PD-L1 overexpressing MOC2 variants *in vitro* showed intermediate and high PD-L1 expression at early passages (2-3) (Fig.3-6a-d). However, longitudinal analysis revealed a passage-dependent loss of PD-L1 (Fig.3-6d), indicating unstable expression of the protein. Unstable expression of CMV promoter-controlled transgenes in mouse cancer cell lines has also been observed by others (personal communication with Antonio Rullan, Francis Crick Institute, UK). Although CMV promoters are strong viral transcriptional promoters, one major limitation is their susceptibility to silencing (Radhakrishnan et al., 2008). Promoter silencing is caused by gradual methylation of the transfected promoter leading to a decrease in transcription (Brooks et al., 2004). To overcome this particular issue a promoter type which is less susceptible to silencing, e.g. the internal spleen focus-forming virus (SFFV) promoter, could be tested in future studies (Demaison et al., 2002). Alternatively, work published by Chi-Ping Day *et al* suggests the use of the ferritin heavy chain (FerH) or RNA polymerase II (Pol

II) promoters for stable expression of transgenes in murine cell lines (Day et al., 2009; Day et al., 2014). Similarly, a CMV-enhanced b-albumin (bAlb) promoter (personal communication with Antonio Rullan, Francis Crick Institute, UK) or the murine phosphoglycerate kinase (mPGK) promoter (Nieuwenhuis et al., 2021) might improve transgene expression in MOC2 cells. A head-to-head comparison of these promoters controlling *CD274* expression performance in MOC2 cells could be conducted in future studies. For the purpose of this project however, I opted to simply freeze a large stock of both cell lines and use them solely within the first three passages after thawing. PD-L1 expression analyses of cell and tumour samples indicated reproducible expression levels within this early passage window.

Of note, protein expression analysis in tumours, was performed via IHC and WB only. Whilst IHC allowed to localise the PD-L1 protein within the tumour section and confirm the cell surface as its predominant expression site, WB results of whole tumour lysates showed overall protein abundance (across PD-L1 expressing cell populations and all cellular compartments) in the tissue chunk. Consequently, the two methods provided somewhat complementary information on PD-L1 protein expression, but neither of them allowed for a quantitative analysis of expression levels. The use of a multiparameter FC panel on tumour samples would have enabled to quantitate protein expression and confirm the overexpression of PD-L1 in tumour cells and directly compare these with expression levels of cells cultured *in vitro*. However, this methodology was not accessible for me at the early stages of my project. Nevertheless, such FC-based characterisation of MOC1 and MOC2 tumours and PD-L1 overexpressing variants could be pursued as part of future work.

In summary, I confirmed the authenticity of MOC1 and MOC2 cell lines via genetic and phenotypic markers. Additionally, I identified a pan-CK panel as a marker mix for MOC2 and EpCAM as a marker for MOC1 cells *in vitro*. Both proteins are frequently expressed by HNSCC (Andratschke et al., 2015; Ligtenberg et al., 2018). I confirmed that MOC1 exhibited an indolent growth behaviour, while MOC2 showed rapid growth. Characterisation of PD-L1 expression levels confirmed low baseline expression for both cell lines, either grown in culture or as tumours *in vivo*. I generated two variants of PD-L1 overexpressing MOC2 cells as a positive control for characterisation studies of the PD-L1 targeted PET radioconjugate, as presented in the next chapter.

Chapter 4: Characterisation and optimisation of ^{89}Zr-DFO-PD-L1$_{\text{mAb}}$ to monitor the expression of murine PD-L1 via PET *in vivo*

4.1 Introduction

As mentioned in the previous chapter, my PhD project aimed at studying PD-L1 expression upon oncolytic virotherapy in head and neck cancer mouse models. For this purpose, I chose to employ PD-L1 targeted immuno-positron emission tomography (immunoPET) using an antibody-based radioconjugate (RC) to image the systemic expression of murine PD-L1. The work performed to characterise this PD-L1 targeted antibody-based RC and establish an imaging protocol in MOC1 and MOC2 mouse models is presented in this chapter.

PD-L1-targeted immunoPET has recently gained interest as a diagnostic tool to assess PD-L1 expression systemically and non-invasively *in vivo* (Bensch et al., 2018; Niemeijer et al., 2018; Verhoeff et al., 2020; Verhoeff et al., 2022). So far, antibody-based RCs have spearheaded the range of tracers suited for PD-L1 immunoPET (Wierstra et al., 2019). The use of antibodies as targeting moieties in RCs benefits from their high inherent specificity and affinity for the target. It further allows the use of clinically approved antibody candidates which can readily be re-purposed as targeting moieties for PET RCs, as exemplified by Bensch *et al* and others (Bensch et al., 2018; Verhoeff et al., 2020). Consequently, numerous preclinical (Chatterjee et al., 2016; Heskamp et al., 2015; Heskamp et al., 2019; Josefsson et al., 2016; Kikuchi et al., 2017; Kurino et al., 2020; Nedrow et al., 2017) and a growing number of clinical studies (Bensch et al., 2018; Verhoeff et al., 2020) (NCT04006522; NCT04222426) using anti-PD-L1 antibody RCs have been reported.

In line with this trend and the advantage of its relatively straightforward application, I decided to use an antibody-based RC to monitor changes of PD-L1 in syngeneic mouse cancer models in my project. In the interest of availability and reproducibility, I selected a commercially available anti-mouse PD-L1 monoclonal antibody (mAb, also referred to as PD-L1$_{\mathrm{mAb}}$) offered for *in vivo* applications (0.2 µm sterile-filtered; endotoxin level <2 EU/mg). This PD-L1$_{\mathrm{mAb}}$ clone (10F.9G2) was generated via cDNA immunisation of female Lewis strain rats, using purified murine PD-L1 cDNA (Eppihimer et al., 2002). Clone 10F.9G2, a rat IgG2b isotype, was selected for its high target selectivity and specificity towards murine PD-L1 (Eppihimer et al., 2002). In addition, this PD-L1$_{\mathrm{mAb}}$ clone interacts with all mouse Fc gamma receptors (FcγR), which are frequently expressed by myeloid cell populations (Dahan et al., 2015). *In vivo* pharmacokinetic studies in mice have shown that the concentration of antibody in circulation remains high within 72 h after PD-L1$_{mAb}$ administration (~90 µg/mL; 100 µg i.v.), and starts to decrease thereafter (Dahan et al., 2015). The dose-dependent pharmacokinetic behaviour for clone 10F.9G2 has only been reported using radiolabelled versions of the mAb and will be addressed in a subsequent paragraph. The importance of such dose-dependent pharmacokinetics was emphasised by results from clinical trials of anti-PD-L1 mAbs, which showed that a relatively high antibody dose was required to saturate systemic antigen expression sites and ensure increased serum availability (Herbst et al., 2014; Lamberts et al., 2015). Importantly, clone 10F.9G2 is most frequently applied for therapeutic purposes, i.e. PD-L1-targeted immune checkpoint blockade (ICB) (Aloulou et al., 2016; Deng et al., 2014; Mosely et al., 2017), but has also been utilised for diagnostic implications, e.g. as targeting moiety for PD-L1 immunoPET and single photon emission tomography (SPECT) RCs (Heskamp et al., 2019; Kikuchi et al., 2017; Kurino et al., 2020; Nedrow et al., 2017).

I radiolabelled the PD-L1$_{mAb}$ (clone 10F.9G2) with the PET-radioisotope Zirconium-89 (^{89}Zr; positron yield ~23%) as its physical decay half-life ($t_{1/2}$ ~78.4 h) matches the circulation half-life of antibodies (Holland et al., 2010; Vugts and van Dongen, 2011). In addition, ^{89}Zr has a relatively short positron range by emitting low energy positrons ($E_{\beta+mean}$ ~396 keV), which facilitates high-resolution PET imaging ($R_{\beta+mean}$ ~1.2 mm), as compared to other long-lived PET radioisotopes, including Iodine-124 (^{124}I, $E_{\beta+mean}$ ~826 keV, $R_{\beta+mean}$ ~3.4 mm) (Holland et al., 2010; Kumar and Ghosh, 2021). Moreover, ^{89}Zr yields higher contrast in PET images as compared to ^{124}I due to its capability to accumulate in cells upon internalisation (Knowles et al., 2014). Logistically, ^{89}Zr is easily accessible in the UK via a commercial provider from a cyclotron in the Netherlands, albeit incurring considerable cost (40 MBq ^{89}Zr cost ~300 GBP). One downside of ^{89}Zr-based antibody-conjugates is their dosimetric burden due to the long physical decay half-life of the isotope and the slow systemic clearance of antibodies (Börjesson et al., 2009; Jagoda et al., 2019; Pandit-Taskar et al., 2014).

The most commonly used chelator for ^{89}Zr-radiolabelling of antibodies is desferrioxamine (DFO), including specific derivatives such as the *p*-iothiocyanatobenzyl-derivative referred to as DFO-NCS (Perk et al., 2010; Vosjan et al., 2010). DFO-NCS robustly forms stable linkages with the lysine residues of antibodies (Perk et al., 2010). Both, conjugation and radiolabelling procedures via DFO-NCS are considered relatively facile and can be achieved within a few hours (Vosjan et al., 2010; Zeglis and Lewis, 2015). ^{89}Zr-DFO-antibody complexes have been shown to exhibit high serum stability *in vitro*, while *in vivo*, low-grade release of ^{89}Zr was only observed in mice but not in humans (Abou et al., 2011; Vosjan et al., 2010; Vugts et al., 2017). The latter might be due to the suboptimal compatibility between ^{89}Zr to DFO-NCS, with preferences for octadentate and hexadentate complexes respectively (Heskamp et al., 2017; Vugts et al., 2017). However, others speculate that the bone uptake observed in mice is merely owed to faster RC degradation rather than RC instability (Abou et al., 2011; Vivier et al., 2018). Free ^{89}Zr exhibits a tropism for calcified compartments of the bone, most importantly the epiphysis and the bone shafts (Abou et al., 2011; Holland et al., 2010). Historically, DFO has been used as a chelator to treat iron and aluminium intoxications and is therefore considered clinically safe.

As mentioned previously, radiolabelled versions of the anti-mouse PD-L1$_{\mathrm{mAb}}$ clone 10F.9G2 have been used for preclinical molecular imaging studies via PET and SPECT by others. For example, Kikuchi *et al.* have employed the ^{89}Zr-labelled PD-L1$_{\mathrm{mAb}}$ for their studies and reported an average specific activity (sp.act.) of ~74 kBq/µg and a high immunoreactivity ranging from 55% to 75% upon radiolabelling (Kikuchi et al., 2017). Further, high target specificity upon radiolabelling with ^{89}Zr and other radioisotopes (e.g. Indium-111, Iodine-125) was reported (Heskamp et al., 2019; Kikuchi et al., 2017; Kurino et al., 2020). The *in vivo* pharmacokinetic behaviour of PD-L1$_{\mathrm{mAb}}$ labelled with Indium-111 (^{111}In) and Iodine-125 (^{125}I) was studied by Kurino *et al* and others and showed high, immediate consumption of radiolabelled PD-L1$_{\mathrm{mAb}}$ by the spleen (Heskamp et al., 2019; Kurino et al., 2020). Co-injection of an excess of unlabelled antibody led to antigen saturation in the spleen and increased the serum availability of the RC resulting in enhanced target saturation in PD-L1 expressing tumours, thus confirming the dose-dependent pharmacokinetic behaviour of PD-L1 targeted antibodies. Other systemic organs which express PD-L1 at lower levels than the spleen, include lungs, lymph nodes and brown adipose tissue (BAT). According to published work, their PD-L1 expression levels did not significantly impact RC pharmacokinetics (Eppihimer et al., 2002; Heskamp et al., 2019; Ingram et al., 2017; Kurino et al., 2020). The high and non-specific uptake of RC in the liver is owed to its role as an antibody metabolising organ (Wang et al., 2008).

In this chapter, I present the basic characterisation of the anti-mouse PD-L_{mAb} radiolabelled with ^{89}Zr (^{89}Zr-DFO-PD-$L1_{mAb}$) following its in-house production. The characterisation comprises a variety of *in vitro* radioimmunoassays to assess binding properties, such as immunoreactivity, target affinity and specificity. These studies were performed using a panel of murine cell lines, including MOC1 and MOC2. Furthermore, PD-L1 targeting and the pharmacokinetic behaviour of ^{89}Zr-DFO-PD-$L1_{mAb}$ is evaluated in the MOC2 tumour model *in vivo*. Dose titration studies of ^{89}Zr-labelleld and co-injected unlabelled PD-$L1_{mAb}$ are also presented, allowing the selection of a dose which provides optimal image contrast and tumour uptake according to antigen expression levels. Finally, the specificity of the radiotracer was evaluated against a non-specific control RC, ^{89}Zr-DFO-IgG_{mAb}, *in vivo* and *in vitro*.

4.2 Results

4.2.1 Characterisation of ^{89}Zr-DFO-PD-L1$_{mAb}$ *in vitro*

At first, ^{89}Zr-DFO-PD-L1$_{mAb}$ and its precursor DFO-PD-L1$_{mAb}$ were tested in several well-established *in vitro* assays to ensure integrity and purity of both products. DFO-PD-L1$_{mAb}$ was tested in regard to its molecular weight, integrity and homogeneity. The radiolabelled product, ^{89}Zr-DFO-PD-L1$_{mAb}$, was checked in regard to its radiochemical purity and stability. The binding characteristics of ^{89}Zr-DFO-PD-L1$_{mAb}$ were assessed via various cell binding assays and will be addressed in a subsequent paragraph.

The molecular weight and integrity of DFO-PD-L1$_{mAb}$ and DFO-IgG$_{mAb}$ were analysed via sodium dodecyl sulphate–polyacrylamide gel electrophoresis (SDS-PAGE) and subsequent silver staining, under reducing and non-reducing conditions. The unconjugated PD-L1$_{mAb}$ and IgG$_{mAb}$ were added as controls. Under non-reducing conditions, DFO-conjugated and unconjugated antibodies, presented as sharp bands at ~150 kDa, while under reducing conditions bands appeared at ~25 kDa and ~50 kDa, indicating light and heavy chain components respectively (Fig.4-1a). High pressure liquid chromatography (HPLC) analysis of DFO-PD-L1$_{mAb}$ corroborated its integrity and confirmed the absence of aggregates and fragments as sources for impurities (Fig.4-1b). The HPLC elution profile of PD-L1$_{mAb}$ served as a baseline. The number of DFO molecules per antibody was estimated based on mass spectrometry measurements comparing DFO-PD-L1$_{mAb}$ and PD-L1$_{mAb}$ samples and showed that a representative batch of conjugate had an average of 0.83 DFO molecules per antibody.

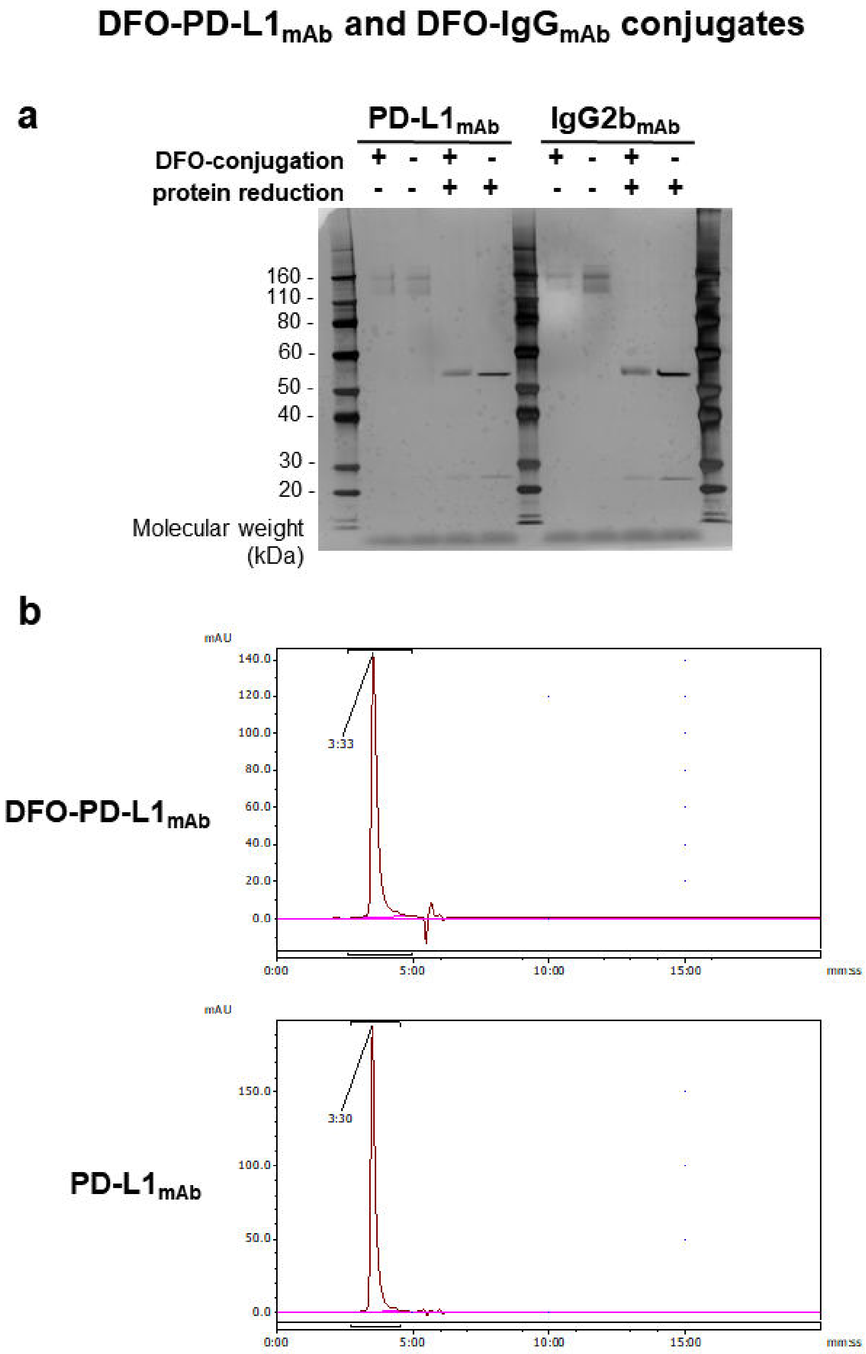

*Figure 4 - 1: **a.** Silver stain of PD-L1$_{mAb}$ and IgG$_{mAb}$ (0.05 µg both) in non-reduced and reduced conditions separated via SDS-PAGE (4-12% Tris-Bis NuPAGE gel). Silver stain was performed once. **b.** HPLC chromatograms of DFO-PD-L1$_{mAb}$ and PD-L1$_{mAb}$. Y-axis shows milli-absorbance unit (mAu) and x-axis shows time (mm:ss). HPLC was performed once.*

Upon radiolabelling of DFO-PD-L1$_{mAb}$ or DFO-IgG$_{mAb}$ with ^{89}Zr, radiochemical yield (RCY) and radiochemical purity (RCP) of the products were checked using instant thin layer chromatography (ITLC). ^{89}Zr-DFO-PD-L1$_{mAb}$ and the control ^{89}Zr-DFO-IgG$_{mAb}$ were produced with moderate to high RCY with 45-

67.5% (n=12) and 86.4-95.7% (n=5) respectively. Further, a high average RCP (>98%, n=12) was confirmed for both products via ITLC, as shown by the absence of free ^{89}Zr at the solvent front (Fig.4-2a; Suppl.Fig.14 to 21). The specific activity for ^{89}Zr-DFO-PD-L1$_{\text{mAb}}$ ranged between 0.11-0.2 MBq/µg (n=12). The *in vitro* stability testing confirmed high ^{89}Zr-DFO-PD-L1$_{\text{mAb}}$ serum stability with fractional ^{89}Zr-disincorporation over a period of 168 h at 37°C in mouse serum (~93%, n=3; Fig.4-2b).

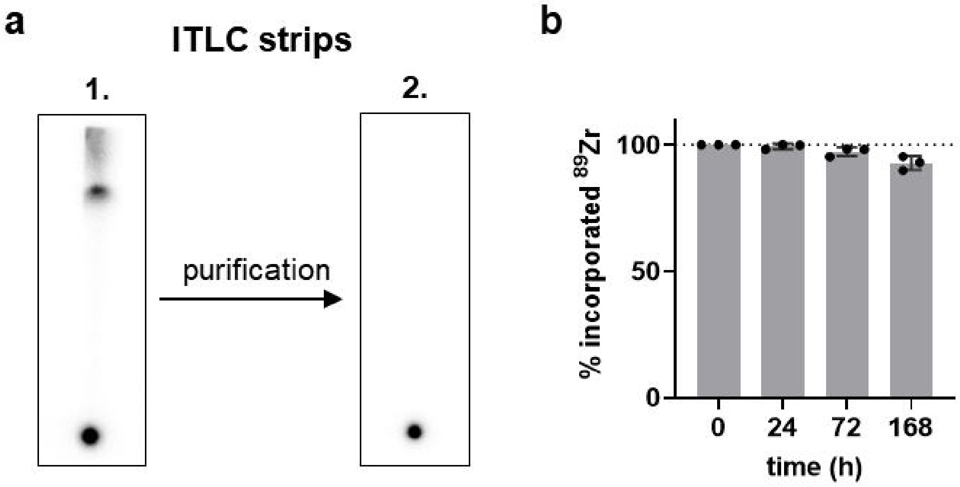

*Figure 4 - 2: **a.** ITLC-SG strips of ^{89}Zr-DFO-PD-L1$_{mAb}$ pre- (1.) and post-purification (2.): dot at the bottom of strip indicates ^{89}Zr-DFO-PD-L1$_{mAb}$ product, black smear at the upper end of strip (solvent front) indicates free ^{89}Zr. **b.** In vitro serum stability of ^{89}Zr-DFO-PD-L1$_{mAb}$. ^{89}Zr incorporation assessed via ITLC and subsequent densitometric measurements. Bars indicate mean of n=3 ± SD; assay was performed once.*

4.2.2 Target binding characteristics of ^{89}Zr-DFO-PD-L1$_{\text{mAb}}$ *in vitro*

To ensure that the radiolabelling procedure did not adversely affect target affinity and specificity of the parental PD-L1$_{\text{mAb}}$, ^{89}Zr-DFO-PD-L1$_{\text{mAb}}$ binding properties were assessed via several well-established radioligand binding assays. Firstly, the Lindmo assay was used to determine the immunoreactive fraction (IRF) of ^{89}Zr-DFO-PD-L1$_{\text{mAb}}$. The IRF is defined as the fraction of radiolabelled antibody which effectively binds the target antigen and is performed on antigen (over)expressing cells *in vitro* (Lindmo et al., 1984; Lindmo and Bunn, 1986). The IRF calculated for ^{89}Zr-DFO-PD-L1$_{\text{mAb}}$ was approximately 80%, as assessed on MOC2*(PD-L1)^{poly}* cells (Fig.4-3a). Secondly, a saturation binding assay was performed to determine the dissociation constant (K_d), as an indication for the binding affinity of ^{89}Zr-DFO-PD-L1$_{\text{mAb}}$ against its target antigen (expressed on

MOC2*(PD-L1)*^{poly} cells). The K_d of ^{89}Zr-DFO-PD-L1$_{\mathrm{mAb}}$ was calculated to be 2.41 ± 0.75 nM (Fig.4-3b). Thirdly, the specificity of ^{89}Zr-DFO-PD-L1$_{\mathrm{mAb}}$ binding against PD-L1 was assessed using a selection of cancer cell lines including MOC1, MOC2 and MOC2*(PD-L1)*^{poly} *and* MOC2*(PD-L1)*^{single} cells, as well as the macrophage cell line RAW264.7, representing blood-borne cell populations. Additionally, IFN-γ stimulation (20 ng/mL, 24 h prior to binding assay) of all cell lines was introduced as a condition to mimic IFN-mediated PD-L1 expression changes which frequently occur in an *in vivo* environment. MOC1, MOC2 and RAW264.7 cells showed negligible to low ^{89}Zr-DFO-PD-L1$_{\mathrm{mAb}}$ binding at baseline (MOC1 5.1 ± 1.2%, MOC2 4.5 ± 0.8%, RAW264.7 4.2 ± 0.4%, mean ± SD of n=3), while MOC2*(PD-L1)*^{poly} and MOC2*(PD-L1)*^{single} showed medium to high levels of bound RC (MOC2*(PD-L1)*^{poly} 49.3 ± 4.5%, MOC2*(PD-L1)*^{single} 100 ± 3.2%) respectively (Fig.4-3c). RAW264.7, MOC1 and MOC2 cells showed markedly increased levels of bound RC upon IFN-γ stimulation (MOC1 20.2 ± 2.6%, MOC2 33.5 ± 2.3%, RAW264.7 31.2 ± 5.0%), as previously observed via FC (Fig.3-3a-b). Interestingly, IFN-γ stimulation only slightly increased PD-L1 expression in both MOC2*(PD-L1)*^{poly} and MOC2*(PD-L1)*^{single} cells (MOC2*(PD-L1)*^{poly} 67.6 ± 2.8%, MOC2*(PD-L1)*^{single} 109.8 ± 8.2%) (Fig.4-3c). Blocking with 100-fold molar excess of unlabelled PD-L1$_{\mathrm{mAb}}$ significantly reduced RC-binding across all conditions with high PD-L1 expression, be it via constitutive overexpression or conditional IFN-γ stimulation ($p<0.0001$ for all but IFN-treated MOC1 $p=0.0003$) (Fig.4-3c). These results confirm that ^{89}Zr-DFO-PD-L1$_{\mathrm{mAb}}$ recognises its target with high specificity *in vitro*. An additional set of specificity of binding results is provided in the thesis appendix to evidence that no major batch-dependent differences in binding specificity were observed across the three batches of DFO-PD-L1$_{\mathrm{mAb}}$ used for radiolabelling throughout my PhD project (Suppl.Fig.15a-c).

^{89}Zr-DFO-PD-L1$_{mAb}$ binding properties *in vitro*

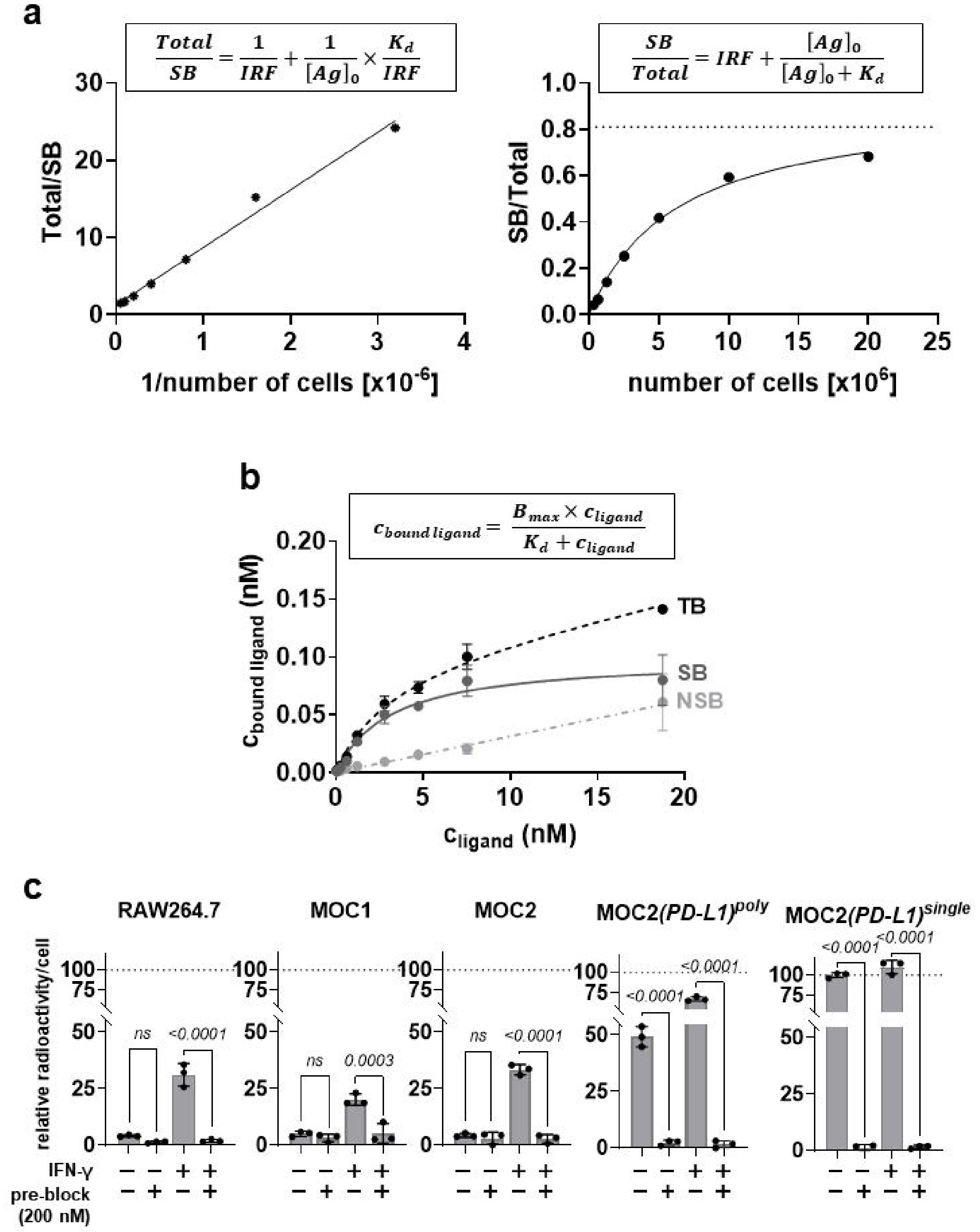

*Figure 4 - 3: **a.** Results obtained from Lindmo assay to determine immunoreactive fraction (IRF) of ^{89}Zr-DFO-PD-L1$_{mAb}$. Linear regression (left) and curve (right) fits show ratios of total amount of radioligand (total) and specifically bound radioligand (SB) plotted against the cell number (or its inverse), also referred to as antigen (Ag) in equation insets. MOC2(PD-L1)^{poly} cells were used. The Lindmo assay was performed once. **b.** Saturation binding assay of ^{89}Zr-DFO-PD-L1$_{mAb}$ on MOC2(PD-L1)^{poly} cells. Curves were fitted for all three fractions, i.e. total binding (TB), specific binding (SB) and non-specifically bound (NSB) fraction, using the equation displayed with K_d denoting the dissociation constant, $c_{bound\ ligand}$ the concentration of bound ligand, c_{ligand} the concentration of ligand and B_{max} denoting the maximum specific binding. Data points show mean ± SD of n=3 (1 of 3 repeats). **c.** Specificity of binding assay of ^{89}Zr-DFO-PD-L1$_{mAb}$ on RAW264.7, MOC1,*

MOC2 and MOC2(PD-L1)^{poly} and MOC2(PD-L1)^{single} cell lines. Cells were treated with IFN-γ (20 ng/mL; 24 h) or medium as a control. ^{89}Zr-DFO-PD-L1$_{mAb}$ was incubated for 1 h (2 nM) and pre-blocked with 100-molar excess of unlabelled PD-L1$_{mAb}$ for 10 min. Radioligand binding expressed as percentage of bound radioligand on untreated MOC2(PD-L1)^{single} cells, bars show mean of n=3 ± SD (1 of 2 repeats). Two-way ANOVA with Bonferroni correction for multiple comparisons was applied. P-values <0.05 were considered statistically significant and are indicated as values.

4.2.3 Pharmacokinetic behaviour of ^{89}Zr-DFO-PD-L1$_{mAb}$ *in vivo*

To explore the pharmacokinetic behaviour of ^{89}Zr-DFO-PD-L1$_{mAb}$ *in vivo,* MOC2 tumour-bearing mice, exhibiting low intratumoural expression of PD-L1, were injected with different co-injection doses of ^{89}Zr-labelled and unlabelled PD-L1$_{mAb}$ (Table 4-1: doses 1, 2 and 3) and biodistribution studies were performed within 96 h after injection. In total, three different co-injection doses were included to address dose-dependent pharmacokinetic differences described for PD-L1 targeting mAbs (Herbst et al., 2014; Kurino et al., 2020; Lamberts et al., 2015). The range of doses was selected based on work published by others (Heskamp et al., 2019; Kikuchi et al., 2017). The biodistribution studies for dose 1 and dose 2 were performed at 48 and 96 h post-injection (p.i.), whilst biodistribution studies for dose 3 were performed at 24, 48, 72 and 96 h p.i. In addition, consecutive PET/CT scans of one mouse injected with ^{89}Zr-DFO-PD-L1$_{mAb}$ (dose 2) and one mouse injected with the isotype control ^{89}Zr-DFO-IgG$_{mAb}$ were performed and RC uptake was quantified computationally. The data presented is pooled from two studies, performed with batches 1 and 2 of DFO-PD-L1$_{mAb}$. Image proof of ITLCs of both ^{89}Zr-DFO-PD-L1$_{mAb}$ products and the ^{89}Zr-DFO-IgG$_{mAb}$ product is not available, but all compounds had a RCP>98% according to experiment records. Ultimately, these studies were laid out to identify the optimal imaging window providing high tumour-to-background contrast and to provide an indication for a RC dose range for subsequent dose titration studies.

Dose reference	**Final PD-L1$_{mAb}$ quantity (µg) and adjusted specific activity in brackets (MBq/µg)**	**^{89}Zr-labelled PD-L1$_{mAb}$ (µg)**	**Unlabelled PD-L1$_{mAb}$ (µg)**
dose 1	10-18 (0.11-0.2)	10-18	-
dose 2	60 (0.03)	10-18	50-42
dose 3	110 (0.02)	10-18	100-92

dose 4	165 (0.01)	10-18	155-147

Table 4 - 1: Co-injection doses of ^{89}*Zr-labelled PD-L1*$_{mAb}$ *(*^{89}*Zr-DFO-PD-L1*$_{mAb}$*) and unlabelled PD-L1*$_{mAb}$ *in vivo.*

The biodistribution results obtained at 48 h following injection of dose 1 (10-18 µg, 2 MBq, ^{89}Zr-DFO-PD-L1$_{mAb}$ only, n=3 in each group) showed very high RC uptake in the spleen which decreased until 96 h (Fig.4-4). The RC uptake in the liver, the main site of antibody clearance, was also high and remained steady over time. The tumour uptake measured at 48 h p.i. was 12.3 ± 6.1 %ID/g and slightly decreased until 96 h reaching 10.3 ± 3.2 %ID/g. Levels of ^{89}Zr-DFO-PD-L1$_{mAb}$ in the blood were low at both times, indicating low bioavailability of the compound. Uptake in the thymus was equally low at both times, while bone uptake was slightly higher at the 48 h than 96 h time point (Fig.4-4). The biodistribution results of dose 2 (10-18 µg, 2 MBq of ^{89}Zr-DFO-PD-L1$_{mAb}$ co-injected with 42-50 µg of PD-L1$_{mAb}$; n=3 in each group) revealed high ^{89}Zr-DFO-PD-L1$_{mAb}$ levels in tumours at 48 h which were slightly decreased at 96 h yielding 29.4 ± 2.9 and 25.1 ± 1.9 %ID/g respectively (Fig.4-4). Liver uptake showed similarly high levels as compared to dose 1 and remained steady over time. The spleen uptake with dose 2 was markedly decreased at both time points, as compared to the uptake measured with dose 1. ^{89}Zr-DFO-PD-L1$_{mAb}$ uptake in the blood was 5.5 ± 1.0 %ID/g at 48 h and decreased until the 96 h time point. The RC uptake in the thymus was marginally lower at 48 h than at 96 h p.i. and the bone uptake showed similar trends to dose 1. Following injection of dose 3 (10-18 µg, 2 MBq of ^{89}Zr-DFO-PD-L1$_{mAb}$ co-injected with 92-100 µg of PD-L1$_{mAb;}$ n=2 for 24 h and 48 h time points and n=3 for all other time points) high RC uptake was measured in the tumours remaining relatively steady over a 96 h period with 21.1 ± 2.1 %ID/g at 24 h, 22.5 ± 11.4 %ID/g at 48 h, 21.4 ± 6.1 %ID/g at 72 h and 23.2 ± 2.7 %ID/g at 96 h (Fig.4-4). Liver uptake varied between time points as a potential effect of data-pooling. Spleen uptake levels were low across all four biodistribution time points and showed minor variations. RC levels in the blood showed a steady decrease over time, however, with marginally higher values than dose 2, indicating increased serum availability. RC uptake in the thymus showed a steady increase over the 96-hour period, similar to the uptake observed in the femur.

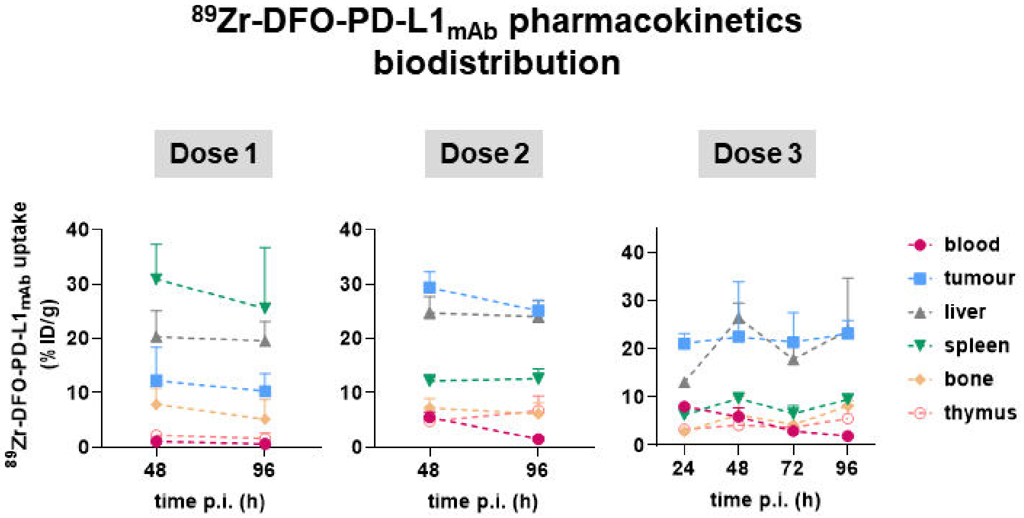

Figure 4 - 4: ^{89}Zr-DFO-PD-L1$_{mAb}$ pharmacokinetic profiles in MOC2 tumour-bearing mice injected with dose 1 (sp.act.~0.11 MBq/µg), dose 2 (adjusted sp.act.~0.03 MBq/µg) or dose 3 (adjusted sp.act.~0.02 MBq/µg) between 24 to 96 h p.i. Graphs show RC uptake (%ID/g) in select organs including tumours (light blue), livers (grey), spleens (green), bone (beige), thymus (pink) and blood (red) as mean ± SD (n=2-3 per time point). Dashed lines indicate trending change. ^{89}Zr-DFO-PD-L1$_{mAb}$ data was pooled from 2 experiments.

The PET scans acquired from one representative mouse injected with dose 2 corroborated the results obtained from biodistribution studies (Fig.4-5a). Accordingly, PET images showed very intense signal arising from the liver and tumour, indicating high RC uptake in these organs across all four imaging time points. Quantification of the uptake in both organs confirmed high RC levels (Fig.4-5b). In contrast, the signal emitted by the spleen was lower and less well differentiated at early time points (e.g. 24 h p.i.), probably owed to the relatively high abdominal background. Again, this observation was confirmed via signal quantification which indicated equally high levels of RC in the spleen and the blood pool. Symmetric and locally confined uptake in the area of both shoulder joints seemed to increase over time and was confirmed via signal quantification (Fig.4-5a/b). The same time-dependent increase was observed with the isotype control conjugate, ^{89}Zr-DFO-IgG$_{mAb}$, suggesting the presence of free ^{89}Zr due to probe disincorporation (Fig.4-5c). A steady increase of ^{89}Zr-DFO-IgG$_{mAb}$ was also observed for the liver and the tumour, which might be due to non-specific uptake of the isotype conjugate. The corresponding biodistribution data (96 h p.i.) of this and another mouse injected with ^{89}Zr-DFO-IgG$_{mAb}$ is provided in Suppl.Fig.16a.

After all the pharmacokinetic data confirmed a dose-dependent behaviour of the RC and showed that image contrast was high across all time points with background signal, as observed in the abdomen, decreasing over time. Furthermore, it showed that RC levels in target expressing organs remained relatively even between 48 to 96 h p.i. (most importantly for dose 2 and 3), indicating systemic target saturation. Therefore, I chose to use 48 h p.i. as the imaging and biodistribution time point for all future studies, considering that a short window between RC injection and imaging would be favourable to study dynamic changes of PD-L1 as presented in chapter 6 of this thesis.

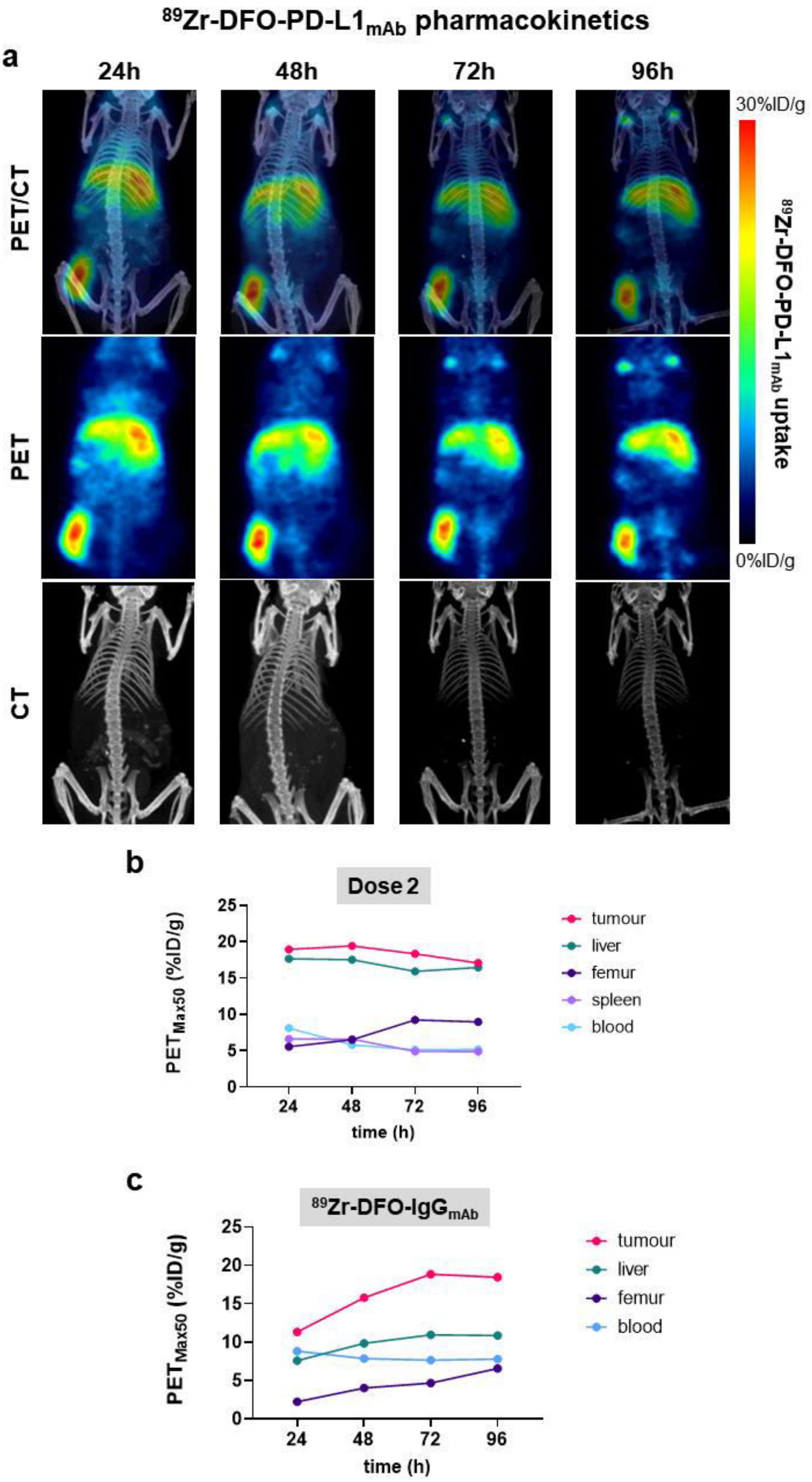

^{89}Zr-DFO-PD-L1$_{mAb}$ pharmacokinetics
a
24h
48h
72h
96h
PET/CT
PET
CT
30%ID/g
0%ID/g
^{89}Zr-DFO-PD-L1$_{mAb}$ uptake
b
Dose 2
PET$_{Max50}$ (%ID/g)
25
20
15
10
5
0
24
48
72
96
time (h)
tumour
liver
femur
spleen
blood
c
^{89}Zr-DFO-IgG$_{mAb}$
PET$_{Max50}$ (%ID/g)
25
20
15
10
5
0
24
48
72
96
time (h)
tumour
liver
femur
blood

Figure 4 - 5: ^{89}Zr-DFO-PD-L1$_{mAb}$ pharmacokinetic profile of MOC2 tumour-bearing mouse injected with dose 2 (adjusted sp.act.~0.03 MBq/µg) between 24 to 96 h p.i. ***a.*** *Co-registered PET/CT scans (PET: single plane slice in coronal projection; CT: 3D reconstruction of MIP) taken at 24, 48, 72 and 96 h post-^{89}Zr-DFO-PD-L1$_{mAb}$ injection.* ***b.*** *PET-based quantification of organ specific uptake (%ID/g) including tumour, liver, spleen, femur, and blood (ROI centred on heart).* ***c.*** *^{89}Zr-DFO-IgG$_{mAb}$ pharmacokinetic profile of MOC2 tumour-bearing mouse injected with non-specific control RC (sp.act.~0.07 MBq/µg; 1.15 MBq i.v) between 24 to 96 h p.i. PET-based quantification of organ specific uptake (%ID/g) for tumour, liver, bone, and blood. The spleen uptake could not be measured due to poor abdominal contrast.*

4.2.4 Dose titration studies to refine tumour uptake of ^{89}Zr-DFO-PD-L1$_{mAb}$ *in vivo*

The data collected from pharmacokinetic studies of ^{89}Zr-DFO-PD-L1$_{mAb}$ showed enhanced tumour accumulation when higher doses of non-labelled PD-L1$_{mAb}$ were co-injected with the RC. To assess whether the co-dosing regimen also allows to distinguish varying expression levels of intratumoural PD-L1, MOC2 and MOC2*(PD-L1)^{poly}* tumour models expressing low and intermediate levels of PD-L1 respectively (Fig.3-4b/c; Fig.3-7b/c) were used. In addition to the previously applied doses 1 to 3, a fourth dose (dose 4: 10-18 µg, 2 MBq of ^{89}Zr-DFO-PD-L1$_{mAb}$ co-injected with 147-155 µg of PD-L1$_{mAb}$; Table 4-1) with an even higher amount of non-labelled PD-L1$_{mAb}$ was used to assess potential effects of systemic antigen blocking. Biodistribution studies were conducted at 48 h post-RC injection, as previous (pharmacokinetic) studies indicated high signal contrast as well as sufficient target saturation at this time point. The data presented is pooled from three independent studies all performed with ^{89}Zr-DFO-PD-L1$_{mAb}$ produced from the second conjugate batch. In addition, the dose titration data of the MOC2 mouse model was also pooled with data previously presented in pharmacokinetic studies (data of doses 1, 2 and 3 at 48 h p.i.). High RCP of all three ^{89}Zr-DFO-PD-L1$_{mAb}$ products was confirmed prior to injection (Suppl.Fig.16b-d).

In both tumour models co-injection dosing studies showed that ^{89}Zr-DFO-PD-L1$_{mAb}$ uptake followed a dose-dependent decrease in systemic PD-L1 expressing organs, including spleen, lungs and BAT (dose 1 < dose 2 < dose 3 < dose 4) (Fig.4-6a). This effect was previously observed in pharmacokinetic studies (Fig.4-4). In contrast, an increased dose of unlabelled PD-L1$_{mAb}$ resulted in higher blood levels of ^{89}Zr-DFO-PD-L1$_{mAb}$, indicating higher bioavailability of the RC once the systemic PD-L1 antigen pool was saturated (Fig.4-6a). The liver showed relatively high uptake regardless of the injected dose or tumour model (Fig.4-6a), most likely due to its role as metabolising organ. The RC uptake in the kidney and the bone was only slightly decreased with increased amounts of unlabelled PD-L1$_{\mathrm{mAb}}$ (Fig.4-6a). With regards to the tumours, low uptake was observed in both MOC2 and MOC2*(PD-L1)*^{poly} tumour types following injection of dose 1 (MOC2 10.9 ± 5.5% ID/g, MOC2*(PD-L1)*^{poly} 13.3 ± 2.2 %ID/g, n=3-6, mean ± SD) (Fig.4-6a/b). Higher tumour uptake was achieved with dose 2 showing slightly higher levels in MOC2*(PD-L1)*^{poly} (31.1 ± 5.2 %ID/g) than MOC2 tumours (26.2 ± 1.9 %ID/g). Injection of dose 3 resulted in reduced ^{89}Zr-DFO-PD-L1$_{\mathrm{mAb}}$ accumulation in MOC2 tumours (21.1 ± 5.7 %ID/g) while MOC2*(PD-L1)*^{poly} tumours exhibited high levels of ^{89}Zr-DFO-PD-L1$_{\mathrm{mAb}}$ uptake (32.7 ± 4.0 %ID/g), allowing for a discrimination of tumour types according to their ^{89}Zr-DFO-PD-L1$_{\mathrm{mAb}}$ uptake ($p=0.012$; multiple unpaired *t*-tests; Fig.4-6b). The marked difference in RC uptake was not reflected in representative autoradiograms obtained from each tumour type, eventually due to technical issues or a sampling bias (Fig.4-6c). Injection of dose 4 resulted in low uptake regardless of tumour type (MOC2 18.4 ± 1.1 %ID/g, MOC2*(PD-L1)*^{poly} 16.9 ± 5.1 %ID/g) indicating that intratumoural PD-L1 epitopes were occupied by unlabelled PD-L1$_{\mathrm{mAb}}$ and thus reducing ^{89}Zr-DFO-PD-L1$_{\mathrm{mAb}}$ uptake. The latter corroborated the target specificity of ^{89}Zr-DFO-PD-L1$_{\mathrm{mAb}}$ in tumours *in vivo*.

In summary, these dose titration studies showed that injection of dose 3 allowed to discriminate MOC2 from MOC2*(PD-L1)*^{poly} tumours according to their PD-L1 expression levels. Consequently, dose 3 was selected for all forthcoming ^{89}Zr-DFO-PD-L1$_{\mathrm{mAb}}$ *in vivo* studies. Further, high target specificity of ^{89}Zr-DFO-PD-L1$_{\mathrm{mAb}}$ was demonstrated by intratumoural PD-L1 blocking, following injection of increased amounts of non-labelled PD-L1$_{\mathrm{mAb}}$ (dose 4).

Co-dosing of ^{89}Zr-DFO-PD-L1$_{mAb}$ with PD-L1$_{mAb}$

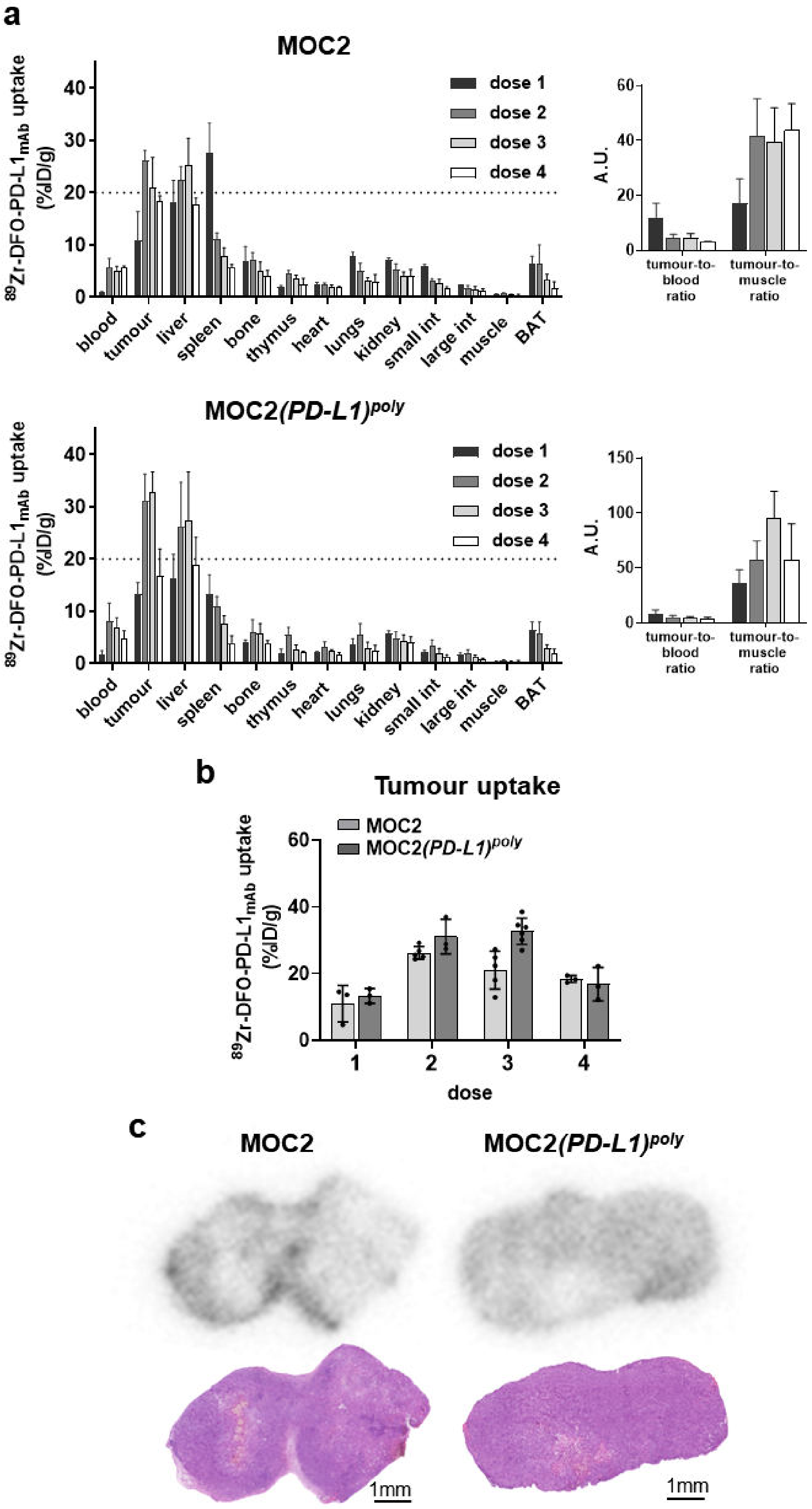

Figure 4 - 6: ***a.*** *^{89}Zr-DFO-PD-L1$_{mAb}$ biodistribution of MOC2 and MOC2(PD-L1)^{poly} tumour-bearing mice injected with 4 different (co-injection) doses: 1 (sp.act.=0.117-0.2MBq/ug), 2 (adjusted sp.act.=0.033MBq/ug), 3 (adjusted sp.act.=0.018MBq/ug), 4 (adjusted sp.act.=0.012MBq/ug). Organs were collected for γ-counting at 48 h p.i. RC uptake is expressed as %ID/g. Tumour to background ratios (presented in arbitrary units, A.U.) for each model and dose are plotted in a separate bar chart to the right hand-side. Bars indicate mean ±SD (n=3-6 per group). Data was pooled from 3 independent studies.* ***b.*** *MOC2 and MOC2(PD-L1)^{poly} tumour uptake of ^{89}Zr-DFO-PD-L1$_{mAb}$ at 48 h p.i. following injection of 4 different doses (listed in a). Multiple unpaired t-tests with Benjamini-Hochberg procedure for FDR correction were applied and p-values <0.01 were considered statistically significant.* ***c.*** *Autoradiograms and H&E-stained sections (10 µm) of MOC2 and MOC2(PD-L1)^{poly} tumours collected 48 h p.i. (dose 3). Sections were exposed to a phosphor screen for 24 h and then used for H&E-staining.*

4.2.5 ^{89}Zr-DFO-PD-L1$_{mAb}$ biodistribution across different syngeneic mouse models

In order to confirm that injection of dose 3 achieved a tumour uptake corresponding to the level of intratumoural PD-L1 expression level, MOC1 (low PD-L1 expression; Fig.3-5a/c) and MOC2*(PD-L1)^{single}* (high PD-L1 expression; Fig.3-11a/c) tumour-bearing mice were injected with this dose 3, followed by biodistribution studies 48 h later. Additionally, the CT26 colon carcinoma mouse model (low PD-L1 expression) was used as a reference control to facilitate a direct comparison with results published by Heskamp *et al*, employing an ^{111}In-labelled version of the same antibody clone (Heskamp et al., 2019). The data was pooled from two independent studies, using ^{89}Zr-DFO-PD-L1$_{mAb}$ produced from the second batch of DFO-PD-L1$_{mAb}$. ITLCs of ^{89}Zr-DFO-PD-L1$_{mAb}$ products showed high RCP (Suppl.Fig.17).

The biodistribution profiles of ^{89}Zr-DFO-PD-L1$_{mAb}$ using CT26, MOC1 and MOC2*(PD-L1)^{single}* models showed similar RC uptake across the majority of systemic organs (Fig.4-7a). However, in some organs including the liver, bone, lungs and BAT RC uptake varied depending on the model (Fig.4-7a). Furthermore, the RC uptake measured in tumours varied between models: CT26 tumours showed the lowest levels of ^{89}Zr-DFO-PD-L1$_{mAb}$ (11.4 ± 2.1 %ID/g; mean ± SD), followed by MOC1 (17.6 ± 2.7 %ID/g) and MOC2*(PD-L1)^{single}* (19.6 ± 2.4 %ID/g). Surprisingly however, the relative differences in tumour uptake between the three models deviated from the PD-L1 expression level previously assessed via IHC and WB (Fig.3-5a/c; Fig.3-11a/c). Accordingly, the marked difference in RC uptake between CT26 and MOC1 models did not reflect the almost equally low levels of PD-L1 in these tumours observed via IHC and

WB (Fig.4-7b/c, Fig.3-5a/c). MOC2*(PD-L1)*^{single} tumours exhibited only a slightly higher RC uptake as compared to MOC1 which did not reflect the antigen abundance in this tumour type as previously assessed via *ex vivo* methods (Fig.3-11a/c).

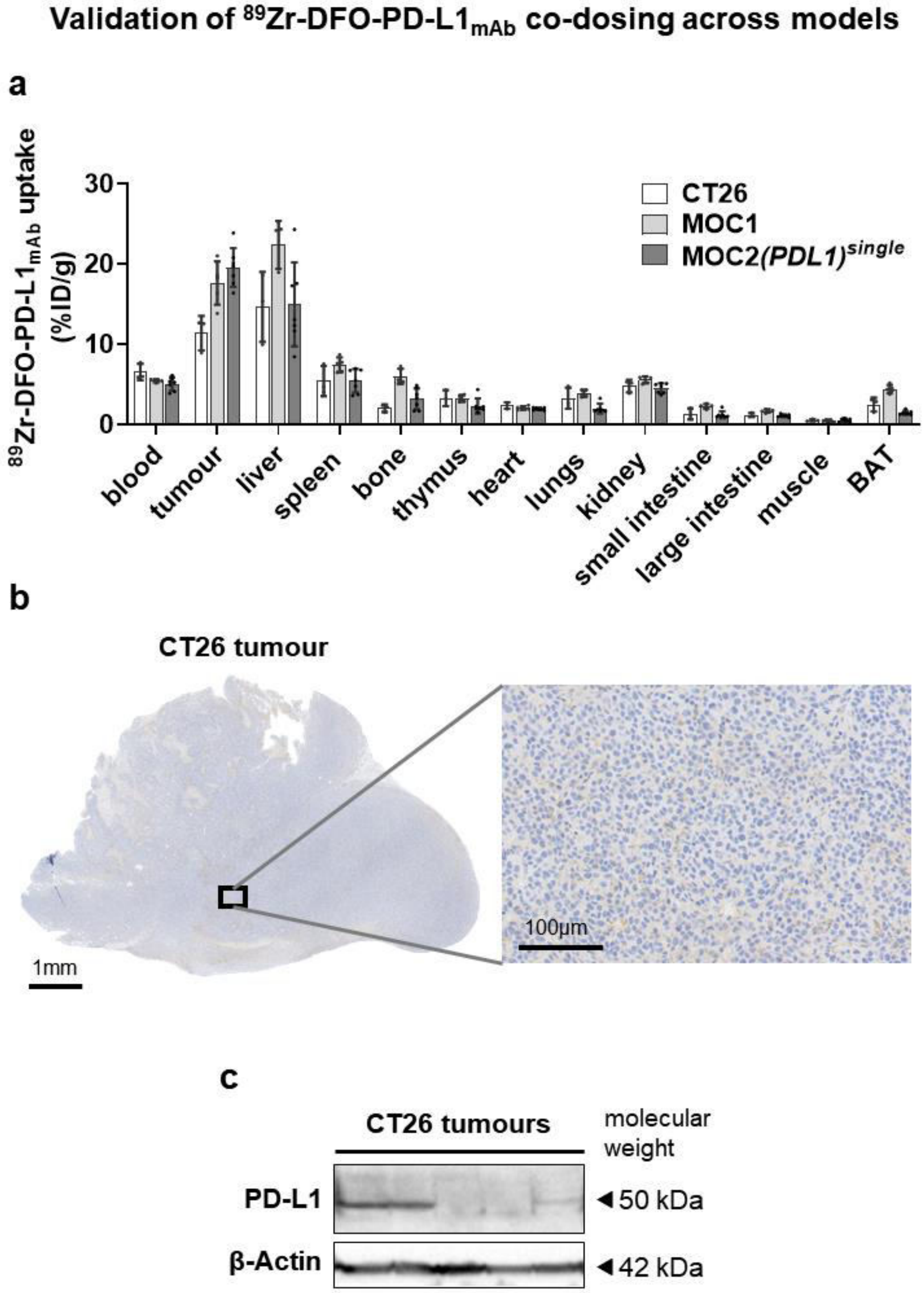

Figure 4 - 7: ***a.*** *^{89}Zr-DFO-PD-L1$_{mAb}$ biodistribution profile of CT26 (n=3), MOC1 (n=5), MOC2(PD-L1)^{single} (n=7) mouse models at 48 h p.i. (dose 3; adjusted sp.act.=0.018 MBq/µg). Data was pooled from three independent studies. Bars indicate*

*mean ± SD. **b.** PD-L1 IHC of CT26 tumour (4 μm section). **c.** PD-L1 expression in tumour lysates (five lysates) assessed via WB.*

4.2.6 Determination of non-specific binding via biodistribution of ^{89}Zr-DFO-IgG$_{mAb}$

To additionally check for non-specific binding, an ^{89}Zr-labelled IgG2b isotype was used as a control and tested *in vivo* and *in vitro*. For in vivo testing, biodistribution studies in MOC1, MOC2, MOC2*(PD-L1)^{single}* and CT26 tumour-bearing mice were performed and PET/CT scans of a few representative mice were acquired. *In vitro* testing comprised a specificity of binding assay. The *in vivo* data presented is pooled from two independent studies, all performed with ^{89}Zr-DFO-IgG$_{mAb}$ produced from the same conjugate batch. High RCP was confirmed for both ^{89}Zr-DFO-IgG$_{mAb}$ products prior to injection, however image proof only exists for one (Suppl.Fig.18a).

^{89}Zr-DFO-IgG$_{mAb}$ (9.74-12.2 μg; sp.act.=0.16-0.21 MBq/μg) was injected to MOC1, MOC2, MOC2*(PD-L1)^{single}* and CT26 tumour-bearing mice and major organs collected 48 h later for biodistribution. PET/CT scans were acquired of a few representative mice prior to biodistribution. The RC uptake profile was very similar across the four tumour models and showed negligible uptake in the majority of organs (Fig.4-8a/b). A small subset of organs including blood, tumour, liver and spleen showed increased uptake levels as observed via representative PET scans and biodistribution likewise (Fig.4-8a/b). Accordingly, RC uptake in the blood was equally high in all four models (~10 %ID/g), indicating high serum availability of the control RC. Similarly, spleen uptake reached equal levels across the models between 6.2-8.3 %ID/g. In contrast, liver uptake varied across the models, which was also observed in previous experiments. The tumours showed model-dependent differences (Fig.4-8b/c): MOC1 tumours showed the lowest RC uptake (13.1 ± 2.5 %ID/g, mean ± SD), CT26 exhibited slightly higher mean uptake values (18.7 ± 4.6 %ID/g), surprisingly exceeding the average tumour uptake of ^{89}Zr-DFO-PD-L1$_{mAb}$, MOC2 (21.6 ± 0.3 %ID/g) and MOC2*(PD-L1)^{single}* (21.7 ± 0.8 %ID/g) showed the highest levels of ‘non-specific’ RC accumulation, reaching values similar to the uptake of ^{89}Zr-DFO-PD-L1$_{mAb}$. After all, only MOC1 tumours showed lower uptake of ^{89}Zr-DFO-IgG$_{mAb}$ compared to the target specific ^{89}Zr-DFO-PD-L1$_{mAb}$ counterpart (Fig.4-8c). Results obtained from an *in vitro* radioligand binding assay using ^{89}Zr-DFO-IgG$_{mAb}$ showed a high level of bound RC in CT26 cells (0.034 ± 0.007 CPM/cell) compared to MOC1 (0.007 ± 0.002 CPM/cell), MOC2 (0.015 ± 0.002 CPM/cell) and MOC2*(PD-L1)^{single}* (0.006 ± 0.001 CPM/cell) cells (Fig.4-8d). Blocking with 100-fold molar excess of unlabelled IgG$_{mAb}$ did not significantly reduce ^{89}Zr-DFO-IgG$_{mAb}$, supporting its non-specific target recognition (Fig.4-8d).

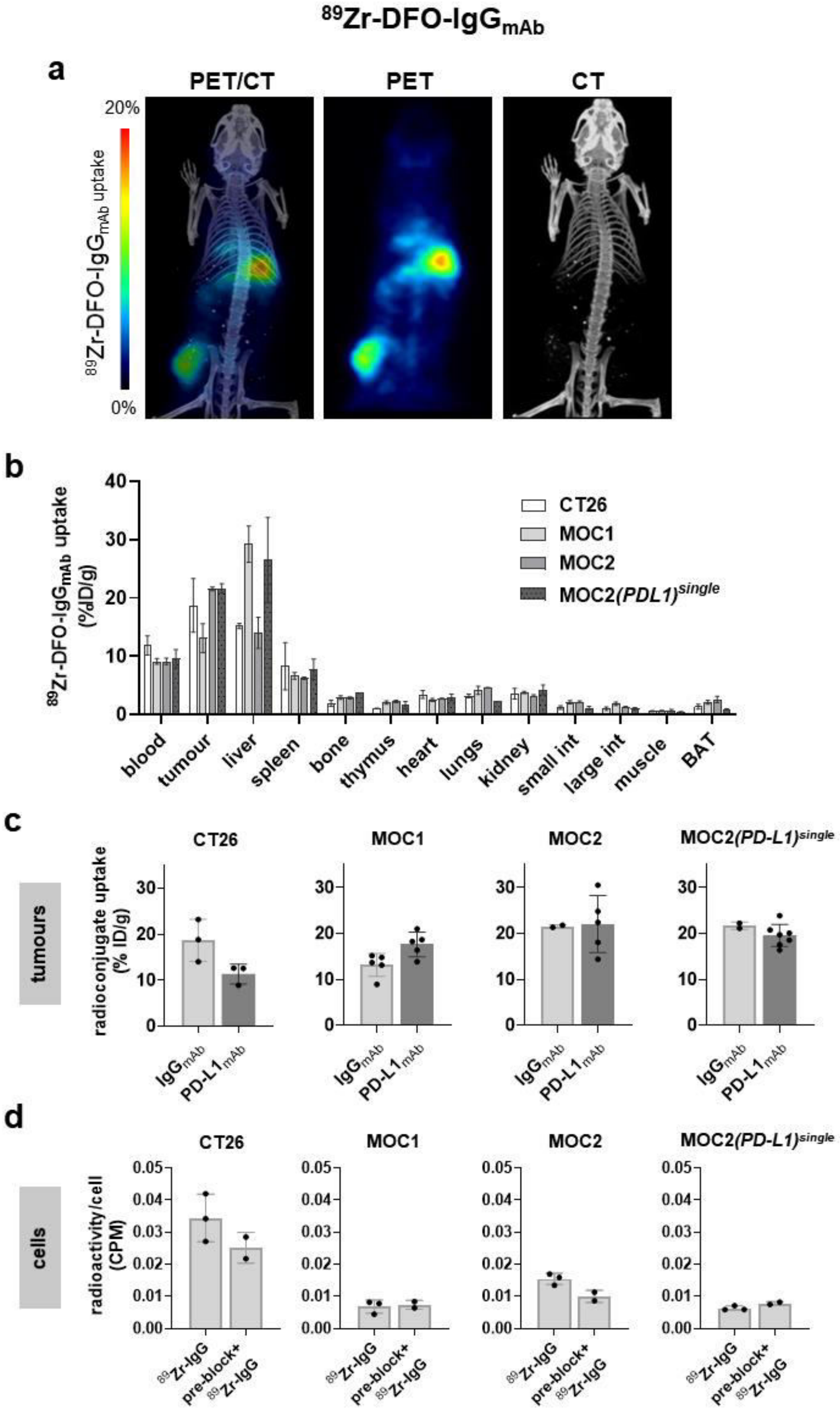

Figure 4 - 8: ***a.*** *^{89}Zr-DFO-IgG$_{mAb}$ biodistribution profile of CT26 (n=3), MOC1 (n=5), MOC2 (n=2) and MOC2(PD-L1)^{single} (n=2) mouse models at 48 h p.i. (9.7-12.2 µg; sp.act.=0.16-0.2 MBq/µg). Data was pooled from two studies. Bars show mean ± SD.* ***b.***

Co-registered PET/CT scans (PET: single plane slice in coronal projection; CT: 3D reconstruction of MIP) taken 48 h post-^{89}*Zr-DFO-IgG*$_{mAb}$ *injection into MOC1 mouse model.* ***c.*** *RC uptake in tumours of* ^{89}*Zr-DFO-IgG*$_{mAb}$ *vs* ^{89}*Zr-DFO-PD-L1*$_{mAb}$ *(dose 3) injected mice and biodistributed at 48 h p.i Bars indicate mean ± SD.* ***d.*** *Specificity of binding assay of* ^{89}*Zr-DFO-IgG*$_{mAb}$ *on CT26, MOC1, MOC2 and MOC2(PD-L1)*^{single} *cells in vitro.* ^{89}*Zr-DFO-IgG*$_{mAb}$ *(2 nM) was incubated for 1 h and pre-blocked with 100-molar excess of unlabelled IgG*$_{mAb}$ *for 10 min. Bars indicate mean ± SD of n=2-3 (experiment was performed once). Unpaired Student's t-tests with Welch's correction were performed for each cell line. P-values <0.05 were considered statistically significant.*

4.2.7 Mouse model-dependent intratumoural vessel density

In an effort to better understand the differences in ^{89}Zr-DFO-PD-L1$_{mAb}$ tumour uptake between the mouse models, I decided to look at the tumour vascularisation as a tumour-dependent characteristic which might influence RC distribution. Vascularisation was determined via CD31, an endothelial cell marker frequently used to assess tumour vessel density. Accordingly, CD31 was stained via IHC in sections collected from MOC1, MOC2, MOC2*(PD-L1)*^{poly}, MOC2*(PD-L1)*^{single} and CT26 tumours at immunoPET studies. Of note, tumour vessel density does not inform on functional parameters of vascularisation such as perfusion and vessel leakiness.

Visual inspection of CD31-stained tumour sections showed a consistent pattern of vascularisation across all five tumour types: Larger vessels (vessels with a clear lumen) were predominantly present in the tumour periphery including the connective tissue surrounding the tumours, while the tumour core showed only small and stellar-shaped vessels without a lumen (Fig.4-9). In order to assess the average vessel density for each section, an automated analysis was applied. One section per tumour was analysed using an ROI covering the whole section. Due to practical reasons no more than one section per tumour was analysed, accepting the risk of such sampling bias. To reduce the impact of a sampling bias, a higher number of sections per tumour should ideally be analysed (e.g. 3 sections across the whole extension of the embedded tumour). The analysis showed a significantly higher vessel density in CT26 tumours (180.3 ± 23.6 1/mm^2, n=7-10 per group, mean ± SD) as compared to MOC1 (87.3 ± 21.9 1/mm^2, $p<0.0001$) and MOC2 tumours (116.0 ± 42.3 1/mm^2, $p=0.0043$) (Fig.4-10a). MOC2*(PD-L1)*^{poly} (129.2 ± 29.6 1/mm^2) and MOC2*(PD-L1)*^{single} (151.6 ± 34.2 1/mm^2) tumours exhibited a slightly higher vessel density than tumours grown from parental MOC2 cells, however the differences were not statistically significant (Fig.4-10a).

Control stains of pancreas and small intestine sections are provided including CD31 and isotype control staining (Fig.4-10b).

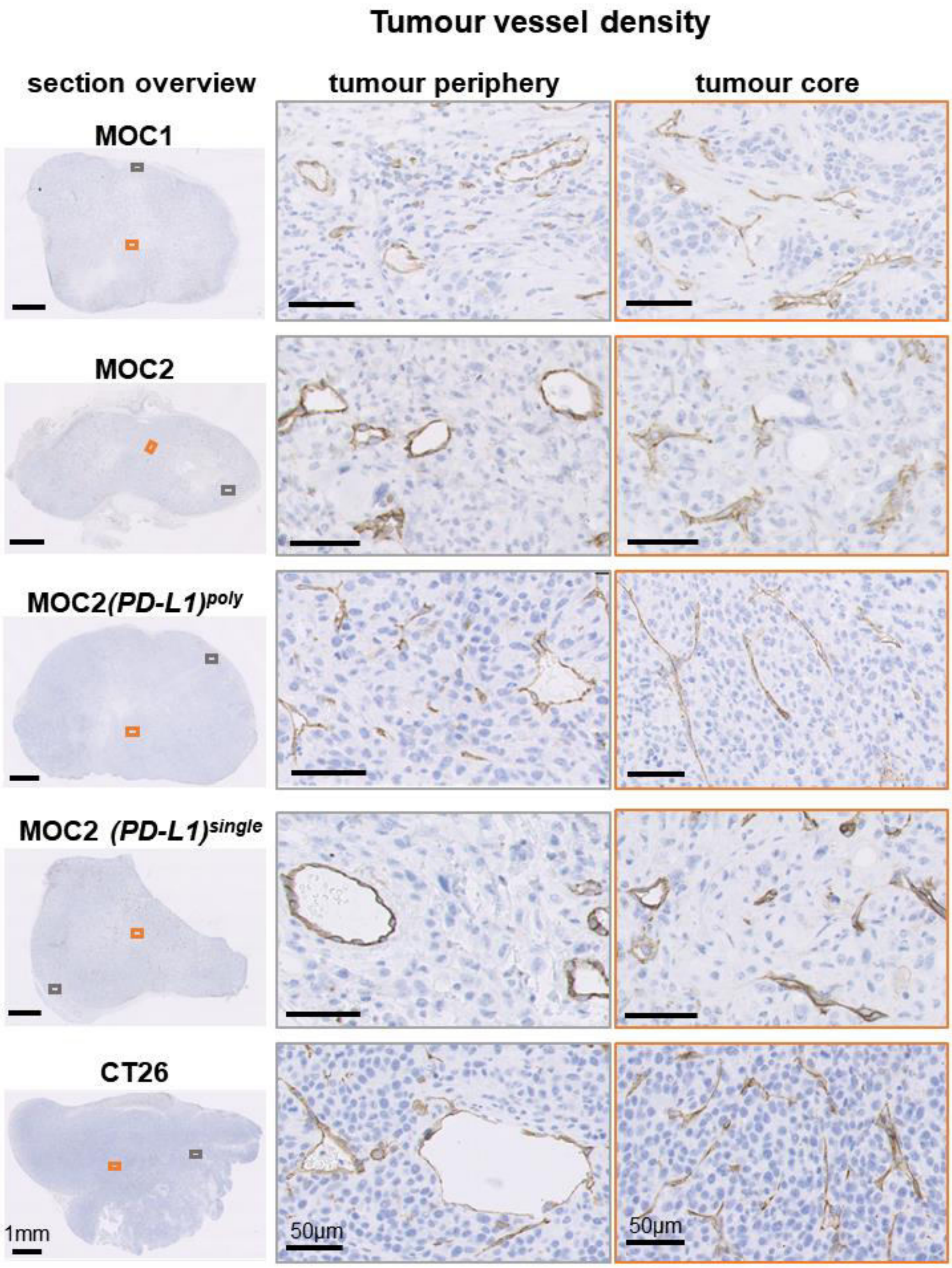

Figure 4 - 9: CD31 IHC of tumour tissue (4 µm sections) of MOC1, MOC2 MOC2(PD-L1)^{poly}, MOC2(PD-L1)^{single} and CT26 models. Each tumour section is shown as an overview (left column), an area representing the tumour periphery (grey frame; middle column) and the tumour core (orange frame; right column).

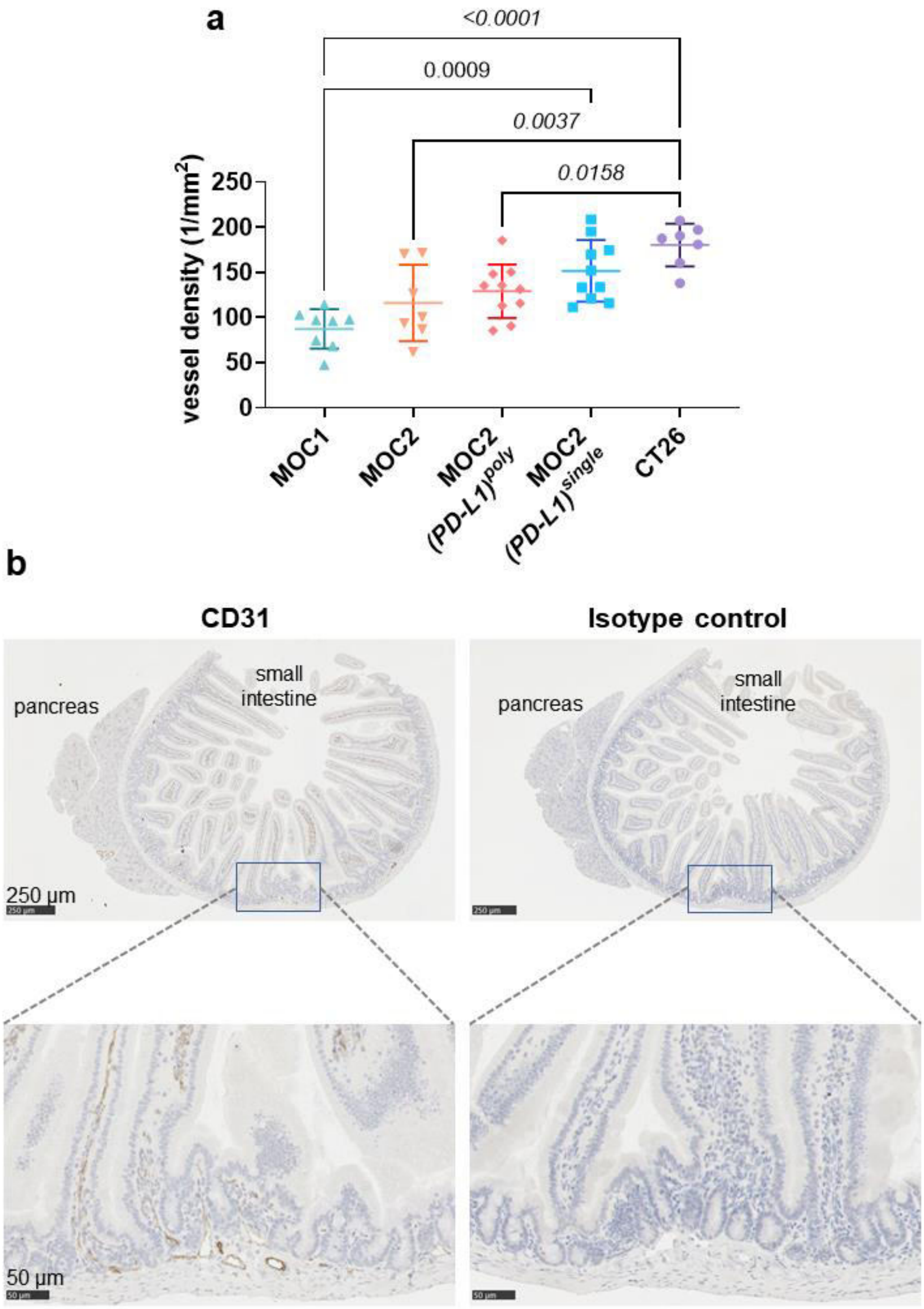

Figure 4 - 10: ***a.*** *Vessel density (CD31-positive area) across tumour types (n=7-10 tumours per group; one representative section for each tumour) assessed via in silico analysis using Definiens Architect XD software. Dot blot with error bars indicating mean ± SD. Data was analysed via one-way ANOVA with Tukey post-hoc correction. P-values<0.05 were considered statistically significant* ***b.*** *CD31 IHC control staining of C57Bl/6J pancreas and small intestine using CD31 (left) and matched isotype control (right) antibodies.*

4.2.8 VOI-based quantification of tumour uptake on PET scans

Finally, volume of interest (VOI)-based RC uptake quantification in PET scans was explored (assessing the %ID/g) and compared to results obtained from biodistribution studies. An overview on VOI-based RC uptake assessment is provided in the introduction of this thesis (1.4.1.4). The method was already used to quantify data presented in section 4.2.3 of this chapter and is frequently preferred over conventional biodistribution studies, as it allows to measure RC uptake non-invasively on PET scans without the need for rigorous organ collection and subsequent gamma-counting. Three representative datasets, where both PET scans and biodistribution results were available, were analysed and the results compared via the Bland-Altman method to determine if there was a bias between the two different uptake measurement strategies.

Firstly, the Bland-Altman method showed an average bias of 1.50 ± 1.10 (mean ± SD of n=3) towards uptake results assessed via conventional biodistribution studies (Fig.4-11a-c). Interestingly, one out of three datasets showed almost no bias with 0.22 ± 2.89 (Fig.4-11a). Pearson correlation analysis confirmed a strong correlation between the biodistribution and VOI-based RC uptake quantification from all three datasets (R^2=0.80 ± 0.08, mean ± SD of n=3), corroborating that both techniques show similar trends albeit the identified bias (Fig.4-11d-f).

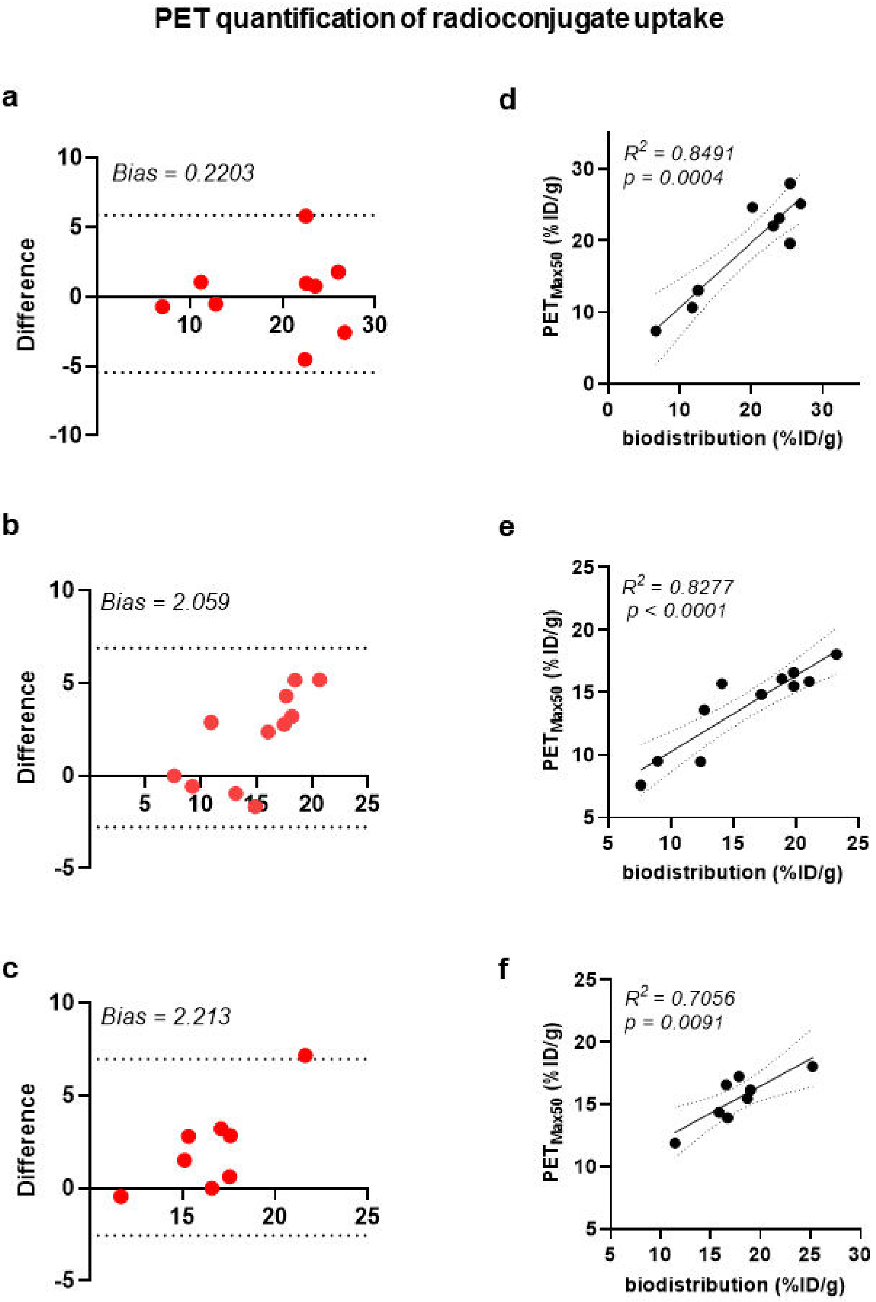

Figure 4 - 11: ***a.-c.*** *Dot plots show Bland-Altman Method comparing* ^{89}*Zr-DFO-PD-L1*$_{mAb}$ *tumour uptake measured via biodistribution and VOI-based PET image analysis. Y-axis presents the difference (A-B) for matched results and x-axis shows the average of matched results.* ***d.-f.*** *Dot plots with linear regression fit and 95% confidence interval (dashed lines) to illustrate correlation between outcomes assessed by these two methods. Pearson correlation was performed and p-values<0.05 considered statistically significant.*

4.3 Conclusion and discussion

Thorough quality control of 'lab-made' antibody-RCs is key to ensure that antibody binding characteristics such as target specificity and affinity are retained and RC immunoreactivity is high upon radiochemical manipulation. Furthermore, the pharmacokinetic behaviour of antibody-RCs shall be assessed in a suitable model *in vivo* to identify the optimal RC injection dose and an adequate time window for subsequent imaging studies. Taken together, these steps ensure the optimal use of antibody-RCs as diagnostic tools, which can then be applied to predict or monitor treatment response in therapy studies.

Initial *in vitro* binding assays indicated favourable binding properties of ^{89}Zr-DFO-PD-L1$_{mAb}$ against its target, suggesting that radiolabelling did not hamper target specificity and affinity of the antibody (Fig.4-3a-c; Suppl.Fig.14a-d). Assessment of the IRF as proposed by Lindmo *et al* (Lindmo et al., 1984; Lindmo and Bunn, 1986), showed high immunoreactivity of the radiolabelled antibody which was similar to previously published results (Fig.4-3a) (Kikuchi et al., 2017). In addition, specificity of binding studies with ^{89}Zr-DFO-PD-L1$_{mAb}$ produced from different DFO-PD-L1$_{mAb}$ batches throughout this project, showed equal specificity across batches (Fig.4-3c, Suppl.Fig.15a/b). It is important to bear in mind that conjugation via lysines causes a certain degree of heterogeneity within, but more so between batches. In order to fully characterise each batch, several *in vitro* analyses can be performed including mass spectrometry to determine the average number of DFO molecules per antibody and functional assays including the Lindmo assay to assess the IRF or specificity of binding assays to determine target specificity. However, such detailed analysis of each batch has not been performed in this thesis following the functional similarity across batches in binding studies. After all, it remains a shortcoming that a more detailed characterisation of each conjugate has not been performed.

The stability of ^{89}Zr-DFO-PD-L1$_{mAb}$ as assessed via a serum stability assay *in vitro* showed negligible ^{89}Zr release within one week (< 7%; Fig.4-2b) which is in line with previously published results (Perk et al., 2010). These findings were corroborated *in vivo,* where low amounts of radioactivity accumulated in bones (< 10%ID/g) upon ^{89}Zr-DFO-PD-L1$_{mAb}$ injection (Fig.4-4, Fig.4-6a). However, the bone uptake observed with the PD-L1 specific RC might also be due to target-specific binding in the bone niche, an anatomical site where PD-L1 expression patterns have not yet been characterised to my knowledge. Furthermore, there is an ongoing debate on the translational relevance of ^{89}Zr bone uptake in mice, as the uptake of free ^{89}Zr frequently observed in mice but not in humans might be caused by the rapid metabolism of the antibody and the ^{89}Zr-DFO complex in this species (Abou et al., 2011; Vivier et al., 2018; Vugts et al., 2017). In order to bypass this debate and assess the stability of a RC *in vivo*, serial blood sampling with concomitant ITLC over a period of one week upon RC injection could be performed. Regardless of that, efforts to further improve the stability of ^{89}Zr-labelled antibody-conjugates are ongoing and focus on chelators which allow for octadentate coordination of the ^{89}Zr-DFO complex (Heskamp et al., 2017). Optimising complex stability with RCs containing long-lived radioisotopes is very important to minimise off-target effects via the accumulation of free ^{89}Zr in healthy tissue.

Pharmacokinetic studies with three different antibody doses were performed to address the dose-dependent PD-L1$_{\text{mAb}}$ kinetics previously described for anti-mouse and anti-human PD-L1$_{\text{mAb}}$ clones *in vivo* (Herbst et al., 2014; Heskamp et al., 2019; Kurino et al., 2020; Lamberts et al., 2015). In line with the literature, low antibody quantities (dose 1) did not achieve target saturation as the majority of compound accumulated in the spleen (Fig.4-4, Fig.4-5a/b). The spleen was previously acknowledged as a systemic PD-L1 antigen sink by others (Heskamp et al., 2019; Kurino et al., 2020). Other natural target expression sites, such as the BAT and lungs did not consume substantial amounts of RC in comparison to the spleen (Fig.4-4, Fig.4-5a/b). Co-injection of an excess of unlabelled PD-L1$_{\text{mAb}}$ alongside ^{89}Zr-DFO-PD-L1$_{\text{mAb}}$ (dose 2 and 3) successfully occupied systemic PD-L1 targets and extended the serum availability of the RC and concomitantly increased its tumour uptake (Fig.4-4, Fig.4-5a/b). Such co-injection strategies for PD-L1$_{\text{mAb}}$ RCs have been successfully employed by others in both preclinical and clinical set-ups (Bensch et al., 2018; Heskamp et al., 2019; Kikuchi et al., 2017). It is important to note that dose-dependent pharmacokinetic effects remain undetected when probes targeting the human PD-L1 epitope, without cross-reactivity for the murine epitope, are tested in immunocompromised xenograft models bearing tumours of human origin (Heskamp et al., 2015; Jagoda et al., 2019). However, the use of a mouse-specific PD-L1 targeted RC in syngeneic mouse models of cancer, as applied in this chapter, overcomes this caveat. The pharmacokinetic data (including PET scans) presented in this chapter indicates that the tumour and other systemic organs expressing PD-L1 are sufficiently saturated with RC after 48 h and RC concentrations in circulation are low enough to provide high contrast images, as for instance compared to images acquired only 24 h after injection (Fig.4-5a). In light of future PD-L1 immunoPET applications (see chapter 6) it was crucial to perform PET imaging/biodistribution studies as soon after RC injection as possible due to the dynamic behaviour of PD-L1 upon therapeutic interventions using OV (Roulstone et al., 2021). Therefore, I chose to schedule all biodistribution and imaging sessions 48 h after RC injection. Of note, such 48 h time points have previously been selected in other preclinical studies using ^{89}Zr-labelled antibody-RCs (Simonetta et al., 2021).

To further elaborate on intratumoural antigen saturation and the capability to study varying levels of intratumoual PD-L1 using ^{89}Zr-DFO-PD-L1$_{\mathrm{mAb}}$, a set of co-dosing experiments was performed comparing intratumoural uptake levels in MOC2 and MOC2*(PD-L1)*^{poly} mouse models. Interestingly, a relatively high amount of unlabelled PD-L1$_{\mathrm{mAb}}$ had to be co-injected alongside ^{89}Zr-DFO-PD-L1$_{\mathrm{mAb}}$ (dose 3) to distinguish MOC2 from MOC2*(PD-L1)*^{poly} tumours according to their PD-L1 expression levels (Fig.4-6a/b). This antibody dose was higher than the doses applied by others (Heskamp et al., 2019; Kikuchi et al., 2017), most likely due to methodological difference including the choice of radioisotope and antibody labelling or the use of different mouse models in these studies. Despite these methodological differences, the tumour uptake levels in the CT26 mouse model were strikingly similar to the levels published by Heskamp *et al* with 11.4 ± 2.1 %ID/g and. 11.1 ± 6.5 %ID/g respectively (Heskamp et al., 2019). In a very recent study, Sandker *et al* co-injected a similarly high dose of unlabelled PD-L1$_{\mathrm{mAb}}$ in order to compensate for drastic systemic increases of PD-L1 in response to an infectious insult (Sandker et al., 2022).

In contrast to the antigen-level dependent uptake observed in MOC2 vs. MOC2*(PD-L1)*^{poly} tumours following injection of dose 3 of ^{89}Zr-DFO-PD-L1$_{\mathrm{mAb}}$, the uptake in MOC2*(PD-L1)*^{single} tumours did not reflect the comparatively higher PD-L1 expression levels in this tumour type (Fig.4-7a; Fig.3-5a/c; Fig.3-11a/c). However, there are several secondary tumour-type specific factors which can influence the uptake of antibody-based RCs including physical (interstitial fluid pressure, IFP), biological (vasculature, immune infiltrate) and biochemical (binding site barrier) parameters which can vary in a tumour-specific manner (Fujimori et al., 1990; Jain, 1990; Jain and Baxter, 1988; Juweid et al., 1992; Welti et al., 2013). Therefore, these parameters need to be addressed in a tumour-type specific manner and taken into account when comparing antibody-RC uptake levels across different tumour models.

One of the aforementioned biological factors impacting tumour-specific antibody-RC uptake is intratumoural vessel density, ultimately determining target accessibility and functional tumour perfusion. Interestingly, intratumoural vessel density varied between the five tumour models presented in this chapter (Fig.4-9, Fig.4-10a). Similar tumour-type dependent variations have also been observed by others (personal communication Emma Reeves, ICR, UK) (Welti et al., 2013). Another important factor which has not been examined as part of this thesis is vessel status, most importantly vessel permeability. To test blood vessel permeability *in vivo*, an intravenous injection protocol with Evans Blue is most frequently used (Radu and Chernoff, 2013). Information on vessel permeability across the tumour models might also help to determine the contribution of non-specific RC accumulation via the enhanced permeability and retention (EPR) effect (Matsumura and Maeda, 1986; Yasunaga et al., 2017). Another factor impacting intratumoural RC distribution is functional tumour perfusion. However, functional tumour perfusion across the five tumour models described in this thesis was not explored. In order to non-invasively measure functional perfusion *in vivo* several imaging methodologies exist including diffusion weighted MRI, contrast-enhanced CT (Mirus et al., 2017), ^{15}O-water PET (Johnson et al., 2020b) and ultrasound imaging using microbubble contrast agents (Cosgrove and Lassau, 2010). Alternatively, intravenous injection of Hoechst® 33342 or fluorescently tagged microspheres (in a terminal setting) are extensively used to assess organ perfusion on tissue sections *ex vivo* (Breitbach et al., 2007; Trotter et al., 1990). Due to the preliminary nature of the tumour vascularisation/perfusion analysis, i.e. the assessment of the vessel density but no functional parameters, no final conclusions on tumour-specific differences across the models used in this chapter can be drawn. Future studies investigating functional perfusion in these mouse models would be required to provide a complete picture. In addition, the contribution of the EPR should be addressed to better understand its impact on non-specific RC uptake. To measure the EPR effect in solid tumours *in vivo* several approaches have been proposed including the use of fluorescently or radioactively labelled liposomes (Børresen et al., 2020; Mikada et al., 2017) or the use of ^{89}Zr-labelled Albumin (Heneweer et al., 2011). The latter was presented in a prototype study to assess the EPR of ^{89}Zr-labelled Ab-conjugates across different tumour types, a strategy which could also be applied to the tumour models in this thesis.

In contrast to all other tumour models presented in this chapter, the CT26 model showed relatively high uptake of the non-specific ^{89}Zr-DFO-IgG$_{\mathrm{mAb}}$ as compared to its PD-L1 targeted counterpart ^{89}Zr-DFO-PD-L1$_{\mathrm{mAb}}$ (Fig.4-8c). Noteworthy, non-specific binding of ^{89}Zr-DFO-IgG$_{\mathrm{mAb}}$ was also found on CT26 cells *in vitro*, corroborating that non-specific binding contributed to the high ^{89}Zr-DFO-IgG$_{\mathrm{mAb}}$ uptake in CT26 tumours *in vivo* (Fig.4-8d). Whilst the uptake of the PD-L1 specific RC is in line with previously published work using the same PD-L1 Ab clone, I could not find any published data on the uptake using the exact same isotype RC as herein (Heskamp et al., 2019). Frequently, an IgG2a isotype control (exhibiting lower inherent affinity towards FcγRs than IgG2b) is used rather than the IgG2b isotype which matches the isotype of the PD-L1$_{\mathrm{mAb}}$ clone 10F.9G2 (Heskamp et al., 2019; Sandker et al., 2022). A biological factor that might have contributed towards a model-dependent, non-specific tumour uptake of ^{89}Zr-DFO-IgG$_{\mathrm{mAb}}$, is the presence of immune cell populations which express high levels of FcγR. A popular example for such an immune cell population are macrophages which express FcγRs and bind full length IgGs (Vivier et al., 2018). Albeit FcγR-binding is generally not expected to significantly affect antibody-RC pharmacokinetics, this might vary depending on the affinity towards FcγR. Accordingly, antibody isotypes which exhibit a high FcγR affinity such as PD-L1$_{\mathrm{mAb}}$ clone 10F.9G2 or its IgG isotype might contribute towards non-specific tumour uptake in tumours abundantly infiltrated with macrophages (Dahan et al., 2015). Therefore, assessing the intratumoural presence of FcγR-expressing cell populations, e.g. via staining of F4/80, a murine macrophage-specific protein, might uncover potential model dependent differences (Austyn and Gordon, 1981; Morris et al., 1991). In order to avoid the potential contribution of FcγR-binding towards non-specific antibody-RC uptake in tumours, the choice of the IgG isotype as the targeting moiety for the imaging probe should be reconsidered. Accordingly, isotypes exhibiting lower inherent affinity towards murine FcγRs, such as the rat IgG2a instead of the rat IgG2b isotype, should be considered if available (Dahan et al., 2015). This might additionally reduce therapeutic effects induced via IgG-FcγR-binding, such as antibody-dependent cellular cytotoxicity (ADCC) (Clynes et al., 2000; Dahan et al., 2015; Musolino et al., 2008; Nimmerjahn and Ravetch, 2012). Unfortunately, mouse targeted antibodies are rarely offered in a variety of isotypes or versions, since their market is very small as compared to antibodies released for use in human patients. Accordingly, the PD-L1$_{\mathrm{mAb}}$ clone 10F.9G2 used as a vector for PET imaging in this thesis was the only product available at the start of my PhD project.

In case issues with non-specific binding occur, but no alternative isotype options are available for the same target, the binding specificity of antibody-based RCs can be improved via radiochemical strategies, most importantly the choice of conjugation approach. Antibody conjugation approaches are divided into two major types, i.e. site-specific conjugation strategies and random conjugation via amino acid residues distributed throughout the whole protein (e.g. lysines). As suggested by the term itself, random conjugation methods lead to random conjugations at amino acid residues accessible throughout the IgG and therefore result in a highly heterogenous mix of antibodies with different sites of conjugation (Dennler et al., 2015). Accordingly, conjugations can also occur in the Fab domain of the antibody and negatively affect RC immunoreactivity. In order to avoid conjugations in the Fab domain, site-specific labelling strategies are employed. One strategy is to incorporate cysteine residues into the antibody backbone as binding sites for the bifunctional chelator (Stimmel et al., 2000). However, the artificial introduction of the cystine residues into the protein structure of a full-length antibody is relatively challenging, which renders site-specific conjugation a rather unpopular approach (Behrens and Liu, 2014; Park et al., 2021). Therefore, coupling at the antibody interchain cysteine residues has been proposed as an alternative type of site-specific reaction but it may generate heterogeneous products and requires preparation of the protein for the attachment of the bifunctional chelator (Park et al., 2021). Furthermore, the carbohydrate moiety of the antibody can serve as a conjugation site distant from the Fab region. Vivier *et al* have recently shown that an antibody-RC, in which glycans were used as a coupling site, showed significantly reduced non-specific binding (Vivier et al., 2020). However, glycan conjugation might suffer from product heterogeneity and eventually affect glycosylation sites in the variable region (Dennler et al., 2015).

If neither another antibody nor the switch from random to site-specific conjugation have led to improved RC specificity, other targeting moieties might be attractive alternatives. These include smaller sized vectors devoid of an Fc portion, such as IgG fragments (e.g. Fab) or derivatives (e.g. scFv or protein scaffolds). For example, Broos *et al* have established a nanobody which binds murine PD-L1 with high specificity *in vitro* and *in vivo* (Broos et al., 2017). With a view to future work, it would be interesting to test this mouse-specific PD-L1 nanobody in the mouse models presented in this thesis, as it might potentially reduce off-target binding with the additional advantage of faster kinetics due to its reduced molecular weight. To my knowledge, no other alternatives of smaller-sized mouse-specific PD-L1 targeting moieties have yet been published. Alternatively, antibody fragmentation could be applied to obtain the Fab domain of the PD-L1 antibody used in this thesis and test whether the lack of the Fc fragment might improve its specificity and tumour targeting *in vivo*. However, antibody fragmentation can be laborious (i.e. optimisation of enzyme-mediated digestion) and requires large quantities of protein to start with (Kinman and Pompano, 2019).

The pharmacokinetic profile of ^{89}Zr-DFO-PD-L1$_{\text{mAb}}$ showed a constant drop of activity in the blood, i.e. in circulation (Fig.4-4, Fig.4-5b). This effect did not change upon injection of dose 3, which eventually saturated peripheral PD-L1 targets. A short serum half-life of ^{89}Zr-DFO-PD-L1$_{\text{mAb}}$ might either be due to i) low inherent affinity of the rat IgG isotype towards murine FcRn or ii) potential immunogenicity of the rat isotype backbone of the antibody. The affinity of a given antibody towards FcRn impacts its binding to FcRn, which ensures systemic antibody recycling and therefore extends the circulation half-life of antibodies (Roopenian and Akilesh, 2007). The affinity of PD-L1$_{\text{mAb}}$ clone 10F.9G2 towards murine FcRn has not been assessed as part of this project. In order to reduce Fc-FcRn interactions and accelerate systemic IgG clearance while preserving antigen targeting, genetic engineering of the Fc portion could be explored. It has been shown that a double-mutant in the Fc portion (H310A/H435Q) reduces FcRn binding, consequently shortening the antibody's circulation half-life (Bouleau et al., 2022; Kenanova et al., 2005). This strategy was successfully applied in an antibody recognising human PD-L1 (Bouleau et al 2022). In line with this, it might be worth exploring the double mutant H310A/H435Q in the mouse specific PD-L1 clone 10F.9G2 as part of future work. Another determinant of the pharmacokinetic behaviour is antibody immunogenicity, which can induce an adaptive immune response towards the injected antibody-RC. Such an immune response involves the generation of antibody-directed antibodies which further form immune complexes that are more likely to undergo FcγR-mediated clearance and can therefore accelerate overall antibody clearance (Bendtzen, 2015). To overcome this issue with clinical grade antibodies for human use, antibody humanisation methods have been developed and are now routinely applied to produce antibodies with minimum immunogenicity (Lee et al., 2014; Safdari et al., 2013). However, to my knowledge, similar strategies are not yet available for antibodies designed for murine use.

Another finding from pharmacokinetic and co-dosing experiments with ^{89}Zr-DFO-PD-L1$_{mAb}$ were the consistently high levels of RC uptake in the liver, including non-specific variabilities (Fig.4-4, Fig.4-6a). The high RC levels proved to be unaffected by the injected dose, corroborating the liver's role in non-target mediated antibody metabolisation, predominantly through FcγR (Wang et al., 2008). The variability in liver uptake in biodistribution data could be an effect of data pooling, including the use of different batches of DFO-PD-L1$_{mAb}$ and biological heterogeneities encountered with different offspring of mice. In regard to differences between antibody-conjugate batches, Sharma *et al* evidenced that an increased number of DFO molecules significantly decreased the liver uptake of their antibody-RC (Sharma et al., 2021). To avoid the batch-differences most likely due to random conjugation methods, site-specific labelling should be employed. The random conjugation approach has been selected for this project due to its straightforward application and its translational relevance as it is currently predominantly used in clinical trials.

In summary, the ^{89}Zr-DFO-PD-L1$_{mAb}$ probe exhibited favourable binding characteristics with nanomolar affinity, high target specificity and high immunoreactivity *in vitro*. *In vitro* and *in vivo* data indicated high RC stability. Pharmacokinetic characterisation of the RC confirmed that systemic targets are saturated via co-injection of excess unlabelled PD-L1$_{mAb}$ alongside ^{89}Zr-DFO-PD-

L1$_{\mathrm{mAb}}$. Further, co-injection dosing achieved high tumour-to-background contrast starting from 48 h after RC injection. Whilst co-injection of ^{89}Zr-DFO-PD-L1$_{\mathrm{mAb}}$ with a relatively high amount of unlabelled PD-L1$_{\mathrm{mAb}}$, i.e. dose 3, allowed discrimination of MOC2 from MOC2*(PD-L1)*^{poly} tumours , it failed to detect the high PD-L1 expression levels in MOC2*(PD-L1)*^{single} tumours, indicating that other factors might affect intratumoural ^{89}Zr-DFO-PD-L1$_{\mathrm{mAb}}$ uptake. The tumour-type dependent vascular density was addressed as one such factor, exhibiting significant variation across the models. Nevertheless, the data presented in this chapter suggests that antibody-based RCs exhibiting high off-target affinities, such as the interaction with FcγRs, cannot be applied at a one fits all injection dose in order to compare intratumoural antigen levels. Efforts to reduce off-target affinities or a more delicate selection of antibody candidates for preclinical use might help to overcome these issues. Ultimately, choosing the PD-L1 specific nanobody developed at Brussels University for future studies might be the best way to overcome the non-specific binding encountered with the IgG2b-based PD-L1$_{\mathrm{mAb}}$.

Chapter 5: Exploring the oncolytic virus RP1 in MOC1 and MOC2 models

5.1 Introduction

RP1 is a novel herpes simplex virus-1 (HSV-1) based oncolytic virus with enhanced potency owing to delicate strain selection and several genetic modifications as described below. It is currently tested clinically for the treatment of solid tumours, as previously addressed in the main introduction (1.2.7). Herein, I am describing the development of RP1 and summarise the results reported from preclinical studies in mouse models of cancer.

RP1 has been derived as the most potent of 29 clinical HSV-1 strains isolated from cold sores of volunteers, following screening of oncolytic potential across a panel of human cancer cell lines. The genes encoding for infected cell proteins (ICP) 34.5 and 47 were deleted. As outlined in the main introduction, ICP34.5 accounts for the neurovirulent potential of HSV and involves mechanisms to escape host-anti-viral responses, such as interferon-mediated mechanisms (Chou et al., 1990; Chou and Roizman, 1994; Orvedahl et al., 2007). Its deletion renders the virus apathogenic to neurons and selective for tumour cells, as ICP34.5 is dispensable for viral replication in tumour cells (Critchley-Thorne et al., 2009; Krabbe and Altomonte, 2018). ICP47 inhibits major histocompatibility complex-I (MHC-I) mediated antigen presentation in HSV-1 infected cells. Therefore, ICP47 deletion restores this functionality and ensures presentation of viral and tumour antigens (Goldsmith et al., 1998). ICP34.5 and ICP34.5/47-deleted versions of HSV-1-based viruses have proven to be clinically safe with the ICP34.5/47-deleted candidate T-VEC currently approved for the treatment of advanced stage melanoma (Andtbacka et al., 2015; Kaufman et al., 2015).

To enhance oncolytic and immunogenic potential, two additional genes were inserted. Firstly, GM-CSF to enhance anti-tumour immunity as GM-CSF promotes the maturation and function of DCs and improves the activity of macrophages (Dranoff et al., 1993; Kim et al., 2000). Of note, for studies in syngeneic mouse cancer models, human GM-CSF was substituted by murine GM-CSF (mGM-CSF; this RP1 virus is also addressed as version 16 in Thomas *et al*)(Thomas et al., 2019). Secondly, GALV-GP-R$^-$ was encoded in the viral backbone to enhance viral spread and tumour cell killing. Details around GALV-GP-R- are addressed in more detail in section 1.2.5.

Preclinical efficacy testing of RP1 showed potent oncolytic activity in several human head and neck cancer, thyroid cancer and melanoma cell lines as well as several murine thyroid cancer cell lines alongside one murine melanoma cell line (Crespo-Rodriguez et al., 2020; Roulstone et al., 2021). The added therapeutic effect arising from GALV-GP-R^{-} expression was demonstrated in xenograft mouse models inoculated with human cancer cell lines as well as in a syngeneic rat cancer model, to enable GALV-GP-R^{-} triggered fusogenic effects through the PiT1 receptor (Roulstone et al., 2021; Thomas et al., 2019). Additionally, Thomas *et al* showed the enhanced capability of GALV-GP-R^{-} expressing RP1 to induce immunogenic cell death in human and rat cancer cell lines *in vitro* (Thomas et al., 2019). Albeit the impaired fusogenic effect of GALV-GP-R^{-} in syngeneic murine cancer models, data obtained in 4434 melanoma and A20 lymphoma models have indicated potent therapeutic effects following repeat intralesional injection of RP1 (Roulstone et al., 2021; Thomas et al., 2019). Additionally, synergistic effects were achieved via the combination of RP1 with anti-PD-1 ICB or BRAF inhibition in the immunocompetent A20 lymphoma model and the murine TBP-B79 thyroid cancer model respectively (Crespo-Rodriguez et al., 2020; Thomas et al., 2019). The compelling preclinical data published by Suzanne Thomas and others, as well as the novelty and the high translational value of the RP1 virus platform convinced me to use RP1 (expressing mGM-CSF) as an oncolytic virus for my PhD project. Furthermore, RP1 has not been tested in syngeneic models of HNSCC, such as MOC1 and MOC2.

In this chapter I present studies demonstrating the effect of the mouse RP1 on MOC1 and MOC2 cell lines *in vitro*, particularly its infectiousness and cytopathic effect (CPE). The expression of the herpesvirus entry mediator (HVEM) was assessed to address the differential response of MOC1 and MOC2 cells to RP1. Following on, I present data obtained from *in vivo* studies exploring the effects of RP1 in the MOC1 mouse model. This work addresses the therapeutic potential of RP1 monotherapy, the biodistribution of the virus upon a single intratumoural injection and the potential effects of intratumoural OV delivery on tumour perfusion. Noteworthy, a single-dosing regimen was selected as a starting point for the *in vivo* work presented in this chapter, with the option to explore effects of repeat dosing at later stages. A map of the RP1 virus and a GFP-tagged variant (RP1 version 15) used in this and the following chapter, are provided below (Fig.5-1).

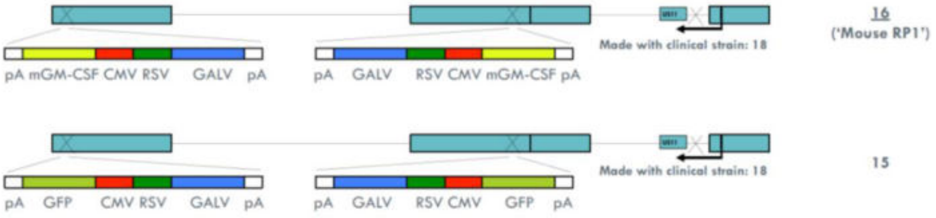

Figure 5 - 1: Schematic representation of the RP1 virus and RP1 version 15 with GFP as a reporter. The construction of both viruses is described in detail by Thomas et al., where these illustrations have been derived from (Thomas et al., 2019).

5.2 Results

5.2.1 Capability of RP1-15 to infect MOC1 and MOC2 cells *in vitro*

To explore whether RP1 was capable of infecting MOC1 and MOC2 cells, the GFP-expressing RP1-15 virus was used and its behaviour monitored via fluorescent imaging. Accordingly, monolayers of MOC1 and MOC2 cells were imaged at 6, 24 and 48 h upon the addition of increasing concentrations of RP1-15. In addition to visual inspection, I attempted to quantify the infected cells as a ratio of the GFP-positive area over the area covered by cells in each well. Both GFP-positive and confluent areas were determined via texture-based auto-segmentation in GFP and brightfield channels respectively (settings for texture algorithm as described in 2.10.2). Of note, although visual inspection of the images showed consistent results, only one of three repeats could be quantified via image analysis due to technical difficulties (differences in image contrast between experiments).

At 6 h post-incubation, MOC1 cells did not express GFP at concentrations lower than 10 PFU/cell (Fig.5-2). At 10 PFU/cell however, a relatively large fraction of cells was infected as observed via visual assessment and image quantification (0.143 at 10 PFU/cell, n=1) (Fig.5-3). In contrast, MOC2 cells did not express GFP at any virus concentration at this stage (Fig.5-2/3). At the following 24 h time point, MOC1 cells showed a dose-dependent expression of GFP (0.002 at 0.01 PFU/cell, 0.210 at 0.1 PFU/cell, 0.349 at 1.0 PFU/cell, 0.502 at 10 PFU/cell) (Fig.5-2/3). Interestingly, MOC2 cells only exhibited signs of infection at the highest concentration (0.224 at 10 PFU/cell). At 48 h, MOC1 cells still showed dose-dependent GFP expression between 0.01 and 1.0 PFU/cell (0.017 at 0.01 PFU/cell, 0.118 at 0.1 PFU/cell, 0.210 at 1.0 PFU/cell), but not beyond (0.033 at 10 PFU/cell). Brightfield images of cells treated with 10 PFU/cell showed that most MOC1 cells were detached and dead at this stage (Fig.5-2). MOC2 exhibited a small number of GFP-positive cells showing signs of infection at 1.0 and 10 PFU/cell, with ratios of 0.040 and 0.155 respectively (Fig.5-2/3). Although only one of three repeats could be quantified via auto-segmentation, the obtained data well-represents the trend observed via visual inspection of all three repeats.

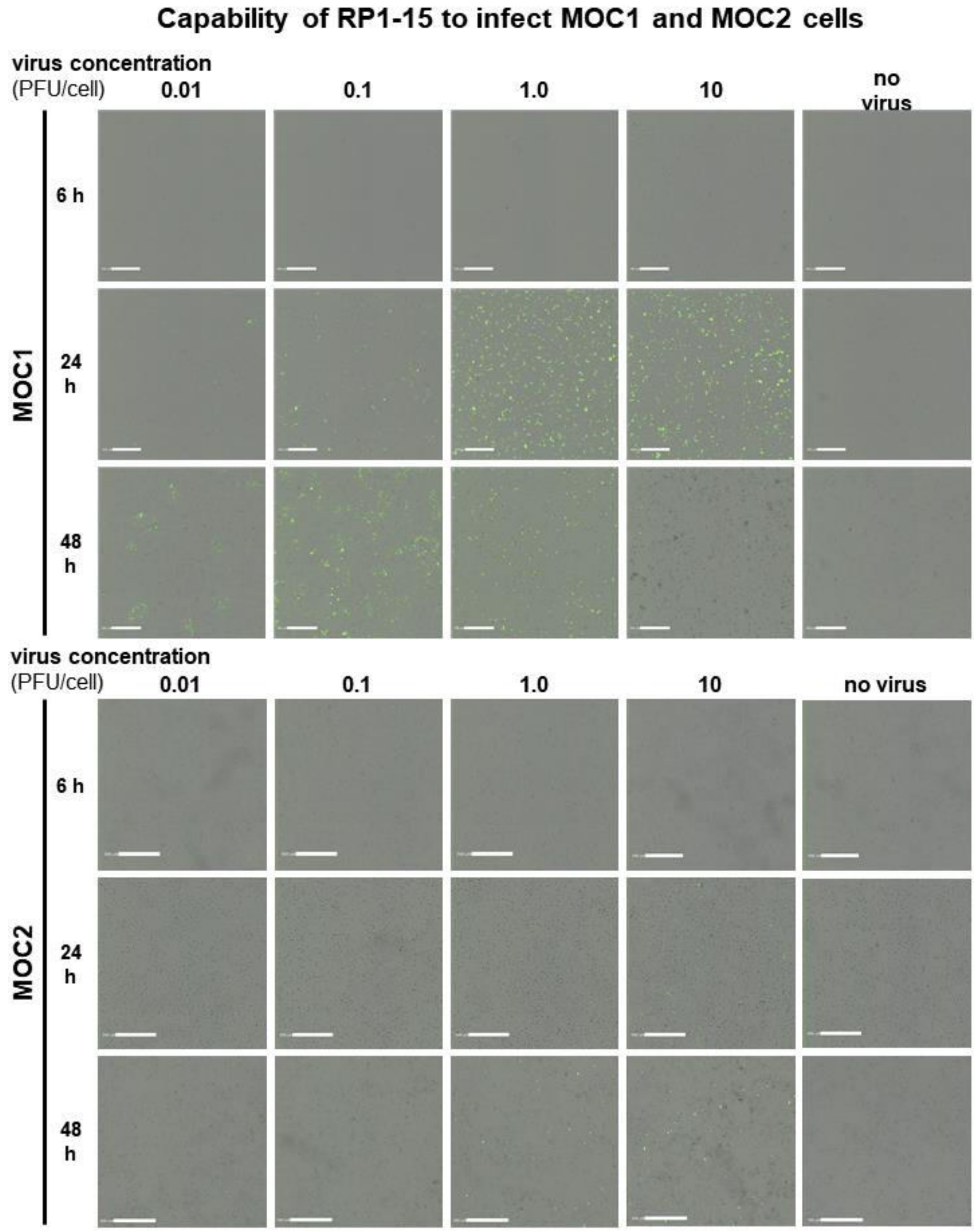

Figure 5 - 2: Images show fused brightfield and fluorescent scans of MOC1 and MOC2 cells during incubation with increasing concentrations of RP1-15 (GFP expressing) at 6, 24 and 48 h. Scale bar represents 500 µm (as indicated by small white label immediately to the left of each scale bar). One of three biological repeats.

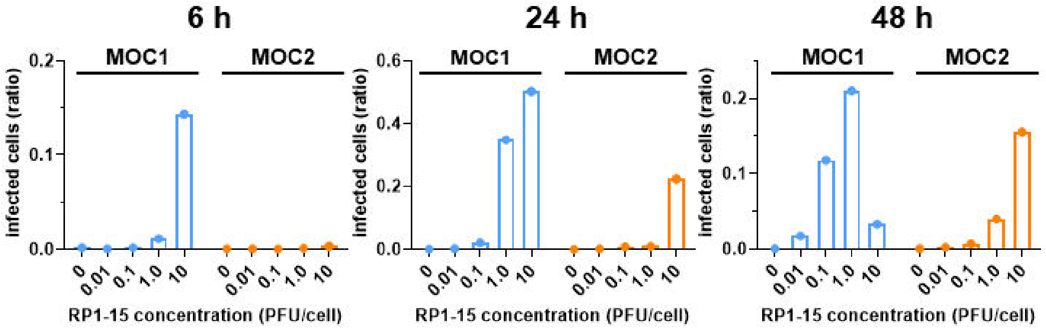

Figure 5 - 3: Bar charts show the ratio of infected cells (GFP positive area) over confluent cells (cell-covered area) per concentration of RP1-15 virus (PFU/cell). Both areas were determined via texture-based auto-segmentation of the whole well in GFP and brightfield channels respectively. Values are presented for MOC1 and MOC2 cells at three different time points (bars show n=1).

5.2.2 Cytopathic effect of RP1 on MOC1 and MOC2 cells *in vitro*

Next, the cytopathic behaviour of RP1 was assessed using both MOC1 and MOC2 cell lines. Based on the infection dynamics observed with RP1-15 in the previous experiment (Fig.5-2, Fig.5-3), the 48 h time point seemed well-suited for the detection of a CPE. Accordingly, the viability of MOC1 and MOC2 cells following a 48 h incubation period with RP1 was determined via CellTiter Glo® assay. The study showed a dose-dependent decrease of MOC1 cell viability in response to RP1 (Fig.5-4). In fact, all tested virus concentrations ranging from 0.1-500 PFU/cell significantly reduced the number of viable cells as compared to the untreated control ($p<0.0001$). This effect remained consistent among all three repeats for all virus concentrations apart from 0.1 PFU/cell, which did not reach a significant CPE in one of three repeats. In contrast, the CPE caused by RP1 in MOC2 cells was not as apparent and quite heterogeneous across the three repeats (Fig.5-4). Overall, the results reported herein were in line with findings obtained from the infection experiment corroborating that MOC1 cells are RP1-sensitive, while MOC2 cells are not. The relative importance of viral replication (as opposed to non-productive viral infection) in inducing cell death was not assessed. This could have been interrogated with UV-inactivated viral preparations, but such experiments were not performed.

Cytopathic effect of RP1 *in vitro*

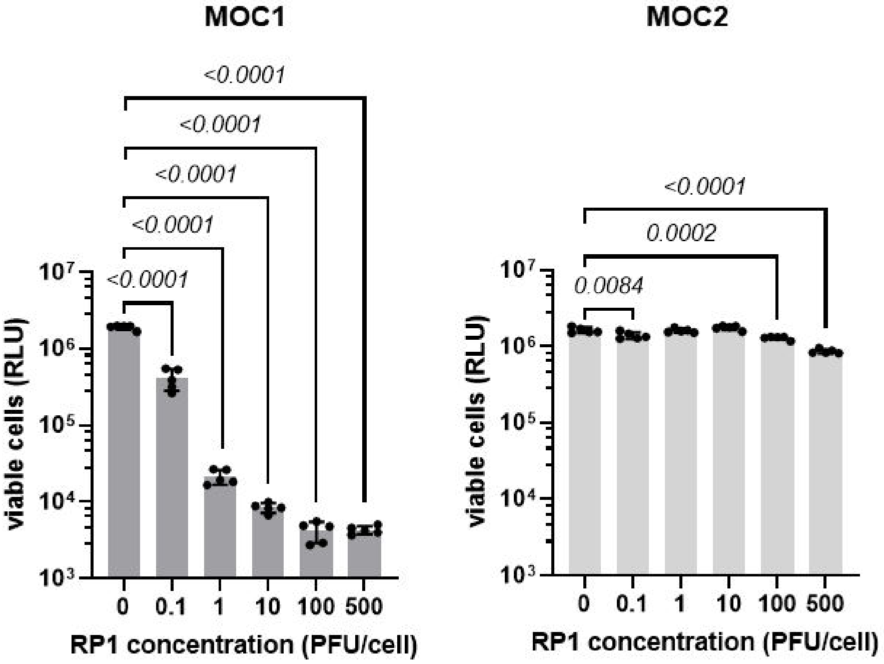

Figure 5 - 4: Bar charts show viable MOC1 and MOC2 cells after 48 h incubation with increasing concentrations of RP1 in vitro. Cell viability was measured via CellTiter Glo assay and is expressed in relative light units (RLU) as log(10)-transformed values (y-axis), bars indicate mean ± SD of n=5. Charts represent one of three individual repeats. Statistical analysis was performed on log(10)-transformed data and each group was compared to the control well (0 PFU) via a one-Way ANOVA with a Dunnett's test for multiple comparisons of all concentrations against the untreated control. P-values<0.05 were considered statistically significant.

5.2.3 HVEM expression as a potential measure of sensitivity to RP1 *in vitro*

The differential sensitivity of MOC1 and MOC2 cells to RP1 *in vitro* might arise from their differential expression of viral entry receptors for HSV-1. One such receptor is a protein called HVEM. It was chosen for expression analysis as its requirement for HSV-1 cell entry was recently emphasised by Ghose *et al* (Ghose et al., 2021). Furthermore, the HVEM antibody was freely available from the lab's antibody stock and financial restrictions did not allow to buy further antibodies, e.g. targeting other receptors involved in HSV-1 cell entry such as Nectin-1. All receptors involved in HSV-1 cell entry are addressed in the introduction of this thesis (1.2.4). With regard to MOC1 and MOC2 cells, FC analysis of HVEM expression indicated negligible levels of HVEM and strikingly similar histograms between the isotype control (IgG) and the HVEM specific antibody (Fig.5-5a/b). The average MFI of HVEM relative to the MFI of IgG levelled around 1 for both cell lines (MOC1 0.92 ± 0.16, MOC2 1.04 ± 0.08; mean ± SD, n=3), which indicated eventual non-specific binding of the anti-HVEM antibody. In light of budgetary constraints, furthermore detailed analysis of the expression of viral entry mechanisms was not conducted.

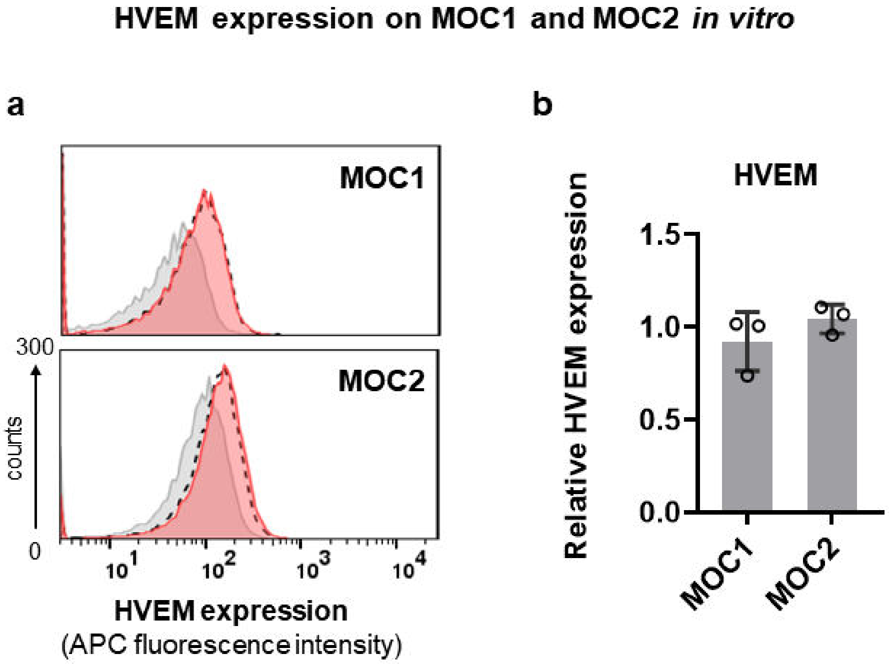

*Figure 5 - 5: **a.** Histograms show expression level of HVEM (red), hamster IgG (dotted line) and unstained (dark grey) samples of MOC1 and MOC2 cells as assessed via flow cytometry **b.** HVEM expression (median fluorescence intensity, MFI) normalised to IgG (MFI) of MOC1 and MOC2. Bars show mean ± SD of n=3.*

5.2.4 Therapeutic effect of RP1 on MOC1 tumours *in vivo*

As MOC1 cells demonstrated high sensitivity to RP1 *in vitro*, the MOC1 cells were engrafted into C56Bl/6J mice to test their response towards the virus *in vivo*. A single dose of RP1 (1×10^6 PFU in 10 µL) or PBS (10 µL) was injected intratumourally and the therapeutic effect of the virus was assessed via calliper measurements to track changes in tumour volume. The cohort size of n=10 was based on previous studies investigating the therapeutic efficacy of RP1 including in mouse models of melanoma (Thomas et al., 2019). This revealed that RP1 treatment slowed MOC1 tumour growth early after injection, as represented by the area under the curve (AUC) between day 0 and day 6 (RP1 767.5 ± 220.9 mm^3, PBS 923.9 ± 298.2 mm^3; mean ± SD of n=10) (Fig.5-6a/b). However, this trend did not persist beyond day 6, indicating there was no significant effect of a single injection on overall MOC1 tumour growth (Fig.5-6a). Of note, several mice had to be culled prematurely, as tumour ulcerations reached the licence limits. Animal body weights were recorded alongside the experiment and showed no marked weight loss from RP1 therapy (Fig.5-6c).

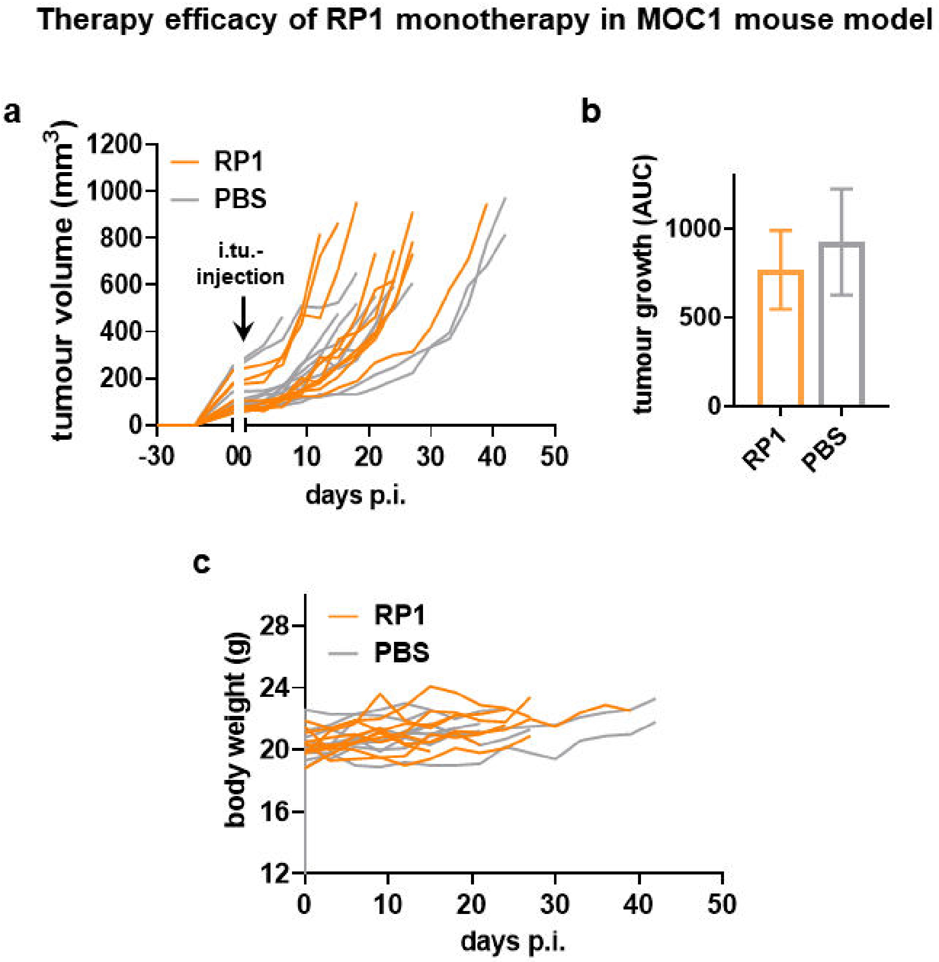

Figure 5 - 6: ***a.*** *Spaghetti plot shows tumour growth of MOC1 tumour-bearing mice following a single intratumoural injection with RP1 (10^6 PFU, 10 µL, orange) or sterile PBS (10 µL, grey) on day 0 (arrow); n=10 mice per group.* ***b.*** *Area under the curve (AUC) of tumour volumes between day 0 and day 6 of treatment, bars indicated mean ± SD, unpaired Student's t-test with Welch's correction was applied and a p-value<0.05 was considered statistically significant* ***c.*** *Animal body weights over the course of treatment.*

5.2.5 Biodistribution and replication of RP1-15 *in vivo*

In order to study the biodistribution and replication potential of RP1 *in vivo*, a small cohort of MOC1 tumour-bearing mice were injected with a single dose of RP1-15 (1×10^6 PFU in 10 µL) and tumours and other organs including tumour-draining lymph nodes (TD Ln) and spleens were collected at day 3 or 7 after injection. Organs were homogenised, and their supernatants incubated on a monolayer of Vero cells to determine the presence of replication-competent RP1-15. The relative number of GFP-expressing cells was determined via fluorescent microscopy.

On day 3 after RP1-15 injection one out of six tumours contained replication-competent virus, as observed by a high number of GFP-expressing Vero cells (Fig.5-7a/b). At the same time point (day 3), some TD Lns contained traces of replication-competent RP1-15, but no signs of replication-competent virus were detected in the spleens (Fig.5-7a). On day 7, none of the organs collected from three different mice showed any replication-competent virus (Fig.5-7a).

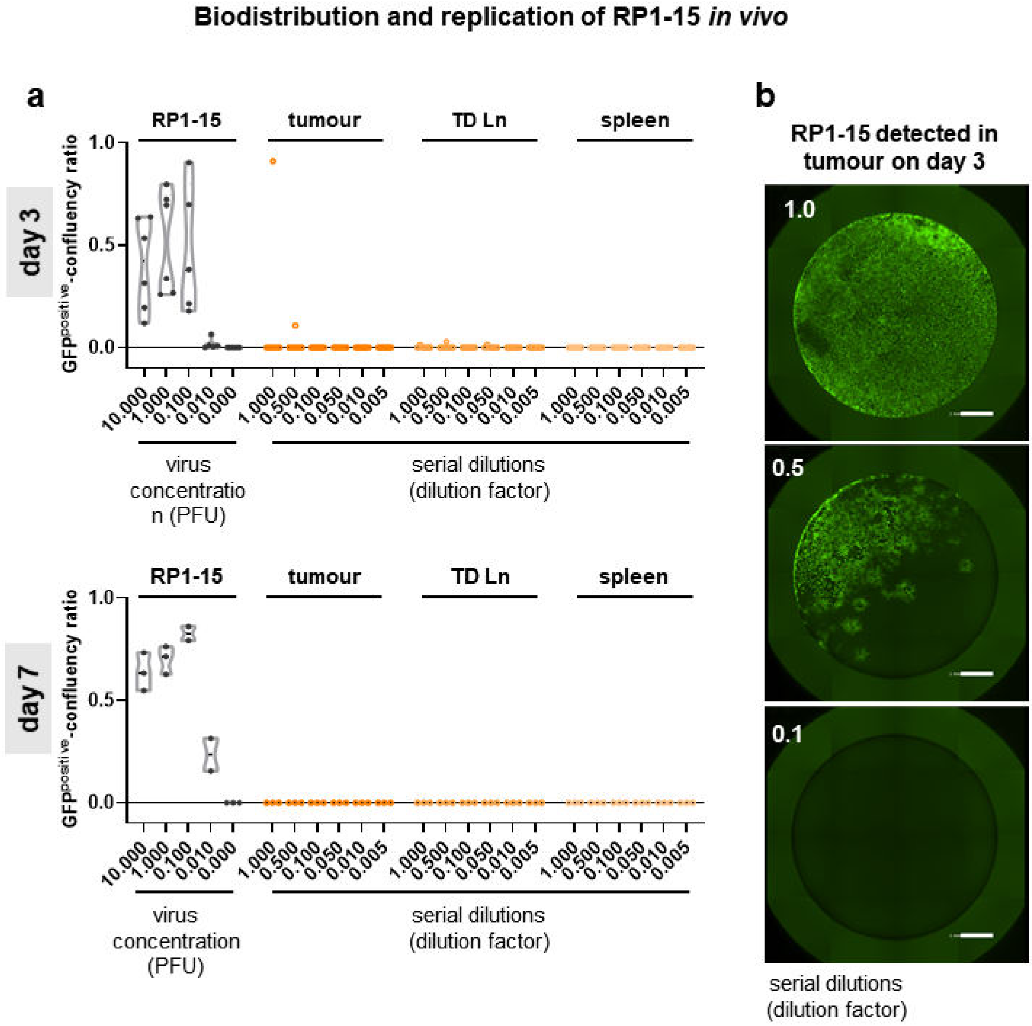

Figure 5 - 7: ***a.*** *Biodistribution of organ supernatants from tumours, tumour draining lymph nodes (TD Ln) and spleens at day 3 and day 7 upon a single intratumoural dose of RP1-15 (10^6 PFU). Serial dilutions of organ supernatants were incubated on a monolayer of Vero cells to detect replication competent RP1-15 virus. Neat RP1-15 was used as a positive control (0.01-10 PFU/well). Each dot indicates a mouse (n=3-6 per time point)* ***b.*** *Fluorescence microscopy images show GFP-expressing (RP1-15 infected) Vero cells*

(in green) following incubation with tumour supernatants (collected 3 days after intratumoural RP-15 injection). Scale bars indicate 1 mm.

5.2.6 MOC1 tumour physical properties upon local RP1 injection

With a view to future PET imaging studies, the potential impact of RP1 on tumour physical properties such as perfusion was explored in a pilot study. Therein, MOC1 tumour-bearing mice treated with a single dose of RP1 (1×10^6 PFU in 10 µL or 5×10^6 PFU in 50 µL) were injected with Hoechst 33342 solution (50 µL, intravenously) and subsequently euthanised for tumour collection. Hoechst 33342 is a cell-permeant blue fluorescent dye which is commonly used to stain DNA and has previously been used in terminal experiments *in vivo* to assess functional tumour perfusion (Breitbach et al., 2007; Latt et al., 1975). Tumour perfusion was evaluated at 2 h or 5 d after intratumoural RP1 administration as these time points were initially selected for RC injection in immunoPET studies presented in the following chapter. MOC1 tumour-bearing mice without intratumoural injection were used as a control.

Fluorescence images acquired from tumour sections collected early (2 h) after RP1 injection showed dark tumour cores, particularly pronounced at the higher viral dose (5×10^6 PFU; Fig.5-8a). Of note, the tumour core was the area targeted for virus injection. The section periphery of both tumours, however, showed bright areas, indicating intact perfusion. Accordingly, both sections exhibited areas of necrosis as evidenced by eosinophilic foci in H&E-stained sections. No effects of necrosis were observed in the uninjected control tumour, which was homogenously stained with Hoechst across the majority of tumour interstitium with some darker areas in-between. The untreated tumour section collected at day 5 post-injection indicated thorough perfusion, however, with limited quality of the scan (Fig.5-8b). RP1 treated tumours collected at day 5 showed homogenous Hoechst staining indicating fully restored tumour perfusion at this time point. However, in the tumour treated with the higher RP1 dose (5×10^6 PFU) two darker foci indicated a residual effect of the virus on tumour perfusion.

Taken together, this pilot study suggested an immediate impact (within 2 h) of a single local RP1 injection on MOC1 tumour perfusion which might be dose-dependent and eventually fades with time. Furthermore, it indicated the need to delay RC injections scheduled at 2 h after RP1-treatment to a later time as tumour perfusion seemed to be very poor at that stage. However, these findings should be confirmed by a repetition of studies. Such studies should ideally be supported by additional stains to determine PD-L1 expression and eventually co-localise with tumour tissue via a second antibody (e.g. pan-CK marker for MOC1).

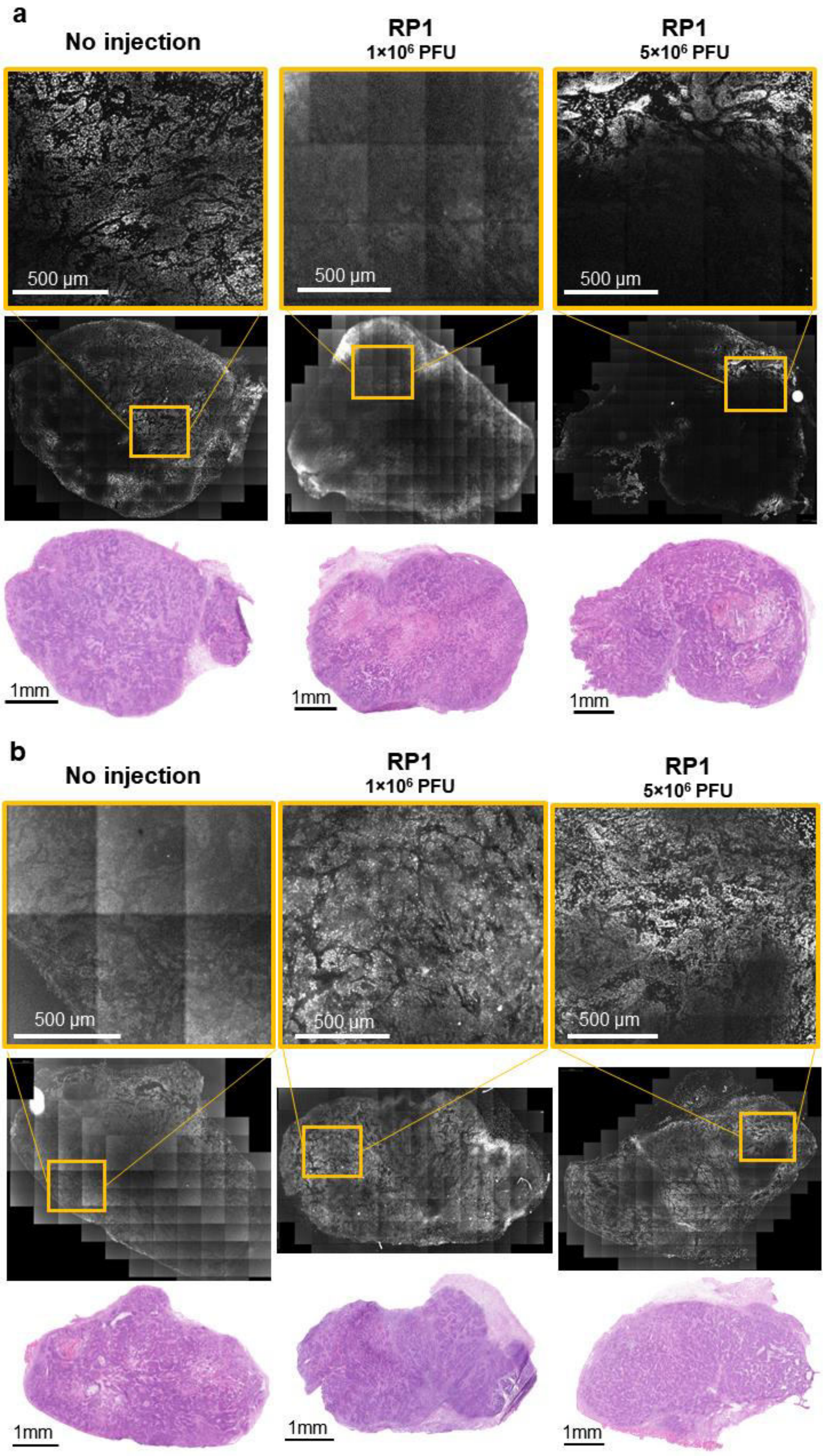
a
No injection
RP1
1×10⁶ PFU
RP1
5×10⁶ PFU
500 µm
500 µm
500 µm
1mm
1mm
1mm
b
No injection
RP1
1×10⁶ PFU
RP1
5×10⁶ PFU
500 µm
500 µm
500 µm
1mm
1mm
1mm

*Figure 5 - 8: Black and white images show fluorescence microscope tile scans of MOC1 tumour sections (6 µm) following Hoechst perfusion in vivo. Perfusion and subsequent tumour collection were carried out at (**a.**) 2 h or (**b.**) 5 d after intratumoural RP1 injection or no injection as a control (n=1 per condition). The patterning effect in some of the fluorescent scans originates from focusing issues of the microscope (automatic acquisition mode) due to poor signal contrast. H&E-stained tumour slices shown underneath fluorescent scans have been performed on consecutive sections.*

5.3 Conclusion and discussion

Oncolytic herpesviruses (oHSV) have proven to be potent biological anti-cancer drugs, with T-VEC approved clinically for the treatment of advanced melanoma (Andtbacka et al., 2015). RP1, a novel HSV-1 based OV, has recently been developed for enhanced oncolytic and immunogenic activity (Thomas et al., 2019). Preclinical data showed potent effects of oncolysis and the induction of immunogenic cell death across various cancer cell lines (e.g. Cal27, Fadu, Mel624, 8505c) (Crespo-Rodriguez et al., 2020; Roulstone et al., 2021). Similarly, antitumour therapeutic effects have been reported for xenograft and syngeneic mouse models of cancer to evidence the full spectrum of biological effects of the RP1 virus. In this chapter, I report on the effects of RP1 in MOC1 and MOC2 models *in vitro* and *in vivo*.

Initial screening of RP1 on MOC1 and MOC2 cells revealed high sensitivity of MOC1 as evidenced by viral infection starting at low doses (0.01-0.1 PFU/cell at 48 h and earlier) and concomitant cell death (Fig.5-2/3/4). In contrast, MOC2 cells were only infected at high viral titres (1.0-10 PFU/cell at 48 h only) and showed almost no cytopathic effect in response, suggesting resistance against RP1-mediated oncolysis *in vitro*, perhaps through resistance to virus-mediated apoptosis (Fig.5-2/3/4). Such cell-type specific difference in oHSV-1 infection can depend on the expression of virus entry receptors such as HVEM or nectin-1 (Ghose et al., 2021; Yu et al., 2007; Yu et al., 2005). Due to resource limitations I chose to look at HVEM expression only (antibody was already in the lab's antibody stock). According to flow cytometric analysis, the differential response of MOC1 and MOC2 cell lines was not related to different expression of HVEM (Fig.5-5). However, the HVEM-targeted antibody used for staining showed signs of poor specificity which is why HVEM expression should ideally be confirmed via alternative routes (e.g. different antibody clone for flow cytometry or HVEM mRNA expression via qPCR) as part of future studies. Furthermore, the expression of nectin-1 in MOC1 and MOC2 cells should be assessed as an alternative entry route for HSV-1.

In contrast to the differential response between MOC1 and MOC2, a comprehensive screening of RP1 on a variety of human HNSCC cell lines showed equally potent oncolytic activity of the virus across these cell lines *in vitro*

(Roulstone et al., 2021). Interestingly, a cell line of murine origin, so-called 4434 melanoma cells, also included in the *in vitro* screening, exhibited lower sensitivity to RP1 than melanoma cells of human origin (Roulstone et al., 2021). *In vitro* screening of RP1 in thyroid cancer cell lines revealed human 8505c and murine TBP-B79 cells as particularly sensitive (Crespo-Rodriguez et al., 2020).

Following the high sensitivity of MOC1 towards RP1 *in vitro*, an *in vivo* study was conducted to assess the response of MOC1 subcutaneous tumours grown in an immunocompetent environment. However, a single intralesional injection of RP1 did not induce a significant therapeutic effect in MOC1 tumours (Fig.5-6a/b). In contrast, therapy studies in syngeneic mouse models of melanoma and lymphoma showed potent anti-tumour effects leading to control or even complete regression of RP1-injected and non-injected lesions (Roulstone et al., 2021; Thomas et al., 2019). However, a less pronounced therapeutic response was observed in a murine thyroid cancer model (Crespo-Rodriguez et al., 2020). Of note, in all three studies repeat dosing (up to 6 injections) was applied (Roulstone et al., 2021; Thomas et al., 2019). After all, only a few examples exist where a single dose of OV achieved tumour regression or cure (Naik et al., 2012).

While pursuing the long-term goal to investigate the PD-L1 response upon RP1 injection via antibody-based immunoPET, a pilot study addressing the potential impact of intralesional RP1 injections on tumour perfusion was performed. As mentioned in chapter 4 (4.3), sustained tumour perfusion is key for RC extravasation and target saturation. Oncolytic viruses however can impact tumour perfusion as previously reported: Using fluorescently labelled microspheres, Caroline Breitbach and colleagues showed that tumour perfusion was significantly reduced after vesicular stomatitis virus (VSV)-based treatment (Breitbach et al., 2007). The data presented in this chapter suggests that MOC1 tumour perfusion is impaired early (2 h) after a single intralesional injection of RP1 but fully restored at later time points (Fig.5-8a/b). The mechanistic basis for this is not clear, but the phenomenon suggests a direct, transient effect on the vasculature. A transient reduction of intratumoural perfusion early after virus injection might arise through an increase in IFP from the injected volume (10 or 50 µL), as well as from the cell lysis triggered by oncolytic virus infection. Over time, both effects might ameliorate through (i) drainage of the excessive fluid and (ii) the anti-viral machinery of the immune system involving direct actions to stop viral spread and associated cell lysis and the removal of cell debris (e.g. macrophages). To better understand the relationship between the intralesional injection of RP1 and MOC1 tumour perfusion, further studies should be pursued. These could be performed via *in vivo* imaging including diffusion weighted MRI, PET or ultrasound imaging, or *ex vivo* via fluorescent microscopy following systemic injection of fluorescently tagged microspheres as previously discussed in 4.3. In contrast to the findings by Breitbach *et al*, almost no replication competent RP1 was found in MOC1 tumours collected at day 3 or 7 post-injection (Fig.5-7a). However, data from Roulstone *et al* showed that in 4434 melanoma tumours high titres of replication competent RP1 were detected following repeat injections (Roulstone et al., 2021).

Taken together, the work presented in this chapter showed that MOC1 cells are highly sensitive to RP1 *in vitro*, with infection and oncolysis occurring at low viral titres. In contrast, MOC2 cells seemed less responsive to RP1. Interestingly, the differential response between MOC1 and MOC2 could not be related to the expression of HVEM, a protein involved in herpesvirus cell entry. MOC1 tumours did not show a therapeutic response following a single intralesional injection of RP1 *in vivo*, possibly owing to the poor replication efficiency of RP1 in MOC1 tumours *in vivo*. Furthermore, MOC1 tumour perfusion is eventually impaired early after intratumoural injection but may be restored at later times. After all, these findings allowed to select the MOC1 mouse model for studies addressing the main hypothesis of this thesis and to design immunoPET studies accordingly (e.g. considering variables such as tumour perfusion upon OV). The outcome of these immunoPET studies will be presented in the subsequent chapter.

Chapter 6: Exploring a RP1-triggered PD-L1 response via PD-L1 immunoPET and complementary methods

6.1 Introduction

The impact of oncolytic virotherapy (OV) on the expression of programmed death ligand 1 (PD-L1), an immune checkpoint protein involved in cancer-immune crosstalk, has recently been reported in several tumour types (Crespo-Rodriguez et al., 2020; Nakao et al., 2020; Ribas et al., 2017; Samson et al., 2018; Thomas et al., 2019). An overview of this topic is provided in the main introduction (section 1.2.6). Therein, an overview of the factors which knowingly mediate PD-L1 expression is also provided (1.3.2). From the sum of possible factors which impact PD-L1, cytokines are expected to play a crucial role in the upregulation of PD-L1 upon OV. Specific cytokines, so-called type I interferons (IFN), are released as a first-line measure upon viral infection (Katze et al., 2002; Yan and Chen, 2012). Type I IFNs act as an initial alert signal for the immune system inducing T-cell recruitment and have the capability to inhibit viral replication (Hwang et al., 1995; Sainz and Halford, 2002). Hence, PD-L1 may be upregulated by type I IFNs on infected and neighbouring cells in an autocrine and paracrine manner respectively. It is important to note that HSV-1 viruses have developed strategies to inhibit type I IFN signalling (Johnson et al., 2008). In the further course following virus injection, antigen-specific T-cells release IFN-γ which might in turn increase PD-L1 on surrounding tumour cells, as a mechanism to evade the cytotoxic activity of T-cells. This concept of PD-L1 upregulation is acknowledged as a strategy of adaptive immune resistance in tumours (Pardoll, 2012; Ribas, 2015). Data from several studies supports this concept reporting a simultaneous increase of CD8+ T-cells, IFN-γ and PD-L1 upon treatment with different OVs likewise (Ribas et al., 2017; Samson et al., 2018). Other studies report only a singular increase of CD8+ T-cells and IFN-γ, without PD-L1 upregulation in tumours, eventually contradicting the concept of an IFN-γ-triggered PD-L1 increase *in vivo* (Shen et al., 2016). While strong evidence for an IFN-mediated upregulation of PD-L1 exists *in vitro* (Garcia-Diaz et al., 2017; Loke and Allison, 2003), additional mechanistic studies are required to decipher the role of IFNs in the context of an OV-triggered PD-L1 increase in tumours *in vivo*.

Local OV has also been described to affect various systemic immune cell compartments providing evidence that the impact of this therapeutic approach extends beyond the site of injection. These effects include enhanced recruitment of immune effector cells, including CD4+ and CD8+ T-cells, to distant non-injected lesions (Nakao et al., 2020; Thomas et al., 2019; Zamarin et al., 2014). Meanwhile, either no increase or a minor increase of immunosuppressive cell populations such as regulatory T-cells has been observed (Thomas et al., 2019). Zamarin *et al*, have linked this increase of CD4+ and CD8+ T-cells to enhanced activation of type I IFN signalling (Zamarin et al., 2014). Moreover, infiltration of immune effector cells to distant tumour sites eventually triggers potent therapeutic effects, as observed in non-injected 4434 melanoma tumours (Roulstone et al., 2021).

As outlined in previous paragraphs and section 1.2.6, there is growing evidence for the systemic impact of intratumoural OV, exemplified by immune effector cell trafficking to distant lesions and the eventual increase of PD-L1 in these lesions. Both examples support the role of cytokines spreading from local to peripheral compartments as mediators of these effects. Therefore, an OV-triggered upregulation of PD-L1, as previously described for local cell compartments, is likely to extend beyond the tumour and affect PD-L1 expression in systemic organs. This led me to formulate the following hypothesis: an oncolytic virus-triggered upregulation of PD-L1 goes beyond tumour-associated cell compartments and exhibits a dynamic behaviour. Such systemic effects of local OV have so far only been studied using conventional *ex vivo* methods such as FC, IHC and WB. Whilst the latter can be powerful tools to measure protein expression in representative organ samples, they usually require large pieces of tissue and therefore the termination of an animal experiment. Further, the sampling procedure itself might introduce a bias. In contrast, immunoPET is an imaging modality that allows for whole-body imaging of a wished antigen in a spatiotemporal manner. Moreover, immunoPET allows to assess protein abundance noninvasively and quantitatively and provides tomographic images to localise a tracer which directly infers protein expression. Therefore, I chose immunoPET to address my hypothesis and capture changes of systemic PD-L1 expression following local OV.

In this chapter, I investigated systemic PD-L1 expression following a single intratumoural injection of RP1 in MOC1 tumours via PD-L1 immunoPET and biodistribution studies. Similarly, these effects were studied following three repeat injections of RP1. To aid interpretation of the immunoPET findings, histopathology of tumours and spleens was performed and levels of pro-inflammatory cytokines in tumours and blood sera were measured. Additionally, a separate study using FC to analyse expression of PD-L1 on different tumour subpopulations was conducted. Finally, an exploratory therapy study was performed to assess possible synergistic effects of RP1 and anti-PD-1 ICB in the MOC1 mouse model.

6.2 Results

6.2.1 Systemic PD-L1 response upon a single intratumoural RP1 dose

In order to address my central hypothesis stating that an upregulation of PD-L1 upon OV goes beyond tumour-associated cell compartments and follows a dynamic behaviour, I applied PD-L1 immunoPET to investigate these effects upon intralesional RP1 administration into MOC1 tumours *in vivo*.

As shown in figure 6-1, MOC1 tumour-bearing mice (tumours sized 131 ± 33 mm^3, mean ± SD; tumour volume was used as the inclusion criterion) were randomly distributed into four groups of n=5-7 mice. A group size of n=5 was determined via power calculations (assuming an effect size of d=2.37 for tumour uptake). On day 0, two groups were injected with a single dose of RP1 (1×10^6 pfu in 10 µL) and the other two groups received a vehicle injection (PBS, 10 µL) instead. One day after treatment, one RP1 and one PBS group were injected with the radioconjugate (dose 3: 10-18 µg/2 MBq ^{89}Zr-DFO-PD-L1$_{mAb}$ co-injected with 92-100 µg of PD-L1$_{mAb}$ to reach 110 µg of PD-L1$_{mAb}$ in total; i.v.) to be PET-scanned and biodistributed on day 3. The two remaining groups (one RP1 and one PBS group) received the radioconjugate 5 days after treatment and were PET-scanned and biodistributed on day 7. This staggered radioconjugate injection regimen enabled the direct comparison of the day 3 vs. day 7 time points to address the dynamic behaviour of PD-L1 following RP1 treatment. No blinding was performed throughout the study. The data presented hereafter was pooled from three PET studies. The RCP of all three radioconjugates used for these studies was confirmed prior to injection (Suppl.Fig.19).

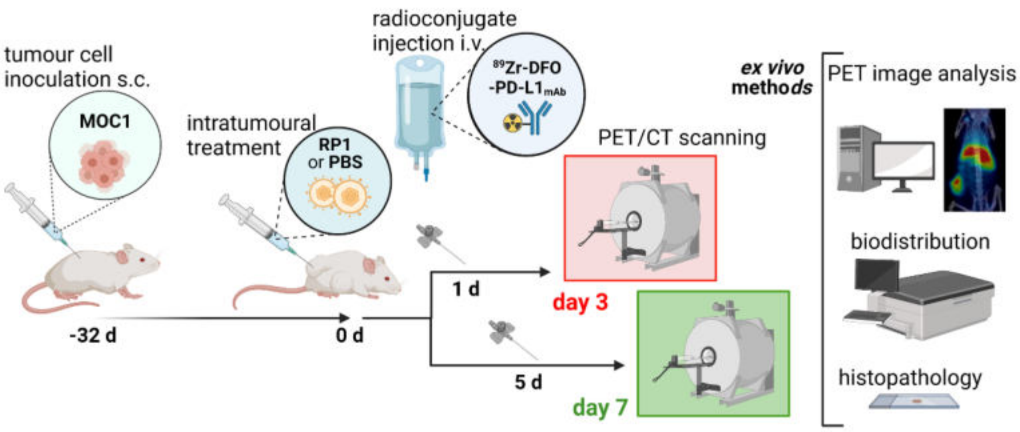

Figure 6 - 1: Schematic of experimental timeline for ^{89}Zr-DFO-PD-L1$_{mAb}$ immunoPET

studies to monitor PD-L1 expression upon a single intratumoural dose of RP1 or vehicle (PBS) in MOC1 tumour-bearing mice on days 3 and 7. Scheme created with Biorender.com.

Visual inspection of PET images acquired on day 3 after treatment showed enhanced ^{89}Zr-DFO-PD-L1$_{\mathrm{mAb}}$ uptake in spleens and TD Lns of RP1-injected mice (Fig.6-2a/b). The uptake observed in other organs including tumours, livers and the bone tissue appeared similar between treatment conditions (Fig.6-2a). Similarly, no difference in systemic signal was discernible on PET images of RP1 and PBS-treated animals. Quantification of the uptake across those organs confirmed these observations, as exemplified by significantly higher uptake of ^{89}Zr-DFO-PD-L1$_{\mathrm{mAb}}$ in spleens of RP1-treated mice ($p=2\times10^{-6}$, multiple unpaired *t*-tests) as well as higher, but non-significant, average uptake in TD Lns ($p>0.01$; Fig.6-2c). The amount of radioconjugate in circulation was lower in RP1 than in PBS-treated animals as assessed via image quantification (ROI centred on the heart). Visual inspection of day 7 scans showed no major differences in radioconjugate uptake between the two treatment conditions, including spleens, TD Lns, as well as tumours (Fig.6-2a/b). Signal quantification confirmed equal uptake in spleens and tumours whilst revealing differences in TD Lns (slightly higher in RP1 group), blood levels (slightly higher in PBS group) (Fig.6-2c). No CT scans were acquired for several animals due to a failure of the CT unit. Those scans were omitted from signal quantification. The issue mostly affected the day 7 cohort (5 scans of RP1 and 2 scans of PBS group and 2 additional scans for day 3 RP1 group), explaining the small number of data points.

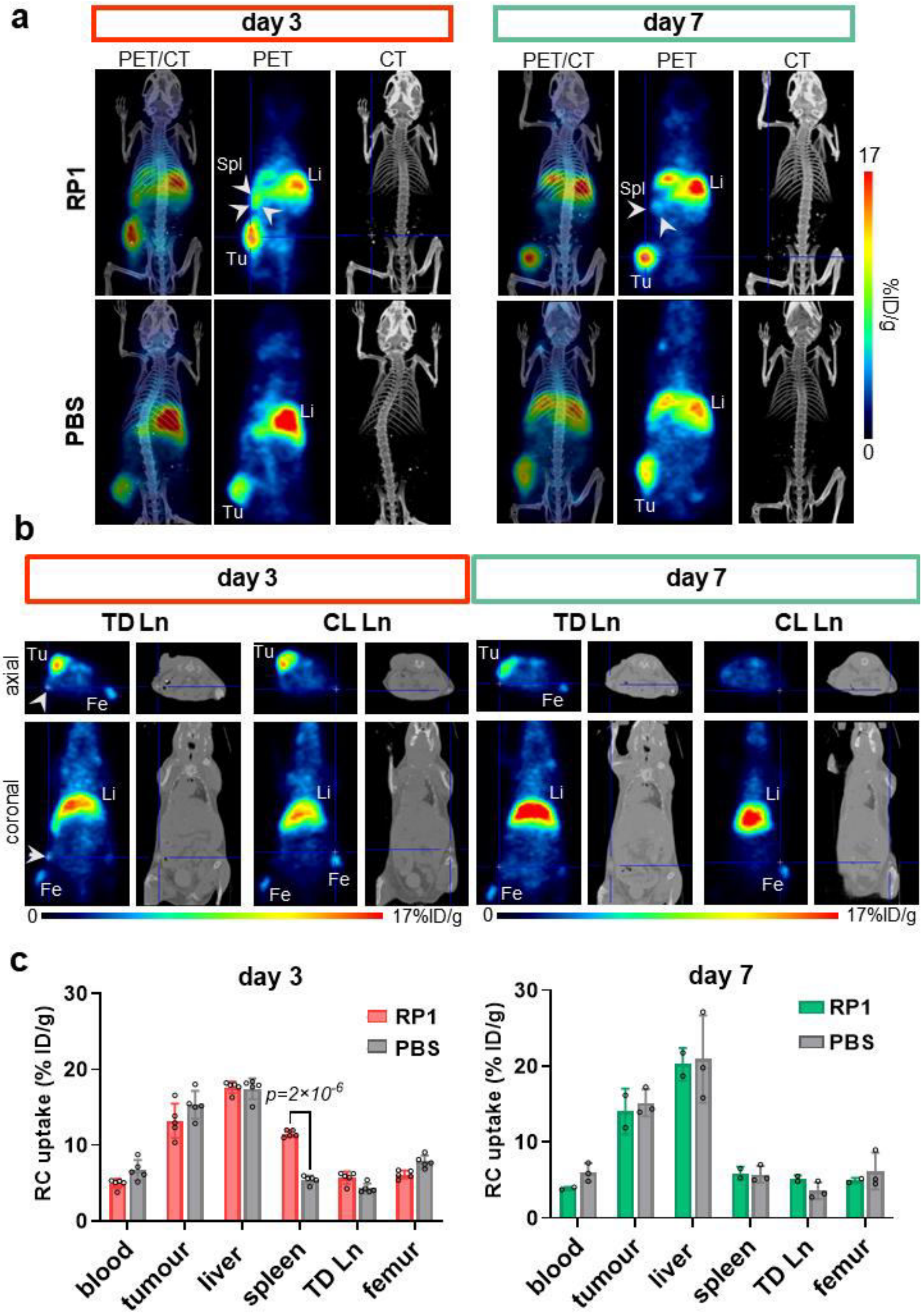

*Figure 6 – 2: **a.** Co-registered PET/CT scans of RP1 and PBS-treated mice on days 3 and 7 post-treatment (PET: single plane slice in coronal projection; CT: 3D reconstruction of MIP). Organs with enhanced uptake are indicated with abbreviations, including liver (Li), tumour (Tu), spleen (Spl) and femur (Fe). Spleens of RP1-treated mice are additionally highlighted with white arrowheads. **b.** PET and CT coronal (upper row) and axial (lower row) plane scans of RP1-treated mice showing tumour draining (TD Ln) and contralateral lymph nodes (CL Ln) on day 3 and 7 post-treatment. Both modalities are shown as corresponding single plane slices in coronal projection. Lns with enhanced RC uptake are indicated with white arrowheads in PET scans. All other visible organs are indicated with abbreviations (as in b.). **c.** Bar charts show* ^{89}*Zr-DFO-PD-L1*$_{mAb}$ *uptake according to*

signal quantification in PET images on day 3 and day 7 following a single injection of RP1 or vehicle. RC uptake is indicated as the percentage of injected dose per gram of tissue (%ID/g). Bars indicate mean ± SD. Statistical analysis of day 3 data was performed via multiple unpaired t-tests on log-transformed data with Benjamini-Hochberg FDR correction (FDR<1%).

Biodistribution studies were performed directly after the PET scans in order to confirm the findings from PET image quantifications and additionally measure the uptake in organs which remained indiscernible in co-registered PET/CT scans. In line with the findings from image quantifications, ^{89}Zr-DFO-PD-L1$_{\mathrm{mAb}}$ levels were higher in spleens (p=0.0003, multiple unpaired t-tests) and TD Lns (p=0.0034) collected on day 3 after RP1 treatment (Fig.6-3a). The average tumour uptake in the RP1 group was lower than in the vehicle group, however not significant (p>0.01). In addition to previous findings, biodistribution data revealed significantly enhanced ^{89}Zr-DFO-PD-L1$_{\mathrm{mAb}}$ uptake in the hearts (p=0.0024) and the lungs (p=0.0033) of RP1-treated mice, suggesting that the systemic impact on PD-L1 expression reaches beyond secondary lymphatic tissue. Furthermore, ^{89}Zr-DFO-PD-L1$_{\mathrm{mAb}}$ levels in the blood were significantly lower among RP1-treated mice (p=0.0023), hinting towards lower systemic radioconjugate availability due to increased consumption by PD-L1 overexpressed in the spleen and other systemic organs. On day 7 after treatment, there were no major differences in RC uptake between RP1- and PBS-treated animals, including the spleens, TD Lns, hearts, lungs and tumours (Fig.6-3a). One exception however was the blood, which again showed significantly higher levels of ^{89}Zr-DFO-PD-L1$_{\mathrm{mAb}}$ in PBS than RP1-treaded animals (p=0.0065). Of note, the femurs were not collected for biodistribution measurements.

To address the dynamic behaviour of PD-L1 expression upon RP1 vs. vehicle injection, RC uptake levels of organs exhibiting the most prominent changes on day 3 were compared with day 7 uptake levels via a two-way ANOVA. The statistical analysis showed that ^{89}Zr-DFO-PD-L1$_{\mathrm{mAb}}$ uptake was significantly different in RP1-treated animals when comparing day 3 and day 7 time points for spleens (p<0.0001, two-way ANOVA), TD Lns (p=0.0003), hearts (p<0.0001) and lungs (p=0.0026), supporting the dynamic expression behaviour of PD-L1 in response to RP1 treatment (Fig.6-3b). Interestingly, RC levels in the blood of RP1-treated mice showed no significant change from day 3 to 7 (p>0.05). Furthermore, the uptake in tumours of RP1-treated mice did not significantly differ between the time points (*p*>0.05). The organs of PBS-treated animals showed fairly equal levels of RC uptake regardless of time point (Fig.6-3b).

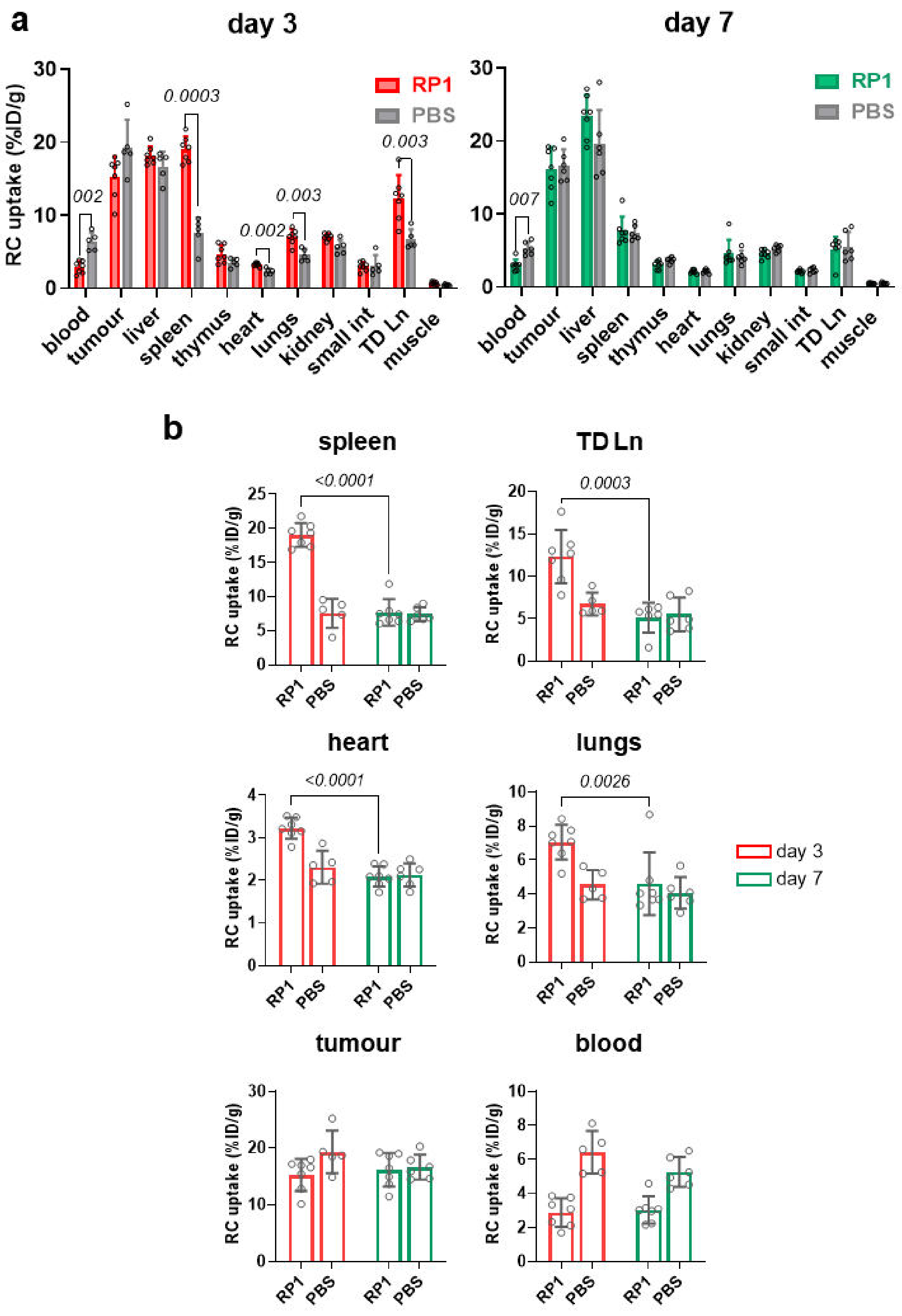

*Figure 6 – 3: **a.** Biodistribution plots of* ^{89}*Zr-DFO-PD-L1*$_{mAb}$ *at day 3 and 7 following a single injection of RP1 or vehicle. RC uptake is indicated as a percentage of the injected dose per gram of tissue (%ID/g). Bars indicate mean ± SD. One TD Ln in RP1 group (day 7) was not found at biodistribution. Statistical analysis was performed via multiple unpaired t-tests on log-transformed data with Benjamini-Hochberg FDR correction*

(FDR<1%). ***b.*** *Bar charts of* ^{89}*Zr-DFO-PD-L1*$_{mAb}$ *uptake in spleens, tumour draining lymph nodes (TD Lns), hearts, lungs, tumours and blood on day 3 (red bars) vs. day 7 (green bars) following a single injection of RP1 or vehicle. RC uptake is indicated as in a. Bars show mean ± SD. Statistical analysis was performed via a two-way ANOVA with Bonferroni multiple comparisons correction on log-transformed data. Comparisons were performed between day 3 and day 7 within each treatment group, i.e. RP1 or PBS. P-values <0.05 were considered statistically significant.*

In order to confirm that the ^{89}Zr-DFO-PD-L1$_{mAb}$ uptake measured in PET and biodistribution studies coincides with overall PD-L1 expression, tumours and spleens collected at biodistribution were stained via PD-L1 IHC *ex vivo* and results assessed visually. Microscopic inspection of tumour sections from RP1 single treatment studies showed no clear difference in net PD-L1 expression between the two treatment groups (RP1 vs. PBS) at both time points, day 3 and day 7 after treatment (Fig.6-4a). In contrast, the spleens collected 3 days after RP1 treatment showed enhanced expression of PD-L1 when compared to sections of all other treatment groups (RP1 on day 7, PBS on day 3 and day 7). Collectively, this data supported the findings made in PET and biodistribution studies, showing that a single intratumoural injection of RP1 had a systemic impact on PD-L1 expression causing a transient increase of PD-L1 in organs such as the spleen early after treatment (day 3 p.i.).

One representative tumour half of each treatment group was cryopreserved and taken for autoradiography and concomitant H&E staining. This method allowed for a more detailed inspection of RC distribution across the tumour section (autoradiogram) alongside confirming tissue integrity (H&E). Radioconjugate distribution seemed quite similar across all four representative sections showing higher intensities along the outer rim and lower intensities in the tumour core (Fig.6-4b). The RP1-tumour section collected on day 3 contained a large area of disintegrated tissue as visible on the H&E stain, which was most likely due to oncolysis. All other H&E tumour stains also contained foci of disintegrated tissue but to a lesser extent. It is important to note that some of the sections (mostly the ones collected on day 7) were relatively brittle and partially ripped during the H&E staining procedure.

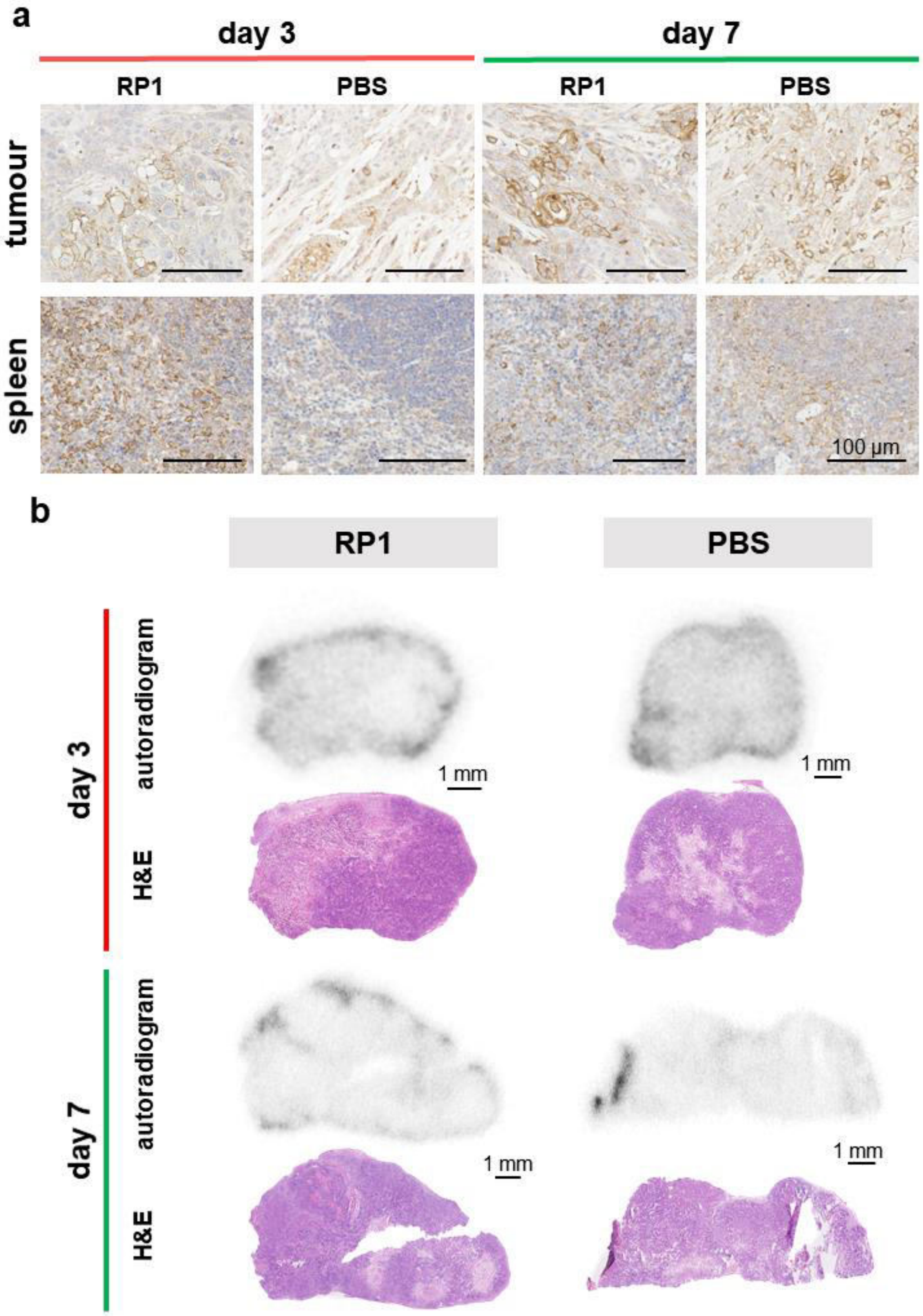

Figure 6 - 4: ***a.*** *PD-L1 IHC of tumour and spleen sections (4 µm) collected on day 3 and 7 after a single intratumoural dose of RP1 or PBS. Tissue from immunoPET studies.* ***b.*** *Tumour sections (~10 µm) as matched autoradiograms (~16 h exposure) and H&E stains (cryopreserved half of tumour).*

Following treatment initiation, the tumour volumes and body weights were monitored to determine whether RP1-treatment impacts these parameters. According to tumour volume records of day 3 and day 7 cohorts, a single intratumoural injection of RP1 showed a negligible effect (Fig.6-5a), corroborating previous findings presented in chapter 5. The body weights remained relatively stable for the duration of the study including a minor dip on day 2 after RP1 administration (Fig.6-5a). To determine the direct effect of a single RP1 or PBS injection on intratumoural tissue integrity, FFPE tumours from immunoPET studies were used to assess the necrotic fraction (herein the equivalent of disintegrated tissue) within a representative H&E-stained section of each tumour. Manual delineation of necrotic areas within each tumour section showed that the necrotic fraction was significantly higher in RP1 compared to PBS-treated tumours on both, day 3 and day 7 time points (p=0.0047 and p=0.0012 respectively, unpaired Student's t-test) (Fig.6-5b/c).

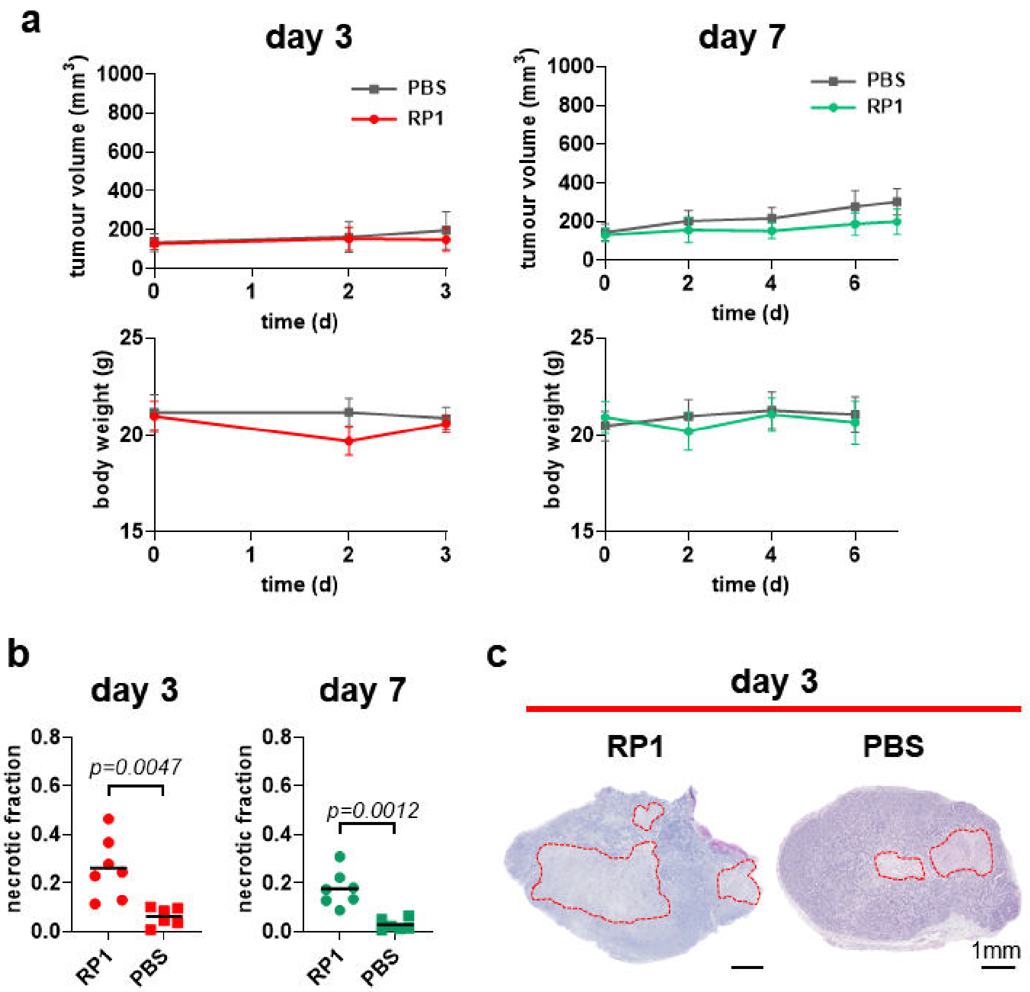

*Figure 6 - 5: **a.** Tumour volume and weight records from treatment initiation (day 0) until the day of PET imaging and biodistribution (day 3 or 7). **b.** Dot plots show the necrotic fraction per treatment group following a single intratumoural dose of RP1 or PBS, as determined on H&E stained sections. Horizontal bars indicate means. An unpaired Student's t-test with Welch's correction was applied and p-values<0.05 were considered statistically significant. **c.** H&E-stained tumour sections (4 µm) collected on day 3 after a*

single dose of RP1 or PBS. Red staggered lines demark disintegrated areas for each section.

Finally, to confirm robustness of the results obtained on day 3 after treatment a second repeat of the experiment was performed (data shown in Suppl.Fig.20). Whilst the majority of results obtained from the repeat study corroborated previously observed changes, it additionally revealed significantly increased PD-L1 levels in the thymus of RP1-treated mice compared to the vehicle group (p=0.0021; multiple unpaired t-tests). In addition, the RC uptake in the mammary Ln located contralaterally to the TD Ln was measured in this study and showed a minor increase in RP1-treated mice (p>0.01).

6.2.2 Systemic PD-L1 response following three repeat doses of RP1

The marked systemic response of PD-L1 following a single dose of RP1 led me to hypothesise that repeat injections might potentiate this effect. Importantly, most published studies which reported a significant increase of PD-L1 following OV in tumours had applied repeat dosing regimen. Therefore, I chose to inject three intratumoural doses of RP1 (10^6 PFU in 10 µL each) or PBS (10 µL each) on day 0, day 2 and day 4 to MOC1 tumour-bearing mice (n=5 per group; inclusion criteria as described in 6.2.1), followed by RC administration on day 5 and PET/CT scanning and concomitant biodistribution on day 7 (Fig.6-6a). No blinding was performed throughout the study. The RCP of ^{89}Zr-DFO-PD-L1$_{\text{mAb}}$ was confirmed prior to injection (Suppl.Fig.21).

Visual inspection of PET scans taken at day 7 after treatment initiation showed no obvious differences between RP1 and PBS-injected mice (Fig.6-6b). Signal quantification confirmed this observation, however, revealing a minor decrease in average RC uptake in livers and femurs of RP1 animals, while the liver uptake in this group was marginally higher than in the vehicle group (Fig.6-6c). In line with image-based findings, biodistribution analysis revealed no significant changes in RC uptake across previously inspected organs (Fig.6-7a). In addition, the hearts of RP1-treated animals showed significantly higher RC uptake than the control (p=0.003; multiple unpaired t-tests). Other tissue including the lungs and the liver showed slightly higher levels of RC in RP1 than PBS-treated mice. The tumour uptake was relatively equal between the treatment conditions, apart from one RP1-treated tumour exhibiting exceptionally high RC uptake of 27.9 %ID/g. The uptake measured in the blood was lower in RP1 vs. PBS-treated mice, a trend consistent with single treatment studies (Fig.6-3a). In addition, the femurs of mice were collected at biodistribution and slightly increased RC levels were measured among PBS-treated mice (Fig.6-7a). Of note, the bone uptake measured herein was within previously observed margins (Fig.4-7a).

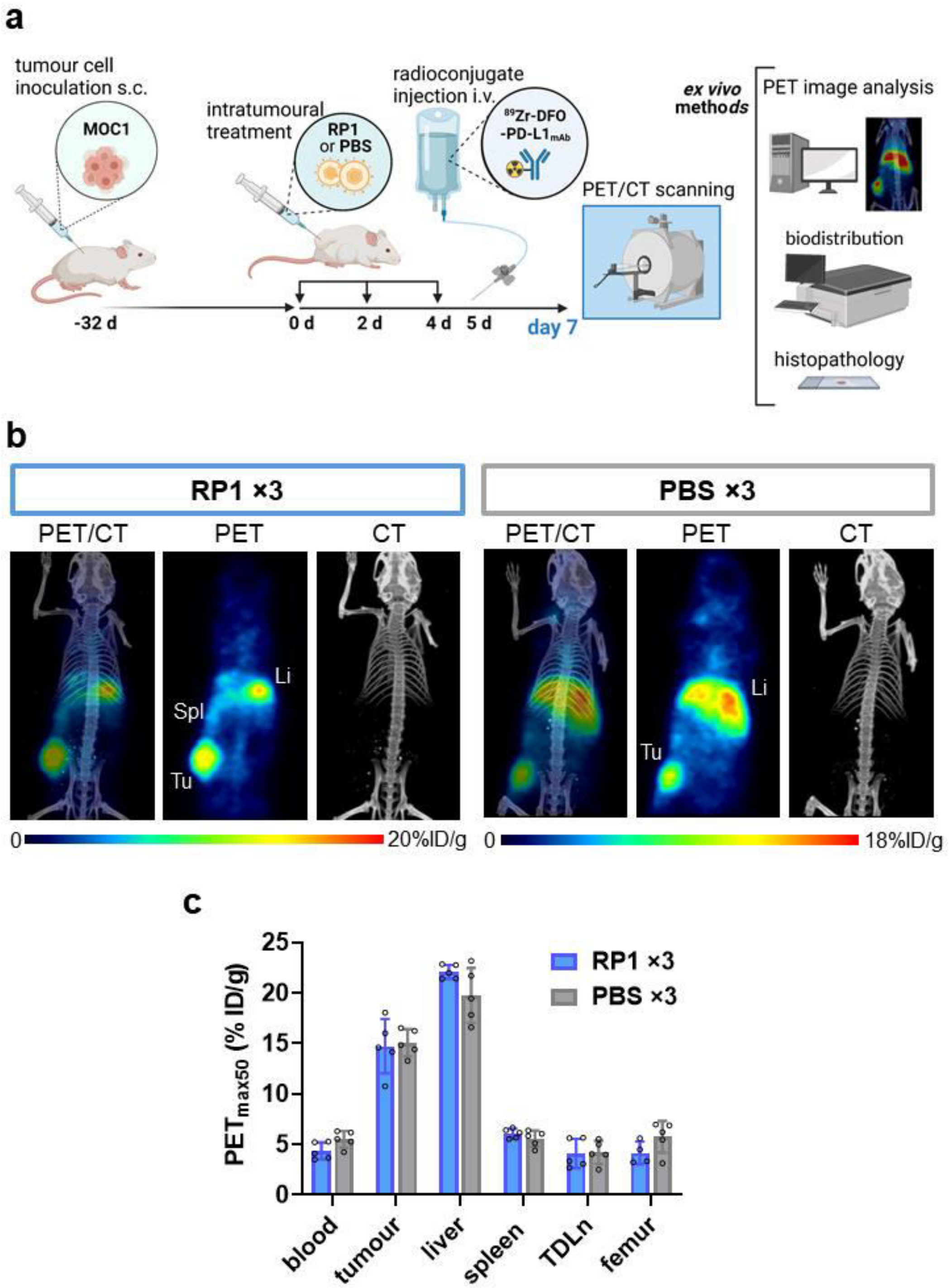

*Figure 6 – 6: **a.** Schematic of experimental timeline of immunoPET study to monitor PD-L1 expression upon three consecutive intratumoural doses of RP1 or vehicle (PBS) in MOC1 tumour-bearing mice. Scheme created with Biorender.com. **b.** Co-registered PET/CT scans of RP1 and PBS-treated mice on day 7 after treatment commencement (PET: single slice in coronal projection; CT: 3D reconstruction). Organs with enhanced uptake are indicated with abbreviations, including liver (Li), tumour (Tu) and spleen (Spl). **c.** Bar chart illustrates ^{89}Zr-DFO-PD-L1$_{mAb}$ uptake according to PET image quantification. Bars indicate mean ± SD. The femur uptake of one RP1 mouse could not be determined as both femurs were located outside the field of view. Statistical analysis was performed via multiple unpaired t-tests on log-transformed data with Benjamini-Hochberg FDR correction (FDR<1%).*

In addition to biodistribution data, autoradiography and concomitant H&E staining was performed in the same fashion as described in the previous section. The autoradiogram of the RP1-treated tumour section showed low RC density in the tumour core and higher density along the outer rim (Fig.6-7b). According to the H&E stain, both areas co-localised with necrotic (disintegrated) and viable tissue, respectively. The autoradiogram of the PBS tumour section showed heterogeneous RC uptake across the whole section with entirely intact tissue according to the matched H&E stain (Fig. 6-7b).

As presented in the previous study, PD-L1 expression in tumours and spleens collected at biodistribution was assessed via PD-L1 IHC *ex vivo*. Following visual inspection of all tumour and spleen sections, no differences in PD-L1 expression were observed between the two treatment groups, supporting the findings from PET and biodistribution studies (Fig.6-7c). It is important to note that this method is a rather crude way of assessing PD-L1 expression, particularly in tumours, which were prone to non-specific staining via PD-L1 IHC. However, PD-L1 IHC of FFPE tissue remained the technique of choice due to regulatory (the transfer of ^{89}Zr tissue to the ICR flow cytometry facility was forbidden) and technical limitations (optimisation of PD-L1 staining on frozen sections remained unsuccessful). A PD-L1 staining protocol suited for frozen tissue sections would have been the method of choice to confirm RC specificity alongside autoradiography on tissue sections *ex vivo*.

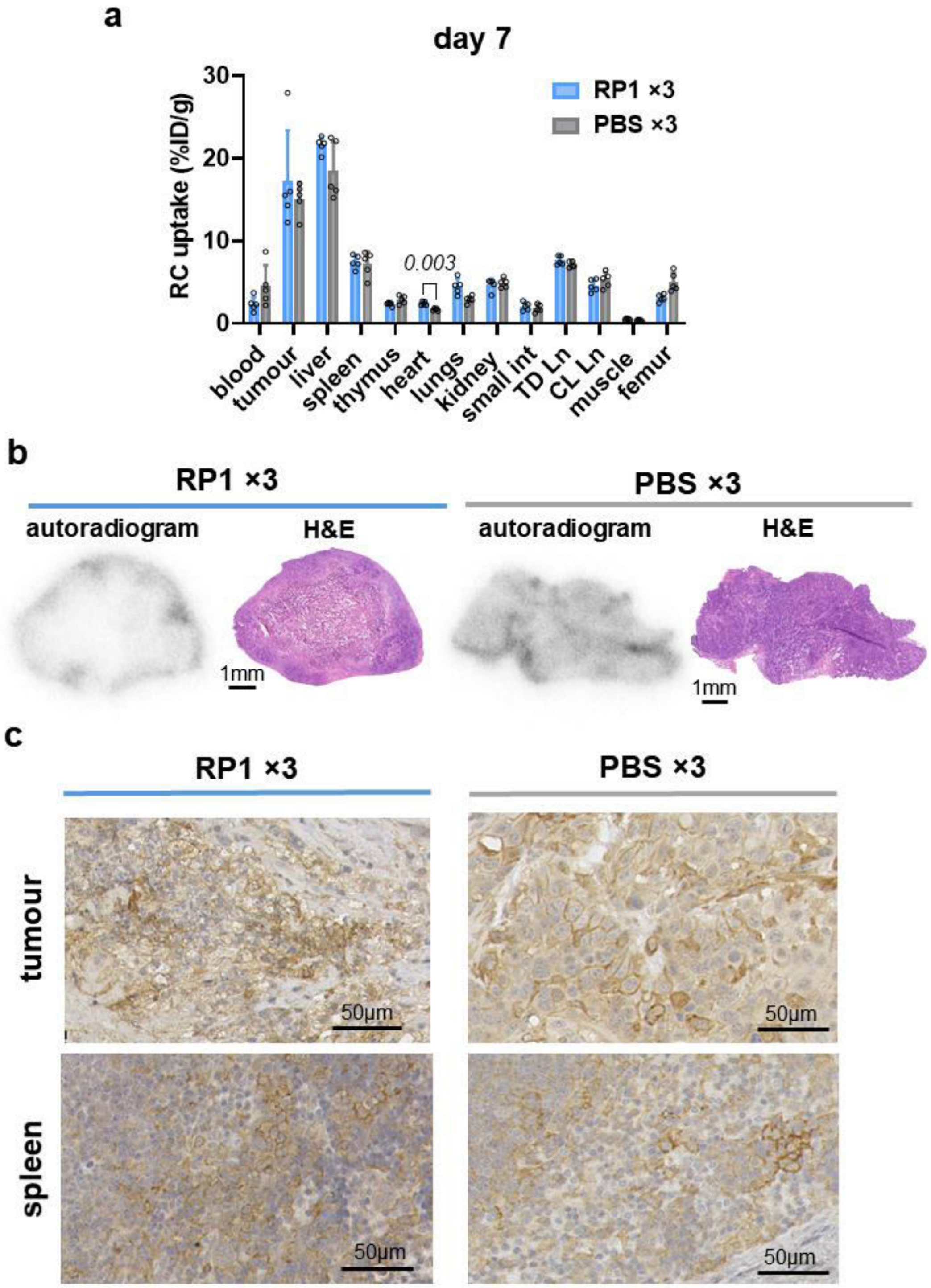

Figure 6 - 7: ***a.*** *Biodistribution plot of* ^{89}*Zr-DFO-PD-L1*$_{mAb}$ *at day 7 following three injections of RP1 or vehicle. RC uptake is indicated as a percentage of the injected dose per gram of tissue (%ID/g). Bars indicate mean ± SD. Statistical analysis was performed via multiple unpaired t-tests on log-transformed data with Benjamini-Hochberg FDR correction (FDR<1%).* ***b.*** *Tumour sections (10 µm) as matched autoradiograms (~24 h exposure) and H&E stains (cryopreserved half of tumour).* ***c.*** *PD-L1 IHC of sections from FFPE tumours and spleens (4 µm). Tissue was collected on day 7 following treatment start.*

Tumour volumes and body weights were monitored starting on the day of treatment in order to screen for any treatment associated effects. Tumour volume records showed no significant difference between RP1 vs. PBS-treated mice (Fig.6-8a). Similarly, the body weights did not differ in a treatment dependent manner apart from a minor dip on day 2 in the RP1-treated group (Fig.6-8a). Similar to the analysis performed on tumours of the single-injection regimen study, FFPE tumours were used to assess the necrotic fraction within one representative H&E-stained section of each mouse. Again, the necrotic fraction was significantly higher in RP1 compared to PBS-treated tumours (*p*=0.0168, unpaired Student's *t*-test) (Fig.6-8b).

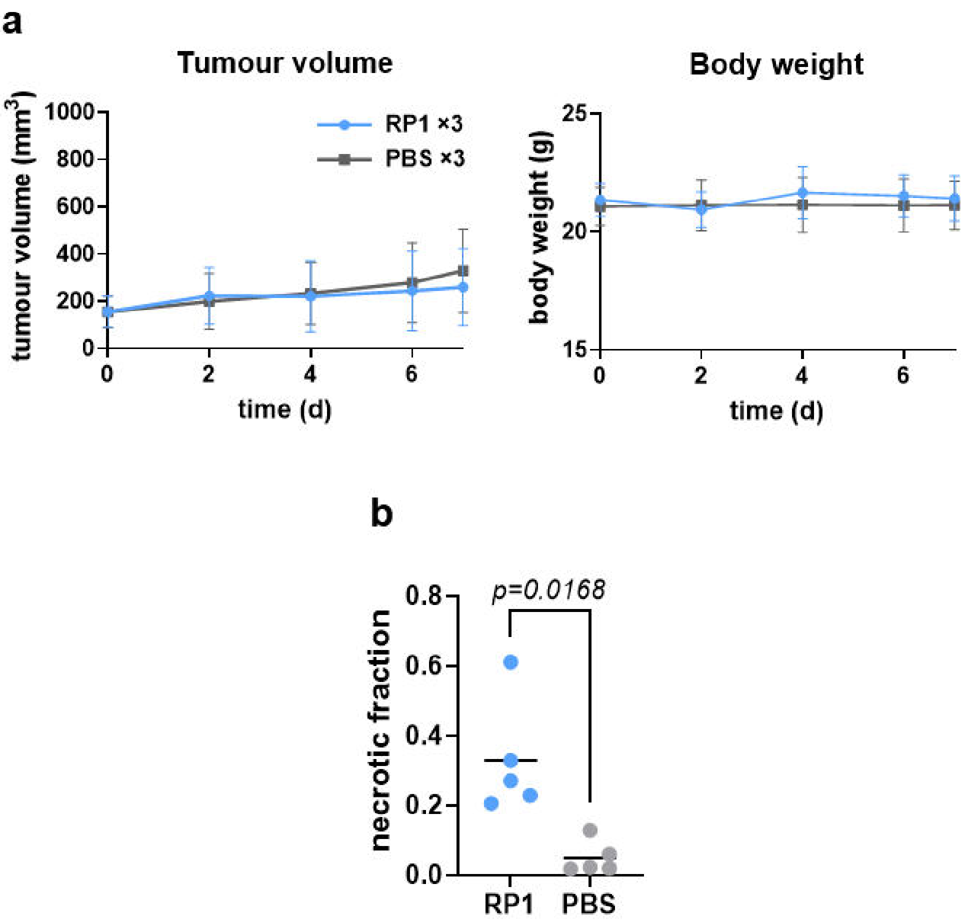

Figure 6 - 8: ***a.*** *Tumour volume and weight records from treatment initiation until the day of PET imaging and biodistribution.* ***b.*** *Dot plot shows the necrotic fraction in each treatment group following three intratumoural doses of RP1 or PBS. Horizontal bars indicate means. The necrotic fraction was determined via manual delineation of H&E-stained tumour sections. An unpaired Student's t-test with Welch's correction was applied and p-values<0.05 were considered statistically significant.*

6.2.3 Cytokine profile on day 3 after a single RP1 injection

Following the high systemic levels of PD-L1 on day 3, I chose to measure the concentration of several inflammatory cytokines as potential drivers for this change. As mentioned previously, inflammatory cytokines such as type I and type II IFNs are released by activated immune cells and other cell types as part of an acute immune response to viral pathogens, eventually inducing an upregulation of PD-L1 (1.3.2). I selected a commercially available panel covering nine pro-inflammatory cytokines and one chemokine relevant during the acute phase of an immune response and applied it on tumour and serum samples. The panel included IFN-γ which is among others secreted by activated NK-cells within a few hours upon viral infection (French and Yokoyama, 2003) as well as IL-1, IL-2, IL-6, IL-12, TNF-α and MCP-1 which are produced upon NF-κB pathway activation (Liu et al., 2017a). To additionally address the role of type I IFNs, I chose to use a second assay designed to measure IFN-α and IFN-β levels in tumour samples. Both cytokines might be increased through the activation of stimulator of interferon genes (STING) in virally infected cells (Barber, 2015). In a scenario of unlimited financial resources, I would have selected an assay panel covering a wider range of cytokines and chemokines.

Among the tumour samples two out of twelve cytokines were significantly increased in RP1-treated animals compared to the vehicle-treated group, including IFN-α and GM-CSF (p=0.007 and $p=2\times10^{-5}$ respectively, multiple unpaired *t*-tests) (Fig.6-7). The increased level of GM-CSF was most likely a direct effect of the GM-CSF expressing RP1 virus. The cytokines IL-6 and TNF-α as well as the chemokine MCP-1, a major regulator of monocyte migration and infiltration, showed a slight increase in RP1-treated tumours but did not reach significance. Furthermore, the IFN-γ level in tumours was not significantly elevated in RP1-treated samples, providing a potential reason for the vastly unchanged PD-L1 levels in this tissue type. Surprisingly, the cytokine signature identified in tumours was not reflected in serum samples. In contrast, no particular cytokine showed distinct changes between the two treatment groups. One RP1-treated mouse however, indicated much higher levels across the majority of serum cytokines, including IL-2, IL-4, IL-6, IL-10, IL-12p70, TNF-α, MCP-1 and IFN-γ, than the others. A few technical hurdles were encountered during the experiment, including bead aggregation leading to low bead counts (IFN-ß in tumours) and signals outside the assay detection range (IL-1ß, IL-2 and GM-CSF in serum samples and IL-12p70 in tumours) leading to the dismissal of several data points (Fig.6-7).

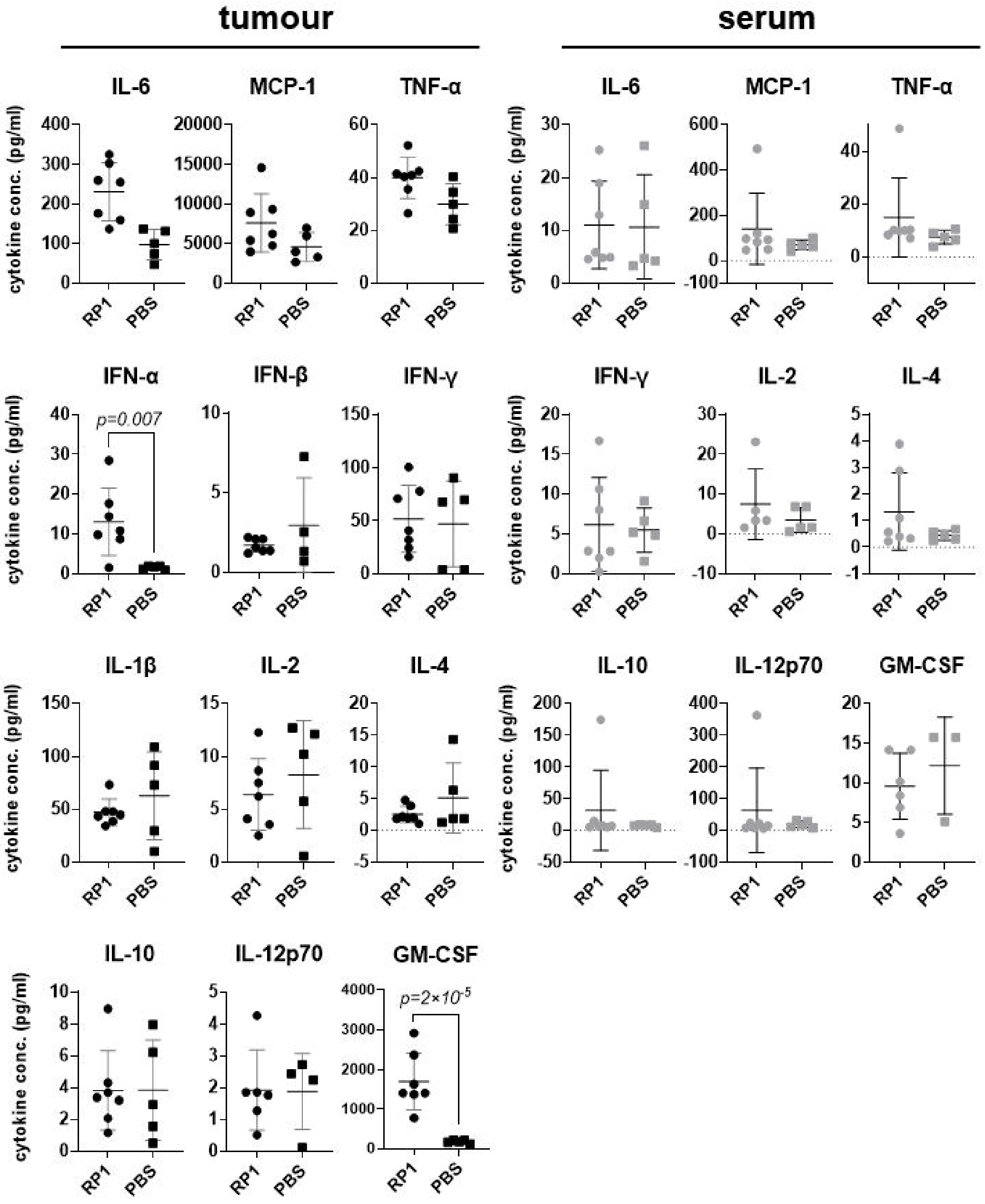

Figure 6 - 9: Dot plots show concentrations of cytokines and one chemokine in tumour and serum samples collected on day 3 after a single RP1 or PBS injection to MOC1 tumours (mean ± SD of n=5-7), including interleukin (IL) 1β, 2, 4, 6, 10, 12p70, tumour necrosis factor-α (TNF-α), interferon-γ (IFN-γ), granulocyte-macrophage colony-stimulating factor (GM-CSF) and monocyte chemoattractant protein-1 (MCP-1). IFN-α and IFN-β levels were only analysed in tumours. Measurements for some analytes were excluded either due to technical issue with the assay (sample clogging) or the concentrations being below the assay detection range, i.e. IL-12p70 and IFN-β of tumours, IL-2 and GM-CSF of sera. For the same reason, the IL-1β measurements of sera

were dismissed completely. Statistical analysis was performed via multiple unpaired t-tests on log-transformed data with Benjamini-Hochberg FDR correction (FDR<1%).

6.2.4 Deciphering a RP1-triggered PD-L1 response among tumour subpopulations

In order to decipher potential differences in PD-L1 expression among tumour subpopulations in response to RP1, the single dose treatment regimen outlined in Fig.6-1 was repeated and FC was used to determine PD-L1 expression across four cell compartments comparing day 3 against day 7. Of note, this analysis could not be performed alongside an immunoPET study due to the very strict safety measures on the handling of radioactivity across the research institute. A mix of five different antibodies was used including EpCAM and CD45 for the discrimination of subpopulations, PD-L1 to measure the expression of the target of interest alongside antibodies against PD-1 and PD-L2 as the other two proteins involved in the formation of the PD-1 co-inhibitory axis. The panel was not extended beyond five markers due to limited access to flow cytometers at the time of the study. No blinding was performed throughout the study. The data was pooled from two mouse studies. For data analysis a hierarchical gating strategy was applied (Fig.6-10a) and tumour-derived cell types were divided into four categories: a mixed population of endothelial cells and fibroblasts (CD45$^-$/EpCAM$^-$), MOC1 tumour cells (EpCAM$^+$/CD45$^-$), immune cells without epithelial features (CD45$^+$/EpCAM$^-$) and immune cells with epithelial features (CD45$^+$/EpCAM$^+$) (Fig.6-10b).

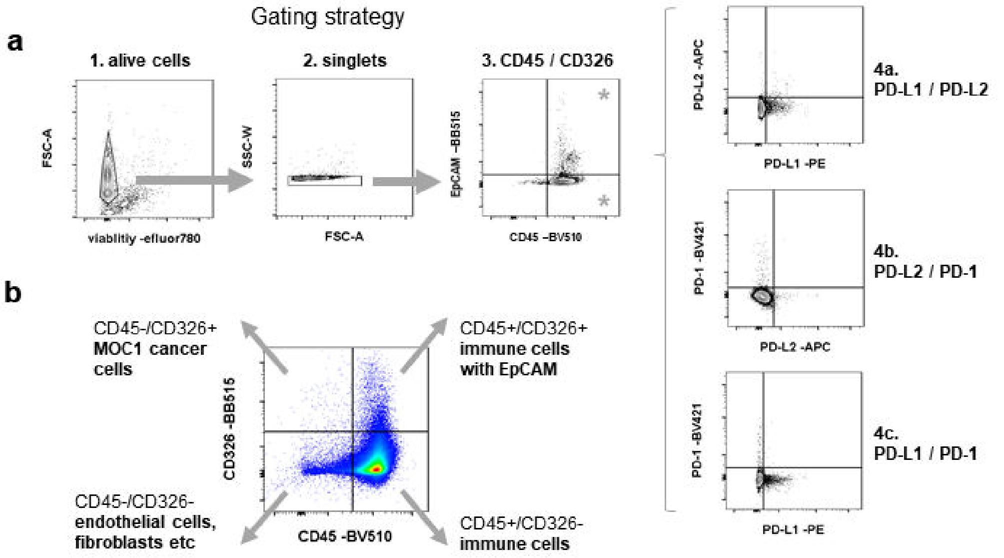

*Figure 6 - 10: **a.** Gating strategy for multiparameter FC on tumour and spleen samples derived from MOC1 tumour-bearing mice on day 3 and day 7 after a single intratumoural RP1 or PBS injection **b.** Differentiation of tumour-derived subpopulations according to their CD45 and EpCAM expression profile.*

FC of tumours and spleens at day 3 and 7 after RP1 or PBS treatment, corroborated the results of the immunoPET study presented in section 6.2.1. Accordingly, PD-L1 expression in tumours was not significantly changed between RP1 and PBS on day 3 and day 7 after treatment (Fig.6-11a), whilst splenic PD-L1 was significantly increased in samples from RP1 as compared to PBS-treated animals on day 3 but not on day 7 (p=0.0001 and p>0.05 respectively, two-way ANOVA). Next, PD-L1 expression was analysed across four different tumour subpopulations: The mixed pool of endothelial cells and fibroblasts ($CD45^-$/$EpCAM^-$) showed a slight increase of PD-L1 in the RP1-treated group on day 3 which was followed by a decrease on day 7 as compared to PBS controls (p>0.05 both, two-way ANOVA; Fig.6-11b). MOC1 tumour cells which were identified via EpCAM ($EpCAM^+$/$CD45^-$) showed similar levels of PD-L1 expression on day 3 followed by a slight decrease in RP1 as compared to PBS-treated tumours on day 7 (p>0.05 both). Interestingly, immune cells without epithelial features ($CD45^+$/$EpCAM^-$) showed slightly elevated levels of PD-L1 on day 3 upon RP1-treatment but no longer on day 7 (p>0.05 both). In contrast, immune cells which exhibited epithelial features ($CD45^+$/$EpCAM^+$) showed significantly decreased PD-L1 expression following RP1 as compared to PBS treatment on day 3 (p=0.0487) and less pronounced on day 7 (p>0.05). A limitation of this experiment was the disproportional distribution between the four subpopulations after sample processing: The biggest population in each tumour sample were the immune cells, while both the tumour and mixed endothelial and fibroblast cell fractions remained underrepresented in numbers (Fig.6-11c). The relative loss of both cell fractions was possibly owed to the high inherent stiffness of MOC1 tumours and the challenges arising at sample processing.

In addition to PD-L1 expression, the levels of PD-1 and PD-L2 in the main pool of immune cells ($CD45^+$/$EpCAM^-$) were analysed as well. As mentioned previously, PD-1 is the main receptor to PD-L1 and PD-L2 (Fig.6-11d). The expression of PD-1 is restricted to immune cell populations (e.g. T-cells), whilst PD-L2 is expressed on immune cells (e.g. APCs) and cancer cells (Yearley et al., 2017). According to the FC analysis, PD-1 exhibited lower levels in RP1-treated tumours on day 3 as compared to PBS (p>0.05) (Fig.6-11e). However, PD-1 expression on immune cells of RP1-treated tumours increased significantly from day 3 until day 7 (p=0.0127) and was significantly higher on RP1-treated as compared to PBS-treated samples on day 7 (p=0.0119). Similar to PD-1, PD-L2 expression was lower in tumour-derived immune cells of RP1 than PBS-treated mice on day 3 but reached similar expression levels between RP1 and PBS groups on day 7 (p>0.05 both) (Fig.6-11f).

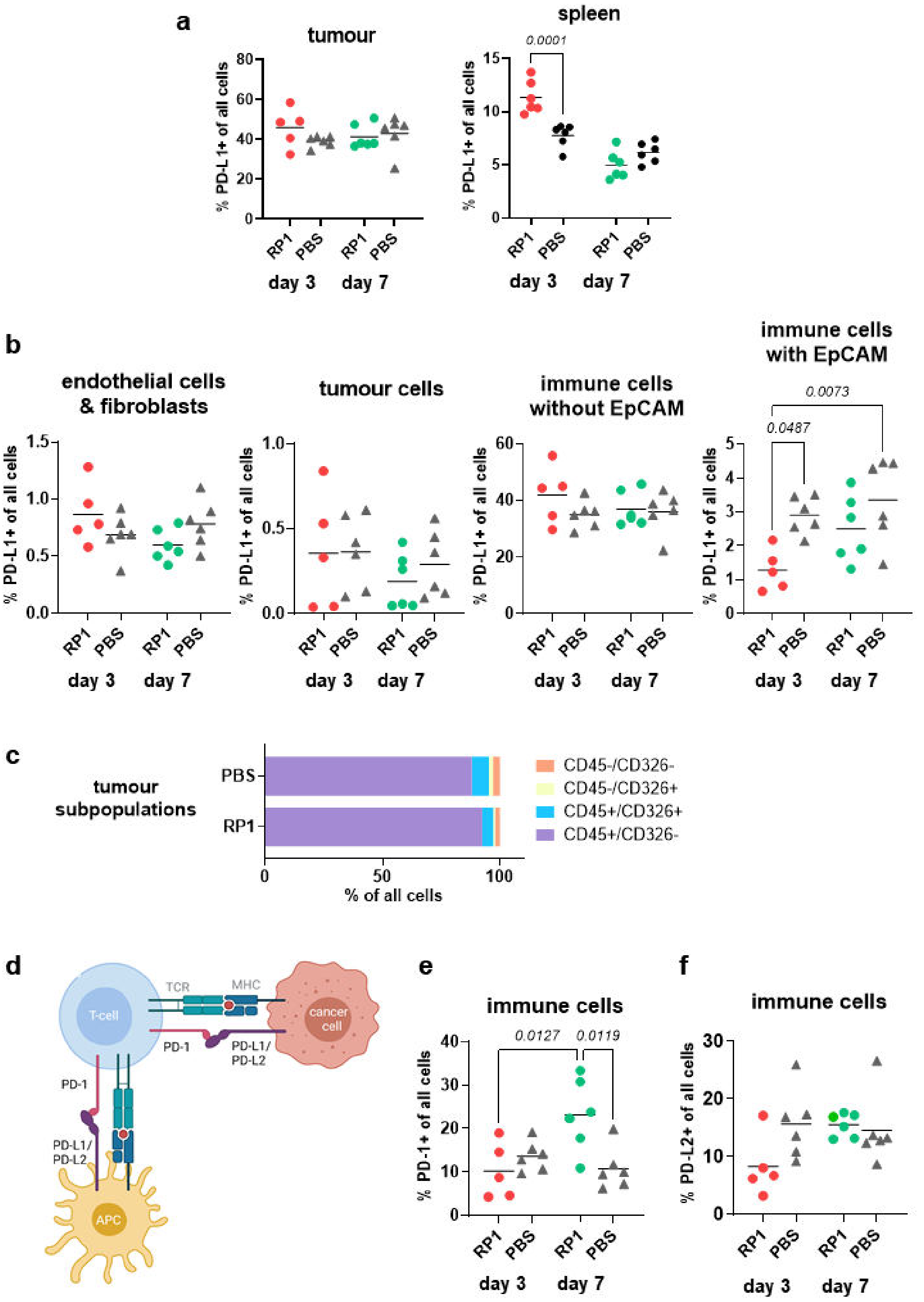

*Figure 6 - 11: **a.** Dot plots show percentage of PD-L1+ cells across all cells isolated from tumours (left) and spleens (right). **b.** Dot plots show percentage of PD-L1+ cells in each of the tumour-derived subpopulations, including a mixed pool of fibroblasts and endothelial cells, tumour cells, immune cells without epithelial features and immune cells with epithelial features. The percentage of PD-L1+ cells refers to the total number of events per sample as 100% (including all singlet and alive events) **c.** Bar chart shows relative distribution of tumour cell subpopulations in RP1 and PBS tumour samples collected on day 7 after treatment **d.** Illustration of PD-1/PD-L1 axis with PD-L2 as a second ligand to PD-1. PD-L1 and PD-L2 are expressed on cancer cells and immune cells (APCs) and others. Figure created with Biorender.com. **e.-f.** Dot plots show percentage*

*of PD-1+ (**f**.) and PD-L2+ (**g**.) tumour-derived immune cells (CD45+/EpCAM-) as the fraction of all single and alive events. All statistical analysis (a./b./e./f.) was performed via a two-way ANOVA with Bonferroni post-hoc correction. P-values <0.05 were considered statistically significant.*

6.2.5 RP1-triggered PD-L1 response of cancer cells *in vitro*

Some viruses have been shown to directly upregulate PD-L1 on cells *in vitro* (Schönrich and Raftery, 2019). Although the data obtained from FC analysis of tumour specimen treated with RP1 did not suggest this *in vivo* (Fig.6-11a/b), the effect might still occur *in vitro*. Accordingly, MOC1 cells were treated with increasing concentrations of RP1 (0, 0.01, 0.1, 1.0, 10 PFU/cell) *in vitro* and their PD-L1 expression was measured after 24 and 48 h via FC. MOC2 cells were also analysed as an RP1-resistant control.

FC analysis showed that RP1 exposure had a minor effect on PD-L1 expression in MOC1 cells, as indicated by a slight dose-dependent increase of PD-L1 expression after 24 h (Fig.6-12a/b). At 48 h, most MOC1 cells were dead from the potent cytopathic effect elicited by RP1. MOC1 cells treated with very low viral titres (0.01 PFU/cell) survived but showed low levels of PD-L1 expression (Fig.6-12a/b). In MOC2 cells, RP1 did not seem to impact PD-L1 expression at 24 h of treatment. Likewise, at the 48 h time point, steady PD-L1 expression was measured for viral titres ranging from 0 to 1.0 PFU/cell, whilst at 10.0 PFU/cell a slight increase of PD-L1 levels was detected (Fig.6-12a/b).

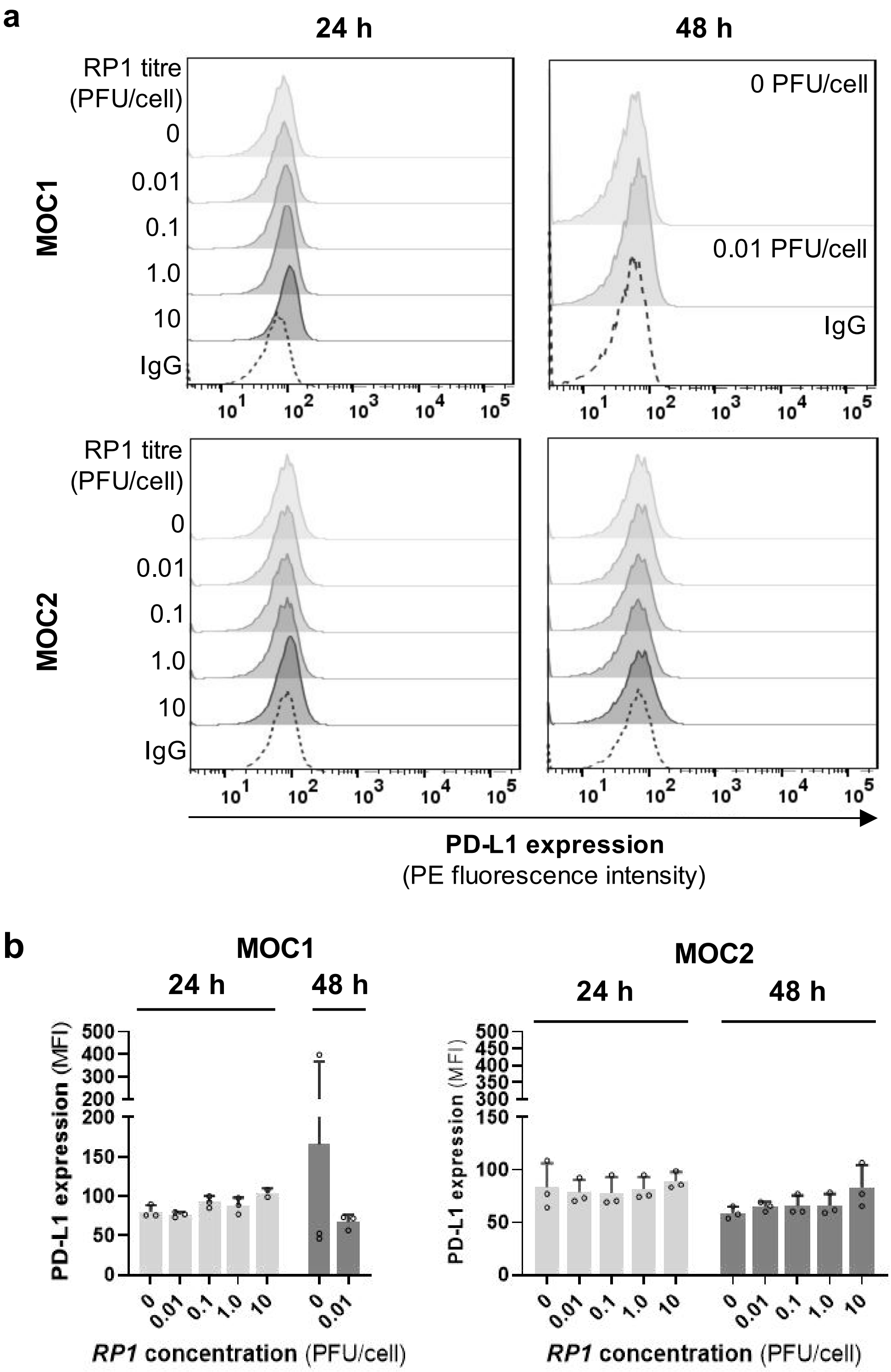

*Figure 6 - 12: **a.** Histograms show PD-L1 expression upon 24 h and 48 h of RP1 treatment (0-10 PFU/cell) in vitro, alongside IgG-stained control (dashed histogram). **b.** Bar charts of MFI as a measure of PD-L1 expression at 24 and 48 h of RP1 treatment. Bars represent mean ± SD of n=3 biological repeats. One data point is missing for MOC1 cells at 10 PFU (24 h) due to very low yield of viable cells at sample collection.*

6.2.6 Therapeutic effect of RP1 in combination with anti-PD-1 ICB

In an effort to determine whether the dynamic change in systemic PD-L1 expression triggered by a single RP1 dose provides a therapeutic benefit when combined with anti-PD-1 ICB, a combination therapy study was performed. Due to financial restrictions, this study was laid out in pilot format using a relatively small number of 4-5 animals for each group. In this study, MOC1-tumour bearing mice received a single intratumoural dose of RP1 (day 0) and were then split in two equal cohorts: one cohort was started on anti-PD-1 ICB or isotype control treatment at day 3 (n=4 per treatment condition), while the other cohort was started on anti-PD-1 or isotype control (IgG2a) treatment on day 7 (n=5 per treatment condition) (Fig.6-13a). The therapeutic effect was assessed via repeated calliper measurements. For anti-PD-1 ICB or isotype control treatment, 200 μg of antibody were injected intravenously per dose, each animal being dosed three times every third day. One shortcoming of the study was the lack of a control group receiving anti-PD-1 as a monotherapy (without prior RP1 injection). No blinding was performed throughout the study.

Tumour volume records of the combination therapy study indicated that there was no therapeutic benefit through the addition of anti-PD-1 ICB regardless of its starting time point (day 3 vs. day 7), suggesting that varying levels of systemic PD-L1 might not impact this therapy regimen (Fig.6-13b). However, a larger cohort size might still allow to see therapeutic benefits either in terms of tumour volume or overall survival. Weight records indicated no significant impact of the treatment apart from a few cases where the body weight decreased towards the end of the study (Fig.6-13c).

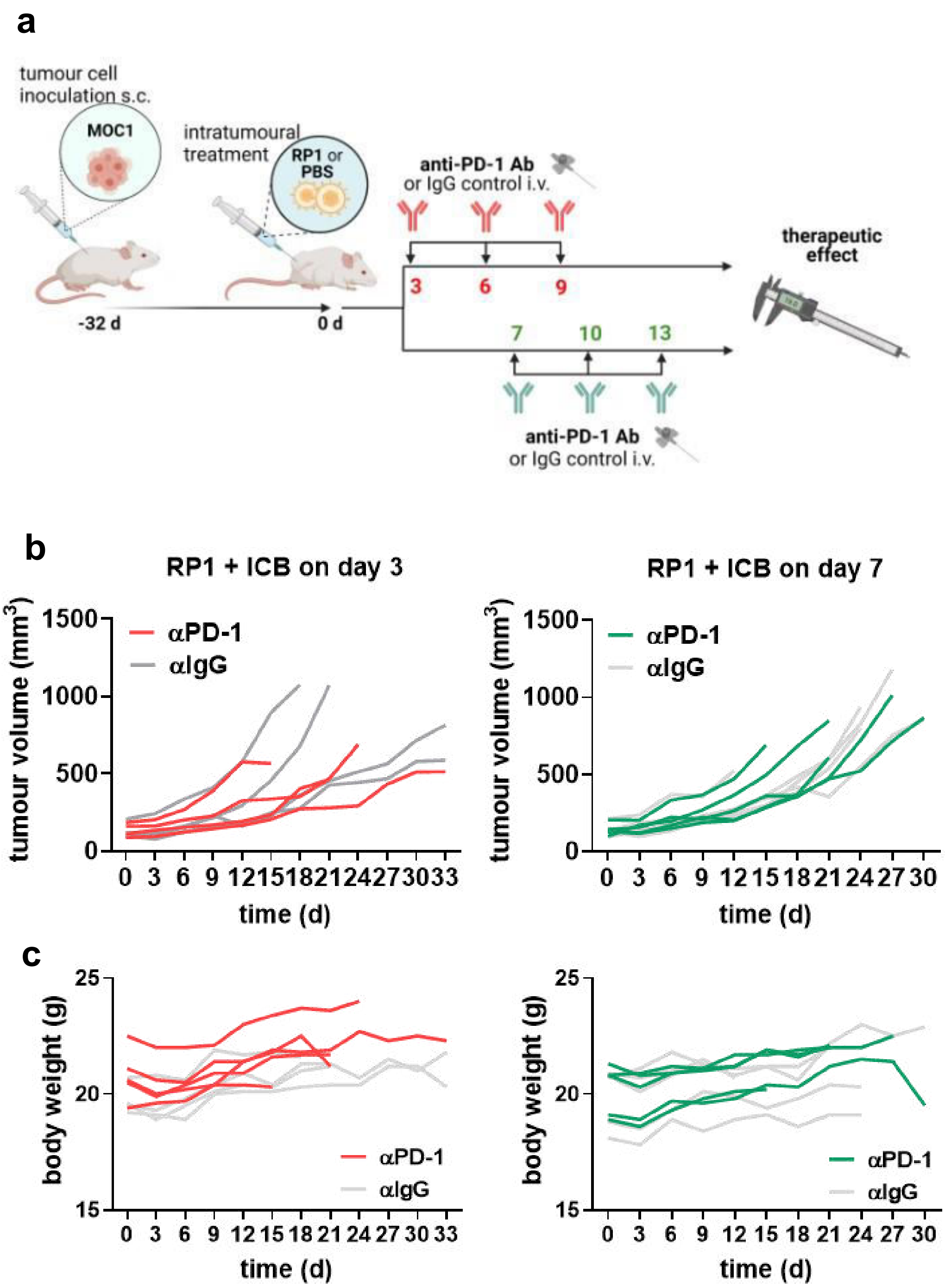

Figure 6 - 13: ***a.*** *Scheme of experimental timeline of therapy study combining intratumoural RP1 with systemic anti-PD-1 ICB or isotype control treatment. Scheme created with Biorender.com.* ***b.*** *Tumour volume records of MOC1 tumour-bearing mice following a single intratumoural injection of RP1 (10^6 PFU, 10 µL) on day 0 with follow-up anti-PD-1 ICB or IgG control treatment (200 µg per dose, three repeat intravenous injections every third day) either started on day 3 (left spaghetti plot, n=4 mice per group) or day 7 (right spaghetti plot, n=5 mice per group).* ***c.*** *Body weight records of all treatment groups with colour code as in previous plots.*

6.2.7 The impact of intratumoural RP1 on PD-1+ and CD8+ immune infiltrate

Following the absence of a therapeutic effect from the combination of RP1 with anti-PD-1 ICB, I decided to assess the presence of cytotoxic T cells as well as PD-1 expressing cells via IHC in tissue previously collected from the RP1 monotherapy study (Fig.6-1). I have chosen to assess the presence of cytotoxic T cells (CD8+) as an indicator for an adaptive immune response. PD-1 in return is frequently addressed as a marker for T cell exhaustion, however, it can also be expressed upon T cell activation. Next to PD-1 there is a range of other inhibitory receptors expressed by exhausted T-cells including T cell immunoglobulin and mucin-domain containing-3 (TIM-3), lymphocyte activation gene 3 (LAG-3), CTLA-4 and T cell immunoreceptor with Ig and ITIM domains (TIGIT) (McLane et al., 2019). Ideally, these targets should be probed in combination via a multiplex IHC platform to identify exhausted T-cells via co-expression of these markers rather than probing for one representative marker alone. Due to financial constraints, I was unable to use such a multiplex IHC platform and opted for simple IHC stains instead. Furthermore, I did not have enough time to establish additional IHC protocols for other markers of exhaustion (e.g LAG-3, CTLA-4, TIGIT) or markers of innate immune cell populations (e.g. F4/80 for macrophages). The number of CD8 and PD-1 positive cells across each tissue section were quantified via computational image analysis which is eluded in 2.11.6 (Fig.6-14).

On day 3, the levels of CD8+ T-cells did not vary significantly between RP1- and PBS-treated groups as observed in tumours and spleens likewise ($p>0.05$ for both, two-way ANOVA) (Fig.6-14a/b; Fig.6-16a). On day 7 however, the number of CD8+ T-cells was significantly increased in RP1-treated tumours ($p=0.0002$), but not spleens ($p>0.05$). The delayed influx of CD8+ T-cells most likely reflects the latency for the activation of the adaptive arm of the immune system. Interestingly, the increase of PD-1 expressing cells occurred with a similar latency, however, affecting both tumour and spleen tissue. Accordingly, tumours and spleens of RP1-treated mice showed increased levels of PD-1 on day 7 (tumour $p=0.0311$; spleen $p>0.05$) but not day 3 ($p>0.05$ for both) as compared to PBS-treated controls (Fig.6-15a/b; Fig.6-16a). In order to find out whether the presence of CD8+ T cells coincides with the presence of PD-1 expressing cells in tumours, I performed a Pearson correlation of both datasets. The analysis outcome indicated a significant correlation of these two proteins on day 3 but not on day 7 (R^2=0.63, *p*=0.0035 and R^2=0.1614, *p*>0.05 respectively, Pearson correlation) (Fig.6-16b). Ideally however, such co-expression analysis should be performed via FC or multiplex IHC.

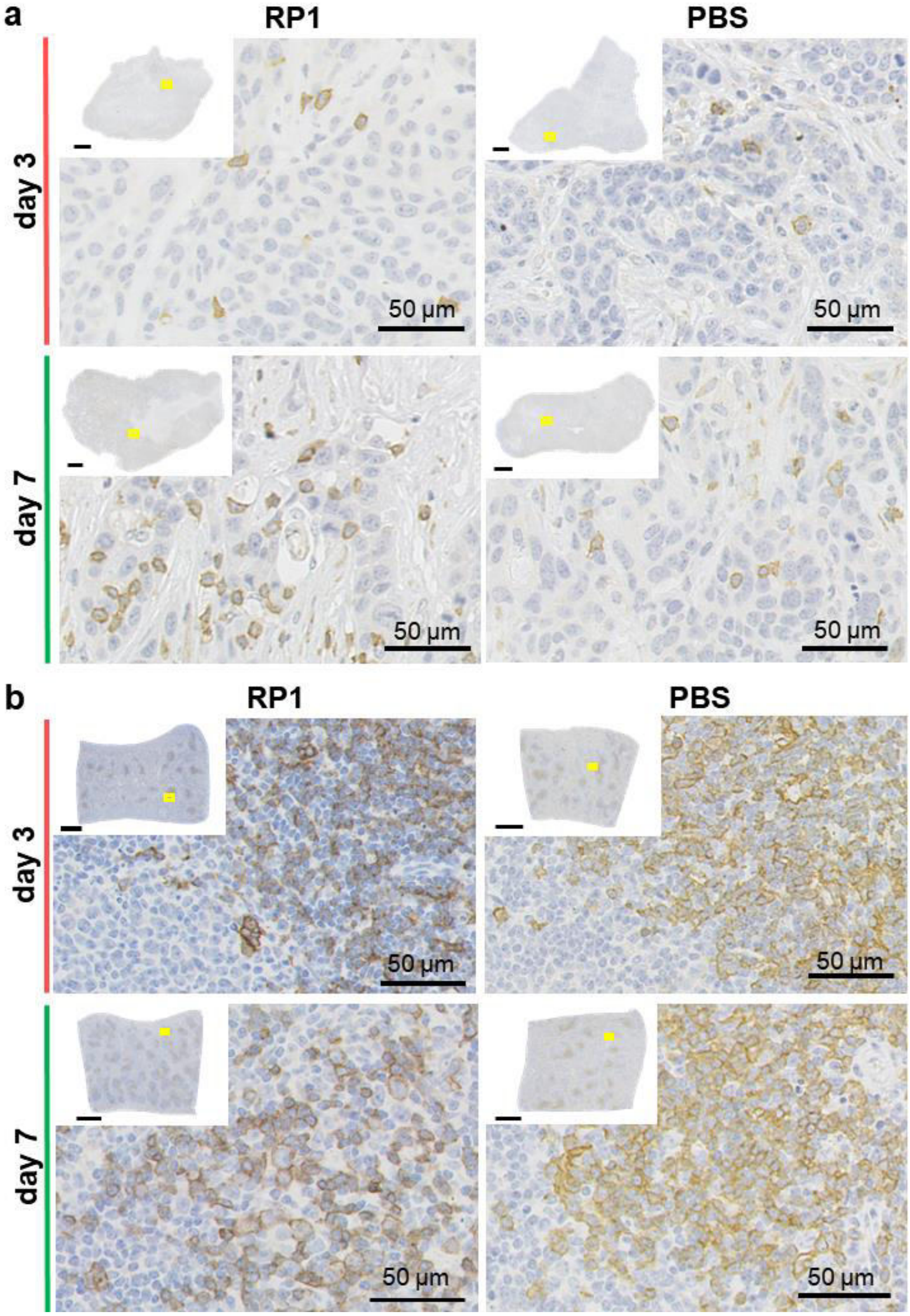

Figure 6 - 14: CD8 IHC of tumour (a) and spleen sections (b) (4 µm each) collected on day 3 and 7 after a single intratumoural dose of RP1 or PBS. Tissue from immunoPET study presented in 6.2.1.

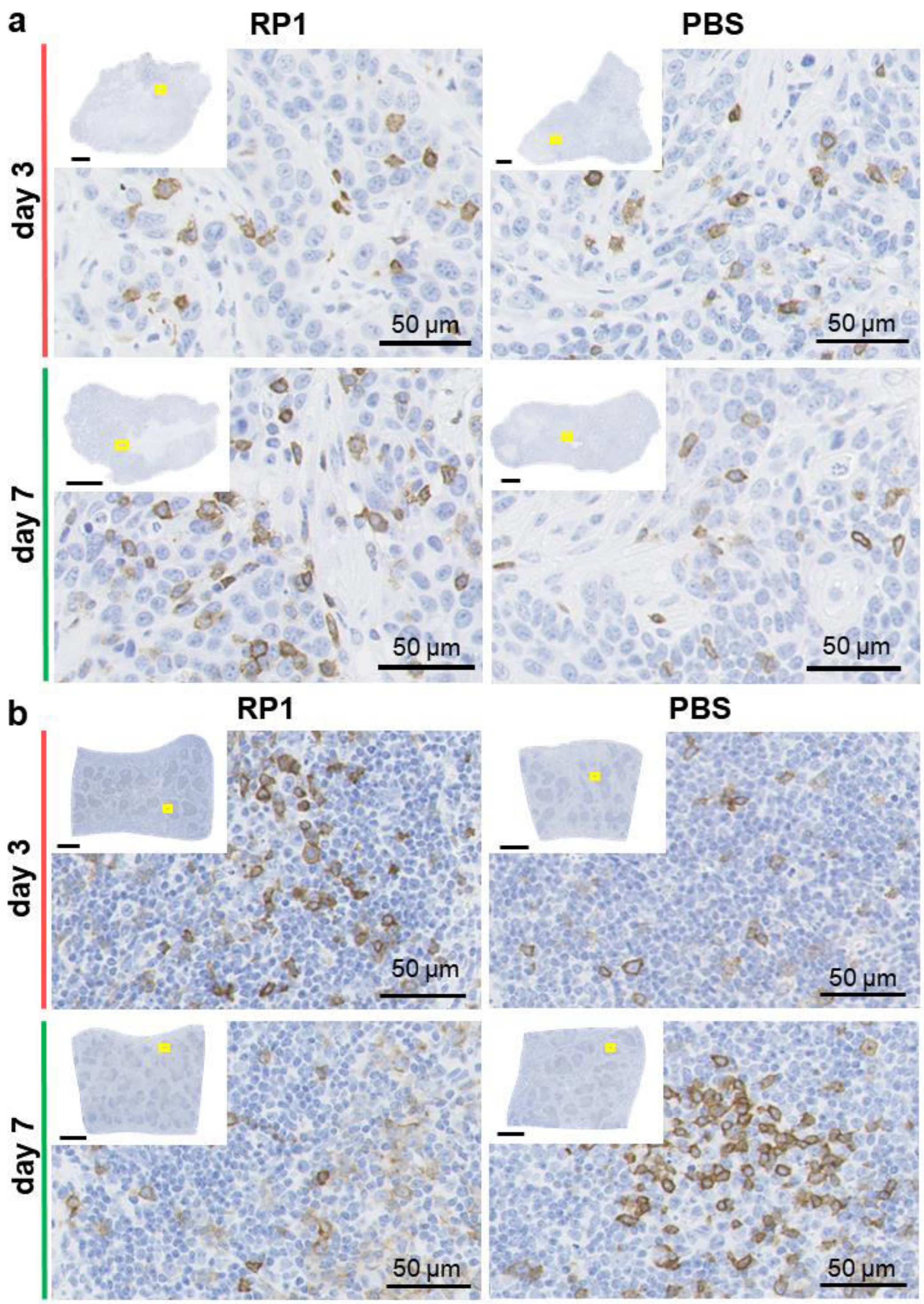

Figure 6 - 15: PD-1 IHC of tumour (a) and spleen sections (b) (4 µm each) collected on day 3 and 7 after a single intratumoural dose of RP1 or PBS. Tissue from immunoPET study presented in 6.2.1.

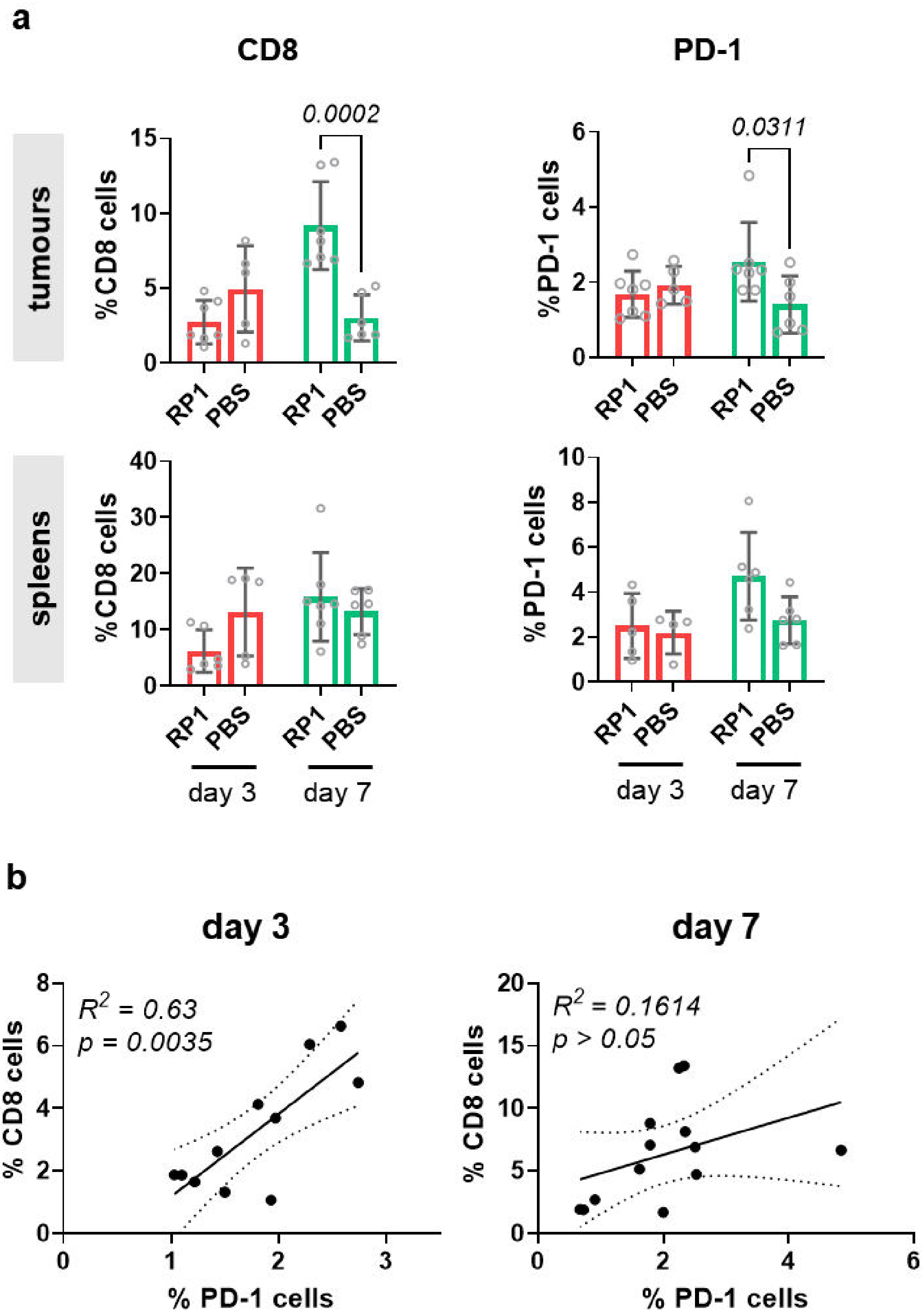

*Figure 6 - 16: **a.** Bar charts show percentages of CD8 and PD-1 positive cells (across all nucleated cells) in tumours and spleens following a single injection of RP1 or PBS (n=5-7). For comparison of RP1 vs. PBS treatments on each time point a two-way ANOVA with Bonferroni post-hoc correction was applied. P-values <0.05 were considered statistically significant. **b.** Linear regression fit of CD8 and PD-1 analysis data in tumours with 95% confidence interval (dashed lines). Pearson correlation coefficients (R^2) are indicated in each plot, p-values <0.05 were considered statistically significant.*

6.3 Conclusion and discussion

RP1 and other oncolytic viruses have been shown to upregulate PD-L1 in intratumoural cell compartments. A few studies have reported an upregulation of PD-L1 beyond the tumour. For example, PD-L1 was increased in TD Lns upon local RP1 injection to 4434 melanoma tumours (Roulstone et al., 2021). A second example is provided by Nakao *et al*, who observed enhanced PD-L1 expression in both injected and non-injected CT26 tumours using a genetically modified vaccinia virus (Nakao et al., 2020). In addition to this, other work has described the systemic impact of local OV on distinct immune cell populations, including an influx of immune effector cells to distant, non-OV injected lesions (Nakao et al., 2020; Thomas et al., 2019; Zamarin et al., 2014). Based on the growing evidence for such systemic effects upon local OV, I chose to explore the impact of local RP1 injections on the systemic expression of PD-L1 in the MOC1 mouse model.

In order to capture these changes on a systemic level, I employed PD-L1 immunoPET to study PD-L1 expression. To further address the dynamic nature of PD-L1 expression, I performed PD-L1 immunoPET on day 3 and day 7 upon a single intratumoural RP1 or PBS injection (Fig.6-1). PD-L1 expression was increased in multiple systemic organs, including TD Ln, spleen, heart, lungs and thymus on day 3 after RP1 treatment (Fig.6-2c; Fig.6-3a/b). Interestingly, these changes were no longer apparent on day 7, corroborating the dynamic expression behaviour of the PD-L1 protein upon OV. As previously addressed, a similar increase of PD-L1 has been observed in TD Lns upon local RP1 treatment in a syngeneic mouse model of melanoma (Roulstone et al., 2021). The latter study also reports a gradual decrease of PD-L1 expression in TD Ln over time, paralleling the results from PD-L1 immunoPET studies presented in this chapter (Fig.6-3a/b). Since the changes reported by Roulstone *et al* were observed upon repeat dosing of RP1 (Roulstone et al., 2021), I chose to perform a similar study applying three repeat injections of RP1 (Fig.6-6a). Interestingly, no increase of PD-L1 expression was observed in MOC1 tumour-bearing mice on day 7 after treatment start (Fig.6-6b/c; Fig.6-7a). In order to address this differential PD-L1 response it might be necessary to perform a head-to-head comparison between the two mouse models (4434 vs. MOC1) including basic profiling of the tumour-immune contexture as a potential reason. Due to the dynamic expression behaviour of PD-L1 it might also be possible that an upregulation of PD-L1 occurs before or after the day 7 time point; another aspect which should be investigated in future studies.

The breadth of organs which upregulated PD-L1 in response to RP1 treatment suggested a systemic trigger such as cytokines released early after viral infection. However, cytokine analysis of serum samples collected on day 3 after RP1 injection showed no elevation in 8 inflammatory cytokines including IL-2, IL-4, IL-6, IL-10, IL-12p70, IFN-γ, GM-CSF, TNF-α and one inflammatory chemokine, MCP-1 (Fig.6-9). Most of the aforementioned cytokines can trigger PD-L1 expression (see 1.3.2). IL-12 for instance, produced by activated APCs (DCs, macrophages), can induce PD-L1 directly or indirectly through the induction of IFN-γ production by T and NK cells (Dorman and Holland, 2000; Eppihimer et al., 2002; Xiong et al., 2014). In fact, Eppihimer *et al* have demonstrated that systemic IL-12 challenge induces a significant increase of PD-L1 in the heart and lungs, however without reporting the PD-L1 levels in other organs such as lymphatic tissue (Eppihimer et al., 2002). Interestingly, no PD-L1 increase was observed in IFN-γ deficient mice, supporting that IFN-γ is involved in IL-12 triggered PD-L1 upregulation (Eppihimer et al., 2002). After all, the lack of evidence for cytokines as a systemic trigger for the changes observed via PD-L1 immunoPET might be due to the limited number of markers covered by the assay panel. The addition of other cytokines mediating PD-L1 expression including IL-17, IL-27 or TGF-ß might provide useful insights: IL-17 can be produced by innate immune populations such as NK cells during an inflammatory response (Cua and Tato, 2010) and IL-27 is expressed at multiple phases of infection exerting both pro- and anti-inflammatory functions (Morita et al., 2021). In contrast, TGF-ß, a potent immune-suppressor regulating the generation and effector function of many immune cell populations (Batlle and Massagué, 2019), impacts PD-L1 expression in a context-dependent manner (see 1.3.2). Furthermore, chemokines should also be considered as direct or indirect sources for PD-L1 upregulation; potential candidates include CCL2, CCL5, CXCL1, CXCL9, CXCL10 and CXCL11 as well as macrophage inflammatory protein 2 (MIP-2). All of these chemokines play a role in the early immune response to inflammatory stimuli and several of them can upregulate PD-L1 on cells in culture, as outlined in the introduction section 1.3.2.

Interestingly, the tumours which did not exhibit increased levels of PD-L1 according to biodistribution studies, showed significantly increased levels of IFN-α and GM-CSF whilst levels of IL-6, MCP-1 and TNF-α were also elevated but without reaching significance (Fig.6-9). This cytokine signature indicated a local inflammatory process in RP1-treated tumours. As mentioned earlier in this chapter, type I IFNs play an important role as first-line antiviral defence. Consistent with this, elevated levels of IFN-α but not IFN-β were measured in RP1-treated tumours (Fig.6-9). However, technical issues hindered the analysis of IFN-β in all samples. IFN-γ, which is released later in the response to viral infection and strongly upregulates PD-L1, was only slightly elevated in RP1-treated tumour samples (Fig.6-9). In fact, Broos *et al* have demonstrated that intratumoural IFN-γ injections increase tumour PD-L1 expression, as exemplified via an immunoSPECT study (Broos et al., 2019). Increased presence of plasmacytoid DCs (with antiviral capacity) at the site of infection can further drive an inflammatory response and the secretion of TNF-α, IL-1β and IL-6 (Davidson et al., 2015). Both, TNF-α and IL-6 were increased in RP1-treated tumour samples on day 3, while IL-1β showed a slight decrease (Fig.6-9). The high levels of GM-CSF in RP1-treated tumours but not serum samples indicate a successful delivery and replication of the virus to tumours without substantial systemic spread. After all, the role of cytokines in an oncolytic virus-induced immune response and their subsequent impact on PD-L1 expression is poorly understood, rendering it challenging to further interpret this cytokine analysis in the context of the PD-L1 expression levels.

As mentioned previously, PD-L1 immunoPET did not indicate increased PD-L1 expression in tumours of RP1 treated mice (Fig.6-2c; Fig.6-3a; Fig.6-6c; Fig.6-7a). This might be due to the substantial damage caused by the RP1 virus within the tumour and its potential impact on intratumoural RC distribution (Fig.6-5b/c; Fig.6-8b). However, only matched tumour autoradiograms and H&E stains of the repeat but not the single dosing study clearly confirmed that damaged parts of the tumour showed less accumulation of RC (Fig.6-4b; Fig.6-7b). RP1 dose-escalation studies might have helped to reduce intratumoural tissue damage (in favour of RC distribution) whilst still achieving an immune-stimulatory effect. The potential impact of OV on tumour perfusion which has previously been addressed in this thesis (Fig.5-8a/b) and elsewhere (Breitbach et al., 2007) might additionally deteriorate RC distribution. Importantly, such effects do not influence *ex vivo* analysis methods like FC, where protein expression analysis is performed on a digested tumour sample and restricted to the population of alive cells (via the exclusion of dead cells at analysis). Furthermore, tissue processing which is required for FC analysis can significantly impact the survival of distinct subpopulations and lead to a sampling bias which is frequently in favour for the gross population of immune cells (personal communication with Antonio Rullan, Emmanuel Patin and Martin McLaughlin). The latter seem to be particularly robust compared to other intratumoural cell compartments such as tumour cells or fibroblasts (Fig.6-11c). In order to determine the effective loss of cells for each of the populations stained with the panel presented in this chapter, it might have been interesting to determine the relative number of each cell compartment via IHC on representative tumour sections. The processing of tumours with a dense stroma such as MOC1 is particularly challenging and so far, there is no adequate way on how to gently disintegrate such samples (personal communication with Miltenyi Biotec scientific advisor). To avoid such processing issues in future experiments I would opt for a multiplex IHC staining platform instead of a multicolour FC panel.

Interestingly, the data obtained from the FC analysis presented in this chapter suggested a slight upregulation of PD-L1 across immune cells (CD45+/EpCAM-) from RP1-treated tumours on day 3 (Fig.6-11b). According to PD-L1 IHC there was no obvious increase in PD-L1 expression across RP1-treated tumours (Fig.6-4a). Furthermore, the substantial contribution of non-specific staining made it difficult to decipher distinct PD-L1-positive subpopulations (e.g. immune cells) (see Suppl.Fig.2 to 7 for PD-L1 IHC optimisation). Instead, I chose to use FC to investigate PD-L1 on different tumour-owed cell compartments. A limitation of the FC panel was its small number of markers which did not allow to further distinguish PD-L1 expressing immune cell populations. However, at the stage when I performed these FC experiments I had difficulties accessing a more advanced cytometer equipped to run more than six fluorochromes at once. Therefore, a panel including a basic set of immune cell markers (of both innated and adaptive arms) should be considered for future studies potentially facilitating interpretation of the findings presented herein. For example, an extended FC panel could help to determine the role of APCs as a PD-L1 expressing subpopulation. Several papers have suggested that these cells upregulate PD-L1 upon recognition of viral DNA/RNA potentially triggered through cellular nucleic acid sensors (Schönrich and Raftery, 2019). While similar effects have also been reported for cancer cells (Chentoufi et al., 2011), neither MOC1 nor MOC2 showed markedly increased levels of PD-L1 upon RP1 exposure *in vitro* (Fig.6-12a/b).

To investigate whether the transient increase of systemic PD-L1 triggered by RP1 might affect a combination with anti-PD-1 ICB, a pilot therapy study was performed (Fig.6-13a). Results from this study showed no added effect regardless of the anti-PD-1 treatment being started on day 3 (high systemic PD-L1 expression) or day 7 (low systemic PD-L1 expression) (Fig.6-13b). Surprisingly however, a similar study which employed a synthetic agonist targeting cellular nucleic acid sensors to stimulate STING, achieved a state of adaptive immune resistance, which could then be exploited therapeutically via the addition of anti-PD-L1 ICB. Eventually, this resulted in the rejection of established MOC1 tumours and the control of distant tumours (Moore et al., 2016a). Despite the molecular similarities between RP1 and STING agonists, RP1 did not induce this state of adaptive immune resistance in MOC1 tumours, which is characterised by increased levels of PD-L1, IFN-γ and CD8+ T-cells, as previously outlined in the introduction (1.2.6). Further, the absence a therapeutic effect in MOC1 upon RP1 and anti-PD-1 combination might also be owed to the differential response between PD-L1, PD-1 and PD-L2 immune checkpoint molecules as shown via FC analysis (Fig.6-11b/e/f). At the time of high systemic PD-L1 expression (day 3), both PD-1 and PD-L2 levels were low on intratumoural immune cells (Fig.6-11e/f) and the presence of CD8+ T-cells, which might also play a role here, was reduced, as determined via IHC (Fig.6-14a; Fig.6-16a). In contrast, on day 7 after treatment, when PD-L1 expression was at control levels, PD-1 was increased in tumour resident immune cells (Fig.6-11e) and accompanied by an influx of CD8+ T-cells (Fig.6-14a; Fig.6-16a). An influx of immune effector cells following OV has also been reported by others and has been shown to improve the outcome of ICB when added in due course (Crespo-Rodriguez et al., 2020; Ribas et al., 2017; Thomas et al., 2019). The preliminary therapy study presented in this chapter was also dedicated to explore the impact of treatment timing on the outcome of combination immunotherapies (Fig.6-13a). Messenheimer *et al.* have previously addressed the impact of treatment timing via combining anti-OX40 and anti-PD-1 therapies in a mouse model of breast cancer (Messenheimer et al., 2017). The relevance of this topic for the success of OV/ICB combinations was recently covered by a review published by Nguyen *et al* (Nguyen et al., 2021) and will certainly gain more interest in the near future. After all, the absence of a therapeutic effect following the RP1 and anti-PD-1 combination treatment might be owed to the small number of animals used for the study (Fig.6-13b). Due to financial constraints, I was unable to repeat this study or perform it with a larger cohort of mice.

In summary, the work presented in this chapter, demonstrates a systemic impact of local RP1 injection into MOC1 tumours as expressed via a transient increase of PD-L1 levels across various organs. In contrast to other studies, an increase of PD-L1 was not observed in tumours with either single or repeat dosing. Cytokine analysis revealed increased levels of distinct inflammatory cytokines in tumours but not the blood, providing an incomplete picture for the observed changes. A small therapy study aimed to explore a potential benefit from the addition of PD-1 blockade upon RP1 treatment, showed no added effect by the combination. A potential reason for an absence of therapy might be the differential response observed between PD-L1, PD-1 and PD-L2 and the late infiltration of CD8+ T-cells, as assessed via FC and IHC. After all, the work presented in this chapter strengthens the role of immunoPET as a tool to non-invasively investigate immune responses on a systemic level. The key finding of this thesis, i.e. the transient PD-L1 response upon a single RP1 injection, might have been missed by other *ex vivo* techniques to measure protein expression, as they all depend on the choice of organs taken for analysis (IHC, WB, FC). Therefore, immunoPET should be further pursued for clinical translation as a method to monitor immune responses during therapeutic interventions in cancer and other diseases.

Chapter 7: Implications for future work

7.1 Translating major findings into other syngeneic mouse models of cancer

The transient increase in PD-L1 expression across several systemic organs following local OV was the key finding in my PhD project. However, an obvious limitation is that it has only been studied in a single syngeneic mouse model of cancer, i.e. MOC1. Therefore, the application of this study set-up in other syngeneic mouse cancer models might provide interesting insights and aid to interpret the observations made in the MOC1 model. Most notably, it would be interesting to perform such a study in the MOC2 mouse model, which in contrary to MOC1 seemed resistant to RP1 *in vitro*. Furthermore, it would be interesting to study PD-L1 expression dynamics in mouse models which have already been characterised in the context of RP1, via *in vitro* assays and *in vivo* therapy studies respectively. This applies to three syngeneic mouse models so far: the TBP-B79 thyroid cancer model in which repeat RP1 injections seemed to slow tumour growth, the 4434 melanoma and A20 lymphoma models in which repeat RP1 injections achieved tumour cures in injected as well as non-injected tumours (both were established as bilateral tumour models) (Crespo-Rodriguez et al., 2020; Roulstone et al., 2021; Thomas et al., 2019). However, there is a large number of other syngeneic mouse models which could be explored towards their PD-L1 response following a single intratumoural RP1 injection, e.g. the CT26 and MC38 colon carcinoma models, the B16 melanoma model (Dahan et al., 2015; Mosely et al., 2017). Moreover, there is a handful of murine HNSCC models which could be used for such purposes as well, e.g. AT-84, MOSC1, MOSC2 and Meer (Hier et al., 1995; Hoover et al., 2007; Schultz-Hector and Haghayegh, 1993; Wang et al., 2019). It is possible that the systemic PD-L1 response observed in MOC1 tumour-bearing mice upon a single RP1 injection depends on the immune contexture in this tumour type or the strong tropism of RP1 towards MOC1 cells. Repeat studies in additional mouse models would help address these questions and eventually increase the translational value of the findings made so far. An additional avenue that could be pursued is the use of a different oncolytic virus in the MOC1 model to compare the effects on PD-L1 expression with the data presented in this thesis.

7.2 Exploring potential sources for the RP1-triggered PD-L1 response

The attempt to explore serum cytokines as a potential source for the RP1-triggered PD-L1 upregulation in the MOC1 mouse model remained inconclusive. An extension of the assay panel beyond the 10 inflammatory cytokines and the addition of relevant chemokines might help to (re-)address cytokines and chemokines as mediators of the observed changes. Furthermore, cytokine stimulation studies could be performed on cells *in vitro* to confirm the impact of candidates identified through the multi-parametric cytokine/chemokine analysis on PD-L1 expression (e.g. similar to the IFN-γ stimulation described in 2.2.1). In this context, it would also be interesting to look at the direct impact of RP1 on PD-L1 expression across various cell types *in vitro*. Whilst my own studies showed that RP1 does not upregulate PD-L1 in MOC1 or MOC2 cells *in vitro*, the effect might look different in other cell types including endothelial cells, fibroblasts or immune cell populations such as APCs. An experiment investigating PD-L1 expression across these cell types after RP1 treatment *in vitro* (each grown in monoculture), might provide additional information on the changes in PD-L1 expression observed *in vivo*.

Furthermore, multiparameter FC could be applied to immune-phenotype cell populations in organs such as the spleen or the tumours, comparing PD-L1 expressing cell populations in RP1- vs. PBS-treated animals. Such analysis would help understand the immunological role of PD-L1 upregulation in response to intratumoural RP1 injection across distinct cell types. Alternatively, transcriptome analysis (RNA-sequencing) of spleen or tumour tissue preserved from PET studies (chapter 6) could be used to characterise the immunologic response patterns induced through local RP1 therapy. Advanced computational methods allow to resolve the transcriptome data and provide a characterisation of the immune infiltrate alongside with distinct immune signatures (Hugo et al., 2016). Theoretically, such analysis could have been performed on frozen tissue chunks preserved from PET studies (reported in chapter 6) but had to be put on hold due to financial restrictions.

Finally, a better understanding of the immunologic role of the PD-L1 response triggered through RP1 might also unveil potential avenues for therapeutic exploitation via rational combinations with other anti-cancer treatments. Although

MOC1 tumour-bearing mice did not seem to benefit from the combination of RP1 and anti-PD-1 ICB, according to a pilot study presented in this thesis, other combinations might yield a therapeutic benefit after all.

7.3 Employing smaller-sized targeting vectors for PD-L1 immunoPET

In this thesis an antibody-based radioconjugate was used to monitor PD-L1 expression via immunoPET *in vivo*. After all, it would be highly interesting to compare the PD-L1mAb radioconjugate performance against a PET probe based on a smaller-sized targeting vector such as a single domain antibody (sdAb). As previously flagged, antibodies are very attractive targeting vectors due to their high inherent target specificity and affinity. However, this goes at the cost of a high molecular weight which limits their capacity to penetrate tissue efficiently. In order to account for this characteristic and ensure thorough penetration of heterogenous target tissue, e.g. the tumour, the imaging time point is usually delayed by a minimum of 48 h after injection. In this time between probe injection and imaging, intracellular accumulation of the radioisotope following target-mediated internalisation might occur, hampering accurate time-resolution of protein expression (dynamics). Therefore, antibodies are considered suboptimal vectors to study receptor dynamics in a timely manner, i.e. within minutes after radioconjugate injection. Being well-aware of these limitations, the PD-L1 mAb I chose as a targeting moiety in my thesis was the only available option to monitor mouse PD-L1 *in vivo* at the time when I started my PhD. However, the use of a smaller-sized construct such as an sdAb labelled with an isotope of significantly shorter half-life (e.g. ^{68}Ga, ^{18}F) would allow to overcome several limitations encountered with full-length antibodies. One such smaller-sized option is the mouse-specific anti-PD-L1 sdAb presented by Broos *et al* (Broos et al., 2017). According to their studies, the Technetium-99 labelled anti-PD-L1 sdAb shows high specificity towards murine PD-L1 *in vitro* and *in vivo*, providing a versatile alternative to monitor PD-L1 expression dynamics.

Appendix

8.1 FMO and isotype controls in flow cytometry

FMO controls are samples stained with all the fluorochromes in a panel, except for one (Roederer, 2002). They are used to set the upper threshold for background signal on the omitted label, and thus to identify and gate positive populations in multicolour experiments. It is crucial to use the same type of sample as used in the experiment (not beads or an irrelevant sample) to capture the signal arising from sample autofluorescence right next to the spillover spread from other dyes in the panel. FMOs however, do not control for non-specific binding or for non-negligible basal expression level. To reduce effects of non-specific binding to Fc receptors expressed on a variety of cell types, the receptors can be blocked via the addition of a Fc-blocking reagent to the cell suspension prior to the antibody mixture as suggested by Andersen *et al* (Andersen et al., 2016).

Isotype controls are antibodies of the same Ig class (isotype) as the specific antibody which either exhibit unknown specificity or are raised against an antigen which is expected not to be present on the cells under study (Hulspas et al., 2009). The ideal isotype control should match the specific antibody in Ig subclass and light chain class (e.g. kappa, lambda), in fluorochrome type and in fluorochrome-protein ratio. Only a perfectly matched isotype control represents a way of determining undesirable antibody binding via Fc-receptors on target cells and/or fluorochrome binding (Keeney et al., 1998). However, a significant limitation of isotype controls is the difference in V_H and V_L regions (determining the antibody binding sites) as compared to the specific antibody. Ultimately, this difference can cause different levels of nonspecific binding (Keeney et al., 1998).

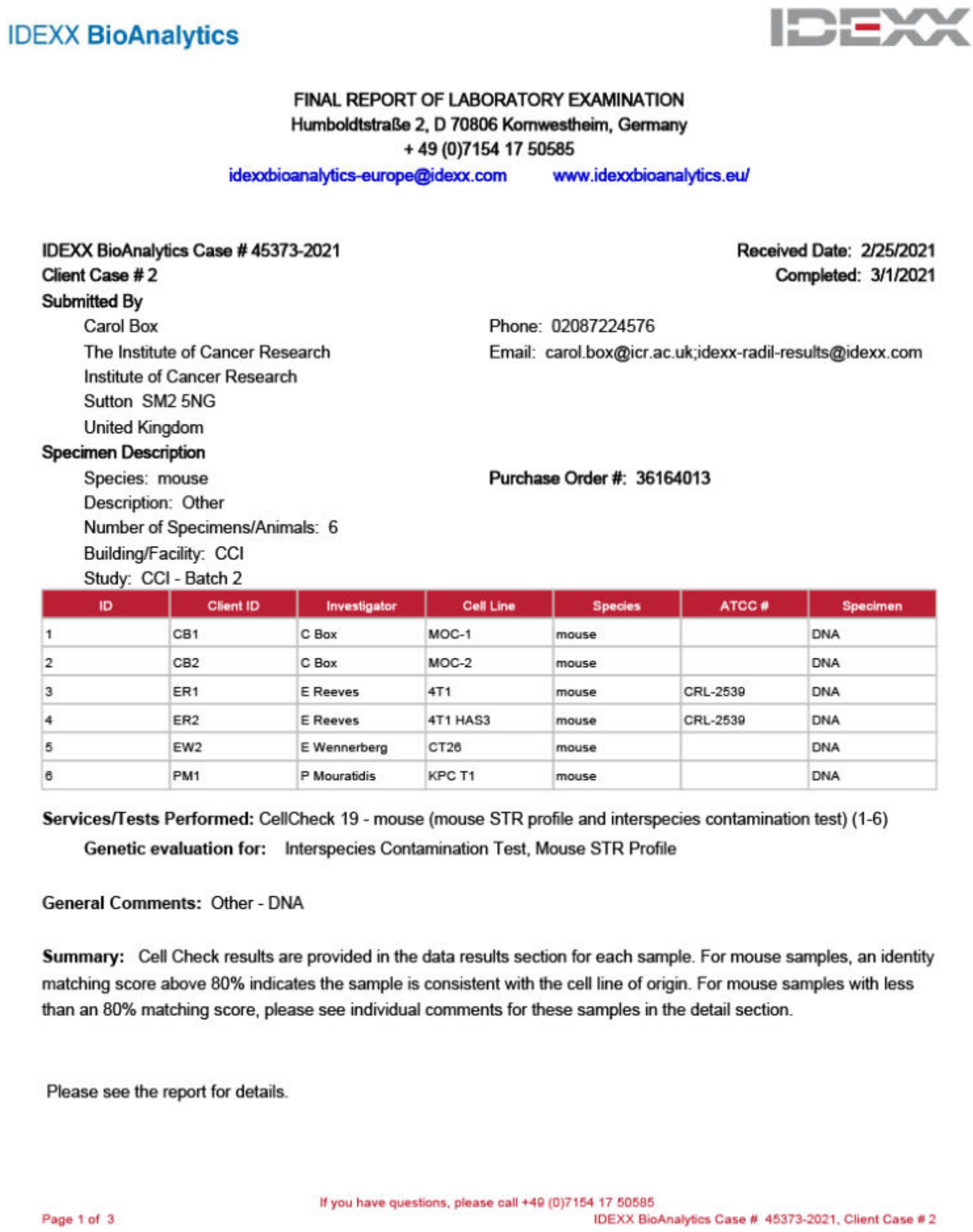

IDEXX **BioAnalytics**

FINAL REPORT OF LABORATORY EXAMINATION

Humboldtstraße 2, D 70806 Kornwestheim, Germany
+ 49 (0)7154 17 50585
idexxbioanalytics-europe@idexx.com www.idexxbioanalytics.eu/

IDEXX BioAnalytics Case # 45373-2021 **Received Date: 2/25/2021**
Client Case # 2 **Completed: 3/1/2021**

Submitted By

Carol Box
The Institute of Cancer Research
Institute of Cancer Research
Sutton SM2 5NG
United Kingdom

Phone: 02087224576
Email: carol.box@icr.ac.uk;idexx-radil-results@idexx.com

Specimen Description

Species: mouse
Description: Other
Number of Specimens/Animals: 6
Building/Facility: CCI
Study: CCI - Batch 2

Purchase Order #: 36164013

ID	Client ID	Investigator	Cell Line	Species	ATCC #	Specimen
1	CB1	C Box	MOC-1	mouse		DNA
2	CB2	C Box	MOC-2	mouse		DNA
3	ER1	E Reeves	4T1	mouse	CRL-2539	DNA
4	ER2	E Reeves	4T1 HAS3	mouse	CRL-2539	DNA
5	EW2	E Wennerberg	CT26	mouse		DNA
6	PM1	P Mouratidis	KPC T1	mouse		DNA

Services/Tests Performed: CellCheck 19 - mouse (mouse STR profile and interspecies contamination test) (1-6)

Genetic evaluation for: Interspecies Contamination Test, Mouse STR Profile

General Comments: Other - DNA

Summary: Cell Check results are provided in the data results section for each sample. For mouse samples, an identity matching score above 80% indicates the sample is consistent with the cell line of origin. For mouse samples with less than an 80% matching score, please see individual comments for these samples in the detail section.

Please see the report for details.

If you have questions, please call +49 (0)7154 17 50585

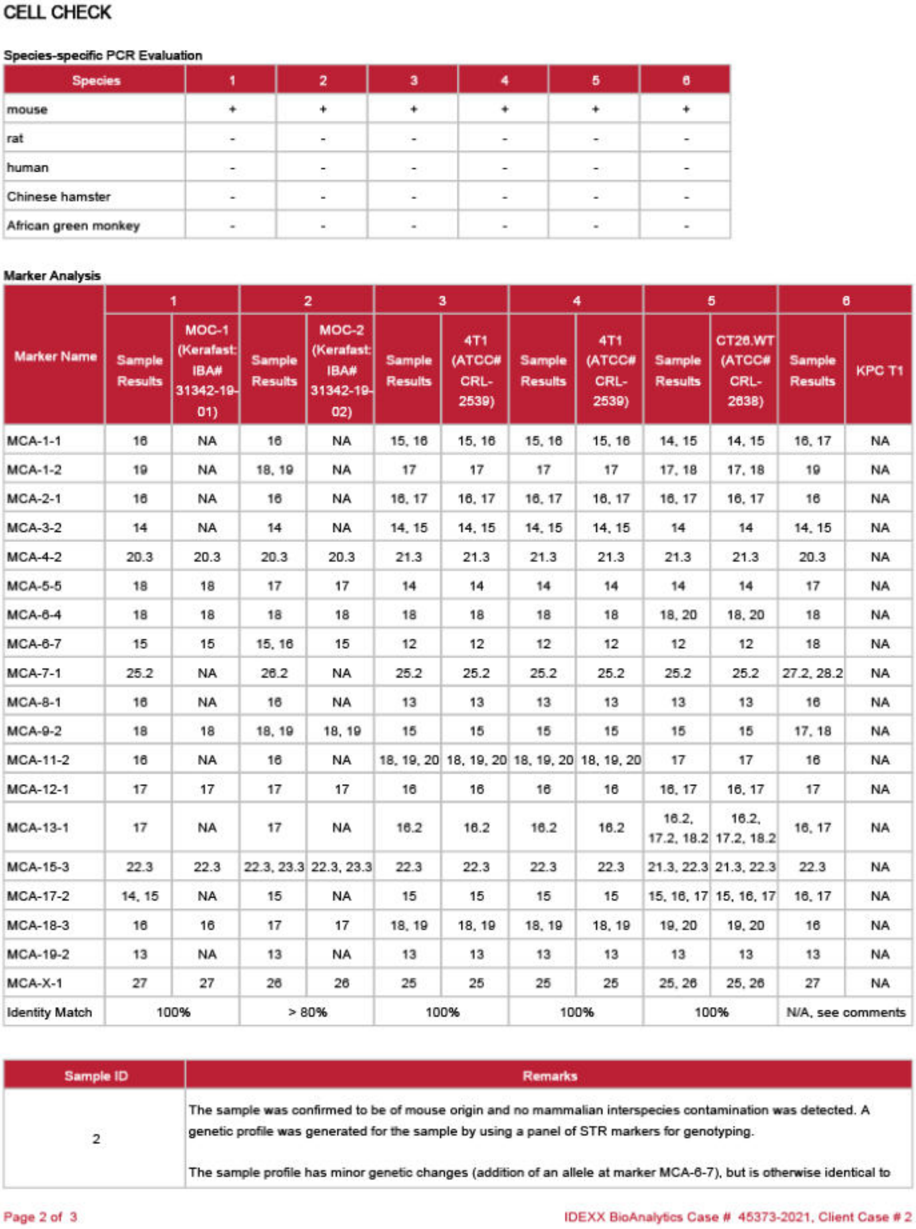

CELL CHECK

Species-specific PCR Evaluation

Species	1	2	3	4	5	6
mouse	+	+	+	+	+	+
rat	-	-	-	-	-	-
human	-	-	-	-	-	-
Chinese hamster	-	-	-	-	-	-
African green monkey	-	-	-	-	-	-

Marker Analysis

Marker Name	1		2		3		4		5		6	
	Sample Results	MOC-1 (Kerafast: IBA# 31342-19-01)	Sample Results	MOC-2 (Kerafast: IBA# 31342-19-02)	Sample Results	4T1 (ATCC# CRL-2539)	Sample Results	4T1 (ATCC# CRL-2539)	Sample Results	CT26.WT (ATCC# CRL-2638)	Sample Results	KPC T1
MCA-1-1	16	NA	16	NA	15, 16	15, 16	15, 16	15, 16	14, 15	14, 15	16, 17	NA
MCA-1-2	19	NA	18, 19	NA	17	17	17	17	17, 18	17, 18	19	NA
MCA-2-1	16	NA	16	NA	16, 17	16, 17	16, 17	16, 17	16, 17	16, 17	16	NA
MCA-3-2	14	NA	14	NA	14, 15	14, 15	14, 15	14, 15	14	14	14, 15	NA
MCA-4-2	20.3	20.3	20.3	20.3	21.3	21.3	21.3	21.3	21.3	21.3	20.3	NA
MCA-5-5	18	18	17	17	14	14	14	14	14	14	17	NA
MCA-6-4	18	18	18	18	18	18	18	18	18, 20	18, 20	18	NA
MCA-6-7	15	15	15, 16	15	12	12	12	12	12	12	18	NA
MCA-7-1	25.2	NA	26.2	NA	25.2	25.2	25.2	25.2	25.2	25.2	27.2, 28.2	NA
MCA-8-1	16	NA	16	NA	13	13	13	13	13	13	16	NA
MCA-9-2	18	18	18, 19	18, 19	15	15	15	15	15	15	17, 18	NA
MCA-11-2	16	NA	16	NA	18, 19, 20	18, 19, 20	18, 19, 20	18, 19, 20	17	17	16	NA
MCA-12-1	17	17	17	17	16	16	16	16	16, 17	16, 17	17	NA
MCA-13-1	17	NA	17	NA	16.2	16.2	16.2	16.2	16.2, 17.2, 18.2	16.2, 17.2, 18.2	16, 17	NA
MCA-15-3	22.3	22.3	22.3, 23.3	22.3, 23.3	22.3	22.3	22.3	22.3	21.3, 22.3	21.3, 22.3	22.3	NA
MCA-17-2	14, 15	NA	15	NA	15	15	15	15	15, 16, 17	15, 16, 17	16, 17	NA
MCA-18-3	16	16	17	17	18, 19	18, 19	18, 19	18, 19	19, 20	19, 20	16	NA
MCA-19-2	13	NA	13	NA	13	13	13	13	13	13	13	NA
MCA-X-1	27	27	26	26	25	25	25	25	25, 26	25, 26	27	NA
Identity Match	100%		> 80%		100%		100%		100%		N/A, see comments	

Sample ID	Remarks
2	The sample was confirmed to be of mouse origin and no mammalian interspecies contamination was detected. A genetic profile was generated for the sample by using a panel of STR markers for genotyping. The sample profile has minor genetic changes (addition of an allele at marker MCA-6-7), but is otherwise identical to

Page 2 of 3

IDEXX BioAnalytics Case # 45373-2021, Client Case # 2

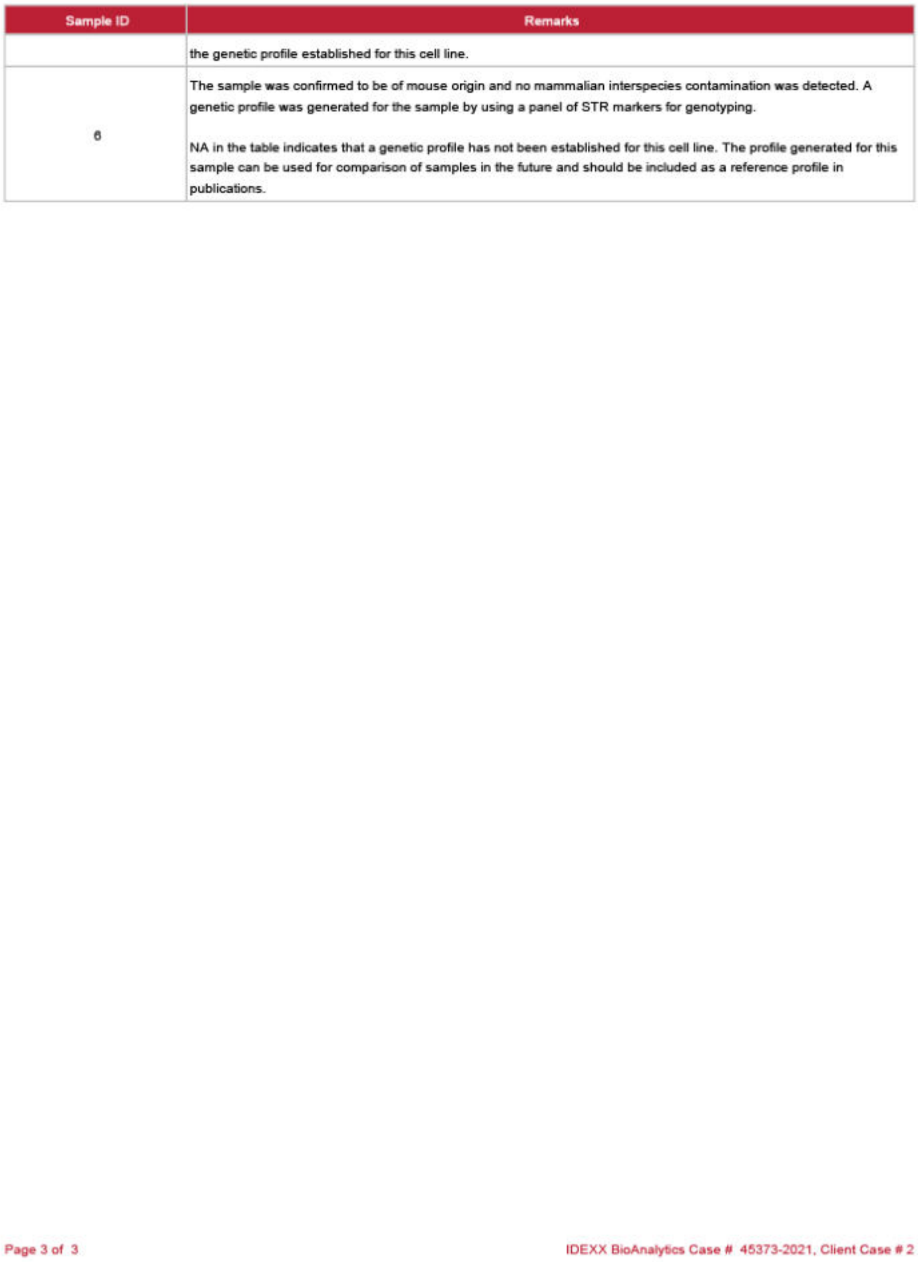

Sample ID	Remarks
	the genetic profile established for this cell line.
6	The sample was confirmed to be of mouse origin and no mammalian interspecies contamination was detected. A genetic profile was generated for the sample by using a panel of STR markers for genotyping. NA in the table indicates that a genetic profile has not been established for this cell line. The profile generated for this sample can be used for comparison of samples in the future and should be included as a reference profile in publications.

Page 3 of 3

IDEXX BioAnalytics Case # 45373-2021, Client Case # 2

Supplementary figure 1: Short tandem repeat (STR) profiling results for MOC1 and MOC2 cell lines.

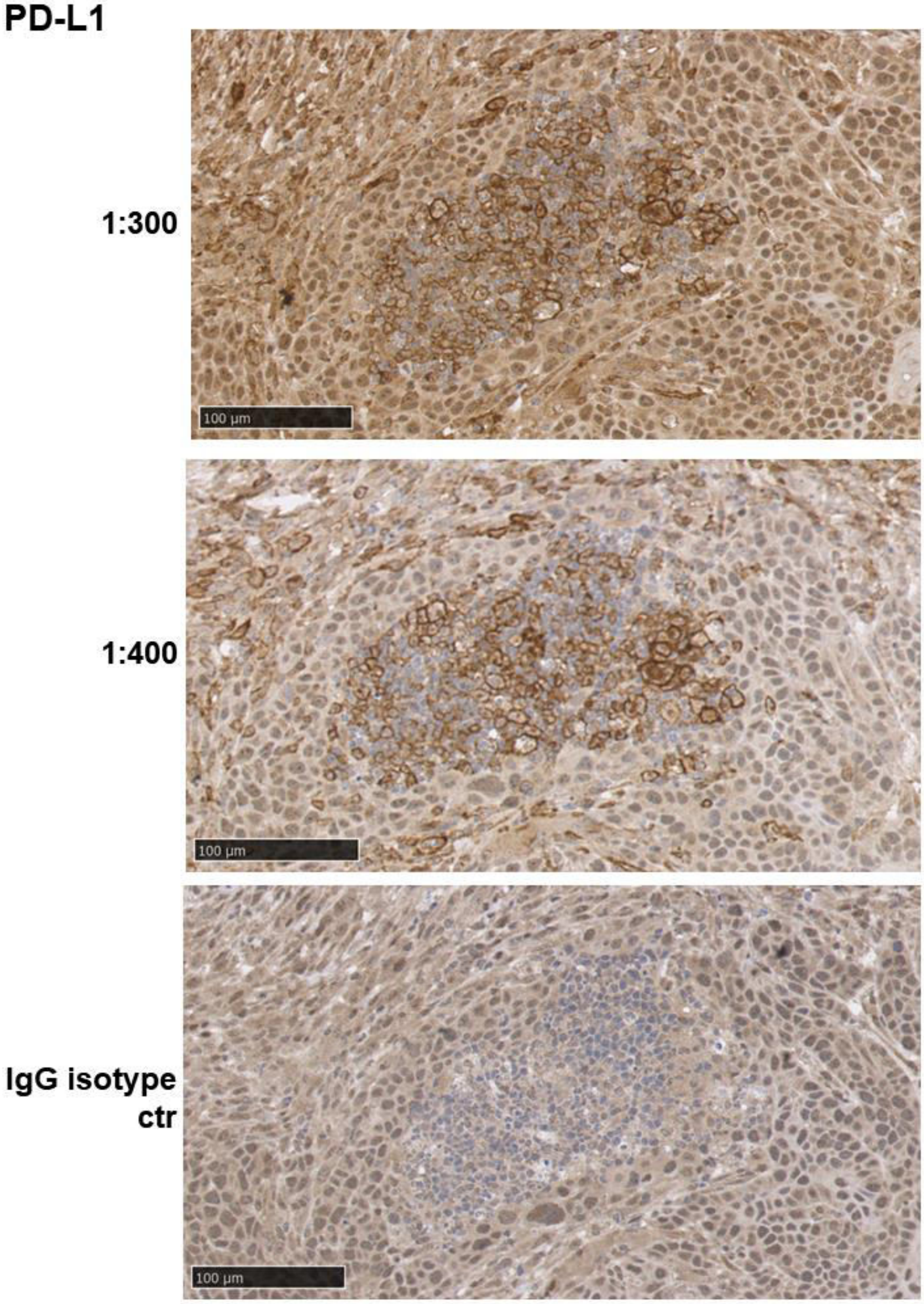

Supplementary figure 2: PD-L1 IHC of MOC2(PDL1)^{poly} *tumour sections (4 µm, consecutive) showing different concentrations of primary antibody and the IgG isotype ctr (1:300). Rabbit serum (2%) was used for blocking and PBS only was used for washes. Bars indicate 100 µm.*

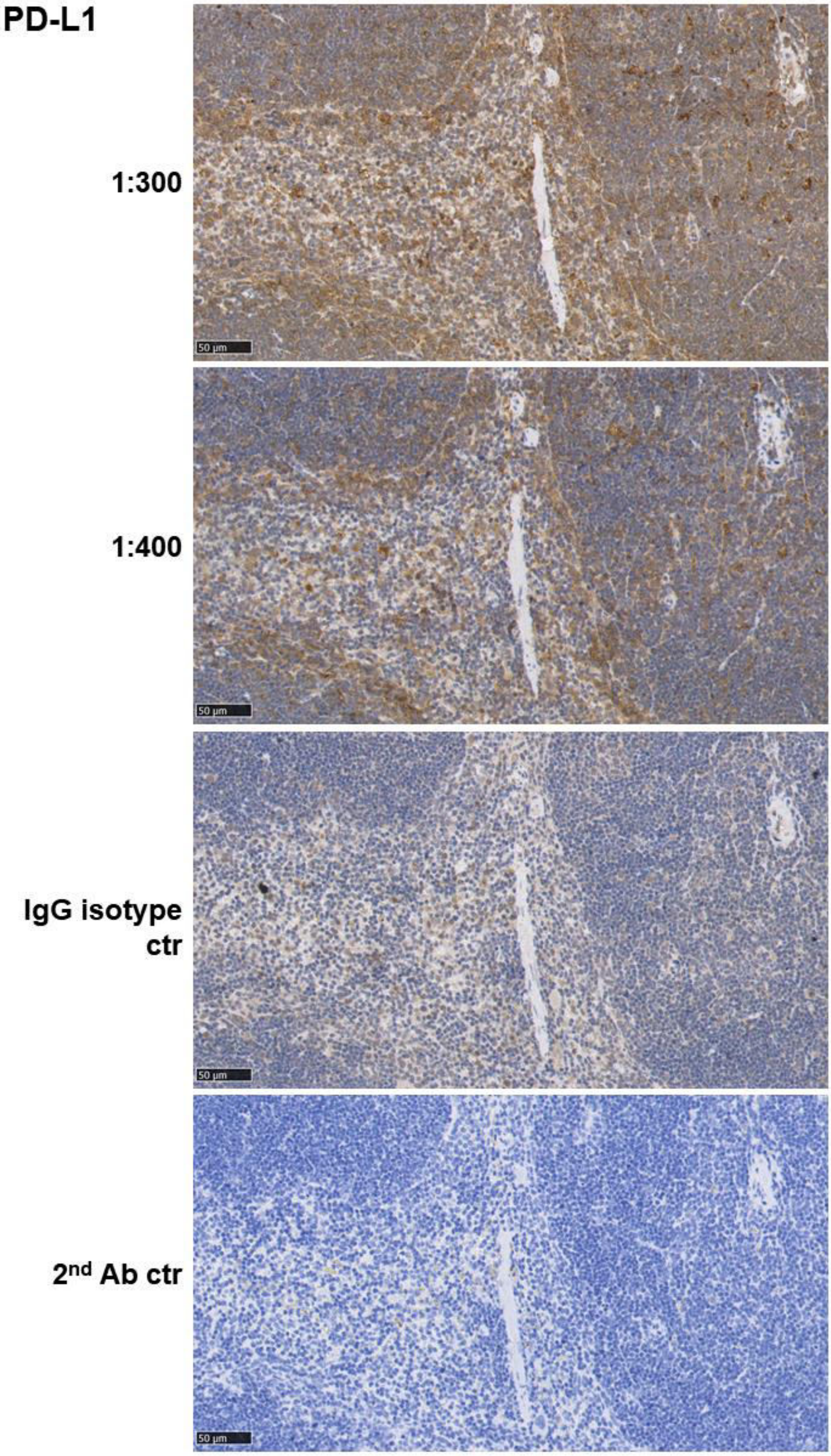

Supplementary figure 3: PD-L1 IHC of spleen sections (4 µm, consecutive) showing two different concentrations of primary antibody as well as IgG isotype and 2nd Ab ctr. Rabbit *serum (2%) was used for blocking and PBS only was used for washes. Bars indicate 50 µm.*

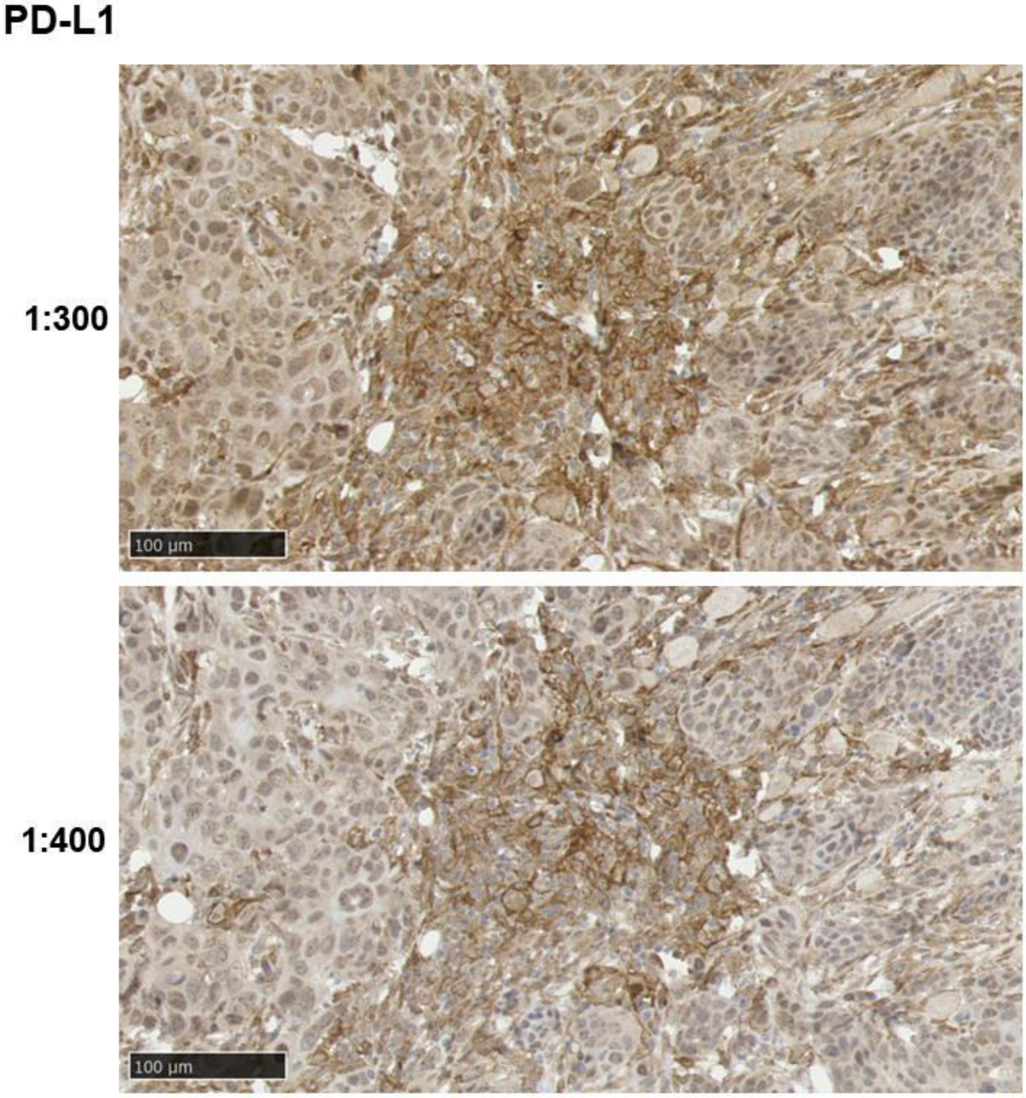

Supplementary figure 4: PD-L1 IHC of MOC1 tumour sections (4 µm) showing two different concentrations of primary antibody. Rabbit serum (10%) was used for blocking and PBS only was used for washes. Bars indicate 100 µm.

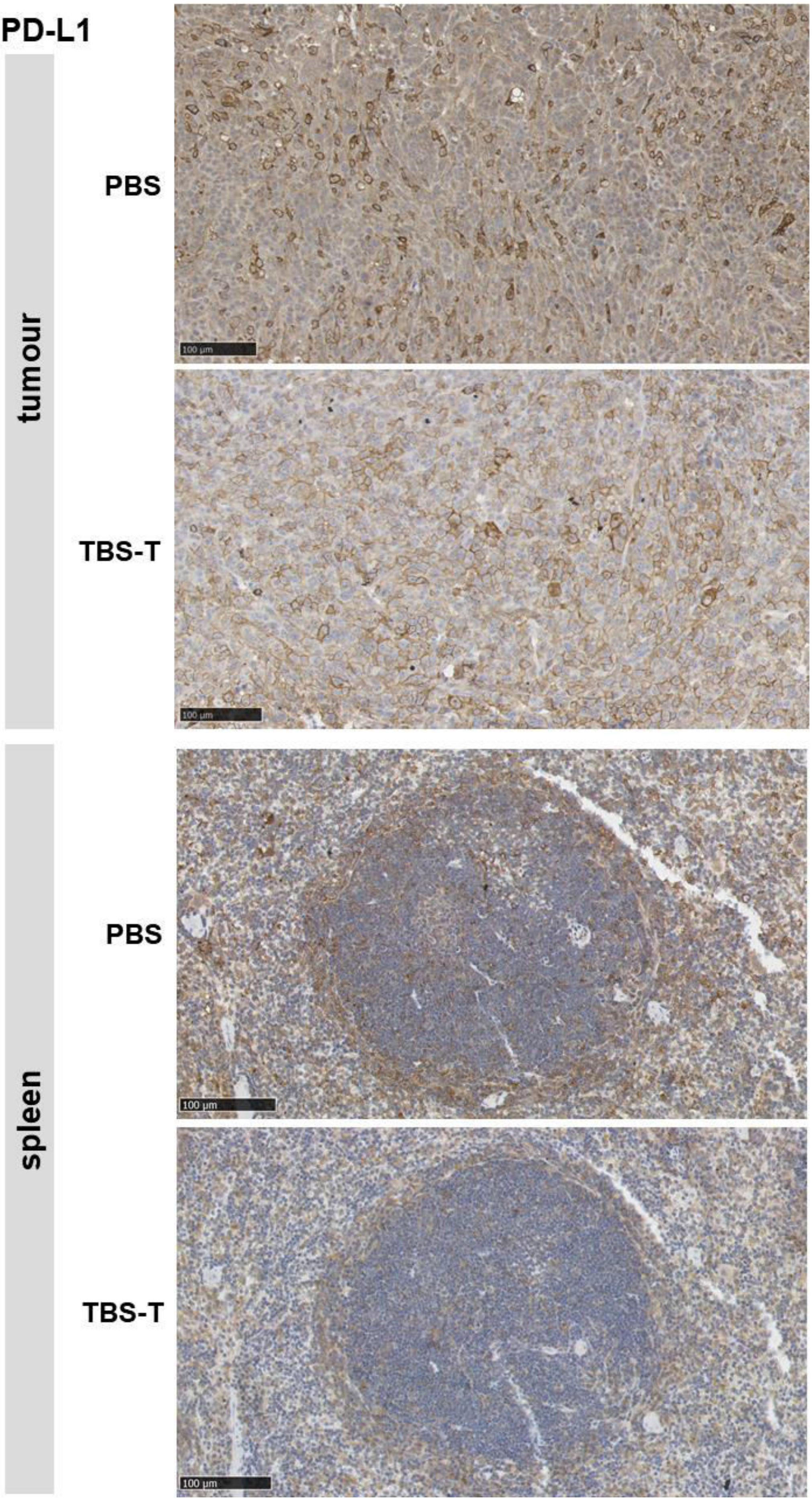
PD-L1
tumour
PBS
100 µm
TBS-T
100 µm
spleen
PBS
100 µm
TBS-T
100 µm

Supplementary figure 5: PD-L1 IHC of $MOC2(PDL1)^{poly}$ *tumour sections and spleen sections (4 µm) stained with primary Ab (1:300). Rabbit serum (10%) was used for blocking and PBS vs. TBS-T was used for washes. Bars indicate 100 µm.*

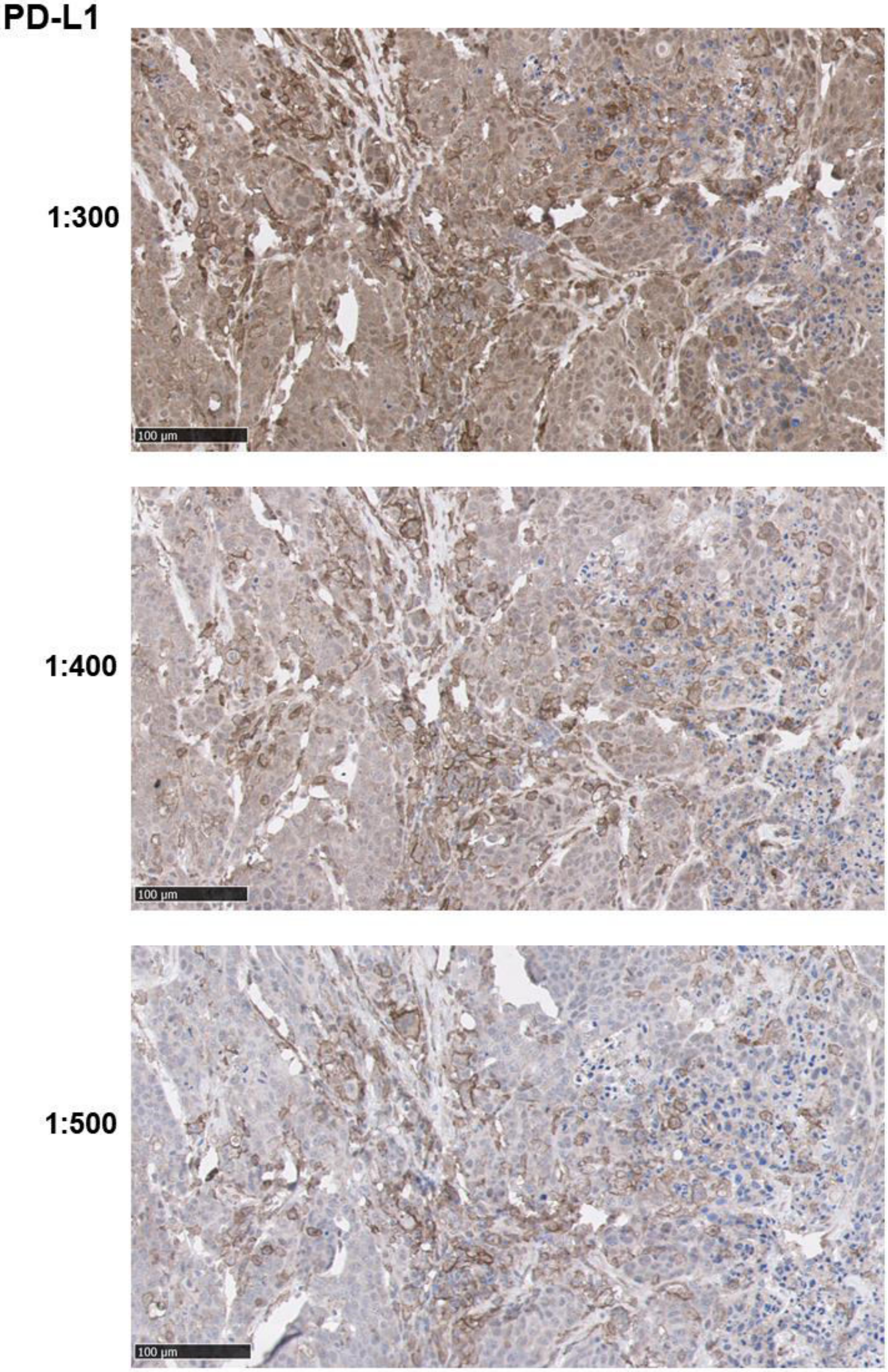

Supplementary figure 6: PD-L1 IHC of MOC1 tumour sections (4 μm) stained with different concentrations of primary Ab. Rabbit serum (10%) was used for blocking and TBS-T was used for washes. Bars indicate 100 μm.

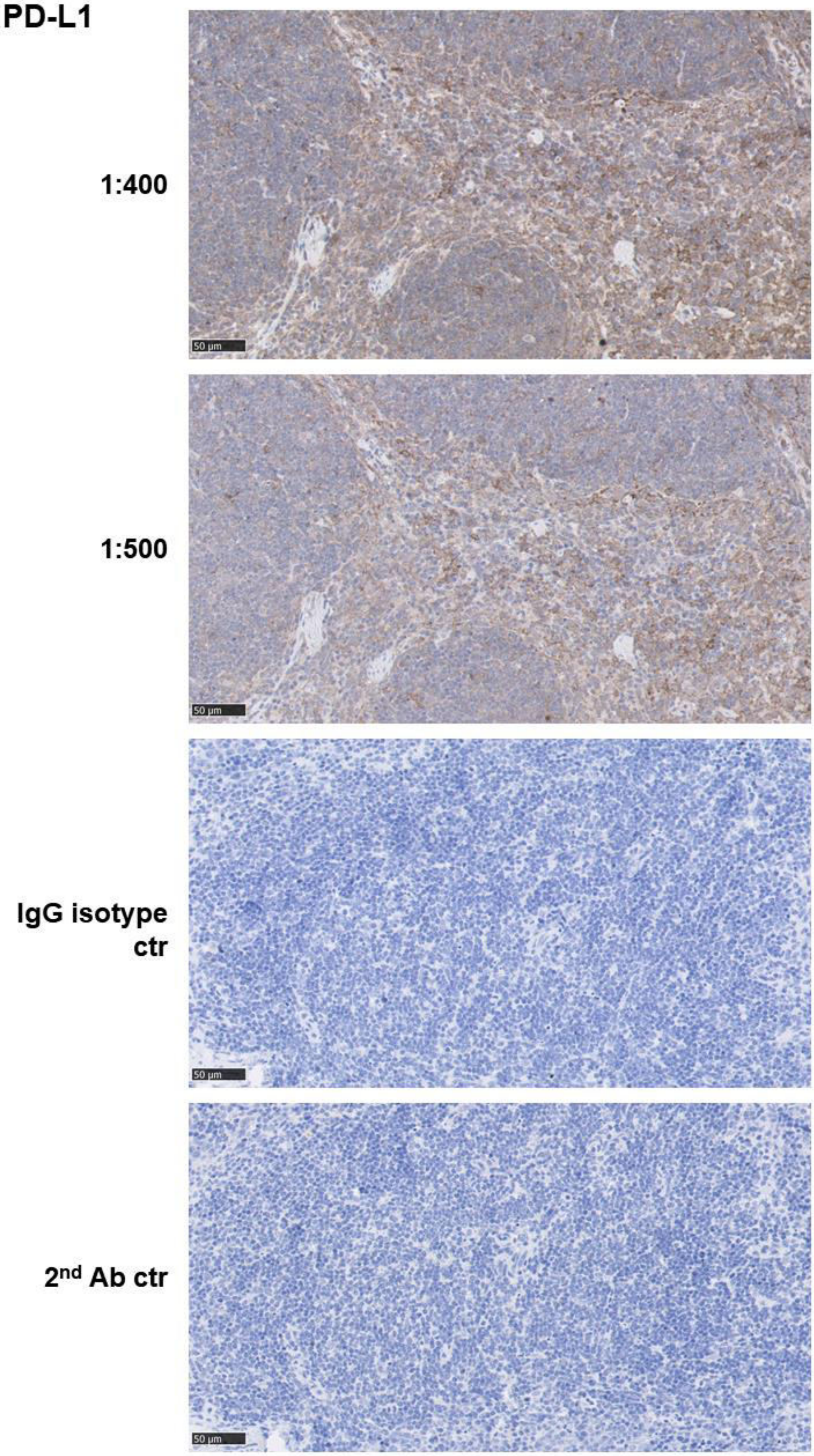
PD-L1
1:400
50 µm
1:500
50 µm
IgG isotype ctr
50 µm
2nd Ab ctr
50 µm

Supplementary figure 7: PD-L1 IHC of spleen sections (4 µm) stained with two different concentrations of primary Ab. Rabbit serum (10%) was used for blocking and TBS-T was used for washes. Bars indicate 50 µm.

CD8

1:50

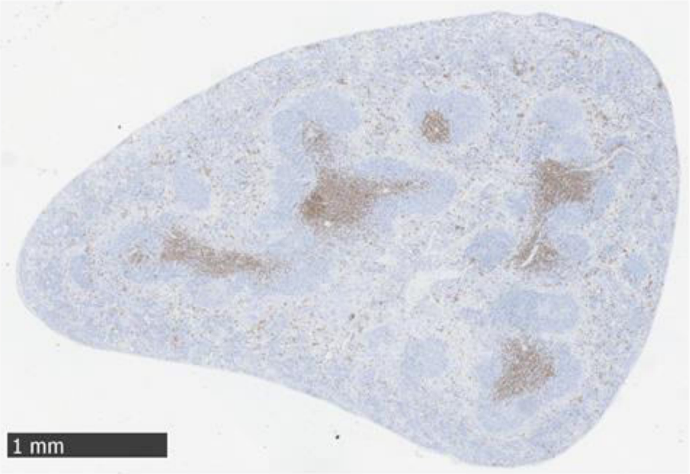

1:100

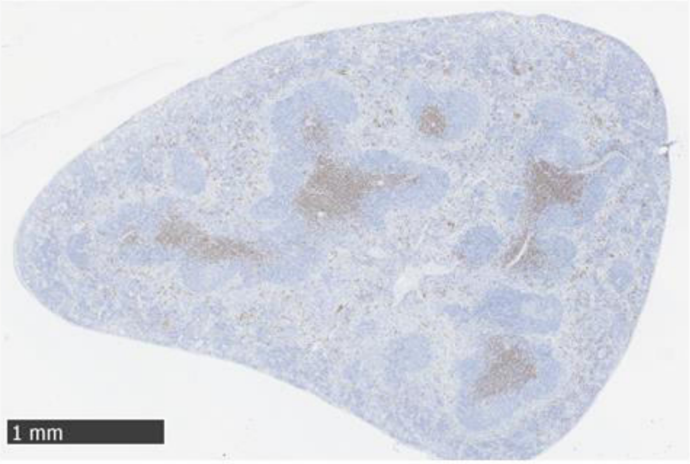

1:300

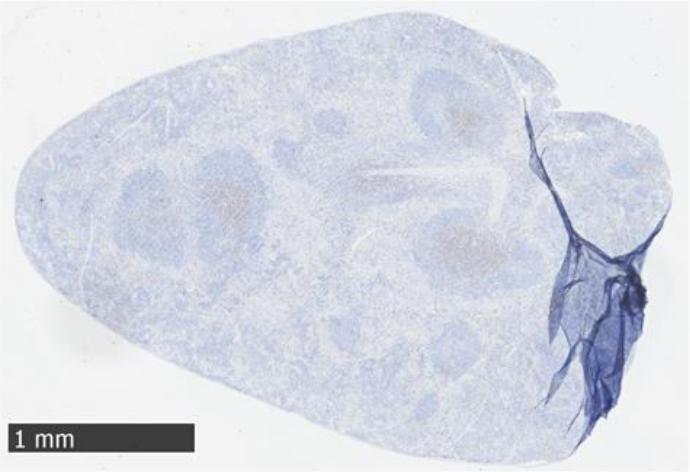

IgG istoype ctr

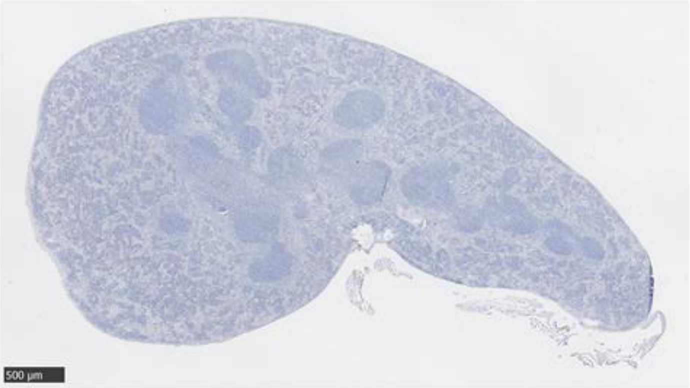

Supplementary figure 8: CD8 IHC of spleen sections (4 µm) showing three different concentrations of primary Ab and an IgG isotype ctr (1:100). Bars indicate 1 mm (first three images) and 500 µm (last image).

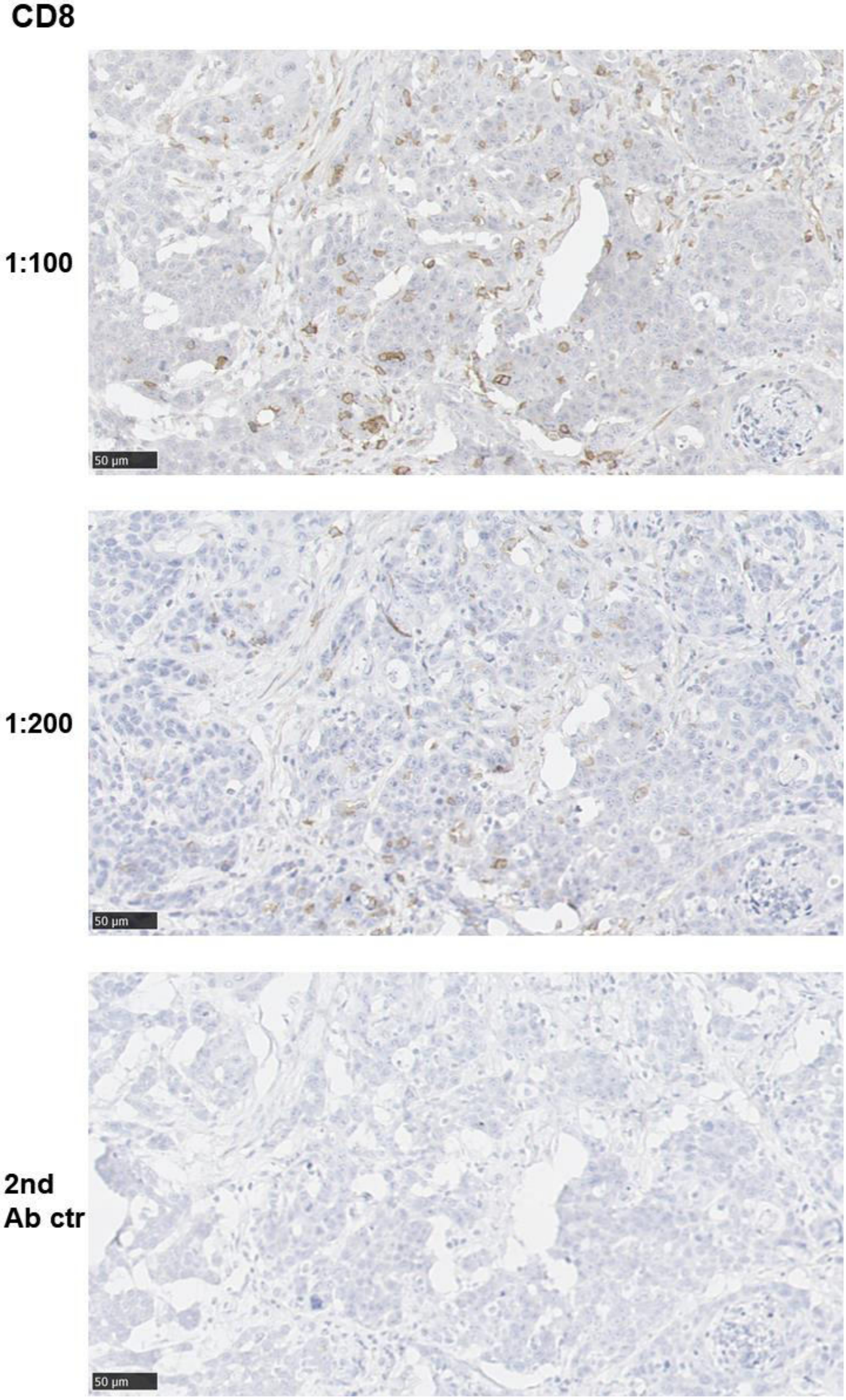

Supplementary figure 9: CD8 IHC of MOC1 tumour sections (4 µm) showing two different concentrations of primary Ab and the 2nd Ab ctr (1:100). Bars indicate 50 µm.

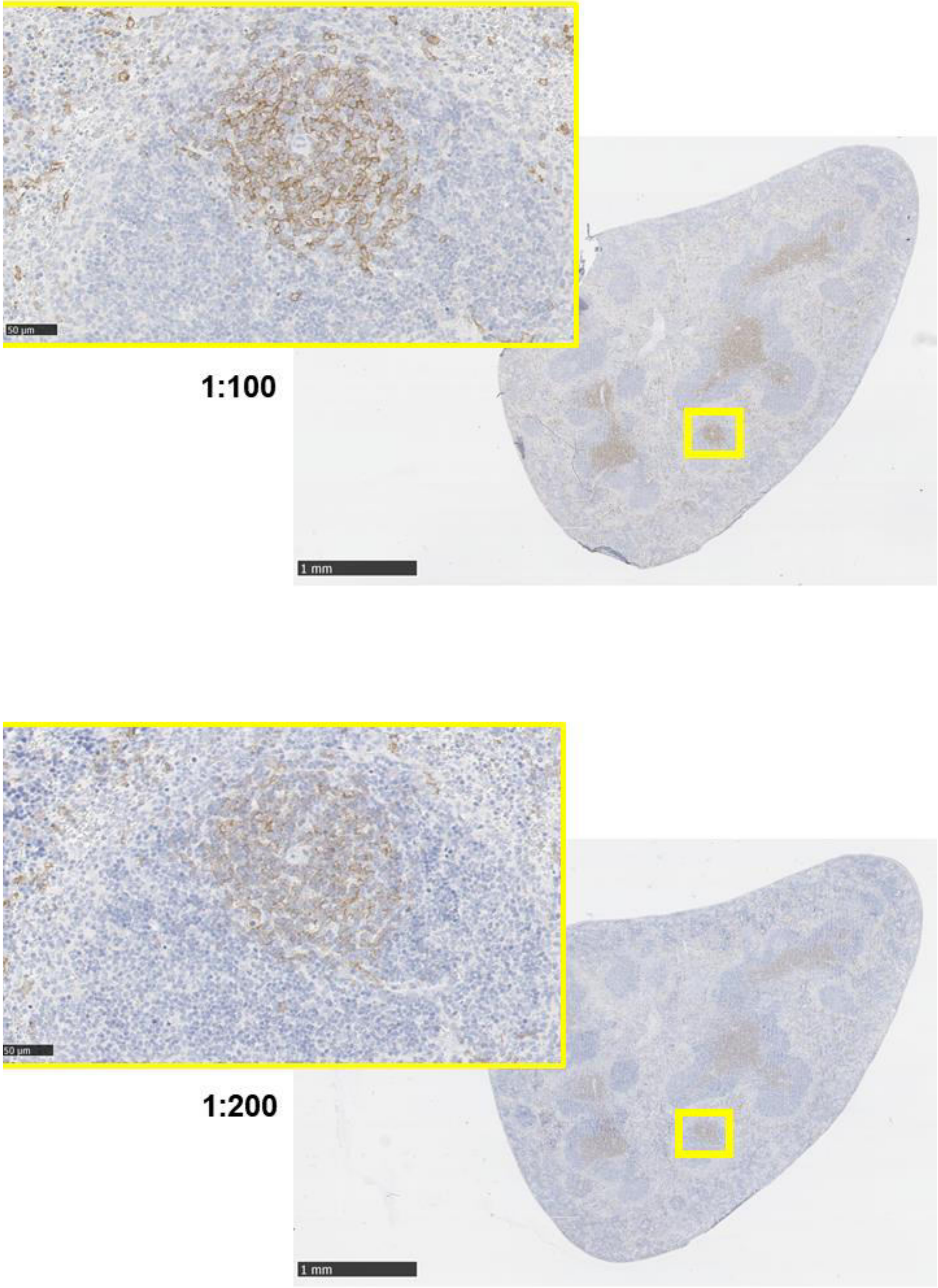

Supplementary figure 10: PD-1 IHC of spleen sections (4 µm, consecutive) showing two different concentrations of primary Ab. Bars indicate 1 mm in overview images and 50 µm in inlets.

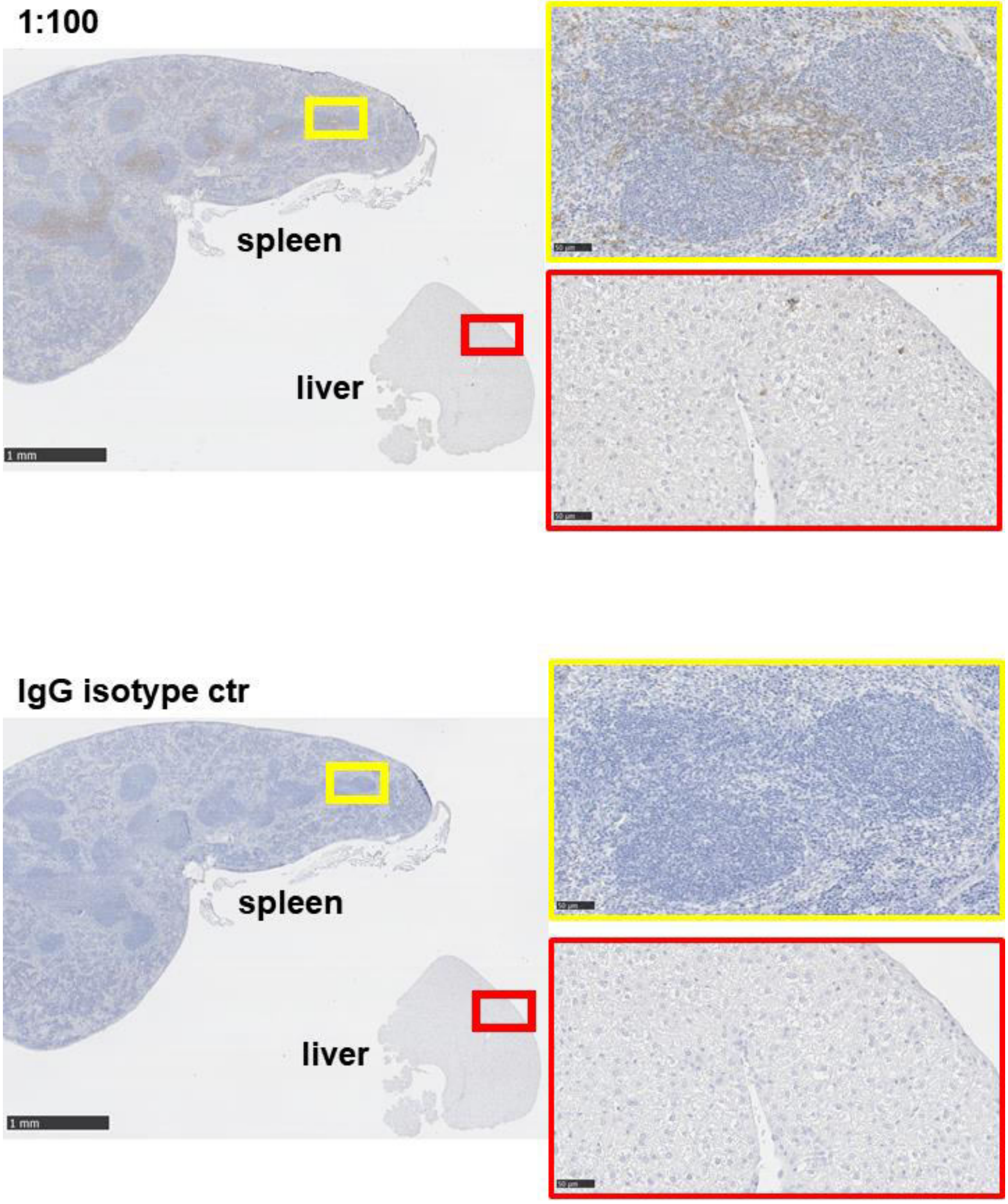

Supplementary figure 11: PD-1 IHC of spleen and liver sections (4 µm) showing full stain and an IgG isotype ctr stain (1:100). Bars indicate 1 mm in overview images and 50 µm in inlets.

1:200

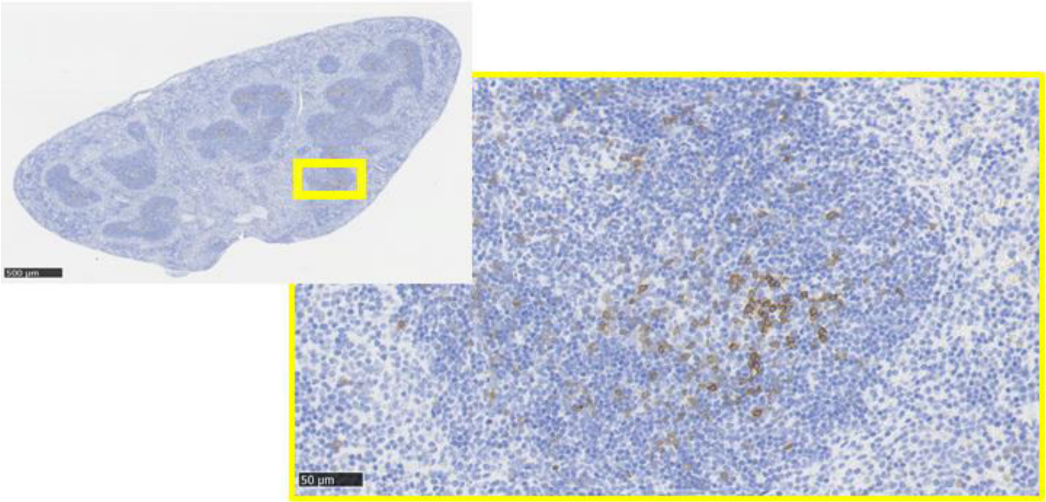

1:300

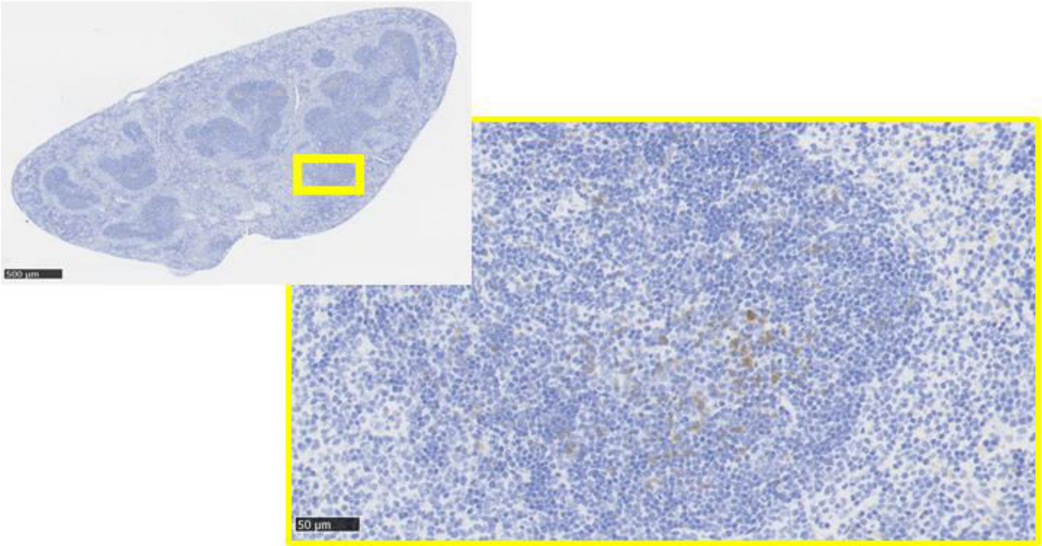

2nd Ab control

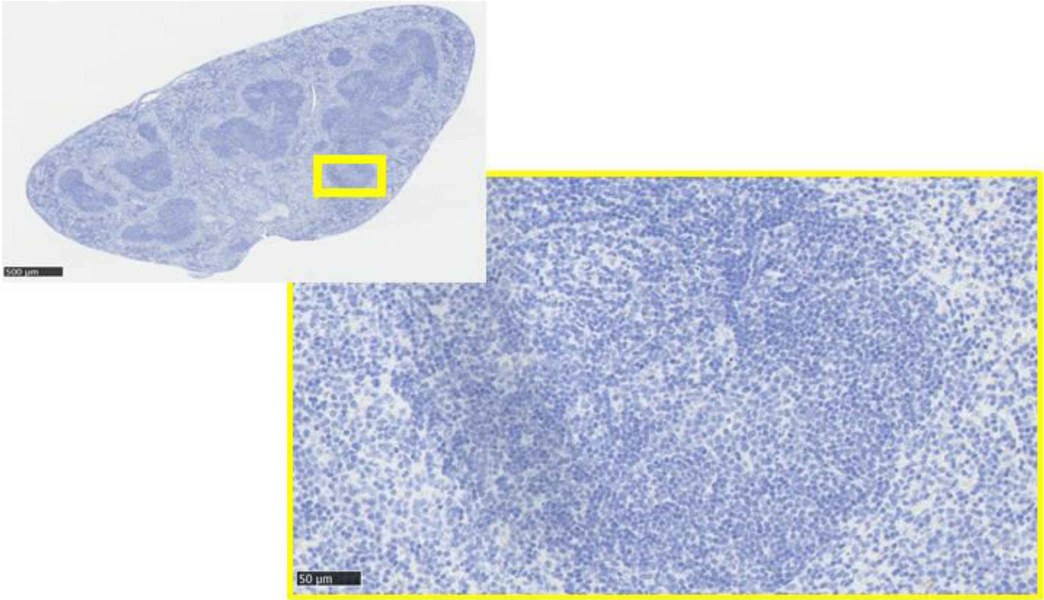

Supplementary figure 12: PD-1 IHC of spleen sections (4 µm) showing two different concentrations of primary Ab and a 2nd Ab ctr stain (1:200). Bars indicate 500 µm in overview images and 50 µm in inlets.

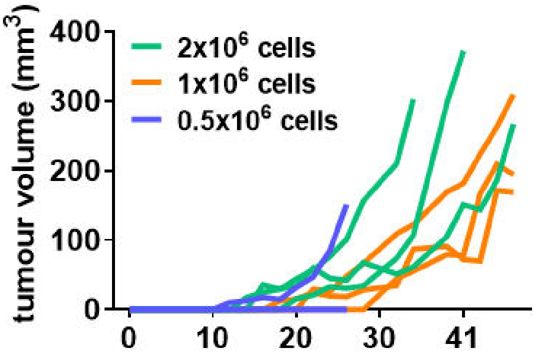

Supplementary figure 13: Tumour growth curves from cell titration studies for MOC1 mouse model (subcutaneous cell injection), n=3 mice per cell concentration.

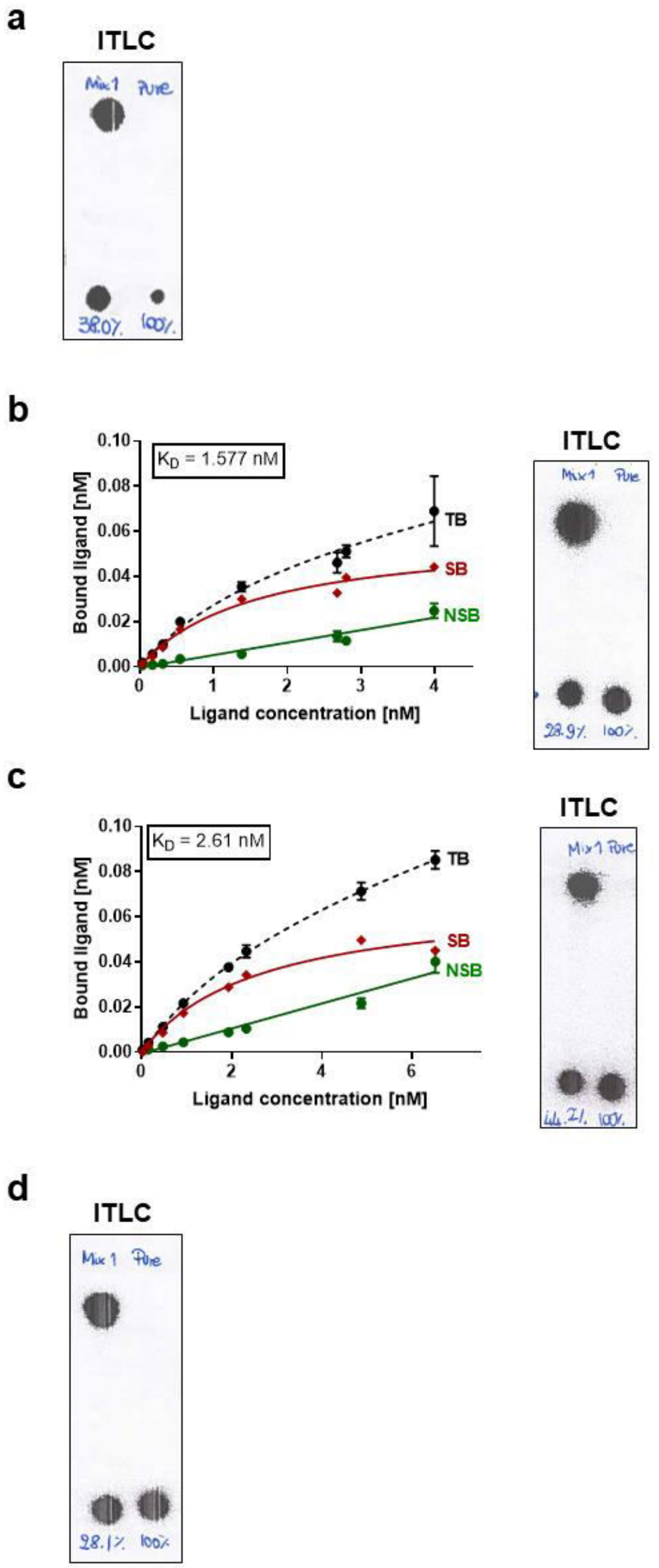

Supplementary figure 14: ITLC-SG strips of ^{89}Zr-DFO-PD-L1$_{mAb}$ produced for the studies shown in Fig.4-3a-b. Each ITLC-SG image shows samples of ^{89}Zr-DFO-PD-L1$_{mAb}$ pre- (left) and post-purification (right), while dots at the bottom of the strip indicate ^{89}Zr-DFO-

PD-L1$_{mAb}$ product and the black smear at the upper end of strip indicates free ^{89}Zr. ***a.*** *ITLC prior to Lindmo assay (second batch of DFO-PD-L1$_{mAb}$ conjugate).* ***b****. ITLC prior to saturation binding assay (first batch of DFO-PD-L1$_{mAb}$).* ***c****. ITLC prior to saturation binding assay (first batch of DFO-PD-L1$_{mAb}$).* ***d.*** *ITLC prior to saturation binding assay shown in Fig.4-3b (second batch of DFO-PD-L1$_{mAb}$).*

a

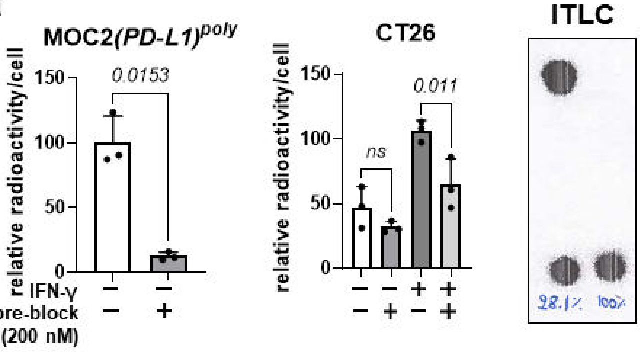

b

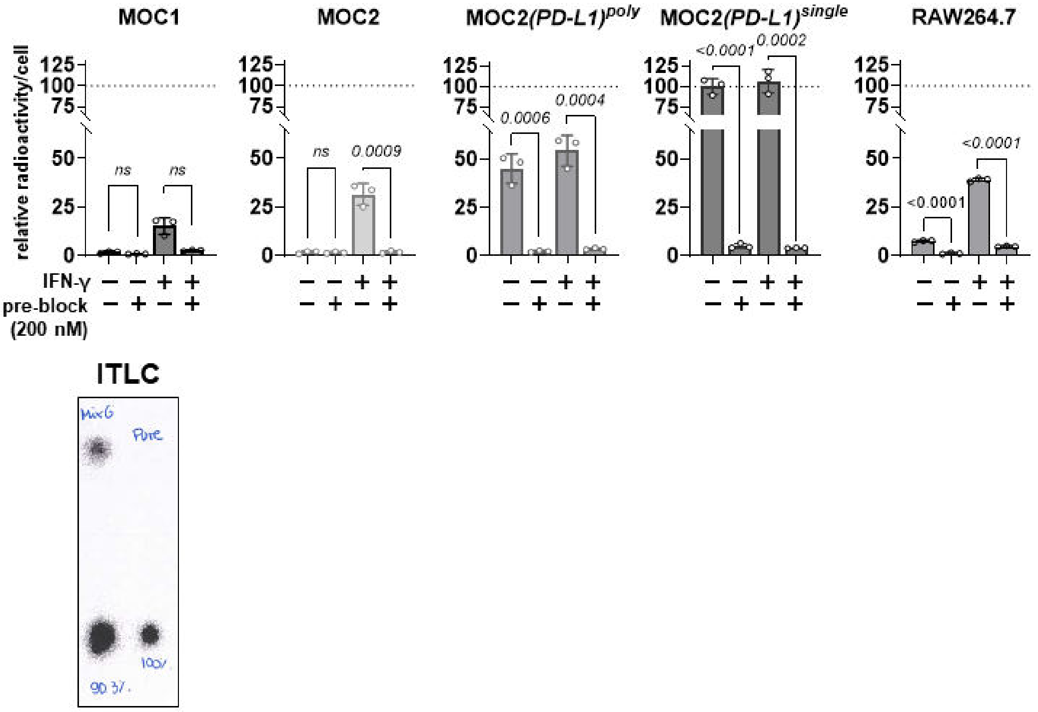

c

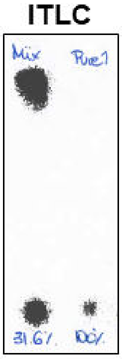

*Supplementary figure 15: ITLC-SG strips of ^{89}Zr-DFO-PD-L1$_{mAb}$ produced from the three different batches of DFO-PD-L1$_{mAb}$ and used in specificity of binding studies. Each ITLC-SG image shows samples of ^{89}Zr-DFO-PD-L1$_{mAb}$ pre- (left) and post-purification (right), while dots at the bottom of the strip indicate ^{89}Zr-DFO-PD-L1$_{mAb}$ product (loading site) and the black smear at the upper end of strip indicates free ^{89}Zr (solvent front). **a.** ITLC and corresponding specificity of binding assay (first batch of DFO-PD-L1$_{mAb}$). **b**. ITLC and corresponding specificity of binding assay (second batch of DFO-PD-L1$_{mAb}$). **c**. ITLC* *corresponding to specificity of binding assay shown in Fig.4-3c (third batch of DFO-PD-*$L1_{mAb}$*). Radioligand binding expressed as percentage of bound radioligand on untreated MOC2(PD-L1)*^{poly} *cells (a) or MOC2(PD-L1)*^{single} *cells (b). Bars show mean of n=3 ± SD. A Student's t-test with Welch correction (for MOC2(PD-L1)*^{poly} *in* ***a****) or a two-way ANOVA with Bonferroni correction for multiple comparisons (all other plots) was applied. P-values <0.05 were considered statistically significant and are indicated as values.*

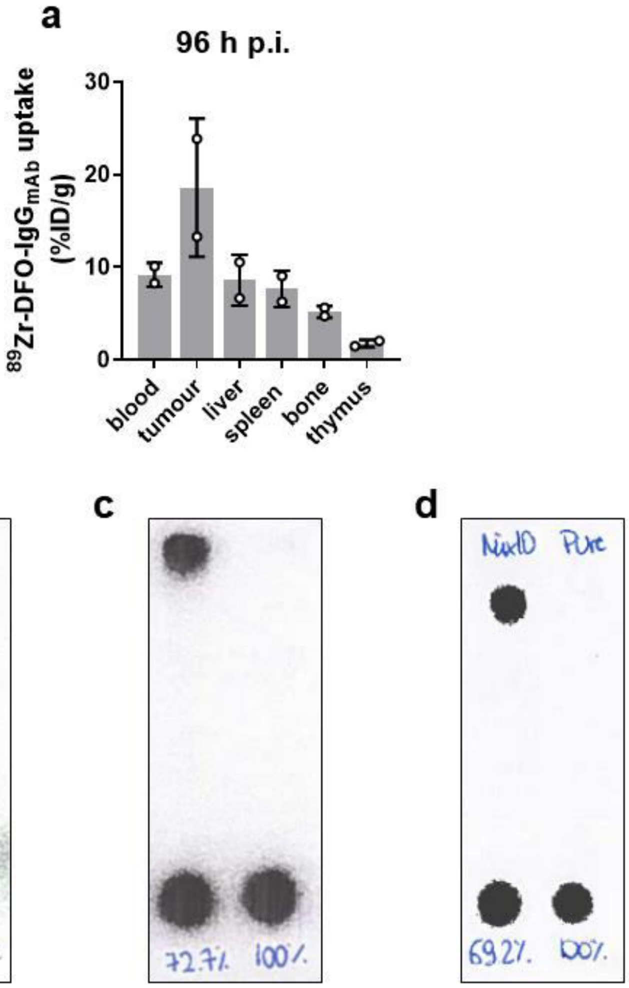

Supplementary figure 16: ***a.*** *Biodistribution data of* ^{89}*Zr-DFO-IgG*$_{mAb}$ *in MOC2 tumour-bearing mice at 96 h p.i.* ***b.-d.*** *ITLC-SG strips of* ^{89}*Zr-DFO-PD-L1*$_{mAb}$ *used for the studies presented in Fig.4-6. Each ITLC-SG image shows samples of* ^{89}*Zr-DFO-PD-L1*$_{mAb}$ *pre- (left) and post-purification (right), while dots at the bottom of the strip indicate* ^{89}*Zr-DFO-PD-L1*$_{mAb}$ *product (loading site) and the black smear at the upper end of strip indicates free* ^{89}*Zr (solvent front).*

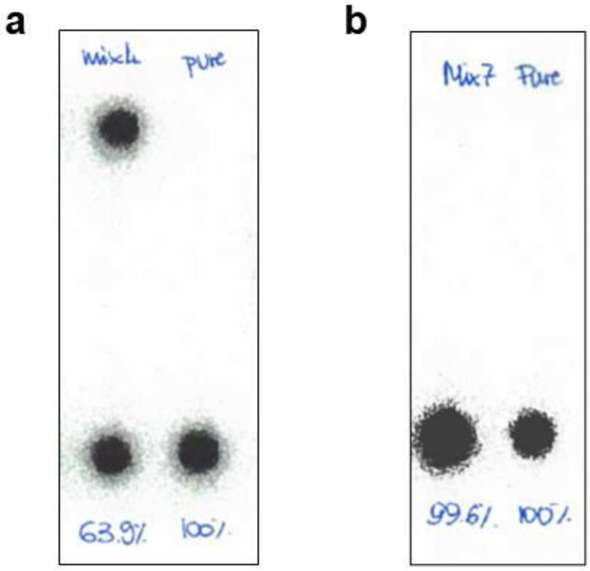

Supplementary figure 17: ITLC-SG strips of ^{89}Zr-DFO-PD-L1$_{mAb}$ used for the studies presented in Fig.4-7. Each ITLC-SG image shows samples of ^{89}Zr-DFO-PD-L1$_{mAb}$ pre- (left) and post-purification (right), while dots at the bottom of the strip indicate ^{89}Zr-DFO-PD-L1$_{mAb}$ product (loading site) and the black smear at the upper end of strip indicates free ^{89}Zr (solvent front). ***a****. 89Zr-DFO-PD-L1mAb used to inject MOC1 mouse model.* ***b****. ^{89}Zr-DFO-PD-L1$_{mAb}$ used to inject CT26 and MOC2(PD-L1)single mouse models.*

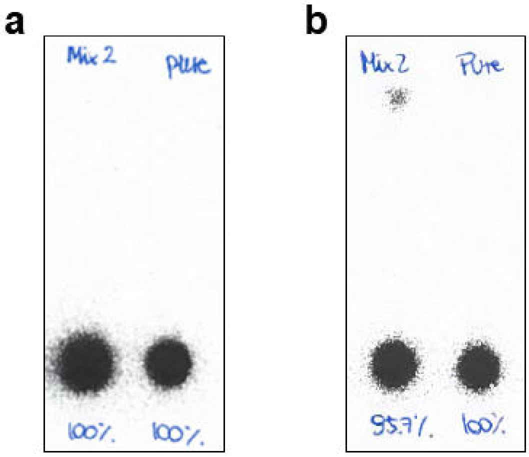

Supplementary figure 18: ITLC-SG strips of ^{89}Zr-DFO-IgG$_{mAb}$ used for the studies presented in Fig.4-8. Each ITLC-SG image shows samples of ^{89}Zr-DFO-IgG$_{mAb}$ pre- (left) and post-purification (right), while dots at the bottom of the strip indicate ^{89}Zr-DFO-PD-L1$_{mAb}$ product (loading site) and the black smear at the upper end of strip indicates free ^{89}Zr (solvent front). ***a.*** *ITLC from in vitro data.* ***b.*** *ITLC from in vivo data. Both studies were performed using the same batch of DFO-IgG$_{mAb}$ conjugate.*

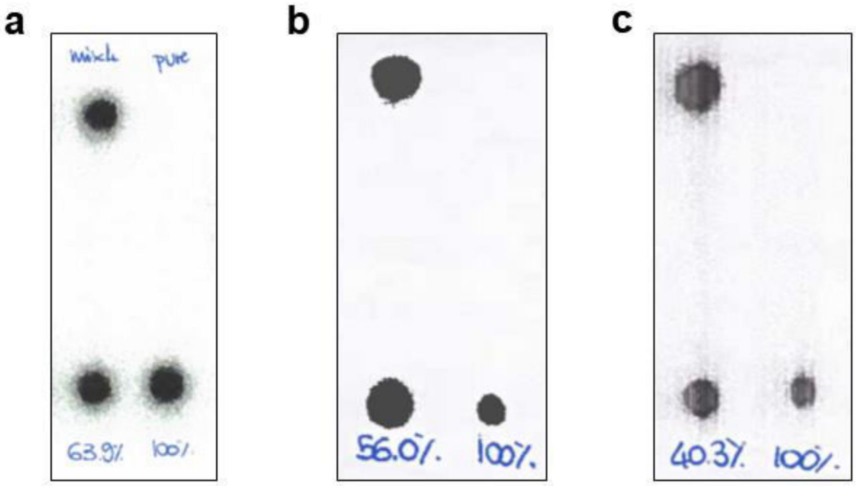

Supplementary figure 19: ITLC-SG strips of ^{89}*Zr-DFO-PD-L1*$_{mAb}$ *used for the studies presented in Fig.6-2 and 6-3. All three imaging studies (**a**, **b** and **c**) were performed with the second batch of DFO-PD-L1*$_{mAb}$ *conjugate. Each ITLC-SG image shows samples of* ^{89}*Zr-DFO-PD-L1*$_{mAb}$ *pre- (left) and post-purification (right), while dots at the bottom of the strip indicate* ^{89}*Zr-DFO-PD-L1*$_{mAb}$ *product (loading site) and the black smear at the upper end of strip indicates free* ^{89}*Zr (solvent front).*

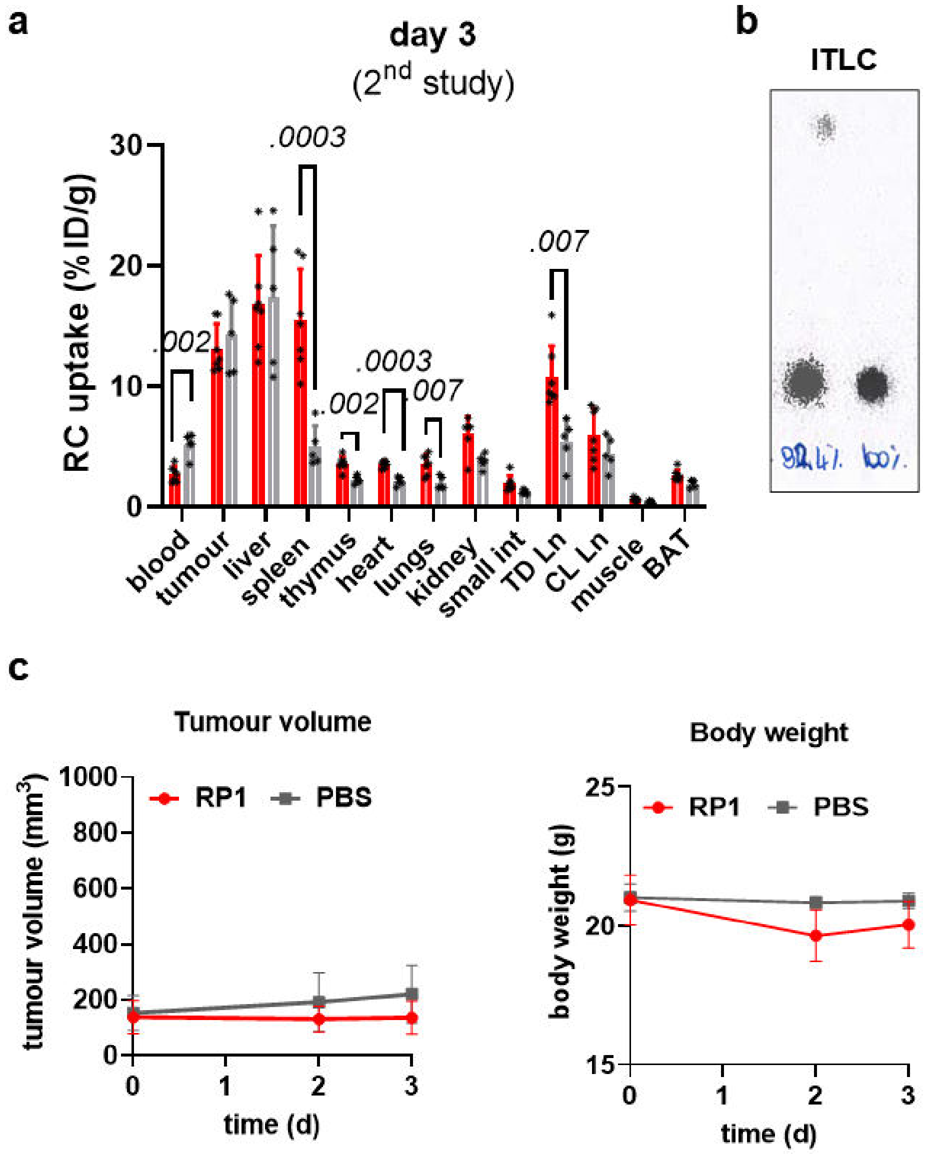

Supplementary figure 20: ***a.*** *Biodistribution chart of repeat study on day 3 after RP1 or PBS treatment in MOC1 mouse model. X-axis indicates radioconjugate (RC) uptake, i.e. ^{89}Zr-DFO-PD-L1$_{mAb}$. Abbreviations stand for small intestine (small int), tumour draining lymph node (TD Ln) and contralateral lymph node (CL Ln), brown adipose tissue (BAT). Multiple unpaired t-tests were applied with Benjamini-Hochberg method (FDR<1%), p-values >0.01 were considered statistically significant and are indicated in the bar chart.* ***b.*** *ITLC-SG strip of ^{89}Zr-DFO-PD-L1$_{mAb}$ used for this study. Image shows samples of ^{89}Zr-DFO-PD-L1$_{mAb}$ pre- (left) and post-purification (right), while dots at the bottom of the strip indicate ^{89}Zr-DFO-PD-L1$_{mAb}$ product (loading site) and the black smear at the upper end of strip indicates free ^{89}Zr (solvent front).* ***c****. Tumour volume and weight records from treatment initiation (day 0) until the day of PET imaging and biodistribution (day 3).*

Supplementary figure 21: ITLC-SG strips of ^{89}*Zr-DFO-PD-L1*$_{mAb}$ *used for the study presented in Fig.6-6 and 6-7. The ITLC-SG image shows samples of* ^{89}*Zr-DFO-PD-L1*$_{mAb}$ *pre- (left) and post-purification (right), while dots at the bottom of the strip indicate* ^{89}*Zr-DFO-PD-L1*$_{mAb}$ *product (loading site) and the black smear at the upper end of strip indicates free* ^{89}*Zr (solvent front).*

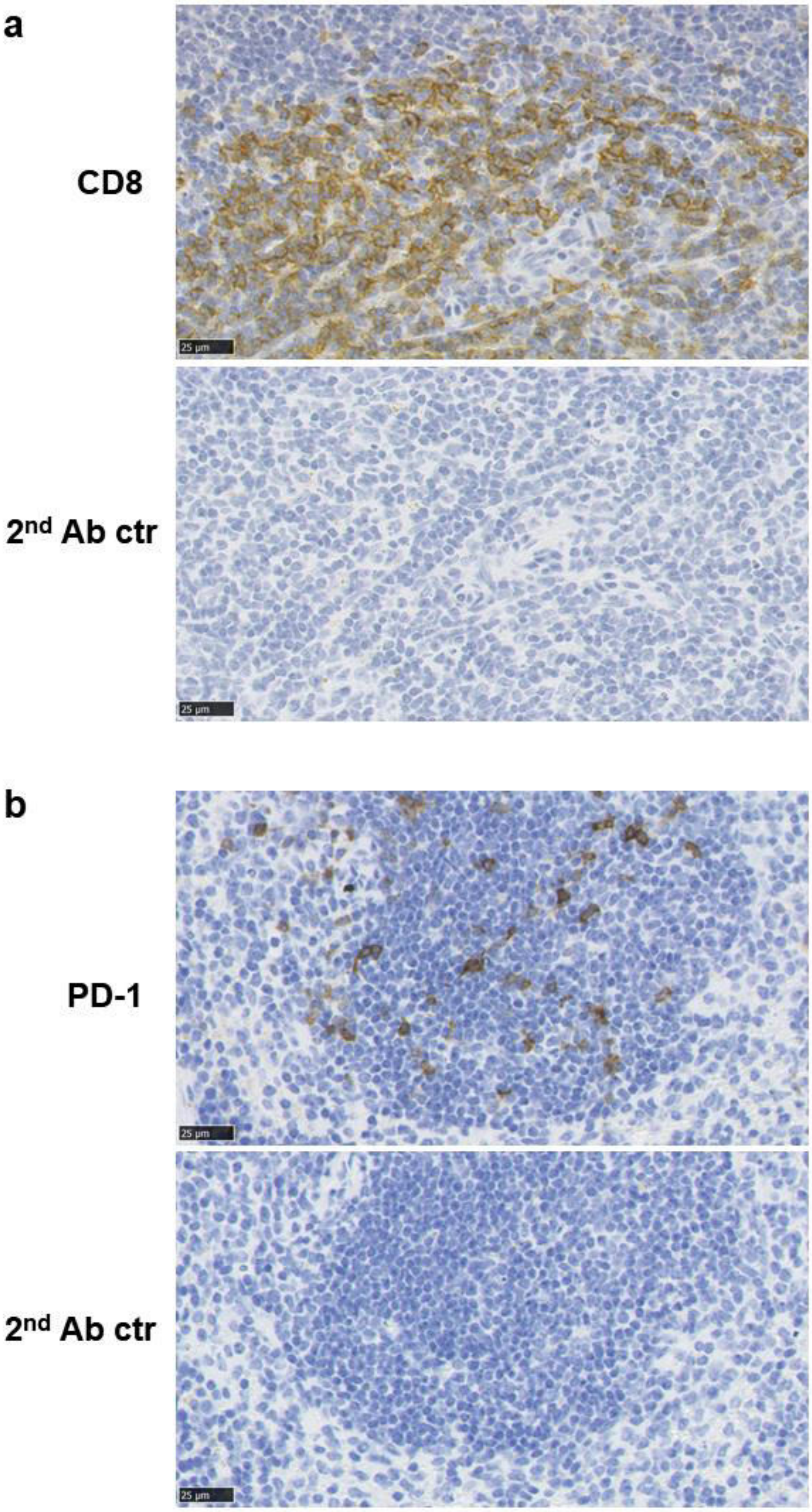

Supplementary figure 22: Control IHC stains corresponding to Fig. 6-14/15. ***a.*** *CD8 and 2nd Ab ctr IHC of spleen sections (4 µm).* ***b.*** *PD-1 and 2nd Ab ctr IHC of spleen sections (4 µm). Bars indicate 25 µm.*

List of figures

List of tables

List of references

Abbott, B.G., Case, J.A., Dorbala, S., Einstein, A.J., Galt, J.R., Pagnanelli, R., Bullock-Palmer, R.P., Soman, P., and Wells, R.G. (2018). Contemporary Cardiac SPECT Imaging-Innovations and Best Practices: An Information Statement from the American Society of Nuclear Cardiology. Journal of nuclear cardiology : official publication of the American Society of Nuclear Cardiology *25*, 1847-1860.

Abou, D.S., Ku, T., and Smith-Jones, P.M. (2011). In vivo biodistribution and accumulation of 89Zr in mice. Nuclear medicine and biology *38*, 675-681.

Aboulkheyr Es, H., Bigdeli, B., Zhand, S., Aref, A.R., Thiery, J.P., and Warkiani, M.E. (2021). Mesenchymal stem cells induce PD-L1 expression through the secretion of CCL5 in breast cancer cells. Journal of cellular physiology *236*, 3918-3928.

Adams, G.P., Schier, R., McCall, A.M., Simmons, H.H., Horak, E.M., Alpaugh, R.K., Marks, J.D., and Weiner, L.M. (2001). High affinity restricts the localization and tumor penetration of single-chain fv antibody molecules. Cancer research *61*, 4750-4755.

Adelstein, D.J. (2003). Systemic chemotherapy for squamous cell head and neck cancer. Expert opinion on pharmacotherapy *4*, 2151-2163.

Adonai, N., Adonai, N., Nguyen, K.N., Walsh, J., Iyer, M., Toyokuni, T., Phelps, M.E., McCarthy, T., McCarthy, D.W., and Gambhir, S.S. (2002). Ex vivo cell labeling with 64Cu-pyruvaldehyde-bis(N4-methylthiosemicarbazone) for imaging cell trafficking in mice with positron-emission tomography. Proc Natl Acad Sci U S A *99*, 3030-3035.

Ahmad, Z.A., Yeap, S.K., Ali, A.M., Ho, W.Y., Alitheen, N.B., and Hamid, M. (2012). scFv antibody: principles and clinical application. Clinical & developmental immunology *2012*, 980250.

Ahn, E., Araki, K., Hashimoto, M., Li, W., Riley, J.L., Cheung, J., Sharpe, A.H., Freeman, G.J., Irving, B.A., and Ahmed, R. (2018). Role of PD-1 during effector CD8 T cell differentiation. Proceedings of the National Academy of Sciences *115*, 4749-4754.

Aichele, P., Unsoeld, H., Koschella, M., Schweier, O., Kalinke, U., and Vucikuja, S. (2006). CD8 T cells specific for lymphocytic choriomeningitis virus require type I IFN receptor for clonal expansion. Journal of immunology (Baltimore, Md : 1950) *176*, 4525-4529.

Alemany, R., Balagué, C., and Curiel, D.T. (2000). Replicative adenoviruses for cancer therapy. Nat Biotechnol *18*, 723-727.

Alexander, C., and Rietschel, E.T. (2001). Bacterial lipopolysaccharides and innate immunity. Journal of endotoxin research *7*, 167-202.

Aloulou, M., Carr, E.J., Gador, M., Bignon, A., Liblau, R.S., Fazilleau, N., and Linterman, M.A. (2016). Follicular regulatory T cells can be specific for the immunizing antigen and derive from naive T cells. Nat Commun *7*, 10579.

Amin, M.B., Greene, F.L., Edge, S.B., Compton, C.C., Gershenwald, J.E., Brookland, R.K., Meyer, L., Gress, D.M., Byrd, D.R., and Winchester, D.P. (2017). The Eighth Edition AJCC Cancer Staging Manual: Continuing to build a bridge from a population-based to a more "personalized" approach to cancer staging. CA: a cancer journal for clinicians *67*, 93-99.

Andersen, M.N., Al-Karradi, S.N., Kragstrup, T.W., and Hokland, M. (2016). Elimination of erroneous results in flow cytometry caused by antibody binding to Fc receptors on human monocytes and macrophages. Cytometry Part A : the journal of the International Society for Analytical Cytology *89*, 1001-1009.

Anderson, C.D. (1932). THE APPARENT EXISTENCE OF EASILY DEFLECTABLE POSITIVES. Science (New York, NY) *76*, 238-239.

Anderson, C.J., and Ferdani, R. (2009). Copper-64 radiopharmaceuticals for PET imaging of cancer: advances in preclinical and clinical research. Cancer biotherapy & radiopharmaceuticals *24*, 379-393.

Anderson, K.G., Stromnes, I.M., and Greenberg, P.D. (2017). Obstacles Posed by the Tumor Microenvironment to T cell Activity: A Case for Synergistic Therapies. Cancer cell *31*, 311-325.

Anderson, N.M., and Simon, M.C. (2020). The tumor microenvironment. Current biology : CB *30*, R921-r925.

Andratschke, M., Hagedorn, H., and Nerlich, A. (2015). Expression of the Epithelial Cell Adhesion Molecule and Cytokeratin 8 in Head and Neck Squamous Cell Cancer: A Comparative Study. Anticancer research *35*, 3953-3960.

Andreyev, A., Sitek, A., and Celler, A. (2014). EM reconstruction of dual isotope PET using staggered injections and prompt gamma positron emitters. Medical physics *41*, 022501.

Andtbacka, R.H., Kaufman, H.L., Collichio, F., Amatruda, T., Senzer, N., Chesney, J., Delman, K.A., Spitler, L.E., Puzanov, I., Agarwala, S.S., *et al.* (2015). Talimogene Laherparepvec Improves Durable Response Rate in Patients With Advanced Melanoma. Journal of clinical oncology : official journal of the American Society of Clinical Oncology *33*, 2780-2788.

Ang, K.K., Berkey, B.A., Tu, X., Zhang, H.Z., Katz, R., Hammond, E.H., Fu, K.K., and Milas, L. (2002). Impact of epidermal growth factor receptor expression on survival and pattern of relapse in patients with advanced head and neck carcinoma. Cancer research *62*, 7350-7356.

Angarita, F.A., Acuna, S.A., Ottolino-Perry, K., Zerhouni, S., and McCart, J.A. (2013). Mounting a strategic offense: fighting tumor vasculature with oncolytic viruses. Trends in molecular medicine *19*, 378-392.

Antonia, S.J., Villegas, A., Daniel, D., Vicente, D., Murakami, S., Hui, R., Yokoi, T., Chiappori, A., Lee, K.H., de Wit, M., *et al.* (2017). Durvalumab after Chemoradiotherapy in Stage III Non-Small-Cell Lung Cancer. The New England journal of medicine *377*, 1919-1929.

Argiris, A., Harrington, K., Tahara, M., Ferris, R., Gillison, M., Fayette, J., Daste, A., Koralewski, P., Nin, R.M., and Saba, N. (2021). LBA36 Nivolumab (N)+ ipilimumab (I) vs EXTREME as first-line (1L) treatment (tx) for recurrent/metastatic squamous cell carcinoma of the head and neck (R/M SCCHN): Final results of CheckMate 651. Annals of Oncology *32*, S1310-S1311.

Aroldi, F., Sacco, J., Harrington, K., Olsson-Brown, A., Nanclares, P., Menezes, L., Bommareddy, P., Thomas, S., Kaufman, H., Samakoglu, S., *et al.* (2020). 421 Initial results of a phase 1 trial of RP2, a first in class, enhanced potency, anti-CTLA-4 antibody expressing, oncolytic HSV as single agent and combined with nivolumab in patients with solid tumors. Journal for immunotherapy of cancer *8*, A256-A257.

Atsaves, V., Tsesmetzis, N., Chioureas, D., Kis, L., Leventaki, V., Drakos, E., Panaretakis, T., Grander, D., Medeiros, L.J., Young, K.H., *et al.* (2017). PD-L1 is commonly expressed and transcriptionally regulated by STAT3 and MYC in ALK-negative anaplastic large-cell lymphoma. Leukemia *31*, 1633-1637.

Austyn, J.M., and Gordon, S. (1981). F4/80, a monoclonal antibody directed specifically against the mouse macrophage. European journal of immunology *11*, 805-815.

Azuma, T., Yao, S., Zhu, G., Flies, A.S., Flies, S.J., and Chen, L. (2008). B7-H1 is a ubiquitous antiapoptotic receptor on cancer cells. Blood *111*, 3635-3643.

Badawi, R.D., Shi, H., Hu, P., Chen, S., Xu, T., Price, P.M., Ding, Y., Spencer, B.A., Nardo, L., Liu, W.*, et al.* (2019). First Human Imaging Studies with the EXPLORER Total-Body PET Scanner. Journal of nuclear medicine : official publication, Society of Nuclear Medicine *60*, 299-303.

Balar, A.V., Castellano, D., O'Donnell, P.H., Grivas, P., Vuky, J., Powles, T., Plimack, E.R., Hahn, N.M., de Wit, R., Pang, L.*, et al.* (2017a). First-line pembrolizumab in cisplatin-ineligible patients with locally advanced and unresectable or metastatic urothelial cancer (KEYNOTE-052): a multicentre, single-arm, phase 2 study. The Lancet Oncology *18*, 1483-1492.

Balar, A.V., Galsky, M.D., Rosenberg, J.E., Powles, T., Petrylak, D.P., Bellmunt, J., Loriot, Y., Necchi, A., Hoffman-Censits, J., Perez-Gracia, J.L.*, et al.* (2017b). Atezolizumab as first-line treatment in cisplatin-ineligible patients with locally advanced and metastatic urothelial carcinoma: a single-arm, multicentre, phase 2 trial. Lancet (London, England) *389*, 67-76.

Barber, G.N. (2015). STING: infection, inflammation and cancer. Nature reviews Immunology *15*, 760-770.

Bartnicka, J.J., and Blower, P.J. (2018). Insights into Trace Metal Metabolism in Health and Disease from PET: "PET Metallomics". Journal of nuclear medicine : official publication, Society of Nuclear Medicine *59*, 1355-1359.

Batlle, E., and Massagué, J. (2019). Transforming Growth Factor-β Signaling in Immunity and Cancer. Immunity *50*, 924-940.

Bé, M.M., Cassette, P., Lépy, M.C., Amiot, M.N., Kossert, K., Nähle, O.J., Ott, O., Wanke, C., Dryak, P., Ratel, G.*, et al.* (2012). Standardization, decay data measurements and evaluation of 64Cu. Applied radiation and isotopes : including data, instrumentation and methods for use in agriculture, industry and medicine *70*, 1894-1899.

Beck, L., Leroy, C., Salaün, C., Margall-Ducos, G., Desdouets, C., and Friedlander, G. (2009). Identification of a novel function of PiT1 critical for cell proliferation and independent of its phosphate transport activity. The Journal of biological chemistry *284*, 31363-31374.

Bedoui, S., and Greyer, M. (2014). The role of dendritic cells in immunity against primary Herpes Simplex Virus infections. Frontiers in Microbiology *5*.

Behrens, C.R., and Liu, B. (2014). Methods for site-specific drug conjugation to antibodies. mAbs *6*, 46-53.

Bellmunt, J., de Wit, R., Vaughn, D.J., Fradet, Y., Lee, J.L., Fong, L., Vogelzang, N.J., Climent, M.A., Petrylak, D.P., Choueiri, T.K., *et al.* (2017). Pembrolizumab as Second-Line Therapy for Advanced Urothelial Carcinoma. The New England journal of medicine *376*, 1015-1026.

Bendtzen, K. (2015). Immunogenicity of Anti-TNF-α Biotherapies: II. Clinical Relevance of Methods Used for Anti-Drug Antibody Detection. Frontiers in immunology *6*, 109.

Benencia, F., Courreges, M.C., Conejo-García, J.R., Buckanovich, R.J., Zhang, L., Carroll, R.H., Morgan, M.A., and Coukos, G. (2005). Oncolytic HSV exerts direct antiangiogenic activity in ovarian carcinoma. Human gene therapy *16*, 765-778.

Benjamini, Y., and Hochberg, Y. (1995). Controlling the False Discovery Rate: A Practical and Powerful Approach to Multiple Testing. Journal of the Royal Statistical Society: Series B (Methodological) *57*, 289-300.

Bensch, F., van der Veen, E.L., Lub-de Hooge, M.N., Jorritsma-Smit, A., Boellaard, R., Kok, I.C., Oosting, S.F., Schröder, C.P., Hiltermann, T.J.N., van der Wekken, A.J., *et al.* (2018). (89)Zr-atezolizumab imaging as a non-invasive approach to assess clinical response to PD-L1 blockade in cancer. Nat Med *24*, 1852-1858.

Bernier, J., Domenge, C., Ozsahin, M., Matuszewska, K., Lefèbvre, J.L., Greiner, R.H., Giralt, J., Maingon, P., Rolland, F., Bolla, M., *et al.* (2004). Postoperative irradiation with or without concomitant chemotherapy for locally advanced head and neck cancer. The New England journal of medicine *350*, 1945-1952.

Bexelius, T.S., Wasti, A., and Chisholm, J.C. (2020). Mini-Review on Targeted Treatment of Desmoplastic Small Round Cell Tumor. Frontiers in oncology *10*, 518.

Bhatt, N.B., Pandya, D.N., and Wadas, T.J. (2018). Recent Advances in Zirconium-89 Chelator Development. Molecules *23*.

Biron, C.A., Nguyen, K.B., and Pien, G.C. (2002). Innate immune responses to LCMV infections: natural killer cells and cytokines. Current topics in microbiology and immunology *263*, 7-27.

Bischoff, J.R., Kirn, D.H., Williams, A., Heise, C., Horn, S., Muna, M., Ng, L., Nye, J.A., Sampson-Johannes, A., Fattaey, A., *et al.* (1996). An adenovirus mutant that replicates selectively in p53-deficient human tumor cells. Science (New York, NY) *274*, 373-376.

Bland, J.M., and Altman, D.G. (1999). Measuring agreement in method comparison studies. Statistical methods in medical research *8*, 135-160.

Boellaard, R., Krak, N.C., Hoekstra, O.S., and Lammertsma, A.A. (2004). Effects of Noise, Image Resolution, and ROI Definition on the Accuracy of Standard Uptake Values: A Simulation Study. Journal of Nuclear Medicine *45*, 1519-1527.

Boes, M., and Meyer-Wentrup, F. (2015). TLR3 triggering regulates PD-L1 (CD274) expression in human neuroblastoma cells. Cancer letters *361*, 49-56.

Boffa, D.J., Graf, R.P., Salazar, M.C., Hoag, J., Lu, D., Krupa, R., Louw, J., Dugan, L., Wang, Y., Landers, M.*, et al.* (2017). Cellular Expression of PD-L1 in the Peripheral Blood of Lung Cancer Patients is Associated with Worse Survival. Cancer epidemiology, biomarkers & prevention : a publication of the American Association for Cancer Research, cosponsored by the American Society of Preventive Oncology *26*, 1139-1145.

Börjesson, P.K., Jauw, Y.W., de Bree, R., Roos, J.C., Castelijns, J.A., Leemans, C.R., van Dongen, G.A., and Boellaard, R. (2009). Radiation dosimetry of 89Zr-labeled chimeric monoclonal antibody U36 as used for immuno-PET in head and neck cancer patients. Journal of nuclear medicine : official publication, Society of Nuclear Medicine *50*, 1828-1836.

Boros, E., and Packard, A.B. (2019). Radioactive Transition Metals for Imaging and Therapy. Chemical reviews *119*, 870-901.

Børresen, B., Hansen, A.E., Fliedner, F.P., Henriksen, J.R., Elema, D.R., Brandt-Larsen, M., Kristensen, L.K., Kristensen, A.T., Andresen, T.L., and Kjær, A. (2020). Noninvasive Molecular Imaging of the Enhanced Permeability and Retention Effect by (64)Cu-Liposomes: In vivo Correlations with (68)Ga-RGD, Fluid Pressure, Diffusivity and (18)F-FDG. International journal of nanomedicine *15*, 8571-8581.

Boswell, C.A., Tesar, D.B., Mukhyala, K., Theil, F.P., Fielder, P.J., and Khawli, L.A. (2010). Effects of charge on antibody tissue distribution and pharmacokinetics. Bioconjugate chemistry *21*, 2153-2163.

Bouleau, A., Nozach, H., Dubois, S., Kereselidze, D., Chevaleyre, C., Wang, C.I., Evans, M.J., Lebon, V., Maillère, B., and Truillet, C. (2022). Optimizing Immuno-PET Imaging of Tumor PD-L1 Expression: Pharmacokinetic, Biodistribution, and Dosimetric Comparisons of (89)Zr-Labeled Anti-PD-L1 Antibody Formats. Journal of nuclear medicine : official publication, Society of Nuclear Medicine *63*, 1259-1265.

Bourgeois-Daigneault, M.C., Roy, D.G., Aitken, A.S., El Sayes, N., Martin, N.T., Varette, O., Falls, T., St-Germain, L.E., Pelin, A., Lichty, B.D., *et al.* (2018). Neoadjuvant oncolytic virotherapy before surgery sensitizes triple-negative breast cancer to immune checkpoint therapy. Science translational medicine *10*.

Boyman, O., and Sprent, J. (2012). The role of interleukin-2 during homeostasis and activation of the immune system. Nature reviews Immunology *12*, 180-190.

Brahmer, J., Reckamp, K.L., Baas, P., Crinò, L., Eberhardt, W.E., Poddubskaya, E., Antonia, S., Pluzanski, A., Vokes, E.E., Holgado, E., *et al.* (2015). Nivolumab versus Docetaxel in Advanced Squamous-Cell Non-Small-Cell Lung Cancer. The New England journal of medicine *373*, 123-135.

Brattain, M.G., Strobel-Stevens, J., Fine, D., Webb, M., and Sarrif, A.M. (1980). Establishment of mouse colonic carcinoma cell lines with different metastatic properties. Cancer research *40*, 2142-2146.

Bray, F., Ferlay, J., Soerjomataram, I., Siegel, R.L., Torre, L.A., and Jemal, A. (2018). Global cancer statistics 2018: GLOBOCAN estimates of incidence and mortality worldwide for 36 cancers in 185 countries. CA: a cancer journal for clinicians *68*, 394-424.

Breitbach, C.J., De Silva, N.S., Falls, T.J., Aladl, U., Evgin, L., Paterson, J., Sun, Y.Y., Roy, D.G., Rintoul, J.L., Daneshmand, M., *et al.* (2011). Targeting Tumor Vasculature With an Oncolytic Virus. Molecular Therapy *19*, 886-894.

Breitbach, C.J., Moon, A., Burke, J., Hwang, T.H., and Kirn, D.H. (2015). A Phase 2, Open-Label, Randomized Study of Pexa-Vec (JX-594) Administered by Intratumoral Injection in Patients with Unresectable Primary Hepatocellular Carcinoma. Methods in molecular biology (Clifton, NJ) *1317*, 343-357.

Breitbach, C.J., Paterson, J.M., Lemay, C.G., Falls, T.J., McGuire, A., Parato, K.A., Stojdl, D.F., Daneshmand, M., Speth, K., Kirn, D., *et al.* (2007). Targeted inflammation during oncolytic virus therapy severely compromises tumor blood flow. Molecular therapy : the journal of the American Society of Gene Therapy *15*, 1686-1693.

Brooks, A.R., Harkins, R.N., Wang, P., Qian, H.S., Liu, P., and Rubanyi, G.M. (2004). Transcriptional silencing is associated with extensive methylation of the CMV promoter following adenoviral gene delivery to muscle. The Journal of Gene Medicine *6*, 395-404.

Broos, K., Keyaerts, M., Lecocq, Q., Renmans, D., Nguyen, T., Escors, D., Liston, A., Raes, G., Breckpot, K., and Devoogdt, N. (2017). Non-invasive assessment of murine PD-L1 levels in syngeneic tumor models by nuclear imaging with nanobody tracers. Oncotarget *8*, 41932-41946.

Broos, K., Lecocq, Q., Keersmaecker, B.D., Raes, G., Corthals, J., Lion, E., Thielemans, K., Devoogdt, N., Keyaerts, M., and Breckpot, K. (2019). Single Domain Antibody-Mediated Blockade of Programmed Death-Ligand 1 on Dendritic Cells Enhances CD8 T-cell Activation and Cytokine Production. Vaccines (Basel) *7*, 85.

Brown, E.B., Boucher, Y., Nasser, S., and Jain, R.K. (2004). Measurement of macromolecular diffusion coefficients in human tumors. Microvascular research *67*, 231-236.

Brown, J.A., Dorfman, D.M., Ma, F.R., Sullivan, E.L., Munoz, O., Wood, C.R., Greenfield, E.A., and Freeman, G.J. (2003). Blockade of programmed death-1 ligands on dendritic cells enhances T cell activation and cytokine production. Journal of immunology (Baltimore, Md : 1950) *170*, 1257-1266.

Brunnström, H., Johansson, A., Westbom-Fremer, S., Backman, M., Djureinovic, D., Patthey, A., Isaksson-Mettävainio, M., Gulyas, M., and Micke, P. (2017). PD-L1 immunohistochemistry in clinical diagnostics of lung cancer: inter-pathologist variability is higher than assay variability. Modern pathology : an official journal of the United States and Canadian Academy of Pathology, Inc *30*, 1411-1421.

Buchbender, C., Heusner, T.A., Lauenstein, T.C., Bockisch, A., and Antoch, G. (2012). Oncologic PET/MRI, part 1: tumors of the brain, head and neck, chest, abdomen, and pelvis. Journal of nuclear medicine : official publication, Society of Nuclear Medicine *53*, 928-938.

Burr, M.L., Sparbier, C.E., Chan, Y.C., Williamson, J.C., Woods, K., Beavis, P.A., Lam, E.Y.N., Henderson, M.A., Bell, C.C., Stolzenburg, S., *et al.* (2017). CMTM6 maintains the expression of PD-L1 and regulates anti-tumour immunity. Nature *549*, 101-105.

Burtness, B., Harrington, K.J., Greil, R., Soulieres, D., Tahara, M., de Castro, G., Jr., Psyrri, A., Baste, N., Neupane, P., Bratland, A., *et al.* (2019). Pembrolizumab alone or with chemotherapy versus cetuximab with chemotherapy for recurrent or metastatic squamous cell carcinoma of the head and neck (KEYNOTE-048): a randomised, open-label, phase 3 study. Lancet (London, England) *394*, 1915-1928.

Butte, M.J., Keir, M.E., Phamduy, T.B., Sharpe, A.H., and Freeman, G.J. (2007). Programmed death-1 ligand 1 interacts specifically with the B7-1 costimulatory molecule to inhibit T cell responses. Immunity *27*, 111-122.

Cantoni, C., Wurzer, H., Thomas, C., and Vitale, M. (2020). Escape of tumor cells from the NK cell cytotoxic activity. Journal of leukocyte biology *108*, 1339-1360.

Carbotti, G., Barisione, G., Airoldi, I., Mezzanzanica, D., Bagnoli, M., Ferrero, S., Petretto, A., Fabbi, M., and Ferrini, S. (2015). IL-27 induces the expression of IDO and PD-L1 in human cancer cells. Oncotarget *6*, 43267-43280.

Carmeliet, P., and Jain, R.K. (2011). Molecular mechanisms and clinical applications of angiogenesis. Nature *473*, 298-307.

Carter, G.C., Law, M., Hollinshead, M., and Smith, G.L. (2005). Entry of the vaccinia virus intracellular mature virion and its interactions with glycosaminoglycans. The Journal of general virology *86*, 1279-1290.

Casey, S.C., Tong, L., Li, Y., Do, R., Walz, S., Fitzgerald, K.N., Gouw, A.M., Baylot, V., Gütgemann, I., Eilers, M.*, et al.* (2016). MYC regulates the antitumor immune response through CD47 and PD-L1. Science (New York, NY) *352*, 227-231.

Castaldi, P., Leccisotti, L., Bussu, F., Miccichè, F., and Rufini, V. (2013). Role of (18)F-FDG PET-CT in head and neck squamous cell carcinoma. Acta otorhinolaryngologica Italica : organo ufficiale della Societa italiana di otorinolaringologia e chirurgia cervico-facciale *33*, 1-8.

Castaldi, P., Rufini, V., Bussu, F., Miccichè, F., Dinapoli, N., Autorino, R., Lago, M., De Corso, E., Almadori, G., Galli, J.*, et al.* (2012). Can "early" and "late"18F-FDG PET-CT be used as prognostic factors for the clinical outcome of patients with locally advanced head and neck cancer treated with radio-chemotherapy? Radiotherapy and oncology : journal of the European Society for Therapeutic Radiology and Oncology *103*, 63-68.

Chan, A.C., and Carter, P.J. (2010). Therapeutic antibodies for autoimmunity and inflammation. Nature reviews Immunology *10*, 301-316.

Chang, T.T., Jabs, C., Sobel, R.A., Kuchroo, V.K., and Sharpe, A.H. (1999). Studies in B7-deficient mice reveal a critical role for B7 costimulation in both induction and effector phases of experimental autoimmune encephalomyelitis. The Journal of experimental medicine *190*, 733-740.

Chatterjee, S., Lesniak, W.G., Gabrielson, M., Lisok, A., Wharram, B., Sysa-Shah, P., Azad, B.B., Pomper, M.G., and Nimmagadda, S. (2016). A humanized antibody for imaging immune checkpoint ligand PD-L1 expression in tumors. Oncotarget *7*, 10215-10227.

Chaturvedi, A.K., Engels, E.A., Pfeiffer, R.M., Hernandez, B.Y., Xiao, W., Kim, E., Jiang, B., Goodman, M.T., Sibug-Saber, M., Cozen, W.*, et al.* (2011). Human papillomavirus and rising oropharyngeal cancer incidence in the United States. Journal of clinical oncology : official journal of the American Society of Clinical Oncology *29*, 4294-4301.

Chaturvedi, A.K., Graubard, B.I., Broutian, T., Pickard, R.K., Tong, Z.Y., Xiao, W., Kahle, L., and Gillison, M.L. (2015). NHANES 2009-2012 Findings: Association of Sexual Behaviors with Higher Prevalence of Oral Oncogenic Human Papillomavirus Infections in U.S. Men. Cancer research *75*, 2468-2477.

Chaudhri, A., Xiao, Y., Klee, A.N., Wang, X., Zhu, B., and Freeman, G.J. (2018). PD-L1 Binds to B7-1 Only In Cis on the Same Cell Surface. Cancer immunology research *6*, 921-929.

Chaurasiya, S., Yang, A., Kang, S., Lu, J., Kim, S.I., Park, A.K., Sivanandam, V., Zhang, Z., Woo, Y., Warner, S.G.*, et al.* (2020). Oncolytic poxvirus CF33-hNIS-ΔF14.5 favorably modulates tumor immune microenvironment and works synergistically with anti-PD-L1 antibody in a triple-negative breast cancer model. Oncoimmunology *9*, 1729300.

Chemnitz, J.M., Parry, R.V., Nichols, K.E., June, C.H., and Riley, J.L. (2004). SHP-1 and SHP-2 associate with immunoreceptor tyrosine-based switch motif of programmed death 1 upon primary human T cell stimulation, but only receptor ligation prevents T cell activation. Journal of immunology (Baltimore, Md : 1950) *173*, 945-954.

Chen, S., Crabill, G.A., Pritchard, T.S., McMiller, T.L., Wei, P., Pardoll, D.M., Pan, F., and Topalian, S.L. (2019). Mechanisms regulating PD-L1 expression on tumor and immune cells. Journal for immunotherapy of cancer *7*, 305.

Chen, X., and Song, E. (2019). Turning foes to friends: targeting cancer-associated fibroblasts. Nature reviews Drug discovery *18*, 99-115.

Chentoufi, A.A., Kritzer, E., Tran, M.V., Dasgupta, G., Lim, C.H., Yu, D.C., Afifi, R.E., Jiang, X., Carpenter, D., Osorio, N.*, et al.* (2011). The herpes simplex virus 1 latency-associated transcript promotes functional exhaustion of virus-specific CD8+ T cells in latently infected trigeminal ganglia: a novel immune evasion mechanism. Journal of virology *85*, 9127-9138.

Cherry, S.R. (2009). Multimodality imaging: beyond PET/CT and SPECT/CT. Seminars in nuclear medicine *39*, 348-353.

Cherry, S.R., Jones, T., Karp, J.S., Qi, J., Moses, W.W., and Badawi, R.D. (2018). Total-Body PET: Maximizing Sensitivity to Create New Opportunities for Clinical Research and Patient Care. Journal of nuclear medicine : official publication, Society of Nuclear Medicine *59*, 3-12.

Chomet, M., van Dongen, G., and Vugts, D.J. (2021). State of the Art in Radiolabeling of Antibodies with Common and Uncommon Radiometals for Preclinical and Clinical Immuno-PET. Bioconjugate chemistry *32*, 1315-1330.

Chong, C.E., Lim, K.P., Gan, C.P., Marsh, C.A., Zain, R.B., Abraham, M.T., Prime, S.S., Teo, S.H., Silvio Gutkind, J., Patel, V*., et al.* (2012). Over-expression of MAGED4B increases cell migration and growth in oral squamous cell carcinoma and is associated with poor disease outcome. Cancer letters *321*, 18-26.

Chou, J., Kern, E.R., Whitley, R.J., and Roizman, B. (1990). Mapping of herpes simplex virus-1 neurovirulence to gamma 134.5, a gene nonessential for growth in culture. Science (New York, NY) *250*, 1262-1266.

Chou, J., and Roizman, B. (1994). Herpes simplex virus 1 gamma(1)34.5 gene function, which blocks the host response to infection, maps in the homologous domain of the genes expressed during growth arrest and DNA damage. Proc Natl Acad Sci U S A *91*, 5247-5251.

Chow, L.Q.M. (2020). Head and Neck Cancer. The New England journal of medicine *382*, 60-72.

Cillo, A.R., Kürten, C.H.L., Tabib, T., Qi, Z., Onkar, S., Wang, T., Liu, A., Duvvuri, U., Kim, S., Soose, R.J*., et al.* (2020). Immune Landscape of Viral- and Carcinogen-Driven Head and Neck Cancer. Immunity *52*, 183-199.e189.

Clynes, R.A., Towers, T.L., Presta, L.G., and Ravetch, J.V. (2000). Inhibitory Fc receptors modulate in vivo cytotoxicity against tumor targets. Nat Med *6*, 443-446.

Coca-Pelaz, A., Rodrigo, J.P., Suárez, C., Nixon, I.J., Mäkitie, A., Sanabria, A., Quer, M., Strojan, P., Bradford, C.R., Kowalski, L.P*., et al.* (2020). The risk of second primary tumors in head and neck cancer: A systematic review. Head & neck *42*, 456-466.

Cohen, E.E.W., Soulières, D., Le Tourneau, C., Dinis, J., Licitra, L., Ahn, M.J., Soria, A., Machiels, J.P., Mach, N., Mehra, R*., et al.* (2019). Pembrolizumab versus methotrexate, docetaxel, or cetuximab for recurrent or metastatic head-and-neck squamous cell carcinoma (KEYNOTE-040): a randomised, open-label, phase 3 study. Lancet (London, England) *393*, 156-167.

Cole, J.E., Navin, T.J., Cross, A.J., Goddard, M.E., Alexopoulou, L., Mitra, A.T., Davies, A.H., Flavell, R.A., Feldmann, M., and Monaco, C. (2011). Unexpected protective role for Toll-like receptor 3 in the arterial wall. Proc Natl Acad Sci U S A *108*, 2372-2377.

Cooper, J.S., Pajak, T.F., Forastiere, A.A., Jacobs, J., Campbell, B.H., Saxman, S.B., Kish, J.A., Kim, H.E., Cmelak, A.J., Rotman, M.*, et al.* (2004). Postoperative concurrent radiotherapy and chemotherapy for high-risk squamous-cell carcinoma of the head and neck. The New England journal of medicine *350*, 1937-1944.

Cooper, T., Biron, V.L., Fast, D., Tam, R., Carey, T., Shmulevitz, M., and Seikaly, H. (2015). Oncolytic activity of reovirus in HPV positive and negative head and neck squamous cell carcinoma. Journal of otolaryngology - head & neck surgery = Le Journal d'oto-rhino-laryngologie et de chirurgie cervico-faciale *44*, 8.

Cosgrove, D., and Lassau, N. (2010). Imaging of perfusion using ultrasound. European journal of nuclear medicine and molecular imaging *37 Suppl 1*, S65-85.

Coyne, C.B., and Bergelson, J.M. (2005). CAR: a virus receptor within the tight junction. Advanced drug delivery reviews *57*, 869-882.

Crespo-Rodriguez, E., Bergerhoff, K., Bozhanova, G., Foo, S., Patin, E.C., Whittock, H., Buus, R., Haider, S., Muirhead, G., Thway, K.*, et al.* (2020). Combining BRAF inhibition with oncolytic herpes simplex virus enhances the immune-mediated antitumor therapy of BRAF-mutant thyroid cancer. Journal for immunotherapy of cancer *8*.

Cripe, T.P., Ngo, M.C., Geller, J.I., Louis, C.U., Currier, M.A., Racadio, J.M., Towbin, A.J., Rooney, C.M., Pelusio, A., Moon, A.*, et al.* (2015). Phase 1 study of intratumoral Pexa-Vec (JX-594), an oncolytic and immunotherapeutic vaccinia virus, in pediatric cancer patients. Molecular therapy : the journal of the American Society of Gene Therapy *23*, 602-608.

Critchley-Thorne, R.J., Simons, D.L., Yan, N., Miyahira, A.K., Dirbas, F.M., Johnson, D.L., Swetter, S.M., Carlson, R.W., Fisher, G.A., Koong, A.*, et al.* (2009). Impaired interferon signaling is a common immune defect in human cancer. Proc Natl Acad Sci U S A *106*, 9010-9015.

Cua, D.J., and Tato, C.M. (2010). Innate IL-17-producing cells: the sentinels of the immune system. Nature reviews Immunology *10*, 479-489.

Curiel, T.J., Wei, S., Dong, H., Alvarez, X., Cheng, P., Mottram, P., Krzysiek, R., Knutson, K.L., Daniel, B., Zimmermann, M.C.*, et al.* (2003). Blockade of B7-H1 improves myeloid dendritic cell-mediated antitumor immunity. Nat Med *9*, 562-567.

D'Souza, C.A., McBride, W.J., Sharkey, R.M., Todaro, L.J., and Goldenberg, D.M. (2011). High-yielding aqueous 18F-labeling of peptides via Al18F chelation. Bioconjugate chemistry *22*, 1793-1803.

Dahan, R., Sega, E., Engelhardt, J., Selby, M., Korman, A.J., and Ravetch, J.V. (2015). FcγRs Modulate the Anti-tumor Activity of Antibodies Targeting the PD-1/PD-L1 Axis. Cancer cell *28*, 285-295.

Davidson, S., Maini, M.K., and Wack, A. (2015). Disease-promoting effects of type I interferons in viral, bacterial, and coinfections. Journal of interferon & cytokine research : the official journal of the International Society for Interferon and Cytokine Research *35*, 252-264.

Day, C.P., Carter, J., Bonomi, C., Esposito, D., Crise, B., Ortiz-Conde, B., Hollingshead, M., and Merlino, G. (2009). Lentivirus-mediated bifunctional cell labeling for in vivo melanoma study. Pigment cell & melanoma research *22*, 283-295.

Day, C.P., Carter, J., Weaver Ohler, Z., Bonomi, C., El Meskini, R., Martin, P., Graff-Cherry, C., Feigenbaum, L., Tüting, T., Van Dyke, T.*, et al.* (2014). "Glowing head" mice: a genetic tool enabling reliable preclinical image-based evaluation of cancers in immunocompetent allografts. PloS one *9*, e109956.

de Kleijn, S., Langereis, J.D., Leentjens, J., Kox, M., Netea, M.G., Koenderman, L., Ferwerda, G., Pickkers, P., and Hermans, P.W. (2013). IFN-γ-stimulated neutrophils suppress lymphocyte proliferation through expression of PD-L1. PloS one *8*, e72249.

de Ruiter, E.J., Ooft, M.L., Devriese, L.A., and Willems, S.M. (2017). The prognostic role of tumor infiltrating T-lymphocytes in squamous cell carcinoma of the head and neck: A systematic review and meta-analysis. Oncoimmunology *6*, e1356148.

De Vos, J., Devoogdt, N., Lahoutte, T., and Muyldermans, S. (2013). Camelid single-domain antibody-fragment engineering for (pre)clinical in vivo molecular imaging applications: adjusting the bullet to its target. Expert opinion on biological therapy *13*, 1149-1160.

Demaison, C., Parsley, K., Brouns, G., Scherr, M., Battmer, K., Kinnon, C., Grez, M., and Thrasher, A.J. (2002). High-level transduction and gene expression in hematopoietic repopulating cells using a human immunodeficiency [correction of imunodeficiency] virus type 1-based lentiviral vector containing an internal spleen focus forming virus promoter. Human gene therapy *13*, 803-813.

Demir, M., Toklu, T., Abuqbeitah, M., Çetin, H., Sezgin, H.S., Yeyin, N., and Sönmezoğlu, K. (2018). Evaluation of PET Scanner Performance in PET/MR and PET/CT Systems: NEMA Tests. Molecular imaging and radionuclide therapy *27*, 10-18.

Deng, L., Liang, H., Burnette, B., Beckett, M., Darga, T., Weichselbaum, R.R., and Fu, Y.-X. (2014). Irradiation and anti–PD-L1 treatment synergistically promote antitumor immunity in mice. The Journal of Clinical Investigation *124*, 687-695.

Deng, R., Jin, F., Prabhu, S., and Iyer, S. (2012). Monoclonal antibodies: what are the pharmacokinetic and pharmacodynamic considerations for drug development? Expert opinion on drug metabolism & toxicology *8*, 141-160.

Dennler, P., Fischer, E., and Schibli, R. (2015). Antibody Conjugates: From Heterogeneous Populations to Defined Reagents. Antibodies *4*, 197-224.

Deri, M.A., Ponnala, S., Zeglis, B.M., Pohl, G., Dannenberg, J.J., Lewis, J.S., and Francesconi, L.C. (2014). Alternative chelator for ^{89}Zr radiopharmaceuticals: radiolabeling and evaluation of 3,4,3-(LI-1,2-HOPO). Journal of medicinal chemistry *57*, 4849-4860.

Derrick, B., and White, P. (2016). Why Welch's test is Type I error robust. TQMP *12*, 30-38.

DeVita, V.T., Lawrence, T.S., and Rosenberg, S.A. (2008). DeVita, Hellman, and Rosenberg's cancer: principles & practice of oncology, Vol 2 (Lippincott Williams & Wilkins).

Dillon, M.T., Bergerhoff, K.F., Pedersen, M., Whittock, H., Crespo-Rodriguez, E., Patin, E.C., Pearson, A., Smith, H.G., Paget, J.T.E., Patel, R.R., *et al.* (2019). ATR Inhibition Potentiates the Radiation-induced Inflammatory Tumor Microenvironment. Clinical cancer research : an official journal of the American Association for Cancer Research *25*, 3392-3403.

Dilworth, J.R., and Pascu, S.I. (2018). The chemistry of PET imaging with zirconium-89. Chemical Society reviews *47*, 2554-2571.

Dong, H., Strome, S.E., Salomao, D.R., Tamura, H., Hirano, F., Flies, D.B., Roche, P.C., Lu, J., Zhu, G., Tamada, K.*, et al.* (2002). Tumor-associated B7-H1 promotes T-cell apoptosis: a potential mechanism of immune evasion. Nat Med *8*, 793-800.

Dong, H., Zhu, G., Tamada, K., and Chen, L. (1999). B7-H1, a third member of the B7 family, co-stimulates T-cell proliferation and interleukin-10 secretion. Nat Med *5*, 1365-1369.

Dong, P., Xiong, Y., Yue, J., Hanley, S.J.B., and Watari, H. (2018). Tumor-Intrinsic PD-L1 Signaling in Cancer Initiation, Development and Treatment: Beyond Immune Evasion. Frontiers in oncology *8*, 386.

Dong, Y., Tu, R., Liu, H., and Qing, G. (2020). Regulation of cancer cell metabolism: oncogenic MYC in the driver's seat. Signal Transduction and Targeted Therapy *5*, 124.

Dorman, S.E., and Holland, S.M. (2000). Interferon-gamma and interleukin-12 pathway defects and human disease. Cytokine & growth factor reviews *11*, 321-333.

Doroshow, D.B., Bhalla, S., Beasley, M.B., Sholl, L.M., Kerr, K.M., Gnjatic, S., Wistuba, II, Rimm, D.L., Tsao, M.S., and Hirsch, F.R. (2021). PD-L1 as a biomarker of response to immune-checkpoint inhibitors. Nature reviews Clinical oncology.

Dranoff, G., Jaffee, E., Lazenby, A., Golumbek, P., Levitsky, H., Brose, K., Jackson, V., Hamada, H., Pardoll, D., and Mulligan, R.C. (1993). Vaccination with irradiated tumor cells engineered to secrete murine granulocyte-macrophage colony-stimulating factor stimulates potent, specific, and long-lasting anti-tumor immunity. Proceedings of the National Academy of Sciences *90*, 3539-3543.

Dunnett, C.W. (1955). A Multiple Comparison Procedure for Comparing Several Treatments with a Control. Journal of the American Statistical Association *50*, 1096-1121.

Dwivedi, R.C., Kazi, R., Agrawal, N., Chisholm, E., St Rose, S., Elmiyeh, B., Rennie, C., Pepper, C., Clarke, P.M., Kerawala, C.J.*, et al.* (2010). Comprehensive review of small bowel metastasis from head and neck squamous cell carcinoma. Oral oncology *46*, 330-335.

Elsner, C., and Bohne, J. (2017). The retroviral vector family: something for everyone. Virus genes *53*, 714-722.

Eppihimer, M.J., Gunn, J., Freeman, G.J., Greenfield, E.A., Chernova, T., Erickson, J., and Leonard, J.P. (2002). Expression and regulation of the PD-L1 immunoinhibitory molecule on microvascular endothelial cells. Microcirculation (New York, NY : 1994) *9*, 133-145.

Erber, R., Stöhr, R., Herlein, S., Giedl, C., Rieker, R.J., Fuchs, F., Ficker, J.H., Hartmann, A., Veltrup, E., Wirtz, R.M.*, et al.* (2017). Comparison of PD-L1 mRNA Expression Measured with the CheckPoint Typer® Assay with PD-L1 Protein Expression Assessed with Immunohistochemistry in Non-small Cell Lung Cancer. Anticancer research *37*, 6771-6778.

Errington, F., Steele, L., Prestwich, R., Harrington, K.J., Pandha, H.S., Vidal, L., de Bono, J., Selby, P., Coffey, M., Vile, R.*, et al.* (2008). Reovirus activates human dendritic cells to promote innate antitumor immunity. Journal of immunology (Baltimore, Md : 1950) *180*, 6018-6026.

Erstad, D.J., Sojoodi, M., Taylor, M.S., Ghoshal, S., Razavi, A.A., Graham-O'Regan, K.A., Bardeesy, N., Ferrone, C.R., Lanuti, M., Caravan, P.*, et al.* (2018). Orthotopic and heterotopic murine models of pancreatic cancer and their different responses to FOLFIRINOX chemotherapy. Dis Model Mech *11*, dmm034793.

Esaki, S., Goshima, F., Ozaki, H., Takano, G., Hatano, Y., Kawakita, D., Ijichi, K., Watanabe, T., Sato, Y., Murata, T.*, et al.* (2020). Oncolytic activity of HF10 in head and neck squamous cell carcinomas. Cancer gene therapy *27*, 585-598.

Evans, H.L., Nguyen, Q.D., Carroll, L.S., Kaliszczak, M., Twyman, F.J., Spivey, A.C., and Aboagye, E.O. (2014). A bioorthogonal (68)Ga-labelling strategy for rapid in vivo imaging. Chemical communications (Cambridge, England) *50*, 9557-9560.

Faul, F., Erdfelder, E., Buchner, A., and Lang, A.G. (2009). Statistical power analyses using G*Power 3.1: tests for correlation and regression analyses. Behavior research methods *41*, 1149-1160.

Faul, F., Erdfelder, E., Lang, A.G., and Buchner, A. (2007). G*Power 3: a flexible statistical power analysis program for the social, behavioral, and biomedical sciences. Behavior research methods *39*, 175-191.

Faustino-Rocha, A., Oliveira, P.A., Pinho-Oliveira, J., Teixeira-Guedes, C., Soares-Maia, R., da Costa, R.G., Colaço, B., Pires, M.J., Colaço, J., Ferreira, R., *et al.* (2013). Estimation of rat mammary tumor volume using caliper and ultrasonography measurements. Lab animal *42*, 217-224.

Ferlay, J., Colombet, M., Soerjomataram, I., Mathers, C., Parkin, D.M., Piñeros, M., Znaor, A., and Bray, F. (2019). Estimating the global cancer incidence and mortality in 2018: GLOBOCAN sources and methods. International journal of cancer *144*, 1941-1953.

Ferlito, A., Shaha, A.R., Silver, C.E., Rinaldo, A., and Mondin, V. (2001). Incidence and sites of distant metastases from head and neck cancer. ORL; journal for oto-rhino-laryngology and its related specialties *63*, 202-207.

Ferris, R.L., Blumenschein, G., Jr., Fayette, J., Guigay, J., Colevas, A.D., Licitra, L., Harrington, K., Kasper, S., Vokes, E.E., Even, C.*, et al.* (2016). Nivolumab for Recurrent Squamous-Cell Carcinoma of the Head and Neck. The New England journal of medicine *375*, 1856-1867.

Ferris, R.L., Gross, N.D., Nemunaitis, J.J., Andtbacka, R.H.I., Argiris, A., Ohr, J., Vetto, J.T., Senzer, N.N., Bedell, C., Ungerleider, R.S.*, et al.* (2014). Phase I trial of intratumoral therapy using HF10, an oncolytic HSV-1, demonstrates safety in HSV+/HSV- patients with refractory and superficial cancers. Journal of Clinical Oncology *32*, 6082-6082.

Fisher, R.A. (1921). 014: On the" Probable Error" of a Coefficient of Correlation Deduced from a Small Sample.

Forastiere, A.A., Ismaila, N., Lewin, J.S., Nathan, C.A., Adelstein, D.J., Eisbruch, A., Fass, G., Fisher, S.G., Laurie, S.A., Le, Q.T.*, et al.* (2018). Use of Larynx-Preservation Strategies in the Treatment of Laryngeal Cancer: American Society of Clinical Oncology Clinical Practice Guideline Update. Journal of clinical oncology : official journal of the American Society of Clinical Oncology *36*, 1143-1169.

Forastiere, A.A., Zhang, Q., Weber, R.S., Maor, M.H., Goepfert, H., Pajak, T.F., Morrison, W., Glisson, B., Trotti, A., Ridge, J.A.*, et al.* (2013). Long-term results of RTOG 91-11: a comparison of three nonsurgical treatment strategies to preserve the larynx in patients with locally advanced larynx cancer. Journal of clinical oncology : official journal of the American Society of Clinical Oncology *31*, 845-852.

Forrest, J.C., Campbell, J.A., Schelling, P., Stehle, T., and Dermody, T.S. (2003). Structure-function analysis of reovirus binding to junctional adhesion molecule 1. Implications for the mechanism of reovirus attachment. The Journal of biological chemistry *278*, 48434-48444.

Fox, T., Elder, E., and Crocker, I. (2008). chapter 3 - Image Registration and Fusion Techniques. In PET-CT in Radiotherapy Treatment Planning, A.C. Paulino, and B.S. Teh, eds. (Philadelphia: Elsevier), pp. 35-51.

Francisco, L.M., Salinas, V.H., Brown, K.E., Vanguri, V.K., Freeman, G.J., Kuchroo, V.K., and Sharpe, A.H. (2009). PD-L1 regulates the development, maintenance, and function of induced regulatory T cells. The Journal of experimental medicine *206*, 3015-3029.

Freeman, G.J., Long, A.J., Iwai, Y., Bourque, K., Chernova, T., Nishimura, H., Fitz, L.J., Malenkovich, N., Okazaki, T., Byrne, M.C.*, et al.* (2000). Engagement of the PD-1 immunoinhibitory receptor by a novel B7 family member leads to negative regulation of lymphocyte activation. The Journal of experimental medicine *192*, 1027-1034.

French, A.R., and Yokoyama, W.M. (2003). Natural killer cells and viral infections. Current opinion in immunology *15*, 45-51.

Fridman, W.H., Zitvogel, L., Sautès-Fridman, C., and Kroemer, G. (2017). The immune contexture in cancer prognosis and treatment. Nature reviews Clinical oncology *14*, 717-734.

Frindel, M., Le Saëc, P., Beyler, M., Navarro, A.-S., Saï-Maurel, C., Alliot, C., Chérel, M., Gestin, J.-F., Faivre-Chauvet, A., and Tripier, R. (2017). Cyclam te1pa for 64Cu PET imaging. Bioconjugation to antibody, radiolabeling and preclinical application in xenografted colorectal cancer. RSC Advances *7*, 9272-9283.

Fueger, B.J., Yeom, K., Czernin, J., Sayre, J.W., Phelps, M.E., and Allen-Auerbach, M.S. (2009). Comparison of CT, PET, and PET/CT for staging of patients with indolent non-Hodgkin's lymphoma. Mol Imaging Biol *11*, 269-274.

Fujimori, K., Covell, D.G., Fletcher, J.E., and Weinstein, J.N. (1990). A modeling analysis of monoclonal antibody percolation through tumors: a binding-site barrier. Journal of nuclear medicine : official publication, Society of Nuclear Medicine *31*, 1191-1198.

Fukuchi, T., Okauchi, T., Shigeta, M., Yamamoto, S., Watanabe, Y., and Enomoto, S. (2017). Positron emission tomography with additional γ-ray detectors for multiple-tracer imaging. Medical physics *44*, 2257-2266.

Fus-Kujawa, A., Prus, P., Bajdak-Rusinek, K., Teper, P., Gawron, K., Kowalczuk, A., and Sieron, A.L. (2021). An Overview of Methods and Tools for Transfection of Eukaryotic Cells in vitro. Frontiers in Bioengineering and Biotechnology *9*.

Gabrilovich, D.I., and Nagaraj, S. (2009). Myeloid-derived suppressor cells as regulators of the immune system. Nature reviews Immunology *9*, 162-174.

Gaggar, A., Shayakhmetov, D.M., and Lieber, A. (2003). CD46 is a cellular receptor for group B adenoviruses. Nat Med *9*, 1408-1412.

Galani, I.E., Triantafyllia, V., Eleminiadou, E.E., Koltsida, O., Stavropoulos, A., Manioudaki, M., Thanos, D., Doyle, S.E., Kotenko, S.V., Thanopoulou, K.*, et al.* (2017). Interferon-λ Mediates Non-redundant Front-Line Antiviral Protection against Influenza Virus Infection without Compromising Host Fitness. Immunity *46*, 875-890.e876.

Gambhir, S.S. (2002). Molecular imaging of cancer with positron emission tomography. Nature reviews Cancer *2*, 683-693.

Ganly, I., Kirn, D., Eckhardt, G., Rodriguez, G.I., Soutar, D.S., Otto, R., Robertson, A.G., Park, O., Gulley, M.L., Heise, C.*, et al.* (2000). A phase I study of Onyx-015, an E1B attenuated adenovirus, administered intratumorally to patients with recurrent head and neck cancer. Clinical cancer research : an official journal of the American Association for Cancer Research *6*, 798-806.

Garcia-Diaz, A., Shin, D.S., Moreno, B.H., Saco, J., Escuin-Ordinas, H., Rodriguez, G.A., Zaretsky, J.M., Sun, L., Hugo, W., Wang, X.*, et al.* (2017). Interferon Receptor Signaling Pathways Regulating PD-L1 and PD-L2 Expression. Cell reports *19*, 1189-1201.

Ghose, J., Dona, A., Murtadha, M., Gunes, E.G., Caserta, E., Yoo, J.Y., Russell, L., Jaime-Ramirez, A.C., Barwick, B.G., Gupta, V.A.*, et al.* (2021). Oncolytic herpes simplex virus infects myeloma cells in vitro and in vivo. Molecular therapy oncolytics *20*, 519-531.

Giavarina, D. (2015). Understanding Bland Altman analysis. Biochemia medica *25*, 141-151.

Giavazzi, R., Sennino, B., Coltrini, D., Garofalo, A., Dossi, R., Ronca, R., Tosatti, M.P., and Presta, M. (2003). Distinct role of fibroblast growth factor-2 and vascular endothelial growth factor on tumor growth and angiogenesis. The American journal of pathology *162*, 1913-1926.

Gillison, M.L., Broutian, T., Pickard, R.K., Tong, Z.Y., Xiao, W., Kahle, L., Graubard, B.I., and Chaturvedi, A.K. (2012). Prevalence of oral HPV infection in the United States, 2009-2010. Jama *307*, 693-703.

Gillison, M.L., Chaturvedi, A.K., Anderson, W.F., and Fakhry, C. (2015). Epidemiology of Human Papillomavirus-Positive Head and Neck Squamous Cell Carcinoma. Journal of clinical oncology : official journal of the American Society of Clinical Oncology *33*, 3235-3242.

Glassman, P.M., Abuqayyas, L., and Balthasar, J.P. (2015). Assessments of antibody biodistribution. Journal of clinical pharmacology *55 Suppl 3*, S29-38.

Glatt, D.M., Beckford Vera, D.R., Parrott, M.C., Luft, J.C., Benhabbour, S.R., and Mumper, R.J. (2016). The Interplay of Antigen Affinity, Internalization, and Pharmacokinetics on CD44-Positive Tumor Targeting of Monoclonal Antibodies. Molecular pharmaceutics *13*, 1894-1903.

Goldsmith, K., Chen, W., Johnson, D.C., and Hendricks, R.L. (1998). Infected cell protein (ICP)47 enhances herpes simplex virus neurovirulence by blocking the CD8+ T cell response. The Journal of experimental medicine *187*, 341-348.

Goldstein, D.J., and Weller, S.K. (1988). Factor(s) present in herpes simplex virus type 1-infected cells can compensate for the loss of the large subunit of the viral ribonucleotide reductase: characterization of an ICP6 deletion mutant. Virology *166*, 41-51.

Gong, A.Y., Zhou, R., Hu, G., Li, X., Splinter, P.L., O'Hara, S.P., LaRusso, N.F., Soukup, G.A., Dong, H., and Chen, X.M. (2009). MicroRNA-513 regulates B7-H1 translation and is involved in IFN-gamma-induced B7-H1 expression in cholangiocytes. Journal of immunology (Baltimore, Md : 1950) *182*, 1325-1333.

Göttgens, E.L., Ostheimer, C., Span, P.N., Bussink, J., and Hammond, E.M. (2019). HPV, hypoxia and radiation response in head and neck cancer. The British journal of radiology *92*, 20180047.

Graham, F.L., Smiley, J., Russell, W.C., and Nairn, R. (1977). Characteristics of a human cell line transformed by DNA from human adenovirus type 5. The Journal of general virology *36*, 59-74.

Grandis, J.R., and Tweardy, D.J. (1993). TGF-alpha and EGFR in head and neck cancer. Journal of cellular biochemistry Supplement *17f*, 188-191.

Gray, L.H., Conger, A.D., Ebert, M., Hornsey, S., and Scott, O.C. (1953). The concentration of oxygen dissolved in tissues at the time of irradiation as a factor in radiotherapy. The British journal of radiology *26*, 638-648.

Greene, S., Robbins, Y., Mydlarz, W.K., Huynh, A.P., Schmitt, N.C., Friedman, J., Horn, L.A., Palena, C., Schlom, J., Maeda, D.Y.*, et al.* (2020). Inhibition of MDSC Trafficking with SX-682, a CXCR1/2 Inhibitor, Enhances NK-Cell Immunotherapy in Head and Neck Cancer Models. Clinical cancer research : an official journal of the American Association for Cancer Research *26*, 1420-1431.

Gujar, S., Pol, J.G., Kim, Y., Lee, P.W., and Kroemer, G. (2018). Antitumor Benefits of Antiviral Immunity: An Underappreciated Aspect of Oncolytic Virotherapies. Trends in immunology *39*, 209-221.

Guleria, I., Khosroshahi, A., Ansari, M.J., Habicht, A., Azuma, M., Yagita, H., Noelle, R.J., Coyle, A., Mellor, A.L., Khoury, S.J.*, et al.* (2005). A critical role for the programmed death ligand 1 in fetomaternal tolerance. The Journal of experimental medicine *202*, 231-237.

Guo, Z.S., Lu, B., Guo, Z., Giehl, E., Feist, M., Dai, E., Liu, W., Storkus, W.J., He, Y., Liu, Z.*, et al.* (2019). Vaccinia virus-mediated cancer immunotherapy: cancer vaccines and oncolytics. Journal for immunotherapy of cancer *7*, 6.

Gutfilen, B., Souza, S.A., and Valentini, G. (2018). Copper-64: a real theranostic agent. Drug design, development and therapy *12*, 3235-3245.

Gutmann, R., Leunig, M., Feyh, J., Goetz, A.E., Messmer, K., Kastenbauer, E., and Jain, R.K. (1992). Interstitial hypertension in head and neck tumors in patients: correlation with tumor size. Cancer research *52*, 1993-1995.

Hamers-Casterman, C., Atarhouch, T., Muyldermans, S., Robinson, G., Hamers, C., Songa, E.B., Bendahman, N., and Hamers, R. (1993). Naturally occurring antibodies devoid of light chains. Nature *363*, 446-448.

Hanahan, D., and Weinberg, R.A. (2011). Hallmarks of cancer: the next generation. Cell *144*, 646-674.

Harrington, K.J., Aroldi, F., Sacco, J.J., Milhem, M.M., Curti, B.D., Vanderwalde, A.M., Baum, S., Samson, A., Pavlick, A.C., Chesney, J.A.*, et al.* (2021). Abstract LB180: Clinical biomarker studies with two fusion-enhanced versions of oncolytic HSV (RP1 and RP2) alone and in combination with nivolumab in cancer patients indicate potent immune activation. Cancer research *81*, LB180-LB180.

Harrington, K.J., Hingorani, M., Tanay, M.A., Hickey, J., Bhide, S.A., Clarke, P.M., Renouf, L.C., Thway, K., Sibtain, A., McNeish, I.A.*, et al.* (2010). Phase I/II study of oncolytic HSV GM-CSF in combination with radiotherapy and cisplatin in untreated stage III/IV squamous cell cancer of the head and neck.

Clinical cancer research : an official journal of the American Association for Cancer Research *16*, 4005-4015.

Harrington, K.J., Kong, A., Mach, N., Chesney, J.A., Fernandez, B.C., Rischin, D., Cohen, E.E.W., Radcliffe, H.S., Gumuscu, B., Cheng, J.*, et al.* (2020). Talimogene Laherparepvec and Pembrolizumab in Recurrent or Metastatic Squamous Cell Carcinoma of the Head and Neck (MASTERKEY-232): A Multicenter, Phase 1b Study. Clinical cancer research : an official journal of the American Association for Cancer Research *26*, 5153-5161.

Hasan, J., Byers, R., and Jayson, G.C. (2002). Intra-tumoural microvessel density in human solid tumours. British journal of cancer *86*, 1566-1577.

Hashibe, M., Brennan, P., Chuang, S.C., Boccia, S., Castellsague, X., Chen, C., Curado, M.P., Dal Maso, L., Daudt, A.W., Fabianova, E.*, et al.* (2009). Interaction between tobacco and alcohol use and the risk of head and neck cancer: pooled analysis in the International Head and Neck Cancer Epidemiology Consortium. Cancer epidemiology, biomarkers & prevention : a publication of the American Association for Cancer Research, cosponsored by the American Society of Preventive Oncology *18*, 541-550.

Hashiro, G., Loh, P.C., and Yau, J.T. (1977). The preferential cytotoxicity of reovirus for certain transformed cell lines. Archives of virology *54*, 307-315.

Hayman, T.J., Baro, M., MacNeil, T., Phoomak, C., Aung, T.N., Cui, W., Leach, K., Iyer, R., Challa, S., Sandoval-Schaefer, T.*, et al.* (2021). STING enhances cell death through regulation of reactive oxygen species and DNA damage. Nat Commun *12*, 2327.

Heldin, C.H., Rubin, K., Pietras, K., and Ostman, A. (2004). High interstitial fluid pressure - an obstacle in cancer therapy. Nature reviews Cancer *4*, 806-813.

Hellmann, M.D., Paz-Ares, L., Bernabe Caro, R., Zurawski, B., Kim, S.W., Carcereny Costa, E., Park, K., Alexandru, A., Lupinacci, L., de la Mora Jimenez, E.*, et al.* (2019). Nivolumab plus Ipilimumab in Advanced Non-Small-Cell Lung Cancer. The New England journal of medicine *381*, 2020-2031.

Hemminki, O., Dos Santos, J.M., and Hemminki, A. (2020). Oncolytic viruses for cancer immunotherapy. Journal of hematology & oncology *13*, 84.

Heneweer, C., Holland, J.P., Divilov, V., Carlin, S., and Lewis, J.S. (2011). Magnitude of enhanced permeability and retention effect in tumors with different phenotypes: 89Zr-albumin as a model system. Journal of nuclear medicine : official publication, Society of Nuclear Medicine *52*, 625-633.

Heo, J., Reid, T., Ruo, L., Breitbach, C.J., Rose, S., Bloomston, M., Cho, M., Lim, H.Y., Chung, H.C., Kim, C.W., *et al.* (2013). Randomized dose-finding clinical trial of oncolytic immunotherapeutic vaccinia JX-594 in liver cancer. Nat Med *19*, 329-336.

Herbst, R.S., Baas, P., Kim, D.W., Felip, E., Pérez-Gracia, J.L., Han, J.Y., Molina, J., Kim, J.H., Arvis, C.D., Ahn, M.J., *et al.* (2016). Pembrolizumab versus docetaxel for previously treated, PD-L1-positive, advanced non-small-cell lung cancer (KEYNOTE-010): a randomised controlled trial. Lancet (London, England) *387*, 1540-1550.

Herbst, R.S., Soria, J.C., Kowanetz, M., Fine, G.D., Hamid, O., Gordon, M.S., Sosman, J.A., McDermott, D.F., Powderly, J.D., Gettinger, S.N., *et al.* (2014). Predictive correlates of response to the anti-PD-L1 antibody MPDL3280A in cancer patients. Nature *515*, 563-567.

Herzog, H., Tellman, L., Qaim, S.M., Spellerberg, S., Schmid, A., and Coenen, H.H. (2002). PET quantitation and imaging of the non-pure positron-emitting iodine isotope 124I. Applied radiation and isotopes : including data, instrumentation and methods for use in agriculture, industry and medicine *56*, 673-679.

Heskamp, S., Hobo, W., Molkenboer-Kuenen, J.D., Olive, D., Oyen, W.J., Dolstra, H., and Boerman, O.C. (2015). Noninvasive Imaging of Tumor PD-L1 Expression Using Radiolabeled Anti-PD-L1 Antibodies. Cancer research *75*, 2928-2936.

Heskamp, S., Raavé, R., Boerman, O., Rijpkema, M., Goncalves, V., and Denat, F. (2017). (89)Zr-Immuno-Positron Emission Tomography in Oncology: State-of-the-Art (89)Zr Radiochemistry. Bioconjugate chemistry *28*, 2211-2223.

Heskamp, S., Wierstra, P.J., Molkenboer-Kuenen, J.D.M., Sandker, G.W., Thordardottir, S., Cany, J., Olive, D., Bussink, J., Boerman, O.C., Dolstra, H., *et al.* (2019). PD-L1 microSPECT/CT Imaging for Longitudinal Monitoring of PD-L1 Expression in Syngeneic and Humanized Mouse Models for Cancer. Cancer immunology research *7*, 150-161.

Hier, M.P., Black, M.J., Shenouda, G., Sadeghi, N., and Karp, S.E. (1995). A murine model for the immunotherapy of head and neck squamous cell carcinoma. The Laryngoscope *105*, 1077-1080.

Higuchi, H., Bronk, S.F., Bateman, A., Harrington, K., Vile, R.G., and Gores, G.J. (2000). Viral fusogenic membrane glycoprotein expression causes syncytia formation with bioenergetic cell death: implications for gene therapy. Cancer research *60*, 6396-6402.

Hirasawa, K., Nishikawa, S.G., Norman, K.L., Alain, T., Kossakowska, A., and Lee, P.W. (2002). Oncolytic reovirus against ovarian and colon cancer. Cancer research *62*, 1696-1701.

Hirst, D.G., Brown, J.M., and Hazlehurst, J.L. (1982). Enhancement of CCNU cytotoxicity by misonidazole: possible therapeutic gain. British journal of cancer *46*, 109-116.

Hoekstra, C.J., Paglianiti, I., Hoekstra, O.S., Smit, E.F., Postmus, P.E., Teule, G.J., and Lammertsma, A.A. (2000). Monitoring response to therapy in cancer using [18F]-2-fluoro-2-deoxy-D-glucose and positron emission tomography: an overview of different analytical methods. European journal of nuclear medicine *27*, 731-743.

Holland, J.P., Divilov, V., Bander, N.H., Smith-Jones, P.M., Larson, S.M., and Lewis, J.S. (2010). 89Zr-DFO-J591 for immunoPET of prostate-specific membrane antigen expression in vivo. Journal of nuclear medicine : official publication, Society of Nuclear Medicine *51*, 1293-1300.

Holliger, P., and Hudson, P.J. (2005). Engineered antibody fragments and the rise of single domains. Nat Biotechnol *23*, 1126-1136.

Honda, T., Egen, J.G., Lämmermann, T., Kastenmüller, W., Torabi-Parizi, P., and Germain, R.N. (2014). Tuning of antigen sensitivity by T cell receptor-dependent negative feedback controls T cell effector function in inflamed tissues. Immunity *40*, 235-247.

Hong, S.D., Hong, S.P., Lee, J.I., and Lim, C.Y. (2000). Expression of matrix metalloproteinase-2 and -9 in oral squamous cell carcinomas with regard to the metastatic potential. Oral oncology *36*, 207-213.

Hoover, A.C., Spanos, W.C., Harris, G.F., Anderson, M.E., Klingelhutz, A.J., and Lee, J.H. (2007). The role of human papillomavirus 16 E6 in anchorage-independent and invasive growth of mouse tonsil epithelium. Archives of otolaryngology--head & neck surgery *133*, 495-502.

Hu, J.C., Coffin, R.S., Davis, C.J., Graham, N.J., Groves, N., Guest, P.J., Harrington, K.J., James, N.D., Love, C.A., McNeish, I., *et al.* (2006). A phase I study of OncoVEXGM-CSF, a second-generation oncolytic herpes simplex virus expressing granulocyte macrophage colony-stimulating factor. Clinical cancer research : an official journal of the American Association for Cancer Research *12*, 6737-6747.

Hu, S., Shively, L., Raubitschek, A., Sherman, M., Williams, L.E., Wong, J.Y., Shively, J.E., and Wu, A.M. (1996). Minibody: A novel engineered anti-carcinoembryonic antigen antibody fragment (single-chain Fv-CH3) which exhibits rapid, high-level targeting of xenografts. Cancer research *56*, 3055-3061.

Huang, G., Wen, Q., Zhao, Y., Gao, Q., and Bai, Y. (2013). NF-κB plays a key role in inducing CD274 expression in human monocytes after lipopolysaccharide treatment. PloS one *8*, e61602.

Hudson, P.J., and Souriau, C. (2003). Engineered antibodies. Nat Med *9*, 129-134.

Hugo, W., Zaretsky, J.M., Sun, L., Song, C., Moreno, B.H., Hu-Lieskovan, S., Berent-Maoz, B., Pang, J., Chmielowski, B., Cherry, G.*, et al.* (2016). Genomic and Transcriptomic Features of Response to Anti-PD-1 Therapy in Metastatic Melanoma. Cell *165*, 35-44.

Hulspas, R., O'Gorman, M.R., Wood, B.L., Gratama, J.W., and Sutherland, D.R. (2009). Considerations for the control of background fluorescence in clinical flow cytometry. Cytometry Part B, Clinical cytometry *76*, 355-364.

Hwang, S.Y., Hertzog, P.J., Holland, K.A., Sumarsono, S.H., Tymms, M.J., Hamilton, J.A., Whitty, G., Bertoncello, I., and Kola, I. (1995). A null mutation in the gene encoding a type I interferon receptor component eliminates antiproliferative and antiviral responses to interferons alpha and beta and alters macrophage responses. Proc Natl Acad Sci U S A *92*, 11284-11288.

Ilkow, C.S., Swift, S.L., Bell, J.C., and Diallo, J.S. (2014). From scourge to cure: tumour-selective viral pathogenesis as a new strategy against cancer. PLoS pathogens *10*, e1003836.

Ingram, J.R., Dougan, M., Rashidian, M., Knoll, M., Keliher, E.J., Garrett, S., Garforth, S., Blomberg, O.S., Espinosa, C., Bhan, A.*, et al.* (2017). PD-L1 is an activation-independent marker of brown adipocytes. Nat Commun *8*.

Ito, T., Matsusaka, Y., Onoguchi, M., Ichikawa, H., Okuda, K., Shibutani, T., Shishido, M., and Sato, K. (2021). Experimental evaluation of the GE NM/CT 870 CZT clinical SPECT system equipped with WEHR and MEHRS collimator. Journal of Applied Clinical Medical Physics *22*, 165-177.

Ivashkiv, L.B. (2018). IFNγ: signalling, epigenetics and roles in immunity, metabolism, disease and cancer immunotherapy. Nature reviews Immunology *18*, 545-558.

Iwai, Y., Ishida, M., Tanaka, Y., Okazaki, T., Honjo, T., and Minato, N. (2002). Involvement of PD-L1 on tumor cells in the escape from host immune system and tumor immunotherapy by PD-L1 blockade. Proceedings of the National Academy of Sciences *99*, 12293-12297.

Jacobson, O., Kiesewetter, D.O., and Chen, X. (2015). Fluorine-18 radiochemistry, labeling strategies and synthetic routes. Bioconjugate chemistry *26*, 1-18.

Jagoda, E.M., Vasalatiy, O., Basuli, F., Opina, A.C.L., Williams, M.R., Wong, K., Lane, K.C., Adler, S., Ton, A.T., Szajek, L.P.*, et al.* (2019). Immuno-PET Imaging of the Programmed Cell Death-1 Ligand (PD-L1) Using a Zirconium-89 Labeled Therapeutic Antibody, Avelumab. Mol Imaging *18*, 1536012119829986-1536012119829986.

Jain, R.K. (1987). Transport of molecules in the tumor interstitium: a review. Cancer research *47*, 3039-3051.

Jain, R.K. (1990). Physiological barriers to delivery of monoclonal antibodies and other macromolecules in tumors. Cancer research *50*, 814s-819s.

Jain, R.K., and Baxter, L.T. (1988). Mechanisms of heterogeneous distribution of monoclonal antibodies and other macromolecules in tumors: significance of elevated interstitial pressure. Cancer research *48*, 7022-7032.

Janeway, C. (2001). Immunobiology 5 : the immune system in health and disease (New York: Garland Pub.).

Jiang, H., Rivera-Molina, Y., Gomez-Manzano, C., Clise-Dwyer, K., Bover, L., Vence, L.M., Yuan, Y., Lang, F.F., Toniatti, C., Hossain, M.B.*, et al.* (2017). Oncolytic Adenovirus and Tumor-Targeting Immune Modulatory Therapy Improve Autologous Cancer Vaccination. Cancer research *77*, 3894-3907.

Johann, S.V., van Zeijl, M., Cekleniak, J., and O'Hara, B. (1993). Definition of a domain of GLVR1 which is necessary for infection by gibbon ape leukemia virus and which is highly polymorphic between species. Journal of virology *67*, 6733-6736.

Johnson, D.E., Burtness, B., Leemans, C.R., Lui, V.W.Y., Bauman, J.E., and Grandis, J.R. (2020a). Head and neck squamous cell carcinoma. Nature reviews Disease primers *6*, 92.

Johnson, G.B., Harms, H.J., Johnson, D.R., and Jacobson, M.S. (2020b). PET Imaging of Tumor Perfusion: A Potential Cancer Biomarker? Seminars in nuclear medicine *50*, 549-561.

Johnson, K.E., Song, B., and Knipe, D.M. (2008). Role for herpes simplex virus 1 ICP27 in the inhibition of type I interferon signaling. Virology *374*, 487-494.

Josefsson, A., Nedrow, J.R., Park, S., Banerjee, S.R., Rittenbach, A., Jammes, F., Tsui, B., and Sgouros, G. (2016). Imaging, Biodistribution, and Dosimetry of Radionuclide-Labeled PD-L1 Antibody in an Immunocompetent Mouse Model of Breast Cancer. Cancer research *76*, 472-479.

Josephs, D.H., Bax, H.J., and Karagiannis, S.N. (2015). Tumour-associated macrophage polarisation and re-education with immunotherapy. Frontiers in bioscience (Elite edition) *7*, 293-308.

Judd, N.P., Allen, C.T., Winkler, A.E., and Uppaluri, R. (2012a). Comparative analysis of tumor-infiltrating lymphocytes in a syngeneic mouse model of oral cancer. Otolaryngology--head and neck surgery : official journal of American Academy of Otolaryngology-Head and Neck Surgery *147*, 493-500.

Judd, N.P., Winkler, A.E., Murillo-Sauca, O., Brotman, J.J., Law, J.H., Lewis, J.S., Jr., Dunn, G.P., Bui, J.D., Sunwoo, J.B., and Uppaluri, R. (2012b). ERK1/2 regulation of CD44 modulates oral cancer aggressiveness. Cancer research *72*, 365-374.

Juweid, M., Neumann, R., Paik, C., Perez-Bacete, M.J., Sato, J., van Osdol, W., and Weinstein, J.N. (1992). Micropharmacology of monoclonal antibodies in solid tumors: direct experimental evidence for a binding site barrier. Cancer research *52*, 5144-5153.

Kanerva, A., Nokisalmi, P., Diaconu, I., Koski, A., Cerullo, V., Liikanen, I., Tähtinen, S., Oksanen, M., Heiskanen, R., Pesonen, S., *et al.* (2013). Antiviral and antitumor T-cell immunity in patients treated with GM-CSF-coding oncolytic adenovirus. Clinical cancer research : an official journal of the American Association for Cancer Research *19*, 2734-2744.

Karakhanova, S., Meisel, S., Ring, S., Mahnke, K., and Enk, A.H. (2010). ERK/p38 MAP-kinases and PI3K are involved in the differential regulation of B7-H1 expression in DC subsets. European journal of immunology *40*, 254-266.

Karapanagiotou, E.M., Roulstone, V., Twigger, K., Ball, M., Tanay, M., Nutting, C., Newbold, K., Gore, M.E., Larkin, J., Syrigos, K.N.*, et al.* (2012). Phase I/II trial of carboplatin and paclitaxel chemotherapy in combination with intravenous oncolytic reovirus in patients with advanced malignancies. Clinical cancer research : an official journal of the American Association for Cancer Research *18*, 2080-2089.

Katze, M.G., He, Y., and Gale, M., Jr. (2002). Viruses and interferon: a fight for supremacy. Nature reviews Immunology *2*, 675-687.

Kaufman, H.L., Kohlhapp, F.J., and Zloza, A. (2015). Oncolytic viruses: a new class of immunotherapy drugs. Nature reviews Drug discovery *14*, 642-662.

Keeney, M., Gratama, J.W., Chin-Yee, I.H., and Sutherland, D.R. (1998). Isotype controls in the analysis of lymphocytes and CD34+ stem and progenitor cells by flow cytometry--time to let go! Cytometry *34*, 280-283.

Keir, M.E., Butte, M.J., Freeman, G.J., and Sharpe, A.H. (2008). PD-1 and its ligands in tolerance and immunity. Annual review of immunology *26*, 677-704.

Kelly, K.R., Espitia, C.M., Zhao, W., Wu, K., Visconte, V., Anwer, F., Calton, C.M., Carew, J.S., and Nawrocki, S.T. (2018). Oncolytic reovirus sensitizes multiple myeloma cells to anti-PD-L1 therapy. Leukemia *32*, 230-233.

Kenanova, V., Olafsen, T., Crow, D.M., Sundaresan, G., Subbarayan, M., Carter, N.H., Ikle, D.N., Yazaki, P.J., Chatziioannou, A.F., Gambhir, S.S.*, et al.* (2005). Tailoring the pharmacokinetics and positron emission tomography imaging properties of anti-carcinoembryonic antigen single-chain Fv-Fc antibody fragments. Cancer research *65*, 622-631.

Keyaerts, M., Xavier, C., Heemskerk, J., Devoogdt, N., Everaert, H., Ackaert, C., Vanhoeij, M., Duhoux, F.P., Gevaert, T., Simon, P.*, et al.* (2016). Phase I Study of 68Ga-HER2-Nanobody for PET/CT Assessment of HER2 Expression in Breast Carcinoma. Journal of nuclear medicine : official publication, Society of Nuclear Medicine *57*, 27-33.

Kikuchi, M., Clump, D.A., Srivastava, R.M., Sun, L., Zeng, D., Diaz-Perez, J.A., Anderson, C.J., Edwards, W.B., and Ferris, R.L. (2017). Preclinical immunoPET/CT imaging using Zr-89-labeled anti-PD-L1 monoclonal antibody for assessing radiation-induced PD-L1 upregulation in head and neck cancer and melanoma. Oncoimmunology *6*, e1329071.

Kil, S.H., Estephan, R., Sanchez, J., Zain, J.M., Kadin, M.E., Young, J.W., Rosen, S.T., and Querfeld, C. (2017). PD-L1 Is Regulated By Interferon Gamma and Interleukin 6 through STAT1 and STAT3 Signaling in Cutaneous T-Cell Lymphoma. Blood *130*, 1458-1458.

Kim, J.J., Yang, J.S., Lee, D.J., Wilson, D.M., Nottingham, L.K., Morrison, L., Tsai, A., Oh, J., Dang, K., Dentchev, T., *et al.* (2000). Macrophage colony-stimulating factor can modulate immune responses and attract dendritic cells in vivo. Human gene therapy *11*, 305-321.

Kim, J.W., Tchernyshyov, I., Semenza, G.L., and Dang, C.V. (2006). HIF-1-mediated expression of pyruvate dehydrogenase kinase: a metabolic switch required for cellular adaptation to hypoxia. Cell metabolism *3*, 177-185.

Kinahan, P.E., Townsend, D.W., Beyer, T., and Sashin, D. (1998). Attenuation correction for a combined 3D PET/CT scanner. Medical physics *25*, 2046-2053.

Kinman, A.W.L., and Pompano, R.R. (2019). Optimization of Enzymatic Antibody Fragmentation for Yield, Efficiency, and Binding Affinity. Bioconjugate chemistry *30*, 800-807.

Klein, D. (2018). The Tumor Vascular Endothelium as Decision Maker in Cancer Therapy. Frontiers in oncology *8*, 367.

Kloten, V., Lampignano, R., Krahn, T., and Schlange, T. (2019). Circulating Tumor Cell PD-L1 Expression as Biomarker for Therapeutic Efficacy of Immune Checkpoint Inhibition in NSCLC. Cells *8*.

Knops, A.M., South, A., Rodeck, U., Martinez-Outschoorn, U., Harshyne, L.A., Johnson, J., Luginbuhl, A.J., and Curry, J.M. (2020). Cancer-Associated Fibroblast Density, Prognostic Characteristics, and Recurrence in Head and Neck Squamous Cell Carcinoma: A Meta-Analysis. Frontiers in oncology *10*.

Knowles, S.M., Zettlitz, K.A., Tavaré, R., Rochefort, M.M., Salazar, F.B., Stout, D.B., Yazaki, P.J., Reiter, R.E., and Wu, A.M. (2014). Quantitative immunoPET of prostate cancer xenografts with 89Zr- and 124I-labeled anti-PSCA A11 minibody. Journal of nuclear medicine : official publication, Society of Nuclear Medicine *55*, 452-459.

Kolumam, G.A., Thomas, S., Thompson, L.J., Sprent, J., and Murali-Krishna, K. (2005). Type I interferons act directly on CD8 T cells to allow clonal expansion and memory formation in response to viral infection. The Journal of experimental medicine *202*, 637-650.

Krabbe, C.A., Pruim, J., van der Laan, B.F., Rödiger, L.A., and Roodenburg, J.L. (2009). FDG-PET and detection of distant metastases and simultaneous tumors in head and neck squamous cell carcinoma: a comparison with chest radiography and chest CT. Oral oncology *45*, 234-240.

Krabbe, T., and Altomonte, J. (2018). Fusogenic Viruses in Oncolytic Immunotherapy. Cancers (Basel) *10*.

Krak, N.C., Boellaard, R., Hoekstra, O.S., Twisk, J.W., Hoekstra, C.J., and Lammertsma, A.A. (2005). Effects of ROI definition and reconstruction method on quantitative outcome and applicability in a response monitoring trial. European journal of nuclear medicine and molecular imaging *32*, 294-301.

Krasniqi, A., D'Huyvetter, M., Xavier, C., Van der Jeught, K., Muyldermans, S., Van Der Heyden, J., Lahoutte, T., Tavernier, J., and Devoogdt, N. (2017). Theranostic Radiolabeled Anti-CD20 sdAb for Targeted Radionuclide Therapy of Non-Hodgkin Lymphoma. Mol Cancer Ther *16*, 2828-2839.

Kumar, K., and Ghosh, A. (2021). Radiochemistry, Production Processes, Labeling Methods, and ImmunoPET Imaging Pharmaceuticals of Iodine-124. Molecules *26*, 414.

Kurino, T., Matsuda, R., Terui, A., Suzuki, H., Kokubo, T., Uehara, T., Arano, Y., Hisaka, A., and Hatakeyama, H. (2020). Poor outcome with anti-programmed death-ligand 1 (PD-L1) antibody due to poor pharmacokinetic properties in PD-1/PD-L1 blockade-sensitive mouse models. Journal for immunotherapy of cancer *8*.

Kyula, J.N., Roulstone, V., Karapanagiotou, E.M., Melcher, A.A., and Harrington, K.J. (2012). Oncolytic reovirus type 3 (Dearing) as a novel therapy in head and neck cancer. Expert opinion on biological therapy *12*, 1669-1678.

Labani-Motlagh, A., Ashja-Mahdavi, M., and Loskog, A. (2020). The Tumor Microenvironment: A Milieu Hindering and Obstructing Antitumor Immune Responses. Frontiers in immunology *11*.

Lai, S.L., Tan, M.L., Hollows, R.J., Robinson, M., Ibrahim, M., Margielewska, S., Parkinson, E.K., Ramanathan, A., Zain, R.B., Mehanna, H., *et al.* (2019). Collagen

Induces a More Proliferative, Migratory and Chemoresistant Phenotype in Head and Neck Cancer via DDR1. Cancers (Basel) *11*.

Lamberts, L.E., Williams, S.P., Terwisscha van Scheltinga, A.G., Lub-de Hooge, M.N., Schröder, C.P., Gietema, J.A., Brouwers, A.H., and de Vries, E.G. (2015). Antibody positron emission tomography imaging in anticancer drug development. Journal of clinical oncology : official journal of the American Society of Clinical Oncology *33*, 1491-1504.

Latchman, Y., Wood, C.R., Chernova, T., Chaudhary, D., Borde, M., Chernova, I., Iwai, Y., Long, A.J., Brown, J.A., Nunes, R.*, et al.* (2001). PD-L2 is a second ligand for PD-1 and inhibits T cell activation. Nature immunology *2*, 261-268.

Latchman, Y.E., Liang, S.C., Wu, Y., Chernova, T., Sobel, R.A., Klemm, M., Kuchroo, V.K., Freeman, G.J., and Sharpe, A.H. (2004). PD-L1-deficient mice show that PD-L1 on T cells, antigen-presenting cells, and host tissues negatively regulates T cells. Proc Natl Acad Sci U S A *101*, 10691-10696.

Latt, S.A., Stetten, G., Juergens, L.A., Willard, H.F., and Scher, C.D. (1975). Recent developments in the detection of deoxyribonucleic acid synthesis by 33258 Hoechst fluorescence. The journal of histochemistry and cytochemistry : official journal of the Histochemistry Society *23*, 493-505.

Lau, J., Cheung, J., Navarro, A., Lianoglou, S., Haley, B., Totpal, K., Sanders, L., Koeppen, H., Caplazi, P., McBride, J.*, et al.* (2017). Tumour and host cell PD-L1 is required to mediate suppression of anti-tumour immunity in mice. Nat Commun *8*, 14572.

Lazear, H.M., Schoggins, J.W., and Diamond, M.S. (2019). Shared and Distinct Functions of Type I and Type III Interferons. Immunity *50*, 907-923.

Lee, E.C., Liang, Q., Ali, H., Bayliss, L., Beasley, A., Bloomfield-Gerdes, T., Bonoli, L., Brown, R., Campbell, J., Carpenter, A.*, et al.* (2014). Complete humanization of the mouse immunoglobulin loci enables efficient therapeutic antibody discovery. Nat Biotechnol *32*, 356-363.

Lee, N.C.J., Kelly, J.R., Park, H.S., An, Y., Judson, B.L., Burtness, B.A., and Husain, Z.A. (2018). Patterns of failure in high-metastatic node number human papillomavirus-positive oropharyngeal carcinoma. Oral oncology *85*, 35-39.

Lee, S., and Lee, D.K. (2018). What is the proper way to apply the multiple comparison test? Korean J Anesthesiol *71*, 353-360.

Less, J.R., Posner, M.C., Boucher, Y., Borochovitz, D., Wolmark, N., and Jain, R.K. (1992). Interstitial hypertension in human breast and colorectal tumors. Cancer research *52*, 6371-6374.

Levin, C.S., and Hoffman, E.J. (1999). Calculation of positron range and its effect on the fundamental limit of positron emission tomography system spatial resolution. Physics in medicine and biology *44*, 781-799.

Li, B., Cui, Y., Nambiar, D.K., Sunwoo, J.B., and Li, R. (2019a). The Immune Subtypes and Landscape of Squamous Cell Carcinoma. Clinical Cancer Research *25*, 3528-3537.

Li, C.W., Lim, S.O., Xia, W., Lee, H.H., Chan, L.C., Kuo, C.W., Khoo, K.H., Chang, S.S., Cha, J.H., Kim, T.*, et al.* (2016). Glycosylation and stabilization of programmed death ligand-1 suppresses T-cell activity. Nat Commun *7*, 12632.

Li, M.O., Wan, Y.Y., Sanjabi, S., Robertson, A.K., and Flavell, R.A. (2006). Transforming growth factor-beta regulation of immune responses. Annual review of immunology *24*, 99-146.

Li, Z., Zhou, J., Zhang, J., Li, S., Wang, H., and Du, J. (2019b). Cancer-associated fibroblasts promote PD-L1 expression in mice cancer cells via secreting CXCL5. International journal of cancer *145*, 1946-1957.

Liang, M. (2018). Oncorine, the World First Oncolytic Virus Medicine and its Update in China. Current cancer drug targets *18*, 171-176.

Ligtenberg, H., Willems, S.M., Ruiter, L.N., Jager, E.A., Terhaard, C.H.J., Raaijmakers, C.P.J., and Philippens, M.E.P. (2018). Verification of HE-based CTV in laryngeal and hypopharyngeal cancer using pan-cytokeratin. Clinical and translational radiation oncology *12*, 21-27.

Lim, S.O., Li, C.W., Xia, W., Cha, J.H., Chan, L.C., Wu, Y., Chang, S.S., Lin, W.C., Hsu, J.M., Hsu, Y.H.*, et al.* (2016). Deubiquitination and Stabilization of PD-L1 by CSN5. Cancer cell *30*, 925-939.

Lin, D.Y.-w., Tanaka, Y., Iwasaki, M., Gittis, A.G., Su, H.-P., Mikami, B., Okazaki, T., Honjo, T., Minato, N., and Garboczi, D.N. (2008). The PD-1/PD-L1 complex resembles the antigen-binding Fv domains of antibodies and T cell receptors. Proceedings of the National Academy of Sciences *105*, 3011-3016.

Lin, K.Y., Guarnieri, F.G., Staveley-O'Carroll, K.F., Levitsky, H.I., August, J.T., Pardoll, D.M., and Wu, T.C. (1996). Treatment of established tumors with a novel vaccine that enhances major histocompatibility class II presentation of tumor antigen. Cancer research *56*, 21-26.

Lindgren, G., Wennerberg, J., and Ekblad, L. (2017). Cell line dependent expression of EpCAM influences the detection of circulating tumor cells with CellSearch. Laryngoscope investigative otolaryngology *2*, 194-198.

Lindmo, T., Boven, E., Cuttitta, F., Fedorko, J., and Bunn, P.A., Jr. (1984). Determination of the immunoreactive fraction of radiolabeled monoclonal antibodies by linear extrapolation to binding at infinite antigen excess. Journal of immunological methods *72*, 77-89.

Lindmo, T., and Bunn, P.A., Jr. (1986). Determination of the true immunoreactive fraction of monoclonal antibodies after radiolabeling. Methods in enzymology *121*, 678-691.

Liu, B.L., Robinson, M., Han, Z.Q., Branston, R.H., English, C., Reay, P., McGrath, Y., Thomas, S.K., Thornton, M., Bullock, P., *et al.* (2003). ICP34.5 deleted herpes simplex virus with enhanced oncolytic, immune stimulating, and anti-tumour properties. Gene therapy *10*, 292-303.

Liu, T., Zhang, L., Joo, D., and Sun, S.-C. (2017a). NF-κB signaling in inflammation. Signal Transduction and Targeted Therapy *2*, 17023.

Liu, Z., Ravindranathan, R., Kalinski, P., Guo, Z.S., and Bartlett, D.L. (2017b). Rational combination of oncolytic vaccinia virus and PD-L1 blockade works synergistically to enhance therapeutic efficacy. Nat Commun *8*, 14754.

Lobo, E.D., Hansen, R.J., and Balthasar, J.P. (2004). Antibody pharmacokinetics and pharmacodynamics. Journal of pharmaceutical sciences *93*, 2645-2668.

Loke, P., and Allison, J.P. (2003). PD-L1 and PD-L2 are differentially regulated by Th1 and Th2 cells. Proc Natl Acad Sci U S A *100*, 5336-5341.

Lu, G., Nishio, N., van den Berg, N.S., Martin, B.A., Fakurnejad, S., van Keulen, S., Colevas, A.D., Thurber, G.M., and Rosenthal, E.L. (2020). Co-administered antibody improves penetration of antibody-dye conjugate into human cancers with implications for antibody-drug conjugates. Nat Commun *11*, 5667.

Lu, Y.-C., Yeh, W.-C., and Ohashi, P.S. (2008). LPS/TLR4 signal transduction pathway. Cytokine *42*, 145-151.

Lubberink, M., and Herzog, H. (2011). Quantitative imaging of 124I and 86Y with PET. European journal of nuclear medicine and molecular imaging *38 Suppl 1*, S10-18.

Lucignani, G., Paganelli, G., and Bombardieri, E. (2004). The use of standardized uptake values for assessing FDG uptake with PET in oncology: a clinical perspective. Nuclear medicine communications *25*, 651-656.

Lütje, S., van Rij, C.M., Franssen, G.M., Fracasso, G., Helfrich, W., Eek, A., Oyen, W.J., Colombatti, M., and Boerman, O.C. (2015). Targeting human prostate cancer with 111In-labeled D2B IgG, F(ab')2 and Fab fragments in nude mice with PSMA-expressing xenografts. Contrast media & molecular imaging *10*, 28-36.

Lyford-Pike, S., Peng, S., Young, G.D., Taube, J.M., Westra, W.H., Akpeng, B., Bruno, T.C., Richmon, J.D., Wang, H., Bishop, J.A., *et al.* (2013). Evidence for a role of the PD-1:PD-L1 pathway in immune resistance of HPV-associated head and neck squamous cell carcinoma. Cancer research *73*, 1733-1741.

Maginnis, M.S., Forrest, J.C., Kopecky-Bromberg, S.A., Dickeson, S.K., Santoro, S.A., Zutter, M.M., Nemerow, G.R., Bergelson, J.M., and Dermody, T.S. (2006). Beta1 integrin mediates internalization of mammalian reovirus. Journal of virology *80*, 2760-2770.

Mahalingam, D., Wilkinson, G.A., Eng, K.H., Fields, P., Raber, P., Moseley, J.L., Cheetham, K., Coffey, M., Nuovo, G., Kalinski, P., *et al.* (2020). Pembrolizumab in Combination with the Oncolytic Virus Pelareorep and Chemotherapy in Patients with Advanced Pancreatic Adenocarcinoma: A Phase Ib Study. Clinical cancer research : an official journal of the American Association for Cancer Research *26*, 71-81.

Mak, D., Corry, J., Lau, E., Rischin, D., and Hicks, R.J. (2011). Role of FDG-PET/CT in staging and follow-up of head and neck squamous cell carcinoma. The quarterly journal of nuclear medicine and molecular imaging : official publication of the Italian Association of Nuclear Medicine (AIMN) [and] the International Association of Radiopharmacology (IAR), [and] Section of the So *55*, 487-499.

Man, F., Koers, A., Karagiannis, P., Josephs, D.H., Bax, H.J., Gilbert, A.E., Dodev, T.S., Mele, S., Chiarruttini, G., Crescioli, S., *et al.* (2021). In vivo trafficking of a tumor-targeting IgE antibody: molecular imaging demonstrates rapid hepatobiliary clearance compared to IgG counterpart. Oncoimmunology *10*, 1966970.

Mandal, R., Şenbabaoğlu, Y., Desrichard, A., Havel, J.J., Dalin, M.G., Riaz, N., Lee, K.W., Ganly, I., Hakimi, A.A., Chan, T.A., *et al.* (2016). The head and neck cancer immune landscape and its immunotherapeutic implications. JCI insight *1*, e89829.

Marcato, P., Dean, C.A., Giacomantonio, C.A., and Lee, P.W. (2009). Oncolytic reovirus effectively targets breast cancer stem cells. Molecular therapy : the journal of the American Society of Gene Therapy *17*, 972-979.

Marganiec-Gałązka, J., Nähle, O.J., and Kossert, K. (2018). Activity determination of (68)Ge/(68)Ga by means of 4πβ(Č)-γ coincidence counting. Applied radiation and isotopes : including data, instrumentation and methods for use in agriculture, industry and medicine *134*, 240-244.

Markert, J.M., Medlock, M.D., Rabkin, S.D., Gillespie, G.Y., Todo, T., Hunter, W.D., Palmer, C.A., Feigenbaum, F., Tornatore, C., Tufaro, F., *et al.* (2000). Conditionally replicating herpes simplex virus mutant, G207 for the treatment of malignant glioma: results of a phase I trial. Gene therapy *7*, 867-874.

Martinive, P., De Wever, J., Bouzin, C., Baudelet, C., Sonveaux, P., Grégoire, V., Gallez, B., and Feron, O. (2006). Reversal of temporal and spatial heterogeneities in tumor perfusion identifies the tumor vascular tone as a tunable variable to improve drug delivery. Molecular Cancer Therapeutics *5*, 1620-1627.

Martone, T., Rosso, P., Albera, R., Migliaretti, G., Fraire, F., Pignataro, L., Pruneri, G., Bellone, G., and Cortesina, G. (2005). Prognostic relevance of CD105+ microvessel density in HNSCC patient outcome. Oral oncology *41*, 147-155.

Marur, S., D'Souza, G., Westra, W.H., and Forastiere, A.A. (2010). HPV-associated head and neck cancer: a virus-related cancer epidemic. The Lancet Oncology *11*, 781-789.

Matsumura, Y., and Maeda, H. (1986). A new concept for macromolecular therapeutics in cancer chemotherapy: mechanism of tumoritropic accumulation of proteins and the antitumor agent smancs. Cancer research *46*, 6387-6392.

Mazanet, M.M., and Hughes, C.C. (2002). B7-H1 is expressed by human endothelial cells and suppresses T cell cytokine synthesis. Journal of immunology (Baltimore, Md : 1950) *169*, 3581-3588.

McDonald, D., Stockwin, L., Matzow, T., Blair Zajdel, M.E., and Blair, G.E. (1999). Coxsackie and adenovirus receptor (CAR)-dependent and major histocompatibility complex (MHC) class I-independent uptake of recombinant adenoviruses into human tumour cells. Gene therapy *6*, 1512-1519.

McKeown, S.R. (2014). Defining normoxia, physoxia and hypoxia in tumours-implications for treatment response. The British journal of radiology *87*, 20130676.

McLane, L.M., Abdel-Hakeem, M.S., and Wherry, E.J. (2019). CD8 T Cell Exhaustion During Chronic Viral Infection and Cancer. Annual review of immunology *37*, 457-495.

McLaughlin, M., Pedersen, M., Roulstone, V., Bergerhoff, K.F., Smith, H.G., Whittock, H., Kyula, J.N., Dillon, M.T., Pandha, H.S., Vile, R.*, et al.* (2020). The PERK Inhibitor GSK2606414 Enhances Reovirus Infection in Head and Neck Squamous Cell Carcinoma via an ATF4-Dependent Mechanism. Molecular therapy oncolytics *16*, 238-249.

Mehanna, H.M., and Morton, R.P. (2006). Deterioration in quality-of-life of late (10-year) survivors of head and neck cancer. Clinical otolaryngology : official journal of ENT-UK ; official journal of Netherlands Society for Oto-Rhino-Laryngology & Cervico-Facial Surgery *31*, 204-211.

Mell, L.K., Brumund, K.T., Daniels, G.A., Advani, S.J., Zakeri, K., Wright, M.E., Onyeama, S.J., Weisman, R.A., Sanghvi, P.R., Martin, P.J.*, et al.* (2017). Phase I Trial of Intravenous Oncolytic Vaccinia Virus (GL-ONC1) with Cisplatin and Radiotherapy in Patients with Locoregionally Advanced Head and Neck Carcinoma. Clinical cancer research : an official journal of the American Association for Cancer Research *23*, 5696-5702.

Messenheimer, D.J., Jensen, S.M., Afentoulis, M.E., Wegmann, K.W., Feng, Z., Friedman, D.J., Gough, M.J., Urba, W.J., and Fox, B.A. (2017). Timing of PD-1 Blockade Is Critical to Effective Combination Immunotherapy with Anti-OX40. Clinical cancer research : an official journal of the American Association for Cancer Research *23*, 6165-6177.

Mestel, R. (2017). Cancer: Imaging with antibodies. Nature *543*, 743-746.

Meyer, J.P., Houghton, J.L., Kozlowski, P., Abdel-Atti, D., Reiner, T., Pillarsetty, N.V., Scholz, W.W., Zeglis, B.M., and Lewis, J.S. (2016). (18)F-Based Pretargeted PET Imaging Based on Bioorthogonal Diels-Alder Click Chemistry. Bioconjugate chemistry *27*, 298-301.

Meza, R., Jimenez-Mendoza, E., and Levy, D.T. (2020). Trends in Tobacco Use Among Adolescents by Grade, Sex, and Race, 1991-2019. JAMA network open *3*, e2027465.

Mezzadra, R., Sun, C., Jae, L.T., Gomez-Eerland, R., de Vries, E., Wu, W., Logtenberg, M.E.W., Slagter, M., Rozeman, E.A., Hofland, I*., et al.* (2017). Identification of CMTM6 and CMTM4 as PD-L1 protein regulators. Nature *549*, 106-110.

Middleton, M., Aroldi, F., Sacco, J., Milhem, M., Curti, B., MBioeth, A.V., Baum, S., Samson, A., Pavlick, A., Chesney, J*., et al.* (2020). 422 An open-label, multicenter, phase 1/2 clinical trial of RP1, an enhanced potency oncolytic HSV, combined with nivolumab: updated results from the skin cancer cohorts. Journal for immunotherapy of cancer *8*, A257-A257.

Mikada, M., Sukhbaatar, A., Miura, Y., Horie, S., Sakamoto, M., Mori, S., and Kodama, T. (2017). Evaluation of the enhanced permeability and retention effect in the early stages of lymph node metastasis. Cancer science *108*, 846-852.

Mirus, M., Tokalov, S.V., Wolf, G., Heinold, J., Prochnow, V., and Abolmaali, N. (2017). Noninvasive assessment and quantification of tumour vascularisation using MRI and CT in a tumour model with modifiable angiogenesis - An animal experimental prospective cohort study. European radiology experimental *1*, 15.

Mok, T.S.K., Wu, Y.L., Kudaba, I., Kowalski, D.M., Cho, B.C., Turna, H.Z., Castro, G., Jr., Srimuninnimit, V., Laktionov, K.K., Bondarenko, I*., et al.* (2019). Pembrolizumab versus chemotherapy for previously untreated, PD-L1-expressing, locally advanced or metastatic non-small-cell lung cancer (KEYNOTE-042): a randomised, open-label, controlled, phase 3 trial. Lancet (London, England) *393*, 1819-1830.

Monaco, G., Chen, H., Poidinger, M., Chen, J., de Magalhães, J.P., and Larbi, A. (2016). flowAI: automatic and interactive anomaly discerning tools for flow cytometry data. Bioinformatics (Oxford, England) *32*, 2473-2480.

Monteran, L., and Erez, N. (2019). The Dark Side of Fibroblasts: Cancer-Associated Fibroblasts as Mediators of Immunosuppression in the Tumor Microenvironment. Frontiers in immunology *10*, 1835.

Moore, E., Clavijo, P.E., Davis, R., Cash, H., Van Waes, C., Kim, Y., and Allen, C. (2016a). Established T Cell-Inflamed Tumors Rejected after Adaptive Resistance Was Reversed by Combination STING Activation and PD-1 Pathway Blockade. Cancer immunology research *4*, 1061-1071.

Moore, E.C., Cash, H.A., Caruso, A.M., Uppaluri, R., Hodge, J.W., Van Waes, C., and Allen, C.T. (2016b). Enhanced Tumor Control with Combination mTOR and PD-L1 Inhibition in Syngeneic Oral Cavity Cancers. Cancer immunology research *4*, 611-620.

Moran, P., and Smith, C. (1918). The correlation between relatives on the supposition of mendelian inheritance. Transactions of the Royal Society of Edinburgh *52*, 899-438.

Morita, Y., Masters, E.A., Schwarz, E.M., and Muthukrishnan, G. (2021). Interleukin-27 and Its Diverse Effects on Bacterial Infections. Frontiers in immunology *12*.

Morris, L., Graham, C.F., and Gordon, S. (1991). Macrophages in haemopoietic and other tissues of the developing mouse detected by the monoclonal antibody F4/80. Development (Cambridge, England) *112*, 517-526.

Mosely, S.I., Prime, J.E., Sainson, R.C., Koopmann, J.O., Wang, D.Y., Greenawalt, D.M., Ahdesmaki, M.J., Leyland, R., Mullins, S., Pacelli, L.*, et al.* (2017). Rational Selection of Syngeneic Preclinical Tumor Models for Immunotherapeutic Drug Discovery. Cancer immunology research *5*, 29-41.

Moses, W.W. (2011). Fundamental Limits of Spatial Resolution in PET. Nuclear instruments & methods in physics research Section A, Accelerators, spectrometers, detectors and associated equipment *648 Supplement 1*, S236-s240.

Mueller, S.N., Vanguri, V.K., Ha, S.J., West, E.E., Keir, M.E., Glickman, J.N., Sharpe, A.H., and Ahmed, R. (2010). PD-L1 has distinct functions in hematopoietic and nonhematopoietic cells in regulating T cell responses during chronic infection in mice. J Clin Invest *120*, 2508-2515.

Musolino, A., Naldi, N., Bortesi, B., Pezzuolo, D., Capelletti, M., Missale, G., Laccabue, D., Zerbini, A., Camisa, R., Bisagni, G.*, et al.* (2008). Immunoglobulin G fragment C receptor polymorphisms and clinical efficacy of trastuzumab-based therapy in patients with HER-2/neu-positive metastatic breast cancer. Journal of clinical oncology : official journal of the American Society of Clinical Oncology *26*, 1789-1796.

Muzi, M., O'Sullivan, F., Mankoff, D.A., Doot, R.K., Pierce, L.A., Kurland, B.F., Linden, H.M., and Kinahan, P.E. (2012). Quantitative assessment of dynamic PET imaging data in cancer imaging. Magnetic resonance imaging *30*, 1203-1215.

Naik, S., Nace, R., Federspiel, M.J., Barber, G.N., Peng, K.W., and Russell, S.J. (2012). Curative one-shot systemic virotherapy in murine myeloma. Leukemia *26*, 1870-1878.

Nakao, S., Arai, Y., Tasaki, M., Yamashita, M., Murakami, R., Kawase, T., Amino, N., Nakatake, M., Kurosaki, H., Mori, M.*, et al.* (2020). Intratumoral expression of IL-7 and IL-12 using an oncolytic virus increases systemic sensitivity to immune checkpoint blockade. Science translational medicine *12*.

Nauta, T.D., van den Broek, M., Gibbs, S., van der Pouw-Kraan, T.C., Oudejans, C.B., van Hinsbergh, V.W., and Koolwijk, P. (2017). Identification of HIF-2α-regulated genes that play a role in human microvascular endothelial sprouting during prolonged hypoxia in vitro. Angiogenesis *20*, 39-54.

Nedrow, J.R., Josefsson, A., Park, S., Ranka, S., Roy, S., and Sgouros, G. (2017). Imaging of Programmed Cell Death Ligand 1: Impact of Protein Concentration on Distribution of Anti-PD-L1 SPECT Agents in an Immunocompetent Murine Model of Melanoma. Journal of nuclear medicine : official publication, Society of Nuclear Medicine *58*, 1560-1566.

Nemunaitis, J., Ganly, I., Khuri, F., Arseneau, J., Kuhn, J., McCarty, T., Landers, S., Maples, P., Romel, L., Randlev, B., *et al.* (2000). Selective replication and oncolysis in p53 mutant tumors with ONYX-015, an E1B-55kD gene-deleted adenovirus, in patients with advanced head and neck cancer: a phase II trial. Cancer research *60*, 6359-6366.

Network, C.G.A. (2015). Comprehensive genomic characterization of head and neck squamous cell carcinomas. Nature *517*, 576-582.

Nguyen, H.M., Bommareddy, P.K., Silk, A.W., and Saha, D. (2021). Optimal timing of PD-1 blockade in combination with oncolytic virus therapy. Seminars in cancer biology.

Nguyen, K.B., Salazar-Mather, T.P., Dalod, M.Y., Van Deusen, J.B., Wei, X.Q., Liew, F.Y., Caligiuri, M.A., Durbin, J.E., and Biron, C.A. (2002). Coordinated and distinct roles for IFN-alpha beta, IL-12, and IL-15 regulation of NK cell responses to viral infection. Journal of immunology (Baltimore, Md : 1950) *169*, 4279-4287.

Ni, X.Y., Sui, H.X., Liu, Y., Ke, S.Z., Wang, Y.N., and Gao, F.G. (2012). TGF-β of lung cancer microenvironment upregulates B7H1 and GITRL expression in dendritic cells and is associated with regulatory T cell generation. Oncology reports *28*, 615-621.

Niculae, D., Dusman, R., Leonte, R.A., Chilug, L.E., Dragoi, C.M., Nicolae, A., Serban, R.M., Niculae, D.A., Dumitrescu, I.B., and Draganescu, D. (2021). Biological Pathways as Substantiation of the Use of Copper Radioisotopes in Cancer Theranostics. Frontiers in Physics *8*.

Niemeijer, A.N., Leung, D., Huisman, M.C., Bahce, I., Hoekstra, O.S., van Dongen, G.A.M.S., Boellaard, R., Du, S., Hayes, W., Smith, R.*, et al.* (2018). Whole body PD-1 and PD-L1 positron emission tomography in patients with non-small-cell lung cancer. Nat Commun *9*, 4664-4664.

Nieuwenhuis, B., Haenzi, B., Hilton, S., Carnicer-Lombarte, A., Hobo, B., Verhaagen, J., and Fawcett, J.W. (2021). Optimization of adeno-associated viral vector-mediated transduction of the corticospinal tract: comparison of four promoters. Gene therapy *28*, 56-74.

Nimmerjahn, F., and Ravetch, J.V. (2008). Fcgamma receptors as regulators of immune responses. Nature reviews Immunology *8*, 34-47.

Nimmerjahn, F., and Ravetch, J.V. (2012). Translating basic mechanisms of IgG effector activity into next generation cancer therapies. Cancer immunity *12*, 13.

Nishimura, H., Nose, M., Hiai, H., Minato, N., and Honjo, T. (1999). Development of lupus-like autoimmune diseases by disruption of the PD-1 gene encoding an ITIM motif-carrying immunoreceptor. Immunity *11*, 141-151.

Nishimura, H., Okazaki, T., Tanaka, Y., Nakatani, K., Hara, M., Matsumori, A., Sasayama, S., Mizoguchi, A., Hiai, H., Minato, N.*, et al.* (2001). Autoimmune dilated cardiomyopathy in PD-1 receptor-deficient mice. Science (New York, NY) *291*, 319-322.

Noble, W.S. (2009). How does multiple testing correction work? Nat Biotechnol *27*, 1135-1137.

Noguchi, T., Ward, J.P., Gubin, M.M., Arthur, C.D., Lee, S.H., Hundal, J., Selby, M.J., Graziano, R.F., Mardis, E.R., Korman, A.J.*, et al.* (2017). Temporally Distinct PD-L1 Expression by Tumor and Host Cells Contributes to Immune Escape. Cancer immunology research *5*, 106-117.

Norman, K.L., Hirasawa, K., Yang, A.D., Shields, M.A., and Lee, P.W. (2004). Reovirus oncolysis: the Ras/RalGEF/p38 pathway dictates host cell permissiveness to reovirus infection. Proc Natl Acad Sci U S A *101*, 11099-11104.

O'Malley, B.W., Jr., Cope, K.A., Johnson, C.S., and Schwartz, M.R. (1997). A new immunocompetent murine model for oral cancer. Archives of otolaryngology--head & neck surgery *123*, 20-24.

Olson, B., Li, Y., Lin, Y., Liu, E.T., and Patnaik, A. (2018). Mouse Models for Cancer Immunotherapy Research. Cancer discovery *8*, 1358-1365.

Onken, M.D., Winkler, A.E., Kanchi, K.L., Chalivendra, V., Law, J.H., Rickert, C.G., Kallogjeri, D., Judd, N.P., Dunn, G.P., Piccirillo, J.F., *et al.* (2014). A surprising cross-species conservation in the genomic landscape of mouse and human oral cancer identifies a transcriptional signature predicting metastatic disease. Clinical cancer research : an official journal of the American Association for Cancer Research *20*, 2873-2884.

Oosting, S.F., and Haddad, R.I. (2019). Best Practice in Systemic Therapy for Head and Neck Squamous Cell Carcinoma. Frontiers in oncology *9*.

Orellana García, L.P., Ehmann, F., Hines, P.A., Ritzhaupt, A., and Brand, A. (2021). Biomarker and Companion Diagnostics-A Review of Medicinal Products Approved by the European Medicines Agency. Frontiers in medicine *8*, 753187.

Orvedahl, A., Alexander, D., Tallóczy, Z., Sun, Q., Wei, Y., Zhang, W., Burns, D., Leib, D.A., and Levine, B. (2007). HSV-1 ICP34.5 confers neurovirulence by targeting the Beclin 1 autophagy protein. Cell host & microbe *1*, 23-35.

Ou, J.-N., Wiedeman, A.E., and Stevens, A.M. (2012). TNF-α and TGF-β Counter-Regulate PD-L1 Expression on Monocytes in Systemic Lupus Erythematosus. Scientific reports *2*, 295.

Oyen, W.J., Boerman, O.C., Subramanian, R., Koenders, E.B., Claessens, R.A., van der Meer, J.W., and Corstens, F.H. (1996). Biodistribution of 111In-labelled IgG and IgM in experimental infection. Nuclear medicine communications *17*, 616-620.

Pagani, M., Stone-Elander, S., and Larsson, S.A. (1997). Alternative positron emission tomography with non-conventional positron emitters: effects of their physical properties on image quality and potential clinical applications. European journal of nuclear medicine *24*, 1301-1327.

Pandit-Taskar, N., O'Donoghue, J.A., Beylergil, V., Lyashchenko, S., Ruan, S., Solomon, S.B., Durack, J.C., Carrasquillo, J.A., Lefkowitz, R.A., Gonen, M., *et al.* (2014). ^{89}Zr-huJ591 immuno-PET imaging in patients with advanced metastatic prostate cancer. European journal of nuclear medicine and molecular imaging *41*, 2093-2105.

Pandit-Taskar, N., Postow, M.A., Hellmann, M.D., Harding, J.J., Barker, C.A., O'Donoghue, J.A., Ziolkowska, M., Ruan, S., Lyashchenko, S.K., Tsai, F., *et al.* (2020). First-in-Humans Imaging with (89)Zr-Df-IAB22M2C Anti-CD8 Minibody in Patients with Solid Malignancies: Preliminary Pharmacokinetics, Biodistribution, and Lesion Targeting. Journal of nuclear medicine : official publication, Society of Nuclear Medicine *61*, 512-519.

Pang, X., Fan, H.Y., Tang, Y.L., Wang, S.S., Cao, M.X., Wang, H.F., Dai, L.L., Wang, K., Yu, X.H., Wu, J.B., *et al.* (2020). Myeloid derived suppressor cells contribute to the malignant progression of oral squamous cell carcinoma. PloS one *15*, e0229089.

Pardoll, D.M. (2012). The blockade of immune checkpoints in cancer immunotherapy. Nature reviews Cancer *12*, 252-264.

Park, J., Lee, S., Kim, Y., and Yoo, T.H. (2021). Methods to generate site-specific conjugates of antibody and protein. Bioorganic & medicinal chemistry *30*, 115946.

Park, J.J., Omiya, R., Matsumura, Y., Sakoda, Y., Kuramasu, A., Augustine, M.M., Yao, S., Tsushima, F., Narazaki, H., Anand, S., *et al.* (2010). B7-H1/CD80 interaction is required for the induction and maintenance of peripheral T-cell tolerance. Blood *116*, 1291-1298.

Passaro, C., Alayo, Q., De Laura, I., McNulty, J., Grauwet, K., Ito, H., Bhaskaran, V., Mineo, M., Lawler, S.E., Shah, K., *et al.* (2019). Arming an Oncolytic Herpes Simplex Virus Type 1 with a Single-chain Fragment Variable Antibody against PD-1 for Experimental Glioblastoma Therapy. Clinical cancer research : an official journal of the American Association for Cancer Research *25*, 290-299.

Passaro, C., Alayo, Q., DeLaura, I., McNulty, J., Grauwet, K., Ito, H., Bhaskaran, V., Mineo, M., Lawler, S.E., Shah, K., *et al.* (2020). Correction: Arming an Oncolytic Herpes Simplex Virus Type 1 with a Single-chain Fragment Variable Antibody against PD-1 for Experimental Glioblastoma Therapy. Clinical cancer research : an official journal of the American Association for Cancer Research *26*, 758.

Patra, M., Bauman, A., Mari, C., Fischer, C.A., Blacque, O., Häussinger, D., Gasser, G., and Mindt, T.L. (2014). An octadentate bifunctional chelating agent for the development of stable zirconium-89 based molecular imaging probes. Chemical communications (Cambridge, England) *50*, 11523-11525.

Paul, S., and Lal, G. (2017). The Molecular Mechanism of Natural Killer Cells Function and Its Importance in Cancer Immunotherapy. Frontiers in immunology *8*, 1124.

Peach, R.J., Bajorath, J., Naemura, J., Leytze, G., Greene, J., Aruffo, A., and Linsley, P.S. (1995). Both extracellular immunoglobin-like domains of CD80 contain residues critical for binding T cell surface receptors CTLA-4 and CD28. The Journal of biological chemistry *270*, 21181-21187.

Pearson, K., and Heron, D. (1913). On theories of association. Biometrika *9*, 159-315.

Perk, L.R., Vosjan, M.J., Visser, G.W., Budde, M., Jurek, P., Kiefer, G.E., and van Dongen, G.A. (2010). p-Isothiocyanatobenzyl-desferrioxamine: a new bifunctional chelate for facile radiolabeling of monoclonal antibodies with zirconium-89 for immuno-PET imaging. European journal of nuclear medicine and molecular imaging *37*, 250-259.

Pesce, G., Marcon, A., Calciano, L., Perret, J.L., Abramson, M.J., Bono, R., Bousquet, J., Fois, A.G., Janson, C., Jarvis, D., *et al.* (2019). Time and age trends in smoking cessation in Europe. PloS one *14*, e0211976.

Peters, C., and Rabkin, S.D. (2015). Designing Herpes Viruses as Oncolytics. Molecular therapy oncolytics *2*, 15010-.

Petrova, V., Annicchiarico-Petruzzelli, M., Melino, G., and Amelio, I. (2018). The hypoxic tumour microenvironment. Oncogenesis *7*, 10.

Pfister, D.G., Spencer, S., Adelstein, D., Adkins, D., Anzai, Y., Brizel, D.M., Bruce, J.Y., Busse, P.M., Caudell, J.J., Cmelak, A.J., *et al.* (2020). Head and Neck Cancers, Version 2.2020, NCCN Clinical Practice Guidelines in Oncology. Journal of the National Comprehensive Cancer Network : JNCCN *18*, 873-898.

Phelps, M.E., Hoffman, E.J., Mullani, N.A., and Ter-Pogossian, M.M. (1975). Application of annihilation coincidence detection to transaxial reconstruction tomography. Journal of nuclear medicine : official publication, Society of Nuclear Medicine *16*, 210-224.

Phelps, M.E., and Los Alamos National, L. (1988). Positron emission tomography ([Los Alamos, N.M.]: [Los Alamos National Laboratory]).

Planès, R., BenMohamed, L., Leghmari, K., Delobel, P., Izopet, J., and Bahraoui, E. (2014). HIV-1 Tat protein induces PD-L1 (B7-H1) expression on dendritic cells through tumor necrosis factor alpha- and toll-like receptor 4-mediated mechanisms. Journal of virology *88*, 6672-6689.

Pollok, K.E., Lahn, M., Enas, N., McNulty, A., Graff, J., Cai, S., Hartwell, J.R., Ernstberger, A., Thornton, D., Brail, L., *et al.* (2009). In Vivo Measurements of Tumor Metabolism and Growth after Administration of Enzastaurin Using Small Animal FDG Positron Emission Tomography. Journal of oncology *2009*, 596560.

Price, D.L., Lin, S.F., Han, Z., Simpson, G., Coffin, R.S., Wong, J., Li, S., Fong, Y., and Wong, R.J. (2010). Oncolysis using herpes simplex virus type 1 engineered to express cytosine deaminase and a fusogenic glycoprotein for head and neck squamous cell carcinoma. Archives of otolaryngology--head & neck surgery *136*, 151-158.

Price, E.W., and Orvig, C. (2014). Matching chelators to radiometals for radiopharmaceuticals. Chemical Society reviews *43*, 260-290.

Provenzano, P.P., Inman, D.R., Eliceiri, K.W., Beggs, H.E., and Keely, P.J. (2008a). Mammary epithelial-specific disruption of focal adhesion kinase retards tumor formation and metastasis in a transgenic mouse model of human breast cancer. The American journal of pathology *173*, 1551-1565.

Provenzano, P.P., Inman, D.R., Eliceiri, K.W., Knittel, J.G., Yan, L., Rueden, C.T., White, J.G., and Keely, P.J. (2008b). Collagen density promotes mammary tumor initiation and progression. BMC medicine *6*, 11.

Pulko, V., Liu, X., Krco, C.J., Harris, K.J., Frigola, X., Kwon, E.D., and Dong, H. (2009). TLR3-stimulated dendritic cells up-regulate B7-H1 expression and influence the magnitude of CD8 T cell responses to tumor vaccination. Journal of immunology (Baltimore, Md : 1950) *183*, 3634-3641.

Puzanov, I., Diab, A., Abdallah, K., Bingham, C.O., 3rd, Brogdon, C., Dadu, R., Hamad, L., Kim, S., Lacouture, M.E., LeBoeuf, N.R.*, et al.* (2017). Managing toxicities associated with immune checkpoint inhibitors: consensus recommendations from the Society for Immunotherapy of Cancer (SITC) Toxicity Management Working Group. Journal for immunotherapy of cancer *5*, 95.

Pynnonen, M.A., Gillespie, M.B., Roman, B., Rosenfeld, R.M., Tunkel, D.E., Bontempo, L., Brook, I., Chick, D.A., Colandrea, M., Finestone, S.A.*, et al.* (2017). Clinical Practice Guideline: Evaluation of the Neck Mass in Adults. Otolaryngology--head and neck surgery : official journal of American Academy of Otolaryngology-Head and Neck Surgery *157*, S1-s30.

Qian, Y., Deng, J., Geng, L., Xie, H., Jiang, G., Zhou, L., Wang, Y., Yin, S., Feng, X., Liu, J.*, et al.* (2008). TLR4 signaling induces B7-H1 expression through MAPK pathways in bladder cancer cells. Cancer investigation *26*, 816-821.

Quandt, D., Jasinski-Bergner, S., Müller, U., Schulze, B., and Seliger, B. (2014). Synergistic effects of IL-4 and TNFα on the induction of B7-H1 in renal cell carcinoma cells inhibiting allogeneic T cell proliferation. Journal of translational medicine *12*, 151.

Quetglas, J.I., Labiano, S., Aznar, M., Bolaños, E., Azpilikueta, A., Rodriguez, I., Casales, E., Sánchez-Paulete, A.R., Segura, V., Smerdou, C.*, et al.* (2015). Virotherapy with a Semliki Forest Virus-Based Vector Encoding IL12 Synergizes with PD-1/PD-L1 Blockade. Cancer immunology research *3*, 449-454.

Quixabeira, D.C.A., Zafar, S., Santos, J.M., Cervera-Carrascon, V., Havunen, R., Kudling, T.V., Basnet, S., Anttila, M., Kanerva, A., and Hemminki, A. (2021). Oncolytic Adenovirus Coding for a Variant Interleukin 2 (vIL-2) Cytokine Re-Programs the Tumor Microenvironment and Confers Enhanced Tumor Control. Frontiers in immunology *12*.

Radhakrishnan, P., Basma, H., Klinkebiel, D., Christman, J., and Cheng, P.W. (2008). Cell type-specific activation of the cytomegalovirus promoter by dimethylsulfoxide and 5-aza-2'-deoxycytidine. The international journal of biochemistry & cell biology *40*, 1944-1955.

Radu, M., and Chernoff, J. (2013). An in vivo assay to test blood vessel permeability. Journal of visualized experiments : JoVE, e50062.

Raftery, M.J., Abdelaziz, M.O., Hofmann, J., and Schönrich, G. (2018). Hantavirus-Driven PD-L1/PD-L2 Upregulation: An Imperfect Viral Immune Evasion Mechanism. Frontiers in immunology *9*, 2560.

Rancati, T., Schwarz, M., Allen, A.M., Feng, F., Popovtzer, A., Mittal, B., and Eisbruch, A. (2010). Radiation dose-volume effects in the larynx and pharynx. International journal of radiation oncology, biology, physics *76*, S64-69.

Reck, M., Rodríguez-Abreu, D., Robinson, A.G., Hui, R., Csőszi, T., Fülöp, A., Gottfried, M., Peled, N., Tafreshi, A., Cuffe, S.*, et al.* (2016). Pembrolizumab versus Chemotherapy for PD-L1-Positive Non-Small-Cell Lung Cancer. The New England journal of medicine *375*, 1823-1833.

Reddy, S., and Robinson, M.K. (2010). Immuno-positron emission tomography in cancer models. Seminars in nuclear medicine *40*, 182-189.

Rettig, E.M., D'Souza, G., Thompson, C.B., Koch, W.M., Eisele, D.W., and Fakhry, C. (2016). Health-related quality of life before and after head and neck squamous cell carcinoma: Analysis of the Surveillance, Epidemiology, and End Results-Medicare Health Outcomes Survey linkage. Cancer *122*, 1861-1870.

Ribas, A. (2015). Adaptive Immune Resistance: How Cancer Protects from Immune Attack. Cancer discovery *5*, 915-919.

Ribas, A., Dummer, R., Puzanov, I., VanderWalde, A., Andtbacka, R.H.I., Michielin, O., Olszanski, A.J., Malvehy, J., Cebon, J., Fernandez, E.*, et al.* (2017). Oncolytic Virotherapy Promotes Intratumoral T Cell Infiltration and Improves Anti-PD-1 Immunotherapy. Cell *170*, 1109-1119.e1110.

Rimm, D.L., Han, G., Taube, J.M., Yi, E.S., Bridge, J.A., Flieder, D.B., Homer, R., West, W.W., Wu, H., Roden, A.C.*, et al.* (2017). A Prospective, Multi-institutional, Pathologist-Based Assessment of 4 Immunohistochemistry Assays for PD-L1 Expression in Non-Small Cell Lung Cancer. JAMA oncology *3*, 1051-1058.

Rippe, B., and Haraldsson, B. (1994). Transport of macromolecules across microvascular walls: the two-pore theory. Physiological reviews *74*, 163-219.

Rittmeyer, A., Barlesi, F., Waterkamp, D., Park, K., Ciardiello, F., von Pawel, J., Gadgeel, S.M., Hida, T., Kowalski, D.M., Dols, M.C.*, et al.* (2017). Atezolizumab versus docetaxel in patients with previously treated non-small-cell lung cancer (OAK): a phase 3, open-label, multicentre randomised controlled trial. Lancet (London, England) *389*, 255-265.

Robbins, Y., Greene, S., Friedman, J., Clavijo, P.E., Van Waes, C., Fabian, K.P., Padget, M.R., Abdul Sater, H., Lee, J.H., Soon-Shiong, P.*, et al.* (2020). Tumor control via targeting PD-L1 with chimeric antigen receptor modified NK cells. eLife *9*.

Roederer, M. (2002). Compensation in flow cytometry. Current protocols in cytometry *Chapter 1*, Unit 1.14.

Roh, J.L., Yeo, N.K., Kim, J.S., Lee, J.H., Cho, K.J., Choi, S.H., Nam, S.Y., and Kim, S.Y. (2007). Utility of 2-[18F] fluoro-2-deoxy-D-glucose positron emission tomography and positron emission tomography/computed tomography imaging in the preoperative staging of head and neck squamous cell carcinoma. Oral oncology *43*, 887-893.

Roopenian, D.C., and Akilesh, S. (2007). FcRn: the neonatal Fc receptor comes of age. Nature reviews Immunology *7*, 715-725.

Rose-Ped, A.M., Bellm, L.A., Epstein, J.B., Trotti, A., Gwede, C., and Fuchs, H.J. (2002). Complications of radiation therapy for head and neck cancers. The patient's perspective. Cancer nursing *25*, 461-467; quiz 468-469.

Rosendahl Huber, S., van Beek, J., de Jonge, J., Luytjes, W., and van Baarle, D. (2014). T cell responses to viral infections - opportunities for Peptide vaccination. Frontiers in immunology *5*, 171.

Roulstone, V., Kyula, J., Thomas, S., Kuncheria, L., Bommareddy, P.K., Smith, H., Whittock, H., Coffin, R.S., and Harrington, K. (2021). Abstract 1917: Immunomodulatory effects of a novel, enhanced potency gibbon ape leukaemia virus (GALV) fusogenic membrane glycoprotein-expressing herpes simplex virus platform with increased efficacy combined with anti PD-1 therapy. Cancer research *81*, 1917-1917.

Rudnick, S.I., and Adams, G.P. (2009). Affinity and avidity in antibody-based tumor targeting. Cancer biotherapy & radiopharmaceuticals *24*, 155-161.

Rudnick, S.I., Lou, J., Shaller, C.C., Tang, Y., Klein-Szanto, A.J., Weiner, L.M., Marks, J.D., and Adams, G.P. (2011). Influence of affinity and antigen internalization on the uptake and penetration of Anti-HER2 antibodies in solid tumors. Cancer research *71*, 2250-2259.

Ruffell, B., and Coussens, L.M. (2015). Macrophages and therapeutic resistance in cancer. Cancer cell *27*, 462-472.

Russell, S.J., and Peng, K.W. (2007). Viruses as anticancer drugs. Trends in pharmacological sciences *28*, 326-333.

Russell, S.J., Peng, K.W., and Bell, J.C. (2012). Oncolytic virotherapy. Nat Biotechnol *30*, 658-670.

Saâda-Bouzid, E., Defaucheux, C., Karabajakian, A., Coloma, V.P., Servois, V., Paoletti, X., Even, C., Fayette, J., Guigay, J., Loirat, D*., et al.* (2017). Hyperprogression during anti-PD-1/PD-L1 therapy in patients with recurrent and/or metastatic head and neck squamous cell carcinoma. Ann Oncol *28*, 1605-1611.

Safdari, Y., Farajnia, S., Asgharzadeh, M., and Khalili, M. (2013). Antibody humanization methods - a review and update. Biotechnology & genetic engineering reviews *29*, 175-186.

Saha, G.B. (2005). Performance Characteristics of PET Scanners. In Basics of PET Imaging: Physics, Chemistry, and Regulations, G.B. Saha, ed. (New York, NY: Springer New York), pp. 81-98.

Sahai, E., Astsaturov, I., Cukierman, E., DeNardo, D.G., Egeblad, M., Evans, R.M., Fearon, D., Greten, F.R., Hingorani, S.R., Hunter, T.*, et al.* (2020). A framework for advancing our understanding of cancer-associated fibroblasts. Nature Reviews Cancer *20*, 174-186.

Sainz, B., Jr., and Halford, W.P. (2002). Alpha/Beta interferon and gamma interferon synergize to inhibit the replication of herpes simplex virus type 1. Journal of virology *76*, 11541-11550.

Salacinski, P., Hope, J., McLean, C., Clement-Jones, V., Sykes, J., Price, J., and Lowry, P.J. (1979). A new simple method which allows theoretical incorporation of radio-iodine into proteins and peptides without damage [proceedings]. The Journal of endocrinology *81*, 131p.

Samson, A., Scott, K.J., Taggart, D., West, E.J., Wilson, E., Nuovo, G.J., Thomson, S., Corns, R., Mathew, R.K., Fuller, M.J.*, et al.* (2018). Intravenous delivery of oncolytic reovirus to brain tumor patients immunologically primes for subsequent checkpoint blockade. Science translational medicine *10*.

Sandker, G.G.W., Adema, G., Molkenboer-Kuenen, J., Wierstra, P., Bussink, J., Heskamp, S., and Aarntzen, E. (2022). PD-L1 Antibody Pharmacokinetics and Tumor Targeting in Mouse Models for Infectious Diseases. Frontiers in immunology *13*, 837370.

Schaaf, M.B., Garg, A.D., and Agostinis, P. (2018). Defining the role of the tumor vasculature in antitumor immunity and immunotherapy. Cell death & disease *9*, 115.

Schmid, P., Adams, S., Rugo, H.S., Schneeweiss, A., Barrios, C.H., Iwata, H., Diéras, V., Hegg, R., Im, S.A., Shaw Wright, G.*, et al.* (2018). Atezolizumab and Nab-Paclitaxel in Advanced Triple-Negative Breast Cancer. The New England journal of medicine *379*, 2108-2121.

Schmitt, A., Barth, T.F., Beyer, E., Borchert, F., Rojewski, M., Chen, J., Guillaume, P., Gronau, S., Greiner, J., Möller, P.*, et al.* (2009). The tumor antigens RHAMM and G250/CAIX are expressed in head and neck squamous cell carcinomas and elicit specific CD8+ T cell responses. International journal of oncology *34*, 629-639.

Schneider, C.A., Rasband, W.S., and Eliceiri, K.W. (2012). NIH Image to ImageJ: 25 years of image analysis. Nature methods *9*, 671-675.

Schönrich, G., and Raftery, M.J. (2019). The PD-1/PD-L1 Axis and Virus Infections: A Delicate Balance. Frontiers in Cellular and Infection Microbiology *9*.

Schreiner, B., Mitsdoerffer, M., Kieseier, B.C., Chen, L., Hartung, H.P., Weller, M., and Wiendl, H. (2004). Interferon-beta enhances monocyte and dendritic cell expression of B7-H1 (PD-L1), a strong inhibitor of autologous T-cell activation: relevance for the immune modulatory effect in multiple sclerosis. Journal of neuroimmunology *155*, 172-182.

Schultz-Hector, S., and Haghayegh, S. (1993). Beta-fibroblast growth factor expression in human and murine squamous cell carcinomas and its relationship to regional endothelial cell proliferation. Cancer research *53*, 1444-1449.

Seiwert, T.Y., Burtness, B., Mehra, R., Weiss, J., Berger, R., Eder, J.P., Heath, K., McClanahan, T., Lunceford, J., Gause, C., *et al.* (2016). Safety and clinical activity of pembrolizumab for treatment of recurrent or metastatic squamous cell carcinoma of the head and neck (KEYNOTE-012): an open-label, multicentre, phase 1b trial. The Lancet Oncology *17*, 956-965.

Semenza, G.L. (2012). Hypoxia-inducible factors in physiology and medicine. Cell *148*, 399-408.

Severin, G.W., Engle, J.W., Barnhart, T.E., and Nickles, R.J. (2011). 89Zr radiochemistry for positron emission tomography. Medicinal chemistry (Shariqah (United Arab Emirates)) *7*, 389-394.

Shah, S., Caruso, A., Cash, H., Waes, C.V., and Allen, C.T. (2016). Pools of programmed death-ligand within the oral cavity tumor microenvironment: Variable alteration by targeted therapies. Head & neck *38*, 1176-1186.

Sharma, S.K., Glaser, J.M., Edwards, K.J., Khozeimeh Sarbisheh, E., Salih, A.K., Lewis, J.S., and Price, E.W. (2021). A Systematic Evaluation of Antibody Modification and (89)Zr-Radiolabeling for Optimized Immuno-PET. Bioconjugate chemistry *32*, 1177-1191.

Sharpe, A.H., and Pauken, K.E. (2017). The diverse functions of the PD1 inhibitory pathway. Nature reviews Immunology.

Shen, W., Patnaik, M.M., Ruiz, A., Russell, S.J., and Peng, K.W. (2016). Immunovirotherapy with vesicular stomatitis virus and PD-L1 blockade enhances therapeutic outcome in murine acute myeloid leukemia. Blood *127*, 1449-1458.

Sheppard, K.A., Fitz, L.J., Lee, J.M., Benander, C., George, J.A., Wooters, J., Qiu, Y., Jussif, J.M., Carter, L.L., Wood, C.R., *et al.* (2004). PD-1 inhibits T-cell receptor induced phosphorylation of the ZAP70/CD3zeta signalosome and downstream signaling to PKCtheta. FEBS letters *574*, 37-41.

Sher, A., Lacoeuille, F., Fosse, P., Vervueren, L., Cahouet-Vannier, A., Dabli, D., Bouchet, F., and Couturier, O. (2016). For avid glucose tumors, the SUV peak is the most reliable parameter for [(18)F]FDG-PET/CT quantification, regardless of acquisition time. EJNMMI research *6*, 21.

Shokeen, M., and Wadas, T.J. (2011). The development of copper radiopharmaceuticals for imaging and therapy. Medicinal chemistry (Shariqah (United Arab Emirates)) *7*, 413-429.

Shukla, A.K., and Kumar, U. (2006). Positron emission tomography: An overview. Journal of medical physics *31*, 13-21.

Siegal, F.P., Kadowaki, N., Shodell, M., Fitzgerald-Bocarsly, P.A., Shah, K., Ho, S., Antonenko, S., and Liu, Y.J. (1999). The nature of the principal type 1 interferon-producing cells in human blood. Science (New York, NY) *284*, 1835-1837.

Simizu, B., and Terasima, T. (1988). Vero Cells: Origin, Properties and Biomedical Applications (Department of Microbiology, School of Medicine, Chiba University).

Simonetta, F., Alam, I.S., Lohmeyer, J.K., Sahaf, B., Good, Z., Chen, W., Xiao, Z., Hirai, T., Scheller, L., Engels, P., *et al.* (2021). Molecular Imaging of Chimeric Antigen Receptor T Cells by ICOS-ImmunoPET. Clinical cancer research : an official journal of the American Association for Cancer Research *27*, 1058-1068.

Simpson, G.R., Han, Z., Liu, B., Wang, Y., Campbell, G., and Coffin, R.S. (2006). Combination of a fusogenic glycoprotein, prodrug activation, and oncolytic herpes simplex virus for enhanced local tumor control. Cancer research *66*, 4835-4842.

Song, S., Yuan, P., Wu, H., Chen, J., Fu, J., Li, P., Lu, J., and Wei, W. (2014). Dendritic cells with an increased PD-L1 by TGF-β induce T cell anergy for the cytotoxicity of hepatocellular carcinoma cells. International immunopharmacology *20*, 117-123.

Sørensen, B.S., Busk, M., Olthof, N., Speel, E.J., Horsman, M.R., Alsner, J., and Overgaard, J. (2013). Radiosensitivity and effect of hypoxia in HPV positive head and neck cancer cells. Radiotherapy and oncology : journal of the European Society for Therapeutic Radiology and Oncology *108*, 500-505.

Spear, P.G. (2004). Herpes simplex virus: receptors and ligands for cell entry. Cellular microbiology *6*, 401-410.

Spinks, T.J., Karia, D., Leach, M.O., and Flux, G. (2014). Quantitative PET and SPECT performance characteristics of the Albira Trimodal pre-clinical tomograph. Physics in medicine and biology *59*, 715-731.

Stimmel, J.B., Merrill, B.M., Kuyper, L.F., Moxham, C.P., Hutchins, J.T., Fling, M.E., and Kull, F.C., Jr. (2000). Site-specific conjugation on serine right-arrow cysteine variant monoclonal antibodies. The Journal of biological chemistry *275*, 30445-30450.

Stojdl, D.F., Lichty, B.D., tenOever, B.R., Paterson, J.M., Power, A.T., Knowles, S., Marius, R., Reynard, J., Poliquin, L., Atkins, H.*, et al.* (2003). VSV strains with defects in their ability to shutdown innate immunity are potent systemic anti-cancer agents. Cancer cell *4*, 263-275.

Student (1908). The Probable Error of a Mean. Biometrika *6*, 1-25.

Sugiura, D., Maruhashi, T., Okazaki, I.-m., Shimizu, K., Maeda, T.K., Takemoto, T., and Okazaki, T. (2019). Restriction of PD-1 function by cis-PD-L1/CD80 interactions is required for optimal T cell responses. Science (New York, NY) *364*, 558-566.

Sugiura, D., Okazaki, I.M., Maeda, T.K., Maruhashi, T., Shimizu, K., Arakaki, R., Takemoto, T., Ishimaru, N., and Okazaki, T. (2022). PD-1 agonism by anti-CD80 inhibits T cell activation and alleviates autoimmunity. Nature immunology *23*, 399-410.

Sun, C., Mezzadra, R., and Schumacher, T.N. (2018). Regulation and Function of the PD-L1 Checkpoint. Immunity *48*, 434-452.

Sun, J., Fang, G., Zuo, Z., Yu, X., Xue, L., Li, C., and Li, S. (2021). Identification of Immune Subtypes for Predicting the Prognosis of Patients in Head and Neck Squamous Cell Carcinoma. Technology in cancer research & treatment *20*, 15330338211045823.

Sundaresan, G., Yazaki, P.J., Shively, J.E., Finn, R.D., Larson, S.M., Raubitschek, A.A., Williams, L.E., Chatziioannou, A.F., Gambhir, S.S., and Wu, A.M. (2003). 124I-labeled engineered anti-CEA minibodies and diabodies allow high-contrast, antigen-specific small-animal PET imaging of xenografts in athymic mice. Journal of nuclear medicine : official publication, Society of Nuclear Medicine *44*, 1962-1969.

Taberna, M., Mena, M., Pavón, M.A., Alemany, L., Gillison, M.L., and Mesía, R. (2017). Human papillomavirus-related oropharyngeal cancer. Ann Oncol *28*, 2386-2398.

Tabrizi, M., Bornstein, G.G., and Suria, H. (2010). Biodistribution mechanisms of therapeutic monoclonal antibodies in health and disease. The AAPS journal *12*, 33-43.

Takano, G., Esaki, S., Goshima, F., Enomoto, A., Hatano, Y., Ozaki, H., Watanabe, T., Sato, Y., Kawakita, D., Murakami, S., *et al.* (2021). Oncolytic activity of naturally attenuated herpes-simplex virus HF10 against an immunocompetent model of oral carcinoma. Molecular therapy oncolytics *20*, 220-227.

Tedcastle, A., Illingworth, S., Brown, A., Seymour, L.W., and Fisher, K.D. (2016). Actin-resistant DNAse I Expression From Oncolytic Adenovirus Enadenotucirev Enhances Its Intratumoral Spread and Reduces Tumor Growth. Molecular therapy : the journal of the American Society of Gene Therapy *24*, 796-804.

Ter-Pogossian, M.M., Phelps, M.E., Hoffman, E.J., and Mullani, N.A. (1975). A positron-emission transaxial tomograph for nuclear imaging (PETT). Radiology *114*, 89-98.

Thomas, G.T., Lewis, M.P., and Speight, P.M. (1999). Matrix metalloproteinases and oral cancer. Oral oncology *35*, 227-233.

Thomas, S., Kuncheria, L., Roulstone, V., Kyula, J.N., Mansfield, D., Bommareddy, P.K., Smith, H., Kaufman, H.L., Harrington, K.J., and Coffin, R.S. (2019). Development of a new fusion-enhanced oncolytic immunotherapy platform based on herpes simplex virus type 1. Journal for immunotherapy of cancer *7*, 214.

Tiraby, M., Cazaux, C., Baron, M., Drocourt, D., Reynes, J.P., and Tiraby, G. (1998). Concomitant expression of E. coli cytosine deaminase and uracil phosphoribosyltransferase improves the cytotoxicity of 5-fluorocytosine. FEMS microbiology letters *167*, 41-49.

Todo, T., Martuza, R.L., Rabkin, S.D., and Johnson, P.A. (2001). Oncolytic herpes simplex virus vector with enhanced MHC class I presentation and tumor cell killing. Proceedings of the National Academy of Sciences *98*, 6396-6401.

Togashi, Y., Shitara, K., and Nishikawa, H. (2019). Regulatory T cells in cancer immunosuppression - implications for anticancer therapy. Nature reviews Clinical oncology *16*, 356-371.

Tong, S., Alessio, A.M., and Kinahan, P.E. (2010). Image reconstruction for PET/CT scanners: past achievements and future challenges. Imaging in medicine *2*, 529-545.

Topalian, S.L., Hodi, F.S., Brahmer, J.R., Gettinger, S.N., Smith, D.C., McDermott, D.F., Powderly, J.D., Carvajal, R.D., Sosman, J.A., Atkins, M.B.*, et al.* (2012). Safety, activity, and immune correlates of anti-PD-1 antibody in cancer. The New England journal of medicine *366*, 2443-2454.

Topolcan, O., and Holubec, L., Jr. (2008). The role of thymidine kinase in cancer diseases. Expert opinion on medical diagnostics *2*, 129-141.

Trinchieri, G. (2003). Interleukin-12 and the regulation of innate resistance and adaptive immunity. Nature reviews Immunology *3*, 133-146.

Trotter, M.J., Olive, P.L., and Chaplin, D.J. (1990). Effect of vascular marker Hoechst 33342 on tumour perfusion and cardiovascular function in the mouse. British journal of cancer *62*, 903-908.

Tu, Z., Pierce, R.H., Kurtis, J., Kuroki, Y., Crispe, I.N., and Orloff, M.S. (2010). Hepatitis C virus core protein subverts the antiviral activities of human Kupffer cells. Gastroenterology *138*, 305-314.

Tukey, J.W. (1949). Comparing individual means in the analysis of variance. Biometrics *5*, 99-114.

Turkington, T.G. (2001). Introduction to PET instrumentation. Journal of nuclear medicine technology *29*, 4-11.

Twigger, K., Roulstone, V., Kyula, J., Karapanagiotou, E.M., Syrigos, K.N., Morgan, R., White, C., Bhide, S., Nuovo, G., Coffey, M.*, et al.* (2012). Reovirus exerts potent oncolytic effects in head and neck cancer cell lines that are independent of signalling in the EGFR pathway. BMC cancer *12*, 368.

Twumasi-Boateng, K., Pettigrew, J.L., Kwok, Y.Y.E., Bell, J.C., and Nelson, B.H. (2018). Oncolytic viruses as engineering platforms for combination immunotherapy. Nature reviews Cancer *18*, 419-432.

Uchihashi, T., Nakahara, H., Fukuhara, H., Iwai, M., Ito, H., Sugauchi, A., Tanaka, M., Kogo, M., and Todo, T. (2021). Oncolytic herpes virus G47Δ injected into tongue cancer swiftly traffics in lymphatics and suppresses metastasis. Molecular therapy oncolytics *22*, 388-398.

Uusi-Kerttula, H., Hulin-Curtis, S., Davies, J., and Parker, A.L. (2015). Oncolytic Adenovirus: Strategies and Insights for Vector Design and Immuno-Oncolytic Applications. Viruses *7*, 6009-6042.

Vanderhoek, M., Perlman, S.B., and Jeraj, R. (2012). Impact of the definition of peak standardized uptake value on quantification of treatment response. Journal of nuclear medicine : official publication, Society of Nuclear Medicine *53*, 4-11.

Veiga-Parga, T., Sehrawat, S., and Rouse, B.T. (2013). Role of regulatory T cells during virus infection. Immunological reviews *255*, 182-196.

Verhoeff, S., Donk, P.P.v.d., Aarntzen, E.H.J.G., Miedema, I.H.C., Oosting, S., Voortman, J., Brouwers, A.H., Slingerland, M., Heskamp, S., and Herpen, C.M.L.-V. (2020). 89Zr-durvalumab PD-L1 PET in recurrent or metastatic (R/M) squamous cell carcinoma of the head and neck. Journal of Clinical Oncology *38*, 3573-3573.

Verhoeff, S.R., van de Donk, P.P., Aarntzen, E., Oosting, S.F., Brouwers, A.H., Miedema, I.H.C., Voortman, J., Menke-van der Houven van Oordt, W.C., Boellaard, R., Vriens, D*., et al.* (2022). (89)Zr-DFO-Durvalumab PET/CT Before Durvalumab Treatment in Patients with Recurrent or Metastatic Head and Neck Cancer. Journal of nuclear medicine : official publication, Society of Nuclear Medicine *63*, 1523-1530.

Visser, E.P., Disselhorst, J.A., Brom, M., Laverman, P., Gotthardt, M., Oyen, W.J., and Boerman, O.C. (2009). Spatial resolution and sensitivity of the Inveon small-animal PET scanner. Journal of nuclear medicine : official publication, Society of Nuclear Medicine *50*, 139-147.

Vivier, D., Fung, K., Rodriguez, C., Adumeau, P., Ulaner, G.A., Lewis, J.S., Sharma, S.K., and Zeglis, B.M. (2020). The Influence of Glycans-Specific Bioconjugation on the FcγRI Binding and In vivo Performance of (89)Zr-DFO-Pertuzumab. Theranostics *10*, 1746-1757.

Vivier, D., Sharma, S.K., and Zeglis, B.M. (2018). Understanding the in vivo fate of radioimmunoconjugates for nuclear imaging. J Labelled Comp Radiopharm *61*, 672-692.

Vogel, W.V., van Dalen, J.A., Wiering, B., Huisman, H., Corstens, F.H., Ruers, T.J., and Oyen, W.J. (2007). Evaluation of image registration in PET/CT of the liver and recommendations for optimized imaging. Journal of nuclear medicine : official publication, Society of Nuclear Medicine *48*, 910-919.

Vogelstein, B., Lane, D., and Levine, A.J. (2000). Surfing the p53 network. Nature *408*, 307-310.

Vosjan, M.J., Perk, L.R., Visser, G.W., Budde, M., Jurek, P., Kiefer, G.E., and van Dongen, G.A. (2010). Conjugation and radiolabeling of monoclonal antibodies with zirconium-89 for PET imaging using the bifunctional chelate p-isothiocyanatobenzyl-desferrioxamine. Nat Protoc *5*, 739-743.

Vugts, D.J., Klaver, C., Sewing, C., Poot, A.J., Adamzek, K., Huegli, S., Mari, C., Visser, G.W.M., Valverde, I.E., Gasser, G.*, et al.* (2017). Comparison of the octadentate bifunctional chelator DFO*-pPhe-NCS and the clinically used hexadentate bifunctional chelator DFO-pPhe-NCS for (89)Zr-immuno-PET. European journal of nuclear medicine and molecular imaging *44*, 286-295.

Vugts, D.J., and van Dongen, G.A. (2011). (89)Zr-labeled compounds for PET imaging guided personalized therapy. Drug discovery today Technologies *8*, e53-61.

Vuky, J., Balar, A.V., Castellano, D., O'Donnell, P.H., Grivas, P., Bellmunt, J., Powles, T., Bajorin, D., Hahn, N.M., Savage, M.J.*, et al.* (2020). Long-Term Outcomes in KEYNOTE-052: Phase II Study Investigating First-Line Pembrolizumab in Cisplatin-Ineligible Patients With Locally Advanced or Metastatic Urothelial Cancer. Journal of clinical oncology : official journal of the American Society of Clinical Oncology *38*, 2658-2666.

Wacholz, C., Hruska, C., and OConnor, M. (2020). Veriton Multi-CZT Detector SPECT/CT System Acceptance Testing. Journal of Nuclear Medicine *61*, 3003-3003.

Wang, W., Wang, E.Q., and Balthasar, J.P. (2008). Monoclonal antibody pharmacokinetics and pharmacodynamics. Clinical pharmacology and therapeutics *84*, 548-558.

Wang, X., Yang, L., Huang, F., Zhang, Q., Liu, S., Ma, L., and You, Z. (2017). Inflammatory cytokines IL-17 and TNF-α up-regulate PD-L1 expression in human prostate and colon cancer cells. Immunology letters *184*, 7-14.

Wang, Z., Wu, V.H., Allevato, M.M., Gilardi, M., He, Y., Luis Callejas-Valera, J., Vitale-Cross, L., Martin, D., Amornphimoltham, P., McDermott, J.*, et al.* (2019). Syngeneic animal models of tobacco-associated oral cancer reveal the activity of in situ anti-CTLA-4. Nat Commun *10*, 5546.

Warburg, O. (1956). On the origin of cancer cells. Science (New York, NY) *123*, 309-314.

Wei, W., Rosenkrans, Z.T., Liu, J., Huang, G., Luo, Q.Y., and Cai, W. (2020). ImmunoPET: Concept, Design, and Applications. Chemical reviews *120*, 3787-3851.

Weinstein, G.S., O'Malley, B.W., Jr., Magnuson, J.S., Carroll, W.R., Olsen, K.D., Daio, L., Moore, E.J., and Holsinger, F.C. (2012). Transoral robotic surgery: a multicenter study to assess feasibility, safety, and surgical margins. The Laryngoscope *122*, 1701-1707.

Welch, B.L. (1947). The generalisation of student's problems when several different population variances are involved. Biometrika *34*, 28-35.

Welti, J., Loges, S., Dimmeler, S., and Carmeliet, P. (2013). Recent molecular discoveries in angiogenesis and antiangiogenic therapies in cancer. J Clin Invest *123*, 3190-3200.

Wherry, E.J., and Kurachi, M. (2015). Molecular and cellular insights into T cell exhaustion. Nature reviews Immunology *15*, 486-499.

Wierstra, P., Sandker, G., Aarntzen, E., Gotthardt, M., Adema, G., Bussink, J., Raavé, R., and Heskamp, S. (2019). Tracers for non-invasive radionuclide imaging of immune checkpoint expression in cancer. EJNMMI radiopharmacy and chemistry *4*, 29.

Windon, M.J., D'Souza, G., Rettig, E.M., Westra, W.H., van Zante, A., Wang, S.J., Ryan, W.R., Mydlarz, W.K., Ha, P.K., Miles, B.A.*, et al.* (2018). Increasing prevalence of human papillomavirus-positive oropharyngeal cancers among older adults. Cancer *124*, 2993-2999.

Woller, N., Gürlevik, E., Fleischmann-Mundt, B., Schumacher, A., Knocke, S., Kloos, A.M., Saborowski, M., Geffers, R., Manns, M.P., Wirth, T.C.*, et al.* (2015).

Viral Infection of Tumors Overcomes Resistance to PD-1-immunotherapy by Broadening Neoantigenome-directed T-cell Responses. Molecular therapy : the journal of the American Society of Gene Therapy *23*, 1630-1640.

Wong, J.S.S.P.B., and Richard, S. (2019). Head and Neck Surgery and Oncology (New York USA: Elsevier).

Wong, W.L., Ross, P., and Corcoran, M. (2013). Evidence-based guideline recommendations on the use of positron emission tomography imaging in head and neck cancer from Ontario and guidelines in general--some observations. Clinical oncology (Royal College of Radiologists (Great Britain)) *25*, 242-245.

Workman, P., Aboagye, E.O., Balkwill, F., Balmain, A., Bruder, G., Chaplin, D.J., Double, J.A., Everitt, J., Farningham, D.A., Glennie, M.J.*, et al.* (2010). Guidelines for the welfare and use of animals in cancer research. British journal of cancer *102*, 1555-1577.

World Health, O. (2015). WHO global report on trends in prevalence of tobacco smoking 2015 (Geneva: World Health Organization).

Wu, A.M. (2014). Engineered antibodies for molecular imaging of cancer. Methods (San Diego, Calif) *65*, 139-147.

Xiong, H.Y., Ma, T.T., Wu, B.T., Lin, Y., and Tu, Z.G. (2014). IL-12 regulates B7-H1 expression in ovarian cancer-associated macrophages by effects on NF-κB signalling. Asian Pacific journal of cancer prevention : APJCP *15*, 5767-5772.

Xu, F., Sternberg, M.R., Kottiri, B.J., McQuillan, G.M., Lee, F.K., Nahmias, A.J., Berman, S.M., and Markowitz, L.E. (2006). Trends in Herpes Simplex Virus Type 1 and Type 2 Seroprevalence in the United States. JAMA *296*, 964-973.

Xu, R.H., Yuan, Z.Y., Guan, Z.Z., Cao, Y., Wang, H.Q., Hu, X.H., Feng, J.F., Zhang, Y., Li, F., Chen, Z.T.*, et al.* (2003). [Phase II clinical study of intratumoral H101, an E1B deleted adenovirus, in combination with chemotherapy in patients with cancer]. Ai zheng = Aizheng = Chinese journal of cancer *22*, 1307-1310.

Yamada, Y., Nakano, S., Gatate, Y., Okano, N., Muramatsu, T., Nishimura, S., Kuji, I., Fukushima, K., and Matsunari, I. (2021). Feasibility of simultaneous (99m)Tc-tetrofosmin and (123)I-BMIPP dual-tracer imaging with cadmium-zinc-telluride detectors in patients undergoing primary coronary intervention for acute myocardial infarction. Journal of nuclear cardiology : official publication of the American Society of Nuclear Cardiology *28*, 187-195.

Yan, N., and Chen, Z.J. (2012). Intrinsic antiviral immunity. Nature immunology *13*, 214-222.

Yang, Y., Xu, W., Peng, D., Wang, H., Zhang, X., Wang, H., Xiao, F., Zhu, Y., Ji, Y., Gulukota, K.*, et al.* (2019). An Oncolytic Adenovirus Targeting Transforming Growth Factor β Inhibits Protumorigenic Signals and Produces Immune Activation: A Novel Approach to Enhance Anti-PD-1 and Anti-CTLA-4 Therapy. Human gene therapy *30*, 1117-1132.

Yasunaga, M., Manabe, S., Tsuji, A., Furuta, M., Ogata, K., Koga, Y., Saga, T., and Matsumura, Y. (2017). Development of Antibody-Drug Conjugates Using DDS and Molecular Imaging. Bioengineering (Basel, Switzerland) *4*.

Yates, F. (1934). The Analysis of Multiple Classifications with Unequal Numbers in the Different Classes. Journal of the American Statistical Association *29*, 51-66.

Yearley, J.H., Gibson, C., Yu, N., Moon, C., Murphy, E., Juco, J., Lunceford, J., Cheng, J., Chow, L.Q.M., Seiwert, T.Y.*, et al.* (2017). PD-L2 Expression in Human Tumors: Relevance to Anti-PD-1 Therapy in Cancer. Clinical cancer research : an official journal of the American Association for Cancer Research *23*, 3158-3167.

Yi, C.H., Jim Zhai, Q., and Wang, B.Y. (2017). Updates on Immunohistochemical and Molecular Markers in Selected Head and Neck Diagnostic Problems. Archives of pathology & laboratory medicine *141*, 1214-1235.

Yoo, J., Henderson, S., and Walker-Dilks, C. (2013). Evidence-based guideline recommendations on the use of positron emission tomography imaging in head and neck cancer. Clinical oncology (Royal College of Radiologists (Great Britain)) *25*, e33-66.

Young, J.S., Lumsden, C.E., and Stalker, A.L. (1950). The significance of the tissue pressure of normal testicular and of neoplastic (Brown-Pearce carcinoma) tissue in the rabbit. The Journal of pathology and bacteriology *62*, 313-333.

Yu, Z., Adusumilli, P.S., Eisenberg, D.P., Darr, E., Ghossein, R.A., Li, S., Liu, S., Singh, B., Shah, J.P., Fong, Y.*, et al.* (2007). Nectin-1 expression by squamous cell carcinoma is a predictor of herpes oncolytic sensitivity. Molecular therapy : the journal of the American Society of Gene Therapy *15*, 103-113.

Yu, Z., Chan, M.K., P, O.c., Eisenberg, D.P., Shah, J.P., Singh, B., Fong, Y., and Wong, R.J. (2005). Enhanced nectin-1 expression and herpes oncolytic sensitivity in highly migratory and invasive carcinoma. Clinical cancer research : an official journal of the American Association for Cancer Research *11*, 4889-4897.

Zainab, H., Sultana, A., and Shaimaa (2019). Stromal desmoplasia as a possible prognostic indicator in different grades of oral squamous cell carcinoma. Journal of oral and maxillofacial pathology : JOMFP *23*, 338-343.

Zamarin, D., Holmgaard, R.B., Subudhi, S.K., Park, J.S., Mansour, M., Palese, P., Merghoub, T., Wolchok, J.D., and Allison, J.P. (2014). Localized oncolytic virotherapy overcomes systemic tumor resistance to immune checkpoint blockade immunotherapy. Science translational medicine *6*, 226ra232.

Zamarin, D., Ricca, J.M., Sadekova, S., Oseledchyk, A., Yu, Y., Blumenschein, W.M., Wong, J., Gigoux, M., Merghoub, T., and Wolchok, J.D. (2018). PD-L1 in tumor microenvironment mediates resistance to oncolytic immunotherapy. J Clin Invest *128*, 1413-1428.

Zeglis, B.M., and Lewis, J.S. (2015). The bioconjugation and radiosynthesis of 89Zr-DFO-labeled antibodies. Journal of visualized experiments : JoVE.

Zetter, B.R. (1998). Angiogenesis and tumor metastasis. Annual review of medicine *49*, 407-424.

Zhai, N., Li, H., Song, H., Yang, Y., Cui, A., Li, T., Niu, J., Crispe, I.N., Su, L., and Tu, Z. (2017). Hepatitis C Virus Induces MDSCs-Like Monocytes through TLR2/PI3K/AKT/STAT3 Signaling. PloS one *12*, e0170516.

Zhang, C., Li, Z., Xu, L., Che, X., Wen, T., Fan, Y., Li, C., Wang, S., Cheng, Y., Wang, X.*, et al.* (2018). CXCL9/10/11, a regulator of PD-L1 expression in gastric cancer. BMC cancer *18*, 462.

Zhang, N., and Bevan, M.J. (2011). CD8(+) T cells: foot soldiers of the immune system. Immunity *35*, 161-168.

Zhang, Y., and Bergelson, J.M. (2005). Adenovirus receptors. Journal of virology *79*, 12125-12131.

Zhang, Y., Hong, H., Engle, J.W., Bean, J., Yang, Y., Leigh, B.R., Barnhart, T.E., and Cai, W. (2011). Positron emission tomography imaging of CD105 expression with a 64Cu-labeled monoclonal antibody: NOTA is superior to DOTA. PloS one *6*, e28005.

Zhao, Q., Xiao, X., Wu, Y., Wei, Y., Zhu, L.Y., Zhou, J., and Kuang, D.M. (2011). Interleukin-17-educated monocytes suppress cytotoxic T-cell function through B7-H1 in hepatocellular carcinoma patients. European journal of immunology *41*, 2314-2322.

Zheng, S., Shen, T., Liu, Q., Liu, T., Tuerxun, A., Zhang, Q., Yang, L., Han, X., and Lu, X. (2021). CXCL6 fuels the growth and metastases of esophageal squamous cell carcinoma cells both in vitro and in vivo through upregulation of PD-L1 via activation of STAT3 pathway. Journal of cellular physiology *236*, 5373-5386.

Zhou, Z., Meshaw, R., Zalutsky, M.R., and Vaidyanathan, G. (2021). Site-Specific and Residualizing Linker for (18)F Labeling with Enhanced Renal Clearance: Application to an Anti-HER2 Single-Domain Antibody Fragment. Journal of nuclear medicine : official publication, Society of Nuclear Medicine *62*, 1624-1630.

Ziai, P., Hayeri, M.R., Salei, A., Salavati, A., Houshmand, S., Alavi, A., and Teytelboym, O.M. (2016). Role of Optimal Quantification of FDG PET Imaging in the Clinical Practice of Radiology. Radiographics : a review publication of the Radiological Society of North America, Inc *36*, 481-496.

Zitvogel, L., Pitt, J.M., Daillère, R., Smyth, M.J., and Kroemer, G. (2016). Mouse models in oncoimmunology. Nature reviews Cancer *16*, 759-773.

Zolkind, P., Przybylski, D., Marjanovic, N., Nguyen, L., Lin, T., Johanns, T., Alexandrov, A., Zhou, L., Allen, C.T., Miceli, A.P., *et al.* (2018). Cancer immunogenomic approach to neoantigen discovery in a checkpoint blockade responsive murine model of oral cavity squamous cell carcinoma. Oncotarget *9*, 4109-4119.